Transactions of the ASME

HEAT TRANSFER DIVISION
Chairman, R. J. SIMONEAU
Secretary, F. A. KULACKI
Senior Technical Editor, G. M. FAETH
Technical Editor, I. CATTON
Technical Editor, R. GREIF
Technical Editor, P. J. MARTO
Technical Editor, R. H. PLETCHER
Technical Editor, R. K. SHAH
Technical Editor, R. VISKANTA
Technical Editor, M. M. YOVANOVICH

BOARD ON COMMUNICATIONS
Chairman and Vice President
K. N. REID, JR.

Members-at-Large
W. BEGELL
J. T. COKONIS
W. G. GOTTENBERG
F. LANDIS
J. R. LLOYD
R. E. NICKELL
J. E. ORTLOFF
C. F. PHILLIPS
R. E. REDER
F. W. SCHMIDT

President, L. S. FLETCHER
Executive Director,
PAUL ALLMENDINGER
Treasurer,
ROBERT A. BENNETT

PUBLISHING STAFF
Mng. Dir., Publ., J. J. FREY
Dep. Mng. Dir., Pub.,
JOS. SANSONE
Managing Editor,
CORNELIA MONAHAN
Production Editor,
VALERIE WINTERS
Editorial Prod. Asst.,
MARISOL ANDINO

The Journal of Heat Transfer (ISSN 0022-1481) is published quarterly for $100 per year by The American Society of Mechanical Engineers, 345 East 47th Street, New York, N Y 10017. Second class postage paid at New York, NY and additional mailing offices. POSTMASTER: Send address changes to The Journal of Heat Transfer, c/o THE AMERICAN SOCIETY OF MECHANICAL ENGINEERS, 22 Law Drive, Box 2300, Fairfield, NJ 07007-2300.
CHANGES OF ADDRESS must be received at Society headquarters seven weeks before they are to be effective. Please send old label and new address.
PRICES: To members, $24.00, annually; to nonmembers, $100.00. Add $6.00 for postage to countries outside the United States and Canada.
STATEMENT from By-Laws. The Society shall not be responsible for statements or opinions advanced in papers or . . . printed in its publications (B7.1, para. 3).

INDEXED by the Engineering Index, Inc.

Journal of Heat Transfer

Published Quarterly by The American Society of Mechanical Engineers

VOLUME 107 • NUMBER 4 • NOVEMBER 1985

ANNOUNCEMENTS

TECHNICAL PAPERS

TECHNICAL NOTES

DISCUSSION

A. D. Kraus
U.S. Naval Postgraduate School,
Monterey, CA
Fellow ASME

A. D. Snider
College of Engineering,
University of South Florida,
Tampa, FL
Mem. ASME

Choking and Optimization of Extended Surface Arrays

When individual extended surface components such as fins or spines are assembled into an array, the performance of the array may become limited by the performance of the fin closest to the base of the array. This paper draws upon previous work of the authors and provides guidance for the selection of the width or diameter of the innermost fin or spine.

Introduction

The exact analysis of the heat transfer over an extended surface is a very complicated problem involving such considerations as three-dimensional heat flow in the fins and the coolant, convection between the fins and coolant, boundary layer inhibition at the fin-coolant interface, and the flow pattern of the coolant. Thus, to compare the performance of any two proposed fin configurations in a realistic setting may be an enormous, perhaps impossible, undertaking. The traditional approach of design engineers has been to invoke a set of idealizing assumptions usually attributed to Murray [1] and Gardner [2]. This simplification results in a model whose mathematical description is tractable (cf. [3-6] and the classic papers of Schmidt [7], Duffin [8], and Harper and Brown [9]). The model presumably approximates reality sufficiently well to justify design decisions; i.e., if one array performs twice as well as another under the idealized conditions, it is hoped that it will perform roughly twice as well in practice.

The authors have applied initial value data to characterize all regular fins (those with a finite tip thickness) by a thermal transmission matrix [Γ] which relates fin base conditions of temperature excess and heat flow to similar conditions at the fin tip [10, 11, 12]

$$\begin{bmatrix} \theta_a \\ q_a \end{bmatrix} = \begin{bmatrix} \gamma_{11} & \gamma_{12} \\ \gamma_{21} & \gamma_{22} \end{bmatrix} \begin{bmatrix} \theta_b \\ q_b \end{bmatrix} = [\Gamma] \begin{bmatrix} \theta_b \\ q_b \end{bmatrix} \tag{1}$$

Here, the matrix [Γ] may be thought of as a linear transformation which maps base conditions into tip conditions and it may be observed that base conditions do indeed induce tip conditions.

The matrix [Γ] has an inverse, which in what follows will be designated as [T]

$$[T] = \begin{bmatrix} \tau_{11} & \tau_{12} \\ \tau_{21} & \tau_{22} \end{bmatrix} = [\Gamma]^{-1} = \frac{1}{\det[\Gamma]} \begin{bmatrix} \gamma_{22} & -\gamma_{12} \\ -\gamma_{21} & \gamma_{11} \end{bmatrix} \tag{2}$$

and because all regular fins and spines (with the height coordinate having its origin at a point either at the fin tip or remote from the fin tip and proceeding in a positive direction toward the fin base) exhibit a property known as reciprocity [14], $\det[\Gamma] = \det[T] = 1$.

$$\begin{bmatrix} \tau_{11} & \tau_{12} \\ \tau_{21} & \tau_{22} \end{bmatrix} = \begin{bmatrix} \gamma_{22} & -\gamma_{12} \\ -\gamma_{21} & \gamma_{11} \end{bmatrix}$$

Thus, the representation using [T] becomes

$$\begin{bmatrix} \theta_b \\ q_b \end{bmatrix} = [T] \begin{bmatrix} \theta_a \\ q_a \end{bmatrix} \tag{4}$$

Both [Γ] and [T] uniquely characterize any particular fin and [Γ] has been developed for several of the common fin shapes [10, 11, 12].

It is easily shown [10] that the ratio $\mu = q_b/\theta_b$ which is termed the input admittance or thermal transmission ratio of an individual fin is related to the tip q_a/θ_a ratio by the bilinear transformation (or reflection relationship)

$$\frac{q_b}{\theta_b} = \frac{\gamma_{21} - \gamma_{11}(q_a/\theta_a)}{-\gamma_{22} + \gamma_{12}(q_a/\theta_a)} = \frac{\tau_{21} + \tau_{22}(q_a/\theta_a)}{\tau_{11} + \tau_{12}(q_a/\theta_a)} \tag{5}$$

Of course, the ratio q_b/θ_b will exist in general at the base of any fin in an array and in particular at the base of an array. In this case, q_b/θ_b is called the input admittance at point k

$$Y_{IN,k} = \left.\frac{q_b}{\theta_b}\right|_k \tag{6}$$

where some appropriate numbering scheme can be used to indicate the various values of k.

If several fins are brought together at a point in an array as in Fig. 1, the point is called a cluster point and the input admittance of the cluster is the sum of the individual thermal transmission ratios of the n-fins comprising the cluster

$$Y_{IN,C} = \left.\frac{q_b}{\theta_b}\right|_C = \sum_{k=1}^{n} \mu_k \tag{7}$$

Observe that the input admittance for the entire array which consists of four fins, three of which are in cluster as shown in Fig. 1, can be quickly obtained presuming that the μ's for fins -1, 2, and 3 and [T] for fin -4 are known

$$Y_{IN,4} = \left.\frac{q_b}{\theta_b}\right|_4 = \frac{\tau_{21} + \tau_{22}(Y_{IN,C})}{\tau_{11} + \tau_{12}(Y_{IN,C})}$$

where

$$Y_{IN,C} = \mu_1 + \mu_2 + \mu_3 = \left.\frac{q_b}{\theta_b}\right|_1 + \left.\frac{q_b}{\theta_b}\right|_2 + \left.\frac{q_b}{\theta_b}\right|_3$$

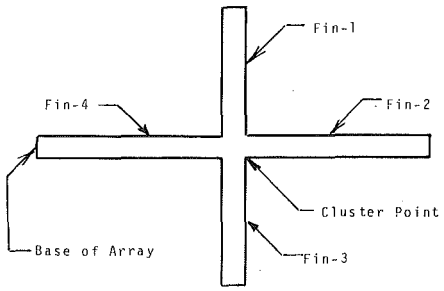

Fig. 1 An array of four fins: Fins -1, 2, and 3 are said to be in cluster

Contributed by the Heat Transfer Division for publication in the JOURNAL OF HEAT TRANSFER. Manuscript received by the Heat Transfer Division January 6, 1984. Paper No. 84-HT-53.

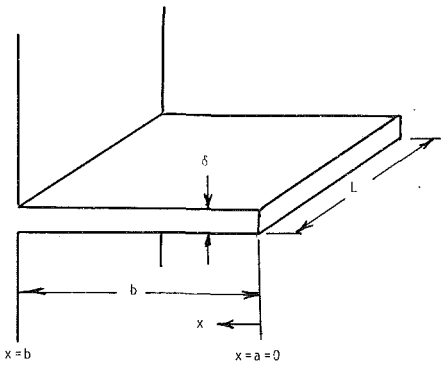

Fig. 2 Longitudinal fin of rectangular profile

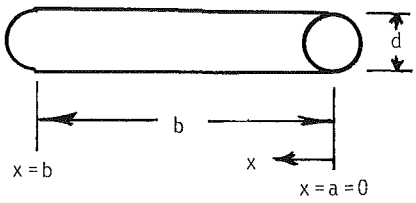

Fig. 3 Cylindrical spine

Parameterizations

Parameterizations for several common fin shapes have been provided [10, 11, 12] and those necessary for the development that follows are provided in this section.

For the longitudinal fin of rectangular profile shown in Fig. 2 and the cylindrical spine displayed in Fig. 3, both with origin of the height coordinate at the tip ($a = 0$),

$$[T] = \begin{bmatrix} \cosh mb & \frac{1}{Y_0}\sinh mb \\ Y_0 \sinh mb & \cosh mb \end{bmatrix}$$

where for the longitudinal fin of rectangular profile

$$m = \left[\frac{2h}{k\delta}\right]^{1/2} \tag{9a}$$

and

$$Y_0 = (2hk\delta)^{1/2} L \tag{9b}$$

and for the cylindrical spine

$$m = \left[\frac{4h}{kd}\right]^{1/2} \tag{10a}$$

and

$$Y_0 = \frac{\pi}{4} kd^2 m = \frac{\pi}{2} (d^3 hk)^{1/2} \tag{10b}$$

For either an individual rectangular longitudinal fin or a cylindrical spine with insulated tip ($q_a = 0$), equation (5) may be employed to show that

$$\mu = \frac{\tau_{21}}{\tau_{11}}$$

and then use of equation (8) yields

$$\mu = Y_0 \tanh mb \tag{11}$$

The important quantity Y_0 is a function of the width of the fin or the diameter of the spine and the pertinent thermal properties k and h. It is called the characteristic admittance of the fin or spine.

The Choking Problem and an Optimization

The fin or spine closest to the base of an array may exhibit a heat flow choke because the fin or spine dimensions may not permit, in a cooling application, the transfer of a sufficient amount of heat to the remote fins in the array. For example, in Fig. 1, the choking situation is dramatically evident when $Y_{IN,4}$ is less than $Y_{IN,C}$ or when the value of Y_{IN} for the entire array is less than the value of Y_{IN} for the cluster composed of fins -1, 2, and 3.

In both cases, the tip heat flow to temperature excess ratio can be designated as Y_a and use of equation (5) with the elements of $[T]$ given by equation (8) provides

$$Y_{IN} = \frac{Y_0 \sinh mb + Y_a \cosh mb}{\cosh mb + (Y_a/Y_0)\sinh mb} \tag{12}$$

If numerator and denominator are both divided by cosh mb, the result is

$$Y_{IN} = \frac{Y_0 \tanh mb + Y_a}{1 + (Y_a/Y_0)\tanh mb} \tag{13}$$

Observe that

$$\lim_{b \to 0} Y_{IN} = Y_a$$

and

$$\lim_{b \to \infty} Y_{IN} = Y_0$$

and these provide the extremes for Y_{IN} for the extreme values of the fin height b.

In order to find the fin height b that makes Y_{IN} a maximum, the customary method of finding where $\partial Y_{IN}/\partial b$ vanishes is employed. In equation (12), once again observe that neither Y_0 nor Y_a is a function of b, and let the numerator be designated as u and the denominator as v. Then

Nomenclature

a = coordinate of fin or spine tip, m
b = coordinate of fin or spine base, m and fin or spine height, m
d = spine diameter, m
h = heat transfer coefficient, W/m^2-°C
k = thermal conductivity, W/m-°C
L = fin length, m
m = fin performance factor, m^{-1}
q = heat flow, W
u = a combination of terms, W/°C
v = a combination of terms, dimensionless
x = length coordinate, m
Y = with subscript, admittance, W/°C or admittance ratio, dimensionless
$[\Gamma]$ = thermal transmission matrix
γ = elements of thermal transmission matrix, dimensions vary
δ = fin width, m; also indicates small change in a variable
θ = temperature excess, °C
μ = thermal transmission ratio, W/°C
$[T]$ = inverse thermal transmission matrix (inverse of $[\Gamma]$)
τ = elements of the matrix $[T]$, dimensions vary

Subscripts

a = designates tip condition
b = designates base condition
o = designates characteristic value
IN = designates input condition

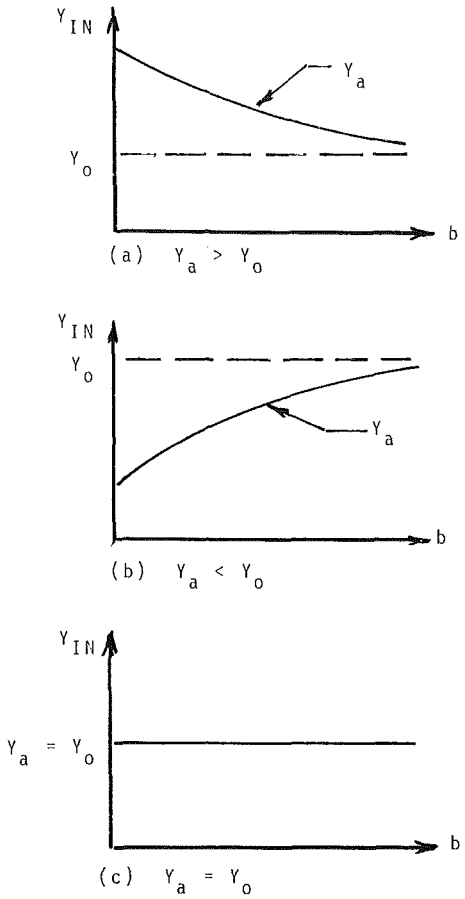

Fig. 4 Three possibilities

$$\frac{\partial Y_{IN}}{\partial b} = \frac{vm[Y_0 \cosh mb + Y_a \sinh mb]}{v^2}$$

$$- \frac{um[\sinh mb + Y \cosh mb]}{v^2} = 0$$

where $Y = Y_a/Y_0$. The m's in the numerator may be cancelled and the denominator v^2 is immaterial. Thus

$$v[Y_0 \cosh mb + Y_a \sinh mb] = u[\sinh mb + Y \cosh mb]$$

and the use of v and u provides a simple yet tedious algebraic exercise

$$[\cosh mb + Y \sinh mb][Y_0 \cosh mb + Y_a \sinh mb]$$
$$= [Y_0 \sinh mb + Y_a \cosh mb][\sinh mb + Y \cosh mb]$$

with the result

$$Y_0 = Y \; Y_a = \frac{Y_a}{Y_0} Y_a$$

or

$$Y_a = Y_0 \tag{14}$$

Because equation (14) does not involve b, it implies that the slope of $Y_{IN} = f(b)$ is never zero unless $Y_0 = Y_a$ in which case it is always zero. Thus, there is no question of optimizing with respect to the fin height and the situation must be as displayed in Fig. 4.

Therefore, if the characteristic admittance $Y_0 < Y_a$ for the innermost fin or spine (the fin or spine closest to the base of the array), the fin or spine will choke the heat flow regardless of its height b, and b should be made as low as possible. If $Y_0 > Y_a$, then no choking occurs and b should be made as high as possible. Finally, if $Y_0 = Y_a$, b has no effect whatsoever.

This conclusion may appear somewhat surprising but it is certainly useful as a design guideline. For the longitudinal fin of rectangular profile, $Y_0 = L(2hk\delta)^{1/2}$ so that to achieve the optimum

$$\delta \geq \frac{Y_a^2}{2hkL^2}$$

and for the cylindrical spine with $Y_0 = \frac{\pi}{2} d^{3/2}(hk)^{1/2}$

$$d > \left[\frac{4Y_a^2}{\pi^2 hk} \right]^{1/3} \tag{16}$$

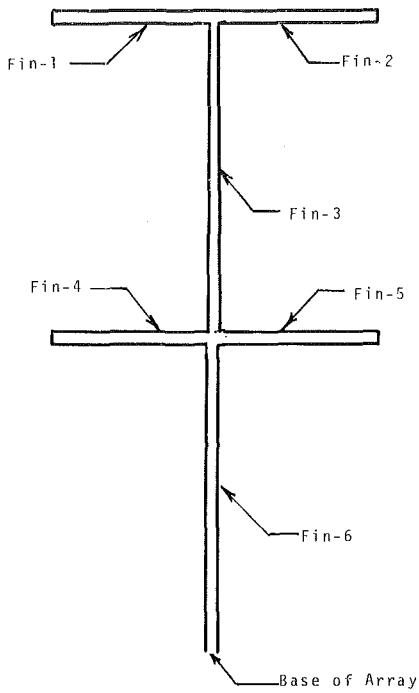

Fig. 5 An array of six fins

Table 1 Data for example with array described by Fig. 5; $h = 80$ W/m^2-K; $k = 160$ W/m-K

Fin	b, cm	δ, cm
1	0.254	0.0254
2	0.254	0.0254
3	1.27	0.0152
4	0.254	0.0254
5	0.254	0.0254
6	1.27	0.0152

Example

Consider the finned array consisting of six fins as shown in Fig. 5. Suppose that fins -1 and 2 are dissipating from one face only and that physical dimensions are as listed in Table 1. It is desired to obtain the input admittance at the base of fin -6 and to determine if a heat flow choke occurs anywhere in this array if $k = 160$ W/m-K and $h = 80$ W/m^2-K.

For fins -1 and 2, application of equation (9b) modified for single side heat dissipation [10, 12] with $L = 1$ m yields

$$Y_{01} = Y_{02} = (hk\delta)^{1/2} L = [(80)(160)(0.000254)]^{1/2}(1)$$

or

$$Y_{01} = Y_{02} = 1.8031 \text{ W/°C}$$

Then use of equation (9a), again for single side dissipation, provides

$$m_1 = m_2 = \left[\frac{h}{k\delta} \right]^{1/2} = \left[\frac{80}{(160)(0.000254)} \right]^{1/2} = 44.368 \text{ m}^{-1}$$

so that

$$mb_1 = mb_2 = 44.368(0.00254) = 0.1127$$

Thus by equation (11) this makes

$$\mu_1 = \mu_2 = Y_{IN1} = Y_{IN2} = Y_{01} \tanh\, mb_1$$

or

$$Y_{IN1} = Y_{IN2} = 1.8031(0.1122) = 0.2023 \text{ W/°C}$$

Fins −4 and 5 have the same dimensions as fins −1 and 2 but dissipate from both sides. Here then, equations (9*b*) and (9*a*) may be used directly (with L = 1 m)

$$Y_{04} = Y_{05} = (2hk\delta)^{1/2} = \sqrt{2}\ Y_{01} = \sqrt{2}\ (1.8031) = 2.5500 \text{ W/°C}$$

and

$$mb_4 = mb_5 = \left[\frac{2h}{k\delta}\right]^{1/2} b_4 = \sqrt{2}\ mb_1 = \sqrt{2}\ (0.1127) = 0.1594$$

so that

$$Y_{IN4} = Y_{IN5} = Y_{04} \tanh\, mb_4 = (2.5500)(0.1580) = 0.4030 \text{ W/°C}$$

For fins −3 and 6, using equations (9*b*) and (9*a*), again with L = 1 m yields

$$Y_{03} = Y_{06} = (2hk\delta)^{1/2} L = [2(80)\ (160)\ (0.000152)]^{1/2} \quad (1)$$
$$= 1.9726 \text{ W/°C}$$

$$m_3 = m_6 = \left[\frac{2h}{k\delta}\right]^{1/2} = \left[\frac{2\ (80)}{160\ (0.000152)}\right]^{1/2} = 81.111 \text{ m}^{-1}$$

and

$$mb_3 = mb_6 = 81.111\ (0.0127) = 1.0301$$

The matrix $[T]$ is determined from equation (8)

$$[T] = \begin{bmatrix} 1.5792 & 0.6196 \\ 2.4109 & 1.5792 \end{bmatrix}$$

At the tip of fin −3

$$Y_{a3} = Y_{IN1} + Y_{IN2} = 2(0.2023) = 0.4046 \text{ W/°C}$$

and by equation (12) at the base of fin −3

$$Y_{IN3} = \frac{\tau_{21} + \tau_{22}(Y_{a3})}{\tau_{11} + \tau_{12}(Y_{a3})} = \frac{3.0500}{1.8299} = 1.6667 \text{ W/°C}$$

Observe that fin −3 does *not* choke the heat flow because $Y_{IN3} > Y_{a3}$ (1.6667 > 0.4046 W/°C).

At the tip of fin −6

$$Y_{a6} = Y_{IN3} + Y_{IN4} + Y_{IN5} = 1.6667 + 2(0.4030) = 2.4727 \text{ W/°C}$$

and again by equation (12) the sought-after Y_{IN6} is

$$Y_{IN6} = \frac{\tau_{21} + \tau_{22}(Y_{a6})}{\tau_{11} + \tau_{12}(Y_{a6})} = \frac{6.3158}{3.1112} = 2.0300 \text{ W/°C}$$

which indicates that fin −6 chokes the heat flow, $Y_{IN6} < Y_{a6}$ (2.0300 < 2.4727 W/°C). This result was to be expected because $Y_{06} < Y_{a6}$ (1.9726 < 2.4727 W/°C).

The choke can be avoided by adjusting the width of fin −6 in accordance with equation (15)

$$\delta > \frac{Y_a^2}{2hkL^2} = \frac{(2.4727)^2}{2(80)(160)(1)^2}$$

or

$$\delta > 0.0002388 \text{ m } (0.02388 \text{ cm})$$

Observe that an attempt to change the height of fin −6 will result in an improved or further degraded value of Y_{IN6}, but not an escape from the heat flow choke. For example, if the height of fin −6 is changed to 1.00 cm, Y_{06} remains the same (for L = 1 m and δ = 0.000152 m, the original dimension)

$$Y_{06} = 1.9726 \text{ W/°C}$$

m_6 remains the same

$$m_6 = 81.111 \text{ m}^{-1}$$

but mb_6 changes

$$mb_6 = 81.111(0.01) = 0.8111$$

The change in mb makes $[T]$ by equation (8)

$$[T] = \begin{vmatrix} 1.3474 & 0.4578 \\ 1.7813 & 1.3474 \end{vmatrix}$$

and then Y_{IN6}, calculated from equation (12), becomes

$$Y_{IN6} = \frac{\tau_{21} + \tau_{22}(Y_{a6})}{\tau_{11} + \tau_{12}(Y_{a6})} = \frac{5.1130}{2.4793} = 2.0622 \text{ W/°C}$$

Observe that the choke still exists but that the array input admittance has improved.

Clearly, if the heat flow choke in fin −6 is to be removed, the fin width must be adjusted in accordance with equation (15). The input admittance of fin −6 can be seen to be *equal* to the tip admittance of fin −6 in the limiting case of a zero height of fin −6. This, of course, carries the physical implication that if the width of fin −6 is less than that dictated by equation (15), fin −6 should be eliminated entirely putting the base of the array at the intersection of fins −3, 4, and 5.

Acknowledgments

Some of the material contained in this paper was developed under National Science Foundation Grant ENG-7701297.

References

1 Murray, W. M., "Heat Dissipation Through an Annular Disk or Fin of Uniform Thickness," *Journal of Applied Mechanics*, 5:A78, 1938.

2 Gardner, K. A., "Efficiency of Extended Surfaces," *Trans. ASME*, Vol. 67, 1945, p. 621.

3 Jakob, M., *Heat Transfer*, Vols. I and II, assisted by S. P. Kezios, Wiley, New York, 1949, 1957.

4 Kreith, F., *Principles of Heat Transfer*, 3rd ed., Intext Educational Publishers, New York, 1973.

5 Chapman, A. J., *Heat Transfer*, 3rd ed., Macmillan, New York, 1974.

6 Holman, J. P., *Heat Transfer*, 4th ed., McGraw-Hill, New York, 1976.

7 Schmidt, E., "Die Wärmeübertragung durch Rippen," *Zeitschrift des Vereines Deutscher Ingenieure*, Vol. 70, 1926, pp. 885–889, 947–951.

8 Duffin, R. J., "A Variational Problem Relating to Cooling Fins," *Journal Math. Mech.*, Vol. 8, No. 1, 1959, pp. 47–56.

9 Harper, D. R., and Brown, W. B., "Mathematical Equations for Heat Conduction in the Fins of Air Cooled Engines," NACA Report No. 158, 1922.

10 Kraus, A. D., Snider, A. D., and Doty, L. F., "An Efficient Algorithm for Evaluating Arrays of Extended Surface," ASME JOURNAL OF HEAT TRANSFER, Vol. 100, May 1978, p. 288.

11 Kraus, A. D., and Snider, A. D., "New Parameterizations for Heat Transfer in Fins and Spines," ASME JOURNAL OF HEAT TRANSFER, Vol. 102, Aug. 1980, p. 415.

12 Kraus, A. D., *Analysis and Evaluation of Extended Surface Thermal Systems*, Hemisphere, New York, 1982.

13 Snider, A. D., and Kraus, A. D., "A General Extended Surface Analysis Method," ASME JOURNAL OF HEAT TRANSFER, Vol. 103, Nov. 1981, p. 699.

14 Kraus, A. D., Snider, A. D., and Landis, F., "The Reciprocity of Extended Surface and the Node Analysis of Finned Arrays," *Proceedings of the Seventh International Heat Transfer Conference*, Munich, Federal Republic of Germany, 1982, Vol. 6, p. 223.

Photographic Observations of Bubble Formation in Flashing Nozzle Flow

R. S. Miller
Mechanical Engineer.
Thermal Processes Program,
General Electric Co.,
Schenectady, NY 12301

Visual observations have been made of bubble growth in the nucleation region of flashing flow of initially subcooled water in a converging-diverging nozzle. Experiments performed under various flow rates, saturation temperatures, turbulence levels, noncondensable gas content, and artificial nucleation sites failed to produce isolated spherical bubbles of the size or density predicted by common bubble nucleation and growth models. Heterogeneous nucleation in the bulk flow was never observed and it is concluded from bubble growth rates that the role of convection in the heat and mass transfer environment of the bubbles is an important consideration in the physics of flashing flows near the nucleation region.

Introduction

Analytical prediction of mass flows in flashing of subcooled flows through orifices, short pipes, and nozzles has proven reasonably effective by incorporating nucleation criteria and bubble growth models into the equations for frictionless, homogeneous flow. Conduction-controlled bubble growth, using, or building on the results of Plesset and Zwick [1] is the most common approach for predicting vapor generation rates. Various approaches have been used for the nucleation superheat criteria including nucleation delay times, static depressurization correlations, and kinetic models. The nucleation site or bubble density is frequently left as the adjustable parameter in the models. Models based on these assumptions appear to predict flow in the bubbly regime quite well based on measured void fractions, pressure distributions and mass flow rates, but little direct evidence exists to validate the bubble growth, nucleation site density, nucleation frequency, or bubble and nucleation site distribution assumptions.

Described below are some results from an effort to directly measure bubble growth rates during flashing flow of an initially subcooled water in a rectangular cross-section, converging-diverging nozzle. Early in the tests it was found that there was neither a very large bubble density nor small bubbles. In addition, the bubbles that occurred were highly distorted, nucleated at the wall and not amenable to (the originally planned) laser visibility sizing. Instead, micrographs were taken of the bubble formation in the test section under various flow and temperature conditions.

Background

The critical bubble size, nucleation superheat, nucleation site density and nucleation frequency govern the appearance of the flow in the nucleation region and, as such, provide the framework in which to view the photographs.

The creation of a stable vapor bubble requires that surface tension be compensated for by superheat in the surrounding liquid, hence the existence of a critical bubble radius for a given fluid and liquid superheat condition. While the critical radius is easily computed, the degree of superheat is not so easily determined and requires additional assumptions. Edwards [3] used an empirical nucleation delay time which implied superheats in the range of several degrees (C) for the conditions against which the model was compared [8]. Ardron [9] used the nucleation site density and the local liquid superheat as adjustable constants; a kinetic expression was then used to estimate the number of bubbles. When matched to the data of Zaloudek [8], Sozzi et al. [10], and Fauske [11], a value for the superheat at nucleation inception of 3.0°C was found. Simpson and Silver [2] also used a kinetic model for nucleation, but superheat was not specifically separated from other nucleus activation energies; a value of 5.6°C was used for comparison to data. Wu et al. [6] used a static depressurization correlation (Alamgir and Lienhard [7]) for nucleation inception which included a dependence on temperature and depressurization rate. This model was used successfully to predict the converging-diverging nozzle water flow data (voidage, mass flux, and pressure) of Abuaf et al. [12] up to a voidage of 0.3. The depressurization rate in the current tests in no case exceeds 4×10^8 Pa/s and occurs upstream of the throat. As a result, depressurization effects would appear to be negligible and the nucleation superheat would be estimated by this model to be less than 10°C for the current tests. Turbulence has been suggested as a potential effect in influencing nucleation by Simpson and Silver, and Wu et al., but is expected to be small in a converging nozzle as in the current experiment. The exact value of superheat at nucleation inception remains poorly characterized, but based on these studies, liquid superheats are expected to be less than 10°C.

Another key parameter in all models is the bubble density in the nucleation inception region, but this quantity appears in various forms. Edwards correlated a volume average bubble density as a function of the superheat at time of inception, the latter being a result of the assumed nucleation delay time, geometry and flow conditions. Simpson and Silver and Ardron [9] vary the nucleation site density and allow the nucleation frequency to be determined by kinetic considerations. Typically the kinetic considerations include a correction for heterogeneous nuclei such as an activation energy multiplier including a wetting angle [2]. Rohatgi et al. [4], following this method, specify the nucleation site density and adopt the same value of the activation energy multiplier used by Simpson et al. Wu et al. varied the volume average bubble density to match nozzle flow data. An effort has been made to summarize in Table 1 the values for nucleation sites, and/or volume-averaged bubble density derived from these various models. Especially striking is the prediction of very high bubble densities by most models, while low bubble densities appear in the meager experimental data.

All modeling efforts assume that the bubbles become uniformly distributed in the flow regardless of the site for

Contributed by the Heat Transfer Division for publication in the JOURNAL OF HEAT TRANSFER. Manuscript received by the Heat Transfer Division March 26, 1984.

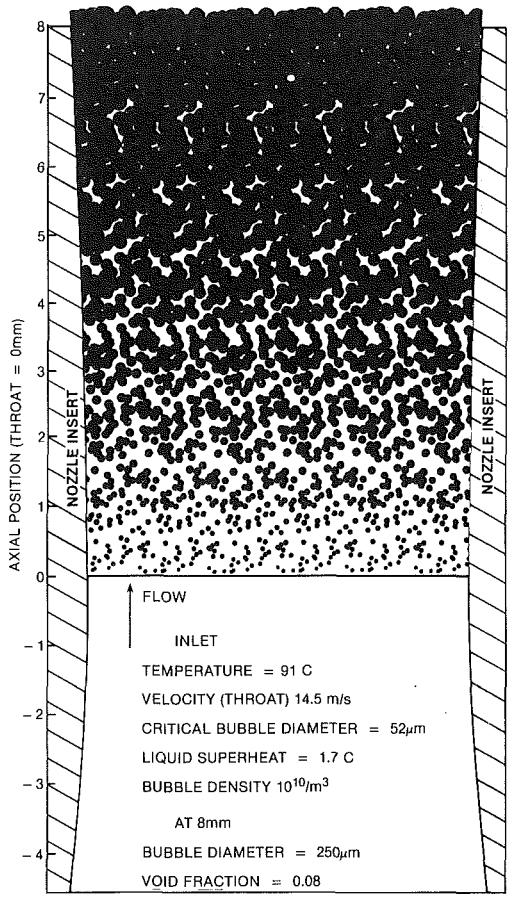

Fig. 1 Representative predicted appearance of bubble growth in the throat region of the test section

nucleation, but no consensus exists on the location or distribution of the heterogeneous nucleation sites. Simpson et al., Rohatgi et al., Malnes [5], and Ardron [9] all assume that the heterogeneous nucleation sites occur in the bulk fluid. Malnes, for example, assumes that dissolved gases form the nucleation sites. Wu et al. assume that the important sites are at the perimeter of the channel. Failure of the bubbles to become uniformly distributed would invalidate conduction-controlled models at far lower voidages than currently assumed, yet very few direct measurements of the nucleation site density or bubble density are available. Ardron and Ackerman [14] measured bubble densities in flashing pipe flow and found them to be smaller than predicted (Table 1), but also noted that the distribution of bubbles in the pipe suggested uniform volumetric bubble nucleation. Photographs of flashing flow in a circular cross section glass converging-diverging nozzle by Klein [15, 16] suggest that nucleation sites are relatively few in number and occur at the wall. No analytical or experimental consensus appears to exist on this aspect of bubble nucleation.

To quickly illustrate for the reader the meaning of these bubble densities in the context of the current experiments, a drawing has been prepared illustrating the expected appearance of the flow (at inlet conditions and a magnification typical of the micrographs) in the throat area of the nozzle for an average bubble density of 10^{10} per m^3. In Fig. 1, the critical radius bubbles are assumed to appear randomly across the nozzle at the throat plane and grow in a 1.7°C uniformly superheated liquid at 91°C inlet temperature (flow from bottom to top). No assumptions are necessary about nucleation site densities since nucleation frequencies are not specified.

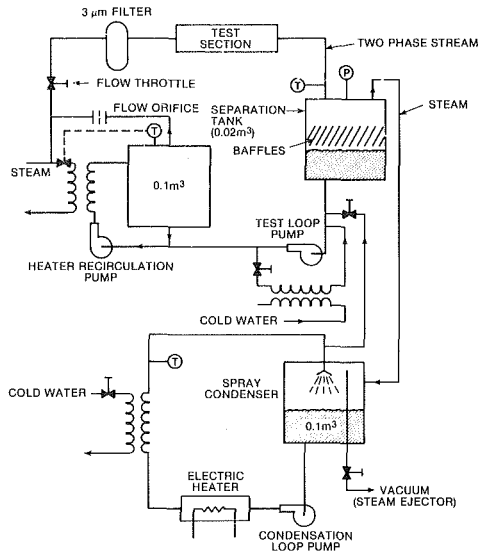

Fig. 2 Schematic of test loop water-conditioning system

Table 1 Calculated and measured bubble and nucleation site densities

Investigator/ data source	Density (sites per m^3) Bubbles	Nucleation
Simpson and Silver [2]/ Silver and Mitchell	–	1.8×10^{5}
Edwards [3]/ Zaloudek [8]	1.2×10^{11}	–
Rohatgi and Reshotko [4]/Simoneau [13]	–	$1\text{–}2\times10^{6}$
Ardron [9]/Zaloudek [8],	–	7×10^{5}
Sozzi and Sutherland [10],	–	7×10^{5}
Fauske [11]	8×10^{12}	7×10^{5}
Wu, Abuaf, Saha [6]/ Abuaf, Zimmer, Wu [12]	10^{9}–10^{12}	–
Ardron and Ackerman [14] (measured)	10^{5}–10^{7}	
(predicted)	10^{9}–10^{10}	1(*a*)
Klein [15, 16]	10^{7}–10^{9}	10^{7}–10^{8}(*b*)

Notes: (*a*) Although only one site was available it generated bubbles at a rate of 7×10^{11} bubbles per m^3 per s. (*b*) Nucleation densities are misleading on a volume basis since the sites were wall sites; there are 80 to 800 sites/m of perimeter for the photographs in [15, 16]. The higher bubble densities are estimates since the nucleation sites appear to create nearly continuous vapor streams rather than bubbles.

Experimental Test Facility

The test loop was designed to supply clean, deaerated water at temperatures up to 120°C with inlet subcooling between a couple of degrees and 100°C at flows up to 10^{-3} m^3/s (10 gpm). Pressures downstream of the test section could be held well below one bar. These conditions were realized in a closed water supply and steam condensation system. The hot water supply to the test section consisted of a recirculating pump, water heater (steam), flow orifice, throttle, particulate filter, test section, and a steam–water separation tank supplying the recirculation pump. The steam was removed to a separate condensing loop. The closed condensing loop consisted of a spray condenser for the steam from the test section loop, a recirculating pump, and a water-cooled heat exchanger feeding back to the spray condenser. Water was tapped off the condensing loop and fed back to the test loop as condensate makeup. The entire system was connected to a vacuum system at the spray condenser to remove noncondensables. The basic test loop is shown in Fig. 2 and includes additional trim heaters and heat exchangers needed for ease of operation.

The entire test facility was constructed of brass, copper, stainless steel, and glass components. A particulate filter with 98 percent efficiency at 3 μm was used during the cleaning

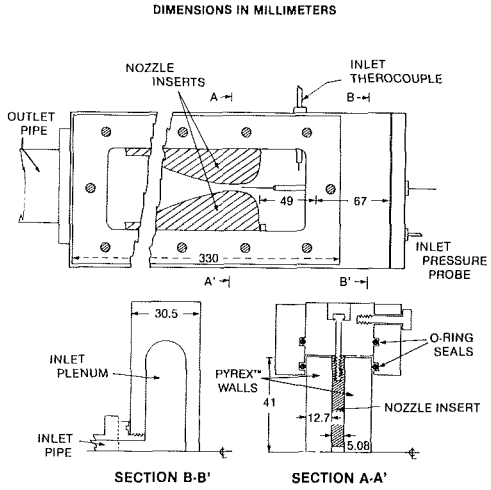

Fig. 3 Test section

process and replaced and used continuously during the tests. The filter was placed immediately upstream of the test section. Operation was initiated by charging the system with deionized water and drawing the maximum attainable vacuum on the system, typically 0.03 bar (28 mm Hg vacuum). Both recirculating loops were then started and the test loop steam heater activated; vigorous outgassing occurred in the test loop until the water temperature allowed flashing in the test section. At this point, steam generated in the flashing process was drawn into the condensation loop at the spray condenser. The vacuum was drawn from the top of the spray condenser, maximizing the fraction of noncondensable gas removal. This process was continued until the condensation loop reached about 90°C, well above the saturation temperature attempting to be held by the vacuum system. The condensation recirculating flow was then cooled by the water-to-water heat exchanger to establish the desired steam saturation conditions. The vacuum was throttled, but left in operation for all the testing since the relatively low steam densities in the tests did not result in a significant loss of water from the system and the removal of any leaked noncondensables was assured. The amount of gas in the water was not measured, but was implied by the flashing and condensation behavior; the reduction in gas content of the water stream was accompanied by an increase in sharpness of the condensation front in the diffusing section and the disappearance of residual gas bubbles after the condensation front. Approximately 0.5 to 1.0 hr of operation were required to deaerate the water.

The test section is shown in Fig. 3 with a typical shaped nozzle insert. The nozzle inserts could be modified to provide a variety of profiles but only one set was used in these experiments with a throat cross-sectional area of 3.0×10^{-5} m^2 (0.0053×0.0056 m). The profile consisted of a rapidly converging section followed by a very gently changing cross section in the vicinity of the throat and then a diverging section with about a 10-deg (half) angle. The space between the glass and the inserts was filled with thin silicone rubber gaskets formed *in situ*. The gaskets introduced rough surfaces in the test section which were the predominant source of nucleation sites. Occasionally nucleation did occur on the glass walls and these instances provided the most interesting photographic bubble definition.

Microphotography was done at magnifications from 10 to 40 times directly onto large-format instant black and white film. Lighting was provided by single pulses of a strobe light with the bubbles in silhouette. The pulse duration was approximately 3 μs (85 percent of total light delivered). Since average flow speeds in the test section were 10–20 m/s, substantial axial blur of the bubbles would be expected (30–60 μm), but all the bubbles of small size originated at the wall at lower speeds and appear distinctly in the micrographs. The light source was well removed from the focal plane of the microscope so the light source was effectively collimated.

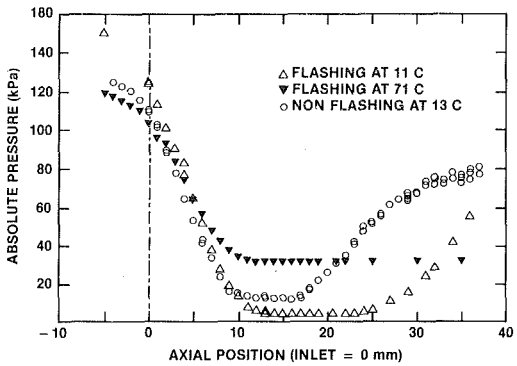

Fig. 4 Pressure as a function of axial position for three flow conditions

Measurements of the axial pressure variation in the nozzle were made with a 1.65-mm-dia probe, axially inserted through the centerline with four, 0.254 mm flush pressure taps located 6.4 mm from the probe tip. Axial traverses were made with the probe tip downstream of the pressure taps.

Microscopic Bubble Characteristics

The pressure probe was used to determine pressure profiles in the nozzle under single-phase flow and two flashing flow conditions [17]. The results for the single-phase flow case agreed with one-dimensional frictionless predictions within the accuracy of the channel cross-sectional area measurement. The pressure traces for the two flashing flow conditions are shown in Fig. 4 along with the single-phase case. The first flashing condition at 11°C inlet condition has such a low throat pressure that accurate determination of the superheat is not possible (a maximum accuracy of ± 4°C). The 11°C condition does show the pressure recovery occurring after the condensation front, minus irreversible pressure drop associated with the flashing. The 71°C flashing condition allows a more accurate determination of superheat; the superheat was less than 2°C ± 0.5°C. This measurement is based on the pressure undershoot at the probe location; however, it is not known if the flow was strictly one-dimensional in the throat. Some evidence indicates pressure undershoot may have been higher at the surface of the nozzle inserts; no nucleation took place on the probe pressure taps, but pressure taps located in the nozzle inserts had to be removed as they invariably acted as nucleation sites.

The flow field developed entirely from bubbles nucleated at the perimeter of the nozzle in the throat region and the bubbles were highly distorted and rarely represented distinct vapor volumes. Two distinct regions existed from the throat downstream: a region of flow with vapor as the continuous phase at the edges coexisting with a continuous liquid core until well into the diverging portion of the nozzle. Since this situation hardly corresponded to the ideal of Fig. 1, an unsuccessful effort was made to locate a flashing condition which might have reasonably well-behaved bubbles. The efforts may be roughly divided into two areas: (1) variations in flow and saturation conditions to change the shear and the vapor density for heterogeneously nucleated bubbles at the wall, and (2) attempts to introduce heterogeneous nucleation sites in the bulk flow. Both efforts were made with and without the presence of noncondensable gas.

In almost all tests, the four contact edges between glass and the nozzle inserts were sources of nucleation. Because of the large size of the bubbles and the coincidence of two edges when viewed from the side, photographs of these bubbles are not especially revealing. With only one nucleation site per

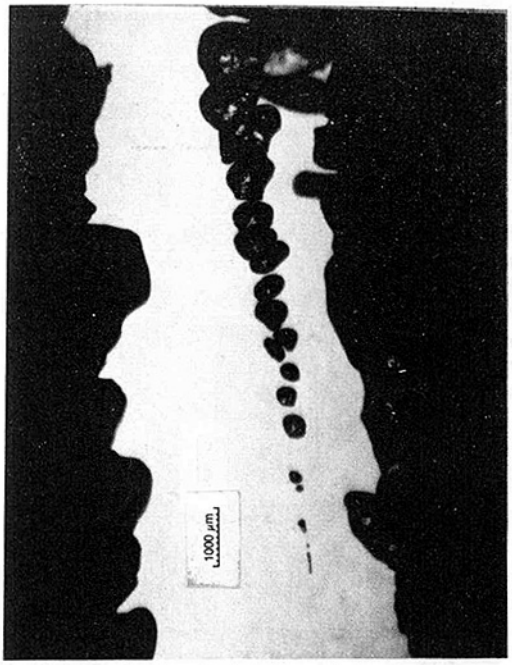

Fig. 5 A short nucleation site bubble and detached bubble stream; inlet temperature 79°C and throat flow speed 18.8 m/s; inlet subcooling ~25°C

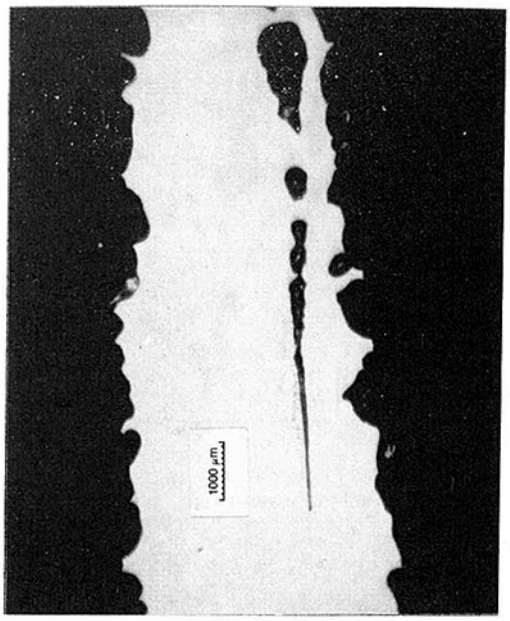

Fig. 6 A long nucleation site bubble and detached bubble stream; inlet temperature 91°C and throat flow speed 14.5 m/s; inlet subcooling ~20°C

edge active, the equivalent of 180 sites per meter of perimeter is attained, in reasonable agreement with the results of Klein on a circular cross section nozzle. A volume density of sites for this case is not particularly meaningful, but if a volume is chosen as a rectangular region in the throat having an axial depth equal to the nozzle throat width, then the volume density of nucleation sites is about 10^7 per m^3. Efforts to roughen the nozzle inserts were ineffective at introducing new nucleation sites. While the definition of an individual bubble becomes somewhat vague when they are connected by ligaments of various sizes and shapes, between 10^7–10^8 bubbles per m^3 might be estimated for a typical case, orders of magnitude less than generally predicted. The presence or absence of noncondensable gas had no qualitative effect on the bubble formation.

The concentration of voidage at the wall made observation difficult, but in some cases an active site on the glass wall would occur, providing bubbles which were readily photographed. The significant persistent feature of nucleation site bubbles illustrated by the glass wall nucleation site cases is an elongated bubble of at least ten diameters. The individual bubbles that appear downstream of the initiation site appear to be the result of the nucleation site bubble breaking up, rather than distinct bubbles forming and leaving the nucleation site. Figures 5 and 6 show the extremes which were observed (flow is from bottom to top in the photographs). The bubbles are seen to grow very rapidly, but the initial diameter of 40–50 μm implies a low superheat (~3°C), especially since a cylindrical bubble has a lower critical superheat than a spherical bubble. Maximum optical resolution was about 10 μm, but the presence of extremely small bubbles acting as precursors to the measured nucleation bubble would have been apparent due to their light scattering ability, even though photographic reproduction is impossible. In Fig. 5 a spherical bubble of initial diameter 45 μm (the approximate diameter of the cylindrical nucleation bubble) could have nucleated in water with 3°C of superheat. That bubble would have grown to a size of 530 μm by the time it exited the photograph (0.48 ms later traveling at the mean flow speed) if its growth had been conduction controlled. It has, however, grown to 1200–1300 μm in this same period. This implies a vapor generation rate which is 13 times as great as theory (Mikic et al. [18]). Similarly, in Fig. 6, a 45-μm bubble nucleating in a 91°C, 2.0°C superheat environment, would have grown to 290 μm in 0.54 ms, but has instead grown to 820 μm; a factor of 22 increase in vapor generation rate compared to theory. The 3 and 2°C superheats deduced from the nucleation bubble diameter compare to values of 2.9 and 5.7 computed from the correlation of Alamgir and Lienhard [7].

The bubbles in Figs. 5 and 6 do not travel at the throat mean flow speed since they originate at the wall; an appreciable voidage has developed and the channel is slowly diverging. An estimate of the average bubble speed was derived by assuming: (1) the bubble speed is equal to the flow speed in a fully developed turbulent flow at a distance from the wall equal to the bubble radius, (2) the mean flow speed is determined from the actual nozzle position, and (3) the void fraction (~4 percent) is based on all five sites (four corner sites and one glass wall site) generating identical bubbles. This estimate is expected to be conservative since the flow is not fully developed ($1/d \cong 2$), the bubbles may move into the stream without remaining tangent to the glass wall, and the four corner nucleation sites are active upstream of the glass wall site so calculated voidage is likely to be low. Average bubble speeds for Figs. 5 and 6 are thus computed to be 13.4 and 11.1 m/s and using conservative superheats of 3.5 and 3.0°C (critical bubble diameters of 40 and 30 μm) the excess vapor generation rate for both cases is a factor of 5. If superheats are 1.5°C, vapor generation rates are 40–30 times theory. It is noted that Ardron et al. [14] find 10^4 times as great a rate.

If all five nucleation sites in Fig. 5 generate bubbles at the same rate as the glass wall site, a bubble density of 3×10^8 bubbles/m^3 results. With real vapor generation rates per bubble between 5 and 50 times as great as used in existing models, bubble densities would have been incorrectly calculated to be between 10^9 and 10^{10} bubbles per m^3 for these tests.

A relatively blunt object was placed across the inlet of the nozzle at the inlet plane in order to generate turbulence. The results are not appreciably different than those above. The object did have the effect of distorting the inlet flow to the extent that nucleation occurred upstream of the throat even at

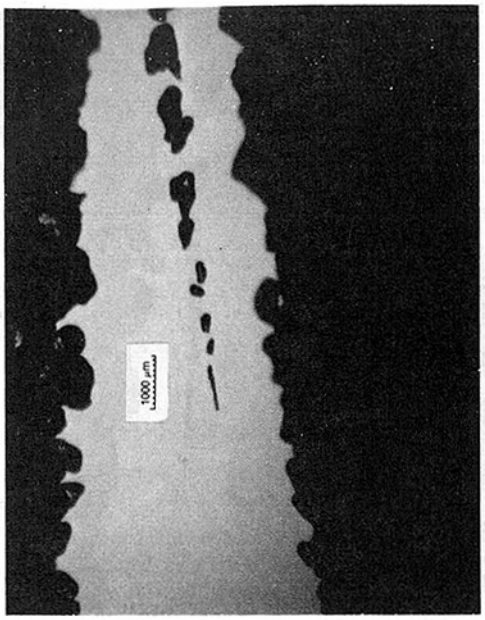

Fig. 7 Nucleation site bubble and detached bubble stream with upstream introduced turbulence; inlet temperature 92°C and throat flow speed 13.7 m/s; inlet subcooling ~20°C

very low flows; at these low flows nucleated bubbles did approach spherical shapes, but they grew as they moved along the wall and did not depart into the free stream. At successively higher flows the results resemble those of Figs. 5 and 6. The only difference appears as rougher bubble shapes, but a continued presence of an elongated nucleation bubble (Fig. 7).

These tests were performed over a range of saturation conditions from 10°C to 110°C (a 90-fold change in vapor density) with no qualitative change in flashing character. Changes in noncondensable content had no apparent effect. Noncondensable content was not measured, but no effort was made to remove the gas from the water. Qualitatively, the presence (or absence) of noncondensable gas was observed by the persistence of bubbles downstream of the condensation front in the diverging section.

Variations in flow and saturation conditions, with and without the presence of noncondensables, addition of upstream turbulence and changes in inlet subcooling failed to produce nucleation in the bulk flow while wall nucleated bubbles were severely distorted. Further contrived attempts were made to create bubbles in the bulk flow that might be more spherical and grow without being subjected to high shear. Two basic attempts were made which both involved introducing blunt surfaces which would serve as cavitation sites. The first cavitation site was introduced upstream of the nozzle throat assuming that gas or steam bubbles so formed would persist into the throat region and serve as favorable spherical steam bubble nucleation sites. This technique was effective in introducing bubbles into the bulk flow and in generating large numbers of gas bubbles for nucleation, but the number of steam bubbles remained very limited and they were not spherical.

A hemispherically capped probe (0.00165 m diameter) axially inserted into the throat region was used as the other blunt object with comparable results. Figures 8 and 9 compare the bubbles formed with and without noncondensables in the system. While gas bubbles can be seen persisting in the flow (Fig. 8), the steam bubbles appear to be growing independently. The presense of gas seems to have little effect on the shape of the steam bubbles. The local formation downstream of the probe does, however, show differences in steam bubble formation; gas bubbles appear first if gas is present.

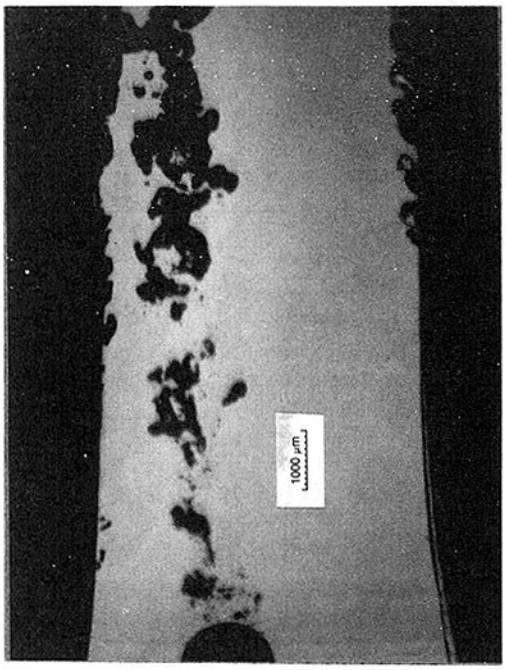

Fig. 8 Steam and air bubbles formed downstream of a blunt probe in the throat region with noncondensables present; inlet temperature 15°C and throat flow speed 16.1 m/s; inlet subcooling ~95°C

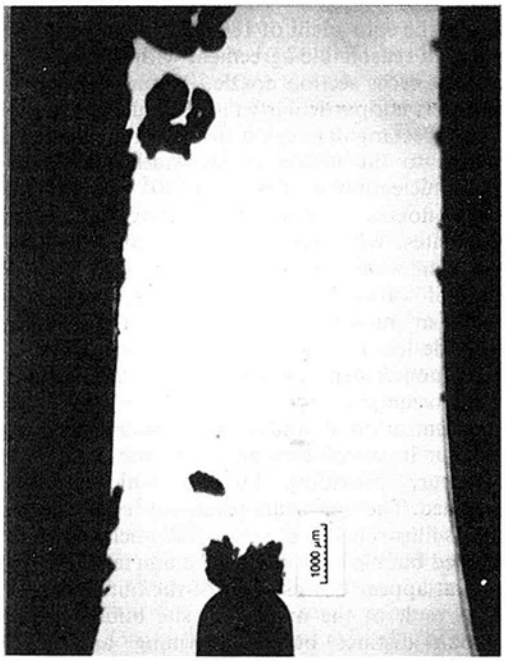

Fig. 9 Steam bubbles formed downstream of a blunt probe in the throat region without noncondensables; inlet temperature 69°C and throat flow speed 15.6 m/s; inlet subcooling ~35°C

Discussion

The density, size, and shape of bubbles formed in flashing nozzle flows have been found to be substantially different than described by various theoretical treatments. The bubbles are fewer in number (one to two orders of magnitude), nonspherical even at low velocities, and larger and faster growing than expected. In addition, the nucleation sites were exclusively confined to the wall and bubbles did not disperse themselves into the bulk flow. A possible explanation is that convection has a significant, perhaps dominant, effect on heat and mass transfer at the interface of the bubbles. Unfortunately, the current study was not geared to the quantification of these effects.

Greater depressurization rates or higher operating pressures might have resulted in greater nucleation superheats and smaller bubbles, and indeed, many of the data to which the theories have been compared are at higher reduced pressures. Higher nucleation superheats might have activated the (absent) bulk fluid nucleation sites and provided a low-shear, dispersed environment for bubble growth, but over a substantial range of flow velocity, vapor density and noncondensable content in the experiments, no significant departure occurred from the pattern of wall nucleation and bubble growth. In addition, published results at higher flows and pressures show concentrations of voidage at the perimeter of a nozzle consistent with the observed perimeter nucleation. Finally, the results are qualitatively in agreement with limited published experimental data showing bubble growth to be much faster and bubble density to be much lower than predicted using conduction-controlled bubble growth theory.

References

1 Plesset, M. S., and Zwick, S. A., "The Growth of Vapor Bubbles in Superheated Liquids," *J. Applied Physics*, Vol. 25, 1954, pp. 493–500.

2 Simpson, H. C., and Silver, R. S., "Theory of One-Dimensional, Two-Phase Homogeneous Non-Equilibrium Flow," *Proc. Inst. Mech. Engrs.*, Paper No. 6, 1962.

3 Edwards, A. R., "Conduction Controlled Flashing of a Fluid, and the Prediction of the Critical Flow Rates in a One Dimensional System," UKAEC Report AHSB(S)R.147, 1968.

4 Rohatgi, U.S., and Reshotko, E., "Non-Equilibrium One-Dimensional Two-Phase Flow in Variable Area Channels," *Non-Equilibrium Two-Phase Flows*, ASME, New York, 1975, pp. 47–54.

5 Malnes, D., "Critical Two-Phase Flow Based on Non-Equilibrium Effects," *Non-Equilibrium Two-Phase Flows*, ASME, New York, 1975, pp. 11–17.

6 Wu, B. J. C., Abuaf, N., and Saha, P., "A Study of Nonequilibrium Flashing of Water in a Converging-Diverging Nozzle," USNRC report NUREG/CR-1864, BNL-NUREG-51317, Vol. 2, June 1981.

7 Alamgir, M. D., and Lienhard, H. H., "Correlation of Pressure Undershoot During Hot-Water Depressurization," ASME JOURNAL OF HEAT TRANSFER, Vol. 103, Feb. 1981, pp. 52–55.

8 Zaloudek, F. R., "The Critical Flow of Hot Water Through Short Tubes," USAEC report HW-77594, 1963.

9 Ardron, K. H., "A Two-Fluid Model for Critical Vapour–Liquid Flow," *Int. J. Multiphase Flow*, Vol. 4, 1978, pp. 323–337.

10 Sozzi, G. L., and Sutherland, W. A., "Critical Flow of Saturated and Subcooled Water at High Pressure," *Non-Equilibrium Two-Phase Flows*, ASME, New York, 1975, pp. 19–25.

11 Fauske, H. K., "The Discharge of Saturated Water Through Tubes," *Chem. Eng. Prog. Symp.*, Ser. 61, 1965, pp. 211–216.

12 Abuaf, N., Zimmer, G. A., and Wu, B. J. C., "Study of Nonequilibrium Flashing of Water in a Converging-Diverging Nozzle," Nuclear Regulatory Commission Report NUREG/CR-1864, BNL-NUREG-51317, Vol. 1, June 1981.

13 Simoneau, R. J., "Pressure Distribution in a Converging-Diverging Nozzle During Two-Phase Choked Flow of Subcooled Nitrogen," *Non-Equilibrium Two-Phase Flows*, ASME, New York, 1975, pp. 37–45.

14 Ardron, K. H., and Ackerman, M. C., "Studies of the Critical Flow of Subcooled Water in a Pipe," CEGB report RD/B/N4299, May 1978.

15 *An Album of Fluid Motion*, M. Van Dyke, ed., Parabolic Press, Stanford, California, 1982, p. 109.

16 Klein, E., Personal communication, July 1983.

17 Miller, R. S., "Photographic Observations of Bubbles in a Flashing, Two-Phase Flow in a Rectangular Cross-Section, Converging-Diverging Nozzle," MS Thesis, RPI, Dec. 1983.

18 Mikic, B. B., Rohsenow, W. M., and Griffith, P., "On Bubble Growth Rates," *Int. J. Heat Mass Transfer*, Vol. 13, 1970, p. 657.

Transition Boiling Heat Transfer on a Vertical Surface[1]

T. D. Bui[2]

V. K. Dhir

Mem. ASME

School of Engineering and Applied Science, University of California, Los Angeles, CA 90024

Transition boiling heat transfer on a vertical surface in a pool of saturated water is investigated experimentally. Local heat transfer rates are obtained on a 6.3-cm-wide and 10.3-cm-high surface which was machined from a large block of copper. Experiments conducted with water show that even for relatively slow transient cooling rates ($|dT/dt| < 11$ K/s), the transient maximum heat fluxes are as much as 60 percent lower than the maximum steady-state heat fluxes. It is found that transition boiling heat transfer is very sensitive to the surface condition as well as to the history of the process. Two distinct transition boiling curves are observed during transient heating and cooling of clean surfaces. However, the difference between the two curves diminishes as the wettability of the surface increases. A correlation is developed to relate the transient quenching and steady-state peak heat fluxes for the range of temperature transient rates and surface conditions used in this investigation. Although the transient transition boiling curves obtained during heating and cooling are distinct because of different initial conditions, it is found that they possess the same rate of change of heat transfer coefficient with surface temperature when a correction factor equal to the ratio of steady to transient maximum heat fluxes is used.

Introduction

Of all the regimes observed in boiling the chaotic region identified as transition boiling has remained controversial. The heat transfer process in this regime is characterized by a reduction in surface heat flux resulting from an increase in wall superheat. Hence the process is inherently unstable for all boiling systems unless some stability mechanism is incorporated [1].

Transition boiling has been believed to be a mixed mode of nucleate and film boiling occurring alternately at the heated surface [2]. On a typical boiling curve where surface heat flux is plotted against surface temperature superheat, this region is bounded by the temperature corresponding to the maximum heat flux in nucleate boiling and that corresponding to the minimum heat flux in film boiling. These temperatures are denoted here as the maximum temperature and the minimum temperature, respectively.

A search of the literature reveals that relatively few investigations have been performed on transition boiling heat transfer in comparison to those on nucleate and film boiling. Most of the reported transition boiling studies utilized the unsteady quenching method. Peyayopanakul and Westwater [3] observed transient boiling of liquid nitrogen on horizontal copper surfaces and concluded that a minimum time for the boiling phenomena to traverse the top 10 percent of the boiling curve near the peak heat flux is required if the boiling process is to be considered quasi-steady. From their data, however, it was noted that characteristic boiling curves in transition boiling differ significantly for various runs, even on the same setup.

Because of the lack of reproducible data, heat transfer in transition boiling has been generally represented by a straight line connecting the maximum point in nucleate boiling and the minimum point in film boiling on a log-log plot. In this way, heat transfer in the transition region is readily determined once information about the maximum and minimum points is obtained.

Using an experimental setup similar to that built by Peterson and Zaalouk [4], Sakurai and Shiotsu [5] obtained characteristic boiling curves of water on small wires and concluded that there are thermal hysteresis effects in both the nucleate boiling region and in the transition boiling region near the maximum heat flux point. However, Sakurai and Shiotsu pointed out in their paper that their transition boiling data may represent mixtures of different modes of boiling along the axial length of the wire—a mixture that may or may not include transition boiling. Sakurai and Shiotsu argued that hysteresis in nucleate boiling is physically the same as that pointed out by Corty and Foust [6] but gave no explanation for the thermal hysteresis in transition boiling.

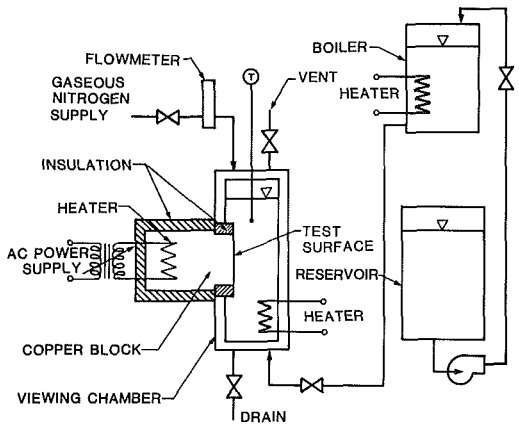

Fig. 1 Schematic diagram of the experiment

Reinforced by observation of jumps in heat fluxes in the transition boiling region from quenching experiments of small spheres, Witte and Lienhard [7] suggested that the thermal hysteresis observed by Sakurai and Shiotsu is caused by the existence of two transition boiling curves, called transitional film boiling and transitional nucleate boiling curves. The jumps in transition boiling heat fluxes were thus thought to have resulted from jumps from one curve to another.

Referring to the classic experiment of Berenson [2] in which heat transfer had been observed to increase with a surfactant added to the liquid, Witte and Lienhard argued that the increase in heat flux was the result of a jump from the transitional film boiling curve to the transitional nucleate boiling curve, in contrast to Berenson's conclusion that wetting lifted the transition boiling curve.

[1]Work supported by National Science Foundation Grant CME 7918253.

[2]Presently at Hughes Aircraft, El Segundo, CA.

Contributed by the Heat Transfer Division and presented at the 22nd National Heat Transfer Conference, Niagara Falls, New York, August 5-8, 1984. Manuscript received by the Heat Transfer Division, May 3, 1984.

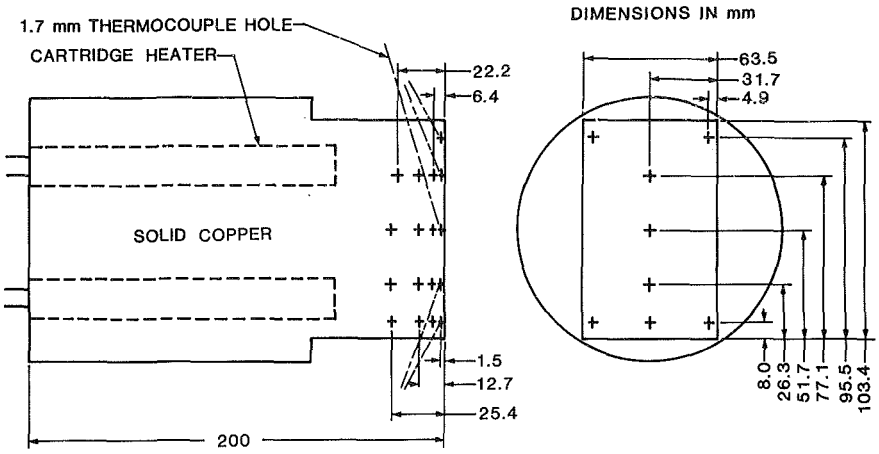

Fig. 2 Details of the test surface machined from a copper block

Very recently Winterton [8] substantiated Berenson's conclusion by examining heat transfer data in transition boiling of liquids with different values of contact angle. Winterton pointed out that contact angle is one of the parameters that control boiling heat transfer in this region and suggested that there should be a continuous variation of the transition boiling curve with this parameter. No experimental data were available to support this speculation, however.

From the above brief discussion it can be concluded that understanding of transition boiling behavior is very limited. Various hypotheses and concepts need to be verified with experiments. The objective of this study is to experimentally investigate the behavior of transition boiling heat transfer under well-controlled conditions. The experiments are conducted with saturated water boiling on an isothermal vertical surface.

Experiments

Figure 1 shows the apparatus. It includes a test section, a viewing chamber and a flow line that is used to start and to maintain the boiling process. The test section is mounted on one side of the viewing chamber and glass windows are placed on the remaining three sides for simultaneous observations of the front and side views of the heating surface. The rectangular heating surface has a width of 6.3 cm and a height of 10.3 cm, and it was machined from one end of a 99.99 percent pure copper solid cylinder. The other end of the cylinder was drilled to fit four cartridge heaters, each rated at 2 kW.

Thirty-gage chromel-alumel thermocouples are positioned along the vertical axis of the rectangular boiling surface at four locations: 8, 26, 52, and 77 mm from the lower edge. At each of the first three locations, four thermocouples are embedded at 1.5, 6.4, 12.7, and 25.4 mm from the surface. The last location, which is at 77 mm from the bottom, has four thermocouples at 1.5, 6.4, 12.7, and 22.2 mm from the surface. Four more thermocouples are also placed at the corners of the rectangular surface to verify the uniformity of surface temperature. Figure 2 shows the location of the various thermocouples.

The test liquid is contained in a square duct having a 14 cm by 14 cm cross section. This duct is also used as a viewing chamber. The test liquid level was maintained at about 30 cm

Nomenclature

a, b = constants

C_t = parameter defined in equation (3)

f, f_1, f_2 = functions defined in equations (1) and (2)

Δf = forward difference of f

$h = q/\Delta T$ = heat transfer coefficient, W/m^2 K

$\frac{dh}{dT}$ = rate of change of h with T

L = thickness of the slab whose temperature is solved by equation (1)

q_{max} = maximum heat flux in nucleate boiling, W/m^2

q_{maxZ} = q_{max} predicted by Zuber's theory

q_{min} = minimum heat flux in film boiling, W/m^2

q_t = transient cooling heat flux

$\left.\frac{dq}{dT}\right|_t$ = rate of change of q with T for transient cooling

$\left.\frac{dq}{dT}\right|_{ps}$ = rate of change of q with T for the approximated pseudo-steady-state curve

T = heater surface temperature, K

T_{sat} = saturation temperature of liquid, K

$\Delta T = T - T_{sat}$ = wall superheat

ΔT_{max} = ΔT at q_{max}, K

ΔT_{min} = ΔT at q_{min}, K

$\frac{dT}{dt}$ = rate of change of T with time, K/s

t = time, s

Δt = step size in time, s

$\Delta t^* = \frac{\alpha(\Delta t)}{L^2}$ = scaled step size in time

x = spatial length, m

Δx = step size in length, m

$\Delta x^* = \frac{\Delta x}{L}$ = scaled step size in length

α = thermal diffusivity of heater material, m^2/s

β = contact angle, measured from the liquid-solid interface, deg

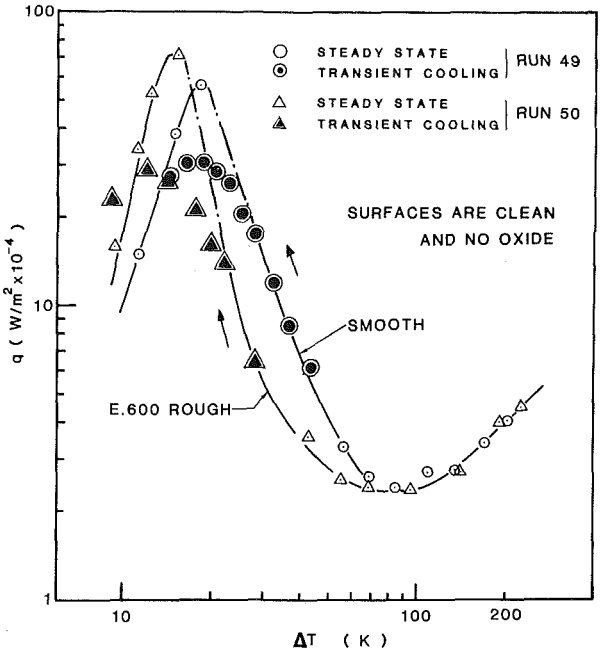

Fig. 3 Effect of surface roughness on boiling curve

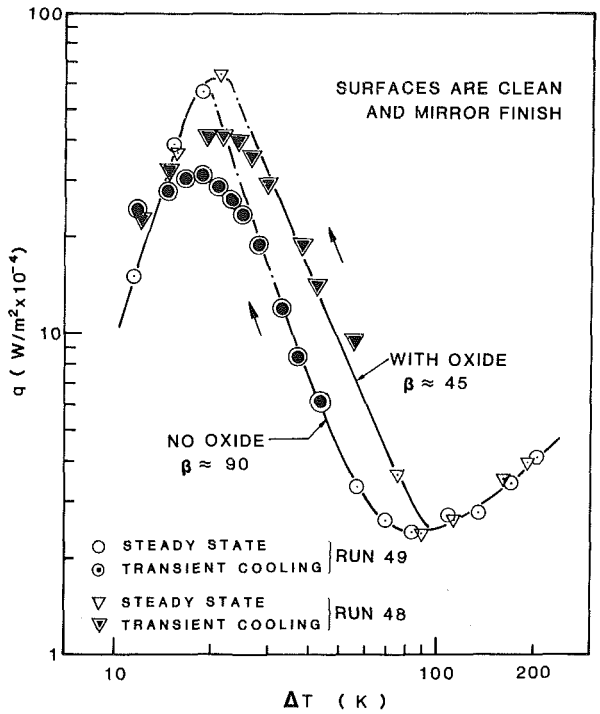

Fig. 4 Effect of surface oxide on boiling curve

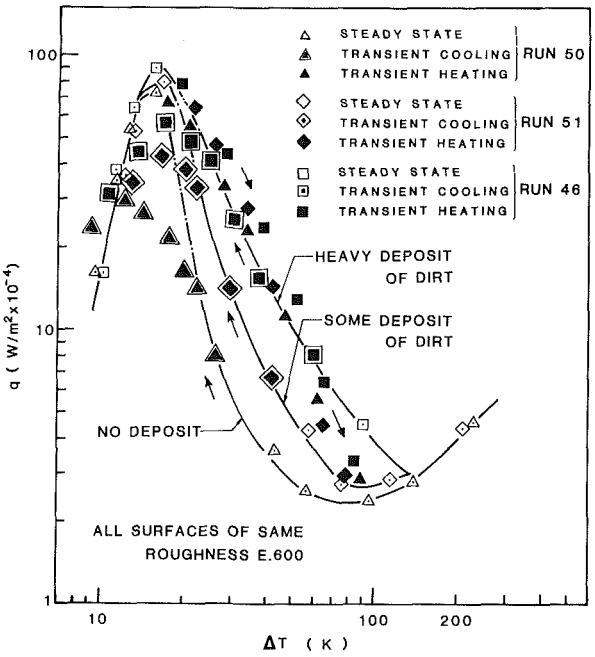

Fig. 5 Effect of surface deposit on boiling curve

above the top of the test surface during the experiments. An immersion heater located at the bottom of the chamber was used to keep the liquid at saturation temperature. The liquid temperature was determined with a thermocouple located in the pool at about 3 cm from the boiling surface.

Start-up of a typical experimental run began with deaeration of the working fluid by vigorous boiling in a reservoir and with preheating of the test section. The chamber was then filled with water from the reservoir and the boiling process was commenced. The power to the heaters was controlled with a variable autotransformer and was determined by voltmeter and ammeter readings. In steady-state tests thermocouple outputs were recorded directly using a Fluke data logger (model 2280 A) with calibrated electronic cold junction compensation. Transient signals were recorded using high-gain direct current differential amplifiers (HP model 8875 A), an analog-to-digital converter, a DEC LSI 11/2 computer, and a Winchester disk drive. The sampling rate, controlled by a programmable real time clock, was set at a convenient value of 10 samplings per second since the temperature transient rate never exceeded 10 K/s. Proper data acquisition technique was assured since the time constant for the entire data acquisition system was found with a step-change calibration method to be about an order of magnitude less than the sampling period. Tests were considered to be steady state when the temperature of the test block changed less than 1 K in 5 min. More details of the experimental apparatus and procedure can be found in [9].

Data Reduction

In steady-state tests, surface heat fluxes were readily calculated using the spatial temperature distribution recorded from thermocouples. One-dimensional heat flow was found to exist inside the test block up to at least 2.5 cm from the boiling surface. Temperature variation along the surface in nucleate boiling was found to be less than 0.7 K, and the maximum deviation was 1.2 K for film boiling. The steady-state three-dimensional heat conduction equation with appropriate boundary conditions was solved using Fourier series to estimate the error in the heat flux calculated with one-dimensional heat flow assumption. It was found that the maximum error was less than 5 percent. The surface temperature was obtained by simply extrapolating the temperature profile to the surface. The q versus ΔT relation for transient runs was reduced from the temperature versus time data by solving the heat conduction problem numerically using the Crank–Nicolson scheme. Temperatures at 1.5 and 12.7 mm from the surface were used as boundary conditions for the initial-boundary value problem. The initial condition was obtained from the steady-state temperature profile before the system experienced a temperature transient. The one-dimensional conduction equation with initial and boundary conditions was written as

$$\frac{\partial T}{\partial t} = \alpha \frac{\partial^2 T}{\partial x^2}$$

$$T(x,0) = ax + b$$
$$T(1.5\text{ mm}, t) = f_1(t)$$
$$T(12.7\text{ mm}, t) = f_2(t) \quad (1)$$

The surface temperature and heat flux were obtained by extrapolation to $x=0$ using the Gregory-Newton forward formula truncated after the fourth term with forward differences [10]

$$f(x) = f(0) + x\Delta f_0 + \frac{x(x-1)}{2!}\Delta^2 f_0 + \frac{x(x-1)(x-2)}{3!}\Delta^3 f_0 + \frac{x(x-1)(x-2)(x-3)}{4!}\Delta^4 f_0 \quad (2)$$

Double precision arithmetic and step sizes of about 0.01 in time and space (Δt^*, Δx^*) were employed to keep round-off and truncation errors to a minimum. The computational errors were therefore considered negligible compared to the measurement uncertainties. The estimated uncertainties are thus based on measurements alone. The maximum uncertainty in heat flux occurred near the minimum and was about 20 percent. However, at higher heat fluxes the uncertainty was much smaller. The details of the calculations are given in [9].

Results

Steady-state experiments could be performed in the nucleate boiling, the film boiling, and partway into the transition boiling regime by careful adjustments of power to the test heater. It was observed during cooling experiments that at heat fluxes above 5×10^4 W/m^2 boiling heat flux changed faster than could be attained by increasing power to the cartridge heaters. Thus transition boiling data with heat fluxes about 5×10^4 W/m^2 are transient data. Similarly, after the maximum heat flux had occurred, the large amount of energy stored in the back of the test block did not allow steady-state conditions to be attained even if the power to the cartridge heaters was totally cut off. Steady-state data are denoted by open symbols; transient cooling and heating data are denoted by double symbols and closed symbols, respectively.

Steady-State Nucleate Boiling and Maximum Heat Flux. Figures 3, 4, and 5 show the steady-state nucleate and film boiling heat transfer data along with the transient transition boiling data obtained during the cooling mode. These data were found to be reproducible to within ±3 percent. In Fig. 3, the boiling curves are plotted for mirror finish and emery 600 finish surfaces. Both surfaces are clean and free of oxides. There is a noticeable effect of roughness on the wall superheat for a given heat flux in nucleate boiling. Surface heat flux is proportional to wall superheat raised to a power estimated to be 3.3 for the mirror finish surface and 4.2 for the rough surface. The maximum heat flux for the rough surface is 72 W/cm^2 while it is only 57 W/cm^2 for the mirror finish surface. The ΔT_{max} on the other hand is smaller for the rough surface. Berenson [2] observed the same trend for ΔT_{max} but concluded that q_{max} was independent of roughness, though his data did show a similar increase in maximum heat flux with increase in surface roughness.

Figure 4 shows the boiling curves for two identically clean and rough surfaces except that one surface has an oxide layer on it. The surface was oxidized by heating it in air at 473 K for 15 min. The associated contact angles were obtained by placing droplets of water on these surfaces when oriented horizontally. The surface oxides appear to have no identifiable effect on the nucleate boiling heat transfer. However, the maximum heat flux on the surface with oxide is about 10 percent higher than that on the surface without an oxide layer. Berenson made similar observations for *n*-pentane boiling on a horizontal surface.

The boiling curves obtained on surfaces having different degrees of dirtiness are plotted in Fig. 5. A clean surface became contaminated with dirt particles when it continued to operate in nucleate boiling for several hours in the liquid pool exposed to the laboratory environment. The heavy deposit of dirt was obtained when boiling was continued for about 30 hr over a period of one week. The details of surface preparation are given in [9]. As was the case with oxides, the nucleate boiling heat flux is found to be independent of the extent to which the surface is dirty. The maximum heat flux is, however, higher for the dirty surfaces, but the temperature at which maximum flux occurs appears to be insensitive to the surface condition. This latter observation is in contradiction to Berenson's observation since he found considerable increases in ΔT_{max} with dirtiness.

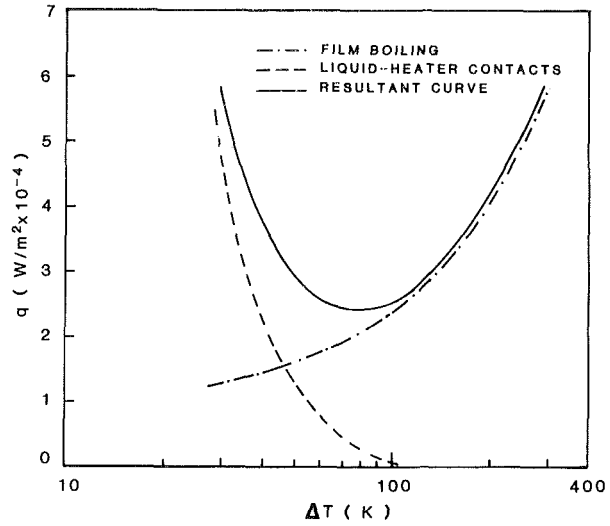

Fig 6 Variation of stable film boiling, liquid-solid contact, and total heat transfer rates with wall superheat

All of the data plotted in Figs. 3, 4, and 5 indicate that the maximum heat flux is sensitive to surface conditions. The maximum heat flux is highest for the dirtiest surface and is lowest for the clean, polished surface. The corresponding ratios of q_{max}/q_{maxZ} are 0.82 and 0.53, respectively. In contrast, the hydrodynamic model of Lienhard and Dhir [11], based on several modifications of Zuber's [12] original theory and supported by high gravity data of Adams [13], gives $q_{max}/q_{maxZ} = 0.9$ for vertical surfaces subjected to boiling on one side. The hydrodynamic model is based on Helmholtz instability of vapor jets away from the boiling surface and is independent of surface conditions. The differences between the present observations and the prediction from the hydrodynamic model might be reconciled if it is accepted that the hydrodynamic conditions near the surface control the maximum heat flux. The maximum heat fluxes given by the hydrodynamic conditions near and far away from the surface tend to approach each other as the wettability or roughness of the surface increases. Further work is needed to make a conclusive argument however.

Steady-State Film Boiling and Minimum Heat Flux. From examination of Figs. 3, 4, and 5, it found that the film boiling heat transfer is independent of surface conditions for wall superheats greater than 160 K. For these superheats the film boiling is unconditionally stable. This mode of boiling is characterized by a continuous, wavy layer of vapor covering the heated surface. The vapor generation rate is relatively low for wall superheats from 160 to 400 K. The maximum Reynolds number is calculated to be about 150. The vapor film is thus laminar even though ripples and large waves are always present at the vapor-liquid interface. An analysis of saturated film boiling heat transfer can be found in [9].

The homogeneous nucleation temperature for water is

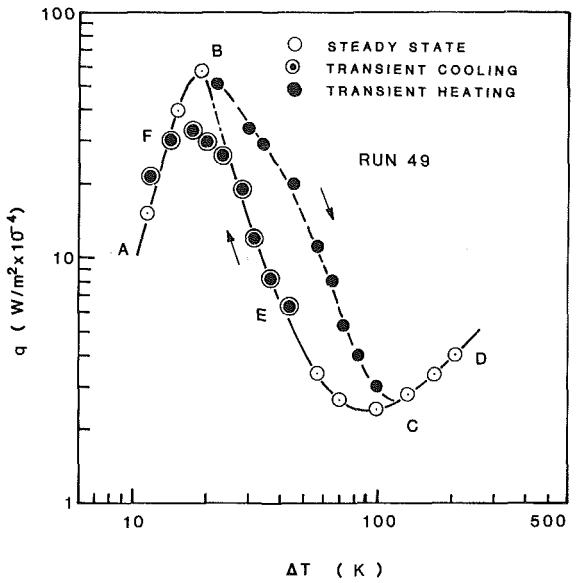

Fig. 7 Boiling curves on a smooth clean surface during heating and cooling modes

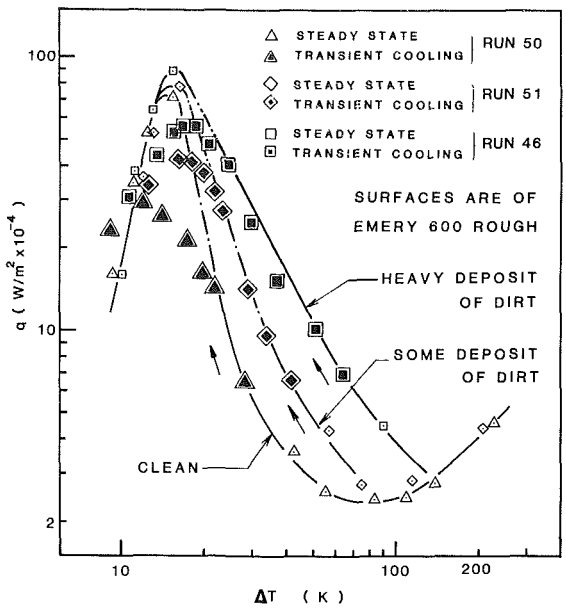

Fig. 8 Boiling curves on clean and dirty rough surfaces during heating and cooling modes

about 543 K. Thus if the interfacial temperature of the metallic surface is above this temperature and no protrusions deeper than the film thickness exist, a meaningful liquid-solid contact will never be possible. For temperatures greater than 543 K, the film boiling process is thus unconditionally stable and independent of surface conditions.

At temperatures below the homogeneous nucleation temperature, the boiling mechanism is strongly influenced by the surface conditions. For a clean mirror finish and oxide-free surface, liquid-solid contacts were visually observed at 105 K wall superheat which is well above the temperature where the heat flux is at a minimum. These contacts were nonpermanent, unstable, nonlocal, and nonwetting. Contacts without wetting occur as liquid touches the heated surface momentarily but is repelled immediately. Therefore no significant amount of vapor is generated from this type of contact as opposed to the heavy nucleation resulting in large bubbles that follows a wetting contact. The onset of this phenomenon depends on the surface condition and wall superheat as has been observed in these experiments.

For wall superheats in the range of 50 to 80 K, contacts are local but still unstable and nonwetting. Wetting contacts appear only at large cavities such as dents on the surface. The minimum heat flux occurs at a wall superheat of 80 K and has a value 2.4 W/cm^2. This value is about 35 percent higher than would be predicted from Berenson's [14] correlation for horizontal plate heaters. Between wall superheats of 40 to 50 K, nonwetting contacts occur over most of the surface. At wall superheats of less than 40 K wetting contacts occur; the vapor bubble layer thickens quickly and the boiling heat transfer rate increases dramatically. The wall temperature at which the heat transfer rate increases very rapidly is denoted as the wetting temperature.

At this point it also should be noted that occurrence of contacts does not always mean an increase in heat flux especially as the wall temperature is decreased. For nonwetting contacts the total heat flux has been observed to decrease with decreasing wall superheat. Since the nonwetting contacts begin at temperatures above the temperature at which the minimum heat flux occurs, the minimum heat flux is the result of a delicate balance between film boiling heat transfer and the heat removed through nonwetting contacts. Figure 6 shows qualitatively the heat fluxes associated with film boiling and various types of contacts. For stable film boiling the heat flux is proportional to $\Delta T^{3/4}$ [9]. Depending

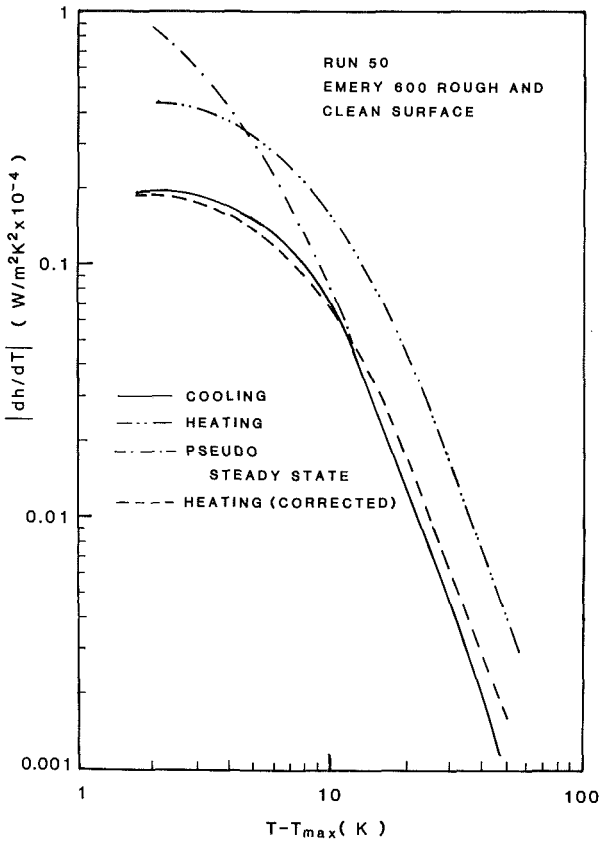

Fig. 9 The dependence of dh/dT on $T - T_{max}$ during transient transition boiling on a clean rough surface

on the variation with wall superheat of the heat flux associated with liquid-solid contacts, it is possible to have a range of wall superheats at which the total heat flux will be minimum. At a given wall superheat the magnitude of the heat flux associated with the various types of contacts will however depend on the fluid-solid combination and surface parameters such as surface chemistry, roughness, and cleanliness. Thus the magnitude of q_{min} and ΔT_{min} are influenced by the surface condition. From Figs. 3, 4, and 5, it is

seen that the q_{min} and ΔT_{min} are the lowest for a clean surface, but increase with oxidation and dirtiness of the surface. These observations reveal that most of q_{min} and ΔT_{min} data reported in the literature (e.g., [16]) are specific to the surface conditions, fluid–surface material combination, and probably geometry of the heater. The controversies resulting from large differences in q_{min} and ΔT_{min} data of various investigators will continue to exist as long as the surface effects are not quantified and the heat fluxes associated with wetting and nonwetting contacts are not known.

Transition Boiling. As mentioned earlier, the steady-state transition boiling data during cooling could only be obtained up to heat fluxes of 5 W/cm^2. Because of the large thermal mass of the test block, the transient cooling rate was relatively slow. The power to the cartridge heaters in these runs was generally maintained at its last steady-state value. Various cooling rates are listed in [9] but were always less than −11 K/s. The reproducibility of these data is within ±5 percent. The maximum heat fluxes attained during transient cooling are smaller than those obtained under steady-state conditions. For a rough and clean surface, the transient maximum flux is only 40 percent of the steady-state value. As observed in the steady-state tests, the maximum heat flux in transient tests is also higher for surfaces having oxides and deposits. Except for a clean rough surface, the temperature at which maximum heat flux occurs is about the same in transient tests as it is in steady-state tests.

Figure 3 shows that the transition heat flux for a clean and rough surface is about ⅓ of that for a mirror finish surface. However, Figs. 4 and 5 show that the transition heat fluxes are higher for surfaces having oxides or deposits. Since surface wettability increases with oxides and deposits [2], higher wettabilities are seen to yield higher heat fluxes. In fact the transition boiling heat fluxes on the dirtiest surface are as much as eight times those on a clean surface.

Another interesting observation that can be made from Figs. 3, 4, and 5 is that the transition boiling curves, when extrapolated (chained lines) from wall superheats for which nearly steady-state conditions existed, tend to approach the steady-state q_{max} and ΔT_{max}. This suggests that a steady-state transition boiling curve might be given by the combined chained and solid lines in these figures. The transient data deviate more and more from the chained curve as the maximum heat flux is approached. This will be elaborated in the Discussion Section.

Figures 7 and 8 show the transient transition boiling curves obtained during cooling and heat periods. During the heating experiments power to the cartridge heaters was generally cut off completely after occurrence of the maximum heat flux. However, in a few runs the power was maintained at a reduced level. The results of these two types of experiments showed no distinguishable difference. To distinguish the cooling and heating data double symbols are used for the cooling data. The data plotted in Fig. 7 are for a clean mirror finish surface. It is noted that two distinct curves are obtained while coming from film boiling and from nucleate boiling sides of the boiling curve. For a given wall superheat the transition boiling heat flux for the heating curve is much more than that for the cooling curve. This would seem consistent with the hypothesis of Witte and Lienhard [7]. However, they thought that the two transition boiling curves were possible in steady state as well as during transient cooling. Now if the heat flux in the region *BE could be controlled*, the pseudo-steady-state curve would be that shown approximately by the solid and chained line connecting *B* and *E*. In steady state, a single boiling curve will exist while approaching either from nucleate boiling or from film boiling side.

A comparison of the effect of surface condition on the heating and cooling curves is made in Fig. 8. The surface

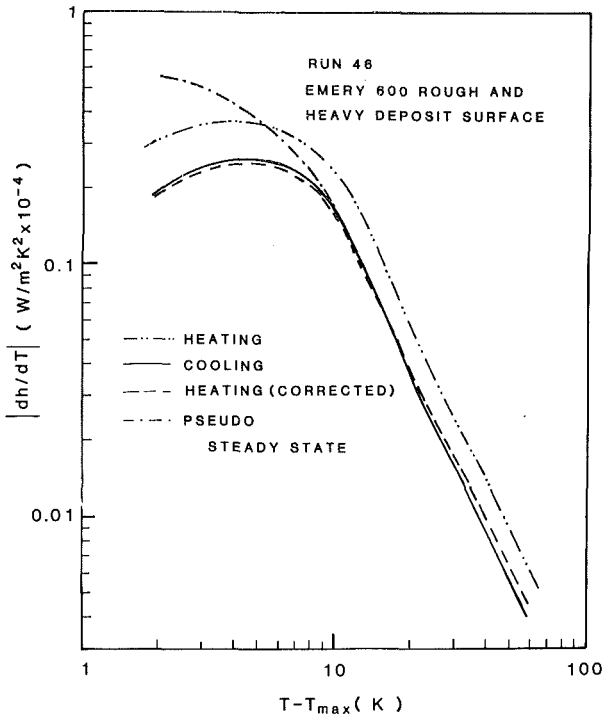

Fig. 10 The dependence of *dh/dT* on $T - T_{max}$ during transient transition boiling on a rough dirty surface

wettability has a relatively smaller effect on the transition boiling curves obtained during heating. The difference between the heating and cooling curves decreases as wettability of the surface increases. For the dirtiest surface the two transition boiling curves nearly overlap.

Discussion of Results

In this section discussion of the common feature of the transient transition boiling curves obtained during heating and cooling is presented. Also, the transient transition boiling data are correlated with a possible steady-state curve.

Relationship Between Transient Heating and Cooling Transition Boiling Curves. It was noted in the previous section that two distinct transition boiling curves exist when the transition boiling region is approached from the nucleate or the film boiling side. The difference between the transition boiling heat fluxes at a given superheat for the two curves strongly depends on the surface conditions. Since the heat transfer coefficient rather than the heat flux is the parameter that is more basic to the physical process at the wall, it is postulated that *the rate of change of the heat transfer coefficient with temperature should be the same for the two curves once a proper account for the differences in the transient and steady-state maximum heat fluxes is made.* Physically this postulate implies that the rate at which wet or dry area frictions change with temperature is the same for both heating and cooling curves.

The rate of change of heat transfer coefficient with temperature $|dh/dT|$ is plotted in Fig. 9 for a clean rough surface. In Fig. 9 the abscissa denotes the difference between the wall temperature and the temperature at which the maximum heat flux occurs. The $|dh/dT|$ curves for the heating and cooling modes almost run parallel to each other. The heating curve is shifted upward since the starting heat flux or heat transfer coefficient is higher for this curve. The ratio of steady state to transient maximum heat fluxes for a clean rough surface is found from Fig. 8 to be 2.41. If the $|dh/dT|$ of the heating curve is divided by this value, the dashed curve

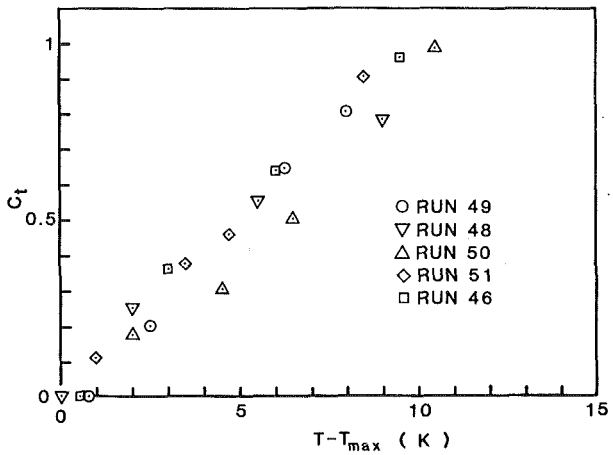

Fig. 11 Correlation of C_t with $T - T_{max}$

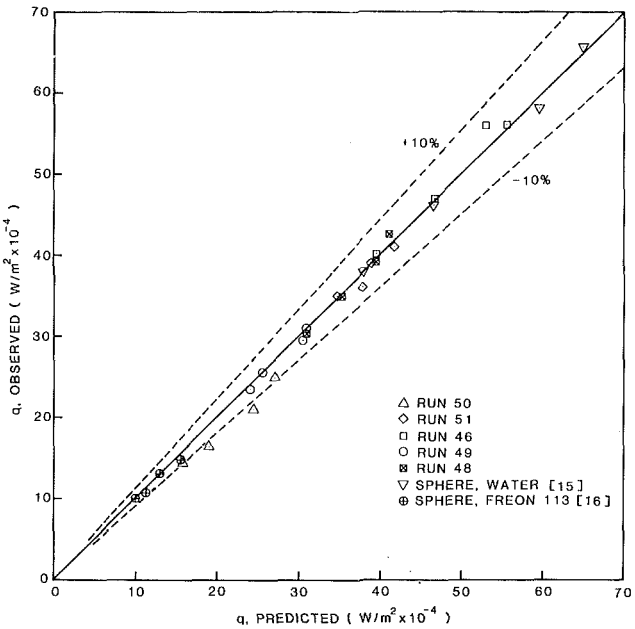

Fig. 12 Comparison of predicted and measured transient heat fluxes during cooling

results. The dotted curve is seen to nearly overlap the cooling curve over the whole range of transition boiling superheats.

The $|dh/dT|$ curves for the dirtiest surface in both heating and cooling modes are plotted in Fig. 10. The ratio of steady-state and transient maximum heat fluxes for this surface is 1.57. The dotted curve obtained by dividing the $|dh/dT|$ of the heating curve by this ratio is again seen to overlap the cooling curve. Thus the good agreement between the corrected heating curves and the cooling curves lends strong support to the above advanced postulate. Although the initial conditions seem to influence the maximum heat fluxes, we do not presently have a sound rationalization as to how the differences in initial conditions manifest themselves into large differences in maximum heat fluxes. The postulate is consistent with the idea of the pseudo-steady-state curve if such a curve is experimentally possible. For a steady-state curve, the q_{max} will be unique and $|dh/dT|$ in both heating and cooling modes will be identical.

An Approximate Relationship Between Transient Cooling and Pseudo-Steady-State Transient Boiling Curves. As seen in Figs. 3, 4, and 5, the transient maximum heat fluxes obtained during cooling are much lower than those obtained in steady-state tests. If the curve joining the steady-state transition boiling data with the steady-state maximum heat flux is taken to be the approximated pseudo-steady-state transition boiling curve, the transient transition boiling data are seen to gradually deviate from this curve. It should be pointed out that, as drawn, the pseudo-steady-state curve does not have zero value of dq/dT at q_{max}. The maximum deviation occurs at the wall superheat where the two heat fluxes are maximum. If a parameter C_t is defined such that

$$C_t = \frac{dq/dT|_t}{dq/dT|_{ps}} \tag{3}$$

the parameter C_t should be a function of dT/dt, wall superheat, and the surface conditions. In Fig. 11, C_t obtained from all of the present data is plotted as a function of $T - T_{max}$. For the range of temperature transients and surface conditions studied in the present work [9], the parameter C_t is found to be nearly insensitive to dT/dt and surface conditions. The parameter C_t is found to vary linearly with $T - T_{max}$. It is interesting to note that transient cooling heat fluxes start to deviate from the pseudo-steady-state curves at about 10 to 11 K above T_{max}; thus the parameter C_t can be correlated as

$$C_t = \frac{T - T_{max}}{10.5} \qquad 0 \le T - T_{max} \le 10.5 \tag{4}$$

From equation (3), the transient transition boiling during cooling can be represented as

$$\left.\frac{dq}{dT}\right|_t = C_t \left.\frac{dq}{dT}\right|_{ps} \tag{5}$$

Integration of equation (5) yields

$$q_t = q_{ref} + \int_{T_{ref}}^{T} C_t \left.\frac{dq}{sT}\right|_{ps} dT \tag{6}$$

where the subscript ref denotes the point where heat flux starts to deviate from the pseudo-steady-state curve.

To evaluate the transient heat flux at a certain temperature from equation (6), an expression for steady-state heat flux as a function of wall superheat in this region is required. By approximating the chained lines in Figs. 3, 4, and 5 as straight lines the pseudo-steady-state heat flux can be represented as

$$q_{ps} = b(\Delta T)^a \tag{7}$$

or

$$\left.\frac{dq}{dT}\right|_{ps} = ab(\Delta T)^{a-1}$$

The values of a and b are listed in [9] for tests with different surface conditions.

The transient heat flux is then expressed as

$$q_t = q_{ref} + \frac{ab}{10.5(a+1)}[(T - T_{sat})^{a+1} - (T_{ref} - T_{sat})^{a+1}]$$

$$- \frac{b}{10.5}(T_{max} - T_{sat})[(T - T_{sat})^a - (T_{ref} - T_{sat})^a]$$

$$\text{for } 0 \le T - T_{max} \le 10.5 \tag{8}$$

Figure 12 shows that the data of the present work are predicted within ± 10 percent by equation (8). The quenching data of Dhir [15] on 19-mm copper spheres in saturated water, and of Veres and Florschuetz [16] on 23.8-mm copper spheres in Freon-113, are also predicted well by equation (8). Since the steady-state maximum heat fluxes were not available from these tests on spheres, the approximate maximum heat flux is obtained by extending the curves for both nucleate and transition boiling. The point of intersection gives values of q_{max} and ΔT_{max}. These values are also listed in [9].

Here it should be reemphasized that the correlation of C_t with $T - T_{max}$ for all the surfaces and the range of temperature

transients studied in the present work implies that the transient transition boiling curves for all the surfaces deviate from the pseudo-steady-state curves in the same manner.

General Remarks About Some of the Existing Transition Boiling Data. The earliest, best-documented steady-state data are those of Berenson [2]. As has been pointed out by Witte and Lienhard [7], Berenson's apparatus did not allow him to have total control over the wall superheats and the corresponding heat fluxes. Thus it seems that he not only had two sets of transition boiling data corresponding to heating and cooling modes but also the data were somewhat transient in nature (slow transient). The transient occurred as the process entered from nucleate to transition and from film to transition boiling. Berenson's observation of increase in transition boiling heat flux with addition of oleic acid is consistent with the present observations (e.g., Fig. 8) in which increased wettability of the surface gives high transition boiling heat fluxes during heating and cooling modes. The increase does not mean that the process shifts from a transient cooling curve to a transient heating curve. Hesse [1] does not report whether he obtained the transition boiling curves while increasing or decreasing the tube wall temperature. However, his data seem to correspond to a transient heating mode. It is not known at what rate he changed the temperature of the liquid heating the tube.

The jumps in transition boiling during quenching of spheres in pool and forced flow boiling (e.g., [7, 15, 17, 18]) result from the sensitivity of the small heater to large area liquid–solid contacts. Visual observations in the present work revealed that in low superheat transition boiling, local liquid–solid contacts persisted for a few seconds. Soon after, these contacts gavg way to a smooth vapor film which also lasted for another few seconds and the process repeated itself. Liquid contacts correspond to good heat transfer while the presence of film leads to degradation in heat transfer. A heater of small thermal mass will be sensitive to these changes in surface heat flux. However, the present heater had a large thermal mass and as such thermocouples did not show any oscillations in temperature. Even an attempt to destabilize the transition boiling process by wiping the surface with a brush during the cooling mode did not lead to a jump in heat flux.

Conclusions

1. Even for relatively slow transients, the transient maximum heat fluxes are found to be much lower than the steady-state maximum heat fluxes.

2. The surface conditions strongly influence the film boiling heat transfer near the minimum heat flux and the transition boiling heat transfer. The steady and transient maximum heat fluxes are also found to be influenced by the surface conditions.

3. Because of different initial conditions, two distinct transient transition boiling curves are obtained during heating and cooling of the surface.

4. The rate of change of heat transfer coefficient with temperature is found to be the same for the two transient transition boiling curves if a correction for the differences in steady-state and transient heat transfer coefficients at the maximum heat flux is made.

5. For all the surface conditions and temperature transients studied in the cooling mode, the parameter C_t defining the ratio of transient to pseudo-steady-state transition boiling heat fluxes can be correlated with $T-T_{\max}$.

References

1 Hesse, G., "Heat Transfer in Nucleate Boiling, Maximum Heat Flux and Transition Boiling," *Int. J. Heat Mass Transfer*, Vol. 16, 1973, pp. 1611–1627.

2 Berenson, P. J., "Experiment on Pool Boiling Heat Transfer," *Int. J. Heat Mass Transfer*, Vol. 5, 1962, pp. 985–999.

3 Peyayopanakul, W., and Westwater, J. W., "Evaluation of the Unsteady State Quenching Method of Determining Boiling Curves," *Int. J. Heat Mass Transfer*, Vol. 21, 1978, pp. 1437–1445.

4 Peterson, W. C., and Zaalouk, M. G., "Boiling-Curve Measurements From a Controlled Heat-Transfer Process," *Trans. ASME*, Vol. 93, 1971, pp. 408–412.

5 Sakurai, A., and Shiotsu, M., "Temperature-Controlled Pool-Boiling Heat Transfer," *Proc. Fifth Int. Heat Transfer Conf.*, Vol. 4, B3.1, 1974, pp. 81–85.

6 Corty, C., and Foust, A. S., "Surface Variables in Nucleate Boiling," *Chem. Engr. Progr. Symp. Ser.*, Vol. 51, 1955, pp. 1–12.

7 Witte, L. C., and Lienhard, J. H., "On the Existence of Two 'Transition' Boiling Curves," *Int. J. Heat Mass Transfer*, Vol. 25, 1982, pp. 771–779.

8 Winterton, R. H. S., "Comments on 'On the Existence of Two 'Transition' Boiling Curves'," *Int. J. Heat Mass Transfer*, Vol. 26, 1983, pp. 1103–1104.

9 Bui, T. D., "Film and Transition Boiling Heat Transfer on an Isothermal Vertical Surface," Ph.D. dissertation, University of California, Los Angeles, CA, 1984.

10 Hornbeck. R. W., *Numerical Methods*, Chap. 4, Quantum, New York, 1975.

11 Lienhard, J. H., and Dhir, V. K., "Hydrodynamic Prediction of Peak and Pool Boiling Heat Fluxes From Finite Bodies," ASME JOURNAL OF HEAT TRANSFER, Vol. 95, 1973, pp. 152–158.

12 Zuber, N., Tribus, M., and Westwater, J. W., "The Hydrodynamic Crisis in Pool Boiling of Saturated and Subcooled Liquids," *Int. Devel. in Heat Transfer*, ASME, New York, 1963, pp. 230–235.

13 Adams, J. M., "A Study of the Critical Heat Flux in an Accelerating Boiling System," Ph.D. thesis, University of Washington, Seattle, WA, 1962.

14 Berenson, P. J., "Film Boiling Heat Transfer From a Horizontal Surface," ASME JOURNAL OF HEAT TRANSFER, Vol. 83, 1961, pp. 351–358.

15 Dhir, V. K., "Study of Transient Transition Boiling Heat Fluxes From Spheres Subjected to Forced Vertical Flow," Sixth Inter. Heat Transfer Conf., Toronto, Canada, Paper No. FB-31, Aug. 7–11, 1978.

16 Veres, D. R., and Florschuetz, L. W., "A Comparison of Transient and Steady State Pool Boiling Data Obtained Using the Same Heating Surface," ASME JOURNAL OF HEAT TRANSFER, Vol. 93, 1971, pp. 229–232.

17 Purohit, G. P., "Subcooled Film Boiling of Water From Spheres," M.S. thesis, University of California, Los Angeles, CA, 1977.

18 Ungar, E. K., "Construction and Initial Testing of an Apparatus for Studying Flow Boiling From a Heated Sphere," M.S. thesis, University of Kentucky, 1981.

Film Boiling Heat Transfer on an Isothermal Vertical Surface[1]

T. D. Bui[2]
Student Mem. ASME

V. K. Dhir
Mem. ASME

School of Engineering and Applied Science,
University of California—Los Angeles,
Los Angeles, CA 90024

Natural convection film boiling heat transfer of saturated liquids on an isothermal vertical surface is investigated both experimentally and theoretically. Local heat transfer coefficients are obtained at steady-state conditions on a 6.3-cm-wide and 10.3-cm-high heated surface which was machined from a large block of copper. Effectively isothermal surface conditions are achieved even for wall superheats up to 450 K. Experiments conducted with water at 1 atm pressure show that predictions from existing theoretical models are inadequate and a detailed consideration of the liquid–vapor interface behavior is required. Still and motion pictures of the vapor film are taken and data on vapor film thickness, interfacial wave behavior, and bubble detachment characteristics are obtained to build an analytical model for predicting film boiling heat transfer. This time-dependent model based on laminar flow in the film incorporates the effects of both large-scale and small-scale waves. Results from analysis are compared with experimental data.

Introduction

Film boiling heat transfer of a saturated liquid on an isothermal vertical surface has been investigated extensively in the past. Analyses of film boiling heat transfer can be grouped into two major categories: the laminar film vapor flow approach and the turbulent film vapor flow approach.

Bromley [1] first investigated the phenomena in a manner similar to that of Nusselt [2] for laminar film condensation and supported his correlation with experimental data obtained from horizontal tubes of relatively small diameters. Improvements on this simple model have been carried out with analyses employing boundary layer-type equations with much greater details such as that done by McFadden and Grosh [3], Cess [4], and Koh [5]. For near atmospheric pressures, the heat transfer rates predicted from these studies are close to Bromley's result, however.

The results of analytical work of the above type in which a stable laminar vapor film with a smooth vapor–liquid interface is assumed appear to agree with experimental data for boiling on a vertical surface no longer than a few centimeters. For longer surfaces these analyses tend to underpredict average heat transfer coefficient and inaccurately predict the dependence of local heat transfer coefficient on length. This approach however yields the correct dependence of heat transfer coefficient with fluid property as well as surface temperature superheats.

A modification of the laminar film approach has been attempted by Andersen [6]. Assuming that the smooth vapor film breaks up due to Helmholtz instability, Andersen used the most unstable wavelength as a good approximation for the length of the film. At each point of film breakup vapor left the film as bubbles and a new film was assumed to grow until it also became unstable. However, no film breakup has been observed in experiments with Freon-113 or water either by Sherman [7] or in the present work.

Greitzer and Abernathy [8] recognized the importance of the presence of bulges of vapor at the vapor–liquid interface on the film boiling heat transfer mechanism. Nevertheless the correlation derived from their mechanistic argument approach appears to be incomplete since different values of the empirical proportionality constant are needed to accurately predict heat transfer coefficients for different fluids. The dependence of heat transfer coefficients on the plate length is not accurately predicted for long surfaces either.

Noting that the heat transfer coefficients predicted by laminar models were lower than the experimental data, several investigators [9, 10, 11] argued that the vapor flow in the film must be turbulent after short distances from the leading edge. Hsu and Westwater [9] assumed that the heat transfer is by conduction across the laminar sublayer only and obtained results that generally overpredict experimental data. Coury and Dukler [10] assumed appropriate distributions of eddy diffusivities in the vapor film while Suryanarayana and Merte [11] hypothesized that the universal velocity profile proposed by Spalding for single phase flow is also valid for the vapor flow in film boiling. Baum et al. [12] proposed a semi-empirical model in which the heat removal capability of the vapor film was assumed to be directly proportional to the average vapor velocity. By assuming the average vapor film thickness and vapor Reynolds number to be invariant in the vertical direction, the eddy diffusivity in turbulent flow was accounted for by using an effective thermal conductivity. The latter three models based on turbulent flow however predict significantly lower heat transfer coefficients than the experimentally determined values. The difference was attributed to the action of the interfacial waves and correlations to account for wave action were proposed.

For common fluids boiling on vertical surfaces of the length of the order of ten centimeters or so, the vapor film Reynolds number is certainly not high enough to justify the assumption of a turbulent vapor film. Turbulent vapor flow, if it exists, will be created by the time-dependent wave oscillation. This turbulent flow will be confined to the region under large amplitude waves. However, as will be seen later, the contribution of the region under large amplitude waves (bubbles) to the overall heat transfer rate is small.

From the brief discussion presented above it is clear that both laminar and turbulent models themselves do not explain the underprediction of the heat transfer data. These models need to be corrected for the influence of the wave action at the vapor–liquid interface. However, up to now the contribution of the wave action to the heat transfer has been obtained only by matching the predictions with the data and at present no mechanistic model that describes the various facets of saturated film boiling on vertical wall exists. The purpose of this work is to develop such a model. This model derives its support from visual observations of film boiling in two planes at right angles to each other. The experimental part of the study also provides previously nonexistent water data on a plane vertical surface.

Analysis

Visual observations of saturated film boiling on a vertical

[1]Work supported by NSF Grant CME 7918253
[2]Presently at Hughes Aircraft, El Segundo, CA
Contributed by the Heat Transfer Division for publication in the JOURNAL OF HEAT TRANSFER. Manuscript received by the Heat Transfer Division May 3, 1984.

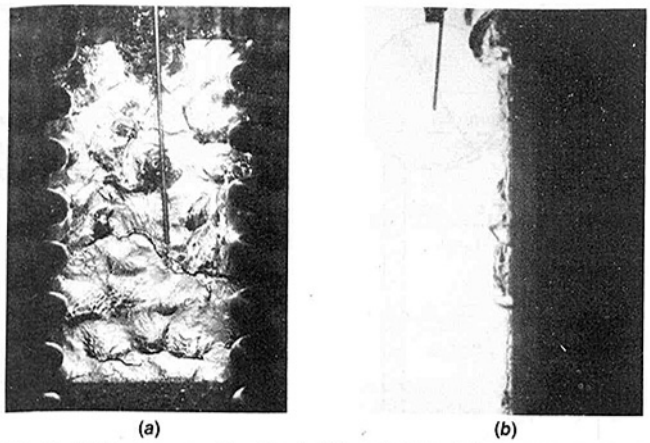

(a) (b)

Fig. 1 Natural convection film boiling of saturated water on a plane vertical surface ($\Delta T = 386$ K): (*a*) front view; (*b*) side view

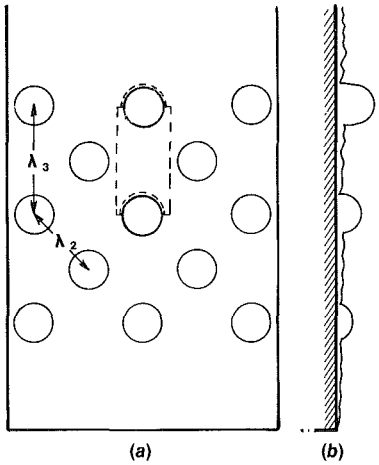

(a) (b)

Fig. 2 Configuration of the vapor–liquid interface for the present heat transfer model: (*a*) front view; (*b*) side view

surface reveal that the interface is far from smooth. The interface is covered with waves of different wavelengths and amplitudes. However, the waves can be generally grouped into two categories: the large-scale waves with a wavelength of the order of a few centimeters and the small-scale waves which resemble ripples on a gas/vapor–liquid interface. The wavelength of these ripples is about an order of magnitude smaller than that of long waves.

The amplitude of large-scale waves grows with distance from the leading edge. The peaks of these waves soon evolve into bulges of vapor which appear like bubbles attached to the interface. The height of these vapor bulges is one to two orders larger than the thickness of the film surrounding them.

The amplitude of the small waves is only a fraction of the average vapor film thickness. These waves are found only on the film area surrounding the large vapor bulges and their amplitude appears to be independent of distance from the leading edge. The waves can be seen in Figs. 1(*a*) and 1(*b*), which show natural convection film boiling of saturated water on a vertical surface at atmospheric pressure.

From the front view of the vapor–liquid interface during film boiling the bulges can be identified with the peaks of a three-dimensional wave. This is shown schematically in Fig. 2(*a*). The circles in Fig. 2(*a*) represent these peaks which appear like bubbles moving with the interface. The bubbles interrupt the vapor path such that the vapor path length is only the average distance between the bubbles rather than the total distance from the leading edge. These vapor bubbles act as vapor sinks so that vapor generated in the region preceding a bubble is fed into that bubble. For this reason the bulges/bubbles grow in size as they move upward. Figure 2(*b*) shows this behavior schematically. The drag experienced by the vapor flowing in the film occupying the region between the bubbles is balanced by the hydrostatic head difference between the vapor and the liquid.

Since the bulges of vapor bubbles are surrounded by the liquid, buoyancy forces act in the bubble resulting in bubble motion. The terminal velocity of the bubbles is given by the balance between buoyancy and the drag force exerted on the bubbles by the liquid. Figure 3 shows schematically the relative flow of liquid around these bubbles. The flow configuration is drawn assuming bubbles are fixed while the liquid and the wall move past them. Since bubbles are part of the interface and have to encounter liquid inertia, the bubbles and the interface move at the same velocity. It has been shown that in the absence of the bubbles' action the interfacial velocity is relatively small compared with the average vapor velocity in the film [5]. The existence of bubbles and their motion cause the interface to move faster at a velocity determined by the forces acting on these bubbles.

Visual observations show that waves start to appear at the interface at about half a wavelength away from the leading edge of the heater surface. Thus all locations on the surface beyond this point experience alternately the presence of bubbles and the film boiling region between the bubbles. Since the heat transfer under the film is expected to be different from that under the bubble, the steady-state heat transfer

Nomenclature

$A_c = \lambda_2^2$ = area of one cell, m^2

$A_f = \lambda_2^2 - \frac{\pi d^2}{4}$ = film area of each cell, m^2

B = film boiling property group defined in equation (23)

C_D = drag coefficient

c_{pv} = specific heat of vapor, J/kg K

D = drag force, N

$d = \frac{1}{2}\lambda_2$ = bubble diameter at the base, m

F_b = buoyancy force, N

g = gravitational acceleration, m/s^2

H = height of bubble top above film, m

h = film boiling heat transfer coefficient, W/m^2K

$\bar{h}_f$ = surface-average h of the film, W/m^2K

$\langle h \rangle$ = time-averaged heat transfer coefficient, W/m^2K

h_{fg} = latent heat of evaporation, J/kg

h'_{fg} = effective latent heat of evaporation, J/kg

$\mathrm{Ja} = \frac{c_{pv}\Delta T}{h_{fg}} \frac{\rho_l - \rho_v}{\rho_v}$ = Jacob number

k_v = vapor thermal conductivity, W/m K

l = effective flow path length, m

$l^\dagger$ = approximated l, m

Pr_v = Prandtl number of vapor

q_b = heat flow rate under a bubble per A_c, W/m^2

$q_{b,0}$ = q_b when $H = 0$

q_f = heat flow rate under film per A_c, W/m^2

R = radius of curvature of bubble, m

$\mathrm{Re} = \frac{\bar{u}\delta}{\nu_v}$ = vapor Reynolds number

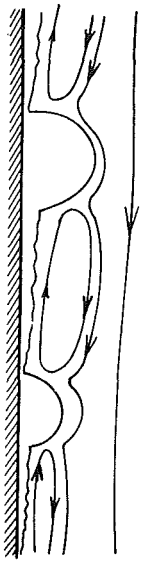

Fig. 3 The relative flow configuration of liquid around bubbles

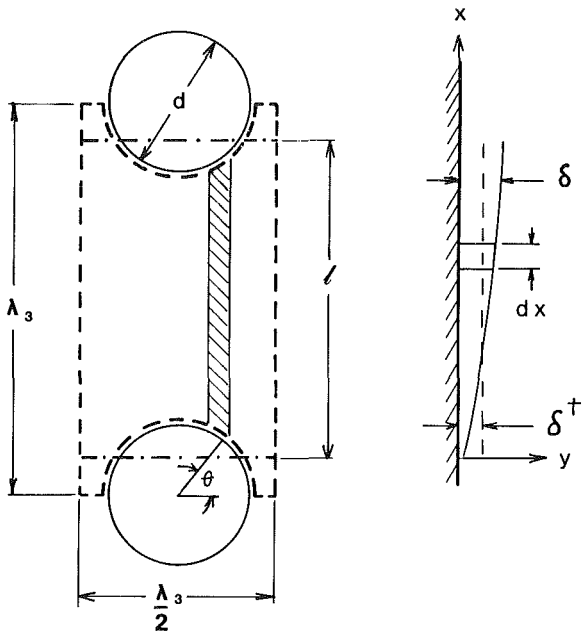

Fig. 4 Film configuration for heat transfer analysis and for calculating the flow path length

coefficient will be the time-averaged heat transfer coefficient over the movement of one cell. Also, because the same pattern is repeated all along the heater surface the heat transfer is anticipated to depend only weakly, if at all, on the distance from the leading edge. After bubbles grow large enough and detach from the interface, the wave pattern will reestablish and the entire process will repeat.

In the following, analyses of the heat transfer under the film and under the bubble are made. The bubble size and shape affect the bubble terminal velocity or the film interfacial velocity which in turn influences the film heat transfer. An expression for the bubble terminal velocity, which is necessary for the evaluation of the heat transfer under the film, is obtained.

(*a*) Heat Transfer Under the Thin Film. Analysis of this dominant contributor to heat transfer is based on the following assumptions:

(*i*) The wall is held at a constant temperature T_w while the liquid is maintained at its saturation temperature T_{sat}.

(*ii*) The vapor and liquid are incompressible.

(*iii*) The flow in the film is laminar.

(*iv*) The film is thin so that inertia terms in the momentum equation and convective terms in the energy equation can be ignored. However, correction for the sensible heat carried by vapor is made.

(*v*) The heat transfer by radiation is assumed to be additive to the heat transfer by conduction across the film. The error resulting from this assumption is small as long as contribution of the radiative heat transfer is not large.

(*vi*) The properties are evaluated at the mean film temperature. The momentum equation for the vapor film as shown in Fig. 4 is written as

$$\mu_v \frac{\partial^2 u}{\partial y^2} = -g(\rho_l - \rho_v) \tag{1}$$

The velocity profile satisfying the boundary conditions

$$\begin{aligned} u &= 0 \qquad \text{at} \quad y = 0 \\ u &= U_i = \text{ const at } y = \delta \end{aligned} \tag{2}$$

can be written as

$$u = \frac{g}{2\mu_v}(\rho_l - \rho_v)(y\delta - y^2) + U_i \frac{y}{\delta} \tag{3}$$

Nomenclature (cont.)

$Sh = \dfrac{c_{pv}\Delta T}{h_{fg}}$ = vapor superheat number
T_{sat} = saturation temperature of liquid, K
T_w = heater surface temperature, K
$\Delta T = T_w - T_{sat}$ = wall superheat, K
u = vapor velocity in film, m/s
U_i = vapor–liquid interfacial velocity, m/s
U_i^* = dimensionless U_i defined in equation (7*b*)
x = coordinate along heater surface for each cell, m
x^* = dimensionless x defined in equation (7*c*)
y = coordinate normal to x for each cell, m
z = distance from the leading edge, m
γ = a constant
δ = vapor film thickness, m
$\bar{\delta}$ = average δ where bubble attaches to the film, m
δ^* = dimensionless δ defined in equation (7*a*)
δ_0 = film thickness at $x = 0$
ϵ_l = emissivity of boiling liquid
ϵ_w = emissivity of heater surface
η = ratio of ripple amplitude to mean film thickness
θ = angular coordinate, rad
λ_2 = two-dimensional wavelength, m
$\lambda_3 = \sqrt{2}\lambda_2$ = three-dimensional wavelength, m
λ_D = the most dangerous wavelength, m
μ_v = vapor viscosity, kg/ms
ν_l = kinematic viscosity of liquid, m^2/s
ν_v = kinematic viscosity of vapor, m^2/s
ρ_l = liquid density, kg/m^3
ρ_v = vapor density, kg/m^3
σ = Stefan–Boltzmann constant

Mass and energy balance applied on a thin vapor section gives

$$\frac{d}{dx}\left[h'_{fg}\int_0^\delta \rho_v u dy\right] = \frac{k}{\delta}\Delta T \tag{4}$$

where h'_{fg} is the effective latent heat of evaporation introduced to take into account the vapor superheating and is evaluated as

$$h'_{fg} = h_{fg} + \frac{1}{2}c_{pv}\Delta T\left[1 - 1/\left(3 + \frac{g(\rho_l - \rho_v)\delta^2}{2\mu_v U_i}\right)\right]$$

Substitution of (3) in (4) gives

$$\frac{d}{dx}(\delta^4) + \frac{4\mu_v U_i}{(\rho_l - \rho_v)g}\frac{d}{dx}(\delta^2) = \frac{16\mu_v k_v \Delta T}{\rho_v(\rho_l - \rho_v)g h'_{fg}} \tag{5}$$

The vapor film thickness δ can be determined at any value of x if the film thickness δ_0 at $x=0$ is given. This represents an additional unknown to be found. Fortunately δ_0 can be assumed to be zero without a significant error in heat transfer. This is ascertained by noting that the constant film analysis [13] gives a heat transfer coefficient that differs only by 4 percent from the case in which δ_0 is assumed to be zero at $x=0$. By integrating equation (5) with $\delta=0$ at $x=0$, we get

$$\delta^4 + \frac{4\mu_v U_i}{g(\rho_l - \rho_v)}\delta^2 - \frac{16\mu_v k_v \Delta T x}{\rho_v h'_{fg}(\rho_l - \rho_v)g} = 0 \tag{6}$$

or in a dimensionless form

$$\delta^{*4} + 4U_i^*\delta^{*2} - 16x^* = 0 \tag{7}$$

where

$$\delta^* = \frac{\delta}{\left(\frac{\nu_v^2}{g}\right)^{1/3}} \tag{7a}$$

$$U_i^* = \frac{U_i}{\frac{g}{\mu_v}(\rho_l - \rho_v)\left(\frac{\nu_v^2}{g}\right)^{2/3}} \tag{7b}$$

$$x^* = \frac{x\mathrm{Ja}(\rho_l - \rho_v)^2}{\left(\frac{\nu_v^2}{g}\right)^{1/3}\mathrm{Pr}_v\rho_v{}^2} \tag{7c}$$

A nonnegative solution of (7) is

$$\delta^* = \sqrt{2}[(U_i^{*2} + 4x^*)^{1/2} - U_i^*]^{1/2} \tag{8}$$

The local heat transfer coefficient along the thin film is

$$h(x) = \frac{k_v}{\delta(x)} = \frac{k_v}{\delta^*}\left(\frac{\nu_v^2}{g}\right)^{-1/3} \tag{9}$$

The average heat transfer coefficient for the film $\bar{h}_f$ is defined as

$$\bar{h}_f = \frac{1}{l}\int_0^l h(x)dx. \tag{10}$$

Note that l is the effective flow path length. The derivation of effective flow path length is given in Appendix 1. Thus for a bubble-film pattern such as the one shown in Fig. 2(*a*) the average heat transfer coefficient for the film area can be readily evaluated with given values of λ_2 and U_i. The contribution of the film to the total heat transfer per unit cell area is

$$q_f = \bar{h}_f\frac{A_f}{A_c}\Delta T = \bar{h}_f\left(1 - \frac{\pi}{4}\frac{d^2}{\lambda_2^2}\right)\Delta T \tag{11}$$

(*b*) Estimation of the Vapor-Liquid Interfacial Velocity. Figure 3 shows the streamline pattern of liquid moving relative to the liquid-vapor interface. Because of the presence of bubbles or vapor bulges circulatory motion is expected to exist in the film area between two bubbles. The circulation will introduce additional drag on the vapor film-liquid interface. Since the interface is assumed to be rigid

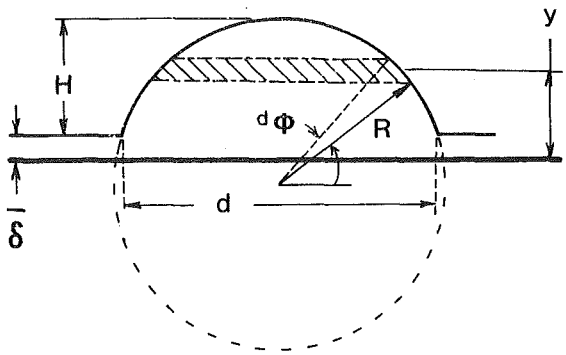

Fig. 5 Bubble geometry for calculation of heat transfer under bubbles

a discontinuity of shear stress will exist at the interface. The precise evaluation of the liquid drag is difficult to make; however, here this drag will be accounted for by including form drag on the bubble. The interfacial velocity is calculated by making a force balance on the bubbles. In making the force balance, the following assumptions are made:

(*i*) The buoyancy force acting on the bubble is calculated with a bubble volume which is the average of bubble volume from formation to detachment. The volume of a bubble at detachment is taken to be equal to the volume of a sphere having the same diameter as the diameter of the base of the bubble.

(*ii*) The viscous drag on the bubble is equivalent to that acting on a circular disk oriented parallel to liquid flow and having the same diameter as the base of the bubble.

(*iii*) The form drag on the bubble is equal to the viscous drag. The form drag accounts for discontinuity in shear stress resulting from the rigid wall assumption. By equating the sum of the form drag and the viscous drag with buoyancy, the interfacial velocity is obtained as

$$U_i = 0.37\left[\frac{(\rho_l - \rho_v)g}{\rho_l \nu_l{}^{1/2}}\right]^{2/3} d \tag{12}$$

The details of the derivation of equation (12) are given in Appendix 2.

(*c*) Heat Transfer Under Bubbles. Though heat transfer under the bubbles is small, it can not be neglected since bubbles cover a significant portion of the heater surface area. For the bubble geometry shown in Fig. 5, the following assumptions are made

(*i*) The film thickness around the bubble is assumed to be constant. The average value of this thickness is obtained as

$$\bar{\delta} = \frac{1}{2\pi}\int_0^{2\pi}\delta(\theta)d\theta = \frac{\delta(l)}{2}$$

(*ii*) The bubble is a segment of a sphere.

(*iii*) The heat transfer through the bubble is by conduction only.

(*iv*) The properties are evaluated at mean film temperature.

Then the heat transfer rate under the bubble is calculated as [13]

$$Q_b = \Delta T 2\pi R k_v \ln\left[1 + \frac{H}{\bar{\delta}}\right] \tag{13}$$

The heat flux per unit cell area is obtained from equation (13) as

$$q_b = \frac{\Delta T 2\pi R k_v}{\lambda_2^2}\ln\left[1 + \frac{H}{\bar{\delta}}\right] \tag{14}$$

In equations (13) and (14) H is defined as

$$H = R\left(1 - \sqrt{\left(\frac{d}{2R}\right)^2}\right) \tag{15}$$

From equation (15) as $H\to 0$ or $R\to\infty$, the heat flux approaches that under the film and is given by

$$q_{b,0} = \frac{k_v}{\bar{\delta}} \frac{\pi d^2}{4\lambda_2^2} \Delta T \tag{16}$$

The ratio of heat fluxes given by equations (14) and (16) is obtained as

$$\frac{q_b}{q_{b,0}} = \frac{8R\bar{\delta}}{d^2} \ln\left[1 + \frac{H}{\bar{\delta}}\right] \tag{17}$$

Figure 6 shows a plot of this ratio as a function of H/R for $d = 0.01075$ m and $\bar{\delta} = 0.0002$ m. It is seen that for H/R from 0.1 to 1, the ratio $q_b/q_{b,0}$ changes only from 0.34 to 0.25. This relatively small change indicates that right after a peak of the large-scale waves evolves into a vapor bulge, the heat transfer under the bubble will quickly approach a near-constant value. This simple evaluation also shows that heat transfer under the bubbles cannot be totally neglected as has been done by Berenson [14]. In the present analysis a mean value of 0.3 for $q_b/q_{b,0}$ was used.

(d) Overall Heat Transfer Coefficient. Near the leading edge the interface is free of any waves and Bromley type analysis is applicable for the film. The heat transfer coefficient very close to the leading edge is thus a function of distance from the leading edge but is independent of time. At short distances away from the leading edge, waves with both long and short wavelengths develop. Vapor bulges or bubbles and ripply film sweep a given location on the wall alternatively. Since rates of heat transfer under the bubble and the film are different, the heat transfer coefficient is time dependent but is independent of distance from the leading edge if the cell model is based on the average conditions between formation and detachment of the bubble. The time-averaged heat transfer coefficient can be written as

$$\langle h \rangle = \underbrace{C\bar{h}_f\left(1 - \frac{\pi d^2}{4\lambda_2^2}\right)}_{\text{under thin film}} + \underbrace{\frac{q_b}{q_{b,0}} \cdot \frac{k_v}{\bar{\delta}} \frac{\pi d^2}{4\lambda_2^2}}_{\text{under bubble}}$$

$$+ \underbrace{\frac{\sigma}{\left[\frac{1}{\epsilon_w} + \frac{1}{\epsilon_l} - 1\right]} \frac{[T_w^4 - T_{\text{sat}}^4]}{[T_w - T_{\text{sat}}]}}_{\text{radiation}} \tag{18}$$

In equation (18) the constant C accounts for the enhancement in the film heat transfer as a result of the presence of ripples. Since the heat transfer rate through the film varies as the inverse of the film thickness, the time-averaged heat transfer rate will be different from that based on the average film thickness. Coury and Dukler [10] have shown that for sinusoidal wave, the constant C is

$$C = \frac{1}{\sqrt{1 - \eta^2}} \tag{19}$$

where η is the ratio of ripple amplitude to the mean film thickness. For $\eta = 0.5$, the constant C will have a value of 1.15. For assumed values of η and the ratio d/λ_2, the evaluation of the time-averaged heat transfer coefficient from equation (18) solely depends on the knowledge of the dominant wavelength λ_2.

(e) Prediction of Large-Scale Wavelength λ_2. A linearized two-dimensional stability analysis for film boiling on a vertical surface has been carried out by Sherman [7]. The analysis is similar to the earlier work of Ünsal and Thomas [15] for film condensation and takes into account the evaporation at the interface. In the present work such an analysis was redone [13] with the assumptions of laminar flow in the film and a velocity U_i at the interface. The most dominant unstable wavelength was found to be

$$\lambda_D = f(\text{Re}, \text{Pr}_v, Sh) \tag{20}$$

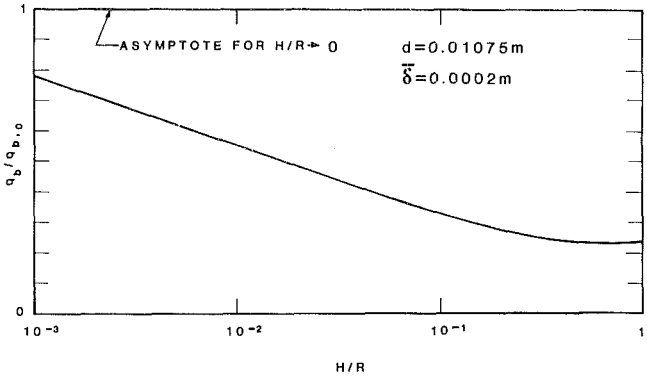

Fig. 6 Variation of $\frac{q_b}{q_{b,0}}$ with $\frac{H}{R}$

The two-dimensional wavelength λ_2 used in the present work is expected to be the same as the most dangerous wavelength λ_D given by equation (20).

From equation (20) it would seem that the wavelength will be a function of distance from the leading edge since the Reynolds number depends on this distance. However, the present observations show that the peaks of the long wavelengths act as vapor sinks and interrupt the flow regularly. The effective flow path length is about a wavelength. The work of Dhir and Taghavi-Tafreshi [16] shows that the peaks of the waves always locate themselves about half a wavelength away from the end. Thus for a wave pattern to develop, the distance from the leading edge of the plate should be about 1 1/2 λ_D, or, to determine the dominant wavelength from equation (20), the Re should be evaluated at 1 1/2 λ_D from the leading edge.

Figure 7 shows the wavelength λ_D predicted from the stability theory as a function of Re for water vapor at $Sh = 0.35$. Also plotted on this figure is the relationship between λ_D and Re when Re is evaluated at λ_D, 1 1/2 λ_D, and $2\lambda_D$ using Bromley-type analysis with nonzero U_i. The point of intersection of the two curves obtained from the stability theory and the heat transfer theory gives the expected value of λ_D. For the heat transfer curve evaluated at λ_D, the point of intersection gives $\lambda_D = 8$ mm and Re = 18. The evaluation at 1 1/2 λ_D gives $\lambda_D = 22$ mm at Re = 49, and finally the heat transfer curve evaluated at $2\lambda_D$ yields $\lambda_D = 57$ mm at Re = 119.

Experiments

All of the film boiling data were obtained under steady-state conditions. The test apparatus and the experimental procedure employed were the same as those already described in the previous paper on transition boiling.

Results and Discussion

Saturated film boiling heat transfer data for water were taken at several wall superheats. The data were found to be highly reproducible. One such set of data for wall superheats of 150, 200, 300, and 400 K is plotted in Fig. 8. These data were taken at 8, 26, 52, and 77 mm from the leading edge. At all the locations the heat transfer coefficient is seen to decrease with wall superheat. At a given superheat the heat transfer coefficient data show little dependence on the distance from the leading edge. The data at all the locations lie within ±5 percent of each other. This is almost the magnitude of uncertainty in the data.

The film boiling heat transfer coefficient data divided by the fluid property group that results from laminar film analysis such as that performed by Bromley are plotted in Fig. 9 as a function of wall superheat. After elimination of the

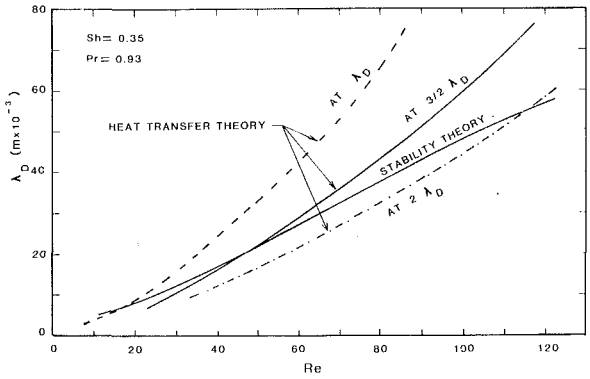

Fig. 7 The dependence of the most dangerous wavelength λ_D on Re obtained from heat transfer analysis and from stability theory

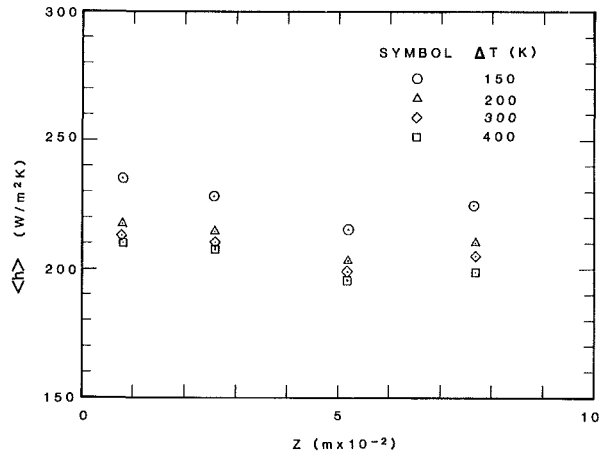

Fig. 8 Measured heat transfer coefficient along the vertical surface

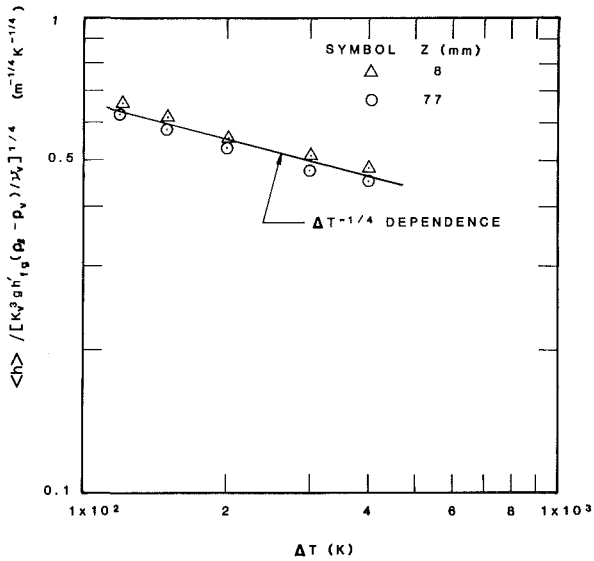

Fig. 9 The dependence of measured heat transfer coefficient on wall superheat

dependence of the fluid properties on temperature, the data are seen to correlate well with wall superheat as $\Delta T^{-1/4}$. This is exactly the dependence which is predicted from Bromley-type analysis and is indicative of the fact that the vapor film is laminar.

The heat transfer coefficients obtained at 77 mm from the leading edge are plotted in Fig. 10 for various wall superheats. While plotting the data the range of uncertainty in the data is also marked. The solid lines show the prediction from the present model when the correction for the sensible heat of the vapor is made from the present analysis and that of Koh [5].

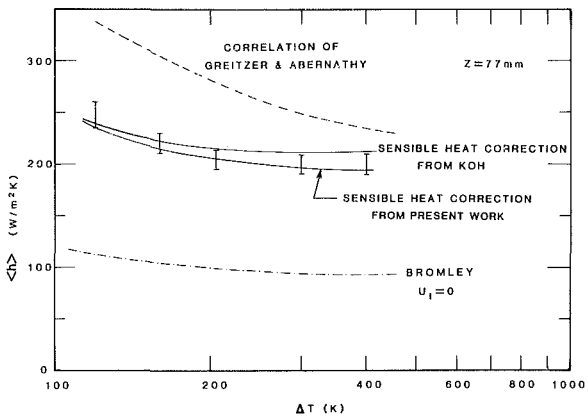

Fig. 10 Comparison of predicted and observed dependence of heat transfer coefficient on wall superheat

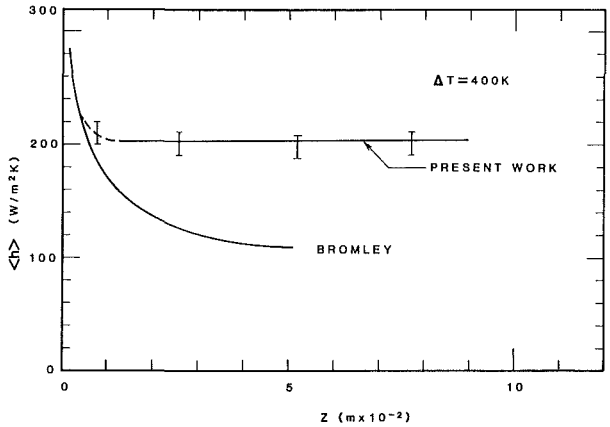

Fig. 11 Comparison of predicted and observed dependence of heat transfer coefficient on distance from leading edge

In obtaining the contribution of the radiative heat transfer, the temperature-dependent emissivity ($\simeq$0.1) of polished copper was used. The emissivity of water was taken to be 1.0. For the temperatures of interest the radiative contribution to the total heat transfer coefficient was less than 2 percent. The present model with either of the corrections for vapor superheat fares very well with the data. The heat transfer coefficients obtained with the correction to latent heat of vaporization made from Koh's analysis are generally 3–6 percent higher. In Koh's analysis both inertia and convective terms in the momentum and energy equation of the vapor were included. Correction made from his analysis should thus be considered to be more accurate. In Fig. 10, the predictions made from Bromley's laminar film analysis with rigid interface and the correlation of Greitzer and Abernathy [8] are also plotted. It is seen that Bromley's model yields heat transfer coefficients that are about 50 percent lower than the data but it gives a correct dependence of heat transfer coefficient on wall superheat. The model of Greitzer and Abernathy gives heat transfer coefficients that are not only 20–40 percent higher than the data but the predicted dependence on wall superheat is also incorrect.

For a wall superheat of 400 K, the heat transfer coefficient obtained at various locations from the leading edge are plotted in Fig. 11. The data as well as the present model show hardly any dependence of the heat transfer coefficient on the distance z. Bromley's model predicts a continuous reduction in the heat transfer with distance. Predictions made from Bromley's model with nonzero U_i may be valid in the first 8 mm from the leading edge. The present model is valid only at distances greater than 10-12 mm from the leading edge. The transition from Bromley's model to the present model will occur in the intermediate region. The visual observations

showed that the interface in this intermediate region was free of large-scale waves but was occupied by ripples.

Validation of the Model With Visual Observations. Still pictures and movies of the film boiling process were taken in two normal planes. The photographs show that surface waves evolve into vapor bulges as they move away from the leading edge. The height of these vapor bulges is one or two orders of magnitude larger than the film thickness. As bubbles grow larger, they are torn away from the vapor film. A three-dimensional wave structure on the vapor–liquid interface is clearly evident from the photographs. However, no signs of film breakup have been discovered.

At a wall superheat of 400 K, 14 bubbles are found to be present on the interface. For a total wall surface area of 64.9 cm^2, this corresponds to a cell area of 4.63 cm^2 or a two-dimensional wavelength $\lambda_2 = 21.5$ mm. In contrast the wavelength obtained from the stability analysis is about 24 mm. The three-dimensional wavelength λ_3 is found to be 29 mm. This gives the ratio of observed three-dimensional and two-dimensional wavelengths to be 1.35 as opposed to the theoretical value of 1.414. The ratio d/λ_2 of the average bubble base diameter to the two-dimensional wavelength is found to be 0.61 while the value assumed in the analysis was 0.5. From the movies the bubble velocity at a wall superheat of 400 K is found to lie between 2.8 and 3 m/s. The value obtained from equation (12) is 3.05 m/s.

The location b where a bubble will detach from the interface can be determined by making an overall energy balance as[3]

$$\langle h \rangle \Delta T \frac{\lambda_3}{2} \frac{b^2}{U_i} = \frac{\pi d^3}{6} \rho_v h_{fg}$$

or

$$b = \left[\frac{\pi d^3 \rho_v h_{fg} U_i}{3\lambda_3 \langle h \rangle \Delta T} \right]^{1/2} \tag{21}$$

For film boiling of water at a wall superheat of 400 K, equation (21) gives b to be 43 mm. This distance is equivalent to $2\lambda_2$. The observations made from the movies indicated that the first bubbles detached between 2.5 to 3 λ_2 from the leading edge. The observed bubble base diameter is about 20 percent larger than that assumed in the analysis. If the observed value of d was used in equation (21), the predicted value of b will be about the same as that obtained from the movies.

Validation of the Model With Experimental Data of Previous Studies. Except very close to the leading edge, every location of the boiling surface will experience alternately the presence of a vapor bubble and a thin film. The vapor film and the bubble are associated with different heat transfer coefficients. Figure 12 shows the variation of the local heat transfer coefficient normalized with its time-averaged value with dimensionless time. The time is non-dimensionalized with the time period of one cycle. The time period for repetition of a cycle is λ_3/U_i, which in the experiments was about 15 ms. The thermocouples used in the present work had a time constant greater than 15 ms and thus did not show any fluctuations in temperature with time. Coury and Dukler [10] in their experiments with Freon-113 used microthermocouples on a nickel block and were able to observe the fluctuation in wall temperature with time. Interestingly, the signature of the dimensionless heat transfer coefficient obtained from their thermocouple data and shown in Fig. 12 very much resembles that predicted from the present model.

The present heat transfer model, when compared to the film boiling data of Sherman [7] on a vertical cylinder of 12.7 mm in diameter, underpredicts the heat transfer coefficients for water by nearly 10 percent. At a wall superheat of 400 K, the

[3] Sensible heat correction has been ignored in making this energy balance.

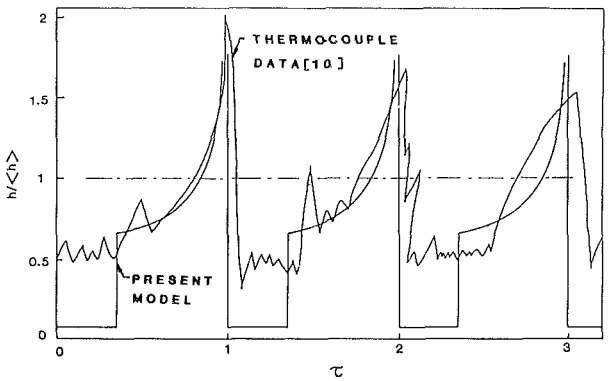

Fig. 12 The predicted time variation of heat transfer coefficient at a vertical location along the wall

present experiments showed a wavelength of 29 mm along the vertical length while Sherman observed a wavelength of 22 mm. It should be mentioned at this point that, in the present model, the three-dimensional wave is assumed to align with the vertical axis. This assumption has been confirmed from visual observations. Physically also, it seems more realistic that the longer wavelength should align with the longer side. However, if the two-dimensional wave were assumed to align with the vertical axis, the predicted time-averaged heat transfer coefficient would be about 8 percent higher. This is shown in Appendix 3. The circumference of the cylindrical heater used in Sherman's experiments was about 40 mm. For film boiling of water, this size cannot support 2 λ_2, which is the minimum requirement for symmetry. Thus it appears that the two-dimensional wavelength aligned along the vertical direction in Sherman's experiments with water. With this consideration, the present two-dimensional model underpredicts Sherman's water data by only a few percent. For Freon-113, Sherman observed a wavelength of 12.7 mm along the vertical length of the heater. In this case a three-dimensional wave could possibly align along the vertical axis. The present three-dimensional model underpredicts the Freon data by only about 5 percent. In this calculation the emissivity of the inconel surface of the cartridge heater in his experiments was taken to be 0.7. Such a value is justified since Freon-113 decomposes at high temperatures which in turn leads to deposits on the surface. The model also correctly predicts the observed dependence of the heat transfer coefficient on wall superheat and distance from the leading edge.

Conclusions

1 Film boiling transfer data obtained on a 10.3-cm-tall vertical surface show no dependence of heat transfer coefficient on distance from the leading edge.

2 The heat transfer data show the film to be laminar. The evolution into bubbles of the peaks of long waves results in shortening of the flow path length and an increase in the heat transfer rate.

3 A model which accounts for the presence of both long and short waves at the interface and the heat transfer under the film and the vapor bubble has been developed. The model fares well with the data.

4 The dominant wavelength, the spacing of the bubbles, the size of the bubbles, and location of detachment of bubbles predicted from the analysis compare well with the data.

References

1 Bromley, L. A., "Heat Transfer in Stable Film Boiling," *Chem. Engr. Prog.*, Vol. 46, 1950, pp. 221–227.

2 Nusselt, W., "Die Oberflachenkondensation des Wasserdampfes," *VDI Z.*, Vol. 60, 1916, pp. 541–569.

3 McFadden, P. W., and Grosh, R. J., "High Heat Flux Heat Transfer Studies—An Analytical Investigation of Laminar Film Boiling," AEC Res. and Dev. Rep., ANL-6060, 1959.

4 Cess, R. D., "Analysis of Laminar Film Boiling From a Vertical Plate," Res. Rep. 405 FF 340-R2-X, Westinghouse Research Lab., 1959.
5 Koh, J. C. J., "Analysis of Film Boiling on Vertical Surfaces," ASME JOURNAL OF HEAT TRANSFER, Vol. 84, No. 1, 1962, pp. 55-62.
6 Anderson, J. G. M., "Low-Flow Film Boiling Heat Transfer on Vertical Surfaces, Part I: Theoretical Model," *AIChE Symp. Ser.*, Vol. 73, No. 164, 1976, pp. 2-6.
7 Sherman, D. C., "Natural Convection Film Boiling on a Vertical Surface," Ph.D. Dissertation, California Institute of Technology, Pasadena, CA, 1980.
8 Greitzer, E. M., and Abernathy, F. H., "Film Boiling on Vertical Surfaces," *Int. J. Heat Mass Transfer*, Vol. 15, 1972, pp. 475-491.
9 Hsu, Y. Y., and Westwater, J. W., "Approximate Theory for Film Boiling on Vertical Surfaces," *Chem. Engr. Prog. Symp. Ser.*, Vol. 56, No. 30, 1960, pp. 15-24.
10 Coury, G. E., and Dukler, A. E. "Turbulent Film Boiling on Vertical Surfaces. A Study Including the Influence of Interfacial Waves," *Proc. Inter. Heat Transfer Conf.*, Paris, 1970, Paper No. B.3.6.
11 Suryanaryana, N. V., and Merte, H., Jr., "Film Boiling on Vertical Surfaces," ASME JOURNAL OF HEAT TRANSFER, Vol. 94, 1972, pp. 371-384.
12 Baum, A. J., Purcipile, J. C., and Dougall, R. S., "Transition and Film Boiling Heat Transfer From Vertical Surfaces," ASME Paper No. 77-HT-82, 1977.
13 Bui, T. D., "Film and Transition Boiling Heat Transfer on Vertical Surfaces," Ph.D. Dissertation, University of California, Los Angeles, CA, 1984.
14 Berenson, P. J., "Film Boiling Heat Transfer From a Horizontal Surface," ASME JOURNAL OF HEAT TRANSFER, Vol. 83, 1961, pp. 351-358.
15 Unsal, M., and Thomas, W. C., "Linearized Stability Analysis of Film Condensation," ASME JOURNAL OF HEAT TRANSFER, Vol. 100, 1978, pp. 629-634.
16 Dhir, V. K., and Taghavi-Tafreshi, K., "Hydrodynamic Transitions During Dripping of a Liquid From Underside of a Horizontal Tube," ASME Paper No. 81-WA/HT-12, presented at the ASME Winter Annual Meeting, November 15-20, 1981, Washington, D.C.

APPENDIX 1

Evaluation of the Effective Flow Path Length

Owing to the presence of bubbles the heat transfer rate over the film area per unit cell is obtained by summing up the heat transfer rates over narrow strips as shown in Fig. 4. The result of such an integration is

$$q_f = \frac{B}{A_c}\left[\frac{1}{2}\int_0^{\pi}(\lambda_3 - d\sin\theta)^{3/4} d\sin\theta\, d\theta + {\lambda_3}^{3/4}\left(\frac{\lambda_3}{2} - d\right)\right] \quad (22)$$

where

$$B = \gamma\left[\frac{\rho_v k_v^3 g(\rho_l - \rho_v) h_{fg} \Delta T^3}{\mu_v}\right]^{1/4} \quad (23)$$

The effective vapor flow length l is related to the heat flux as

$$q_f = \frac{B}{A_c} l^{3/4} \frac{\lambda_3}{2} \quad (24)$$

Combining equations (22) and (24) yields

$$l = \left[2\left\{\frac{\frac{1}{2}\int_0^{\pi}(\lambda_3 - d\sin\theta)^{3/4} d\sin\theta\, d\theta + {\lambda_3}^{3/4}\left(\frac{\lambda_3}{2} - d\right)}{\lambda_3}\right\}\right]^{4/3} \quad (25)$$

An approximate value of this length l can be obtained by using the length $l^{\dagger}$ that would give the same area of film per cell

$$l^{\dagger}\frac{\lambda_3}{2} = \frac{\lambda_3^2}{2} - \frac{\pi d^2}{4} \quad (26)$$

$$l^{\dagger} = \sqrt{2}\lambda_2 \frac{A_f}{A_c} \quad (27)$$

The error in heat transfer rate with the use of $l^{\dagger}$ instead of l is only a few percent.

APPENDIX 2

Estimation of Bubble Velocity

With the assumption that the average bubble volume from its inception to detachment is half of that of a sphere of diameter equal to the base of the bubble, the buoyancy force acting on the bubble can be written as

$$F_b = (\rho_l - \rho_v) g \frac{\pi}{12} d^3 \quad (28)$$

From the flow configuration shown in Fig. 3, the drag in the vertical direction results from flow near the top of the bubble. Assuming the top of the bubble to be equivalent to a circular disk of diameter d, the drag coefficient for laminar flow over the disk with zero angle of attack can be written as

$$C_D = \frac{1.328}{\left(\frac{U_i x}{\nu_l}\right)^{1/2}} \quad (29)$$

where x is the length of travel of the fluid on the plate. The total viscous drag on the disk is obtained by carrying out an integration in a direction normal to the flow. Such an integration yields

$$D = 0.58 \rho_l {\nu_l}^{1/2} {U_i}^{3/2} d^{3/2} \quad (30)$$

Assuming that viscous and form drags are equal and equating the buoyancy and drag forces, an expression for U_i is obtained as

$$U_i = 0.37\left[\frac{(\rho_l - \rho_v) g}{\rho_l {\nu_l}^{1/2}}\right]^{2/3} d \quad (31)$$

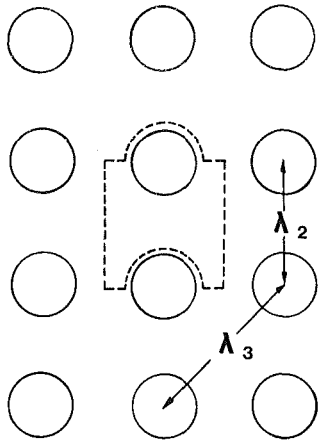

Fig. 13 An alternative configuration of the vapor-liquid interface

APPENDIX 3

Alternate Configuration of the Interface

An alternative configuration of the interface is shown in Fig. 13. Here the two-dimensional wavelength λ_2 is oriented along the vertical axis. Thus vapor flows along λ_2 instead of λ_3. It is seen that though the cell area remains the same, the effective flow path length l is shorter. In fact it can be shown that

$$l_{\lambda_2} = \frac{1}{\sqrt{2}} l_{\lambda_3} \quad (32)$$

Since heat transfer coefficient in the film is nearly proportional to $l^{-1/4}$, the overall heat transfer coefficient will be nearly proportional to $l^{-1/4}$. Thus

$$\langle h \rangle_{\lambda_2} \simeq (2)^{1/8} \langle h \rangle_{\lambda_3} \quad (33)$$

The difference is only about 8 percent.

Thermosyphon Boiling in Vertical Channels

A. Bar-Cohen[1]
Fellow ASME

H. Schweitzer

Department of Mechanical Engineering,
Ben Gurion University,
Beer Sheva, Israel

The high heat flux capability and modest temperature differences associated with boiling heat transfer make immersion cooling one of the primary candidates for VHSIC and VLSI microelectronic component thermal control. While the literature contains many references to pool boiling heat transfer from single *integrated circuit packages or transistor cans, there is as yet little information on ebullient thermal transport from vertical* arrays *of parallel, densely packaged Printed Circuit Boards or ceramic modules. The present study represents an attempt to explore the thermal performance of such ebullient cooling systems by analytically and empirically investigating boiling heat transfer in water from a pair of flat, isoflux plates. Experimental results for wall temperature as a function of axial location, heat flux, and plate spacing are presented. A theoretical model for liquid flow rate through the channel is developed and used as a basis for correlating the rate of heat transfer from the channel walls.*

Introduction

The continued growth in functional density of microelectronic devices is today constrained by available thermal design and heat removal techniques. Rapidly escalating heat fluxes at the package level, as line widths shrink and chip gate-counts increase, have prompted a broad reassessment of thermal control strategies in the electronics industry. Complete immersion of electronic assemblies in fluids of appropriately high dielectric strength and low dielectric constant offers a most promising alternative to conventional thermal control measures. Immersion cooling has been the subject of considerable research [1–7] and has recently been adopted by Cray Research Inc. for the Cray-2 "supercomputer" [8].

The successful implementation of this technique in high-power radar equipment, as far back as the 1940s [9–11], and the laboratory data gathered during the past two decades on immersion of logic and memory devices, provide a firm base for the engineering development of immersion cooling. In both these application categories reliance on boiling heat transfer at the heat-dissipating surfaces can provide a benign local environment for microelectronic devices and accommodate substantial heat flux variations while minimizing temperature excursions and component failure rates.

While the literature contains many references to pool boiling heat transfer from single integrated circuit packages or transistor cans, there is as yet little information on ebullient thermal transport from vertical arrays of parallel, densely packaged Printed Circuit Boards (PCB) or ceramic modules. Saturated boiling from the surfaces of such elements can be expected to produce an axial quality or vapor fraction gradient in the vertical channel formed by each pair of elements. This vapor fraction may be expected to increase the rate of fluid circulation past the PCB, in thermosyphon-like fashion, and modify the thermal performance relative to simple pool boiling. The influence of PCB spacing on the heat transfer rate from the individual elements is of particular concern in electronic cooling applications where miniaturization and minimization of packaging volume is of paramount importance.

The present study represents an attempt to explore the thermal characteristics of such ebullient cooling systems, by analytically and experimentally investigating boiling heat transfer from a pair of flat, closely spaced, isoflux plates immersed in saturated water.

Theoretical Background

Two-Phase Flow Regimes in a Vertical Channel. The axial variation in steam quality, or vapor fraction, in an ebulliently heated channel gives rise to distinct flow regimes in various sections of the channel. While the precise location of the flow regime boundaries depends on fluid and geometric parameters, as well as the imposed heat flux, it has been found that annular flow, with a thin liquid film on the pipe wall, is the dominant regime in saturated, vertical channel, two-phase flow. Specifically, for water/steam mixtures at near-atmospheric pressure, transition from slug to annular flow in vertical up-flow is often found to occur at flow qualities of approximately 5 percent. Empirical, vertical flow, heat transfer correlations for water are, thus, often identified as pertaining to either subcooled and low-quality (≤ 5 percent) flow or high-quality flow.

Heat Transfer Rate. One of the most widely used correlations for flow boiling heat transfer in vertical pipes is that of Chen [12]. In this approach, the two-phase heat transfer coefficient is assumed to be a summation of boiling and convective components. The boiling component h_b is derived from the Forster and Zuber correlation for nucleate pool boiling [13] while the convective component h_c is based on the standard forced convection correlations, with the Reynolds number modified to reflect liquid flow alone.

The Chen correlation includes two empirical factors F_b and F_c which were evaluated by Chen for a wide range of data and presented in graphical form [12]. The F_b factor, multiplying the usual boiling coefficient, is meant to accommodate the suppression of nucleate boiling due to reduced liquid film thickness and was found by Chen to vary from 0.9 to 0.1 as the two-phase Reynolds number varied from 10^4 to 10^6. The convective factor F_c was postulated by Chen to reflect heat transfer enhancement due to the high-velocity core flow of vapor and was found to increase from 1 to 100 as the Martinelli parameter X_{tt} varied from 10 to 10^{-2}.

In a more recent study by Bjorge, Hall, and Rohsenow [14], the method of superpositioning for correlating forced convection boiling heat transfer data is extended to cover subcooled to high quality flows, using single-phase and two-phase forced convection equations, a pool boiling for-

[1]Currently at Control Data Corporation, Minneapolis, Minnesota

Contributed by the Heat Transfer Division and presented at the ASME Winter Annual Meeting, Boston, Massachusetts, November 13–18, 1983. Manuscript received by the Heat Transfer Division July 12, 1983.

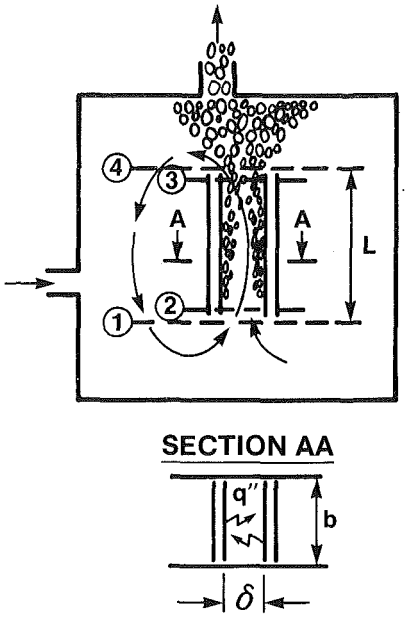

Fig. 1 Schematic and geometric definition of thermosyphonic boiling in parallel-plate channel

mulation, and a boiling incipience criterion. Only one empirically determined coefficient is needed in this approach and the agreement with water data is better than that provided by the Chen correlation.

Comparison of these two approaches reveals that, in the Bjorge, Hall, and Rohsenow formulation, the Chen boiling suppression factor F_b is replaced by an analytic function based on the incipient superheat, i.e., $1 - (\Delta T_{sat,ib}/\Delta T_{sat})^3$. Similarly, the Chen empirical convective enhancement factor F_c is replaced by an analogous function $F(X_{tt})/F_2$ which is again dependent on the Martinelli parameter, as well as the Reynolds and Prandtl numbers for the liquid.

Thermosyphonic Channel Flow. Use of the preceding correlations for the two-phase heat transfer rate requires knowledge of the mass flux G traversing the channel of interest. In the present configuration, this flow rate arises from density differences between the two-phase mixture in the channel and the ambient saturated liquid surrounding the channel. Unfortunately, however, the literature contains no ready expression for this thermosyphonic flow rate and its determination, albeit in approximate fashion, is a central aspect of the present study.

The requisite flow rate can, in principle, be found by use of an extended Bernoulli equation formulation along an assumed streamline, starting at the channel inlet and looping back through the ambient fluid to this same point. Along this path, marked in Fig. 1, all pressure changes must sum to zero. The axial pressure variations in the channel are composed of inlet and exit losses and, most importantly, flow losses in the channel itself.

Following [15] the single-phase inlet loss may be taken as

$$\Delta P_{\text{inlet}} = 0.65\rho_f u_i^2/2g \tag{1}$$

Based on the data presented in [16], the exiting two-phase mixture can be expected to dissipate the entire velocity head, i.e., $\Delta P_{\text{exit}} = \rho_f u_L^2/2g$, so that the static pressure at the channel outlet would be approximately equal to the static ambient pressure at that height.

The channel pressure drop incorporates the contributions of shear stress, fluid acceleration, and hydrostatic terms. For the flow of an ideal homogeneous mixture of vapor and liquid, this ΔP can be determined in a straightforward manner [17]. However, for the flow of a real two-phase mixture, and especially in the post-bubbly regimes, it has been found necessary to express this pressure drop in terms of empirically determined factors accounting for (1) the variation of vapor fraction with quality, and (2) shear stress between the mixture and the wall as well as between the two phases.

In their classic study, Lockhart and Martinelli [18] developed a systematic presentation of such factors for adiabatic pipe flow. These were later modified by Martinelli and Nelson [19] for the flow boiling of water in circular pipes. Unfortunately, these factors are, strictly speaking, valid only for water/steam flow in circular pipes and may well be inappropriate for calculating two-phase pressure drop in a parallel-plate channel.

As a result of this limitation and in the absence of detailed pressure drop data for a parallel-plate channel, which would make it possible to determine the correct Martinelli/Nelson factors for this geometry, attention must be turned toward an alternate pressure drop formulation. This formulation, presented in detail in [20], is based on the assumption of an axially invariant slip ratio S ($\equiv u_g/u_f$) between the liquid and vapor phases and a further assumption that shear stress along the channel walls is governed by the liquid properties. With these assumptions, the in-channel pressure drop for saturated two-phase flow in a uniformly heated channel can be shown to equal [20]

Nomenclature

A = channel cross-sectional area
C_{fr} = friction factor
c_p = specific heat
C_{sf} = characteristic constant, defined in equation (4)
D_b = bubble departure diameter
D_e = hydraulic diameter
g = gravitational acceleration
g_c = gravitational constant
G = mass flux (mass flow rate per unit area)
h = heat transfer coefficient
i_{fg} = latent heat of vaporization
k = thermal conductivity
L = channel length
P = pressure
ΔP = pressure difference
Pr = Prandtl number $\equiv c_p\mu/k$
q'' = heat flux
Re = Reynolds number
S = slip ratio
T = temperature
u = velocity
v = specific volume
x = quality
X_{tt} = Martinelli parameter
z = length location
α = void fraction
δ = channel width (Fig. 2)
ϕ, γ = weighting functions in equation (3)
μ = dynamic viscosity
ρ = density
σ = surface tension

Subscripts

b = boiling
c = convection
CSR = Constant Slip Ratio
f = liquid
fg = liquid vapor transition
fr = friction
g = gas
incip = boiling incipience
ib = boiling incipience
inlet = inlet
L = outlet from channel
MN = Martinelli/Nelson
s = saturation state
ST = surface tension
TP = two phase
w = wall
z = length location

$$\Delta P_{2-3} = \frac{2C_{fr}G^2 v_f}{D_e} \frac{\left[1+\left(\frac{v_g}{Sv_f}-1\right)x_L\right]^3 - 1}{3\left(\frac{v_g}{Sv_f}-1\right)\frac{x_L}{L}}$$

$$+ G^2 v_f x_L \left[(S-1)\left(\frac{v_g}{Sv_f}-1\right)x_L + \left(\frac{v_g}{Sv_f}-1\right) + (S-1)\right] \quad (2)$$

$$+ \frac{g(\rho_f-\rho_g)\frac{Sv_f}{v_g}\frac{L}{x_L}}{\left(1-\frac{Sv_f}{v_g}\right)^2} \ln\left[\left(\frac{Sv_f}{v_g}-1\right)x_L + 1\right]$$

$$+ \rho_f g L - \frac{\rho_f - \rho_g}{1+\frac{Sv_f}{v_g}} gL$$

The availability of the Martinelli/Nelson and the Constant Slip Ratio relations for the in-channel pressure drop makes it possible to determine the requisite mass flow rate through the parallel plate channel. Prior to performing the necessary algebraic manipulation it is well to recall that $D_e = 2\delta$ and that the flow quality equals $2q''z/G\delta i_{fg}$ for symmetric, isoflux heating or $q''z/g\delta i_{fg}$ when one channel wall is adiabatic. It should be noted, as well, that solution for G generally requires iterative or computer-assisted calculations.

Analytical Development of Heat Transfer Relation

Introduction. The successful correlation of the heat transfer rate in flow boiling by Chen [12] and Bjorge, Hall, and Rohsenow [14], as well as the more modest success of other researchers, appears to validate reliance on a superposition of convective and boiling heat transfer mechanisms in evaluating two-phase thermal transport for annular-like flows. It may thus be anticipated that the surface heat flux in thermosyphonic boiling will be expressible as

$$q'' = \phi q_c'' + \gamma q_b'' \quad (3)$$

where ϕ and γ are to be evaluated empirically. Due to the relatively low mass fluxes anticipated to develop in the thermosyphon mode, q_b'' may be taken as in pool boiling, via the familiar Rohsenow correlation for water [15]

$$c_{pf}(T_w - T_s)/i_{fg} = C_{sf}\left\{q_b''[\sigma g_c/(\rho_f-\rho_g)g]^{0.5}/\mu_f i_{fg}\right\}^{0.333} \mathrm{Pr} \quad (4)$$

The determination of q_c'' is discussed below.

Convective Component. In annular two-phase flow in relatively narrow channels, the average velocity of the vapor in the core is substantially higher than the average liquid velocity along the channel walls. This difference gives rise to the so-called slip ratio and, due to the identity of the liquid and vapor velocities at the interface, induces a steep velocity gradient in the thin liquid film. The resulting velocity profile, nearly uniform in the core and sharply changing near the wall, is similar to the fully developed turbulent velocity profile and suggests that a conventional forced convection correlation, with an appropriately defined Re, might be applicable to the determination of the convective component without the need to determine the appropriate slip ratio between the liquid and vapor phases.

In keeping with the turbulent flow analogy, Re should be based on the average fluid velocity in the channel $\bar{u}$, which for two-phase flow is given by

$$\bar{u} = G\bar{v} = G(xv_{fg} + v_f) \quad (5)$$

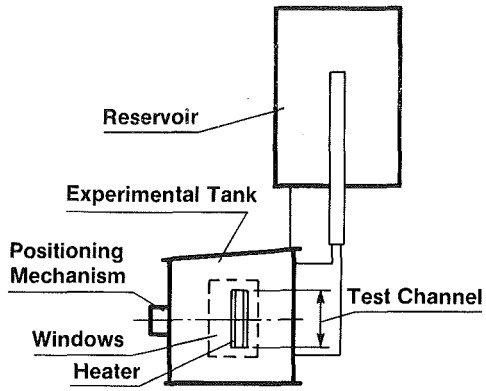

Fig. 2 Schemtic representation of the experimental system

Consequently, with the hydraulic diameter equal to 2δ, the two-phase Re can be defined as

$$\mathrm{Re}_{TP} \equiv G\left(x\frac{v_{fg}}{v_f} + 1\right)(2\delta/\mu_f) \quad (6)$$

It should be noted that the Re_{TP} thus defined does not properly account for the relationship between inertia and viscous forces in the two-phase flow and, as a result of the use of $\bar{u}$, overestimates the momentum flux in the flow. The proper relationship is maintained in the previously discussed formulations [12, 14], but a very large enhancement factor (approaching 10^2) must then be used to adjust the predicted h_c to the observed values. The Re_{TP} definition offered in equation (6) is thought to eliminate the need for a large enhancement factor associated with the "slip ratio" between the liquid and vapor phases. Inserting this two-phase Reynolds number in the standard McAdams correlation for convective heat transfer [15], h_c is found to be

$$h_c = 0.023\frac{k_f}{2\delta}\mathrm{Pr}_f^{0.4}\left(\frac{2\delta G}{\mu_f}\right)^{0.8}\left(x\frac{v_{fg}}{v_f}+1\right)^{0.8} \quad (7)$$

The flow quality x can in general be found by integrating the heat flux along the channel walls. For uniform heat flux, the quality can be easily shown to equal $2q''z/G\delta i_{fg}$ for the symmetric case, and one half this value when one channel wall is adiabatic.

***G*—Insensitivity of h_c.** For the symmetrically, uniform heat flux, heated channel, substitution of the relation for x into equation (7) yields

$$h_c = 0.023\frac{k_f}{2\delta}\mathrm{Pr}_f^{0.4}\left(\frac{2\delta G}{\mu_f}\right)^{0.8}\left(\frac{2q''z}{G\delta i_{fg}}\cdot\frac{v_{fg}}{v_f}+1\right)^{0.8} \quad (8)$$

For the relatively narrow channels of interest and at operating conditions significantly below the critical pressure (for both water and candidate dielectric fluids), $(2q''z/G\delta i_{fg})$ (v_{fg}/v_f) can be shown to be much greater than unity everywhere except the channel inlet [20].

Using this approximation and following integration of equation (8), the height-averaged convective heat transfer coefficient is found to equal

$$\bar{h}_c \simeq 0.0064\frac{k_f}{\delta}\mathrm{Pr}_f^{0.4}\left[\frac{4q''L}{\mu_f i_{fg}}\cdot\frac{v_{fg}}{v_f}\right]^{0.8} \quad (9)$$

for the symmetric configuration. A similar relation for the asymmetric case can be derived by reducing equation (9) by a factor of $2^{0.8}$.

It should be noted that the convective heat transfer coefficient thus depends on the total wall heat flux. The role of q'' in this relation is to establish the average quality in the channel which, in turn, determines the average two-phase velocity and the two-phase Reynolds number.

Most significantly, the average convective coefficient is

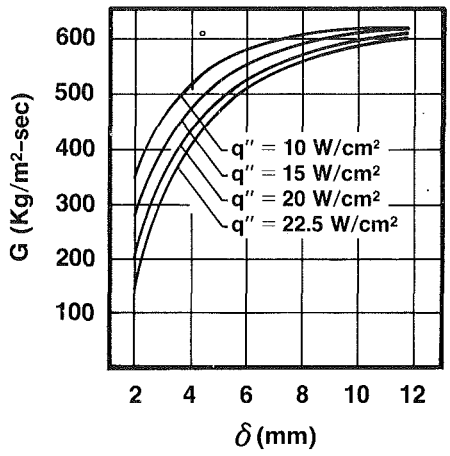

Fig. 3 Mass flux as a function of channel width—symmetric heat flux, Martinelli, and Nelson correlation [19]

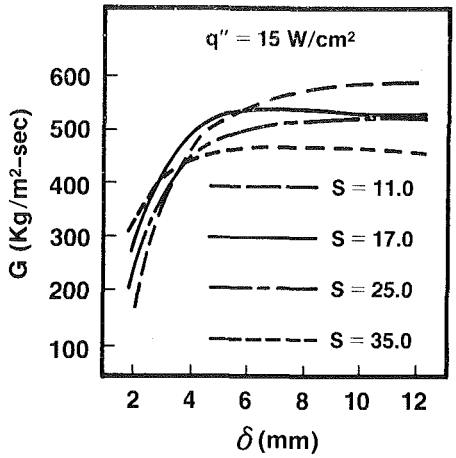

Fig. 5 Influence of slip ratio on the mass flux

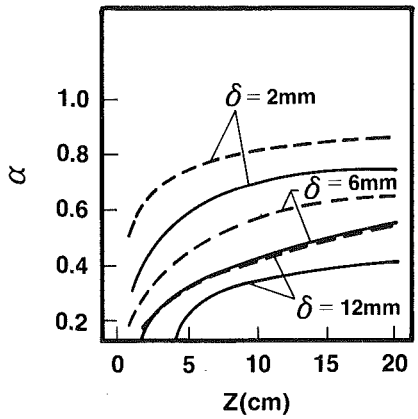

Fig. 4 Axial variation of void fraction: Martinelli/Nelson correlation [19]; —q'' symmetric equals 10 W/cm^2, asymmetric equals 20 W/cm^2; - - - q'' symmetric 20 W/cm^2, asymmetric 40 W/cm^2

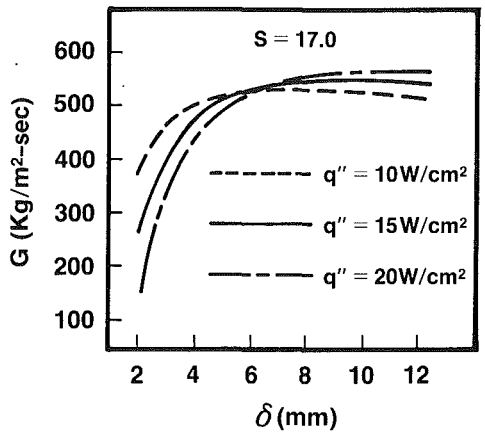

Fig. 6 Influence of symmetric heat flux on mass flux for constant slip ratio

thus found to be explicitly independent of the mass flux G in the parallel-plate channel. Considering the difficulty involved in determining the thermosyphonic mass flux, this is a most fortuitous result, and at the very least, reduces the precision with which G must be calculated.

Experimental Apparatus

The experimental apparatus, shown schematically in Fig. 2, consists of a metal tank enclosing two heaters and a liquid reservoir. The tank includes glass windows, on the front and rear walls, to facilitate visual observation of the boiling phenomena.

The parallel-plate channel, formed by the two heaters, is 240 mm high and 66 mm wide. The distance between the heated surfaces constituting the channel can be varied continuously during operation of the apparatus in the range of 0–60 mm, with an accuracy of ± 0.1 mm.

The heating element inside each heater is a thin metal foil covered with Kapton and manufactured by Minco, Inc. (USA). This foil is attached to the heater plate by a flat, steel "pressure plate." A very thin layer of thermal grease was applied to both sides of the heating element, to minimize the thermal contact resistances. A 6-mm layer of rock wool insulation was placed between the pressure plate and the rear surface of the heater. After assembly, the edges of each heater were covered with a layer of RTV Silicone Elastomer, approximately 1.5 mm in thickness, to provide sealing and some additional insulation. As a result of this design and careful heater assembly, it was found possible to obtain heat fluxes as high as 25 W/cm^2 at the heater surface.

In the subject apparatus, the individual heaters are supported by cylindrical hollow bars, within which pass the electrical power cables. One of the cylinders is fixed to the wall of the tank while the other is part of a mechanism whose purpose it is to vary the distance between the heated surfaces.

In the course of this investigation, the heated surface temperatures were measured by K-type thermocouples, inserted into the heater plate at a depth of 1.5 mm from the wetted surface at seven distinct heights. At each height, a single thermocouple was placed at the center of the plate and an additional one or two thermocouples at the lateral edge(s).

During an experiment, the vapor generated in the channel is dispersed, in the form of a bubble spray, into a slightly subcooled, elevated liquid reservoir. Fluid from the reservoir flows down into the tank through a branched pipe, connected to the tank near the top and bottom, respectively.

Thermosyphonic Mass Flux

The determination of the induced mass flux is central to the understanding of the thermal behavior of ebulliently cooled, parallel plates immersed in a saturated fluid. While the heat transfer relation proposed in this work is relatively insensitive to G, this is not the case with the commonly used correlations (e.g., [12, 14]). Furthermore, a knowledge of G is essential for the evaluation of the axial variations of the quality and vapor fraction and, ultimately, the calculation of the channel height at which dryout, associated with either the evaporation of the

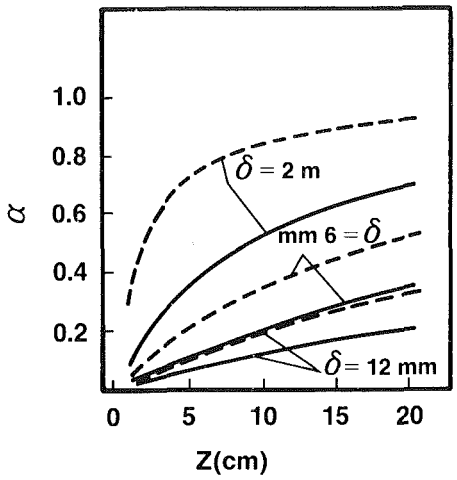

Fig. 7 Axial variation in void fraction for slip ratio = 17; —q'' symmetric equals 10 W/cm^2, asymmetric equals 20 W/cm^2; - - - q'' symmetric 20 W/cm^2, asymmetric 40 W/cm^2

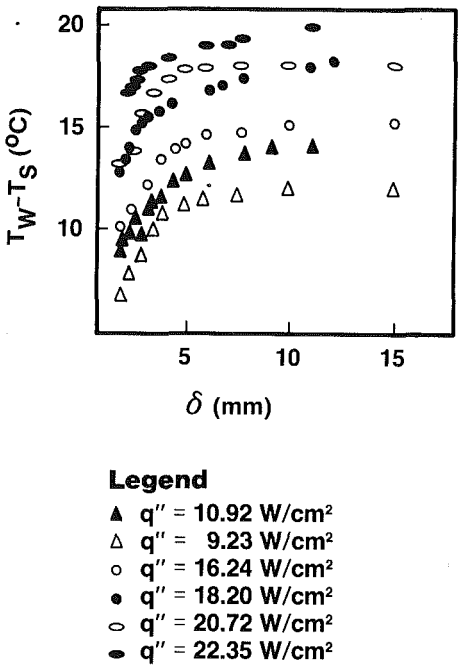

Fig. 8 Influence of channel spacing on wall superheat; open symbols = asymmetric heating, full symbols = symmetric heating

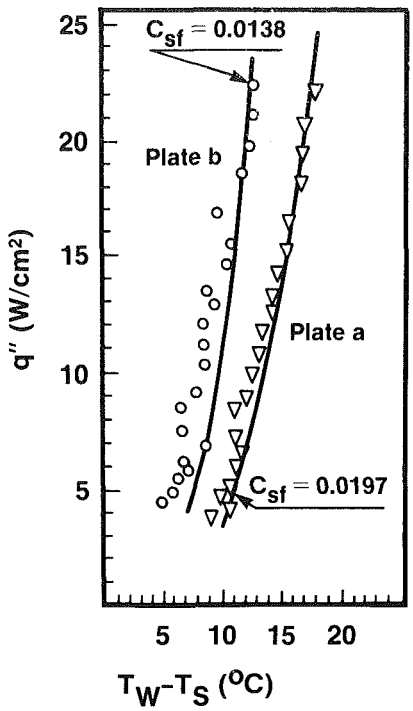

Fig. 9 Pool boiling curve for widely spaced parallel plates in water

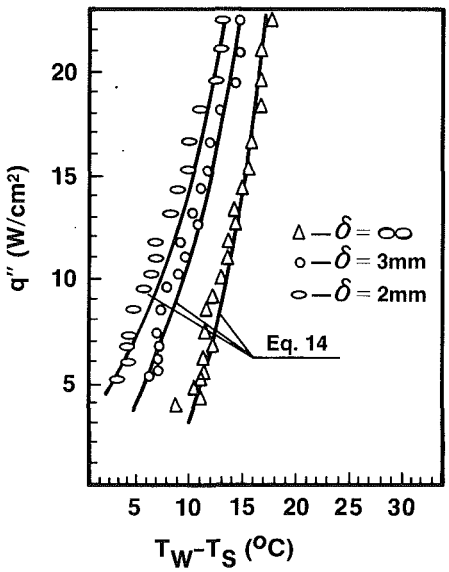

Fig. 10 Pool boiling curves for different channel widths in water

liquid film or, alternately, complete vaporization of the flow, may be expected to occur.

The variation of G for a symmetrically applied heat flux, based on the Martinelli/Nelson factors, is shown in Fig. 3. It may be noted that G appears to reach an asymptotic value at large spacings (>12 mm) which is nearly independent of q''. However, as the plate spacing decreases, the mass flux is seen to decline at a progressively greater rate for the higher heat fluxes.

Based on the value of G and the void fraction relations in [19], it is possible to determine the vapor fraction α along the channel, as shown in Fig. 4. For the parametric range studied, α at the top of the channel is seen to generally exceed 0.5 and to approach 0.85 for the high heat fluxes and narrow spacings. The calculated values of α are, thus, significantly higher than normally associated with bubbly flow and are thus indicative of the existence of churn and/or annular flow in the channel [20].

As noted earlier, the mass flux may also be calculated via equation (2), the constant slip ratio relation for the channel pressure loss. For different assumed values of S, this approach yields a family of mass fluxes, as can be seen for example in Fig. 5. Based on a comparison between predicted flow regime transitions and visual observations in the present apparatus, as well as flow boiling data documented in the literature [21], S may be taken approximately equal to 17 [20]. The variation in the "constant slip ratio" mass flux with a symmetrically imposed heat flux and channel spacing is shown in Fig. 6.

The axial dependence of the vapor fraction, associated with the "constant slip ratio" formulation, is expressed by equation (10)

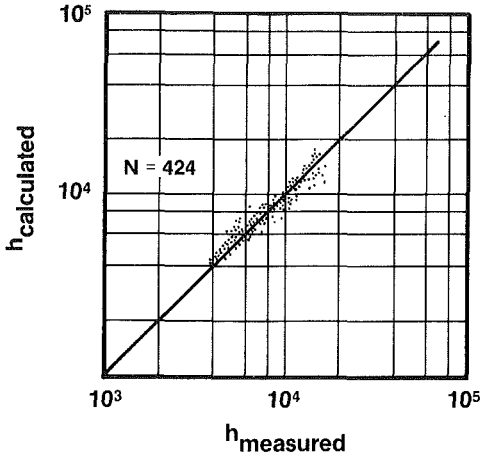

Fig. 11 Comparison of calculated and measured heat transfer coefficients

$$\alpha = \left[1 + Sv_f\left(\frac{1}{x} - 1\right)/v_g\right]^{-1} \tag{10}$$

This relation is plotted in Fig. 7 for a range of channel spacings and heat fluxes. It may be noted that the α values in Fig. 7, based on $S = 17$, are nearly identical to those derived via the Martinelli/Nelson factors and shown in Fig. 4.

Experimental Results and Discussion

Qualitative Trends. Typical experimental results, obtained with the present apparatus, are shown in Fig. 8 and illustrate the influence of the channel spacing on the wall temperature. It may be seen that, at constant imposed heat flux, the wall temperature decreases as the spacing narrows below approximately 10 mm. It may thus be argued that for channel spacings greater than 15 mm, the data reflect the usual nucleate pool boiling behavior. Indeed, as shown in Fig. 9, the relationship between heat flux and wall superheat for data obtained with a 30 mm gap is expressible via the Rohsenow correlation of equation (4). The Fig. 10 comparison of the empirical boiling curves for narrow spacings, with the curve appropriate to pool boiling behavior, reveals the channel spacing to exert a greater influence on wall superheat at the low heat fluxes where natural convection effects are of importance.

The observed thermal behavior may be explained by the interaction between heat transfer and hydrodynamic aspects of thermosyphon boiling in narrow channels. Clearly, as the channel narrows, the quality and vapor fractions, for a fixed heat flux, increase, leading to an increase in the velocity of the two-phase mixture and to a change in the prevailing flow regime from bubbly to slug to churn and finally to annular flow. It might thus be expected that, as the interplate spacing decreases, the effective heat transfer coefficient will increase until the annular liquid film approaches the breakdown condition and local dryout occurs. At this point the local wall temperature would rise sharply endangering the survival of the apparatus or the ebulliently cooled components. The latter condition was obviously not encountered in the parametric range of the present experiments.

At the lower heat fluxes thermal transport from the immersed surfaces is dominated by the relatively weak single phase natural convection. In this range, an increase in the void fraction, associated with a reduced interplate spacing, is most effective in increasing the velocity of the two-phase fluid and, consequently, providing a substantial reduction in wall superheat. As the range of heat fluxes appropriate to fully developed nucleate pool boiling is approached, the channel width appears to exert a less significant influence on wall superheat due, perhaps, to the more moderate velocity changes and the difficulty involved in improving an already highly effective heat transfer process.

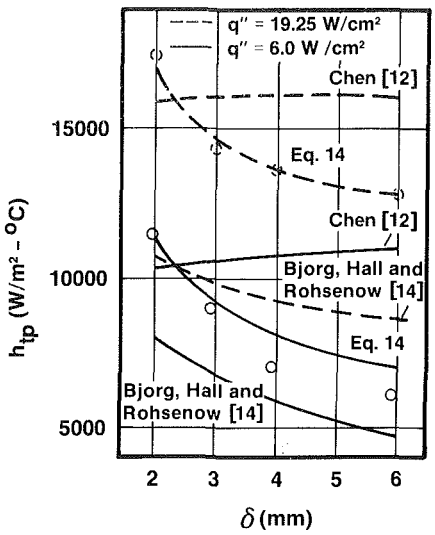

Fig. 12 Comparison of two-phase heat transfer coefficient correlation with symmetric experimental data

Correlation. The observed parametric trends can serve as a basis for correlating the values of the effective heat transfer rate from the immersed surfaces to saturated water in the form of equation (3). Based on previous results [12, 14], it might have been anticipated that a "suppression" factor, multiplying the nucleate boiling term, would be needed in the correlation. However, since nucleate boiling was visually observed to occur over the entire experimental heat flux range, for all but the narrowest gap, and since it is desirable that equation (3) merge smoothly into the usual pool boiling expression, for large gaps, it was decided to set $\gamma = 1$ and focus the correlating effort on the coefficient of the convective component.

As a result of setting $\gamma = 1$, the coefficient of the convective component ϕ must vanish for sufficiently wide channels. Furthermore, reflecting the trends noted, in the range of interest it can be expected to be a relatively strong function of the channel width δ, and to display a weak dependence on the imposed flux q'' or, alternatively, on the quality x. The channel width may be of importance both in terms of flow development, i.e., the ratio of channel length to width L/δ, and in terms of the relationship between the bubble departure diameter and the width, i.e., D_b/δ. The bubble departure diameter can generally be related to the ratio between surface tension forces and buoyancy forces $D_b \sim [g_c\sigma/g(\rho_f - \rho_g)]^{1/2}$ [15]. Consequently, a correlation for ϕ in the form of

$$\phi = a\left\{\frac{[g_c\sigma/g(\rho_f - \rho_g)]^{1/2}}{\delta}\right\}^b (L/\delta)^c x_L^d \tag{11}$$

is to be sought.

Based on a regression analysis of the data obtained in this investigation, including approximately 400 distinct points, and incorporating the Martinelli/Nelson mass flux to determine x_L and h_c, ϕ is found to equal

$$\phi_{MN} = 0.0214[g_c\sigma/g(\rho_f - \rho_g)\delta^2]^{1/2} x_L^{-0.541} \tag{12}$$

Alternately, when the constant slip ratio model with $S = 17$ is used to determine the mass flux through the ebulliently heated channel, the requisite correlation is found as

$$\phi_{CSR} = 0.022[g_c\sigma/g(\rho_f - \rho_g)\delta^2]^{1/2} x_L^{-0.533} \tag{13}$$

Due to the similarity between the G values calculated via the two methods and the relative insensitivity of h_c to G,

previously discussed, ϕ_{CSR} and ϕ_{MN} are seen to be nearly identical. It is also to be noted that in both ϕ correlations, the exponent of the (L/δ) term was found to equal zero, signifying the independence of ϕ from the channel aspect ratio for the conditions of the experimental study.

Incorporating ϕ_{CSR} into the superposition relation for q'', with $\gamma = 1$, yields the proposed semi-empirical correlation for the heat transfer rate in thermosyphon boiling between parallel plates, as

$$q'' = 0.022[g_c\sigma/g(\rho_f-\rho_g)\delta^2]^{1/2}\bar{h}_c(T_w-T_s)x_L^{-0.533} + (k_f/C_{sf}^3)(k_f/\mu_f i_{fg})^2[g(\rho_f-\rho_g)/g_c\sigma]^{1/2}(T_w-T_s)^3 \quad (14)$$

where $\bar{h}_c$ is given by equation (9).

The excellent agreement (an average discrepancy of 2 percent) between the observed data and the proposed correlation is shown in the Fig. 11 comparison between the experimental two-phase heat transfer coefficient and the value calculated via equation (14) using a numerical successive substitution procedure necessitated by the q'' dependence of the convective heat transfer term. Interestingly, as may be noted in Fig. 10, the proposed correlation agrees equally well with the data for large and small channel widths.

A further comparison between the proposed correlation and the observed thermal performance is shown in Fig. 12 where the dependence of the two-phase heat transfer coefficient on the channel width is displayed for two values of heat flux. It may be noted that while the Bjorge, Hall, and Rohsenow formulation [14] (based on the constant slip ratio G) yields h_{TP} values that are approximately 30 percent below the measured values, it clearly displays the correct trend, increasing as the interplate spacing decreases. This is not the case for the Chen correlation [12] which yields nearly constant h_{TP} values and tends toward lower values as the channel narrows.

Summation

In the course of the present investigation of an ebulliently heated, parallel-plate channel, immersed in a near-infinite, saturated fluid, the wall superheat at constant imposed heat flux was found to decrease as the channel narrowed. It was found possible to explain this somewhat anomalous behavior with the aid of a boiling thermosyphon analysis which yielded the mass flux through the channel and which, together with a formulation for the convective component of heat transfer (based on a uniquely defined Reynolds number) formed the basis for an accurate correlation of all the near-atmospheric water data gathered in this investigation.

References

1 Megerlin, F., and Markowitz, A., "Advanced Cooling and Thermal Control Techniques," IEEE NEREM Conf., Boston, MA 1971.

2 Marto, P. J., and Lepere, V. J., "Pool Boiling Heat Transfer From Enhanced Surfaces to Dielectric Fluids," ASME JOURNAL OF HEAT TRANSFER, Vol. 104, 1982, pp. 292–299.

3 Nakayama, W., et al., "Dynamic Model of Enhanced Boiling Heat Transfer From Micro-Porous Surfaces," in: *Advances in Enhanced Heat Transfer*, ASME, New York, 1979, pp. 39–45.

4 Fujii, M., Nishiyama, E., and Yamanaka, G., "Nucleate Pool Boiling Heat Transfer From Micro-Porous Surfaces," ibid., pp. 45–51.

5 Oktay, S., "Departure From Natural Convection (DNC) in Low Temperature Boiling Heat Transfer Encountered in Cooling Micro-Electronic LSI Devices," *Proc. 7th International Heat Transfer Conf.*, Munich, Germany, 1982, Vol. 4, pp. 113–118.

6 Ciccio, J. A., and Thun, R. E., "Ultra-High Density VLSI Modules," *IEEE Trans.*, Vol. CHMT-1, No. 3, Sept. 1978, pp. 242–248.

7 Kraus, A. D., and Bar-Cohen, A., *Thermal Analysis and Design of Electronic Equipment*, McGraw-Hill, New York, 1983, Chapter 16.

8 "Supercomputer Will Use Immersion Cooling," Industrial Research and Development, Jan. 1982, p. 80.

9 Goltsos, C. E., and Mark, M., "Packaging With a Flexible Container for Oil-Filled or Evaporative-Cooled Electronic Equipment," *IRE Trans.*, Vol. PEP-6, 1962, pp. 44–48.

10 Fairbanks, D. R., Goltsos, C. E., and Mark, M., "The Submerged Condenser," ASME Paper No. 67-HT-15, 1967.

11 Paradis, L. R., "Simplified Transmitter Cooling System," 8th International Circuit Packaging Symp., San Francisco, Aug. 21–22, 1967.

12 Chen, J. C., "A Correlation for Boiling Heat Transfer to Saturated Fluid in Convective Flow," ASME Paper No. 63-HT-34, 1963.

13 Forster, H. K., and Zuber, N., "Dynamics of Vapour Bubbles and Boiling Heat Transfer," *AIChE J.*, Vol. 1, No. 4, 1955, pp. 531–539.

14 Bjorge, R. W., Hall, G. R., and Rohsenow, W. M., "Correlation of Forced Convection Boiling Heat Transfer Data," *Int. J. Heat Mass Transfer*, Vol. 25, No. 6, 1982, pp. 753–757.

15 Rohsenow, W. M., and Choi, H., *Heat, Mass and Momentum Transfer*, Prentice-Hall, Englewood Cliffs, NJ, 1961.

16 Ferrel, J. K., and McGee, J. W., "Two-Phase Flow Through Abrupt Expansions and Contractions," TID-23394, Dept. of Chem. Eng., North Carolina State Univ., Raleigh, NC, 1966, Vol. 3.

17 Wallis, G. B., *One Dimensional Two-Phase Flow*, McGraw-Hill, 1969.

18 Lockhart, R. W., and Martinelli, R. C., "Proposed Correlation of Data for Isothermal Two-Phase, Two-Component Flow in Pipes," *Chem. Eng. Progress*, Vol. 45, No. 1, 1949, pp. 39–46.

19 Martinelli, R. C., and Nelson, D. B., "Predictions of Pressure Drop During Forced-Circulation Boiling of Water," *Trans. ASME*, Vol. 70, Aug. 1948.

20 Schweitzer, H., "Thermosyphonic Boiling in Parallel Plate Channel," M.Sc. Thesis, Dept. of Mech. Eng., Ben-Gurion Univ., 1983.

21 Davidson, W. F., Hardie, P. H., Hamphreys, C. G. R., Markson, A. A., Munford, A. R., and Ravese, T., "Studies of Heat Transmission Through Boiler Tubing at Pressures From 500 to 3000 Pounds," *Trans. ASME*, Vol. 65, 1943, pp. 553–591.

Heat Transfer and Evaporation From Heated Water Bodies

M. Chattree
Student Mem. ASME

S. Sengupta
Mem. ASME

Department of Mechanical Engineering,
University of Miami,
Coral Gables, FL 33124

It is known that there is a sharp temperature gradient in a thin water layer at the air-water interface. Systematic measurements of this temperature difference and meteorological parameters were made at a cooling pond in East Mesa, CA. The water loss was measured directly, and the water temperatures were in the range of 30–46°C. Existing formulae which use the surface temperature difference and wind speeds to predict the net heat flux have been examined. Examination of the well-known Saunders' equation shows that a parameter λ does not have a constant value. Nondimensional correlations have been developed to predict the net heat flux and the evaporative heat flux at the interface. A dimensional correlation which includes the effect of the surface temperature variation is found to give the most accurate prediction of the net heat flux.

Introduction

Heat exchange at the air-water interface, both for natural and artificially heated water bodies, is of increasing importance in the abatement of thermal pollution, design of cooling ponds and in modeling water temperature as an important element of water quality. The design of a cooling pond depends critically on accurate predictions of the heat and mass flux to the atmosphere through the air-water interface.

Radiometric measurement of surface temperature of a water body is usually different from the temperature a few millimeters below the surface. The difference can be as much as 2°C. Saunders (1967) assumed that a thin water layer at the air-water interface is laminar. He proposed a formula relating the temperature difference ΔT across the depth δ of the thermal skin to the net heat flux Q_n through the surface

$$Q_n \sim k_w \Delta T/\delta \tag{1}$$

where k_w is the thermal conductivity of water. With the assumption that the depth of skin thickness for heat transfer is proportional to that for momentum transfer, dimensional arguments lead to the relationship

$$\delta \sim \nu_w(\tau_w/\rho_w)^{-1/2} \tag{2}$$

where τ_w is the viscous stress, ν_w is the viscosity of water, and ρ_w is the water density.

By combining equations (1) and (2) and assuming that τ_w is proportional to the shear stress τ in the atmospheric surface layer, Saunders finds the relationship

$$Q_n = k_w(\tau/\rho_w)^{1/2}\frac{\Delta T}{\lambda \nu_w} \tag{3}$$

where λ is widely known as Saunders' constant which absorbs the relationship between τ_w and τ and other unknown factors.

It has been conjectured that λ is independent of τ and ΔT; hence Q_n can be known if only ΔT and τ are known. In equation (3) no direct adjustment has been made for the difference between the thickness of the thermal boundary layer and the viscous boundary layer. Since the Prandtl number (ν_w/α, where α is the thermal diffusivity of water) is greater than 1, the thermal layer should be thinner than the viscous layer. According to Wesley (1979), this can be approximated, using the theory of flow near a rigid boundary, by multiplying the right-hand side in equation (3) by a new coefficient Λ such that $\lambda = \Lambda \mathrm{Pr}^{-1/3}$. This results in

$$Q_n = k_w(\tau/\rho_w)^{1/2}\Delta T/(\Lambda \nu_w^{2/3}\alpha^{1/3}) \tag{4}$$

Deacon [4] derives an equation similar to equation (3) but with modifications for ΔT being measured across very large depths of water as compared to a millimeter or so for the earlier formulations. His equation in the present notation after rearrangement can be written as

$$Q_n = k_w(\tau/\rho_w)^{1/2}\Delta T[\nu_w \phi(\mathrm{Pr})]^{-1} \tag{5}$$

where, for water

$$\phi(\mathrm{Pr}) = 15.2\ \mathrm{Pr}^{-0.39} \tag{6}$$

Another somewhat similar approach for describing the thermal skin behavior is given by Hasse [5] who finds that the temperature difference across the 35 cm of sea water not exposed to solar (shortwave) radiation can be represented by

$$\Delta T = C_1 Q_n/U_\infty \tag{7}$$

where C_1 is a constant which varies slowly with the skin thickness [5] and U_∞ is the wind speed at 10 m height. In the case of shortwave radiation, following Hasse's one-dimensional model for deriving ΔT, the following formula is obtained

$$\Delta T = C_1(H/U_\infty) + C_2(Q/U_\infty) \tag{8}$$

where Q is the sum of latent heat, sensible heat, and back radiation. H is the shortwave radiation.

McAlister and McLeish [12] discuss the mechanism (i.e. conduction, convection, and radiation) of heat transfer at the interface. Paulson and Parker [13] and Hill [6] found that presence of surface waves plays a major role in the surface exchange processes. Wu [18] and McLeish and Putland [11] have measured velocity profiles in air and water at the interface region. Howe et al. [7] have measured the mean temperature and velocity profiles along with their RMS values and covariances of fluctuations in the water sublayer below the interface. They also showed that by using laser doppler anemometer and fast response thermistors one can obtain direct measurements of the heat and momentum fluxes in the aqueous surface layer beneath the interface. Howe et al. [8] compared the mean profiles in the air and water and also provided an analysis of the RMS values for the velocity and temperature in the water. The heat flux in water was computed by using the measurements of fluctuating temperature and velocity. The measured heat flux in the water agrees well with that determined by measurements in air.

Klotz and Street [9] present a solution for the coupled laminar boundary layer equations of energy, mass, and momentum at a smooth interface. They also describe the numerical solution of the turbulent boundary layers at a rough air-water interface. A key problem lies in the parameterization of the roughness effects at the interface and

Contributed by the Heat Transfer Division and presented at the ASME Winter Annual Meeting, New Orleans, Louisiana, December 11–14, 1984. Manuscript received by the Heat Transfer Division March 13, 1984.

their influence on the eddy coefficients in the near interface regions.

Evaporative heat is the predominant component of the net heat flux. Therefore, expressions for evaporation are also examined in this study. A widely used evaporation expression is the Ryan–Harleman (Ryan, Harleman, and Stolzenbach [15]) equation. This equation for evaporative heat flux in metric units is

$$Q_e = [2.6(\Delta\theta_v)^{1/3} + 3.1U_2][e_s - e_2] \quad (9)$$

where

$$\Delta\theta_v = \theta_{vs} - \theta_{va} \quad (10)$$

and $\Delta\theta_v$ is the virtual temperature difference between the air and water surface in °C; θ_{vs} and θ_{va} are virtual temperatures evaluated at the water surface and the air, respectively in °C. The air temperature and wind speeds are measured at 2 m height. The virtual temperature is defined as the temperature of dry air having the same density as the moist air; it accounts for the mass transfer by natural convection.

The units of e_s, e_2, U_2, and Q are millibar, m/s, and W/m^2, respectively, in equation (9). There was a lack of reliable field data for heat-loaded water bodies to verify/calibrate evaporation formulae (Adams et al., [1]). Thus, the present experiments helped to generate a useful data base.

The objectives of the present study are to develop methods for predicting net heat flux and evaporation across the air–water interface. The net heat flux will be predicted using simple measurements of surface and bulk temperatures and wind speeds. Dimensional and nondimensional correlations which use the above measurements have been developed. Existing empirical relationships have also been examined.

The salient features of the present study are:

(*a*) ΔT takes a broad range of values from 0.1°C to 2°C. T_s and bulk temperature were measured by the same instrument. Therefore, no cross calibration was required.

(*b*) A wide range of values for meteorological data makes this study particularly useful. The water temperature varied from 30°C to 46°C. The air temperature varied widely from 22°C to 44°C. The relative humidity varied from 28 to 68 percent, and the wind speed at 4.5 m height was in the range of 0.7 m/s to 5.8 m/s.

(*c*) The evaporative heat flux, which is a major component of net heat flux, is known very accurately because the pond bottom has a plastic lining and there was no rain during the experiments.

Experiments

Site Description. All measurements were taken at a cooling pond on the East Mesa site. The East Mesa site is managed by Westec Services, Inc., for the U.S. Department of Energy, San Francisco operations office. This site was chosen because (*a*) hot geothermal water was available at the site; (*b*) the pond has a regular geometry: square constant depth pond with essentially homogeneous temperature; (*c*) there is a special bottom liner which prevents seepage, making water budget calculations simple. Figures 1 and 2 show schematic and cross-sectional views of the pond. There is a protective layer of soil on top of the bottom linear. The liner and the protective soil extend to the other face of the berm. While the geothermal fluid contains dissolved minerals, the relevant properties of this fluid compared well with tap water. The experiments were conducted between 27th June, 1981 and 5th July, 1981. The ranges of the various measured quantities are mentioned in Section 1.

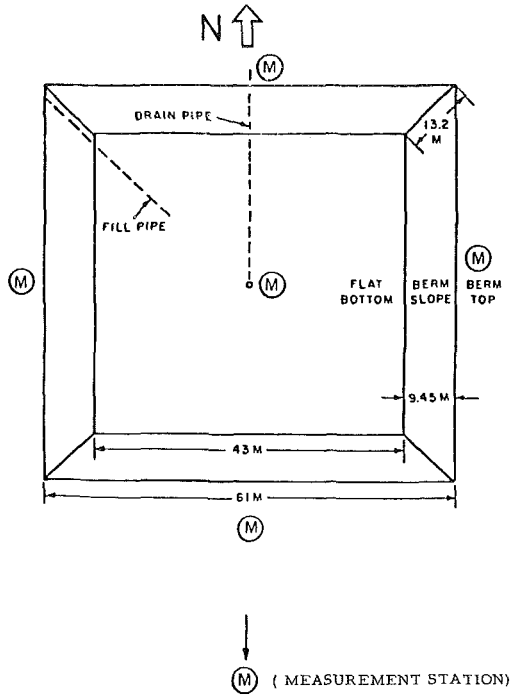

Fig. 1 Plan view of East Mesa Pond (from [1])

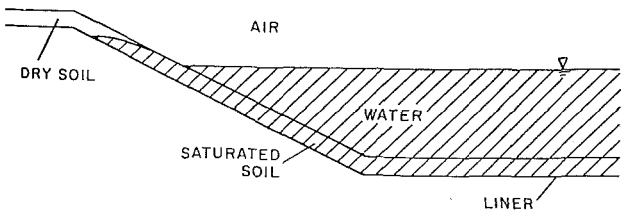

Fig. 2 Cross-sectional view of East Mesa Pond (from [1])

Water Level Measurement. The pond surface elevation was determined with respect to an arbitrary reference level by

Nomenclature

C_{pw} = specific heat of water
e_s = saturated vapor pressure of air at water surface temperature
e_2 = vapor pressure of air at 2 m height
k_w = thermal conductivity of water
Pr = Prandtl number = $C_{pw}\mu_w/k_w$
Q_{an} = net absorbed atmospheric radiation
Q_{br} = back radiation
Q_c = conductive heat flux
Q_e = evaporative heat flux
Q_n = net heat flux at the interface
Q_r = net all-wave radiative heat flux
Q_s = net absorbed shortwave radiation
T_a = air temperature
T_s = surface temperature of water
U_∞ = wind speed at 10 m height
U_2 = wind speed at 2 m height
α = thermal diffusivity
ΔT = difference between bulk and surface temperature
δ = skin thickness
Λ = Wesley's constant
λ = Saunders' constant
μ_w = dynamic viscosity of water
ν_w = kinematic viscosity of water
ϕ = relative humidity
ρ_a = density of moist air
ρ_w = density of water
τ = shear stress
θ_v = virtual temperature

reading water levels in stilling wells using hook gauges. The wells were located on the outside slope of a berm and connected to the pond by approximately 35 m of flexible plastic tubing.

Radiation Measurement. Total downward solar radiation (direct and diffuse) was measured with an Eppley precision pyranometer located within 10 m of the pond edge. Net radiation for all wavelengths was measured over the pond surface with a dual hemisphere Fritschen type radiometer.

Measurements of Temperatures. A PRT-5 radiometer was used to measure the surface temperature of the water. No thermal stratification was observed in the horizontal direction. The radiometer was placed vertically facing the water surface. It monitored the surface temperature continuously and the readings were averaged, using a RMS voltmeter, for 2-min intervals. The skin was broken by a jet from a pump submerged about 20 cm below the water surface. The radiometer then measured the bulk temperature and averaged it for 10-s intervals.

Air temperatures and humidities were measured by use of aspirated bead thermistors (dry and wet wicks). The nested aspirator tubes functioned as solar radiation shields. A remote reference tower was located approximately 100 m from the pond to provide an undisturbed reference data base for comparison purposes. Wind velocity, and thereby wind direction, was measured at the reference tower with three orthogonal propellers at each height. These temperature and wind sensors were located on short towers around the periphery and on a towable raft located near the pond center.

Data Reduction

Data collected included water surface elevation, wet and dry bulb air temperature, net radiation, downward radiation, wind speed and direction and water surface and bulk temperatures.

The evaporative heat flux was calculated by finding the difference between the averaged stilling well readings at 1-hr time intervals. Correction was made for the difference in density of the pond and the stilling well water, i.e., $\rho_p \Delta H_p = \rho_s \Delta H_s$ where ρ_p is density of pond water, ρ_s is density of stilling well water, ΔH_p is change in pond level, and ΔH_s is change in stilling well level. The conduction heat flux has been calculated using Bowen's ratio, which gives the conductive heat flux as

$$Q_c = 0.610 Q_e (T_s - T_a)/(e_s - e_2) \tag{11}$$

The radiative components of the net heat flux (i.e., back radiation, shortwave radiation, and atmospheric radiation) are calculated using well-established relationships (see Lee and Sengupta [10]).

The wind speeds measured at 1.8 and 4.5 m height were extrapolated according to a logarithmic profile to obtain the speed at 10 m height. The wind speed at 2 m height was used for the evaporative heat flux correlation, and the wind speed at 10 m height was used for net heat flux correlation. The shear stress has been calculated as $\tau = \rho_a C_d U_\infty{}^2$ where C_d is the coefficient of drag with a value of 0.00121.

Results and Discussion

The results are based on the analysis of 70 data points covering both night and day conditions. The nighttime data points are identified by the absence of measured shortwave radiation. A total of 35 data points lies in the nighttime division and 35 in the daytime division. The net heat flux at the interface is out of the surface and is negative at all times. The surface temperature is lower than the bulk temperature at all times.

Standard deviations are computed according to the definition of the unbiased standard deviation

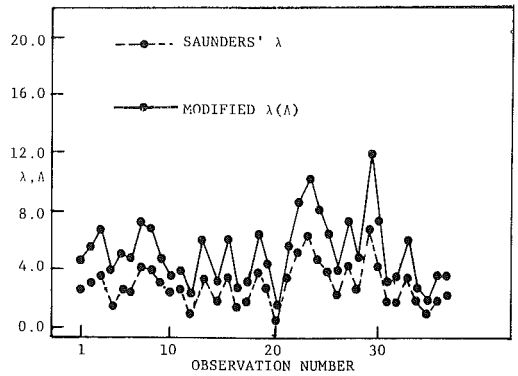

Fig. 3 Plot showing values of λ and Λ calculated using Saunders' equation

$$s_x = \sqrt{\frac{\Sigma (x_i - \bar{x})^2}{(n-1)}} \tag{12}$$

Evaluation of Existing Formulae. This section discusses Saunders' equation, Hasse's equations, and variation of λ.

Saunders' equation is

$$\lambda = \frac{k_w C_d{}^{1/2} \rho_a{}^{1/2} U_\infty \Delta T}{\nu_w \rho_w{}^{1/2} Q} \tag{13}$$

Calculation of λ was done using the following heat fluxes (see nomenclature)

$$Q = Q_n$$
$$Q = Q_e + Q_c$$
$$Q = Q_n - Q_s$$

Quantity Λ was calculated in a similar manner in Wesley's equation

$$\Lambda = \lambda \mathrm{Pr}^{1/3} \tag{14}$$

Typical values of Λ and λ are plotted in Fig. 3. Hasse's C_1 was calculated using the following equation

$$\Delta T = C_1 Q / U_\infty \tag{15}$$

The three heat fluxes mentioned earlier and the following additional heat fluxes (see nomenclature) were used to calculate C_1.

$$Q = Q_s$$
$$Q = Q_c$$
$$Q = Q_{an} + Q_{br}$$

The best results (least scatter in values of λ, Λ, and C_1) were obtained for the net heat flux and net heat flux from which the shortwave radiation has been excluded. The results using other heat fluxes have a large standard deviation, which means that the values of λ and C_1 are widely scattered. Therefore, in the discussion that follows we will discuss λ and C_1 calculated using the net heat flux only.

Saunders' Formula. Saunders' λ has an average value of 2.80 with a standard deviation of 1.28 with the values of λ ranging from 0.7 to 6.9. For the daytime data the average value of λ was 2.90 with a high standard deviation of 1.60, but for the nighttime data the average value of λ was 2.70 with a relatively low standard deviation of 1.00.

The shortwave radiation was excluded in the calculation of net heat flux (which was used to calculate λ). On the basis of 70 data points, λ had a mean value of 2.69 with a low standard deviation of 1.10.

Wesley's Formula. There was no appreciable improvement in the constancy of λ calculated by introducing the Prandtl number according to Wesley's formulation. In equation (14) the modified λ could not take any constant value. The mean value of λ increased from 2.80 to 4.62 and the corresponding standard deviation from 1.28 to 2.10.

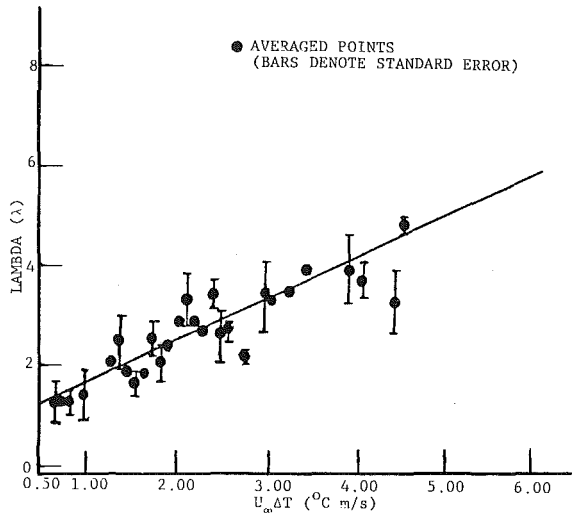

Fig. 4 Plot of λ versus $U_\infty \Delta T$ showing the best fit line

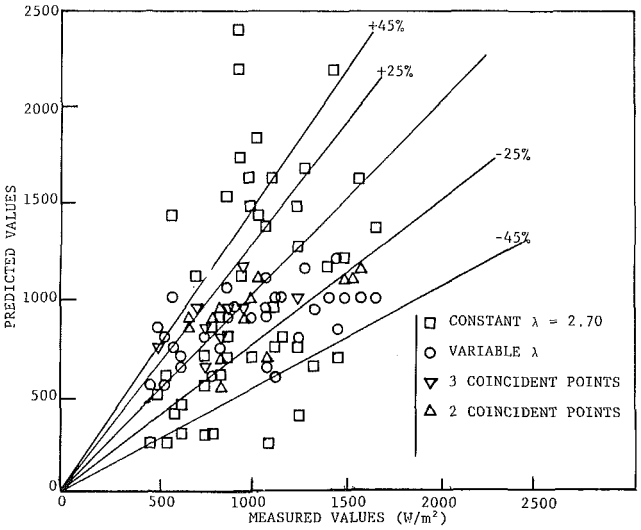

Fig. 5 Prediction of net heat flux using constant and variable λ

Hasse's Formula. Hasse's equation does not perform well: Quantity C_1 (units of °C m/s/Langley*/ min) takes a mean value of 1.85 with a standard deviation of 0.83 with values of C_1 ranging from 0.75 to 3.1. For the nighttime data alone C_1 has an average value of 1.76 with a standard deviation of 0.65; for the daytime data the mean C_1 is 1.95 with a standard deviation (S.D.) of 1.00.

C_1 calculated from equation (15) with Q substituted as Q_s is not a constant. The mean value of C_1 is 94.1 with a very high S.D. of 244. Hence ΔT is not linearly correlated with the shortwave radiation.

From the above results it is clear that λ and C_1 are not constants. In the absence of shortwave radiation the values of λ lie close to a mean of 2.70 and those of C_1 around a mean of 1.77°C m/s/langley/min. The values of λ and C_1 are more scattered when shortwave radiation is present. When the values of λ with a mean of 2.70 and S.D. of 1.00 are compared with other field measured values between 4 and 10 (Chattree [3]), we note that for the present measurements the mean value of λ is considerably lower.

Saunders' λ. The following is a table of correlation coefficients of λ with some measured variables:

λ	Q_n	T_s	U_∞	$U_\infty \Delta T$	$T_s - T_a$	ΔT	Pr
1.00	0.08	0.093	0.23	0.80	0.09	0.53	0.11

We note that λ is significantly correlated with the product $U_\infty \Delta T$ and λ increases when $U_\infty \Delta T$ increases.

Wesley's (1979) finding that λ increases with the surface temperature is not substantiated, as λ does not correlate significantly with the surface temperature (T_s versus λ coefficient of 0.093). A best fit (Fig. 4) for λ versus $U_\infty \Delta T$ is given by

$$\lambda = 0.87 U_\infty \Delta T + 0.59 \tag{16}$$

with a standard deviation (S.D.) of 0.75 in estimating λ from this fit, where U_∞ is in m/s and ΔT in °C. Figure 4 plots the averaged points, and the bars denote the standard error for each average. Hence Saunders' equation can be modified to give an empirical correlation for Q_n with λ substituted as

$$\lambda = A_1 U_\infty \Delta T + A_2 \tag{17}$$

where A_1 and A_2 are empirically determined constants.

When equation (16) is substituted in equation (13) to predict Q_n, we get promising results: 80 percent of all data points lie within an error band of ±25 percent (Fig. 5). For nighttime case the fit for λ is better, and the scatter is also less. The equation is

$$\lambda = 0.77 U_\infty \Delta T + 0.85 \tag{18}$$

with a standard error of 0.60 as compared to 0.75 before in estimating λ from equation (16).

Correlations for Net Heat Flux. *This section presents the* dimensional and nondimensional correlations for predicting the net heat flux.

Nondimensional Variables for Net Heat Flux Correlation. The net heat flux depends on the thermal conductivity of the water, ΔT, and thermal skin thickness. The thermal skin thickness is related to the viscous skin thickness, which in turn depends on the shear stress or the wind speed. The following variables were obtained as a result of nondimensional analysis:

$$P_1 = \frac{Q_n}{U_\infty \tau} = \frac{\text{net heat flux at the interface}}{\text{wind convected kinetic energy flux}}$$

$$\text{Pr} = \frac{C_{pw}\mu_w}{k_w} = \text{Prandtl number}$$

$$P_3 = \frac{\nu_w \tau}{k_w \Delta T} = \text{Reynolds number based on skin thickness} \times \frac{\text{wind convected kinetic energy flux}}{\text{heat conducted across water surface layer}}$$

In the above we note that $\tau \sim \rho U_\infty^2$ and Reynolds number = $U_\infty \delta / \nu_w$.

Nondimensional Correlations. Multiple regression analysis was carried out using log (Pr) and log (P_3) as the independent variables and log (P_1) as the dependent variable. Log (Pr) was found to be insignificantly correlated with the dependent variable, but log (P_1) and log (P_3) correlated significantly with a correlation coefficient of 0.93. The correlation between the nondimensional numbers is

$$Q_n / U_\infty \tau = 0.383 \times 10^{-3} \left(\frac{k_w \Delta T}{\nu_w \tau} \right)^{1.01} \tag{19}$$

When τ is substituted as $\rho_a C_d U_\infty^2$ and equation (19) is solved for Q_n, we get

$$Q_n = C_1 U_\infty^{0.98} \Delta T^{1.01} \tag{20}$$

Hasse's relationship is

*1 langley = 41869 J/m²

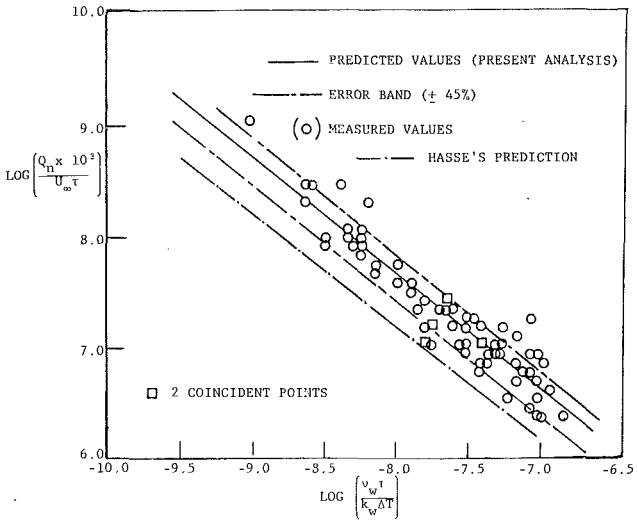

Fig. 6 Plot of nondimensional net heat flux

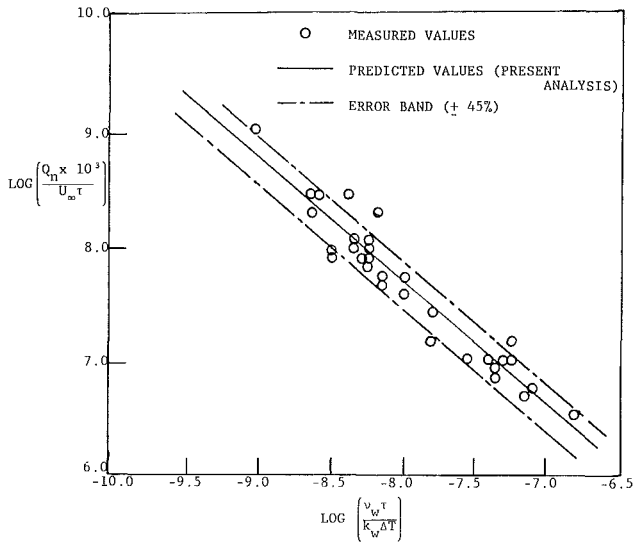

Fig. 7 Plot of nighttime nondimensional net heat flux

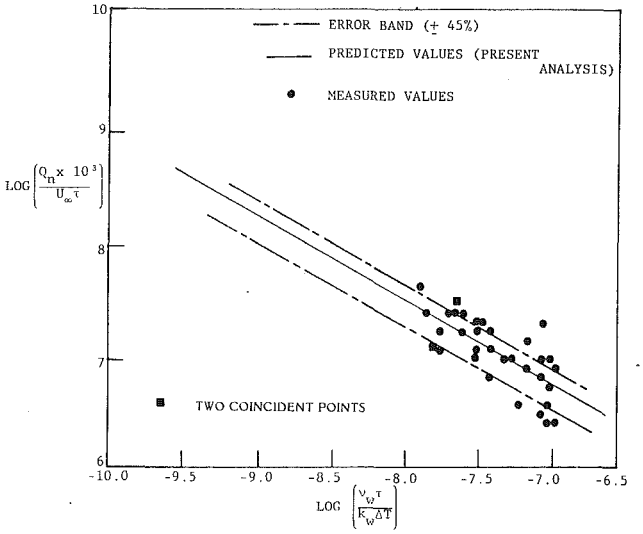

Fig. 8 Plot of daytime nondimensional net heat flux

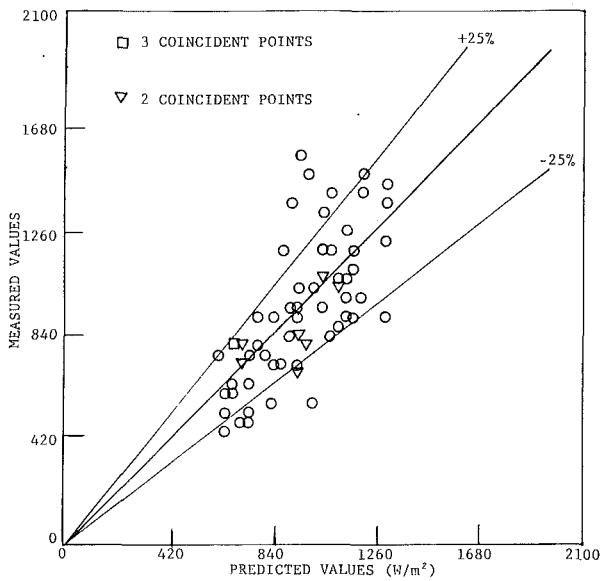

Fig. 9 Prediction of net heat flux using linear dimensional correlation

$$Q_n = C_2 U_\infty \Delta T \tag{21}$$

Hence, we observe that the correlation developed is similar to Hasse's relation with modified exponents and constant.

It is observed that Hasse's relation consistently underpredicts the net heat flux with 90 percent of the points having errors more than 60 percent. The main reason is the difference in the values of C_1 and C_2. 75 percent of all the data points (measured values) lie within a ±45 percent error band of equation (20).

The data were divided into daytime and nighttime periods, and the regression analysis was done separately for the two divisions. The following sections discuss the results.

The correlation coefficient, between the relevant parameters, for the nighttime data is found to be 0.96. The regression equation is

$$Q_n / U_\infty \tau = 0.139 \times 10^{-3} \left(\frac{k_w \Delta T}{\nu_w \tau} \right)^{1.067} \tag{22}$$

Equation (22) can be written as

$$Q_n = C_1 U_\infty{}^{0.86} \Delta T^{1.07} \tag{23}$$

This equation is slightly different in terms of exponents and constant from Hasse's well-known form ($Q_p = U_\infty \Delta T$). The results are promising (as compared to 75 percent data points lying within a ±45 percent error band) for nighttime heat flux prediction as 85 percent of all data points lie within ±40 percent error band (Fig. 7).

For daytime data the correlation coefficient between the relevant prameters is 0.70. The regression equation is

$$Q_n / U_\infty \tau = 48.24 \times 10^{-3} \left(\frac{k_w \Delta T}{\nu_w \tau} \right)^{0.724} \tag{24}$$

In the above case 68 percent of all data points lie within a ±45 percent error band (Fig. 8).

Dimensional Correlation. A linear regression was performed for predicting Q_n using the product $U_\infty \Delta T$ and the surface temperature T_s. $U_\infty \Delta T$ was used as a variable, keeping Saunders' relation in mind. T_s was used to include the effect of surface temperature on the net heat loss. Q_n was obtained as a best fit as

$$Q_n = -51.92 U_\infty \Delta T - 49.40 T_s + 1013.20 \tag{25}$$

where U_∞ is in m/s, ΔT and T_s in °C, and Q_n in W/m^2.

The standard error in calculating Q_n from the above equation is 2.25 × 10^5 W/m^2, and 80 percent of all data points lie within an error band of ±25 percent (Fig. 9). This is in contrast to the nondimensional regression correlations

for which 75 percent of all data points lie within an error band of ±45 percent. This correlation is more accurate than the previous correlation because it takes the surface temperature change into consideration. As the surface temperature increases the heat loss increases. When this linear regression is carried out for the nighttime data only, the standard error for predicting Q_n reduces to 1.79×10^5 W/m^2 (from 2.21×10^5 W/m^2) and the equation is

$$Q_n = -79.13U_\infty \Delta T - 46.89T_s + 983.9 \quad (26)$$

This prediction is quite accurate, as 90 percent of all data points lie within an error band of ±25 percent.

An examination of the above results indicates that different correlations are applicable for day and night periods. This has also been noted by Hasse in equations (7) and (8). The predicted and measured values are much closer to each other for the nighttime data. The forms of the two correlations are different with respect to an exponent and a constant [equations (22) and (23)]. When the combined correlation [equation (20)] is used to predict both the nighttime and the daytime heat flux, it predicts the nighttime heat flux more accurately. This correlation also predicts the net heat flux, which excludes the shortwave radiation satisfactorily for daytime. The results indicate that prediction of Q_n is satisfactory in the absence of shortwave radiation. It is difficult to identify the reason for this, but it is presumed to be related to the absorption of the shortwave radiation at the surface. A simple formulation which includes the effect of shortwave radiation and is similar to Hasse's equation [equation (9)] was tried and found to give unsatisfactory results.

Some of the differences in predicting the net heat flux for daytime as well as nighttime are due to the fact that the response of the skin temperature to a change in meteorological conditions is of the order of minutes or maybe seconds, while the major component of the net heat flux is the evaporative flux which is averaged over an hour in this analysis using the water budget method. There is a lack of confidence in the equations which predict the instantaneous evaporative heat flux especially for heat loaded water bodies. This inherently limits the development of a comprehensive theory for skin temperature difference, because of the uncertainty in the value of the net heat flux. The most rigorous analysis would be to measure complete vapor profiles and other parameters simultaneously to get the value of the instantaneous net heat flux.

The above discussion was related to heat flux (W/m^2) centered at the hour. This represented the average heat flux during that hour. When heat loss is added for each hour, we get the cumulative heat loss (J/m^2) for 70 hr. Measured cumulative net heat flux (J/m^2) was compared to the cumulative net heat flux calculated using the nondimensional correlation developed in the present study [equation (19)], cumulative net heat flux calculated using variable λ [equation (16)], and constant λ [equation (13)], and cumulative net heat flux using linear dimensional correlation [equation (24)].

The best agreement was found for the dimensional correlation, which predicted the cumulative heat loss to an accuracy of 99 percent. When variable λ was used, the net loss

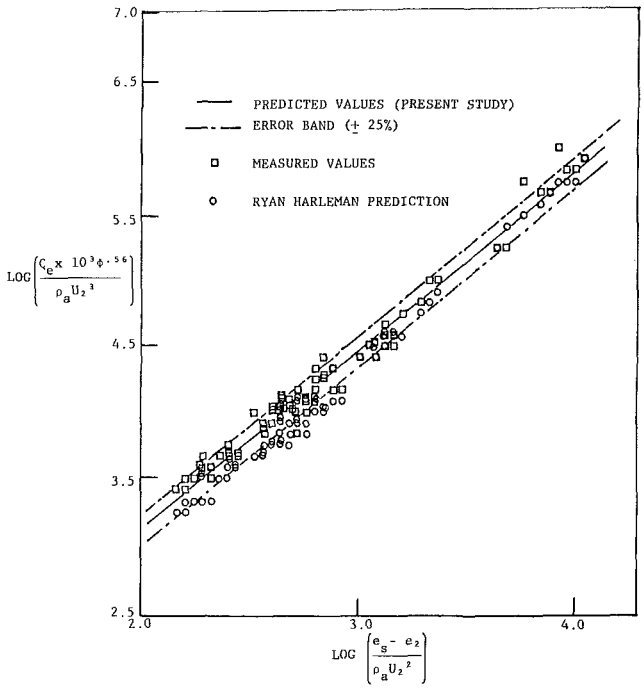

Fig. 10 Plot of nondimensional evaporative heat flux

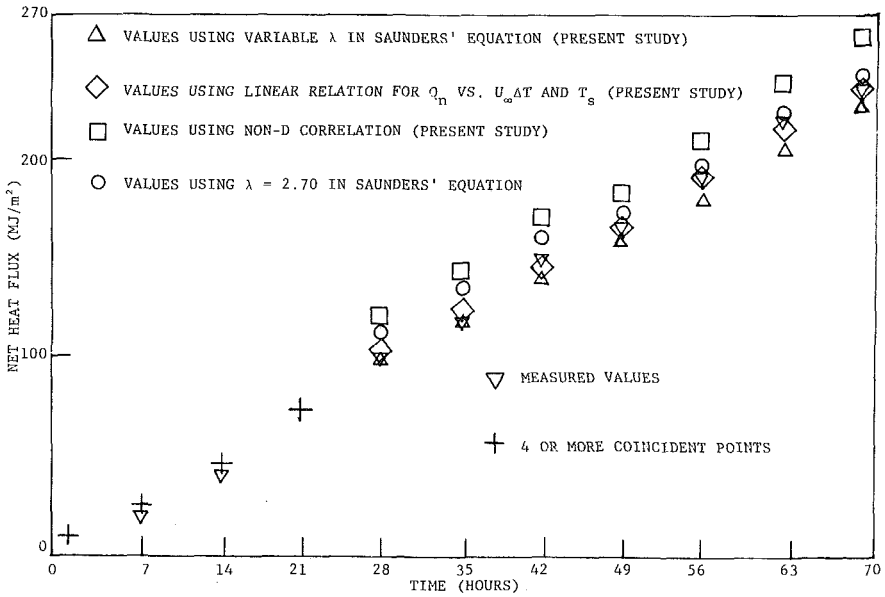

Fig. 11 Plot of cumulative net heat flux versus time

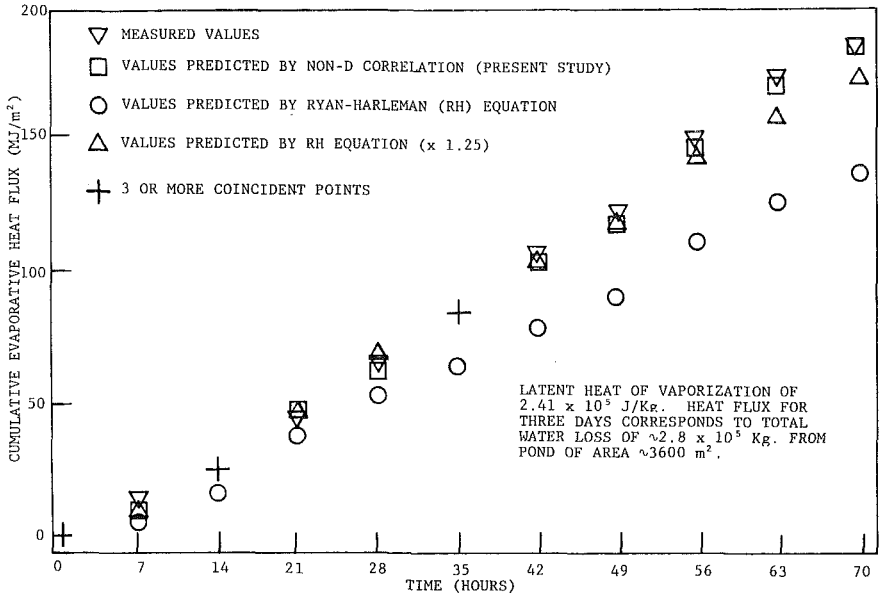

Fig. 12 Plot of cumulative evaporative heat flux versus time

was underpredicted by 7 percent, constant λ heat loss was underpredicted by 2 percent, and the nondimensional correlation overpredicted by 9 percent. Thus for predicting cumulative heat loss, variable λ, constant λ, nondimensional correlation, Hasse's equation with modified constant, and the linear dimensional correlation can be used to achieve a fair degree of accuracy (Fig. 11).

For predicting heat loss centered on the hour (W/m^2) linear dimensional correlation is the most accurate. The second best prediction is achieved using variable λ, whereas constant λ, nondimensional correlation, and Hasse's equation predict net heat flux with the same least accuracy.

Correlation for Evaporative Heat Flux

Nondimensional Variables for Evaporative Heat Flux Correlation. The relevant quantities used are ρ_a, ϕ, $(e_s - e_2)$, Q_e, and U_2.

The nondimensional numbers obtained are

$$E_1 = Q_e/\rho_a {U_2}^3 = \frac{\text{total evaporative heat loss}}{\text{wind convected kinetic energy flux}}$$

$$E_2 = (e_s - e_2)/\rho_a {U_2}^2 = \frac{\text{vapor pressure difference}}{\text{dynamic head of the flow field}}$$

ϕ = relative humidity of the free-stream air

In using the above variables, various minor effects like berm height flow alteration and sloping sides have been neglected to avoid an overly complicated model. It is assumed that the berm is not very much higher than the water surface level.

Multiple regression analysis was performed using log (ϕ) and log (E_2) as the independent variables and log (E_1) as the dependent variable; log (E_1) and log (E_2) correlated significantly with a correlation coefficient of 0.98. The correlation between the dimensionless variables is

$$\frac{Q_e}{\rho_a {U_2}^3} = 8.78 \times 10^{-3} \left(\frac{e_s - e_2}{\rho_a {U_2}^2} \right)^{1.245} \phi^{-0.56} \qquad (28)$$

When this correlation is used to compute Q_e, we observe that 85 percent of all data points lie within an error band of ±25 percent (Fig. 10).

The above correlation is different from the Ryan-Harleman equations, as it explicitly includes humidity, and the exponents of U_2 and $(e_s - e_2)$ are different. The exponents in the RH equation are 1.00 and 1.00, respectively. We see that as the humidity of the outside air increases the evaporation rate decreases. Also, the evaporative heat flux increases at a faster rate than given by the Dalton Law, which approximates that Q_e goes linearly with $(e_s - e_2)$. The exponent in the present correlation is 1.245 instead of 1.00. This can be explained in light of enhanced evaporation rates for heat-loaded ponds.

In the calculations for the evaporation regressions evaporation was available as the average evaporation rate during an hour. Wind speeds and air temperature data were available as half hour averages centered on the hour. The surface temperature was available instantaneous at the hour. Therefore the data available were not a uniform data set at one point of time. This mismatch puts an inherent limitation on an accurate prediction of the evaporative heat flux. Partial care of this mismatch was taken by centering the stilling well levels and surface temperatures on the hour, using linear interpolation and extrapolation.

When the RH equation is used to predict the evaporative heat flux, we observe that only 60 percent of all data points lie within ±25 percent error band (Fig. 10). The RH equation underpredicts the evaporation, because it was originally calibrated for lakes much larger in size than East Mesa. The fetch effect (Chattree [3]) reduces evaporation in larger ponds. When the constants in the RH equation are multiplied by 1.25, the prediction of the hour-to-hour evaporation is much better. In the RH equation the free and forced convection terms are summed linearly. However the processes of free and forced convection are not independent but related. The dimensionless correlation developed in the present study includes the effect of natural convection and couples it to the forced convection. This equation is valid only if forced and natural convection are occurring together.

The nondimensional correlation for predicting the evaporative heat flux predicts the cumulative evaporative heat loss for 3 days within 99 percent. The Ryan-Harleman equation underpredicts the cumulative evaporative heat loss for 3 days by 25 percent. When the RH equation is modified by a factor of 1.25, it underpredicts the evaporation by 7 percent (Fig. 12).

Conclusions

In this study an attempt has been made to predict the net heat and the evaporative heat flux crossing the surface of a heated water body. Table 1 summarizes various existing

Table 1 Summary of predictive equations

Description of equation		*Comments*
Saunders' equation (Fig. 5)	$Q_n = \dfrac{k_w C_d^{1/2} \rho^{1/2} U_\infty \Delta T}{\nu_w \rho_w^{1/2} \lambda}$	75 percent data points within ±45 percent error band
Modified Saunders' equation using variable λ (Fig. 5)	$\lambda = A_1 + A_2 U_\infty \Delta T$	80 percent of all data points with in ±25 percent error band; correlation coefficient of λ versus $U_\infty \Delta T$ is 0.80
Hasse's equation (Eqn. 21) (Figs. 6 and 7)	$Q_n = C_1 U_\infty \Delta T$	The values are underpredicted because Hasse's value of C_1 is not applicable here
Nondimensional correlation for net heat flux (*a*) Alltime (similar to Hasse) (Fig. 6)	$\dfrac{Q_n}{U_\infty \tau} = 0.38 \times 10^{-3} \left(\dfrac{k_w \Delta T}{\nu_w \tau} \right)^{1.01}$	75 percent data points within ±45 percent error band
(*b*) Nighttime (Fig. 7)	$\dfrac{Q_n}{U_\infty \tau} = 0.138 \times 10^{-3} \left(\dfrac{k_w \Delta T}{\nu_w \tau} \right)^{1.067}$	85 percent data points within ±40 percent error band
(*c*) Daytime (Fig. 8)	$\dfrac{Q_n}{U_\infty \tau} = 48.24 \times 10^{-3} \left(\dfrac{k_w \Delta T}{\nu_w \tau} \right)^{0.724}$	65 percent data points within ±45 percent error band
Dimensional correlation for net heat flux (*a*) Alltime (Fig. 9)	$Q_n = -51.92 U_\infty \Delta T - 49.40 T_s + 1013.20$	*80 percent data points within ±25 percent error band;* predicts cumulative heat loss for 3 days with 99 percent accuracy (Fig. 11)
(*b*) Nighttime	$Q_n = -79.13 U_\infty \Delta T - 46.89 T_s + 983.9$ Q_n: W/m², U_∞: m/s, ΔT: °C	90 percent data points within ±25 percent error band
Nondimensional evaporation correlation (Fig. 10)	$\dfrac{Q_e}{\rho_a U_2^3} = 8.78 \times 10^{-3} \left(\dfrac{e_s - e_2}{\rho_a U_2^2} \right)^{1.245} \phi^{-0.56}$	85 percent data points within ±25 percent error band; on cumulative basis for 3 days predicts evaporative heat loss with 99 percent accuracy (Fig. 12)
Ryan – Harleman Equation (Fig. 10)	$Q_e = [2.6(\Delta\theta_v)^{1/3} + 3.1 U_2][e_s - e_2]$ Q_e: W/m², ($e_s - e_2$: mbar, U_2: m/s, $\Delta\theta_v$: °C	On cumulative basis for 3 days underpredicts evaporative heat loss by 25 percent (Fig. 12)

relations and equations developed in this study. The following conclusions can be drawn after reviewing the results:

1 For formulae similar to Saunder's equation, λ increases as $U_\infty \Delta T$ increases. When this dependence of λ is used to predict Q_n, 80 percent of all data points lie within an error band of ±25 percent.

2 Wesley's Λ, which accounts for the difference between the thermal and the viscous skin thicknesses, does not give better results when compared to Saunders' λ.

3 There are two regimes for the predictive equations, one for daytime and the other for nighttime heat fluxes. This has also been noted by Hasse [5]. The prediction of heat fluxes is better when the shortwave radiation is absent. This can be seen from equations (23-24) and Figs. 7-8. A linear correlation [equation (26)] for predicting Q_n with respect to $U_\infty \Delta T$ and T_s is most satisfactory for the present study. This relation places 90 percent of all data points within a ±25 percent error band.

4 The correlation coefficient between the relevant nondimensional numbers for the evaporative heat flux correlation was found to be 0.98; the correlation [equation (28)] developed for predicting the evaporative heat flux is satisfactory, as 85 percent of all data points lie within an error band of ±25 percent.

5 For cumulative heat loss we observe that

(*a*) Actual heat loss and heat loss predicted using linear regression [equation (25)] for Q_n versus $U_\infty \Delta T$ and T_s differ by less than 1 percent. When heat loss is predicted using variable λ, constant λ in Saunders' equation and using nondimensional correlation, there is an error in the range of 8 percent (Fig. 11). Therefore these relations can also be used to predict cumulative heat loss with a fair degree of accuracy;

(*b*) the nondimensional correlation for predicting evaporative heat flux predicts the cumulative evaporative loss within 99 percent of the actual loss. The Ryan-Harleman equation underpredicts the heat loss for 3 days by 25 percent. When the RH equation is multipled by a factor of 1.25, the error reduces to 7 percent underprediction.

Acknowledgments

This work was supported by EPRI through a subcontract from MIT. The authors wish to acknowledge the help of Mr. John Bartz for the support, Dr. Eric Adams for valuable suggestions and assistance in data collection, and Mr. George Athey of BPNL for help in skin temperature data collection and for supplying the supporting data. The support of the NSF through an equipment grant is also acknowledged.

References

1 Adams et al., *Progress Report on Evaluation of Models for Predicting Evaporative Water Loss and Hydrothermal Performance in Cooling Impoundments*, Report of Energy Laboratory, MIT, 1980.

2 Athey, G. F., Hadlock, R. K., and Abbey, O. B., Measurements on Cooling Pond at East Mesa Site (Data supplied by Pacific Northwest Laboratory, Richland, Washington), 1981.

3 Chattree, M., "An Examination of Transport Processes at the Air-Water Interface with Special Emphasis on Prediction of the Net Heat Flux and Evaporative Heat Flux across the Interface," M.S. thesis, University of Miami, 1982.

4 Deacon, E. L., *Gas Transfer to and Across an Air-Water Interface*, Tellus, Vol. 29, 1977, pp. 363-374.

5 Hasse, L., *The Sea Surface Temperature Deviation and the Heat Flow at the Sea-Air Interface*, Boundary Layer Meteorology 1, 1971, pp. 368-379.

6 Hill, R. H., "Laboratory Measurements of Heat Transfer and Thermal Structure Near an Air-Water Interface," *J. of Physical Oceanography*, Vol. 2, 1972, pp. 190-198.

7 Howe, B. M., Chambers, A. J., and Street, R. L., "Heat Transfer at a Mobile Boundary," in: *Advances in Heat and Mass Transfer at Air-Water Interface*, ASME, 1978, pp. 1-10.

8 Howe, B. M., Chambers, A. J., Klotz, S. P., Cheung, T. K., and Street, R. L., "Comparison of Profiles and Fluxes of Heat and Momentum Above and Below an Air-Water Interface," ASME Paper 80-WA/HT-68, 1980.

9 Klotz, S. P., and Street, R. L., "On the Simulation of the Coupled Laminar Boundary Layer at a Smooth, Phase-Changing Gas-Liquid Interface," *Proc. Second Int. Conf. on Numerical Methods in Laminar and Turbulent Flow*, Venice, Italy, 1981.

10 Lee, S. S., Sengupta, S., and Lee, C. R., "Surface Skin Temperature Gradients in Cooling Lakes," *Proceedings of the 2nd Waste Heat Management and Utilization Conference*, Miami Beach, FL, 1979.

11 McLeish, W., and Putland, G. E., "Measurement of Wind Driven Flow Profiles in the Top Millimeter of Water," *J. of Physical Oceanography*, Vol. 5, 1975, pp. 516-518.

12 McAlister, F. D., and McLeish, W., "Heat Transfer in the Top Millimeter of the Ocean," *Journal of Geophysical Research*, Vol. 74, No. 13, 1979.

13 Paulson, C. A., and Parker, T. W., "Cooling of Water Surface by Evaporation, Radiation and Heat Transfer," *Journal of Geophysical Research*, Vol. 77, No. 3, 1972.

14 Reznjevic, K., *Handbook of Thermodynamic Tables and Charts*, Hemispherre, 1976.

15 Ryan, P. J., Harleman, R. F., and Stolzenbach, K. D., "Surface Heat Loss from Cooling Ponds," *Water Resources Research*, Vol. 10, No. 5, 1974, pp. 930-938.

16 Saunders, P. M., "The Temperature of the Ocean-Air Interface," *Journal of Atmospheric Sciences*, Vol. 25, 1967, pp. 269-273.

17 *Sperry Univac—Large Scale System Stat-Pack Programmer Reference* (UP 7502), Section 9, pp. 1-11.

18 Wu, J., "Wind Induced Drift Currents," *J. of Fluid Mechanics*, Vol. 68, 1975, pp. 49-70.

N. Kaji
Assistant Professor.
Department of Automobiles,
The Institute of Vocational Training,
Sagamihara 229, Japan

Y. H. Mori
Associate Professor.
Department of Mechanical Engineering,
Keio University,
Yokohama 223, Japan

Y. Tochitani
Associate Professor.
Department of Mechanical Engineering,
Kanazawa Institute of Technology,
Nonoichi 921, Japan

Heat Transfer Enhancement Due to Electrically Induced Resonant Oscillation of Drops

By applying a low-frequency alternating field with a specially designed waveform, we succeeded in making water drops in a medium of silicone oil undergo a resonant shape oscillation of the second mode. The resonant oscillation was found to be quite effective for enhancing heat transfer between the medium and drops.

Introduction

This paper reports on some of our continuing efforts to seek effective methods for electrohydrodynamic augmentation of direct contact heat transfer to or from drops passing through an immiscible liquid. A novel augmentation technique is presented which has not been attempted successfully in either our previous works [1-6] or any other related works reported so far. The background of the technique is as follows.

When a liquid drop suspended in a second liquid phase with a much higher electrical resistivity is subjected to a steady electric field, at the drop half-surface facing an electrode a charge is induced that is opposite in sign to the electrode. The drop undergoes deformation into a prolate spheroid, with its axis of revolution parallel to the direction of the field, because of electric stresses acting on the surface charge [7]. If the field is interrupted suddenly, the drop will of course recover an almost spherical form again due to the interfacial tension force. Thus, it is readily assumed that if a field is applied intermittently with an appropriate frequency, the drop will undergo a shape oscillation, i.e., a reciprocating deformation between a sphere and a prolate spheroid. In fact we succeeded in inducing such a shape oscillation of single water drops rising in a denser silicone oil by applying an intermittent electric field and thereby enhancing the heat transfer to the drops [1-3]. The field was applied perpendicular to the drop path, crossing the parallel electrode plates installed vertically, as illustrated in Fig. 1. In order to prevent drops from migrating parallel to the field, the direction of the field was alternated. The correspondence in phase between the field and the drop oscillation is illustrated in Fig. 2. It should be noted that drops oscillated twice in each period of the field, $1/f$; in other words, the field frequency f is equal to half the oscillation frequency f'. The appearance of the oscillation differed from that of usual drop oscillations of the second mode in that the "neutral" drop shape was not spherical but was biased to a prolate spheroid (see Fig. 2*b*). Experiments with varying field frequency f and constant field strength E_f showed that while the oscillation amplitude ($\sim (D_p/D_n)_{max}$) is maintained constant over a frequency range below a certain critical frequency f_{cr}, it starts to decrease monotonically as f increases exceeding f_{cr}; and that the heat transfer coefficient takes a maximum at that very f_{cr}. We expected that a resonant oscillation of the second mode would occur when f is adjusted to a particular frequency f_{r2} which is half the resonance frequency f'_{r2} of drops, and that the resonant oscillation would yield a more intensive augmentation of heat transfer. Although f_{r2} was predicted to fall in the f range covered by our experiments, we never recognized a resonant oscillation. We assume that this fact should be ascribed to higher-

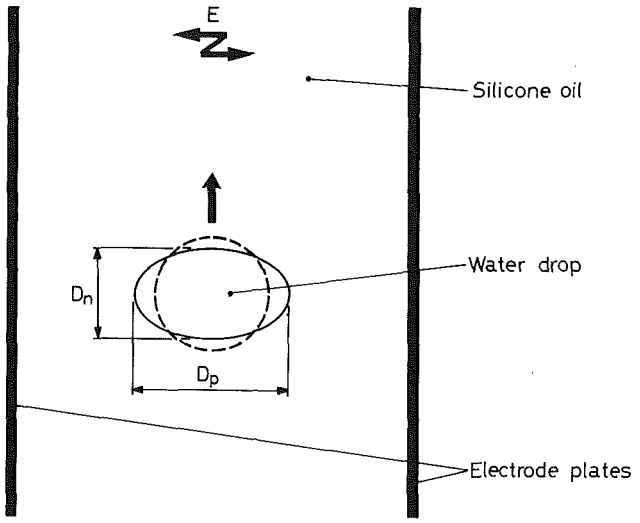

Fig. 1 Scheme of applying an electric field on a water drop rising in denser silicone oil

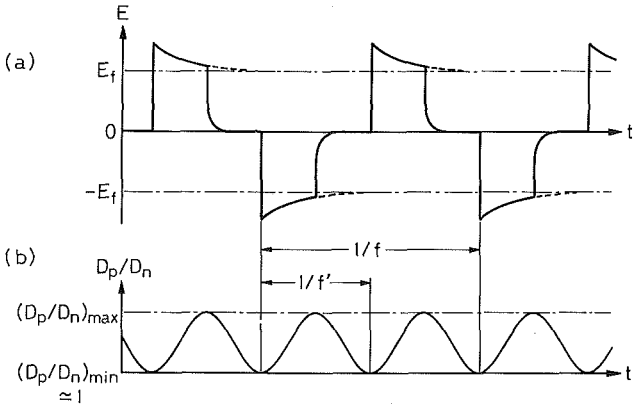

Fig. 2 Pulsed quasi-square waveform of an intermittent field (*a*) and induced shape oscillation of a drop (*b*)

Contributed by the Heat Transfer Division for publication in the JOURNAL OF HEAT TRANSFER. Manuscript received by the Heat Transfer Division October 12, 1984.

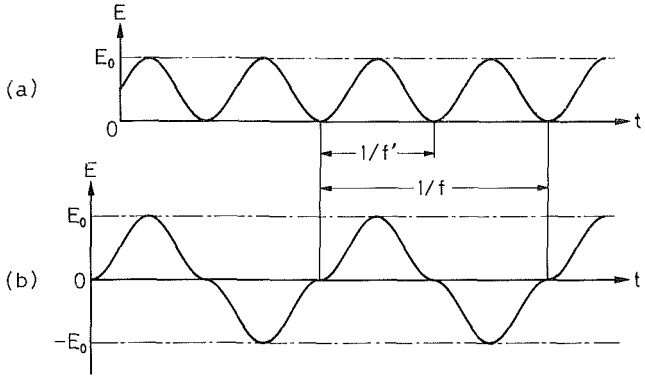

Fig. 3 Modified sinusoidal waveform of a field for inducing a resonant oscillation of drops

frequency components having been involved in the waveform employed, which is illustrated in Fig. 2(*a*).

The purpose of this study is to produce a resonant oscillation and to examine its effectiveness for heat transfer augmentation. For this purpose we intended to employ a field waveform which is considered the most favorable for giving drops the resonant oscillation whenever the fundamental frequency component f of the field is adjusted to the resonance frequency f'_{r2} or f_{r2}. This waveform may be such that the field strength E changes sinusoidally with time between two limiting values, $E = 0$ and $E = E_0 > 0$, as illustrated in Fig. 3(*a*) or expressed as

$$E = \frac{E_0}{2}(\sin 2\pi f' t + 1) \tag{1}$$

If we simply assume that the drop deformation depends on the magnitude of the field and not on its direction, the above waveform can be replaced by one such as the one illustrated in Fig. 3(*b*) or expressed as

$$E = (-1)^{[2ft]}\frac{E_0}{2}\left[\sin\left(4\pi ft - \frac{\pi}{2}\right) + 1\right] \tag{2}$$

where the brackets in the exponent of (-1) denote Gauss' notation; i.e., $[2ft]$ means the maximum integer that does not exceed $2ft$. The above assumption is valid under a steady field, but not exactly correct under an unsteady field unless the charge relaxation at the drop surface is instantaneous. Despite this problem we decided to employ the alternating waveform given in Fig. 3(*b*) or by equation (2) in order to prevent the drop migration which may have a secondary effect on heat transfer and thus hinder a correct evaluation of the effect of shape oscillation on heat transfer. In practical operations in heat exchangers, however, the drop migration may rather be a favorable factor contributing to the heat transfer, and thus we may be able to employ the waveform given in Fig. 3(*a*) or by equation (1).

Experimental

The general arrangement of the experiments was almost the same as that described in references [2, 5]. Isolated water drops of a specified volume rose in a stagnant, hotter medium of methylphenyl silicone oil (KF 54 fluid prepared by Shin-Etsu Chemical Co., Tokyo) contained in a space between a pair of vertical brass-plate electrodes set parallel to each other. The distance between the electrodes was 38 mm. The undisturbed temperature of the medium was maintained between 49.5 and 50.2°C throughout the experiments, while it was maintained constant within ± 0.1 K in each run. Each run consisted of a recording of drop motions by means of cinephotography as well as a series of drop temperature measurements – which are only briefly described below – under specific field conditions. The free rise of each drop was interrupted by a glass funnel which was inserted at an arbitrary elevation in the medium, and then the drop was swallowed slowly into the funnel. The lowest temperature that a thermocouple located at the entrance of the funnel showed while each drop passed over the thermocouple junction was recorded, and it was regarded as the reference drop temperature at that elevation. By traversing the funnel vertically we got the elevation dependence of the drop temperature from which we deduced the quasi-steady overall heat transfer coefficient α related to the equivalent spherical surface area of each drop. More details of the measurements and the process of deducing α are described in [2].

A special power supply yielding such a field as illustrated in Fig. 3(*b*) was newly designed by one of us (Y. T.) and was constructed for the sake of this study. Its output voltage can be varied between 1.5 and 12.5 kV, and its frequency can be varied in a range above 0.5 Hz. The distortion of waveform increases gradually with an increasing frequency. A detailed description of the design and the performance of the power supply is given elsewhere [8].

Results and Discussion

Drop Dynamics. Drop motions observed in this study under fields with the modified sinusoidal waveform (Fig. 3*b*) were almost the same in appearance as those observed in the previous study [2, 3] under intermittent fields with a pulsed quasi-square waveform (Fig. 2*a*). That is, drops rose rectilinearly making prolate-biased shape oscillations. As the field strength E_0 increased, the amplitude of the shape

Nomenclature

D_n = axis of drop normal to electric field, mm
D_p = axis of drop parallel to electric field, mm
D_0 = equivalent spherical diameter of drop, mm
$(D_p/D_n)_{max}$ = maximum distortion ratio of drop shown in Fig. 2
$(D_p/D_n)_{min}$ = minimum distortion ratio of drop shown in Fig. 2
d = duty ratio of intermittent electric field
E = strength of electric field, MV/m
E_f = strength of electric field shown in Fig. 2, MV/m
E_0 = strength of electric field shown in Fig. 3, MV/m
f = frequency of electric field, Hz
f' = frequency of drop oscillation, Hz
f_{cr} = critical field frequency shown in Figs. 4 and 6, Hz
f_{r2} = field frequency yielding second mode resonant oscillation of drop, Hz
f'_{r2} = resonance frequency of second mode oscillation of drop, Hz
t = time, s
α = heat transfer coefficient based on surface area of spherical drop, W/(m²K)
α_0 = α under no electric field, W/(m²K)

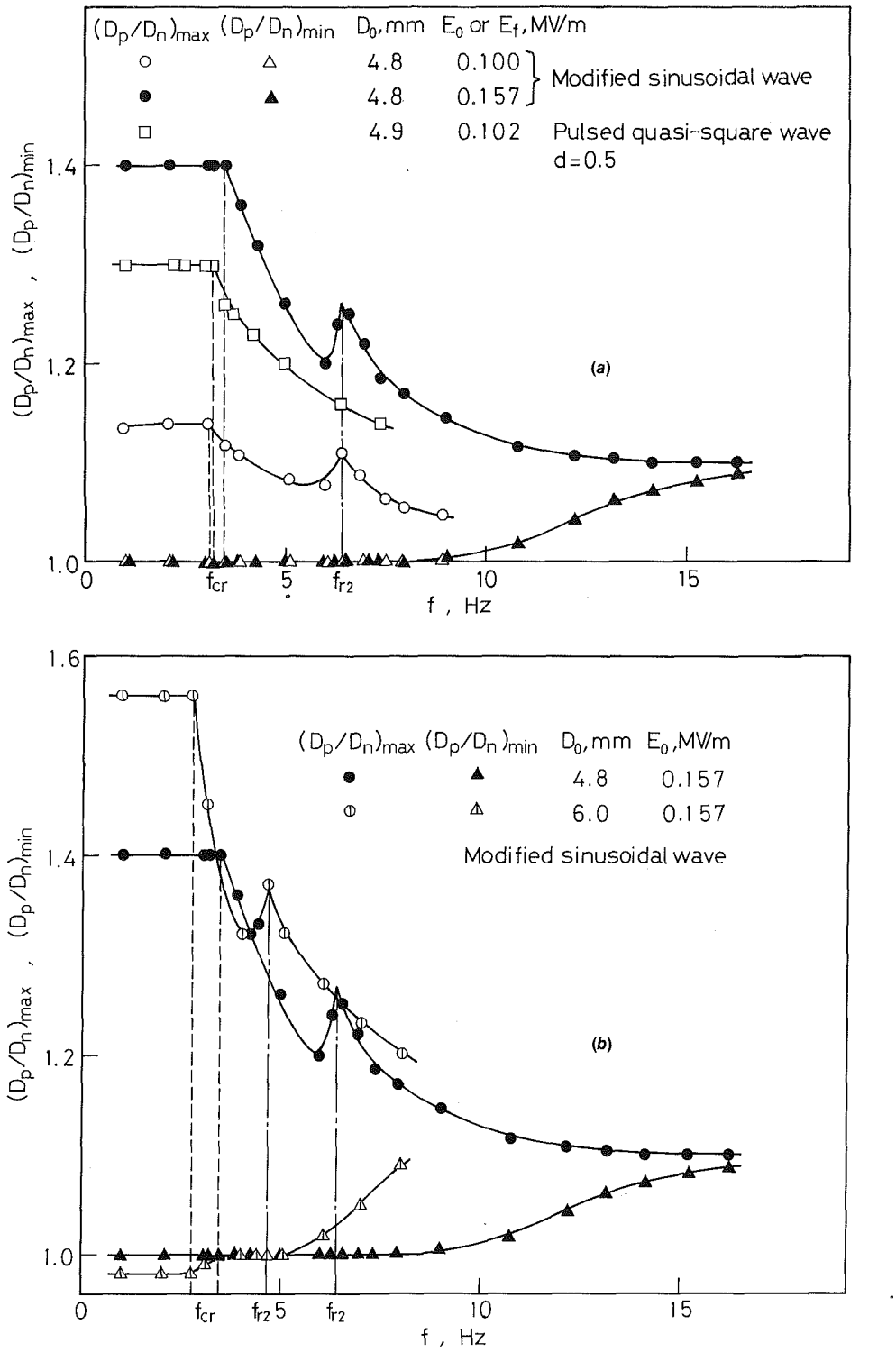

Fig. 4 Dependences of $(D_p/D_n)_{max}$ and $(D_p/D_n)_{min}$ on the field frequency: Parameters of interest are strength and waveform of the field in (a) and drop diameter in (b)

oscillation increased, and the rise velocity of drops decreased only slightly. More details of drop dynamics are given below.

Dependences of $(D_p/D_n)_{max}$ and $(D_p/D_n)_{min}$ on the field frequency f are shown in Figs. 4(*a*) and 4(*b*). Three sets of data for drops of almost the same size are compared in Fig. 4(*a*); two sets were obtained in this study under fields with the same modified sinusoidal waveform but with different E_0, and the other set was obtained in the previous study [3] under intermittent fields with a pulsed quasi-square waveform. In Fig. 4(*b*) two sets of data for drops of different sizes are compared. Every set of data shows the existence of a critical frequency f_{cr} where $(D_p/D_n)_{max}$ starts to decrease with an increasing f. The value of f_{cr} depends appreciably on the drop size but very weakly on the strength and waveform of applied field. Although $(D_p/D_n)_{max}$ decreases monotonically, in the case of pulsed quasi-square waveform, as f increases ex-

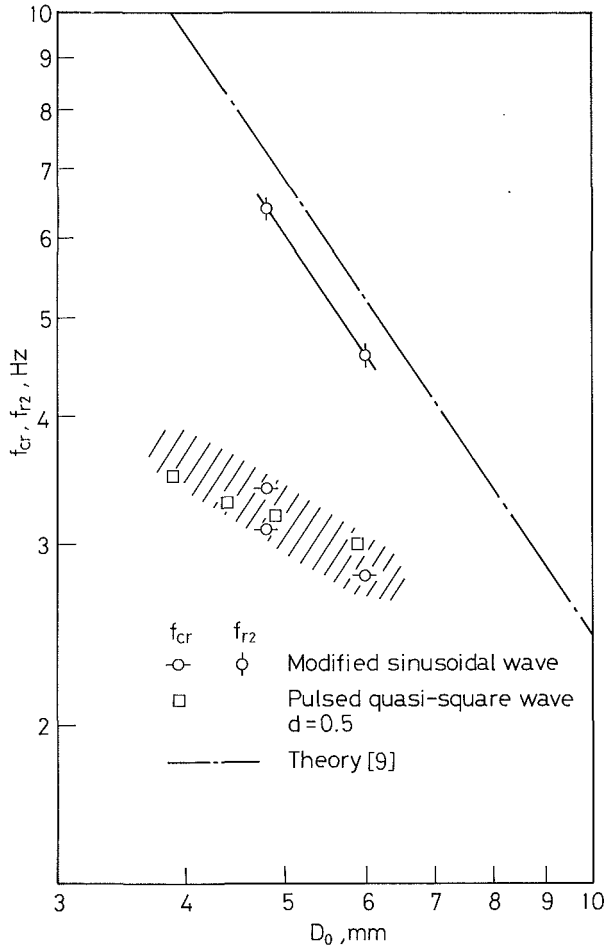

Fig. 5 Dependences of f_{r2} and f_{cr} on drop diameter

ceeding f_{cr}, $(D_p/D_n)_{max}$ exhibits a peak at a certain frequency in the case of modified sinusoidal waveform. We assume that the peak is caused by the resonant oscillation of the second mode, and we regard the frequency where the peak is located as f_{r2}, half of the resonance frequency f'_{r2} of drops. On the other hand, $(D_p/D_n)_{min}$ is equal to or slightly less than unity over a frequency range less than 8 Hz when $D_0 = 4.8$ mm or 5 Hz when $D_0 = 6.0$ mm. (Nothing special is recognized at $f = f_{r2}$ which falls in the above range.) This means that each drop recovers its spherical shape once in every half period $1/(2f)$. As f increases further, drops no longer return to the spherical shape and thus $(D_p/D_n)_{min}$ increases asymptotically to the same level to which $(D_p/D_n)_{max}$ decreases asymptotically.

The frequency f_{r2} can be determined approximately to be 6.4 Hz when $D_0 = 4.8$ mm and 4.6 Hz when $D_0 = 6.0$ mm based on Figs. 4(*a*) and 4(*b*). These two experimental f_{r2} values are lower by 22 percent than half of f'_{r2}, for the same D_0, as predicted by introducing appropriate physical-property values (see Table 1 in [6]) into conventional hydrodynamic theory for small-amplitude driven oscillations of spherical drops [9]. However, such a deviation is not always significant in view of uncertainties of the property values.

As E_0 increases, the amplitude of oscillation increases, and at the same time the "neutral" drop shape is biased more and more into a prolate spheroid. Although such changes in the oscillation amplitude or in the neutral drop shape are expected to cause a decrease of the resonance frequency f'_{r2} [10, 11] and thus f_{r2}, no dependence of f_{r2} on E_0 could be recognized in the range of the present experiments.

The difference between f_{r2} and f_{cr} is dependent on the drop size as illustrated in Fig. 5. The excess of f_{r2} over f_{cr} decreases with an increasing D_0, since f_{r2} is approximately proportional to $-3/2$ power to D_0 while f_{cr} exhibits a weaker negative dependence on D_0. As D_0 further increases far beyond the range of our experiments, f_{r2} will presumably become lower than f_{cr}; this will be preceded by $(D_p/D_n)_{max}$ at $f = f_{r2}$ exceeding the level of $(D_p/D_n)_{max}$ which prevails over the frequency range less than f_{cr}. This matter is not only of physical interest but also of potential importance, as discussed briefly in the following section, in selecting the optimum frequency for heat transfer augmentation.

Heat Transfer. Since fields yield no detectable change in the translational motion of drops (except a slight decrease of the rise velocity) as stated before, any increases in the heat transfer rate under fields are practically ascribed to the induced shape oscillations of drops. It should further be noted that fractional increases, due to the shape oscillations, in the instantaneous surface area of each drop over the equivalent spherical surface area are only 3.3 percent at most in the range of the present experiments. Thus, the primary factor yielding such increases in the heat transfer rate as shown below is no doubt reciprocating convections induced inside and outside drops by the oscillations. We investigate in this paper, however, neither the convections themselves nor their roles in heat transfer, but rather show the heat transfer enhancements obtained and simply relate them to the oscillations observed.

The relative increases in quasi-steady heat transfer coefficient α due to fields are presented in Figs. 6(*a*) and 6(*b*). Note that the data shown in Fig. 6(*a*) correspond to those in Fig. 4(*a*) and those in Fig. 6(*b*) correspond to Fig. 4(*b*). In the case of the modified sinusoidal waveform tested in the present experiments, α exhibits one peak at $f = f_{cr}$ just as in the case of the pulsed quasi-square waveform, and another peak at $f = f_{r2}$. The existence of some peak of α at either of those frequencies is plausible, because the time-averaged oscillation velocity – which is roughly evaluated by $f(D_{p,max} - D_{p,min})$ – takes the maximum at either of them. However, the peaks shown in Figs. 6(*a*) and 6(*b*) are somewhat too sharp to be simply interpreted in terms of the time-averaged oscillation velocity depending on the frequency f. A full interpretation of the matter will require an intensive analysis of the convections developed over the drop surface, which is beyond the scope of this paper.

As long as we judge by the results given in Figs. 6(*a*) and 6(*b*), α at $f = f_{r2}$ is a little inferior to that at $f = f_{cr}$ under the same E_0. This fact may be a consequence of the rise of the oscillation amplitude at $f = f_{r2}$, being rather limited as can be seen in Figs. 4(*a*) and 4(*b*). However, these findings should be accepted with some caution. The waveform yielded by our power supply was not always perfect over the frequency range covered by the present experiments. As a matter of fact, it suffered an appreciable distortion at, for example, $f = 5$ Hz and larger distortions at higher frequencies [8]. Therefore, the experimental results do not always represent correctly such quantities as those to be obtained under fields with an ideal waveform. In other words, the oscillation at $f = f_{r2}$ might have been excited more intensively resulting in a stronger enhancement of heat transfer, if we could have applied fields with a more regular waveform.

It seems worthwhile to note a potential advantage of selecting f_{r2} instead of f_{cr} even if f_{r2} yields a still lower α than f_{cr} does after perfect regulation of the waveform. Figure 7 shows α/α_0 versus $(D_p/D_n)_{max}$ relations at $f = f_{cr}$ and $f = f_{r2}$. (It may be interesting to note that a difference in waveform yields little difference in the α/α_0 versus $(D_p/D_n)_{max}$ relation at $f = f_{cr}$.) Apparently f_{r2} yields a higher α than f_{cr} does at every level of $(D_p/D_n)_{max}$ in the whole range of the experiments. This fact sounds reasonable, because

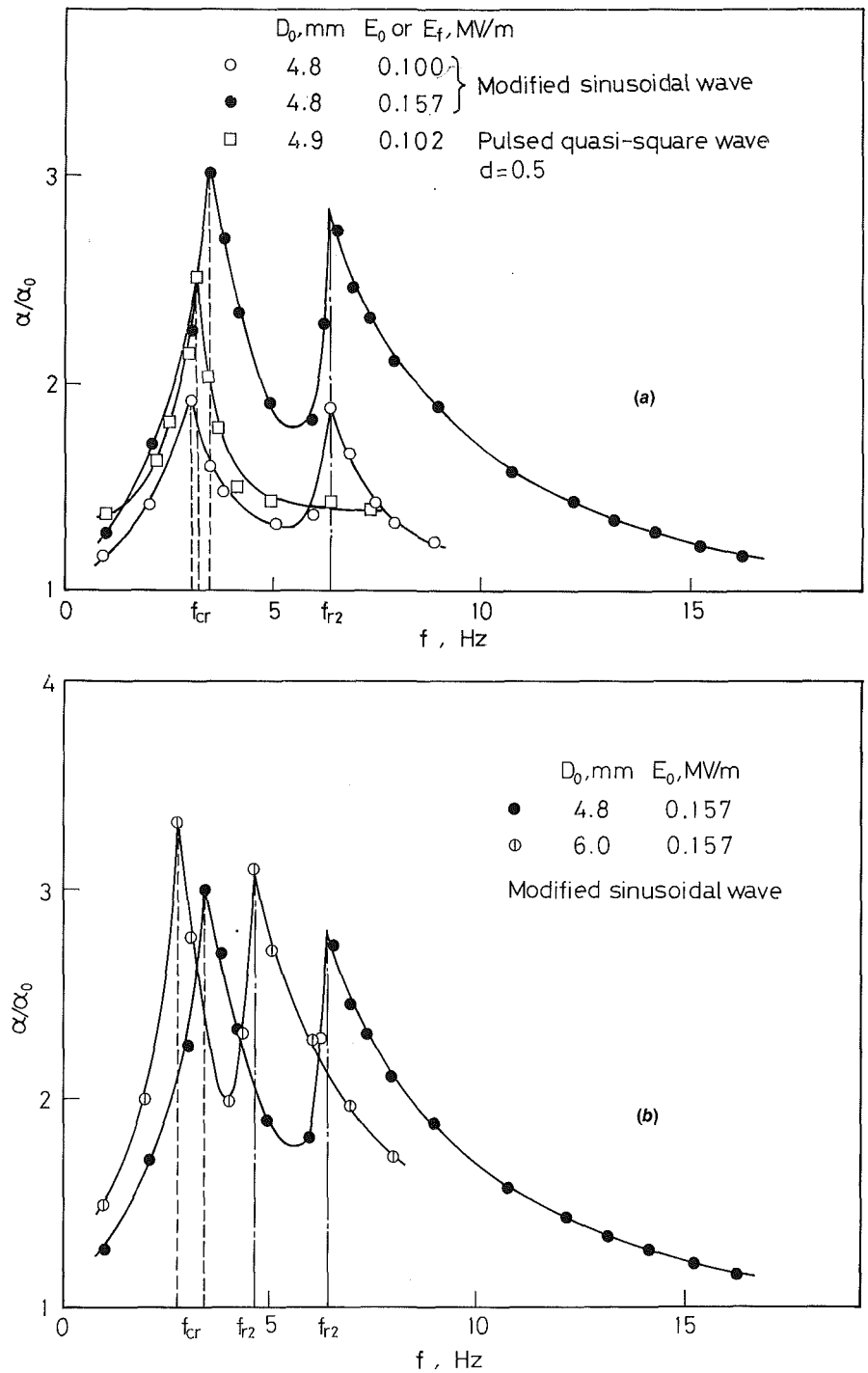

Fig. 6 Dependence of relative increase of heat transfer coefficient on the field frequency: Parameters of interest are strength and waveform of the field in (*a*) and drop diameter in (*b*)

under the same level of $(D_p/D_n)_{max}$ a faster motion of the interface is available at f_{r2} than at f_{cr} as long as $f_{r2} > f_{cr}$. Therefore, such superiority of α at f_{r2} to that at f_{cr} will be the same at higher levels of $(D_p/D_n)_{max}$ beyond the range of the experiments. In order to prevent drops from bursting which would cause a serious difficulty in heat exchanger operations [6], $(D_p/D_n)_{max}$ must not be increased too much. (The possible upper limit of $(D_p/D_n)_{max}$ is 2.8 in the case of water/KF 54 system [6], but a much lower level will be required for safe operations.) Thus, selecting f_{r2} instead of f_{cr} seems appropriate for the purpose of realizing the highest α avoiding a risk of drop burst, as long as the condition that $f_{r2} > f_{cr}$ is satisfied in the given system. The advantage of selecting f_{r2} will be lost if $f_{r2} < f_{cr}$.

In either case, it is important to clarify the dependences of both f_{r2} and f_{cr} on system properties. This task is left to future study. For the present, we can roughly predict f_{r2} with the aid of conventional theory on small-amplitude drop oscillations [9], but we have no means to express a general f_{cr} in terms of system properties.

Conclusions

We have succeeded in making drops undergo resonant

shape osciliation of the second mode by utilizing an alternate field with a specially designed waveform as illustrated in Fig. 3(*b*). The heat transfer coefficient peaks at two different frequencies: the critical frequency f_{cr} beyond which the oscillation amplitude exhibits a sudden drop, and the frequency f_{r2} yielding the resonant oscillation (Fig. 6). The highest heat transfer coefficient will be available by selecting f_{r2}, at least under some conditions.

Acknowledgments

We would like to express our sincere thanks to Dr. Kazuo Yoshida of Department of Mechanical Engineering, Keio University for his valuable suggestions on the aspect of physical interpretation of drop oscillations observed in our previous study [3]. His suggestions led us to the basic idea of this study. We also acknowledge H. Hirano, H. Suzuki, and Y. Nishiyama, former students at the Institute of Vocational Training, for their assistance in a part of the experimental work. This study was supported by the Ministry of Education, Science and Culture of Japan which appropriated Grants in Aid for Scientific Research Nos. 57045105 and 58045105 and also by Kurata Foundation.

References

1 Mori, Y. H., Kaji, N., and Tochitani, Y., "An Augmentation Method of Heat or Mass Transfer With an Intermittent Electric Field," Japanese Patent No. 1043731.

2 Kaji, N., Mori, Y. H., Tochitani, Y., and Komotori, K., "Direct-Contact Heat Transfer to Drops in an Intermittent Electric Field," *Proceedings of the 6th International Heat Transfer Conference*, Toronto, Aug. 1978, Vol. 3, pp. 165–170.

3 Kaji, N., Mori, Y. H., Tochitani, Y., and Komotori, K., "Augmentation of Direct-Contact Heat Transfer to Drops With an Intermittent Electric Field," ASME JOURNAL OF HEAT TRANSFER, Vol. 102, 1980, pp. 32–37.

4 Mori, Y. H., and Kaji, N., "An Augmentation Method of Heat or Mass Transfer Between Drops and a Continuous Fluid Phase With an Electric Field," Japanese Patent pending.

5 Kaji, N., Mori, Y. H., Tochitani, Y., and Komotori, K., "Electrohydrodynamic Augmentation of Direct-Contact Heat Transfer to Drops Passing Through an Immiscible Dielectric Liquid: Effect of Field-Induced Shuttle Migration Between Parallel Plane Electrodes of Drops," *Proceedings of the 7th International Heat Transfer Conference*, Munich, Aug. 1982, Vol. 5, pp. 231–236.

6 Kaji, N., and Mori, Y. H., "Direct Contact Heat Transfer to a Drop Translating in a Transverse Electric Field," *Warme- und Stoffubertragung*, Vol. 18, 1985, to be published.

7 Torza, S., Cox, R. G., and Mason, S. G., "Electrohydrodynamic Deformation and Burst of Liquid Drops," *Philosophical Transactions of the Royal Society of London*, Series A, Vol. 269, 1971, pp. 295–319.

8 Tochitani, Y., "High Voltage ac Power Supply With Variable Frequency Output from 0.5 to 10 Hz," *Review of Scientific Instruments*, to be published.

9 Trinh, E., Zwern, A., and Wang, T. G., "An Experimental Study of Small-Amplitude Drop Oscillations in Immiscible Liquid Systems," *Journal of Fluid Mechanics*, Vol. 115, 1982, pp. 453–474.

10 Trinh, E., and Wang, T. G., "Large-Amplitude Free and Driven Drop-Oscillations: Experimental Observations," *Journal of Fluid Mechanics*, Vol. 122, 1982, pp. 315–338.

11 Sample, S. B., Raghupathy, B., and Hendricks, C. D., "Quiescent Distortion and Resonant Oscillations of a Liquid Drop in an Electric Field," *International Journal of Engineering Science*, Vol. 8, 1970, pp. 97–109.

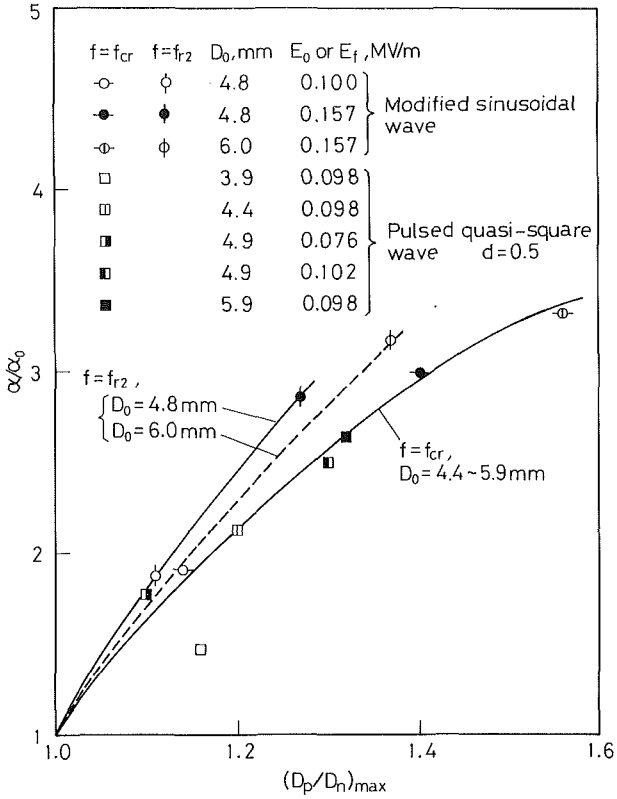

Fig. 7 α/α_0 **versus** $(D_p/D_n)_{max}$ **relations at** $f = f_{r2}$ **and** $f = f_{cr}$

C. Bénard

D. Gobin

F. Martinez

ERA 1028-CNRS,
Bâtiment 502,
Campus Universitaire,
91405 Orsay, France

Melting in Rectangular Enclosures: Experiments and Numerical Simulations

This paper presents a numerical and experimental analysis of the heat transfer process that takes place while melting a solid material, in a rectangular enclosure. Natural convection is present in the melt layer, and the solid phase is assumed to be isothermal. Very detailed and precise experimental results are given that are used to validate a particularly rapid numerical code. Some insights into the kinetics of the melting process lead to a deeper understanding of the coupling between convection and phase change and allow us to propose a simple algebraic correlation that predicts the time evolution of the melting front to within 5 percent.

Introduction

Over the last few years, a great deal of experimental [1-9] and numerical [10-21] research has dealt with the influence of natural convection on the kinetics of heat transfer during the melting process of a solid material.

The experimental studies mainly provide observations of the solid-liquid interface during melting of phase change materials (PCMs), such as paraffins or other organic compounds, and occasionally present temperature measurements in the melt [1, 7]. For the experiments that have been performed with the horizontal direction being the direction of initial propagation of the melting front, it has been experimentally observed that as soon as the thickness of the melt layer is of the order of several millimeters (corresponding to a Rayleigh number, based on the melt layer thickness and the maximum temperature difference in the liquid phase, of the order of 10^3), the onset of natural convection in the melt modifies the shape and velocity of the melting front. These results have been obtained for several different geometries, generally allowing a two-dimensional approach. The configurations studied are the vertical cylinder [1, 2], the horizontal cylinder [3, 4] and the rectangular enclosure [5-7]. Generally, these papers do not include parametric studies, with the exception of experimental investigations of the role of the aspect ratio of the cavity [2, 5].

Apart from the phenomenological observations referred to above, an interferometric analysis [8] of the melting process of heptadecane in a rectangular cavity with a free top surface has shown that the convection regime is laminar for Rayleigh numbers (based on the height of the cavity) up to 5×10^7. During the review process of the present paper an experimental study of melting in enclosures of different geometries was published [9], and correlations giving the heat transfer at the interface as a function of the governing parameters are proposed.

A great many papers [10-19] deal with the numerical simulation of the problem and present results of numerical parametric studies. In these analyses however, the Rayleigh number is always kept smaller than 10^8, though, for most thermal storage applications using parafins, the magnitude of Ra in the melt layer is in the range: $10^8 \leq \mathrm{Ra} \leq 10^{10}$.

Some numerical studies consider cases in which it is not necessary to solve the complete set of coupled equations describing natural convection and phase change [10, 11, 20]. In the other studies, the complete coupled problem is analyzed for various geometric configurations: around a vertical cylinder [12, 19], around a horizontal cylinder [13], inside a horizontal cylinder [14-16], and in a rectangular enclosure [17, 18, 21]. Generally, qualitative agreement with experimental results is reported, but apart from [18, 21], no comparison between experimental and numerical results is presented. In the comparison presented in [21], the authors relate their numerical results to the experiments reported in [6]. Unfortunately, the absence of detailed information about the experiments did not allow a completely satisfactory comparison. In [18], a comparison is presented for the beginning of the melting process in a rectangular cavity with Rayleigh numbers of the order of $10^7 - 10^8$. Good qualitative agreement is obtained for the shape of the melting front; however, the simulations predict systematically lower values for the speed of propagation of the interface as compared to the experiments, for reasons that are not fully understood.

This short review of the state of the art indicates that, for the Rayleigh numbers typically found in practical applications such as latent heat storage, there are very few experiments and no thoroughly validated numerical models. Moreover, the numerical codes presented in the literature, though capable of simulating only lower Rayleigh number flows, require prohibitively large computer time for simulating a full fusion cycle.

The objectives of this paper are:

1 to present detailed and reliable experimental results of the melting process in a rectangular enclosure heated from one vertical side

2 to use these results to validate an efficient numerical simulation program presented earlier [21]

3 to present some insights into the problem of time development of the melting process in a two-dimensional rectangular enclosure in the absence of conduction in the solid phase. A deeper understanding of the convection and melting problem leads to a simple algebraic correlation that predicts the time development of the melting process to within 5 percent.

In the typical process under study, the material is initially in the solid state at fusion temperature. Fusion is started by raising the temperature of one vertical wall of the rectangular cell containing the material to a temperature $T_1 > T_f$, while the opposite wall of the cell is maintained at T_f. The top boundary condition is one of free surface, since the cell is not completely filled up to allow for the expansion of the PCM upon melting.

The process is characterized by four dimensionless numbers: the Rayleigh number, based on the height Ra_H, the

Contributed by the Heat Transfer Division for publication in the JOURNAL OF HEAT TRANSFER. Manuscript received by the Heat Transfer Division August 20, 1984.

Prandtl number, the Stefan number, and the aspect ratio A of the cavity. The present study is valid for the following orders of magnitude of these parameters

$$\mathrm{Ra} \cong 10^8 - 10^9;\ \mathrm{Pr} \gtrsim 10;\ \mathrm{Ste} < 0.2;\ 5.5 \gtrsim \mathrm{A} \gtrsim 1.2$$

In part I, the numerical method is briefly explained. In part II, the experimental set is described. In parts III and IV, experiment and simulation are compared progressively by considering first the problem of the convecting liquid alone (Part III), and then the coupled problem of natural convection in the liquid phase and melting of the isothermal solid (Part IV). In part V, simple correlations are established.

I Numerical Method

In this section, the main assumptions and characteristics of the numerical method already described in [21] are summed up briefly.

First, the PCM is a pure substance, changing phase at a well-defined temperature T_f with a known enthalpy.

Moreover, it is assumed that the liquid PCM is

1 newtonian
2 incompressible
3 satisfies the Boussinesq approximation

The heat transfer is supposed to fulfill the following hypotheses:

4 the flow is two dimensional (end-wall effects are negligible)
5 heat transfer at the solid–liquid interface is not strongly perturbed by the expansion of the PCM on melting
6 the melting front surface is smooth: There are no effects arising from dendrite formation or coarse-grained crystal structure in the solid.
7 the convection flow in the melt is in the laminar regime
8 the convective flow is not strongly influenced by the movement of the melting front, since for the order of magnitude of the characteristic dimensionless parameters defining the range of our study, the front velocity is negligible compared to the liquid boundary layer velocities. As a consequence, natural convection can be computed for a fixed cavity at a given time step.
9 natural convection is in a steady state at every time step since the characteristic time for convection to reach steady state is much less than the time needed by the front to make a significant move

As a consequence, the numerical procedure consists in computing the steady-state convection regime in a nonrectangular cavity at every time step. The resulting local heat transfer at the interface is then used to determine the position of the melting front at the end of the time step. The procedure is repeated until complete melting of the PCM.

With θ, $\mathbf{V}$, P being the dimensionless temperature, velocity, and pressure, respectively, the equations of natural convection in the liquid phase (conservation of mass, momentum and energy) are written

$$\nabla \cdot \mathbf{V} = 0 \tag{1}$$

$$(\mathbf{V} \cdot \nabla) \cdot \mathbf{V} = \nabla^2 \mathbf{V} - \nabla P - \mathrm{Gr} \cdot \theta \mathbf{g} / |\mathbf{g}| \tag{2}$$

Nomenclature

A = aspect ratio of the enclosure $= H/L$
$\bar{A}$ = equivalent aspect ratio of the nonrectangular liquid cavities
$c^*(z^*, t^*)$ = position of the solid–liquid interface
C_p = specific heat capacity of the liquid phase
D = depth of the enclosure
$F(t)$ = melted fraction $= \dfrac{1}{HL}\int_0^H c^*(z^*, t^*)dz^*$
F_0 = $F(t_0)$
g = acceleration due to gravity
Gr = Grashof number (based on height) $= g\beta\Delta T \cdot H^3/\nu^2$
H = height of the enclosure (z direction)
$I[z_D]$ = $\int_0^{z_D} S(z)\,dz$; equation (19)
k = thermal conductivity of the liquid phase
L = width of the enclosure (y direction)
L_f = latent heat of fusion
$\mathbf{n}$ = normal vector to the interface
$\hat{\mathrm{Nu}}(z)$ = local Nusselt number at the cold wall of a rectangular cavity (scale: $k\Delta T/H$), equation (6)
$\mathrm{Nu}_E(z)$ = dimensionless amount of heat at the interface per unit of the vertical surface (experimental)
$\mathrm{Nu}_S(z)$ = the same, for simulation
$\overline{\mathrm{Nu}}$ = average Nusselt number at the interface
$\overline{\mathrm{Nu}}_C$ = average Nusselt number at the interface in the conduction regime
$\overline{\mathrm{Nu}}_0$ = average Nusselt number at the cold wall of a rectangular enclosure
P = pressure $= P^*H^2/\rho\nu^2$
Pr = Prandtl number of the liquid PCM $= \nu/\alpha$
Ra = Rayleigh number (based on height) = Pr•Gr
s = displacement of the interface along $\mathbf{n}$
Ste = Stefan number $= \dfrac{C_p \cdot \Delta T}{L_f}$
$S(z)$ = equation (6)
t = dimensionless time $= t^*\nu/H^2$
t_0 = time of the end of the conduction regime in the liquid phase
t_F = time of contact of the melting front with the cold wall
$\hat{t}$ = dimensionless time; equation (11)
T = dimensional temperature
T_f = melting point of the PCM
T_1 = temperature of the *hot* wall
T_0 = temperature of the *cold* wall
T_m = average temperature $= (T_1 + T_0)/2$
$\mathbf{V}$ = velocity $= \mathbf{V}^*H/\nu$
v^* = horizontal velocity of the melting front
y^* = horizontal dimensional coordinate
Y = horizontal transformed coordinate $= \dfrac{y^*}{H} \cdot \dfrac{L}{c^*(z^*, t^*)}$
z^* = vertical dimensional coordinate
z_D = position of contact of the interface with the cold wall
α = thermal diffusivity
β = expansion coefficient of the liquid PCM
δ = average width of the liquid cavity
ΔT = temperature difference $= T_1 - T_0$
θ = dimensionless temperature
ρ = density (ρ_s: solid, ρ_L: liquid)
ν = kinematic viscosity
τ = dimensionless time $= A\hat{t}$
∇ = gradient operator

Superscript

* = dimensional quantities

Table 1 Thermophysical properties of *n*-octadecane

Thermophysical Property	Unit	
Latent heat : L_F	J/kg	$241\ 10^3$
Thermal conductivity : k	W/m°C	0.157
Specific heat : C_p	J/kg°C	2200
Density : ρ_L at 30°C, (40°C)	kg/m³	775.5 (768.4)
ρ_S	"	814
Expansion coefficient : β	$°C^{-1}$	$0.91\ 10^{-3}$
Kinematic viscosity : ν at 30°C,(35°C)	m²/s	$5.005\ 10^{-6}$ $(4.468\ 10^{-6})$

$$(\mathbf{V}\cdot\nabla)\cdot\theta=\frac{1}{\mathrm{Pr}}\nabla^2\theta \tag{3}$$

where **g** is the gravity, ∇ the gradient operator, Gr the Grashof number built on the height of the cell and the temperature difference ΔT between the two vertical walls, and Pr the Prandtl number of the liquid PCM. The two vertical walls bounding the liquid are considered isothermal and no-slip. The bottom wall is adiabatic and no-slip. The top surface, in contact with air, is treated full slip and adiabatic.

The interface motion equation is

$$-\mathbf{n}\cdot\nabla\theta=\frac{\rho_s}{\rho_L}\frac{\mathrm{Pr}}{\mathrm{Ste}}\frac{\partial s}{\partial t} \tag{4}$$

where **n** is the local normal to the melting front and $\partial s/\partial t$ the local dimensionless velocity of the interface along **n**. The quantity ρ_s is the solid density, ρ_L the liquid density.

The cavity is a nonrectangular domain, due to the irregular shape of the melting front. The position of the interface at time t^* and level z^* is defined by its distance from the hot vertical wall $c^*(z^*, t^*)$. A nonorthogonal coordinate transformation is used to map the physical liquid cavity into a rectangular computational space. The transformed equations are simplified by neglecting the cross terms due to nonorthogonality. This has no significant effect on the precision if

$$\frac{\partial c^*}{\partial z^*}\lesssim 0.3$$
$$H\frac{\partial^2 c^*}{\partial z^{*2}}\lesssim 0.3 \tag{5}$$

The validity of this approximation has been checked experimentally, but this is however a limitation of the code.

The numerical simulation technique is a finite difference method based on Patankar-Spalding differencing scheme [23] that solves the steady-state convection problem using a false transient procedure to accelerate convergence. An unevenly spaced rectangular grid is used in the computational space and we could check that this allows a good resolution of the boundary layers and a good estimation of the heat transfer at the solid-liquid interface using a limited number of nodes [21, 24].

The initialization of the numerical procedure uses an approximate analytical solution of the one-dimensional Stefan problem [25].

The CPU time presently required for one calculation step (natural convection plus interface movement) is about 500 s on a UNIVAC-1110 computer. A complete melting process may be simulated using 15 to 30 steps.

II Experimental Set

The PCM used in the experiments is pure *n*-octadecane. Most of its thermophysical properties are known within a few percent from the literature [26–29]. The melting temperature of the PCM has been checked to be $T_f=28.05\pm0.05$°C, which is in agreement with the published data. The average values of the thermophysical properties are summed up in Table 1.

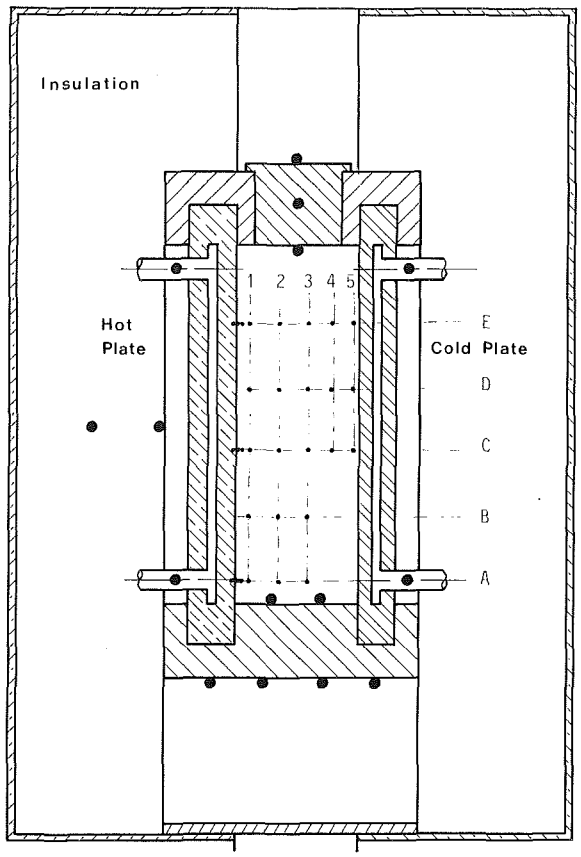

Fig. 1 Vertical cross section of the experimental cell; location of the thermocouples (10^{-2}m):
$z_A^*=1.24$, $z_B^*=4.71$, $z_C^*=8.20$, $z_D^*=11.72$, $z_E^*=15.26$; $y_1^*=0.82$, $y_2^*=2.33$, $y_3^*=3.83$, $y_4^*=5.33$, $y_5^*=6.63$

The experimental cell containing the phase change material is a rectangular parallelepiped (height $H=0.197$ m, width $L=0.0688$ m, depth $D=0.600$ m) (Fig. 1).

II.1 Boundary Conditions. The two largest vertical walls facing each other are metal flat heat exchangers through which water is circulated. They have been designed so that the temperature drop between the water inlet and outlet in each heat exchanger is less than 0.2°C, even when delivering the maximum heat flow rate needed in the experiments. The water flow path machined into the hot wall heat exchanger (made out of brass) has been designed so that no surface temperature nonhomogeneity can be detected on the hot surface within 0.1°C. The cold wall heat exchanger is made out of an aluminum alloy.

The inlet water temperature to each exchanger can be maintained constant throughout each experimental run (several hours) with a precision of 0.05°C. This high stability has been obtained by using two closed-loop water supplies, each one consisting of a thermostat and a 0.5-m^3 well-insulated water bath. The large thermal mass of the water bath is needed to smooth out the short-term fluctuations (±0.15°C) due to the on-off regulation of the thermostat.

Each vertical heat exchanger is protected on its side and back faces by another exchanger which is maintained at the same temperature.

The remaining four walls of the cell are made out of 0.04-m-thick altuglass. All the outside faces of the enclosure are carefully insulated, and the top and bottom walls can thus be considered as adiabatic in a first-order approximation, the heat losses being less than 0.3 W/m²/°C. The insulation on

the vertical endwalls can be removed for photographic observation of the melting front.

Due to the shape of the cell, the heat transfer can be considered as two dimensional [22]; indeed, we could verify during our experiments that the effects of the end walls are confined to a region of about 1 cm near these walls, as evidenced by the uniform melting front propagation.

II.2 Temperature Measurements. Sixty Cr-Al thermocouples are used with a digital voltimeter (resolution 1 μV) to measure temperatures with an accuracy of 0.025°C. The voltimeter outputs are processed by a minicomputer. Since the temperatures in the experiments vary slowly with time, the circuit noise is reduced by time averaging five successive measurements for each thermocouple. The time interval between two successive measurements on the same thermocouple is kept at more than 30 s to fully dissipate the heat generated by operating the thermocouple relay, which would otherwise result in a small error in the measured temperature. All the sixty channels, with the thermocouple and electric relay in place, have been calibrated independently. The accuracy with nonaveraged measurements is ± 0.05°C; for averaged measurements, it increases to ± 0.025°C, equal to the voltimeter accuracy. The uncertainty on averaged temperature differences is ± 0.10°C, and on absolute temperatures, it is ± 0.15°C.

Nine thermocouples (diameter 0.12 mm) are used to measure the hot plate surface temperature in its central part. These thermocouples are placed in blind holes drilled into the hot plate from the outside, and are 1 mm from the inner surface of the hot wall.

Six thermocouples are located very close to the hot wall to study the temperature gradients in the hot boundary layer. In the bulk of the PCM, 22 thermocouples are tightened with springs on a 0.20 m length along the third dimension. The uncertainty on the position of the wire axes with respect to the hot surface is 0.15 mm.

Several 0.2-mm-dia thermocouples are located in the water inlets and outlets, on the side walls of the cell and in the surrounding insulation, as indicated on Fig. 1. They are used to estimate the heat losses through the horizontal walls and to check the stability of the experiments.

During an experimental run, the measurements are generally taken every 300 to 360 s on "slowly" varying thermocouples and every 60 s on "quickly" varying ones. The thermocouple channels are automatically shifted from "slow sampling" to "quick sampling" by the computer when the measured temperature reaches the melting point T_f.

III Validation of the Convection Model

The first step of the methodology used here for validating the numerical code consists in a comparison of experimental and numerical results for natural convection in a rectangular enclosure. Although this problem has been extensively studied in the literature, it was necessary to perform specific experiments to check the validity of the convective part of the code and mainly the values given to the physical parameters of the liquid PCM. Indeed:

- few data are available for high Rayleigh number convection
- the thermophysical properties of the liquid phase are expected to be strongly temperature dependent in the vicinity of the fusion temperature; their influence on the heat transfer at the cold wall has to be known to tackle the melting problem.

In the second step (see section IV), the parameters characterizing the melting process are introduced by considering fusion experiments, without conduction in the solid phase.

In the reference experiment on natural convection, the hot heat exchanger, initially at the same temperature $T_0 = 28.1$°C as the cold plate, is raised to $T_1 = 37.6$°C. The cold temperature is chosen to be very close to T_f: The thermal boundary conditions are thus similar to those met in the melting problem. The height of liquid in the cell is $H = 0.1775 \pm 0.001$ m. With those conditions, the dimensionless parameters characterizing the experiment are: $A = 2.58$, $\mathrm{Pr} = 50.9$, $\mathrm{Ra} = 1.09 \cdot 10^9$. The temperature measurements in the fluid show that the indications of the five thermocouples of a given horizontal level are identical within a 0.1°C margin, indicating that all of them are in the central stratified zone.

The dimensional temperature distributions in the vertical midplane, $T(L/2, z^*)$ obtained experimentally and numerically are compared in the following way [24]:

Two numerical solutions of the problem have been obtained using constant thermophysical properties and a 23×21 irregular grid. These solutions frame the maximum dispersion of the numerical results due to the uncertainties on the physical parameters of the PCM and on the experimental conditions [24]; it is less than 0.1°C. The difference between these solutions and the experimental results is of the order of 0.3°C at midheight ($z^* \cong H/2$) and the asymmetry of the experimental results is not represented by these numerical simulations. These discrepancies that cannot be explained by the uncertainties of the parameters are removed if the kinematic viscosity is taken to be nonlinearly temperature dependent close to T_f: The linear variation between 40°C and 30°C given by the literature [29] and a quadratic extrapolation between 30°C and 28.1°C, leading to $\nu(T_f) \cong 9 \cdot 10^{-6}$ m^2/s, give a very good fit. The corresponding average heat transfer at the cold wall is 4 percent lower than the value obtained with a constant ν, a result that will have to be kept in mind when analyzing the melting problem.

The local Nusselt number distribution at the cold wall of the enclosure obtained in the calculation with constant thermophysical parameters fits very well the correlation proposed for air by Schinkel et al. [30]:

$$\hat{Nu}(z) = 0.33\ \mathrm{Ra}^{1/4} S(z) \tag{6a}$$

where

$$S(z) = 1.594(1-z)^{-1/4}(0.27 + 0.46z)^{5/4}$$

extending the validity of this correlation to the range $\mathrm{Ra} = 10^9$, $\mathrm{Pr} = 50$, and $2.5 \leqq A \leqq 25$.

In spite of the assumption of constant physical parameters the interest of such a correlation, which is not dependent on A if H is used as the reference length to define $\hat{\mathrm{Nu}}(z)$ and Ra, will appear clearly in the analysis of the melting process driven by natural convection in liquid cavities of constant height and changing aspect ratio.

The only drawback of Schinkel correlation is that if $z \to 1$, $S(z) \to \infty$. Our experimental results will allow us to propose a more realistic value for $S(z)$ when z goes to 1

$$S(z) \cong S(0.98) \cong 2.174 \text{ for } 0.98 \leqq z \leqq 1 \tag{6b}$$

IV Analysis of the Melting Process

IV.1 Typical Fusion Experiment: Experimental Procedure. At the beginning of the experiment, the cell is filled with solid *n*-octadecane to a height $H = 0.170 \pm 0.001$ m. The initial temperature in the cell ($T_0 = 27.65$°C) is perfectly uniform within the precision of the measurements. The initial losses are very low, smaller than 0.10 W/m^2. A temperature step, defined at ± 0.1°C, heats up the hot wall from T_0 to $T_1 = 37.05$°C in 150 s. The initial time $t^* = 0$ is when T_1 reaches 37.05°C. Due to the imperfections of the experiment, T_1 drifts very slowly to 37.17°C during the first three hours, to attain 37.30°C after six hours and stabilize at this value until the end of the experiment (complete melting). During the process, the height H of the liquid cavity increases, and the

experiment has been characterized by three periods of constant ΔT and H:

(1) $t^* < 148$ min, $\Delta T = 9.05 \pm 0.1\,^\circ$C,
$H = 0.172$ m, $\mathrm{Ra} = 0.936 \cdot 10^9$, $\mathrm{Ste} = 0.083$

(2) $148 < t^* < 360$ min, $\Delta T' = 9.2 \pm 0.1\,^\circ$C,
$H' = 0.175$ m, $\mathrm{Ra}' = 1.002 \cdot 10^9$, $\mathrm{Ste} = 0.084$

(3) $t^* > 360$ min, $\Delta T'' = 9.25 \pm 0.1\,^\circ$C,
$H'' = 0.180$ m, $\mathrm{Ra}'' = 1.097 \cdot 10^9$, $\mathrm{Ste} = 0.084$

IV.2 Interface Heat Transfer

IV.2.1 Experimental Results. The evolution of the melting front position, obtained from the photographic observations, is displayed on Fig. 2. In the lower part of the cavity, the interface is linear and the tilt increases with time. In the top part, the melting front exhibits a strong curvature.

The uncertainty on the position of the interface from the photographs is of the order of 0.0015 m, due to the depth of the experimental cell (0.60 m). Thus these profiles will be preferably used to fit the shape of the melting front, and the temperature evolution of the thermocouples (Fig. 3) will provide the more accurate information needed to study the overall kinetics of the melting process.

Let us stress that the melting front definition depends on the crystal structure of the solid-liquid interface. As it would not be possible to get a very smooth interface if the temperature of the solid phase were maintained too close to the melting point, the temperature of the cold wall is kept 0.4°C below T_f. The slight heat loss through the solid phase corresponding to this temperature difference is lower than 0.2 percent of the total heat flux and can be neglected.

The temperature evolution of the thermocouples that are close to the hot wall shows that the initial conduction regime is progressively disturbed between 6 min ($\bar{A} = 67$) and 12 min ($\bar{A} \cong 50$), where $\bar{A}$ is the equivalent aspect ratio, based on the half-height thickness of the liquid cavity: $\bar{A} = 1/c(0.5, t)$. From 12 min to 35 min ($\bar{A} \cong 30$), the stratification of temperatures appears and, from 35 min to 60 min ($\bar{A} \cong 20$), the boundary layer regime builds up and remains stable during the whole experiment.

The temperature evolution of the thermocouples located in the bulk of the PCM (Fig. 3) shows a very sharp increase of the temperature when the melting front reaches the location of the thermocouple, corresponding to the high temperature gradient in the boundary layer. Then, after a maximum in the inversion zone, the temperature reaches a steady value when the thermocouple is in the central stratified zone.

The time-dependent position of the melting front, $c^*(z^*, t^*)$, at different heights z^* can be obtained either from the photographic observations or from the thermocouple temperature evolution (Fig. 4). It can be seen on the figure that within the precision of the experiment, the local width of the liquid cavity at height z^* increases linearly with time for

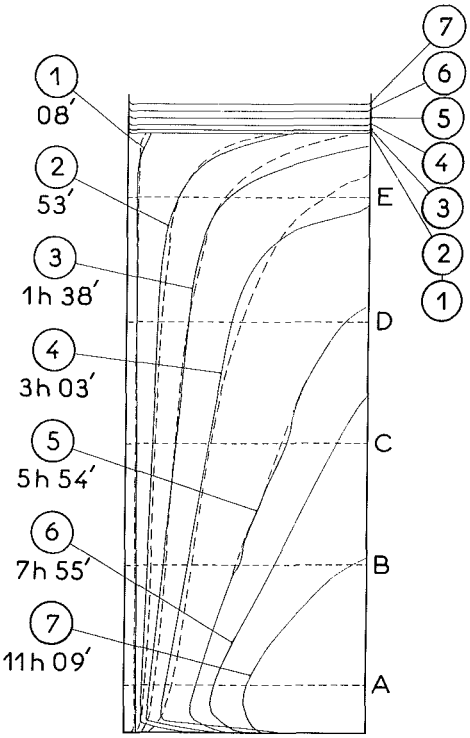

Fig. 2 Time evolution of the melting front: experiment (solid line) and simulation (dashed line)

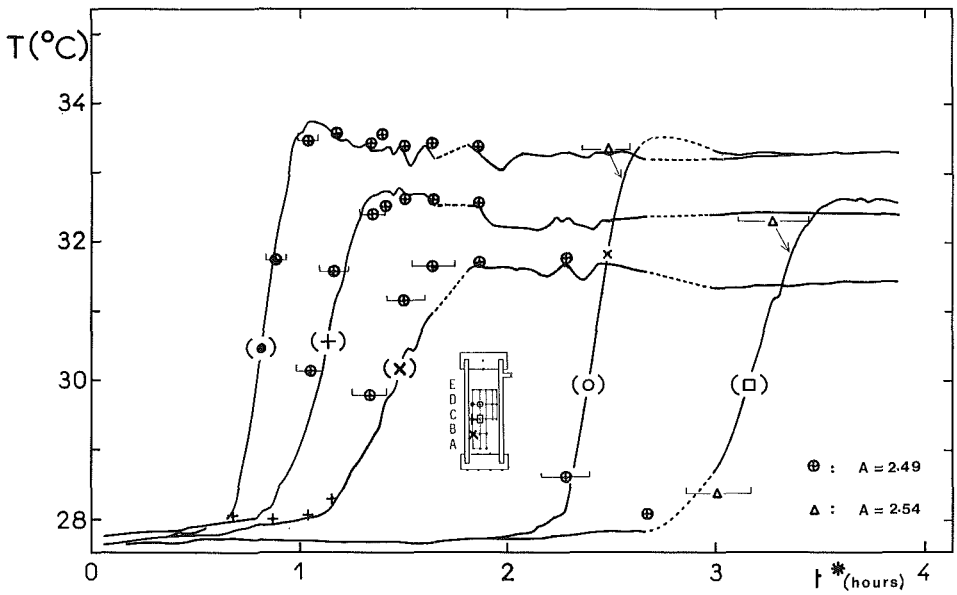

Fig. 3 Temperature evolution of the thermocouples located in the bulk of the PCM (levels B, C, and D): experiment (solid lines) and simulation (points)

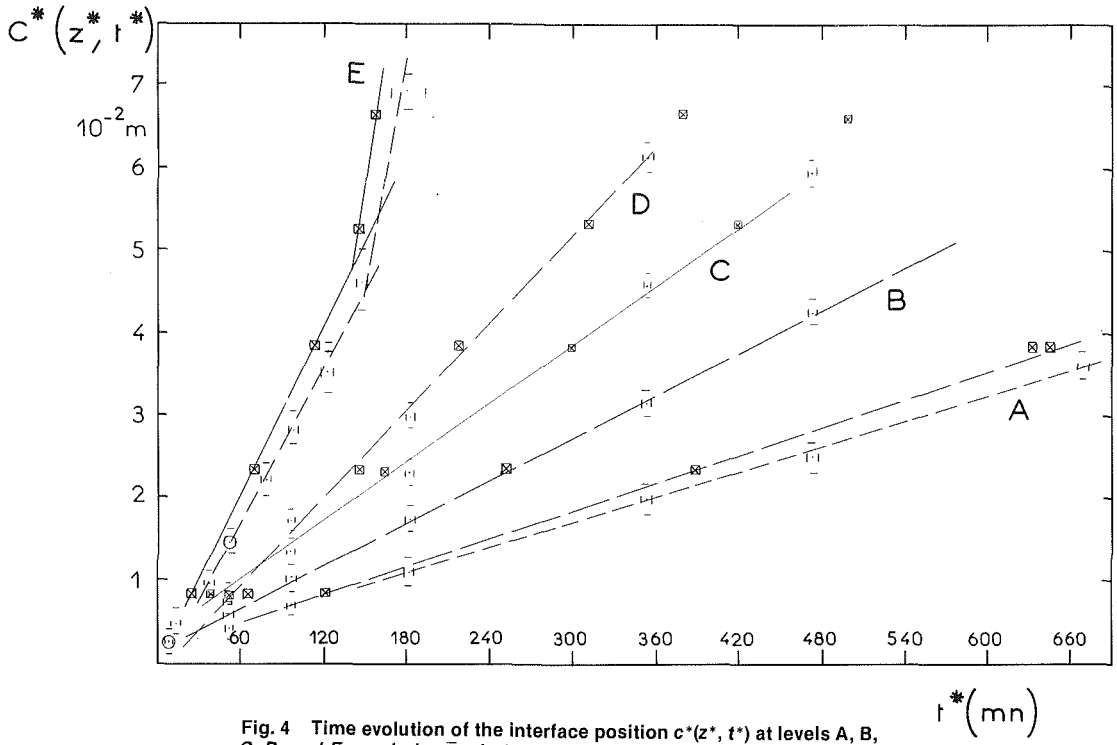

Fig. 4 Time evolution of the interface position $c^*(z^*, t^*)$ at levels A, B, C, D, and E; symbols: ⊟ photographic observations; ⊠ thermocouple measurements

Table 2 Experimental results

LEVEL	Dimensionless height : z	$v_E^*(z^*)$ (10^6 m/s)	$Nu_E(z)$
A	0.072	0.89	21.12
B	0.274	1.44	34.17
C	0.476	1.98	46.99
D	0.681	2.92	69.29
E	0.888	5.40	128.15

$t^* > 50$ min and as long as the melting front has not reached the cold wall at level z^*. The local *horizontal* velocity $v_E^*(z^*, t^*) = \partial c^*(z^*, t^*)/\partial t^*$ may thus be considered as a constant at a given height: The values of $v_E^*(z^*, t^*)$ are obtained with a precision of 5 percent (see Table 2). This important original result will be used in our simplified analysis of the problem.

IV.2.2 Comparison of Numerical and Experimental Results. The numerical and experimental results are compared in Figs. 2 and 3. It can be seen in Fig. 2 that for small enough local tilts and curvatures of the melting front (equation (5)) the simplified coordinate transformation used in the numerical code is a very good approximation. But after about 50 min, the top part of the simulated interface progressively slows down compared with the experimental results due to the higher tilt and curvature of the melting front that the numerical code cannot simulate with sufficient accuracy because of the approximation in the transformation of coordinates. Let us underline that the neglected extra amount of heat transfer to the very top part of the front due to the expansion of the PCM upon melting is an order of magnitude too small to influence significantly the front shape.

The good agreement in the central linear part of the melting front is confirmed by comparison of the temperature evolution in the liquid cavity at levels *B*, *C*, and *D* (Fig. 3). We may notice that the slopes of the thermocouple *T* versus time, $\partial T/\partial t^*$, are identical in the experiment and in the numerical simulation: Both the melting front velocities and the shape of the boundary layer at levels *B*, *C*, and *D* are in good agreement. In particular, the simulation gives constant *horizontal* fusion velocities $v_S^*(z^*, t^*)$ at each level, identical to the experimental results within the error margin. The numerical simulation shows that this is verified for $t^* > 50$ min, which corresponds to the separation of the boundary layers.

IV.2.3 Comparison With Natural Convection in Rectangular Enclosures. Figure 5 shows the local experimental and simulated Nusselt numbers $Nu_E(z)$ and $Nu_S(z)$ as functions of z, during melting, when the *boundary layers are distinct* ($A \leqq 25$). The Nusselt numbers here are defined as the dimensionless amount of heat transferred by unit of time and by unit of vertical surface

$$Nu_{E(S)}(z) = v_{E(S)}^*(z^*) \frac{\rho_S}{\rho_L} \frac{H}{\alpha \mathrm{Ste}} \tag{7}$$

Since the horizontal fusion velocities have been found to be constant, these quantities are constant with time too.

The local Nusselt number at the cold wall of a *rectangular* enclosure $\hat{Nu}(z)$, resulting from the numerical correlation proposed by Schinkel et al. ($2.5 \leqq A \leqq 25$), equation (6), is also represented in Fig. 5. It appears clearly on the figure that, for $z \leqq 0.75$, $Nu_E(z)$ and $Nu_S(z)$ are both identical to $\hat{Nu}(z)$. Thus the local Nusselt at the interface can be represented by correlation (6) for any $z \leqq 0.75$ as long as the melting front has not reached the cold wall for this given z; the simulation of the melting process for practical applications can be significantly simplified by the use of this correlation (see section V.1 below).

In the range $z > 0.75$, the numerical results for rectangular and nonrectangular enclosures are identical, but the experimentally measured local heat transfer is higher as already noticed above. An accurate simulation of this phenomenon implies the complete transformation of coordinates, including all the terms that have been neglected in the present version of the code. In spite of this discrepancy (inferior to 10 percent) between the numerical and experimental local Nusselt number in the top part, we will use relation (6) to describe the local

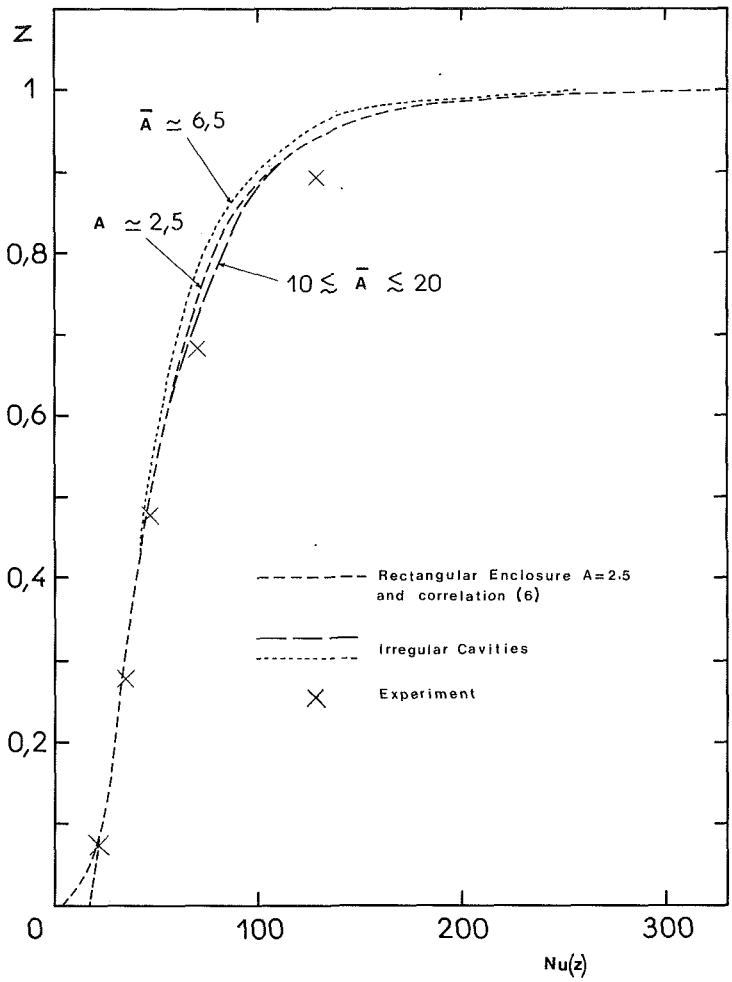

Fig. 5 Local heat transfer at the interface as a function of z: simulation (dashed lines) and experiment (crosses)

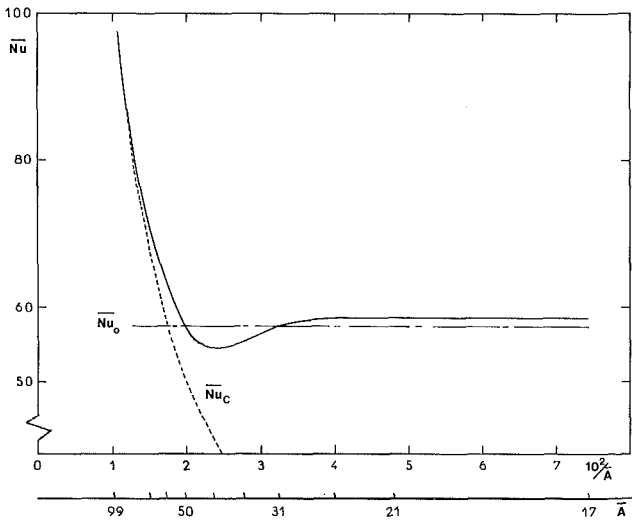

Fig. 6 Average heat transfer at the interface as a function of the time-dependent equivalent aspect ratio of the liquid cavity: simulation of the melting process (solid line), pure conduction solution ($\overline{Nu}_C$), rectangular enclosures ($\overline{Nu}_0$)

heat transfer for any z when establishing simplified correlations of the time evolution of the melted fraction, which involves the *total* heat transfer at the interface.

The transition time t_0, necessary for the boundary layer regime to establish in the liquid cavity, is defined on the basis of the time evolution of the calculated average Nusselt number at the interface $\overline{Nu}$. $\overline{Nu}$ is depicted in Fig. 6 as a function of the time-dependent equivalent aspect ratio $\bar{A}$ of the liquid cavity. The curve first shows a sharp decrease, corresponding to the conduction regime ($\overline{Nu}_c$). The onset of natural convection in the liquid phase causes $\overline{Nu}$ to go through a minimum and then reach a constant value, very close to $\overline{Nu}_0 = 0.33\ Ra^{1/4}$, corresponding to the boundary layer regime in rectangular enclosures. In the following study, time t_0 is defined as the time instant when $\overline{Nu}_c = \overline{Nu}_0$. Using the simplified solution of the Stefan problem [25]

$$\overline{Nu}_c(t) = \left(2\frac{\rho_L}{\rho_S}\frac{Ste}{Pr}t\right)^{-1/2}, \tag{8}$$

t_0 is given by

$$t_0 = 4.59\frac{Pr}{Ste}\frac{\rho_S}{\rho_L}Ra^{-1/2} \tag{9a}$$

and the melted fraction at time t_0 is obtained from (8)

$$F_0 = A/0.33\ Ra^{1/4} \tag{9b}$$

V Correlations

The previous observations are now used to establish simplified correlations for describing the melting process. Two steps are to be considered:

1 before the melting front reaches the cold wall, the interface extends from $z=0$ to $z=1$

2 after the melting front reaches the cold wall, the interface extends from $z=0$ to $z=z_D(t, t_0)$, the height of the solid PCM

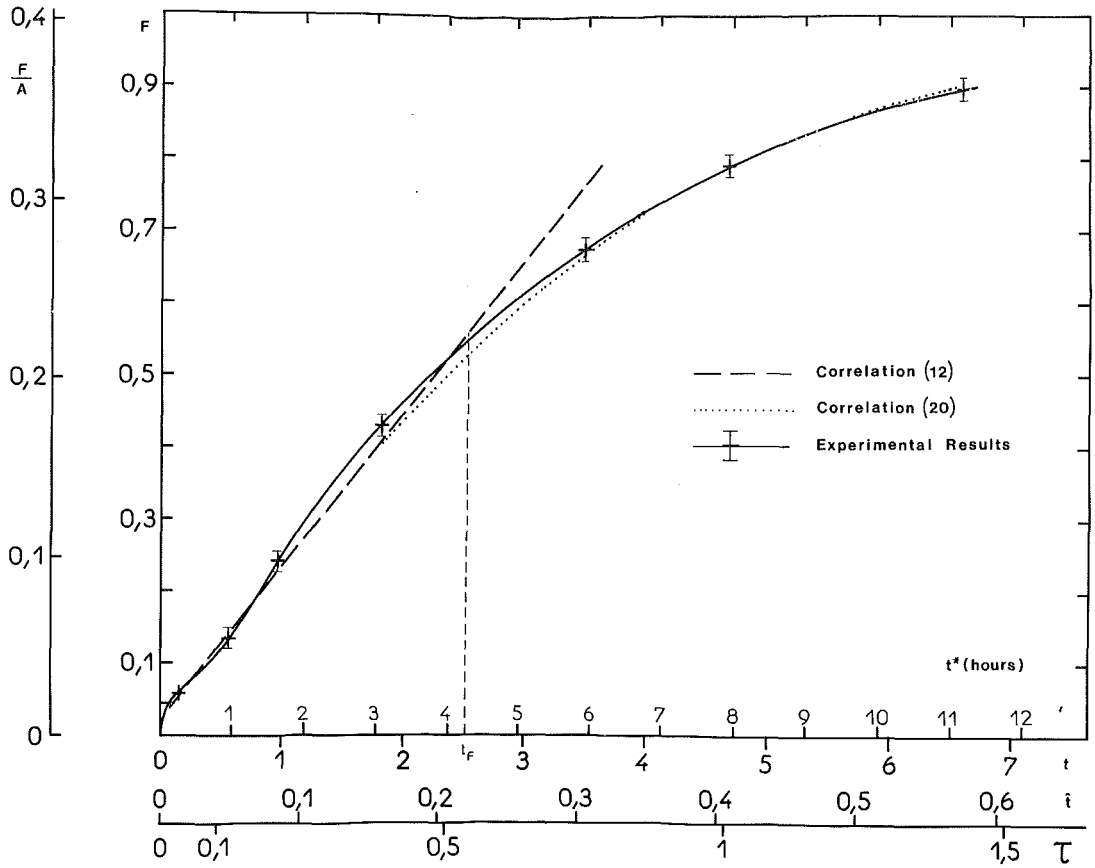

Fig. 7 *Time evolution of the melted fraction: comparison of correlations (12) and (20) with the experimental results*

V.1 Melting Fraction *Before* Contact of the Melting Front With the Cold Wall. The melted fraction growth depends on Nu which is a constant for $t > t_0$, since Nu(z) is considered constant for any z. The melted fraction at time t is thus written

$$F(t,\ t_0) = A\,\frac{\rho_L}{\rho_s}\,\frac{\mathrm{Ste}}{\mathrm{Pr}}\,\overline{Nu}\,(t-t_0) + F_0 \tag{10}$$

If we define a new dimensionless time $\hat{t}$ as

$$\hat{t} = 0.33\mathrm{Ra}^{1/4}\,\frac{\rho_L}{\rho_s}\,\frac{\mathrm{Ste}}{\mathrm{Pr}}\,t \tag{11}$$

equation (10) becomes

$$F(\hat{t},\ \hat{t}_0) = A\,(\hat{t} + \hat{t}_0) \tag{12}$$

where

$$\hat{t}_0 = 1/0.66\mathrm{Ra}^{1/4} \tag{13}$$

In terms of the average width of the liquid cavity $\delta = F/A$, equation (12) gives

$$\delta(\hat{t},\ \hat{t}_0) = \hat{t} + \hat{t}_0 \tag{14}$$

The latter formulation will be preferred as it is more general; indeed the aspect ratio of the whole enclosure, which is not a parameter of the problem so far, has not been kept in the correlation.

V.2 Melted Fraction *After* Contact of the Melted Front With the Cold Wall. At time $t = t_F$, the top part of the melting front reaches the cold wall of the enclosure, and for $t > t_F$ the heat transfer at the interface has to be considered between $z = 0$ and $z = z_D(t,\ t_0) < 1$.

The interface velocity at a given height $z < z_D$ being a constant even if $z_D < 1$, the cold wall is reached for a given z at a time given by

$$(\hat{t} - \hat{t}_0)AS(z) = 1 - 2A\hat{t}_0 \tag{15}$$

according to (6). The aspect ratio is now a parameter of the problem. By using the variable $\tau = A\hat{t}$, we can write

$$(\tau - \tau_0)S(z) = 1 - F_0 \tag{16}$$

The melted fraction at $\tau = \tau_F$ (contact with the cold wall for $z = 1$) is (from (12) and (16))

$$F(\tau_F,\ \tau_0) = \tau_F + \tau_0 = \frac{1}{S(1)} + F_0\left(1 - \frac{1}{S(1)}\right) \tag{17}$$

For $\mathrm{Ra} \simeq 10^9$ and $\mathrm{Ste} \lesssim 0.2$, $F_0 \ll F(\tau_F, \tau_0)$ and

$$F(\tau_F, \tau_0) \simeq \tau_F \simeq 1/S(1) \tag{18}$$

This relation shows that, for these orders of magnitude of Ra and Ste, the melted fraction at time τ_F does not depend on the parameters of the problem. Relation (6*b*) was used to estimate $S(1)$, which leads to $F(\tau_F,\ \tau_0) = 0.46$.

For $\tau > \tau_F$, the average melting rate decreases with time

$$\frac{dF(\tau,\ \tau_0)}{d\tau} = \int_0^{z_D} S(z)\,dz = I[z_D(\tau,\ \tau_0)] \tag{19}$$

where the function $z_D(\tau, \tau_0)$ is implicitly given by (16). The integration of equation (19) gives:

$$F(\tau, \tau_0) = 1 - z_D(\tau, \tau_0)(1 - 2\tau_0) + (\tau - \tau_0)I[z_D(\tau, \tau_0)] \tag{20}$$

which can be used in the whole range $\tau > \tau_0$ since

$$z_D(\tau, \tau_0) = 1 \text{ and } I[z_D] = 1 \text{ for } \tau_0 < \tau < \tau_F \tag{21}$$

It is clear from (20) that $F(\tau, \tau_0)$ can be expressed in terms of the functions $z_D(\tau, \tau_0)$ and $I[z_D(\tau, \tau_0)]$ which are independent of the parameters of the problem. Thus τ and τ_0 are the only quantities that determine the value of the melted fraction.

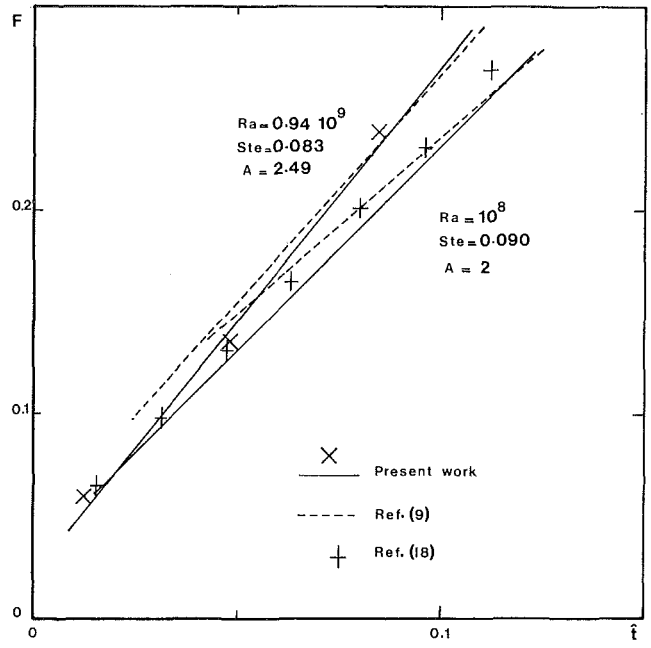

Fig. 8 Time evolution of the melted fraction: comparison of the present correlation (12) and the correlation established in [9] with the experimental results from this study ($Ra = 10^9$) and from [18] ($Ra = 10^8$)

The time variation of the melted fraction given by (12) and (20) is compared with the results of the reference experiment in Fig. 7. The agreement shows that the simplified analysis proposed in this section provides accurate information on the melting process in the range of parameters considered in this study.

Recent studies have presented experimental results concerning the time evolution of the melted fraction in a rectangular enclosure before contact of the melting front with the cold wall [9, 18]. The experimental results obtained by Ho and Viskanta for $Ra = 10^8$ and $Ste = 0.09$ (Fig. 3 of [18]) are plotted on Fig. 8: The linear time dependence of the melted fraction demonstrated in our study appears clearly on the figure. Bareiss and Beer draw similar conclusions from their own experimental measurements and propose a correlation for the average Nusselt number at the interface and a criterion for the transition from the conduction to the convection regime in the melt (equations (11) and (12) of [9]). In Fig. 8, our correlation (solid line) and the expression from [9] (dashed line) are compared to the results of our reference experiment and of [18]. Our correlation is still in good agreement with the experiment at $Ra = 10^8$. The correlation from [9] leads to a lower melting rate (-10 percent for $Ra \cong 10^9$ and -13.5 percent for $Ra = 10^8$); this difference might be due to the fact that this empirical correlation has been established for rather small enclosures (H from 0.01 to 0.08 m) and thus the influence of the end effects might be significant.

V.3 Consequences on the Dimensional Problem. For high Ra, the melted fraction $F(\tau, \tau_0)$ is a function of $\tau = A\hat{t}$. When all the parameters are held constant but the height of the cavity, $\tau \sim H^{-1/4}\, t^*$. This result implies that, for given conditions and for a given width of the enclosure, the same melted fraction $F(\tau, \tau_0)$ is attained in a smaller dimensional time for lower cavities; this is in agreement with experimental observations [2]. For example, the time needed to melt a given amount of phase change material may be reduced by 30 percent when dividing a container of aspect ratio $A = 6$ into four containers of aspect ratio $A = 1.5$, assuming that the total height and volume are kept identical.

VI Conclusion

The experimental set described in this paper has been used to validate the numerical simulation of the melting process in a vertical rectangular enclosure [21]. Results have been presented for high Rayleigh number natural convection in the liquid phase (Ra based on height of the order of magnitude of 10^9). Very good agreement between the numerical and experimental results is shown on the temperature fields for natural convection flow in a rectangular enclosure. As for the melting process, the numerical code, taking account of natural convection in the moving nonrectangular liquid cavity, gives a very good prediction of the melting front shape and position and of the temperature evolution with time in the liquid phase for $Ste < 0.2$. These very precise results allow us to give a real justification to the hypotheses that were used in the construction of our program, for the range of parameters considered in this study. The main hypotheses that have been used in many other methods [12, 17] are:

- the flow in the liquid cavity is laminar
- the density change upon melting has a negligible effect on the process
- the quasi-stationary of the melting process (hypotheses 8 and 9)

The comparison of experimental and numerical results shows that the local heat transfer along the vertical walls is constant at a given level z as soon as the boundary layers are separated and is well represented by a correlation proposed by Schinkel et al. [30] for *rectangular* enclosures. This shows that the only modification of the boundary layer along the vertical wall when small tilts and curvatures are introduced is a slight thickening that maintains a constant boundary heat flux by vertical unit surface. As a consequence, the local heat transfer at the interface may be approximated by this correlation for the *nonrectangular* liquid cavities met in the fusion experiments. This leads to simple analytical expressions of the time evolution of the melted fraction which are not dependent on the parameters of the system as long as we are in the correct parameter range; in particular, we may notice that the melted fraction when the cold wall is attained does not depend on any parameter of the problem.

The next step in this study is the analysis of the role of conduction in the solid PCM, which will be published in a coming paper. The convective and phase-change aspect having been validated in the present study, this coming study will have only to deal with the conductive coupling of the solid PCM with the phase-change process.

Futher exploration in this field should take into account more realistic experimental conditions, such as other boundary conditions on the vertical walls, in order to optimize the melting process in practical applications.

Acknowledgments

The authors wish to express their appreciation to Dr. A. Gadgil for his advice concerning the presentation of the results. This work is supported by SPI Direction and PIRSEM Research Program of CNRS.

References

1 Ramsey, J. W., and Sparrow, E. M., "Melting and Natural Convection Due to a Vertical Embedded Heater," ASME JOURNAL OF HEAT TRANSFER, Vol. 100, 1978, pp. 368-370.

2 Bareiss, M., and Beer, H., "Influence of Natural Convection on the Melting Process in a Vertical Cylindrical Enclosure," *Letters in Heat and Mass Transfer*, Vol. 7, 1980, pp. 329-338.

3 Sparrow, E. M., Schmidt, R. R., and Ramsey, T. W., "Experiments on the Role of Natural Convection in the Melting of Solids," ASME JOURNAL OF HEAT TRANSFER, Vol. 100, 1978, pp. 11-16.

4 Bathelt, A. G., Viskanta, R., and Leidenfrost, W., "An Experimental Investigation of Natural Convection in the Melted Region Around a Heated Horizontal Cylinder," *Journal of Fluid Mechanics*, Vol. 90, 1979, pp. 227-239.

5 Marshall, R. H., "Natural Convection Effects in Rectangular Enclosures Containing a Phase Change Material," in: *Thermal Storage and Heat Transfer in Solar Energy Systems*, ASME, New York, 1978, pp. 61-69.

6 Hale, N. W., and Viskanta, R., "Photographic Observation of the Solid Liquid Interface Motion During Melting of a Solid Heated From an Isothermal Vertical Wall," *Letters in Heat and Mass Transfer*, Vol. 5, 1978, pp. 329-337.

7 Sanson-Ortega, A., Gobin, D., and Benard, C., "Paraffin Trombe Wall for Space Heating," *Proceedings International Conference on Building Energy Management*, Porto, 1980.

8 Van Buren, P. D., and Viskanta, R., "Interferometric Measurement of Heat Transfer During Melting From a Vertical Surface," *Int. J. of Heat and Mass Transfer*, Vol. 23, 1980, pp. 568-571.

9 Bareiss, M., and Beer, H., "Experimental Investigation of Melting Heat Transfer With Regard to Different Geometric Arrangements," *Int. Com. Heat Mass Transfer*, Vol. 11, 1984, pp. 323-333.

10 Kroeger, P. G., and Ostrach, S., "The Solution of a Two-Dimensional Freezing Problem Including Convection Effects in the Liquid Region," *Int. J. of Heat and Mass Transfer*, Vol. 17, 1974, pp. 1191-1207.

11 Yao, L. S., and Chen, F. F., "Effects of Natural Convection in the Melted Region Around a Heated Horizontal Cylinder," ASME JOURNAL OF HEAT TRANSFER, Vol. 102, 1980, pp. 667-672.

12 Sparrow, E. M., Patankar, S. V., and Ramadhyani, S., "Analysis of Melting in the Presence of Natural Convection in the Melt Region," ASME JOURNAL OF HEAT TRANSFER, Vol. 99, 1977, pp. 520-526.

13 Rieger, H., Projahn, U., and Beer, H., "Analysis of the Heat Transport Mechanisms During Melting Around a Horizontal Circular Cylinder," *Int. J. of Heat and Mass Transfer*, Vol. 25, 1982, pp. 137-147.

14 Pannu, J., Joglekar, G., and Rice, P. A., "Natural Convection to Cylinders of Phase Change Material Used for Thermal Storage," *AIChE Symposium Series*, 1980, pp. 47-55.

15 Saitoh, T., and Hirose, K., "High Rayleigh Number Solutions to Problems of Latent Heat Thermal Energy Storage in a Horizontal Cylindrical Capsule," ASME JOURNAL OF HEAT TRANSFER, Vol. 104, 1982, pp. 545-553.

16 Rieger, H., Projahn, U., Bareiss, M., and Beer, H., "Heat Transfer During Melting Inside a Horizontal Tube," ASME JOURNAL OF HEAT TRANSFER, Vol. 105, 1983, pp. 226-234.

17 Ramanchandran, N., Gupta, J. P., and Jaluria, Y., "Two-Dimensional Solidification With Natural Convection in the Melt and Convective and Radiative Boundary Conditions," *Numerical Heat Transfer*, Vol. 4, 1981, pp. 469-484.

18 Ho, C. J., and Viskanta, R., "Heat Transfer During Melting From an Isothermal Vertical Wall," ASME JOURNAL OF HEAT TRANSFER, Vol. 106, 1984, pp. 12-19.

19 Hossfeld, L. M., "A Coordinate Transformation Method for Solving a Convection Phase Change Problem," Ph.D. Thesis, University of Minnesota, 1979.

20 Lapadula, C. A., and Mueller, W. K., "The Effect of Buoyancy on the Formation of a Solid Deposit Freezing Onto a Vertical Surface," *Int. Journal of Heat and Mass Transfer*, Vol. 13, 1970, pp. 13-26.

21 Gadgil, A., and Gobin, D., "Analysis of Two-Dimensional Melting in Rectangular Enclosures in Presence of Convection," ASME JOURNAL OF HEAT TRANSFER, Vol. 106, 1984, pp. 20-26.

22 Mallison, G. D., and De Vahl Davis, G., "Three Dimensional Natural Convection in a Box: a Numerical Study," JOURNAL OF FLUID MECHANICS, Vol. 83, 1977, pp. 1-31.

23 Patankar, S. V., "Numerical Heat Transfer and Fluid Flow," Hemisphere/McGraw-Hill, 1980.

24 Gobin, D., "Changement d'état solide-liquide: Evolution temporelle du couplage entre la convection naturelle dans la phase liquide et la conduction dans la phase solide. Etude numérique et expérimentale," Thèse de doctorat d'état, Université Paris VI, June 1984.

25 Goodman, T. R., "Application of Integral Methods to Transient Nonlinear Heat Transfer," in: *Advances in Heat Transfer*, Vol. 1, Academic Press, 1964, pp. 52-120.

26 Humphries, W. R., and Griggs, E. I., "A Design Handbook for Phase Change Thermal Control and Energy Storage Devices," NASA Technical Paper No. 1074, 1977.

27 Hale, D. V., Hoover, M. J., and O'Neill, M. J., "Phase Change Materials Handbook," NASA Report No. 61363, 1971.

28 Yarbrough, D. W., and Griggs, E. I., "Thermal Conductivity of Solid Alkanes From n-Hexadecane to n-Eicosane," *Proceedings of the 14th South Eastern Seminar on Thermal Sciences*, 1978, pp. 256-267.

29 American Petroleum Institute, Research Project 44, 1973.

30 Schinkel, W. N. M., Linthorst, S. J. M., Hoogendorn, C. J., "The Stratification in Natural Convection in Vertical Enclosures," ASME JOURNAL OF HEAT TRANSFER, Vol. 105, 1983, pp. 267-272.

Freezing in the Presence of Rotation

J. S. Nelson

E. M. Sparrow
Fellow ASME

Department of Mechanical Engineering,
University of Minnesota,
Minneapolis, MN 55455

Freezing of a phase-change medium in a sealed, rotating cylindrical capsule was studied experimentally. The axis of rotation was either colinear with the axis of the capsule or perpendicular to the axis of the capsule, with corresponding maximum centrifugal forces of about 2g and 4½g. The role of rotation differed depending on whether the capsule was fully or partially filled with liquid at the onest of freezing. For the fully filled capsule, rotation-related effects occurred only when the liquid was initially superheated relative to the fusion temperature. Rotation, acting via the Coriolis force, decreased the heat flow from the superheated liquid to the solid-liquid interface which, in turn, gave rise to a small increase in the rate of solidification and in the energy extracted from the capsule, with the net effect being no larger than 5 percent. In the perpendicular mode, rotation had a significant effect on the spatial distributions of the frozen layer thickness and of the voids. For the case of a partially filled capsule, rotation altered the position and shape of the air space associated with the partial filling and in this way gave rise to substantial increases (up to 17 percent) in the rate of solidification.

Introduction

Previous work on solidification in the presence of rotation has been confined to metallurgical applications and to the resulting changes in metal microstructure (e.g., [1-5]). In the present research, attention is focused on the heat transfer. Experiments are performed in which a nonmetallic phase-change medium contained in a cylindrical capsule is rotated as it solidifies. Two orientations of the rotation are investigated, as depicted schematically in Fig. 1. In one, the axis of rotation is colinear with the axis of the cylinder. In the other, the axis of rotation is perpendicular to the axis of the cylinder, with the two axes intersecting midway along the cylinder length. The maximum centrifugal forces for the perpendicular and colinear orientations of rotations were about 4½g and 2g, respectively.

A total of five parameters were varied during the course of the research. These included: (1) the presence or absence of rotation, (2) the orientation of the rotation, (3) the presence or absence of superheat in the solidifying liquid, (4) the temperature of the wall of the cylindrical capsule, and (5) the degree to which the capsule is filled with liquid. The phase-change medium was 99 percent pure *n*-eicosane paraffin, which has a fusion temperature of 36.3°C. The freezing occurred in response to a step-change decrease of the temperature of the capsule wall.

Measurements were made of the frozen mass, the circumferential and axial distributions of the thickness of the solidified layer, and the bulk temperature of the liquid, all as a function of time. The distribution of voids was also carefully monitored. In the presentation of the results, the response of the energy transfer, the liquid superheat decay, the frozen layer thickness, and the void distribution to rotation will be highlighted. The sensitivity of these results to the other investigated parameters will also be documented. Comparisons will be made with numerical results whenever possible.

A survey of the literature revealed a number of studies of the interaction between natural convection and rotation in enclosed single-phase fluids. The two basic geometries dealt with included the fluid-filled rotating cylinder whose end faces are maintained at different temperatures and the rotating fluid annulus in which there is a temperature difference between the bounding cylindrical surfaces. For the most part, natural convection was diminished by rotation (e.g., [6-8]) but not always [8, 9].

Experimental Apparatus and Procedure

As shown in Fig. 1, the axis of rotation was vertical for both the colinear and perpendicular modes, so that the cylindrical capsules were, respectively, oriented with their axes vertical and horizontal. The respective capsules were of identical internal dimensions, 3.80 cm in diameter and 19.0 cm in length, yielding an aspect ratio (length/diamter) of five. Each consisted of an open-ended, thin-walled cylindrical shell (wall thickness ~ 0.3 cm) and disklike caps to close the ends, all of brass. Brass was used because of its relatively high thermal conductivity, easy machinability, and compatibility with both paraffin and water (which served as the thermal environment of the capsule). All surfaces which bounded the paraffin were lapped to a high degree of smoothness. Each of

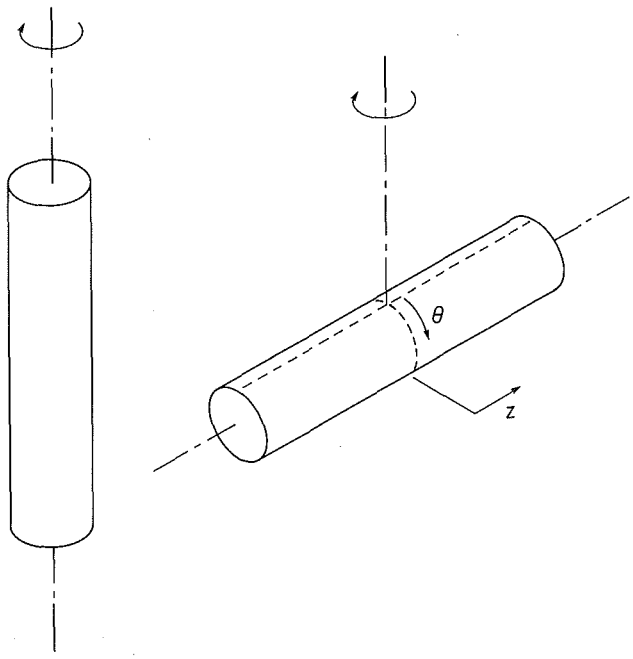

Fig. 1 Illustration of the colinear and perpendicular modes of rotation

Contributed by the Heat Transfer Division for publication in the JOURNAL OF HEAT TRANSFER. Manuscript received by the Heat Transfer Division October 10, 1984.

the capsules was equipped with five fine-gage, precalibrated thermocouples whose junctions were situated about 0.15 cm from the inner surface of the cylindrical wall.

Two constant-temperature water baths were used during the course of each data run. One of these was equipped with a thermostatically controlled heater and was utilized prior to the freezing period to establish a uniform temperature ($=T_0$) of the liquid-paraffin-filled capsule at or above the fusion value (i.e., $\geq$ 36.3°C). The other water bath was used to impose a preselected, lower-than-fusion temperature on the surface of the capsule during the freezing period. During the experiment, this bath was continuously supplied with chilled water at a temperature slightly below the desired temperature value. A thermostat-equipped heating unit was used for temperature control. The agitation provided by the heating unit was supplemented by a rotating, multibladed stirrer.

A variable-speed motor was suspended over the center of the freezing bath with its shaft pointing vertically downward. The motor shaft was coupled to the capsule at the beginning of the freezing period and decoupled at the preselected termination of the period. The maximum rotational speeds were 300 and 205 rpm, respectively, for the colinear and perpendicular modes, the lower speed for the latter being due to greater hydrodynamic resistance.

The mass of the paraffin was measured by a triple-beam balance having a smallest scale division of 0.1 g (the smallest mass measurement was about 40 g). A dial-gage-equipped caliper with a resolution of 0.001 in. was used in the measurement of the thickness of the frozen layer, and the rotational speed was measured to one rpm by a digital tachometer. All thermocouple emfs were read and recorded by a 1-μV programmable datalogger. In general, the accuracy of all measured quantities is believed to be in the 1 percent range.

The first step in the execution of a data run was to fill the then-empty capsule with liquid paraffin, with the filling procedure being tailored to whether the capsule was to be fully or partially filled [10]. The filled capsule was then sealed and placed in the equilibration bath. After equilibrium at temperature T_0 had been attained (as indicated by thermocouple readings), the capsule was transferred to the already readied freezing bath and coupled to the shaft of the motor, which was immediately activated if appropriate to the run (ie., either rotating or nonrotating). The transfer and coupling operations were accomplished in 10 s or less.

The freezing period was allowed to continue for a preselected period of time. For a given set of operating conditions defined by the initial temperature of the liquid paraffin, the temperature imposed on the capsule wall during freezing, and the rotational speed, freezing runs of various durations were performed in order to determine the timewise dependence of the results.

Two different run-termination procedures were employed depending on which results were being sought in the given run. For the determination of the bulk temperature of the unfrozen liquid paraffin, the residual liquid was poured out of the capsule into a specially designed guarded calorimeter which consisted of a styrofoam cup surrounded by a water-filled annular space. The temperature of the water was set to closely approximate the expected value of the bulk temperature. Once poured into the cup, the liquid paraffin was stirred with a two-thermocouple-equipped nylon rod that had also been preheated to the expected bulk temperature. The two thermocouples attained identical and steady values after the liquid paraffin was vigorously stirred for about 15 s.

A different run-termination procedure was used when the mass and thickness of the frozen solid were to be determined. In this case, the residual liquid paraffin was extracted by suction, an operation which was accomplished in about 5 s. The next step was to remove the frozen solid from the capsule, a task which could not be accomplished directly because of the intimate bond between the solid and the capsule wall. To overcome this difficulty, the capsule was resealed and then submerged in a cold bath, either ice/water (0°C) or ethylene glycol/water (−10°C). Since the thermal expansion coefficient of the solid *n*-eicosane paraffin is about thirty times larger than that of brass, the paraffin experienced a greater contraction than the brass, thereby severing the bond between them. Once removed from the capsule, the specimen was weighed and then marked as to the axial and circumferential locations where measurements of the thickness of the solidified layer were to be made. For specimens frozen in the perpendicular mode, 72 measurement sites were used (9 axial stations and 8 circumferential positions at each station). Specimens produced in the colinear mode were nearly axisymmetric. For these specimens, 40 sites were used (10 axial stations with 4 circumferential positions at each station). The measurements were facilitated by sectioning the specimen at each of the axial stations where the thickness was to be determined.

Further information about the apparatus, instrumentation, and experimental procedure is available in [10].

Parameters

The five parameters which were varied during the course of the research will now be characterized. The orientation of the rotation is either colinear or perpendicular (Fig. 1), while the magnitude of the rotation can be expressed via the rotational Froude number

Nomenclature

$\bar{c}_L$ = specific heat of liquid
$\bar{c}_S$ = specific heat of solid
E = energy
E_{L1} = sensible energy release from liquid which freezes
E_{L2} = sensible energy release from unfrozen liquid
E_S = sensible energy release from subcooled solid
$E_{\max}$ = maximum energy release
E_λ = energy release due to phase change
$E_{\lambda,\max}$ = maximum value of E_λ
Fo = Fourier number = $\alpha_S t/R^2$
Fr = Froude number
g = acceleration of gravity
L = internal length of capsule
M_S = mass solidified between $t=0$ and $t=t$
M_S' = solidified mass per unit length
M_T = total mass in capsule
R = inside radius of capsule
Ste_L = liquid-phase Stefan number = $\bar{c}_L(T_0 - T^*)/\lambda$
Ste_S = solid-phase Stefan number = $\bar{c}_S(T^* - T_w)/\lambda$
T = temperature
T_b = bulk temperature of liquid
T_0 = initial temperature of liquid
T_w = temperature of water in freezing bath
T^* = fusion temperature
t = time
z = axial coordinate, Fig. 1
α_S = thermal diffusivity of solid
δ = thickness of frozen layer
θ = angular coordinate, Fig. 1
λ = latent heat of fusion
ρ_S = density of solid
ω = rotational speed
$\omega_{\max}$ = maximum rotational speed

Table 1 Parametric temperature differences and Stefan numbers

$(T_0 - T^*)$	Ste_L	$(T^* - T_w)$	Ste_S
0°C	0	6.0°C	0.0465
44.1	0.414	30.3	0.235

$$\mathrm{Fr} = r_{\mathrm{rot}}\omega^2/g \tag{1}$$

in which r_{rot} is the radius of rotation. For the colinear mode, $r_{\mathrm{rot}} = R$ (inner radius of capsule), while for the perpendicular mode, $r_{\mathrm{rot}} = \frac{1}{2}L$ (half of the internal length of the capsule). Since the maximum values of ω were, respectively, 300 and 205 rpm for the colinear and perpendicular modes, the corresponding maximum values of Fr are 1.92 and 4.48. The minimum value of Fr was zero (no rotation). Results corresponding to the maximum and minimum Fr will be presented here. Between $\mathrm{Fr}_{\min}$ and $\mathrm{Fr}_{\max}$, the results varied more or less linearly with Fr.

The superheat which exists in the liquid prior to the initiation of freezing is $(T_0 - T^*)$, where T^* is the fusion temperature. In dimensionless terms, the initial superheat can be represented by the liquid-phase Stefan number

$$\mathrm{Ste}_L = \bar{c}_L(T_0 - T^*)/\lambda, \quad \bar{c}_L = \int_{T^*}^{T_0} c_L dT/(T_0 - T^*) \tag{2}$$

The values of $(T_0 - T^*)$ and Ste_L used to parameterize the experiments are listed in Table 1.

The freezing process is driven by the temperature difference between the solid–liquid interface and the capsule wall. In practice, it was more convenient to use the temperature T_w of the water bath rather than the wall temperature. Thus, $(T^* - T_w)$ will be utilized as the characteristic temperature difference along with its dimensionless counterpart, the solid-phase Stefan number

$$\mathrm{Ste}_S = \bar{c}_S(T^* - T_w)/\lambda \tag{3}$$

where $\bar{c}_S$ was evaluated using the only available value (= 1.92 kJ/kg − °C). Table 1 lists the $(T^* - T_w)$ and Ste_S values of the experiments.

The last parameter is the degree to which the capsule was initially filled with liquid, either fully filled or 90 percent filled.

The quantities for which data will be presented will now be described. Since the results are time dependent, it is convenient to use a dimensionless time variable

$$\mathrm{FoSte}_S \tag{4}$$

which is suggested by heat conduction theory, where Fo $(= \alpha_S t/R^2)$ is the Fourier number. The properties k_S and ρ_S which appear in FoSte_S were evaluated at T^* (note that c_S has canceled out).

The mass M_S solidified between $t = 0$ and $t = t$ will be presented as the ratio M_S/M_T, where M_T is the total charge of paraffin in the capsule (i.e., M_T is the maximum value of M_S). The latent energy E_λ released during the transformation of M_S from the liquid to the solid states is

$$E_\lambda = \lambda M_S \tag{5}$$

and if $E_{\lambda,\max} = \lambda M_T$, it follows that

$$E_\lambda/E_{\lambda,\max} = M_S/M_T \tag{6}$$

Three sensible heat components were evaluated and will be presented. The sensible heat E_S released due to the subcooling of the solid is given by

$$E_S = M_S\bar{c}_S(T^* - \bar{T}_S) \tag{7}$$

where $\bar{T}_S$ is the spatial-average temperature of the solid at time t, calculated by solving the energy equation for the solid as described in [10]. For the liquid, two sensible heat components E_{L1} and E_{L2} were determined. E_{L1} is the energy released by the liquid which solidified during the data run, while E_{L2} is the energy released by the liquid which did not freeze during the run. These components are given by

$$E_{L1} = M_S\bar{c}_L(T_0 - T^*) \tag{8}$$

$$E_{L2} = (M_T - M_S)\int_{T_b}^{T_0} c_L dT \tag{9}$$

in which T_b is the measured liquid bulk temperature at time t.

The thickness of the frozen layer at any location with axial coordinate z and angular coordinate θ will be denoted by $\delta(z, \theta)$ and will be presented in the ratio δ/R. A measure of the axial nonuniformity of the frozen layer is given by the variation of the solidified mass M_S' per unit length

$$M_S' = \int_0^{2\pi}\int_{r_\delta}^{R} \rho_S r dr d\theta \tag{10}$$

where $r_\delta = (R - \delta)$ and ρ_S is the density of the solid paraffin.

Other quantities for which data are to be presented are the timewise decay of the liquid superheat, expressed as $(T_b - T^*)/(T_0 - T^*)$, and the response of the distribution of the voids to rotation.

The thermophysical properties needed in the evalution of the results were taken from [11] and [12].

Results and Discussion

The bulk of the presentation of results will deal with the case in which the capsule is fully filled when the phase-change medium is in its liquid state. In the final portion of the presentation, results wil be conveyed for the case of partial filling.

Rate of Solidification. The measured rates of solidification, conveyed by plotting the instantaneous value of M_S/M_T $(= E_\lambda/E_{\lambda,\max})$ versus the dimensionless time variable FoSte_S, are presented in Figs. 2 and 3, respectively, for the colinear mode and the perpendicular mode. Each figure contains results for four different thermal operating conditions, respectively characterized by Ste_L and Ste_S. To avoid overlap, the data for each operating condition have been displayed horizontally from the data for the others, the displacement being accomplished by using different abscissa origins for each operating condition. Smooth curves have been passed through the data for continuity.

In Fig. 2, the leftmost and next-to-leftmost groupings of data correspond to no initial liquid superheat ($\mathrm{Ste}_L = 0$) and, respectively, to a moderately cooled capsule wall ($\mathrm{Ste}_S = 0.0465$) and to a more strongly cooled wall ($\mathrm{Ste}_S = 0.235$). The next-to-rightmost and rightmost data groupings are for operating conditions characterized by appreciable initial liquid superheat ($\mathrm{Ste}_L = 0.414$) and to the same degrees of wall cooling as in the foregoing. Figure 3 has a similar structure, except that one of the $\mathrm{Ste}_L = 0$ (no superheat) operating conditions was omitted because ample data had already been collected to establish the behavior of the $\mathrm{Ste}_L = 0$ results.

The main issue addressed in Figs. 2 and 3 is the effect of rotation on the rate of solidification. For each of the operating conditions, solidification data corresponding to the maximum rotational speed $\omega_{\max}$ and to no rotation are plotted, respectively represented by the black and the open symbols.

Inspection of the figures shows that when there is no liquid superheat ($\mathrm{Ste}_L = 0$), no effect of rotation on the rate of solidification can be discerned, neither for the colinear mode (capsule vertical) nor the perpendicular mode (capsule horizontal). The insensitivity to rotation is due to the absence of heat flow from the liquid to the solid–liquid interface, so that motions in the liquid are irrelevant.

The solidification results for operating conditions characterized by initial liquid superheat ($\mathrm{Ste}_L > 0$) do respond to rotation, but the response is modest. For the

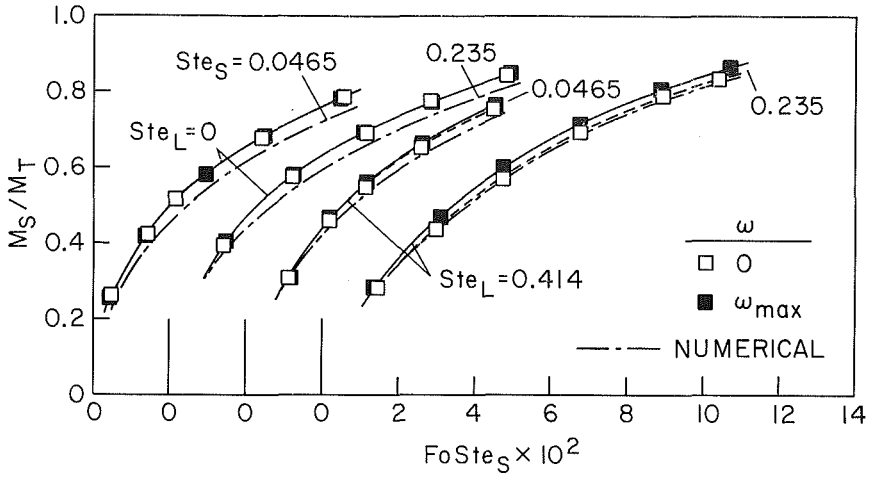

Fig. 2 Solidification results for the colinear mode

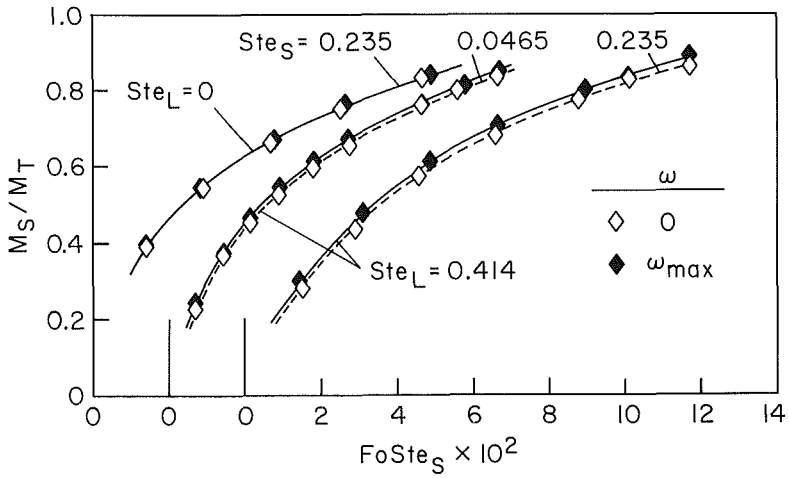

Fig. 3 Solidification results for the perpendicular mode

colinear mode (Fig. 2), the effect of rotation is virtually undetectable for the case of the moderately cooled capsule wall ($Ste_S = 0.0465$) and is in the 3–5 percent range for the more strongly cooled wall ($Ste_S = 0.235$). Rotation in the perpendicular mode evokes a slightly greater response, as witnessed by comparing Figs. 2 and 3. The extreme encountered effect of rotation is in the 6–7 percent range and occurs at the shortest investigated freezing times.

It is noteworthy that the effect of rotation is to increase the rate of solidification compared with the stationary case. To rationalize this finding, it should be noted that the presence of liquid superheat decreases the rate of solidification compared with the no-superheat case. This is a well-established behavior (e.g., [13]), which can be verified by comparing the present no-rotation results for $Ste_L = 0$ and $Ste_L = 0.414$ at a fixed value of Ste_S. The slowing of the solidification occurs because the heat which flows from the superheated liquid to the solid–liquid interface is conducted across the frozen layer and, in doing so, it lays claim to a portion of the heat-carrying capacity of the layer. This reduces the capability of the layer to carry heat liberated by phase change, so that the rate at which the phase change occurs must diminish.

Since rotation increases the solidification rate in the presence of liquid superheat, it may be surmised that rotation inhibits the heat flow from the liquid to the solid–liquid interface. Without rotation, the liquid-to-interface heat flow is by gravity-driven natural convection. When rotation is present, two additional body forces come into play, the centrifugal force and the Coriolis force. The centrifugal force tends to encourage fluid motion, while the Coriolis force is a retarding force. Since the aforementioned decrease of the convective heat transfer with rotation must be due to a retardation of the fluid motion, it may be concluded that the Coriolis force plays a greater role.

Figure 2 conveys the results of numerical finite-difference solutions [14] for freezing in a vertical nonrotating cylindrical capsule having a length/diameter ratio of five (equal to that of the experiments), either with or without initial liquid superheat. As seen there, the numerical results fall slightly below the experimental data (open squares), the maximum deviation being about 8 percent. This difference is readily rationalized by noting that in order to use the method of moving boundary immobilization, the numerical work was performed for a capsule in which there is no freezing on the end faces (i.e., adiabatic ends). On the other hand, freezing occurred on the end faces of the capsules used in the experiments, which is why the experimentally determined M_S values exceed the numerical values. Upon taking account of this, the experimental and numerical results are mutually supportive.

Another relevant result of the numerical solutions is that the heat transfer coefficients at the external surface of the capsule are sufficiently large so as not to have any effect on the freezing which occurs within the capsule.

Decay of Liquid Superheat. Further perspectives on the effect of rotation can be obtained by examining the data for the decay of the liquid superheat. These data are presented in Figs. 4 and 5, respectively, for the colinear and the per-

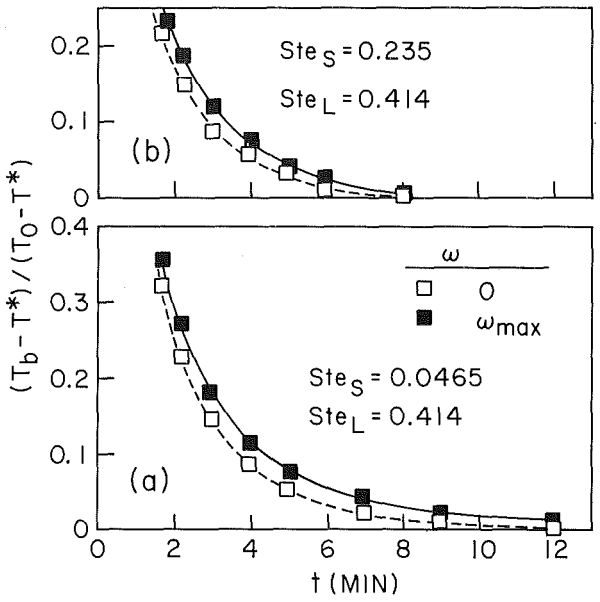

Fig. 4 Decay of liquid superheat for the colinear mode

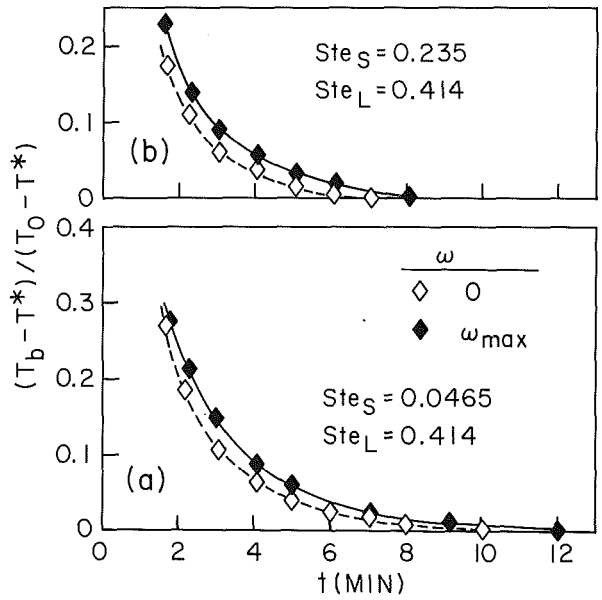

Fig. 5 Decay of liquid superheat for the perpendicular mode

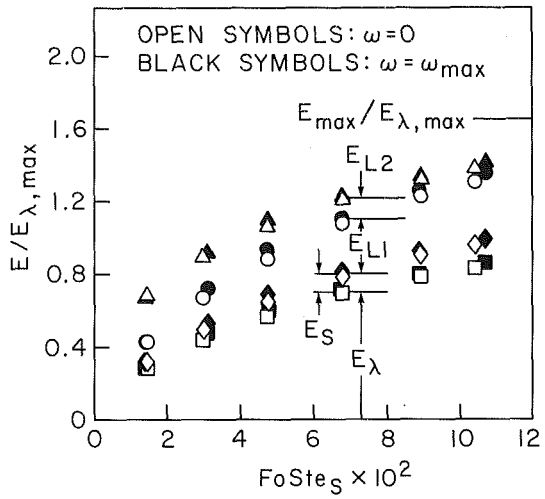

Fig. 6 Energy components and all-component energy extraction for the colinear mode

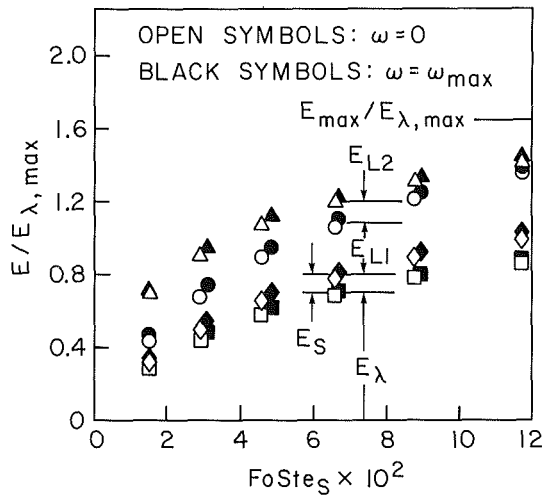

Fig. 7 Energy components and all-component energy extraction for the perpendicular mode

pendicular modes. Each figure is subdivided into (*a*) and (*b*) parts, respectively, for the moderately cooled capsule wall and the more strongly cooled wall. For both parts, $\text{Ste}_L = 0.414$.

In the figures, the instantaneous bulk temperature T_b of the liquid has been expressed in terms of the ratio $(T_b - T^*)/(T_0 - T^*)$ and plotted as a function of time. Note that the physical time t has been used as the abscissa variable rather than the FoSte_S dimensionless time. This choice is based on the realization that the decay of the superheat is a single-phase natural convection process, unrelated to phase change, whereas FoSte_S is a time variable appropriate to phase change. Instead of t itself, a liquid-phase Fourier number $\alpha_L t/R^2$ might have been used, but without benefit since for a given operating condition, $\alpha_L t/R^2$ is directly proportional to t.

Inspection of Figs. 4 and 5 indicates that for all cases, the decay of the liquid superheat is slowed by rotation. A slower decay of the superheat necessarily implies a decrease in the rate of heat flow from the liquid to the interface. This direct finding corroborates an identical finding that was deduced somewhat less directly from the solidification rate results. As discussed previously, the lower rates of heat flow are due to the retarding action of the Coriolis force.

It is relevant to note from Figs. 4 and 5 that although the decay of the superheat is somewhat more rapid for the more strongly cooled capsule than for the more moderately cooled capsule, the periods when significant superheat exists are not too greatly different. On the other hand, upon noting that $t \sim (\text{FoSte}_S)/\text{Ste}_S$, it can be seen from Figs. 2 and 3 that the solidification period is very much shorter for the more strongly cooled case than for the more moderately cooled case (i.e., $\text{Ste}_S = 0.235$ versus 0.0465). Therefore, for the former, the period of significant superheat encompasses a much greater portion of the solidification period than for the latter. Since rotational-related effects can only occur when superheat exists, the greater responsiveness of the more strongly cooled case to rotation is plausible.

In no case was any supercooling of the liquid detected.

Energy Components. All of the components of the energy extracted from the capsule during the freezing period were evaluated from the experimental data as a function of time and will be presented here for the cases which were most sensitive to rotation. Figures 6 and 7 respectively convey the energy components for freezing in the colinear and perpendicular modes, with $\text{Ste}_L = 0.414$ and $\text{Ste}_S = 0.235$ for both figures. In each figure, data are included both for

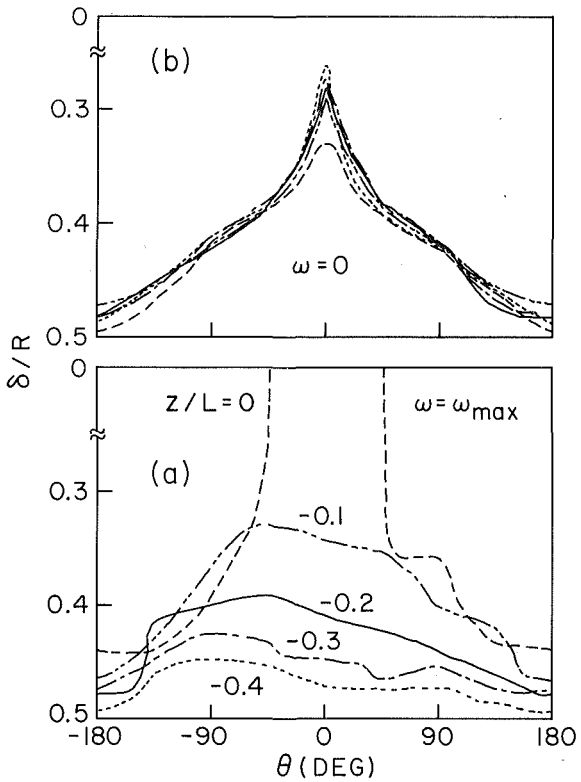

Fig. 8 Illustrative frozen layer thickness distributions, perpendicular mode, $Ste_L = 0.414$, $Ste_S = 0.235$, $FoSte_S \cong 6.6 \times 10^{-2}$

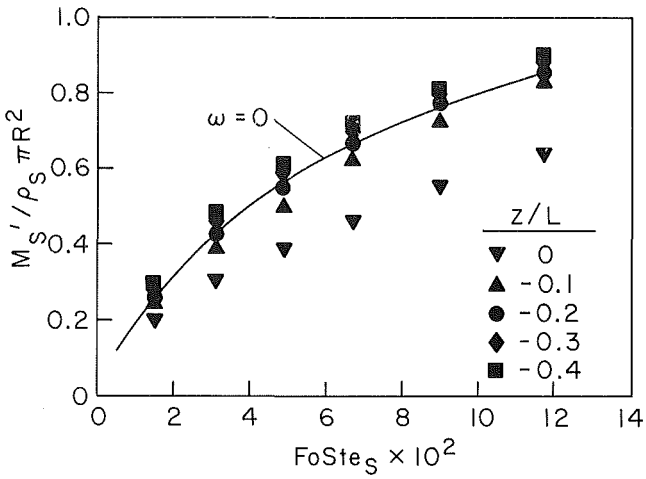

Fig. 9 Solidified mass per unit length, perpendicular mode, $Ste_L = 0.414$, $Ste_S = 0.235$

rotation at λ_{max} (black symbols) and for no rotation (open symbols).

The lowermost tier of data (the square symbols) denotes the energy E_λ liberated as latent heat during the phase change and is so labeled in the figures. The next tier of data, the diamonds, represent the sum $(E_\lambda + E_S)$, where E_S is the sensible heat release due to subcooling of the solid. The vertical gap between the data in the first and second tiers is, therefore, equal to E_S. The sensible heat release E_{L1} from the portion of the initially superheated liquid which solidifies is represented by the vertical gap between the second and third tiers of data. Correspondingly, the third tier represents the sum $(E_\lambda + E_S + E_{L1})$. The vertical gap between the third and fourth tiers is E_{L2}, which is the sensible heat release from the portion of the initially superheated liquid which remains unfrozen. The data symbols in the fourth tier represent the sum of all the energy components, i.e., $(E_\lambda + E_S + E_{L1} + E_{L2})$. It is these all-component data that are needed in applications where the rate of energy extraction is of primary importance (i.e., thermal energy storage).

To attain a dimensionless presentation of the energy results, each of the components and their sums has been normalized by $E_{\lambda,max}$ $(= \lambda M_T)$.

If the freezing were to go to completion and the solid were to attain the temperature T_w, it follows that

$$E_\lambda = E_{\lambda,max}, \quad E_S = M_T \bar{c}_S (T^* - T_w),$$
$$E_{L1} + E_{L2} = M_T \bar{c}_L (T_0 - T^*) \tag{11}$$

and if the sum of these components is denoted by E_{max}, then

$$E_{max}/E_{\lambda,max} = 1 + Ste_S + Ste_L \tag{12}$$

For the operating conditions of Figs. 6 and 7, $E_{max}/E_{\lambda,max} = 1.649$. A horizontal line representing this equation has been drawn at the upper right of each figure. This line serves as an asymptote toward which the upper tier of data is approaching.

With regard to the all-component energy extraction, rotation is seen to bring about a 2–4 percent increase. For the individual components, E_λ and E_{L1} are increased by rotation, E_{L2} is decreased by rotation, and E_S is virtually unaffected. The increased heat transfer associated with the rotation-related increase in freezing exceeds the reduction in the heat transfer from the liquid core to the solid–liquid interface.

It may also be noted that after the superheat has fully decayed (i.e., $T_b = T^*$), the sum $(E_{L1} + E_{L2})$ is a constant, although E_{L1} increases and E_{L2} decreases.

Frozen Layer Thickness. The effects of rotation on the thickness of the frozen layer will now be summarized and highlighted.

For the colinear mode (capsule vertical), the presence of rotation did not have any discernible effect on the shape of the thickness distribution. For freezing without liquid superheat, the frozen layer thickness was spatially uniform at any instant, except near the ends of the capsule. When there was initial liquid superheat, the instantaneous thickness of the frozen layer increased in the downward vertical direction, i.e., from the top of the capsule to the bottom. These same patterns occurred both with and without rotation.

In contrast, the thickness distribution was markedly affected by rotation in the perpendicular mode (capsule horizontal), and Fig. 8 is presented to illustrate the nature of the effects. The figure corresponds to $Ste_L = 0.414$, $Ste_S = 0.235$ and to an instant of time $FoSte_S \cong 6.6 \times 10^{-2}$. The (*a*) and (*b*) parts of the figure respectively pertain to $\omega = \omega_{max}$ and to $\omega = 0$.

To illuminate the format of Fig. 8, it is helpful to take note of the axial and circumferential coordinates z and θ that are illustrated in Fig. 1. Furthermore, from physical reasoning and confirmed by the experimental results, $\delta(z, \theta) = \delta(-z, -\theta)$, where δ is the local thickness of the frozen layer. In view of this relationship, there is no need for a separate presentation of the results for $z \leq 0$ and $z \geq 0$, and those for $z \leq 0$ are presented in Fig. 8. In both Figs. 8(*a*) and (*b*), δ/R is plotted as a function of θ for parametric values of z/L (L = length of capsule).

It may also be noted that for the direction of rotation illustrated in Fig. 1 and for $z \leq 0$, the $\theta < 0$ portion of the capsule advances into the fluid environment and will, therefore, be termed the windward portion. The $\theta > 0$ portion for $z \leq 0$ will be termed the leeward portion.

For the stationary case (Fig. 8*b*), the circumferential distributions of the frozen layer thickness at the five axial stations are virtually coincident, indicating that the freezing is essentially two dimensional. The thickness is a minimum at $\theta = 0$ deg, increases with increasing $|\theta|$, and attains a

maximum at $\theta = \pm 180$ deg. This thickness distribution reflects a natural convection flow which recirculates in the cross section.

In the presence of rotation (Fig. 8*a*), the δ distributions vary with z, with an overall trend of δ increasing with $|z|$. In addition, at any z, the frozen layer is thinner on the windward portion of the capsule than on the leeward portion. Another noteworthy feature of Fig. 8(*a*) is that the frozen layer thickness is zero in the neighborhood of $z = 0$ and $\theta = 0$.

The increase of δ with $|z|$ is attributable to the centrifugal force field, which induces an outward axial motion in the relatively cool, dense liquid adjacent to the solid-liquid interface. The heat transfer coefficient associated with the outflow should decrease with $|z|$ because the boundary layer increases in that direction, enabling δ to increase with $|z|$.

This outwardly directed flow, in conjunction with the steady rotation of the capsule, gives rise to Coriolis forces. In general, the Coriolis force is a deflecting force which is perpendicular to both the axis of rotation and the velocity vector of the flow relative to the rotating frame of reference. In particular, the Coriolis force deflects the outwardly directed flow away from the windward portion of the rotating capsule, which may explain the unsymmetrical nature of the δ versus θ curves in Fig. 8(*a*). Since the cooler, denser liquid is deflected away from the windward surface, the liquid in the proximity of this surface is warmer and, hence, the solid layer is thinner than for the leeward surface.

The zero thickness in the neighborhood of $z = 0$ and $\theta = 0$ reflects the presence of a void. The void is created by density increases associated with the cooling of the superheated liquid and with the transformation of the liquid into solid. The centrifugal force causes the void to coalesce at the center of rotation while gravity acts to position the void at the top of the capsule.

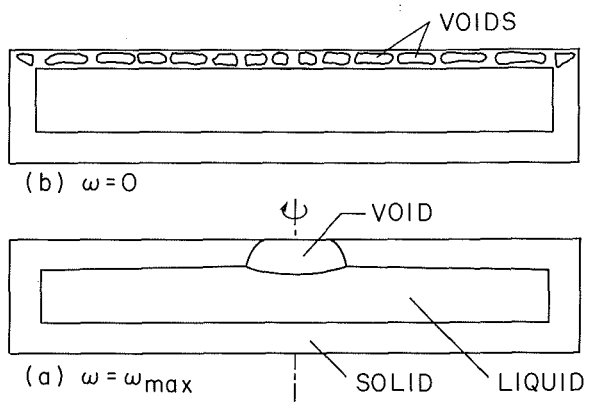

Fig. 10 Void patterns with and without rotation, perpendicular mode, $Ste_L = 0.414$, $Ste_S = 0.235$, $FoSte_S \cong 8.8 \times 10^{-2}$

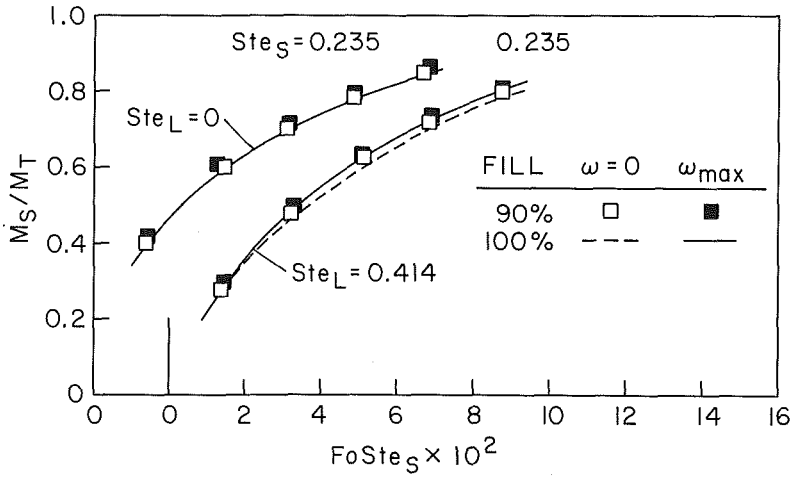

Fig. 11 Solidification results for a partially filled capsule in the colinear mode

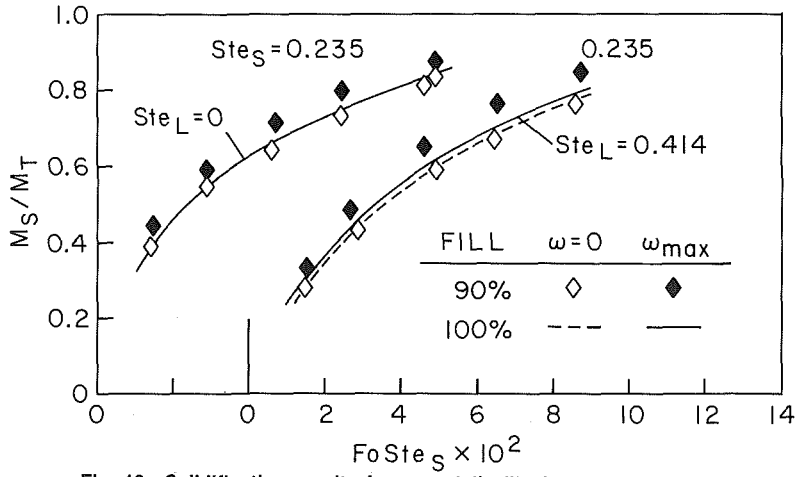

Fig. 12 Solidification results for a partially filled cavity in the perpendicular mode

A measure of the axial nonuniformity of the frozen layer for the perpendicular mode is conveyed by the z dependence of M_S', the solidified mass per unit length. In Fig. 9, M_S' is plotted against time (in dimensionless form) at several fixed axial stations z. The selected z values are the same as for Fig. 8, and, furthermore, the Ste_L and Ste_S values are the same for both figures. In addition to the black data symbols for the $\omega = \omega_{\max}$ case, there is a solid line which depicts the M_s' results for the stationary case.

It may be observed that the data for the rotational case tend to bracket the $\omega = 0$ line, with the average of the data falling only slightly above the line. Aside from the $z = 0$ station, which is strongly affected by the void, the spread in the M_S' data with z varies from about 25 percent at the smallest FoSte_S to slightly less than 10 percent at the largest FoSte_S.

Voids. As was noted in the foregoing, voids are formed because of density increases which occur during the freezing process. In the absence of superheat, the void was found to be situated in the interior of the frozen solid, coaxial with the axis of the capsule. The positioning of the void was insensitive to orientation, rotation, and Ste_S.

When there is initial superheat, a disk-shaped void is formed near the top of the capsule in the colinear mode. The shape of the void is only slightly affected by rotation (Fig. 5.46 of [10]). For the perpendicular mode, the response of the void distribution to rotation is illustrated in Fig. 10. Without rotation (Fig. 10*b*), the voids are distributed all along the top of the horizontal capsule. In the presence of rotation, the centrifugal force brings the voids together into a single void centered at the axis of rotation.

An elaboration of the observations of the voids, including a description of small voids that are formed by rapid freezing, is available in [10].

Partially Filled Capsule. The results presented up to now pertain to the case in which the capsule was fully filled with liquid at the beginning of the freezing period. Attention is now turned to the results for the case where the capsule is charged with 90 percent of the fully filled mass.

The solidification rate results for the partially filled capsule are presented in Figs. 11 and 12, respectively, for the colinear and perpendicular modes. Also appearing in these figures for comparison purposes are results for the fully filled case (solid and dashed lines). Each figure includes both the no-superheat and superheat cases ($\mathrm{Ste}_L = 0$ and 0.414, respectively) for $\mathrm{Ste}_S = 0.235$ (the more strongly cooled capsule wall). Results are presented for both $\omega = 0$ and for $\omega = \omega_{\max}$.

For each case, M_S/M_T is plotted as a function of FoSte_S. In this regard, it is relevant to note that M_T has a different meaning depending on the filling. In particular, for the 90 percent fill, M_T is 90 percent of that for the complete fill.

Turning first to the colinear mode (Fig. 11), it appears that even in the absence of superheating, there is a slight effect of rotation on M_S/M_T for the partially filled capsule. This is in contrast to the fully filled capsule, where no effect was observed. To rationalize this finding, it is relevant to note that the partial filling of the capsule creates an air space which decreases the area of contact between the paraffin and the capsule wall. When the capsule is rotated, a portion of the contact area is recovered because the free surface of the liquid is curved rather than flat. It is this area recovery which is believed responsible for the slight increase of M_S/M_T due to rotation when $\mathrm{Ste}_L = 0$. For $\mathrm{Ste}_L > 0$ in Fig. 11, unexpectedly, the effect of rotation on M_S/M_T appears to be no greater than for the $\mathrm{Ste}_L = 0$ case.

For the perpendicular mode (Fig. 12), the effect of rotation on the solidification rate for the partially filled capsule is appreciable both with and without liquid superheat – up to 17 percent in the investigated range. Thus, in the perpendicular mode, partial filling accentuates the effect of rotation compared with the fully filled capsule. This finding can be explained by noting that in the absence of rotation, the air space created by the partial filling runs along the entire length of the horizontal capsule, at the top. When rotation is present, the air space is drawn toward the center of rotation, significantly increasing the contact area between the paraffin and the capsule wall. This increased contact area is responsible for the increase in M_S/M_T with rotation.

Concluding Remarks

The effect of rotation on freezing differed depending on whether the capsule was fully or partially filled with liquid prior to the onset of freezing. For the case of the fully filled capsule, there were no effects of rotation without initial superheating of the liquid. In the presence of initial superheat, rotation-related increases in the rate of solidification and in the energy extracted from the capsule were generally no larger than 5 percent for the investigated operating conditions (i.e., centrifugal forces no greater than 4½g). For the case of a partially filled capsule, rotation affected the freezing process by altering the position and shape of the air space associated with the partial filling. For a 90-percent-filled capsule, rotation-related increases in solidification rate of up to 17 percent were encountered.

References

1 Chalmers, B., *Principles of Solidification*, Krieger, New York, 1964.

2 Cole, G. S., and Bolling, G. F., "Enforced Fluid Motion and the Control of Grain Structure in Metal Castings," *Transactions of the Metallurgical Society of AIME*, Vol. 239, 1967, pp. 1824–1835.

3 Cole, G. S., and Bolling, G. F., "Importance of Fluid Motion During Ingot Solidification," *The Solidification of Metals*, Iron and Steel Institute Journal, Vol. 110, 1967, pp. 323–329.

4 Howson, H. O., "Macrostructure Comparison of Centrifugal and Static Castings," *The Solidification of Metals*, Iron and Steel Institute Journal, Vol. 110, 1967, pp. 334–348.

5 Cole, G. S., "Transport Processes and Fluid Flow in Solidification," in: *Solidification*, American Society for Metals, Metals Park, Ohio, 1969, pp. 201–274.

6 Chandrasekhar, R. S., *Hydrodynamic and Hydromagnetic Stability*, Oxford University Press, London, 1961.

7 Kaiser, J. A. C., "Rotating Deep Annulus Convection. Part 1. Thermal Properties of the Upper Symmetric Regime," *Tellus*, Vol. 21, 1969, pp. 789–805.

8 Tang, D., and Hudson, J. L., "Experiments on a Rotating Fluid Heated From Below," *International Journal of Heat and Mass Transfer*, Vol. 26, 1983, pp. 943–949.

9 Homsy, G. M., and Hudson, J. L., "Centrifugally Driven Thermal Convection in a Rotating Cylinder," *Journal of Fluid Mechanics*, Vol. 35, 1969, pp. 33–52.

10 Nelson, J. S., "Effects of Rotation on Encapsulated Freezing," Ph.D. thesis, Department of Mechanical Engineering, University of Minnesota, Minneapolis, MN, 1984.

11 Humphries, W. R., and Griggs, E. I., "A Design Handbook for Phase Change Thermal Control and Energy Storage Devices," NASA Technical Paper 1074, 1977.

12 Griggs, E. I., and Yarbrough, D. W., "Thermal Conductivity of Solid Unbranched Alkanes From *n*-Hexadecane to *n*-Eicosane," *Proceedings, 14th Southeastern Seminar on Thermal Sciences*, Raleigh, NC, 1978.

13 Sparrow, E. M., Ramsey, J. W., and Kemink, R. G., "Freezing Controlled by Natural Convection," ASME JOURNAL OF HEAT TRANSFER, Vol. 101, 1979, pp. 578–584.

14 Ohkubo, Y., "Freezing in a Vertical Tube," M.S. thesis, Department of Mechanical Engineering, University of Minnesota, Minneapolis, MN, 1984.

Transient Simultaneous Condensation and Melting of a Vertical Surface

D. Galamba
Student Mem. ASME

V. K. Dhir
Mem. ASME

School of Engineering and Applied Science,
University of California, Los Angeles,
Los Angeles, CA 90024

Transient melting of a vertical wall as a result of condensation of saturated vapor is investigated analytically. Using a Nusselt-type analysis the equations governing the laminar melt and condensate films are solved by a combination of analytical and numerical finite-differencing techniques. The solutions in the axial distance–time plane fall into three regions: the piling region where the melt and condensate thicknesses are only functions of time, the Goursat region where the thicknesses are functions of both the axial distance and time, and the steady-state region where the film thicknesses are only functions of the axial distance. The time to achieve a steady-state condition is obtained analytically.

Introduction

When a solid structure is exposed to saturated vapor and the melting temperature of the solid is less than the temperature of the vapor, simultaneous melting-condensation may occur. This phenomenon is of particular interest in nuclear reactor safety and has several applications in the chemical industry such as desalination. In this work, transient condensation-melting of a vertical wall exposed to saturated vapor of another liquid is studied.

The problems of steady-state condensation and steady-state condensation-melting for vertical surfaces have been studied by several investigators including Taghavi-Tafreshi and Dhir [1]. In [1] steady-state simultaneous melting-condensation on a vertical wall was investigated both analytically and experimentally. Using similarity transformations the full boundary layer equations governing laminar melt and condensate films were solved numerically for high Prandtl number liquids. Melting and condensation heat transfer and the melt-condensate interface temperature were obtained as a function of ρ_c/ρ_m, c_{pc}/c_{pm}, k_c/k_m, μ_c/μ_m, $c_{pc}(T_{sat}-T_{melt})/h_{fg}$, and $c_{pm}(T_{sat}-T_{melt})/h_{sl}$. It is shown in this work's Analysis section that the parameters of the present problem are: $\rho_c/\rho_m \equiv \rho$, $k_c/k_m \equiv k$, $\mu_c/\mu_m \equiv \mu$, and $(\rho_c h_{fg})/(\rho_m h_{sl}) \equiv e$. The parameters c_{pc}/c_{pm}, $c_{pc}(T_{sat}-T_{melt})/h_{fg}$, and $c_{pm}(T_{sat}-T_{melt})/h_{sl}$ do not appear explicitly in the present work because it is assumed that $c_{pc}(T_{sat}-T_c) << h_{fg}$ and $c_{pm}(T_m-T_{melt}) << h_{sl}$.

In comparison to the steady-state case, not much has been done on the problems of transient condensation and transient condensation-melting. Sparrow and Siegel [2] analyzed the problem of transient film condensation. They used a Nusselt-type analysis by ignoring inertia and convective terms. Contreras and Thorsen [3] examined the case of transient condensation and melting when the condensate and melt were of the same chemical composition, such as steam condensing on ice. They ignored the inertia terms in the momentum equation but kept the convective terms in the energy equation. They then obtained an integral solution assuming a quadratic temperature profile.

In this work transient condensation-melting of a vertical wall is analyzed for the case when the condensate and the melt are two immiscible liquids. The governing equations are set up in a manner similar to that used by Sparrow and Siegel [2]. The equations are solved by a combination of analytical and numerical techniques. Once the condensate and melt thicknesses are determined for all x and t of interest, the interface temperature, interface velocity, and Nusselt numbers of the process can be determined.

Analysis

The physical model used in this study is shown in Fig. 1. A vertical isothermal wall at its melting temperature is suddenly exposed to saturated vapor of another immiscible liquid. The melting temperature of the wall is less than the saturation temperature of the vapor such that the latent heat of vaporization released during condensation leads to melting of the solid. The vapor condenses in the form of a film, and both the melt and condensate films flow downward due to gravity. The assumptions are

(*i*) The wall is maintained at its melting temperature;
(*ii*) the pure quiescent saturated vapor has no noncondensable gas in it;
(*iii*) no shape change of the solid occurs during the transient period, i.e., the solid-melt interface remains vertical;
(*iv*) both the condensate and melt layers remain laminar;
(*v*) the problem is two dimensional;
(*vi*) the axes are fixed on the wall and move into the solid as the melt front progresses;
(*vii*) inertia terms in the momentum equations and con-

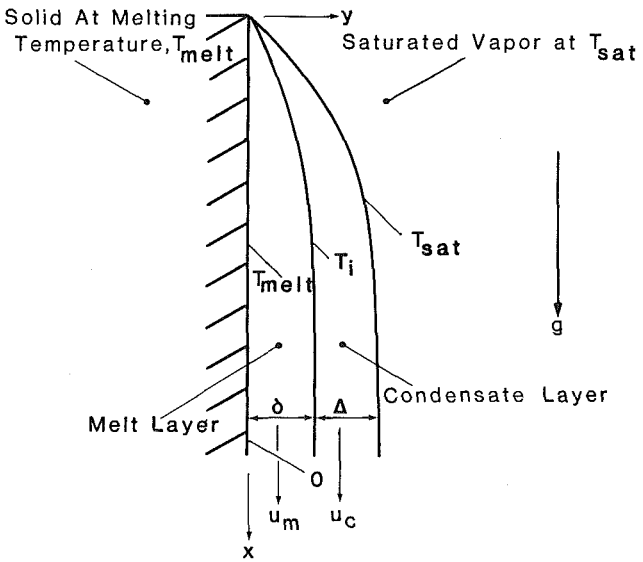

Fig. 1 Physical model for simultaneous melting-condensation on a vertical wall

Contributed by the Heat Transfer Division for publication in the JOURNAL OF HEAT TRANSFER. Manuscript received by the Heat Transfer Division May 21, 1984. Paper No. 83-WA/HT-99.

vective terms in the energy equations are negligible. It is shown in [7] that the inertia terms in the condensate and melt can be ignored when $c_{pc}(T_{sat}-T_{melt})/(h_{fg}\mathrm{Pr}_c)<<1$ and $c_{pm}(T_{sat}-T_{melt})/(h_{sl}\mathrm{Pr}_m)<<1$ respectively. Convective terms are small when $c_{pc}(T_{sat}-T_{melt})/h_{fg}<<1$ and $c_{pm}(T_{sat}-T_{melt})/h_{sl}<<1$;

(*viii*) constant thermophysical properties are assumed; and

(*ix*) the densities of the condensate and the melt are much greater than that of the saturated vapor.

For the assumed velocity and temperature profiles the inertia and convective terms are ignored in the point form momentum and energy equations. The boundary conditions on velocity are: no slip at the solid wall, no shear stress at the free surface, and equal velocities at the interface between the condensate and melt layers. With these boundary conditions the velocity profile for the condensate is

$$u_c = u_i + \frac{\rho_c g}{2\mu_c}(2y\delta + 2y\Delta - 2\delta\Delta - y^2 - \delta^2) \quad \delta \le y \le \delta + \Delta \tag{1}$$

while that for the melt layer is

$$u_m = \left(\frac{u_i}{\delta} + \frac{\rho_m g \delta}{2\mu_m}\right) y - \frac{\rho_m g y^2}{2\mu_m} \quad 0 \le y \le \delta \tag{2}$$

The interface velocity u_i is obtained by matching the shear stress at $y=\delta$ as

$$u_i = (\rho_c g/\mu_m)\Delta\delta + \left(\frac{1}{2}\rho_m g/\mu_m\right)\delta^2 \tag{3}$$

The boundary conditions on temperature are: melting temperature at the wall, saturation temperature at the free surface, and equal temperatures of the melt and the condensate at the interface. With these boundary conditions the condensate temperature profile is

$$T_c = (T_{sat} - T_i)(y - \delta - \Delta)/\Delta + T_{sat} \quad \delta \le y \le \delta + \Delta \tag{4}$$

while the melt temperature profile is

$$T_m = (T_i - T_{melt})y/\delta + T_{melt} \quad 0 \le y \le \delta \tag{5}$$

The interface temperature T_i is determined by matching the heat flux at the condensate-melt interface as

$$T_i = \frac{(k_c/k_m)T_{sat}(\delta/\Delta) + T_{melt}}{1 + (k_c/k_m)(\delta/\Delta)} \tag{6}$$

The continuity and energy equations are applied to both the condensate and melt layers. With the assumptions of $h_{fg} >> c_{pc}(T_{sat} - T_c)$ and $h_{sl} >> c_{pm}(T_m - T_{melt})$ the energy equation for the condensate layer is

$$\frac{\partial}{\partial x}\int_{\delta}^{\delta+\Delta} \rho_c h_{fg} u_c dy + \frac{\partial}{\partial t}\int_{\delta}^{\delta+\Delta} \rho_c h_{fg} dy = k_c \frac{\partial T_c}{\partial y}\bigg|_{y=\delta} \tag{7}$$

and that for the melt layer is

$$\frac{\partial}{\partial x}\int_{0}^{\delta} \rho_m h_{sl} u_m dy + \frac{\partial}{\partial t}\int_{0}^{\delta} \rho_m h_{sl} dy = k_m \frac{\partial T_m}{\partial y}\bigg|_{y=\delta} \tag{8}$$

With the assumed velocity and temperature profiles and the interface velocity and temperature equations (7) and (8) represent two equations in two unknowns: Δ and δ.

These two equations are nondimensionalized to bring out the problem parameters and to have solutions valid for general applications. The dimensionless variables are chosen so that in the limit of $h_{fg} \to \infty$ or $h_{sl} \to \infty$ these equations degenerate to the solutions presented by Sparrow and Siegel [2]. These variables are

$$x^* = x/L \tag{9}$$

Nomenclature

c_p = specific heat
E = $(\rho_c h_{fg})/(\rho_{min} h_{min})$
e = $(\rho_c h_{fg})/(\rho_m h_{sl})$
G = transformation variable = $\Delta^{*3}/3$
g = gravity
H = transformation variable = $\delta^{*3}/3$
h_{fg} = latent heat of vaporization of the condensate
h_{sl} = latent heat of fusion of the solid
K = k_c/k_{min}
k = with a subscript, thermal conductivity; without a subscript, k_c/k_m
L = length of vertical surface aligned with gravity
M = μ_c/μ_{min}
Nu_t^0 = local Nusselt number of the melt layer based on total temperature difference and evaluated at the solid wall; defined in equation (51)
P = ρ_c/ρ_{min}
Pr = Prandtl number
T = temperature
T_{melt} = melting temperature of the solid
T_{sat} = saturation temperature of the vapor
t = time
t_{css} = maximum steady state time for transient condensation defined in equation (16)
t_{min} = lesser of t_{mss} or t_{css}
t_{mss} = maximum steady-state time for transient melting defined in equation (17)
t_p = piling time
t_{ss} = steady-state time
U = vector of variables, (G, H)
u = one component of vector U; or the axial velocity
x = axial coordinate parallel to gravitational acceleration and measured from leading edge of the solid wall
y = coordinate normal to the surface
γ_t^0 = constant proportional to the Nusselt number of the melt layer based on total temperature difference, defined in equation (51)
$\bar{\gamma}_t^0$ = time-averaged value of γ_t^0
Δ = thickness of the condensate layer
Δ_{ss} = maximum steady-state condensate thickness defined in equation (13)
δ = thickness of the melt layer
δ_{ss} = maximum steady-state melt thickness defined in equation (14)
μ = with a subscript, viscosity; without a subscript, μ_c/μ_m
ρ = with a subscript, density; without a subscript, ρ_c/ρ_m

Subscripts

C = refers to values given by Contreras and Thorsen's published paper [3]
CC = refers to values given by Contreras and Thorsen's corrected analysis [7]
c = condensate layer
i = refers to interface between the condensate and melt layers
m = melt layer
min = refers to whether condensate or melt values are used in t_{min}
T = refers to steady-state values obtained from computer program developed in [5]

Superscripts

$*$ = nondimensional variables defined in equations (9–12)
$'$ = nondimensional variables defined in equations (48–50)

$$\Delta^* = \Delta/\Delta_{ss} \tag{10}$$

$$\delta^* = \delta/\delta_{ss} \tag{11}$$

$$t^* = t/t_{\min} \tag{12}$$

where[1]

$$\Delta_{ss} = \left[\frac{4k_c\mu_c(T_{\text{sat}} - T_{\text{melt}})L}{(\rho_c h_{fg})\rho_c g}\right]^{1/4} \tag{13}$$

$$\delta_{ss} = \left[\frac{4k_m\mu_m(T_{\text{sat}} - T_{\text{melt}})L}{(\rho_m h_{sl})\rho_m g}\right]^{1/4} \tag{14}$$

$$t_{\min} = \text{lesser of } t_{css} \text{ or } t_{mss} \tag{15}$$

The steady-state times t_{css} and t_{mss} for the condensate and melt layers alone are defined as

$$t_{css} = \left[\frac{(\rho_c h_{fg})\mu_c L}{k_c g(T_{\text{sat}} - T_{\text{melt}})\rho_c}\right]^{1/2} \tag{16}$$

$$t_{mss} = \left[\frac{(\rho_m h_{sl})\mu_m L}{k_m g(T_{\text{sat}} - T_{\text{melt}})\rho_m}\right]^{1/2} \tag{17}$$

The rationale for using the minimum time $t_{\min}$ is derived from the following considerations:

1 If $h_{fg} \to \infty$ melting alone occurs. Therefore the time scale used should be that of the melt. Using $t_{\min}$ insures that the melt time scale will be used. The same situation exists if $h_{sl} \to \infty$ in which case the proper time scale is that of the condensate.

2 If time was scaled with the greater of t_{css} or t_{mss}, in the case of $h_{fg} \to \infty$ the scaling for time would be $t_{css} \to \infty$. The time to achieve steady state is finite. Therefore the dimensionless time at steady state would be $t_{ss}/t_{css} = 0$. By scaling with the smaller of the two, in the case of $h_{fg} \to \infty$ the scaling for time is t_{mss}, which is finite. The dimensionless time at steady state is t_{ss}/t_{mss} which is also finite. The same situation exists for the case of $h_{sl} \to \infty$.

With the dimensionless variables the condensate energy equation becomes

$$\left[\frac{l\Delta^{*4} + i\delta^*\Delta^{*3} + j\delta^{*2}\Delta^{*2} + r\delta^{*3}\Delta^* + m\delta^{*4}}{c\Delta^{*2} + b\delta^*\Delta^* + d\delta^{*2}}\right]\frac{\partial\Delta^*}{\partial x^*}$$

$$+\left[\frac{a\Delta^{*4} + f\delta^*\Delta^{*3} + g\delta^{*2}\Delta^{*2} + h\delta^{*3}\Delta^*}{c\Delta^{*2} + b\delta^*\Delta^* + d\delta^{*2}}\right]\frac{\partial\delta^*}{\partial x^*} + \frac{\partial\Delta^*}{\partial t^*}$$

$$= \frac{y\Delta^* + n\delta^*}{c\Delta^{*2} + b\delta^*\Delta^* + d\delta^{*2}} \tag{18}$$

while that for the melt layer becomes

$$\left[\frac{o\delta^{*2}\Delta^* + p\delta^{*3}}{w\Delta^* + u\delta^*}\right]\frac{\partial\Delta^*}{\partial x^*}$$

$$+\left[\frac{q\delta^*\Delta^{*2} + s\delta^{*2}\Delta^* + v\delta^{*3}}{w\Delta^* + u\delta^*}\right]\frac{\partial\delta^*}{\partial x^*} + \frac{\partial\delta^*}{\partial t^*} = \frac{-z}{w\Delta^* + u\delta^*} \tag{19}$$

The constants a–z are listed below

$$a = 4\mu\left[\frac{e\rho}{k\mu}\right]^{1/4} \qquad c = 2\left[\frac{EM}{KP}\right]^{1/2}$$

$$b = 4k\left[\frac{EM}{KP}\right]^{1/2}\left[\frac{e\rho}{k\mu}\right]^{1/4} \qquad d = 2k^2\left[\frac{eEM\rho}{kKP\mu}\right]^{1/2}$$

$$f = 4(2k + \rho^{-1})(e\mu\rho/k)^{1/2} \qquad p = 2\rho^{3/4}(k\mu/e)^{1/4}$$

$$g = 4(2k + \rho k^2)(e/k)^{3/4}(\mu/\rho)^{1/4} \qquad q = 4\left[\frac{\mu\rho}{ek}\right]^{1/2}$$

$$h = 4ek \qquad r = 4(2\rho k^2 + k)(e/k)^{3/4}(\mu/\rho)^{1/4}$$

$$i = 8(k+\mu)\left[\frac{e\rho}{k\mu}\right]^{1/4} \qquad s = 4(k + \rho^{-1})(\rho/k)^{3/4}(\mu/e)^{1/4}$$

$$j = 4\left(4k + \frac{1}{2\rho} + \frac{k^2}{\mu}\right)\left[\frac{e\mu\rho}{k}\right]^{1/2} \qquad u = 2\left[\frac{EkM\rho}{eKP\mu}\right]^{1/2}$$

$$l = 4.0 \qquad v = 4.0$$

$$m = 2ek \qquad w = 2\left[\frac{EM}{eKP}\right]^{1/2}\left[\frac{\rho}{ek\mu}\right]^{1/4}$$

$$n = k^{3/4}(e\rho/\mu)^{1/4} \qquad y = 1.0$$

$$o = 2\left[\frac{\mu\rho}{ek}\right]^{1/2} \qquad z = -1.0 \tag{20}$$

The parameters of this problem are:

$(\rho_c h_{fg})/(\rho_m h_{sl}) \equiv e$, $k_c/k_m \equiv k$, $\mu_c/\mu_m \equiv \mu$; and $\rho_c/\rho_m \equiv \rho$. Additional ratios are defined as: $(\rho_c h_{fg})/(\rho_{\min} h_{\min}) \equiv E$, $k_c/k_{\min} \equiv K$, $\mu_c/\mu_{\min} \equiv M$, and $\rho_c/\rho_{\min} \equiv P$. If $t_{\min}$ is t_{css} or t_{mss}, E, K, M, and P are each 1 or e, k, μ, and ρ respectively.

Equations (18) and (19) are a first-order quasi-linear hyperbolic system in two independent variables: x^*, t^*, and two dependent variables: Δ^* and δ^*. The boundary and initial conditions are $\Delta^*(x^* = 0, t^*) = \delta^*(x^* = 0, t^*) = 0$ and $\Delta^*(x^*, t^* = 0) = \delta^*(x^*, t^* = 0) = 0$.

Method of Solution. Equations (18) and (19) comprise mathematically a very difficult system. No closed-form analytical solution is apparent which satisfies both the differential equations and the boundary and initial conditions. Furthermore a numerical solution is not trivial because of the unstable numerical nature of hyperbolic systems and because of the poles which exist with respect to the initial condition and the boundary condition at the leading edge.

In this work a combined numerical and analytical technique is used to obtain solutions. The details of the solution are contained in [7]. Briefly stated Δ^* and δ^* are functions of t^* only and x^* only in two separate regions of the (x^*, t^*) plane. In these two regions, shown in Fig. 2, a closed-form analytical expression exists for $\Delta^*(t^*)$, $\delta^*(t^*)$, $\Delta^*(x^*)$, and $\delta^*(x^*)$. In the area in between, the Goursat region, Δ^* and δ^* are functions of both x^* and t^* and a numerical solution is obtained.

The region in which Δ^* and δ^* are functions of t^* only is called here the piling region. Physically this region corresponds to the case of no net flow. The mass flow rates in the condensate and melt layers are a function of the condensate and melt thicknesses. In the piling region the thicknesses are not a function of x^*. Therefore at a fixed time the flow rate into and out of each layer is constant or no net flow occurs.

The limiting characteristic defining the piling region as shown in Fig. 2 is obtained as

$$x^* = (C_1/2)t^{*2} \tag{21}$$

where

$$C_1 = \frac{C_{11} + C_{22}}{2} + \frac{1}{2}[(C_{11} - C_{22})^2 + 4C_{12}C_{21}]^{1/2} \tag{22}$$

$$C_{11} = [mC^4 + rDC^3 + jD^2C^2 + iD^3C + lD^4]/$$
$$[dC^2 + bDC + cD^2] \tag{23}$$

[1] $(\rho_c h_{fg})/(\rho_m h_{sl})$ is a parameter of the problem regardless of the density of the saturated vapor. When the densities of the condensate and the melt are not much greater than that of the saturated vapor another parameter of the problem is $(\rho_c - \rho_v)/(\rho_m - \rho_v)$ where ρ_v is the density of the vapor. In this case $(\rho_c h_{fg})$ and $(\rho_m h_{sl})$ remain unchanged but ρ_c and ρ_m are replaced by $(\rho_c - \rho_v)$ and $(\rho_m - \rho_v)$, respectively.

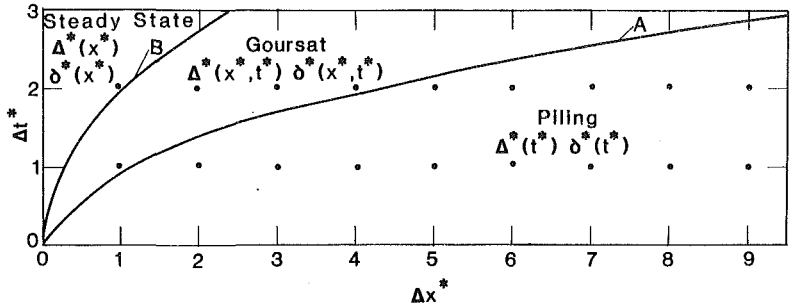

Fig. 2 Steady-state, Goursat, and piling regions with mesh points and limiting characteristics *B* and *A*

$$C_{12}=(D^2/C^2)[hDC^3+gD^2C^2+fD^3C+aD^4]/[dC^2+bDC+cD^2] \quad (24)$$

$$C_{21}=(C^2/D^2)(pC^3+oDC^2)/(uC+wD) \quad (25)$$

$$C_{22}=(vC^3+sDC^2+qD^2C)/(uC+wD) \quad (26)$$

$$C=e\left[\frac{KP\mu}{eEkM\rho}\right]^{1/4}[e+(1/k)]^{-1/2} \quad (27)$$

$$D=\left[\frac{KP}{EM}\right]^{1/4}[ek+1]^{-1/2} \quad (28)$$

The constants a–z have been defined earlier in equations (20). In this piling region:

$$\delta^*=Ct^{*1/2} \quad (29)$$

$$\Delta^*=Dt^{*1/2} \quad (30)$$

For x^* fixed, the dimensionless piling time t_p^* is determined from equation (21). After the piling time t_p net flow in the layers starts to occur.

The region in which Δ^* and δ^* are functions of x^* only is the steady-state region. For x fixed, after a certain time t_{ss}, which is determined from equation (31), Δ and δ attain their local steady-state values. This steady-state time has a fixed value and is the same for both layers. The film thicknesses Δ and δ do not approach their steady-state values asymptotically and do not attain their steady-state values only when $t \to \infty$. The limiting characteristic curve B defining the steady-state region as shown in Fig. 2 is obtained as

$$x^*=(K_1{}^2/4)t^{*2} \quad (31)$$

where

$$K_1=\frac{K_{11}+K_{22}}{2}-\frac{1}{2}[(K_{11}-K_{22})^2+4K_{12}K_{21}]^{1/2} \quad (32)$$

$$K_{11}=[mA^4+rBA^3+jB^2A^2+iB^3A+lB^4]/[dA^2+bBA+cB^2] \quad (33)$$

$$K_{12}=(B^2/A^2)[hBA^3+gB^2A^2+fB^3A+aB^4]/[dA^2+bBA+cB^2] \quad (34)$$

$$K_{21}=(A^2/B^2)[pA^3+oBA^2]/[uA+wB] \quad (35)$$

$$K_{22}=[vA^3+sBA^2+qB^2A]/[uA+wB] \quad (36)$$

$$A=\left[\frac{k}{(k+C_{ss})(1+1.5\rho C_{ss})}\right]^{1/4} \quad (37)$$

$$B=AC_{ss}\left[\frac{e\rho}{k\mu}\right]^{1/4} \quad (38)$$

and C_{ss} is a root of the cubic equation

$$C_{ss}^3+3\mu C_{ss}^2+1.5[(\mu/\rho)-(\mu/e)]C_{ss}-\mu/(e\rho)=0 \quad (39)$$

The constants a–z are once again those given earlier under equation (20). The solution of the cubic equation (39) is given in [6]. The root is chosen so that Δ (dimensional) = $C_{ss}\delta$ (dimensional). In this steady-state region

$$\delta^*=Ax^{*1/4} \quad (40)$$

$$\Delta^*=Bx^{*1/4} \quad (41)$$

The velocity of the steady-state wave front is given by the time derivative of equation (31). If the velocity is desired as a function of x equation (31) is substituted back to express t as a function of x.

The Lax–Friedrichs finite-differencing numerical method is used to determine the solution of Δ^* and δ^* in the Goursat region. This method, which is described in [4], is explicit forward difference in time with a first-order truncation error in Δt and a second-order truncation error in Δx. The poles which exist at both the boundary and initial conditions are removed by the transformation

$$\Delta^*=(3G)^{1/3} \quad (42)$$

$$\delta^*=(3H)^{1/3} \quad (43)$$

Using this transformation equations (18) and (19) take on the form

$$AU_{x^*}+U_{t^*}+D=0 \quad (44)$$

where A is a 2 by 2 matrix, $U_{x^*}=(\partial G/\partial x^*, \partial H/\partial x^*)$, $U_{t^*}=(\partial G/\partial t^*, \partial H/\partial t^*)$, and D is a 2 by 1 vector.

The matrix A and the vector D are evaluated at x^* and t^*. Central differencing is done on the vector components u of U_{x^*}, i.e.,

$$u_{x^*}=[u(x^*+\Delta x^*,t^*)-u(x^*-\Delta x^*,t^*)]/(2\Delta x^*). \quad (45)$$

Explicit forward differencing is done on the components of U_{t^*} but an average value is used to approximate $u(x^*, t^*)$, i.e.,

$$u_{t^*}=\frac{u(x^*,t^*+\Delta t^*)-0.5[u(x^*+\Delta x^*,t^*)+u(x^*-\Delta x^*,t^*)]}{\Delta t^*} \quad (46)$$

The averaging of $u(x^*, t^*)$ by its neighboring values introduces damping into the finite-differencing scheme. This is required to dampen out numerical instabilities which hyperbolic systems have. The stability criterion for this scheme is

$$\Delta t^*\,|e_{\max}|/\Delta x^*<1 \quad (47)$$

where $e_{\max}$ is the maximum eigenvalue of the matrix A. For the present application $e_{\max}$ has been <10. Therefore the first-order truncation error in Δt^* has been a greater concern than the stability criterion.

For the numerical solution of the Goursat problem, as shown in Fig. 2, the initial condition at $t^* = 0$ is used to determine the values of G and H at $t^* = \Delta t^*$. Since the values at $t^* = \Delta t^*$, $x^* = 2\Delta x^*, 3\Delta x^*, \ldots$ fall into the piling region the values of G and H there are given their closed-form analytical values rather than the values which would be obtained from the finite-differencing scheme. For the end point at $t^* = \Delta t^*$, $x^* = n\Delta x^*$, the values of G and H are determined

by their values at $(n-1)\Delta x^*$, $(n-2)\Delta x^*$, $(n-3)\Delta x^*$ and an interpolating polynomial which is third-order correct in Δx^*. The process is repeated at $t^* = 2\Delta t^*$ using the values of G and H at $t^* = \Delta t^*$ and so forth for greater times. At $t^* = 2\Delta t^*$, $x^* = \Delta x^*$ the values of G and H are given their closed-form steady-state analytical values since they are in the steady-state region. The process is continued until the steady-state limiting characteristic curve B in Fig. 2 extends past the maximum x^* of interest. In those cases where the steady-state limiting characteristic remains very close to $x^* = 0$ the computations are stopped at a previously set maximum t^* or when the results for G and H do not change in any meaningful way with an increase in time.

Having the closed-form analytical solutions in the piling and steady-state regions and the numerical solution in the Goursat region, the values of Δ and δ are known for all x and t of interest. Knowing Δ and δ the values of the interface temperature, interface velocity, local and average Nusselt numbers for the layers can be obtained.

Results and Discussion

In order to assure the correctness of the present analysis the limiting solutions were compared with those of other investigators. In [7] the results of this study are compared to those of Sparrow and Siegel [2] for the case of $h_{fg} \to \infty$ and $h_{sl} \to \infty$, i.e., melting alone or condensation alone. Since the present work basically has Sparrow and Siegel's assumptions present results degenerate to theirs in these two limits.

The next case examined was the problem of a vapor condensing onto a solid of the same chemical composition, for example, steam condensing onto ice. In this regard the only transient analysis previously performed has been that of Contreras and Thorsen [3]. In their published paper there are some typographical and analytical errors. Details of these errors and the corrected results are contained in [7].

The results of steam condensing on ice are shown in Fig. 3 for 1 atmosphere pressure and $x = 0.15$ m. The figure compares Contreras and Thorsen's published results [3] given with the subscript C, the present work's which has no subscript, Contreras and Thorsen's corrected results [7] given with the subscript CC, and those obtained from the computer program given in [5] which is denoted with the subscript T. This computer program solves the steady-state problem including both inertia terms in the momentum equations and convective terms in the energy equations. The results obtained from this program are accepted as the standard for steady-state analysis.

As seen from Fig. 3, the condensate layer grows with time until $t = t_p$. After this time it thins down to its steady-state value. The melt layer continues to thicken with time even after t_p until it attains its steady-state value. The sum of two thicknesses $(\Delta + \delta)$, however, remains constant with time after t_p. Contreras and Thorsen's published and corrected results likewise show this constant value of $(\Delta + \delta)$ after their steady-state time t_{ss}. The steady-state time in the case of the condensate and melt of the same species depends upon how the steady time is defined. If the condensate or melt layers are considered alone, the steady-state time corresponds to the present work's t_{ss}. If on the other hand the sum of the two layers is considered, as Contreras and Thorsen did for the steam–ice system, then the present work's piling time corresponds to their steady-state time. The behavior of the individual layers and the difference between the steady-state time for the combined layers versus that for the individual layers cannot be determined from Contreras and Thorsen's work. This is because they considered only the sum of the two layers, not each layer individually. For the one atmosphere steam–ice system at $x = 0.15$ m, the velocity of the steady-state front is found to be 1.09 m/s.

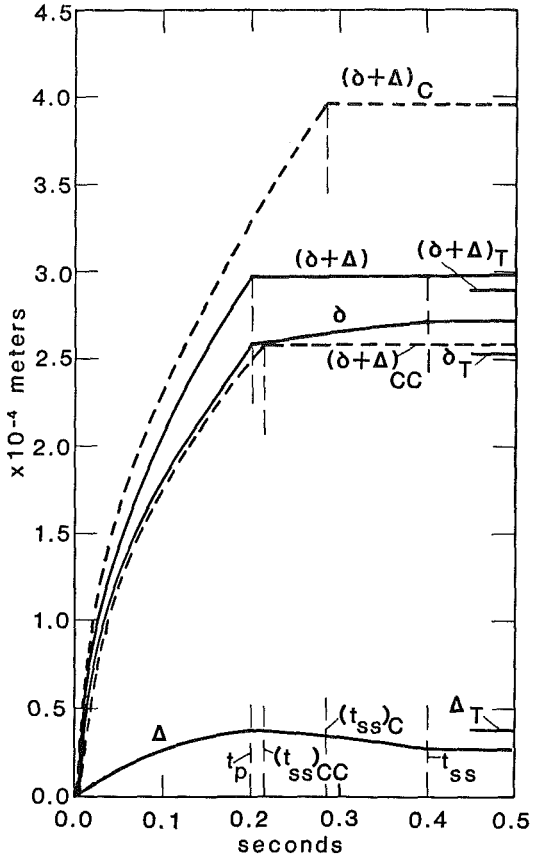

Fig. 3 One atmosphere steam condensing on ice at $x = 0.15$ m; present results compared to those of Contreras and Thorsen [3], Contreras and Thorsen corrected [7], and Taghavi-Tafreshi [5]

To investigate the effect of the variation of the melt and condensate thermophysical properties a base case was selected and the dimensionless property ratios were altered one at a time. For the base case $k = 5$, $\rho = 1$, $\mu = 1/2$, $c_{pc}/c_{pm} = 2$, and $e = 2$. Since the present analysis is valid for small values of $c_{pc}(T_{sat} - T_{melt})/h_{fg}$ and $c_{pm}(T_{sat} - T_{melt})/h_{sl}$, the values of these parameters were chosen to be 0.01 while obtaining the results from [5].

As the thermophysical properties change, Δ_{ss}, δ_{ss}, and t_{min} change. If a comparison is to be made from case to case it is better that a common scaling exist for both film thicknesses as well as for time. For the base case

$$\Delta_{ss}/\delta_{ss} = [(k\mu)/(e\rho)]^{1/4} = 1.25^{1/4} = 1.06,$$

$$t_{css}/t_{mss} = [(e\mu)/(k\rho)]^{1/2} = 0.2^{1/2} = 0.45$$

Here, the melt time scale t_{mss} is greater than the condensate time scale t_{css}, with δ_{ss} approximately equal to Δ_{ss}. Therefore if the melt or the condensate properties are to be used to scale the film thicknesses and time, it is better that the scaling be done with the melt values. The boundary layer thicknesses are thus nondimensionalized with δ_{ss}, and time with t_{mss}.

$$\Delta' = \Delta/\delta_{ss} \tag{48}$$

$$\delta' = \delta/\delta_{ss} \tag{49}$$

$$t' = t/t_{mss} \tag{50}$$

The local Nusselt number is defined the same way as is done in [1]

Table 1 Dimensionless piling and steady-state times, the steady-state temperature drop across the melt layer, and the steady-state coefficient $\gamma_t{}^0$ at $x^* = 0.5$

Case	t'_p	t'_{ss}	$\frac{(T_i - T_{melt})_{ss}}{(T_{sat} - T_{melt})}$	γ^0_{tss}
base*	0.470	1.050	0.945	1.05
$k=1$	0.555	1.155	0.780	0.895
$\mu=0.05$	0.280	0.790	0.960	1.02
$e=1$	0.350	0.900	0.910	1.06
$\rho=½$	0.578	1.150	0.943	1.01

*Base case has: $k=5$, $\mu=½$, $e=2$, $\rho=1$

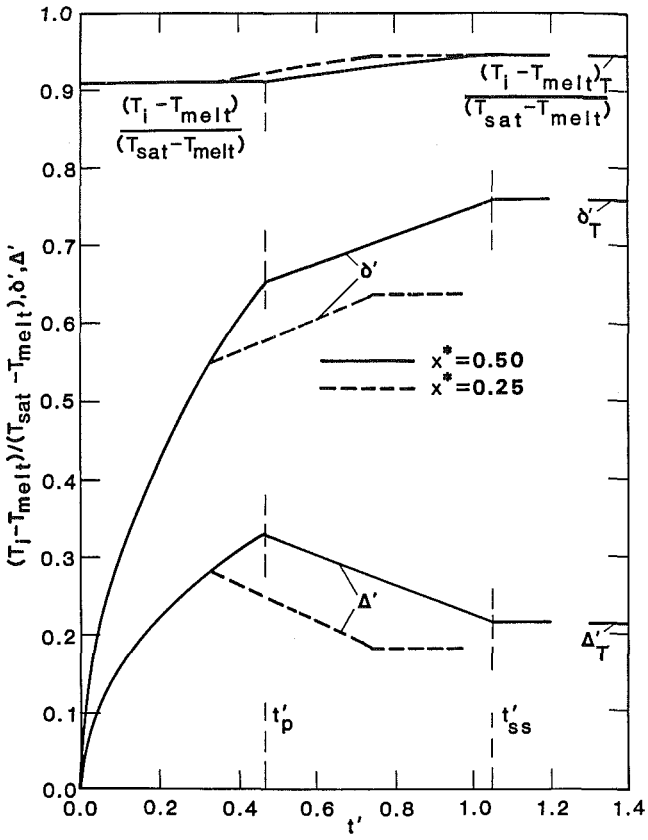

Fig. 4 Dependence of the temperature drop across the melt layer and the melt and condensate thicknesses on t' for base case at different values of x^*

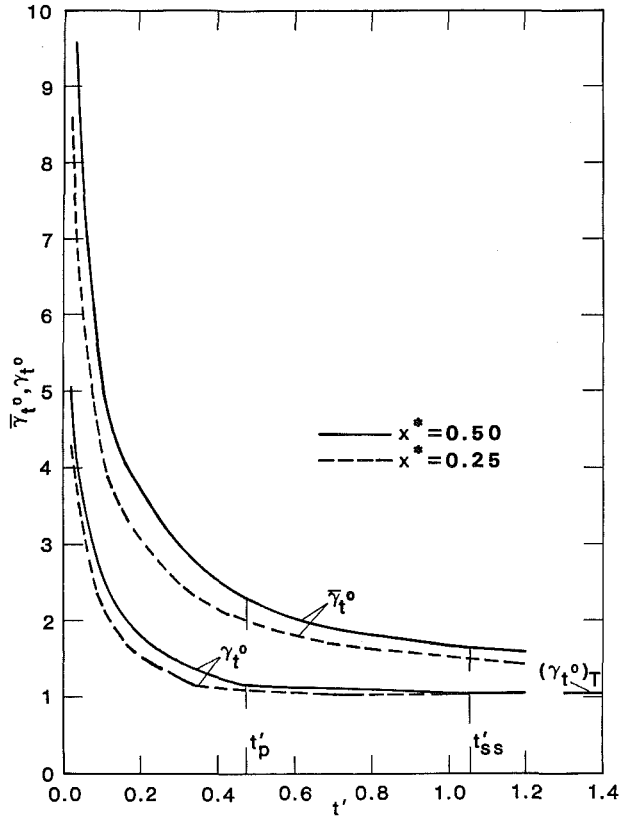

Fig. 5 The dependence of coefficients $\bar{\gamma}_t{}^0$ and $\gamma_t{}^0$ on t' for the base case at different values of x^*

$$\mathrm{Nu}_t{}^0 = \frac{x}{(T_{sat} - T_{melt})} \frac{\partial Tm}{\partial y}\bigg|_{y=0}$$

$$= \gamma_t{}^0 \left[\frac{\rho_m g \rho_m h_{sl} x^3}{4\mu_m k_m (T_{sat} - T_{melt})} \right]^{1/4} \tag{51}$$

The values of Δ', δ', and $(T_i - T_{melt})/(T_{sat} - T_{melt})$ as a function of t' are given in Fig. 4 for the base case at $x^* = 0.5$ and $x^* = 0.25$. Steady-state values obtained from [5] are also given at the right with subscript T. For $t < t_p$ the interface temperature between the two layers is constant. From equation (6) the interface temperature is given as

$$T_i = [kT_{sat}(\delta/\Delta) + T_{melt}]/[1 + k(\delta/\Delta)] \tag{52}$$

In the piling region both δ and Δ are proportional to $t^{½}$. Therefore the ratio of the two is constant and so is the interface temperature. The same situation exists in the steady-state region where both δ and Δ are proportional to $x^{1/4}$. As can be observed from Fig. 4, decreasing x^* decreases the piling and steady-state times as the square root of x^*. In the Goursat region, Δ, δ, and T_i vary with x. This variation is not a simple translation of the result at another x^* value. The coefficient $\gamma_t{}^0$ in the expression for the Nusselt number as well as its time-averaged value $\bar{\gamma}_t{}^0$ are plotted in Fig. 5. In the piling region $\bar{\gamma}_t{}^0$ is twice $\gamma_t{}^0$ since in this region $\gamma_t{}^0$ is proportional to one over the square root of time. At very large times $\bar{\gamma}_t{}^0$ will approach $\gamma_t{}^0$. The time-averaged values can be useful to calculate at a given location the total melting of the wall in the period of interest. The difference in the steady-state values as compared to those obtained from [5] is insignificant. This is expected since $c_{pm}(T_{sat} - T_{melt})/h_{sl}$ and $c_{pc}(T_{sat} - T_{melt})/h_{fg}$ are both much less than 1. The dimensionless piling and steady-state times, as well as the steady-state temperature drop across the melt layer and the steady-state coefficient $\gamma_t{}^0$, are given in Table 1 for both this base case and the variation cases which follow.

In studying the effect of the variation of thermophysical properties, one of the property ratios is varied while the others are kept at the base values. Details of these variations, when k is decreased to 1, μ is decreased to 0.05, and e is decreased to 1, are given in [7].

From these results it is found that the effect of varying k is primarily to change the interface temperature. When k is decreased, the temperature drop across the condensate layer

must increase to transfer approximately the same heat load. This therefore decreases $(T_i - T_{melt})$ by about 20 percent. The major effect of changing μ to 0.05 is to decrease the piling time by about 40 percent and the steady-state time by approximately 25 percent. In the piling region for $t \leq t_p$, the condensate and melt thicknesses are not functions of μ. However, the piling and steady-state times are functions of this parameter because in the Goursat and steady-state regions the film thicknesses are functions of distance.

When the parameter e is decreased from 2 down to 1, the condensate and melt both grow at the same rate in the piling region. This is because a given heat flux will generate the same volume of melt and condensate. Comparing these results with the base case, the greatest variation is in the thickness of the condensate. Since the total amount of heat transferred is still just about the same, more vapor must condense. Therefore the condensate thickens by approximately 64 percent. For the thicker condensate layer $(T_i - T_{melt})$ decreases by about 9 percent in the piling region and 4 percent in the steady-state region.

The major effect of decreasing ρ from 1 to 1/2 while maintaining the rest of the parameters at their base values is to increase the piling time by 23 percent. As is the case when the viscosity ratio is varied, when the density ratio is varied the piling and steady-state times are changed but for $t \leq t_p$ there is no effect of density ratio on the film thicknesses. In the Goursat and steady-state regions when ρ is decreased to 1/2 the effect upon Δ', δ', T_i, and $\gamma_t{}^0$ is small. The steady-state time is increased by about 10 percent.

Conclusions

1 For transient melting-condensation on a vertical wall, the solutions in the (x, t) plane fall into three regions: the piling region which corresponds to the case of no net flow; the Goursat region in which net flow starts to occur and where the solutions are functions of both x and t; and the steady-state region in which the solutions are only functions of x.

2 Analytical expressions are found for both the piling and the steady-state times. After the piling time the condensate layer thins down to its steady-state value while the melt layer thickens. When the melt and condensate are of the same species the sum of the two layers is constant after the piling time.

3 Before the piling time and after the steady-state time the interface temperature between the two layers remains constant. In the Goursat region, the interface temperature increases up to the steady-state value.

4 In the range of thermophysical properties considered, the ratio of thermal conductivities mainly affects the interface temperature, the density ratio mainly affects the piling time, the viscosity ratio affects both the piling and the steady-state times, and the ratio of latent heats significantly affects only the film thicknesses.

Acknowledgments

The authors wish to acknowledge the very kind assistance of Professors Stanley Osher, Kenneth Bube, and James Ralston in the UCLA Mathematics Department for their help in solving the governing equations both analytically and numerically.

References

1 Taghavi-Tafreshi, K., and Dhir, V. K., "Analytical and Experimental Investigation of Simultaneous Melting-Condensation on a Vertical Wall," ASME JOURNAL OF HEAT TRANSFER, Vol. 104, 1982, pp. 24–33.

2 Sparrow, E. M., and Siegel, R., "Transient Film Condensation," ASME *Journal of Applied Mechanics*, Vol. 81, Mar. 1959, pp. 120–121.

3 Contreras, W., and Thorsen, R. S., "Transient Melting of a Solid Heated by a Condensing Saturated Vapor—Case 1: Negligible Interface Curvature," ASME JOURNAL OF HEAT TRANSFER, Vol. 97, Nov. 1975, pp. 570–575.

4 Ames, W. F., *Numerical Methods for Partial Differential Equations*, 2nd ed., Academic Press, New York, 1977.

5 Taghavi-Tafreshi, K., "Condensation of Saturated Vapor on Melting Surfaces," Ph.D. dissertation, UCLA, 1982.

6 *CRC Standard Mathematical Tables*, 19th ed., editor, Samuel Selby, Chemical Rubber Co., Cleveland, 1971, pp. 103–104.

7 Galamba, D., "Some Aspects of Simultaneous Melting-Condensation on Vertical Surfaces," Ph.D. dissertation, UCLA, 1985.

S. Kimura
A. Bejan
Assoc. Mem. ASME
Department of Mechanical Engineering and Materials Science, Duke University, Durham, NC 27706
I. Pop
Faculty of Mathematics, University of Cluj, R-3400, Cluj, CP 253, Romania

Natural Convection Near a Cold Plate Facing Upward in a Porous Medium

It is shown that the phenomenon of natural convection driven in a porous medium by a cold plate facing upward or by a warm plate facing downward consists of a finite-length boundary layer flow chopped off by the sharp edges of the plate. The heat and fluid flow features of the boundary layer are determined analytically employing scale analysis and integral analysis. The overall heat transfer rate between porous medium and plate is found to vary as $Nu/Ra^{1/3} = 0(1)$, where Ra is the Darcy-modified Rayleigh number based on plate half-length. The boundary layer features of the flow and the heat transfer effected by it are confirmed in the Ra range 100–700 by numerical solutions of the complete partial differential equations.

Introduction

The object of this paper is to study the phenomenon of natural convection driven in a fluid-saturated porous medium by a cold plate facing upward (Fig. 1). Assuming that the fluid that fills the pores of the medium expands upon heating at constant pressure ($\beta > 0$), the flow sketched in Fig. 1 is also possible in the vicinity of a warm plate of finite length facing downward. The flow in this second configuration is visualized by rotating Fig. 1 by 180 deg.

In step with the growing interest in porous medium heat and fluid flow processes and in the many engineering applications of these phenomena [1], the horizontal wall geometry has been recognized as one of fundamental importance. Cheng and Chang [2, 3] have developed the similarity solutions for steady-state convection above a heated surface, by representing the wall temperature as a power function of the distance x from the vertical plane of symmetry of the flow. In a subsequent paper, Cheng [4] reported Karman–Pohlhausen solutions to the same problem. The growth of a thermal layer in a porous medium adjacent to a suddenly heated semi-infinite horizontal surface was described analytically by Pop and Cheng [5].

Contrary to the phenomenon documented in [2–5], for which the upward facing plate of Fig. 1 would have to be heated and infinite, the natural convection flow examined in this paper is driven by a finite-length plate whose temperature is lower than the ambient temperature. In such a cooled-from-below configuration there would be no motion if the plate were infinite. In what follows, we employ scale analysis, integral analysis, and numerical simulations to demonstrate that the main feature of the flow is a distinct horizontal boundary layer "chopped off" to finite length by the edges of the plate: This feature is sketched in Fig. 1. An analogous finite-length boundary layer flow occurs in a Newtonian fluid bathing a cooled surface facing upward [6, 7].

Boundary Layer Formulation

The equations accounting for the conservation of mass, momentum, and energy for Darcy flow in the Cartesian frame of Fig. 1 are [2]

$$\frac{\partial u}{\partial x} + \frac{\partial v}{\partial y} = 0 \tag{1}$$

$$\frac{\partial u}{\partial y} - \frac{\partial v}{\partial x} = -\frac{Kg\beta}{\nu}\frac{\partial}{\partial x}(T - T_\infty) \tag{2}$$

$$u\frac{\partial T}{\partial x} + v\frac{\partial T}{\partial y} = \alpha\left(\frac{\partial^2 T}{\partial x^2} + \frac{\partial^2 T}{\partial y^2}\right) \tag{3}$$

where u, v, K, g, T, and ν are the volume-averaged velocity components, the permeability of the porous structure, the gravitational acceleration, the local temperature of the fluid-saturated medium, and the fluid kinematic viscosity, respectively. The Boussinesq approximation was used in order to couple the flow field to the temperature field, by introducing the coefficient of thermal expansion β in equation (2). Equations (1)–(3) are based on the homogeneous porous medium model, where T is the local equilibrium temperature of pore fluid and solid matrix, and where α is the thermal diffusivity calculated as the ratio of the thermal conductivity of the fluid-saturated matrix k, divided by the volumetric heat capacity ρc_p of the fluid alone.

In accordance with the rules of scale analysis outlined in [8], we focus attention on the region of length l and unknown transverse length scale δ, Fig. 1, and make the assumption that the region is slender

$$\delta << l \tag{4}$$

In this region, the velocity scales are u and v, and the scale of the temperature difference $T_\infty - T$ is $\Delta T = T_\infty - T_0$. The slenderness condition (4) is the basis for viewing the $\delta \times l$ region as a boundary layer region in which equations (2, 3) assume the simpler form

$$\frac{\partial u}{\partial y} = \frac{Kg\beta}{\nu}\frac{\partial}{\partial x}(T_\infty - T) \tag{5}$$

$$u\frac{\partial T}{\partial x} + v\frac{\partial T}{\partial y} = \alpha\frac{\partial^2 T}{\partial y^2} \tag{6}$$

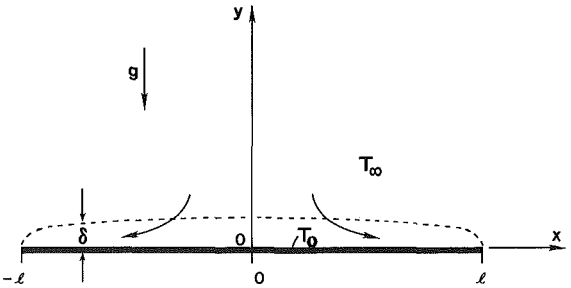

Fig. 1 Schematic of boundary layer flow near a cold plate facing upward in a porous medium

Contributed by the Heat Transfer Division for publication in the JOURNAL OF HEAT TRANSFER. Manuscript received by the Heat Transfer Division November 21, 1983.

In association with the mass continuity equation (1), the boundary layer equations (5, 6) imply two scale equalities

$$\frac{u}{\delta} \sim \frac{Kg\beta\Delta T}{\nu l} \tag{7}$$

$$\frac{u\Delta T}{l} \sim \alpha\frac{\Delta T}{\delta^2} \tag{8}$$

From the above scaling laws we conclude that the unknown boundary layer thickness scale must be

$$\delta \sim l\,\mathrm{Ra}^{-1/3} \tag{9}$$

where Ra is the Darcy-modified Rayleigh number based on the half-length of the plate l

$$\mathrm{Ra} = \frac{Kg\beta l(T_\infty - T_0)}{\alpha\nu} \tag{10}$$

In view of the slenderness condition (4) invoked in the beginning of the scale analysis, the boundary layer thickness scale (9) is valid if

$$\mathrm{Ra}^{1/3} >> 1 \tag{11}$$

The heat transfer rate predicted by the scale analysis is

$$Q_{0-l} \sim kl\frac{\Delta T}{\delta} \tag{12}$$

where Q_{0-l} is the heat transfer rated into the plate, collected from $x = 0$ to $x = l$ (the units of Q_{0-l} are W/m, indicating a heat transfer rate per unit length normal to the plane of Fig. 1). In Nusselt number notation, the heat transfer rate (12) scales as

$$\mathrm{Nu} = \frac{Q_{0-l}}{k\Delta T} \sim \mathrm{Ra}^{1/3} \tag{13}$$

Note that unlike in vertical boundary layer flow, where the Nusselt number scales as the square root of the Rayleigh number based on wall height, in the present problem the Nusselt number scales as the cube root of the Rayleigh number. The Nu $\sim$ $\mathrm{Ra}^{1/3}$ scaling represents a relatively effective heat transfer mechanism in a geometric configuration in which the flow would be motionless if the plate were sufficiently long: The effectiveness of the heat transfer mechanism is also a feature of the corresponding finite-plate configuration in pure fluids [6, 7].

In the next two sections, the heat transfer scaling law Nu $\sim$ $\mathrm{Ra}^{1/3}$ is refined and tested based on integral analysis and numerical experiments.

Integral Solution

Integrating the momentum and energy equations (5, 6) across the boundary layer of thickness $\delta(x)$, Fig. 1, and invoking the boundary conditions

$$v = 0 \text{ and } T = T_0 \text{ at } y = 0$$

$$u = 0,\ T = T_\infty, \text{ and } \frac{\partial T}{\partial y} = 0 \text{ at } y > \delta \tag{14}$$

we obtain

$$(u)_{y=0} = \frac{Kg\beta}{\nu}\frac{d}{dx}\int_0^\delta (T - T_\infty)\,dy \tag{15}$$

$$\frac{d}{dx}\int_0^\delta u(T - T_\infty)\,dy = -\alpha\left(\frac{\partial T}{\partial y}\right)_{y=0} \tag{16}$$

The scale analysis reported in the preceding section recommends the following dimensionless variables

$$\xi = \frac{x}{l} \tag{17}$$

$$\eta = \frac{y}{\delta(x)} \tag{18}$$

$$\Delta(\xi) = \frac{\delta(x)}{l\mathrm{Ra}^{-1/3}} \tag{19}$$

$$\theta(\eta) = \frac{T_\infty - T}{T_\infty - T_0} \tag{20}$$

$$F(\xi, \eta) = \frac{u}{\dfrac{Kg\beta\Delta T}{\nu}\mathrm{Ra}^{-1/3}} \tag{21}$$

Noting the boundary conditions that must be satisfied by the dimensionless temperature profile

$$\theta(0) = 1,\ \theta(1) = 0,\ \theta'(1) = 0 \tag{22}$$

the longitudinal velocity distribution $F(\xi, \eta)$ may be taken as the product

Nomenclature

A, B, C = numerical constants, equations (26)
F = dimensionless longitudinal velocity, equation (21)
F_0 = dimensionless longitudinal velocity along the plate, equation (23)
g = gravitational acceleration
K = permeability
l = half-length of cold plate, Fig. 1
L = length of large square domain, Fig. 3
Nu = Nusselt number, equation (13)
P_0 = pressure along the upper surface of the plate
P_∞ = pressure far from the plate
Q_{0-l} = heat transfer rate into the cold plate, integrated from $x=0$ to $x=l$
Ra = Darcy-modified Rayleigh number, equation (10)
T = temperature
T_0 = plate temperature
T_∞ = porous medium temperature
ΔT = temperature difference, $T_\infty - T_0$
u = longitudinal velocity
v = transverse velocity
x = longitudinal position
y = transverse position
α = thermal diffusivity of fluid-saturated porous medium
β = coefficient of thermal expansion
δ = boundary layer thickness
Δ = dimensionless boundary layer thickness, equation (19)
η = dimensionless transverse position, equation (18)
ρ = density
θ = dimensionless temperature profile, equation (20)
ν = kinematic viscosity
ξ = dimensionless longitudinal position, equation (17)
ψ = streamfunction, equation (43)
$(\hat{\ })$ = dimensionless variables of numerical solutions, equations (44)

$$F(\xi, \eta) = F_0(\xi)\theta(\eta) \tag{23}$$

so that F_0 represents the dimensionless longitudinal velocity along the plate (at $\eta = 0$). Substituting the new variables (17)-(21), (23) into the momentum and energy integrals (15, 16) yields

$$-F_0 = A\frac{d\Delta}{d\xi} \tag{24}$$

$$B\frac{d}{d\xi}(F_0\Delta) = \frac{C}{\Delta} \tag{25}$$

where A, B, C are three numerical coefficients that depend solely on the function θ chosen to represent the temperature and velocity profiles across the boundary layer, equations (20, 23),

$$A = \int_0^1 \theta d\eta; \quad B = \int_0^1 \theta^2 d\eta; \quad C = -\theta'(0) \tag{26}$$

Eliminating F_0 between equations (24) and (25) yields a single equation for the dimensionless boundary layer thickness Δ

$$\Delta\frac{d^2\Delta^2}{d\xi^2} = -\frac{2C}{AB} \tag{27}$$

Separation of variables in equation (27) is achieved using the auxiliary function $p = d\Delta^2/d\xi$; integrating once and invoking the symmetry condition $u = 0$ at $x = 0$, or

$$\frac{d\Delta}{d\xi} = 0 \text{ at } \xi = 0 \tag{28}$$

we obtain

$$\frac{d\Delta}{d\xi} = -\frac{1}{\Delta}\left[\frac{2C}{AB}(\Delta_0 - \Delta)\right]^{1/2} \tag{29}$$

where the constant Δ_0 is the unknown boundary layer thickness in the middle of the plate, $\Delta_0 = \Delta(0)$. Integrating equation (29) once more, and arguing that the boundary layer is terminated by the sharp edge of the plate

$$\Delta(1) = 0 \tag{30}$$

yields the boundary layer thickness $\Delta(\xi)$ in implicit form

$$\xi = \left(1 + \frac{1}{2}\frac{\Delta}{\Delta_0}\right)\left(1 - \frac{\Delta}{\Delta_0}\right)^{1/2} \tag{31}$$

with constant Δ_0 dependent on the choice of temperature and velocity profile

$$\Delta_0 = \left(\frac{9C}{8AB}\right)^{1/3} \tag{32}$$

The boundary layer thickness (31) has been plotted in Fig. 2. It is worth noting that the vanishing of the boundary layer region at the edge of the plate, equation (30), does not mean that the flowrate longitudinally through the boundary layer becomes zero at the edge. The longitudinal flowrate can be found by integrating u across the boundary layer

$$\int_0^{\delta(x)} u\,dy = (A\Delta_0)^2\left[-\frac{\Delta}{\Delta_0}\frac{d(\Delta/\Delta_0)}{d\xi}\right] \tag{33}$$

and, as shown in Fig. 2, the term in the square brackets is finite at the edge of the plate.

The heat transfer rate predicted by the above analysis is

$$Q_{0-l} = \int_0^l k\left(\frac{\partial T}{\partial y}\right)_{y=0} dx \tag{34}$$

or, using the Nusselt number definition (13),

$$\frac{\mathrm{Nu}}{\mathrm{Ra}^{1/3}} = C\int_0^1 \frac{d\xi}{\Delta}, \text{ const} \tag{35}$$

where $\Delta(\xi)$ is given by equation (31). The right-hand side of equation (35) is the numerical factor of order O(1) that was anticipated, but could not be numerically determined, by the scale analysis presented earlier, equation (13).

Table 1 The Nu(Ra) function recommended by three integral solutions

function $\theta(\eta)$, eqs. (20, 23)	$\mathrm{Nu}/\mathrm{Ra}^{1/3}$				
	$\epsilon=0$	0.05	0.1	0.15	0.20
$1 - \eta$	0.794	0.774	0.754	0.734	0.714
$(1 - \eta)^2$	0.928	0.905	0.882	0.858	0.835
$1 - \sin(\frac{\pi}{2}\eta)$	0.848	0.827	0.806	0.785	0.763

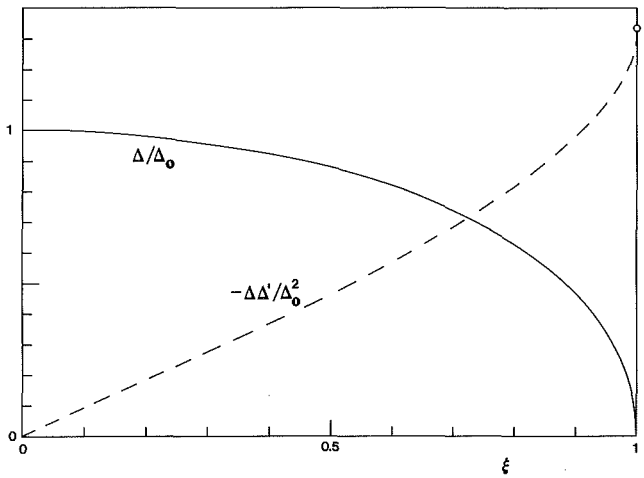

Fig. 2 Integral solution for boundary layer thickness and total longitudinal flowrate

Table 1 shows that the numerical factor in the $\mathrm{Nu} \sim \mathrm{Ra}^{1/3}$ proportionality is relatively insensitive to the choice of temperature and velocity profile shape (see, for example, the numerical values listed under $\epsilon = 0$). The same numerical factor is relatively insensitive to the boundary condition imposed at the edge of the plate. To illustrate this last feature, we replaced equation (30) with the more general condition that the boundary layer thickness at the edge of the plate is finite and equal to a certain percentage of the boundary layer thickness in the middle of the plate

$$\Delta(1) = \epsilon\Delta_0 \tag{36}$$

Repeating the analysis that follows equation (30), in place of equations (32) and (35) we obtain

$$\Delta_0 = \left(\frac{9C}{8AB}\right)^{1/3}\left[(1-\epsilon)\left(1 + \frac{\epsilon}{2}\right)^2\right]^{-1/3} \tag{37}$$

$$\frac{\mathrm{Nu}}{\mathrm{Ra}^{1/3}} = [2ABC\,\Delta_0(1-\epsilon)]^{1/2} \tag{38}$$

Table 1 shows the values of the numerical coefficient $\mathrm{Nu}/\mathrm{Ra}^{1/3}$ for ϵ values ranging from 0 to 20 percent. It is evident that the heat transfer result $\mathrm{Nu}/\mathrm{Ra}^{1/3}$ depends only weakly on ϵ, hence $\epsilon = 0$ [equation (30)] is both reasonable and concise as a boundary condition for the $x = l$ end of the plate.

Using equation (30) as end condition is consistent also with the physical argument that at the edge of the plate the horizontal boundary layer must attain a pressure equal to that of the infinite porous medium at the same level, P_∞. By integrating the vertical Darcy flow equation across the boun-

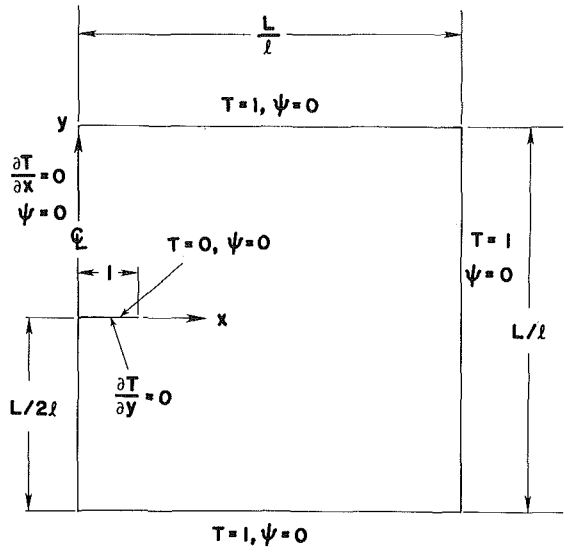

Fig. 3 Square domain used for numerical solutions

dary layer, we obtain the pressure distribution along the upper surface of the plate

$$P_0 = P_\infty + \rho g \beta \int_0^\delta (T - T_\infty)\, dy \tag{39}$$

In the dimensionless notation chosen for the integral solution, the pressure distribution (39) is rewritten as

$$P_0 = P_\infty + \rho g \beta (T_0 - T_\infty)\, l \mathrm{Ra}^{-1/3} A \Delta(\xi) \tag{40}$$

We conclude that, physically, $\Delta(1) = 0$ is the same as stating that the pressure at the end of the boundary layer is the same as the pressure of the fluid-saturated porous reservoir into which the boundary layer flow discharges. One additional note is that the $\Delta(1) = 0$ end condition was invoked also in [7] for pure fluids in the limit of negligible inertia (i.e., large Prandtl numbers).

Numerical Solutions

Relative to the boundary layer analyses discussed so far, whose solutions depended on only one dimensionless parameter, Ra, the finite-difference simulation of the flow is considerably more complicated. This time, since the flow must be calculated in a finite domain (Fig. 3) and only at a finite number of points (nodes), the calculated flow depends on two additional parameters, namely, the relative size of the medium surrounding the horizontal plate (L/l, Fig. 3) and the total number of grid points employed. In developing the numerical solutions described below, special care was taken for these two additional parameters to be large enough so that the resulting heat and fluid flow picture was influenced by Ra only.

The finite-difference formulation started with placing the governing equations (1)–(3) in the dimensionless streamfunction form

$$\frac{\partial^2 \hat{\psi}}{\partial \hat{x}^2} + \frac{\partial^2 \hat{\psi}}{\partial \hat{y}^2} = -\mathrm{Ra} \frac{\partial \hat{T}}{\partial \hat{x}} \tag{41}$$

$$\frac{\partial(\hat{T}, \hat{\psi})}{\partial(\hat{x}, \hat{y})} = \frac{\partial^2 \hat{T}}{\partial \hat{x}^2} + \frac{\partial^2 \hat{T}}{\partial \hat{y}^2} \tag{42}$$

by first defining the streamfunction $\psi(x, y)$

$$u = \frac{\partial \psi}{\partial y}, \quad v = -\frac{\partial \psi}{\partial x} \tag{43}$$

and the dimensionless variables

$$\hat{\psi} = \frac{\psi}{\alpha}, \quad \hat{T} = \frac{T - T_0}{T_\infty - T_0}, \quad (\hat{x}, \hat{y}) = \frac{(x, y)}{l} \tag{44}$$

The Rayleigh number Ra is based on plate half-length, and is given by equation (10).

Equations (41, 42) were solved in the square domain shown in Fig. 3, and were subjected to the boundary conditions sketched on the figure. The square domain is meant to play the role of an infinite porous medium surrounding the horizontal plate. Due to the symmetry about $x = 0$ of the plate geometry, the square domain of length L contains only the right half of the plate sketched in Fig. 1. The four sides of the square domain are all assumed to be impermeable. The plane of symmetry, $x = 0$, is taken as adiabatic, while the remaining L-long walls are assumed isothermal (their temperature is equal to T_∞, which is the infinite reservoir temperature in boundary layer analysis). The horizontal plate is located at midheight in the square domain; its upper side is isothermal (at T_0), while its lower side is adiabatic (this last feature was adopted in order to remove the possibility of downward plume flow driven by a cold surface facing downward; this different phenomenon was dealt with in [2–4]).

In order to control the cost of numerical computations, the square domain was covered with a nonuniform grid placing more points in the regions where steep velocity and temperature gradients are expected. The domain was covered with a network of vertical and horizontal lines whose density was four times higher in the region immediately above the plate and in the plate tip region (i.e., on both sides of the $x = l$ plane).

The numerical scheme consisted of upwind finite-difference approximations [9] for the convection terms in the energy equation (42). The remaining terms in equations (41) and (42) were approximated by centered finite differences. The streamfunction equation (41) was solved by successive overrelaxation. For Ra > 500, the temperature $\hat{T}$ was underrelaxed at each iteration: The underrelaxation factor 0.6 was used for this purpose. The convergence was determined by monitoring the solution for the temperature field. The convergence criterion was

$$\frac{\mathrm{Max} \left| \hat{T}_{ij}^{k+1} - \hat{T}_{ij}^{k} \right|}{\mathrm{Max} \left| \hat{T}_{ij}^{k+1} \right|} \leq \mathrm{Res} \tag{45}$$

where superscript k indicates the iteration order. The residue $\mathrm{Res} = 10^{-4}$ was found to be sufficiently small to guarantee convergence.

The overall accuracy of the numerical solution was determined by observing the dependence of Q_{0-l} on the number of grid points and on the size of the square domain. In terms of the dimensionless variables of the numerical solution, equations (44), the overall Nusselt number defined in equation (13) assumes the form

$$\mathrm{Nu} = \int_0^1 \left(\frac{\partial \hat{T}}{\partial \hat{y}} \right)_{\hat{y}=0} d\hat{x} \tag{46}$$

Figure 4 shows the effect of the number of horizontal plate nodes on the overall heat transfer rate (the relationship between Nu and the total number of grids points in the square domain is reported in Table 2). In Fig. 4, the dependence between Nu and the number of plate nodes is not smooth because in some cases the number of plate nodes was increased by adding nodes only near the plate-tip region (which contributes the most to Q_{0-l}). In view of the test shown in Fig. 4, for the simulations reported later in this section we used a grid with 18 nodes on the horizontal plate, and with a total of nodes varying from 63 × 56 to 100 × 100 for the entire square domain (Table 2).

Figure 5 shows the effect of square domain size L/l on the overall heat transfer rate. At the highest Rayleigh number considered in the numerical part of this study, Ra = 700, acceptable accuracy was achieved when the square domain

Table 2 Summary of numerical results

Ra	Total Number of Grid Points	Number of Grid Points on the Horizontal Plate	L/ℓ	Nu	Figure Number in this paper
	54 x 56	9		5.16	
	58 x 56	13		5.14	
700	63 x 56	18	5	5.29	Fig. 4
	67 x 56	22		5.27	
	73 x 56	28		5.26	
	38 x 35		3	4.89	
	63 x 56		5	5.29	
700	80 x 70	18	7	5.40	Fig. 5
	100 x 100		9.4	5.66	
	104 x 116		14	5.75	
100	63 x 56			3.01	
200	63 x 56			3.81	
300	63 x 56	18	9.4	4.41	Fig. 7
400	63 x 56			4.86	
500	80 x 80			5.06	
600	100 x 100			5.36	
700	100 x 100			5.66	Fig. 6a,b,c

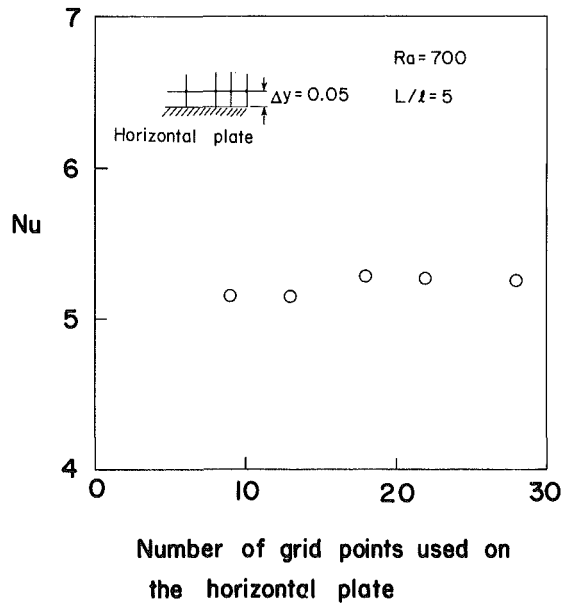

Fig. 4 The dependence between the overall Nusselt number and the total number of nodes used on the plate

was roughly ten times longer than the plate half-length (L/l = 9.4, Table 2).

Representative patterns of streamlines and isotherms are shown in Figs. 6(a, b) for Ra = 700. The upper side of the half-plate is covered by a very clear thermal boundary layer, surrounded from above and from the right by practically isothermal fluid whose temperature is more closely given by $\hat{T} \cong 0.8$ than by the $\hat{T} = 1$ imposed on the impermeable frontier of the large square domain. The boundary layer is chopped off by the edge of the plate, and the stream sinks below $y = 0$ as a nearly vertical cold plume. Velocities are highest in the boundary layer region, especially near the tip. The square domain houses two relatively slow cells that result from the

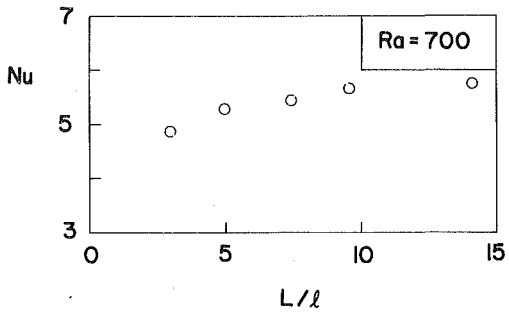

Fig. 5 The effect of domain size on the overall heat transfer rate to the plate

splitting of the cold plume as it hits the bottom frontier. The cell residing under the half-plate is driven by the cold plume from the side and by the hot frontier from below. The larger, counterclockwise, cell is driven by the cold plume and by the bottom and right frontiers of the square domain.

Details of the horizontal and vertical velocity component distributions near the horizontal plate are shown in Fig. 6(c). It is clear that at high Rayleigh numbers the horizontal flow occupies a slender wall region in which the scale of $\hat{v}$ is consistently smaller than the scale of $\hat{u}$, regardless of the position along the plate $\hat{x}$.

The patterns of Figs. 6(a, b) are useful in explaining the Nu(Ra) relationship revealed by numerical simulations in the Ra range 100–700: This relationship is reported in Table 2 and in Fig. 7, which show that the numerical data obey extremely closely (within 1.5 percent) the power law

$$\mathrm{Nu} = 0.65\ \mathrm{Ra}^{1/3} \tag{47}$$

This result confirms strongly the conclusion of scale analysis, equation (13); as shown below, equation (47) validates also the numerical factor $\mathrm{Nu}/\mathrm{Ra}^{1/3}$ predicted by the integral solutions summarized in Table 1.

At first glance, the numerical results (47) fall roughly 25 percent below the results produced by the integral method (Table 1). This, however, is not a sign that the integral solutions are only accurate within 25 percent; actually, the Nu value predicted by any numerical simulation in a finite domain as ours (Fig. 3) *must* always be lower than the Nu values predicted by integral boundary layer analysis (Fig. 1). Relative to the heat transfer part of the problem, an important difference between Fig. 1 and Fig. 3 is that in Fig. 1, ΔT is the temperature difference between the frontier of the large (but finite) square domain and the plate. In all the numerical simulations the "outer fluid" is slightly colder than the periphery of the large domain; hence, the heat transfer is lower than in the case when the outer fluid temperature would equal T_∞. Said another way, in a numerical experiment the overall heat transfer rate from the domain frontier (T_∞) to the plate (T_0) must overcome *two* thermal resistances, first the one associated with the boundary layers lining the periphery of the square domain, and second, the thermal resistance due to the horizontal layer formed along the plate.

In order to compare equation (47) with Table 1 properly, we make the observation that in a numerical simulation such as the one shown in Fig. 6 the (outer fluid)-(plate) temperature difference is about 0.8 ΔT, where ΔT is the (outer fluid)-(plate) temperature difference on which Table 1 is based. Therefore, if the outer fluid temperature in Fig. 6 is to match T_∞ used in the integral analysis, the temperature difference between the periphery of the square domain and the plate in Fig. 3 must be approximately equal to 1.25 ΔT. Thus, replacing ΔT with 1.25 ΔT in the definitions of Nu and Ra in equation (47), we obtain

$$\frac{Nu}{\mathrm{Ra}^{1/3}} \approx (0.65)(1.25)^{4/3} = 0.88 \tag{48}$$

Equation (48), in which Nu and Ra are now based on the same ΔT as in Table 1, is in good agreement with the last two (more refined) entries under $\epsilon = 0$ in Table 1. In other words, the numerical heat transfer results of Fig. 7 and Table 2 support quantitatively the predictions made based on integral analysis.

Concluding Remarks

In this paper we showed that the phenomenon of natural convection driven in a porous medium by a cold plate facing upward or by a warm plate facing downward consists of a boundary layer flow terminated by the sharp edges of the plate (Figs. 1, 2). The length, velocity and heat transfer scales of the boundary layer flow were determined based on scale analysis and integral (Karman-Pohlhausen) analysis. The boundary layer character of the flow and the heat transfer effected by its were confirmed based on numerical simulations in a finite-size domain sufficiently larger than the horizontal plate. The heat transfer rate between the porous medium and the plate is adequately represented by the last two values listed under $\epsilon = 0$ in Table 1.

One final observation concerns the choice of a finite size system, Fig. 3, to simulate natural convection around a small plate buried in an infinite porous medium. The closed box model adopted in the present study is only one of the many ways in which the phenomenon could be studied numerically. For example, another way would be to adopt a through-flow model, that is, a large system for which through-flow conditions are specified around the periphery. With reference to the rectangular domain sketched in Fig. 3, one could specify vertical flow through the top and bottom boundaries, and no flow through the left boundary. However, considerable care must be taken in specifying a flow condition such as "no flow" along the right boundary, because the goodness of this condition depends on how small the plate is relative to the lateral extent of the control volume. If the control volume is not large enough, then the no flow condition imposed along the right boundary would interfere with the natural tendency of the plate region to entrain fluid radially, as illustrated in Fig. 6(*a*) and in plots showing natural convection around concentrated heat sources in porous media (e.g., [10–12]).

If the size of the system is not large enough, then the through-flow model is as inadequate as the closed-box model employed in the present study; the only way to improve the performance of both models is to increase the size ratio L/l. This is why—while adopting the closed-box model—we performed and stressed the sensitivity test reported in Fig. 5. In addition to that test we have strong indicators that L/l values of order 10 are large enough to yield numerical results that compliment the theoretical part of this study. Some of these indicators are discussed below.

First, although the motion is always driven by the differential heating between the horizontal plate and the boundary of the large box, the larger the L/l value the more

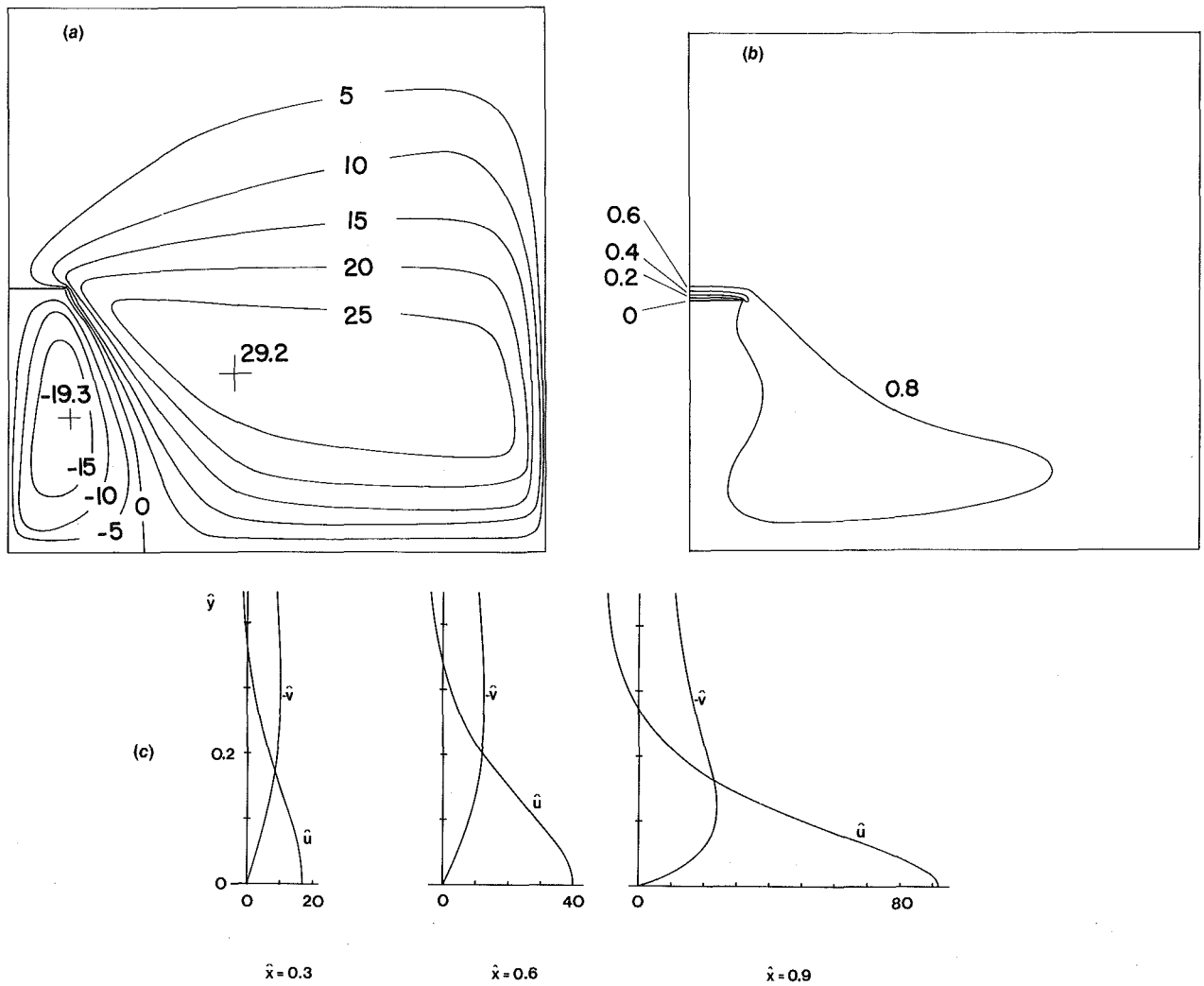

Fig. 6 Numerical solution for Ra = 700; (*a*) streamlines (the numbers indicate the value of $\hat{\psi}$); (*b*) isotherms (the numbers indicate the value of $\hat{T}$); (*c*) velocity profiles at x/l = 0.3, 0.6, and 0.9

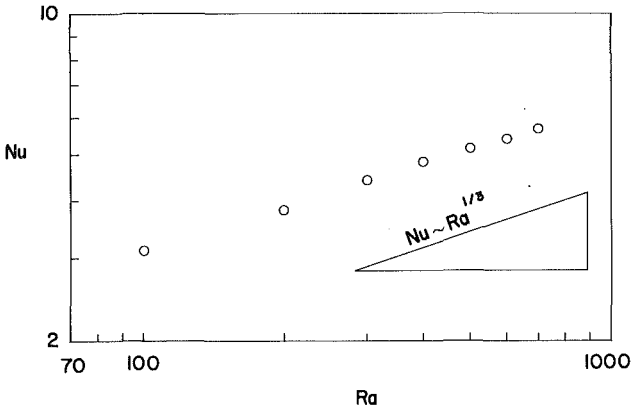

Fig. 7 Numerical results showing the effect of Ra on Nu

the fluid inventory of the box is in thermal equilibrium with the box boundary (i.e., in the large L/l limit, the thermal resistance that dominates the plate-box heat transfer is the plate–fluid resistance, not the fluid–box boundary resistance). Figure 6(*b*) shows that the fluid in the large square domain is almost isothermal and at a temperature much closer to the box boundary temperature than to the plate temperature. This means that when L/l is about 10, the closed-box model comes sufficiently close to simulating convection about a horizontal plate in an infinite porous medium.

Second, one may argue that in the case when the closed box is not large enough the vertical side wall of the box plays the role of "driving wall" and the heat transfer along the horizontal plate is influenced by forced convection. But in forced convection the Nusselt number for the horizontal plate scales as the square root of the Peclet number (see [8], pp. 355–360). Indeed, the $Nu \sim Ra^{1/3}$ scaling revealed by numerical Nu calculations (Fig. 7) is the ultimate proof that the plate-box overall heat transfer is dominated by natural convection, i.e., proof that the square domain chosen for numerical simulations is "large enough."

Acknowledgments

This work was supported in part by the National Science Foundation through Grant No. MEA-82-07779.

References

1 Cheng, P., "Heat Transfer in Geothermal Systems," *Advances in Heat Transfer*, Vol. 14, 1978, pp. 1–105.

2 Cheng, P., and Chang, I-Dee, "Buoyancy Induced Flows in a Saturated Porous Medium Adjacent to Impermeable Horizontal Surfaces," *Int. J. Heat Mass Transfer*, Vol. 19, 1976, pp. 1267–1272.

3 Cheng, P., "Similarity Solutions for Mixed Convection From Horizontal Impermeable Surfaces in Saturated Porous Media," *Int. J. Heat Mass Transfer*, Vol. 20, 1977, pp. 893–898.

4 Cheng, P., "Convective Heat Transfer in Porous Layers by Integral Methods," *Lett. Heat Mass Transfer*, Vol. 5, 1978, pp. 243–252.

5 Pop, I., and Cheng, P., "The Growth of a Thermal Layer in a Porous Medium Adjacent to a Suddenly Heated Semi-infinite Horizontal Surface," *Int. J. Heat Mass Transfer*, Vol. 26, 1983, pp. 1574–1576.

6 Suriano, F. J., and Yang, K. T., "Laminar Free Convection About Vertical and Horizontal Plates at Small and Moderate Grashof Numbers," *Int. J. Heat Mass Transfer*, Vol. 11, 1968, pp. 473–490.

7 Clifton, J. V., and Chapman, A. J., "Natural-Convection on a Finite-Size Horizontal Plate," *Int. J. Heat Mass Transfer*, Vol. 12, 1969, pp. 1573–1584.

8 Bejan, A., *Convection Heat Transfer*, Wiley, New York, 1984, pp. 17–21.

9 Gossman, A., Pun, W. M., Runchal, A. K., Spalding, D. B., and Wolfshtein, M., *Heat and Mass Transfer in Recirculating Flows*, Academic Press, New York, 1969.

10 Bejan, A., "Natural Convection in an Infinite Porous Medium With a Concentrated Heat Source," *J. Fluid Mechanics*, Vol. 89, 1978, pp. 97–107.

11 Hickox, C. E., and Watts, H. A., "Steady Thermal Convection From a Concentrated Source in a Porous Medium," ASME JOURNAL OF HEAT TRANSFER, Vol. 102, 1980, pp. 248–253.

12 Hickox, C. E., "Thermal Convection at Low Rayleigh Number From Concentrated Sources in Porous Media," ASME JOURNAL OF HEAT TRANSFER, Vol. 103, 1981, pp. 232–236.

On the Oscillatory Instability of Closed-Loop Thermosyphons

K. Chen
Department of Mechanical and Industrial Engineering, University of Utah, Salt Lake City, UT 84112
Assoc. Mem. ASME

The stability of natural convection flows in single-phase closed-loop thermosyphons is investigated. The thermosyphons considered in the present analysis are fluid-filled tubes bent into rectangular shapes. The fluid is heated over the lower horizontal segment and cooled over the upper horizontal segment. Analytical and numerical solutions are presented for a range of loop aspect ratios and radii for both laminar and turbulent flows. It is found that the steady-state results for thermosyphons with different aspect ratios and radii can be expressed in terms of a single dimensionless parameter. When this parameter is less than a critical value, the flow is always stable. Above this critical point, oscillatory instability exists for a narrow range of a friction parameter. The calculated neutral stability conditions show that the flow is least stable when the aspect ratio of the loop approaches unity. The frequency of the convection-induced oscillation is slightly higher than the angular frequency of a fluid particle traveling along the loop.

1 Introduction

The problem of heat transfer and stability for flow in natural convection loops (thermosyphons) has stimulated considerable interest in the past due to its important applications in oceanic and geophysical phenomena as well as in such practical engineering systems as nuclear reactors and solar heaters. Keller [1] and Welander [2] considered a simple rectangular thermosyphon consisting of two insulated vertical branches with point heat source and sink at the center of the lower and upper horizontal segments respectively. It was pointed out in these pioneering works that, when a certain parameter which physically represents the ratio of the buoyancy force to the frictional forces exceeds a critical value, an oscillatory motion in the fluid may occur. Such oscillatory instability was also found, experimentally and theoretically, for flow in toroidal thermosyphons by Creveling et al. [3] and Damerell and Schoenhals [4]. Studies of the stability behavior of circular loops have also been carried out by Greif, Zvirin, and Mertol [5–6] and by Kaizerman, Wacholder, and Elias [7]. Bau and Torrance [8] investigated the stability of an open convection loop. Zvirin et al. [9] studied the stability characteristics of the thermosyphonic solar water heater and showed that this system can become unstable at high energy utilizations. The transient behavior of natural convection systems has also been investigated numerically and experimentally by some of the investigators mentioned above and other investigators [10–11]. In most of the previous investigations on the stability of natural convection in closed loops, the influence of loop geometry receives little attention. From the practical viewpoint, the loop configuration is one of the few alterable factors in thermosyphon design. A detailed study of this factor is desirable for better understanding of the operational and safety problems caused by the periodic instability in natural convection loops.

The present work is a theoretical investigation of the stability of natural convection loops with different aspect ratios and radii. The system considered is comprised of two insulated vertical branches with two horizontal connections immersed into the constant temperature heat source and sink, as shown in Fig. 1. These two horizontal connections may not be straight but can be bent into any other shape as long as the friction factor and heat transfer coefficient within the loop will not be significantly affected.

The analysis is based on a one-dimensional approach. All the fluid properties, except for the density in the buoyancy term, are assumed to be constant. With these assumptions the steady volume flow rate is uniform along the loop. Although in an actual thermosyphon the flow may be three dimensional, analytical results of one-dimensional stability analysis compared favorably with experiments [3, 4, 8]. It has been found in a previous paper reported by the author [12] that the steady-state solutions for this problem can be expressed in terms of a single parameter which combines the influences of loop diameter and geometry. When the distance between the heat source and sink is fixed, there exists an optimum value of this parameter for maximum heat transfer rate. In the present stability analysis for natural convection loops, no instability exists when this parameter is less than a critical value for both laminar and turbulent flows, indicating that the flow becomes unstable only when the buoyancy force dominates. Since the computed critical value of this parameter is found to be far above the optimum value for maximum heat transfer rate, the results obtained from the present study make it possible to design a thermosyphon that can operate safely and efficiently.

2 Analysis

The closed-loop thermosyphon to be analyzed is shown in

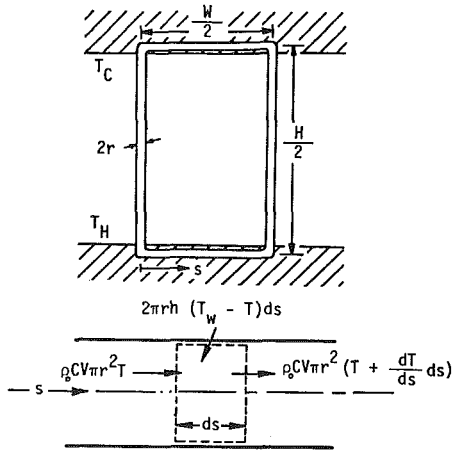

Fig. 1 Rectangular natural convection loop

Contributed by the Heat Transfer Division for publication in the JOURNAL OF HEAT TRANSFER. Manuscript received by the Heat Transfer Division October 6, 1983. Paper No. 83-WA/HT-93.

Fig. 1. This thermosyphon is made of two vertical pipes of equal diameter and length joined together at the top and bottom by two horizontal pipes. Heat is received from a constant-temperature heat source over the bottom horizontal pipe and rejected to a constant-temperature heat sink over the top horizontal pipe.

Assuming the Boussinesq approximation is valid, the continuity equation and the equation of motion for a one-dimensional flow in the loop can be written as

$$\frac{\partial V}{\partial s}=0 \tag{1}$$

$$\rho_0 \pi r^2 \frac{\partial}{\partial t}\oint V ds = -\pi r^2 \oint dP - g\pi r^2 \oint \rho \cos\phi ds - 2\pi r \oint \tau_w ds \tag{2}$$

The energy equation for the circulating fluid, with the axial conduction and viscous dissipation neglected, is

$$\rho_0 C \pi r^2 \left(\frac{\partial}{\partial t}+V\frac{\partial}{\partial s}\right)T = 2\pi r h (T_w - T) \tag{3}$$

To simplify the analysis, the two vertical branches are assumed to be thermally insulated. The relation between ρ and T is assumed to be linear. The wall shear stress τ_w and the heat transfer coefficient h are related to the mean velocity through the following relationships

$$\tau_w = \frac{1}{8}\rho_0 V^2 f \tag{4}$$

and

$$h = m\frac{\kappa}{2r}(2\mathrm{Re}_r)^n \tag{5}$$

where f is the friction factor and usually can be correlated by

$$f = \frac{a}{\mathrm{Re}_r^b} \tag{6}$$

Re_r in equations (5) and (6) is the Reynolds number based on the pipe radius. a, b, m, and n are empirical constants.

In accordance with the above assumptions, the governing equations for this problem reduce to

$$\rho_0 \pi r^2 \frac{d}{dt} V \oint ds = \rho_0 g \beta \pi r^2 \left[\int_{\frac{W}{2}}^{\frac{W+H}{2}} T ds - \int_{\frac{H}{2}+W}^{H+W} T ds\right] - 2\pi r \cdot \frac{\rho_0}{8} V^2 (a\nu^b V^{-b} r^{-b})(H+W) \tag{7}$$

$$\rho_0 C \pi r^2 \left(\frac{\partial}{\partial t}+V\frac{\partial}{\partial s}\right)T = 2\pi r \left[\frac{m\kappa}{2r}\left(\frac{2Vr}{\nu}\right)^n\right](T_w - T) \tag{8}$$

For convenience, dimensionless quantities are now defined

$$s^\circ = \frac{s}{W} \tag{9}$$

$$\theta^\circ = \frac{T - \frac{(T_H+T_C)}{2}}{T_H - T_C} \tag{10}$$

$$V^\circ = \frac{V}{V_{\mathrm{ref}}} = \frac{V}{\left(\frac{mW\kappa}{\rho_0 C r \nu}\right)^{\frac{1}{1-n}}\left(\frac{\nu}{2r}\right)} \tag{11}$$

$$t^\circ = \frac{t V_{\mathrm{ref}}(1+A)}{W} \tag{12}$$

$$\mathrm{G}_m = \frac{4g\beta(T_H - T_C) r^{1+b} {V_{\mathrm{ref}}}^{b-2}}{a\nu^b (1+A)} \tag{13}$$

$$F = \frac{aW\nu^b}{r^{1+b}{V_{\mathrm{ref}}}^b (1+A)} \tag{14}$$

where A is the aspect ratio of the loop

$$A = \frac{W}{H} \tag{15}$$

In terms of these dimensionless variables, the momentum equation (7) and energy equation (8) become

$$\frac{4}{F\mathrm{G}_m}\left(\frac{\partial}{\partial t^\circ}+\frac{1}{1+A}V^\circ\frac{\partial}{\partial s^\circ}\right)V^\circ = A\left(\int_{\frac{1}{2}}^{\frac{1}{2}+\frac{1}{2A}} \theta^\circ ds^\circ - \int_{\frac{1}{2A}+1}^{1+\frac{1}{A}} \theta^\circ ds^\circ\right) - \frac{1}{\mathrm{G}_m} V^{\circ 2-b} \tag{16}$$

$$\left[(1+A)\frac{\partial}{\partial t^\circ}+V^\circ\frac{\partial}{\partial s^\circ}\right]\theta^\circ = 2V^{\circ n}(\theta_w^\circ - \theta^\circ) \tag{17}$$

The mean velocity and temperature are decomposed into a steady solution (denoted by an upper bar) and a small disturbance (denoted by a prime) as follows

$$V^\circ(t^\circ) = \bar{V}^\circ + V^{\circ\prime}(t^\circ) = \bar{V}^\circ + \tilde{V}^\circ e^{K^\circ t^\circ} \tag{18}$$

Nomenclature

A = aspect ratio = W/H
a, b = coefficient and exponent in the expression for the friction coefficient, equation (6)
C = specific heat
C_i = dummy variables
F = friction parameter, equation (14)
f = friction coefficient = a/Re_r^b
G_m = modified Grashof number, equation (13)
g = gravitational acceleration
H = twice the height of thermosyphon (Fig. 1)
h = heat transfer coefficient
K = complex time factor
m, n = coefficient and exponent in the expression for heat transfer coefficient, equation (5)
p = pressure
Re_r = Reynolds number = Vr/ν
r = radius of flow channel (Fig. 1)
s = coordinate along the loop
T = temperature
ΔT = temperature difference across heat source and sink = $T_H - T_C$
t = time
V = mean fluid velocity
V_{ref} = reference velocity, equation (11)
W = twice the width of thermosyphon (Fig. 1)
β = thermal expansion coefficient
γ = dummy variable
θ = dimensionless temperature scaled by ΔT
κ = thermal conductivity
ν = kinematic viscosity
ρ = density
ρ_0 = reference density
τ_w = wall shear stress
ϕ = angle between the tube and the vertical
ω = angular frequency

Subscripts

C = heat sink conditions
H = heat source conditions

Superscripts

$^\circ$ = dimensionless quantities based on length W
$\bar{}$ = steady-state solutions
$'$ = perturbed quantities
$\tilde{}$ = spatial variation of the perturbed quantities

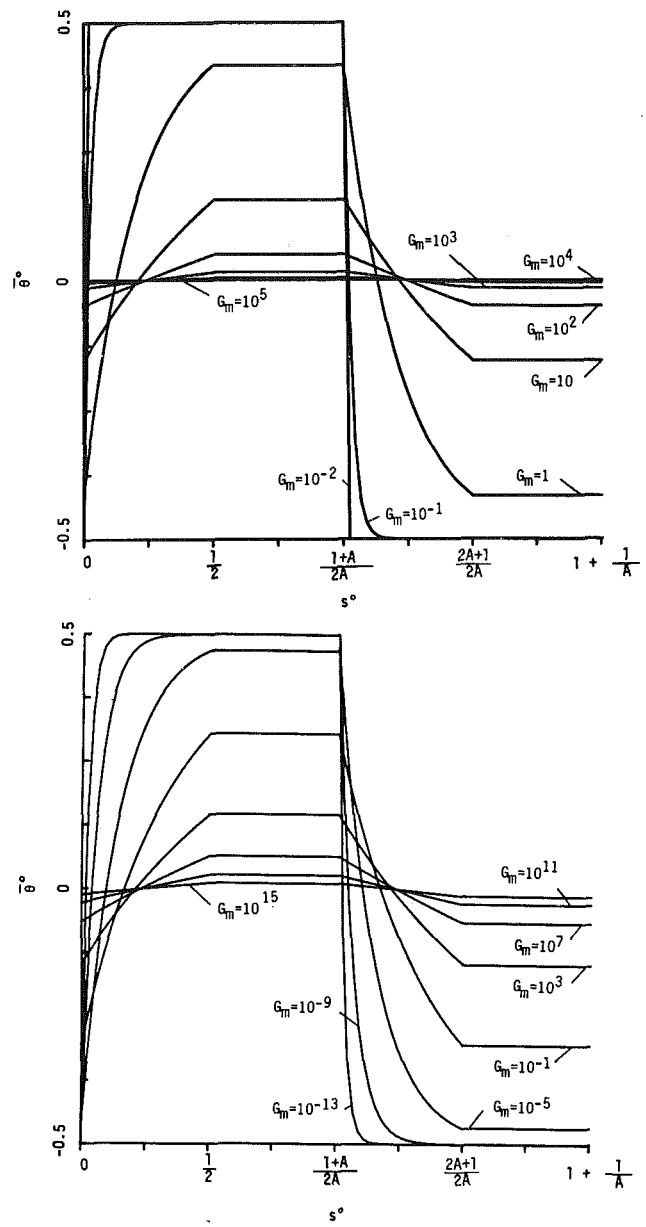

Fig. 2 Steady temperature distribution: (*a*) laminar flow; (*b*) turbulent flow

$$\theta^\circ(s^\circ,t^\circ)=\bar{\theta}^\circ(s^\circ)+\theta^{\circ\prime}(s^\circ,t^\circ)$$
$$=\bar{\theta}^\circ(s^\circ)+\tilde{\theta}^\circ(s^\circ)e^{K^\circ t^\circ} \tag{19}$$

where K° is the dimensionless complex time factor of the disturbances

$$K^\circ=\frac{KW}{V_{\text{ref}}(1+A)} \tag{20}$$

The steady temperature distribution can be solved analytically. The solution is

$$\bar{\theta}^\circ=C_1e^{-2s^\circ/\bar{V}^{\circ 1-n}}+\frac{1}{2} \quad \text{for } s^\circ=0 \text{ to } \frac{1}{2}$$
$$=-C_1e^{-2[s^\circ-(1+A)/2A]/\bar{V}^{\circ 1-n}}-\frac{1}{2} \quad \text{for } s^\circ$$
$$=\frac{1+A}{2A} \text{ to } \frac{1+2A}{2A} \tag{21}$$

where

$$C_1=-\frac{1-e^{-1/\bar{V}^{\circ 1-n}}}{1-e^{-2/\bar{V}^{\circ 1-n}}} \tag{22}$$

The steady-state velocity profile $\bar{V}^\circ$ can be obtained from the following equation

$$\bar{V}^{\circ 2-b}=\frac{C_1G_m}{2}(e^{-1/\bar{V}^{\circ 1-n}}-1) \tag{23}$$

Subtracting the steady-state results from the complete governing equations (16) and (17) yields the disturbance equations

$$\frac{4K^\circ}{FG_m}\tilde{V}^\circ=A\left(\int_{\frac{1}{2}}^{\frac{1}{2}+\frac{1}{2A}}\tilde{\theta}^\circ ds^\circ-\int_{\frac{1}{2A}+1}^{1+\frac{1}{A}}\tilde{\theta}^\circ ds^\circ\right)$$
$$-\frac{(2-b)\tilde{V}^{\circ 1-b}\tilde{V}^\circ}{G_m} \tag{24}$$

$$(1+A)K^\circ\tilde{\theta}^\circ+\bar{V}^\circ\frac{d\tilde{\theta}^\circ}{ds^\circ}=$$

$$\begin{cases} -\tilde{V}^\circ\dfrac{d\tilde{\theta}^\circ}{ds^\circ}+2n\bar{V}^{\circ n-1}\tilde{V}^\circ(\theta_w^\circ-\bar{\theta}^\circ)-2\bar{V}^{\circ n}\tilde{\theta}^\circ \\ \quad \text{for } 0<s^\circ<\dfrac{1}{2} \text{ and } \dfrac{1}{2}+\dfrac{1}{2A}<s^\circ<1+\dfrac{1}{2A} \\ 0 \\ \quad \text{for } \dfrac{1}{2}<s^\circ<\dfrac{1}{2}+\dfrac{1}{2A} \text{ and } \dfrac{1}{2A}+1<s^\circ<1+\dfrac{1}{A} \end{cases} \tag{25}$$

It can be shown mathematically that no real and positive K° can satisfy the disturbance equations above; hence the only unstable solutions in this problem are those which behave in an oscillatory manner. At neutral stability, K° reduces to a pure imaginary number $i\omega^\circ$.

3 Method of Solution

The steady solutions have been solved by this author [12] for both laminar ($b = 1$, $n = 0$) and turbulent ($b = 0$, $n = 0.8$) flows. Since no experimental results are available for rectangular loops, the exponents b and n were chosen to be that for a fully developed forced convection in a circular pipe. The steady temperature distributions shown in Figs. 2(*a*) and 2(*b*) have been presented in [12] with G_m replaced by $1/P^\circ$. Physically, the dimensionless parameter G_m represents the ratio of the buoyancy drive to the friction loss in the loop. The optimum loop configuration for maximum heat transfer rate has been determined [12] to be

$$G_m=2^{\frac{b-n-1}{1-n}} \tag{26}$$

As can be seen from Figs. 2(*a*) and 2(*b*), the change in fluid temperature in the horizontal segments is small for $G_m>>1$, resulting in a lower buoyancy drive. For $G_m<<1$ there is no temperature difference between the fluid and the tube wall in the two horizontal connections except in the very short entrance sections. Both cases should be avoided if maximum heat transfer rate is desired. The heat transfer equations for the limiting cases of $G_m>>1$ and $G_m<<1$ are straight lines when plotted on a semi-log chart. Equation (26) was obtained by equating the heat transfer equations for these two limiting cases. It was found from the calculated heat transfer results than an optimum combination of the buoyancy drive and the temperature difference is obtained when G_m is equal to the optimum value given in equation (26).

With $\bar{\theta}^\circ$ and $\bar{V}^\circ$ determined, the perturbed energy equation can be solved analytically. The results are

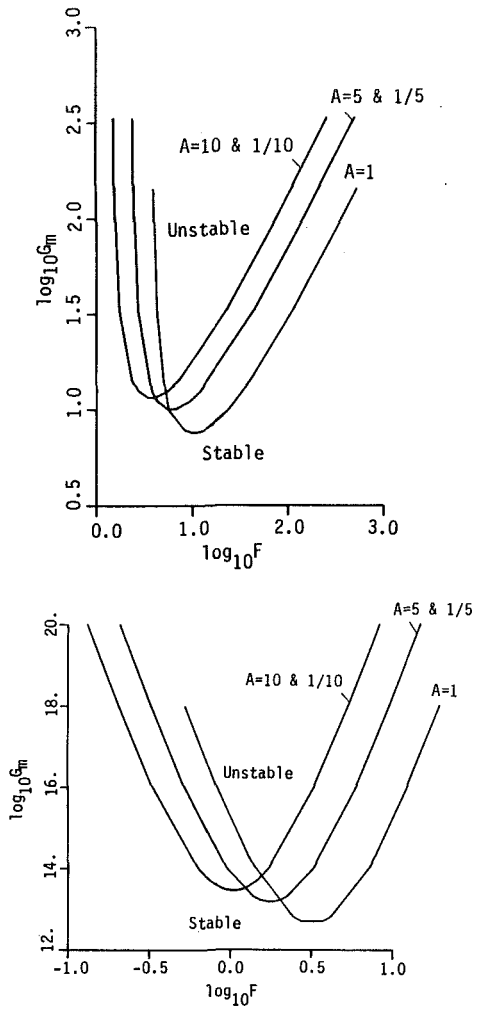

Fig. 3 Neutral stability curves in F, G_m coordinates: (*a*) laminar flow; (*b*) turbulent flow

$$\tilde{\theta}^\circ = C_2 e^{-\gamma s^\circ} + C_3 e^{-2s^\circ/\tilde{V}^{\circ 1-n}} \qquad \text{for } s^\circ = 0 \text{ to } \frac{1}{2}$$

$$= C_4 e^{\frac{-i\omega^\circ(1+A)}{\tilde{V}^\circ}(s^\circ - 0.5)} \qquad \text{for } s^\circ = \frac{1}{2} \text{ to } \frac{1}{2} + \frac{1}{2A} \tag{27}$$

where

$$\gamma = \frac{i\omega^\circ(1+A) + 2\tilde{V}^{\circ n}}{\tilde{V}^\circ} \tag{28}$$

$$C_3 = \frac{2C_1(1-n)\tilde{V}^\circ}{i\tilde{V}^{\circ 1-n}\omega^\circ(1+A)} \tag{29}$$

$$C_2 = C_3\left[\frac{e^{-\left(\frac{\gamma}{2} + \frac{i\omega^\circ(1+A)}{2A\tilde{V}^\circ}\right)} - e^{-\left(\frac{1}{\tilde{V}^{\circ 1-n}} + \frac{i\omega^\circ(1+A)}{2A\tilde{V}^\circ}\right)}}{1 + e^{-\left(\frac{\gamma}{2} + \frac{i\omega^\circ(1+A)}{2A\tilde{V}^\circ}\right)}} - 1\right] \tag{30}$$

$$C_4 = C_2 e^{-\gamma/2} + C_3 e^{-1/\tilde{V}^{\circ 1-n}} \tag{31}$$

Due to the symmetry of the loop, only the perturbed temperature distribution over half of the loop is considered above.

Substitution of the calculated $\tilde{\theta}^\circ$ into the momentum equation yields the following two real algebraic equations

$$\frac{C_5}{G_m}(2-b)\tilde{V}^{\circ 1-b} - \frac{4C_6\omega^\circ}{FG_m} = C_7 \tag{32}$$

$$\frac{4C_5\omega^\circ}{FG_m} + \frac{C_6(2-b)\tilde{V}^{\circ 1-b}}{G_m} = C_8 \tag{33}$$

where

$$C_5 = -e^{1/\tilde{V}^{\circ 1-n}}\tilde{V}^{\circ 1-n}\omega^{\circ 2}(1+A)^2\cos[C_9\omega^\circ(1+A)] - \tilde{V}^{\circ 1-n}\omega^{\circ 2}(1+A)^2\cos[C_{10}\omega^\circ(1+A)] \tag{34}$$

$$C_6 = -e^{1/\tilde{V}^{\circ 1-n}}\tilde{V}^{\circ 1-n}\omega^{\circ 2}(1+A)^2\sin[C_9\omega^\circ(1+A)] + \tilde{V}^{\circ 1-n}\omega^{\circ 2}(1+A)^2\sin[C_{10}\omega^\circ(1+A)] \tag{35}$$

$$C_7 = 4C_1A(1-n)\tilde{V}^\circ\{\cos[C_9\omega^\circ(1+A)] + \cos[C_{10}\omega^\circ(1+A)] - \cos[C_{11}\omega^\circ(1+A)]\} \tag{36}$$

$$C_8 = 4C_1A(1-n)\tilde{V}^\circ\{\sin[C_9\omega^\circ(1+A)] - \sin[C_{10}\omega^\circ(1+A)] - \sin[C_{11}\omega^\circ(1+A)]\} \tag{37}$$

$$C_9 = \frac{1}{2\tilde{V}^\circ} \tag{38}$$

$$C_{10} = \frac{C_9}{A} \tag{39}$$

$$C_{11} = C_{10}(A-1) \tag{40}$$

Since the linear stability analysis cannot determine the magnitude of the disturbances, $\tilde{\theta}^\circ$ or $\tilde{V}^\circ$ can be assigned any value without altering the final results. This explains why neither $\tilde{\theta}^\circ$ nor $\tilde{V}^\circ$ appears in equations (32) and (33).

The procedure to seek the neutral stability solutions is straightforward but very time consuming. For a pair of specified G_m and A, the steady-state solutions are solved first (which are functions of G_m alone). The steady-state solutions are then substituted into equations (32) and (33) to solve for F at different values of ω°. If the curves of F computed from these two equations do not intersect, which indicates that flow is stable in this region, G_m is increased until the two curves first make contact. G_m at this critical point is the smallest G_m for which the flow can become unstable. For G_m greater than this critical value, there are two intersections between the two curves for F. When G_m is very large, more than two real roots for F have been found during the calculation. These higher mode solutions can easily be distinguished from the first mode solutions because they always occur at higher frequency and the temperature disturbance shows two or more waves along the loop.

4 Results and Discussion

The stability of the system studied here is determined by the dimensionless parameters G_m and F. The loci of neutral stability for five different aspect ratios are displayed in Figs. 3(*a*) and 3(*b*) for laminar and turbulent flows, respectively. The corresponding frequency of these neutral stability conditions is shown in Figs. 4(*a*) and 4(*b*). As mentioned in the foregoing, G_m represents the ratio of the buoyancy force to the friction loss in the loop. Flow becomes unstable only when G_m is greater than some critical value. Above this critical point the boundary between the stable and unstable regions is determined by the values of both G_m and F. It is shown in Figs. 3(*a*) and 3(*b*) that the flow is extremely stable at large F as well as at small F for both laminar and turbulent flows. This phenomenon was first found and explained by Welander [2] and will be discussed later.

The critical G_m computed from the stability analysis is found to be far above the optimum operating condition, equation (26). Thus, it is possible to operate a thermosyphon efficiently without oscillation. These computed neutral

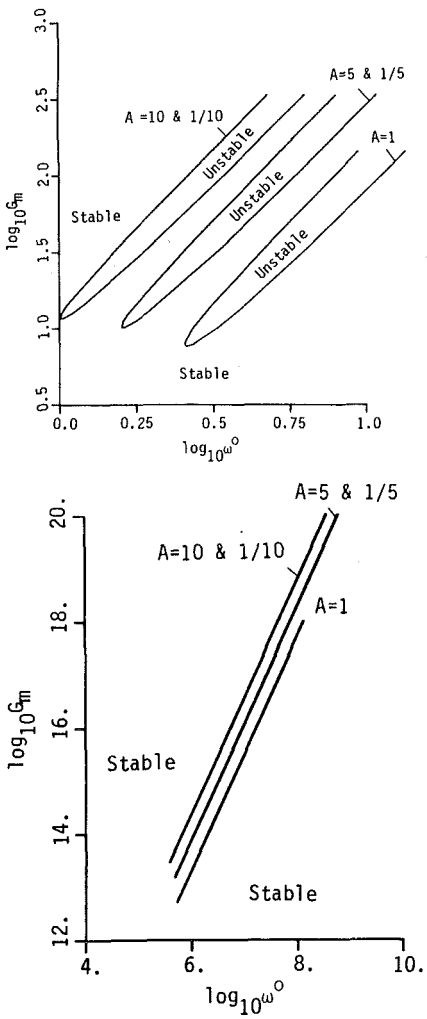

Fig. 4 Neutral stability curves in ω°, G_m coordinates: (*a*) laminar flow; (*b*) turbulent flow

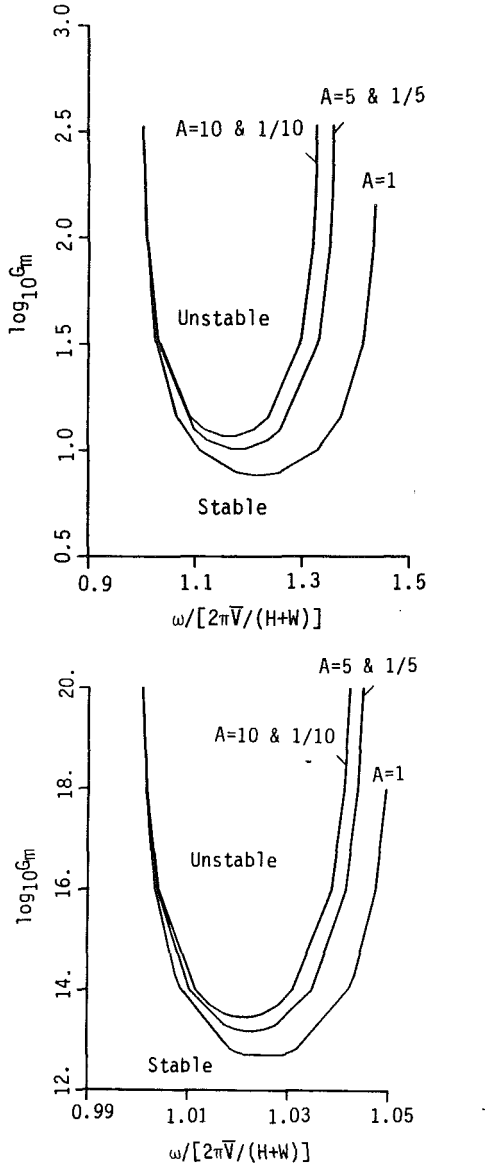

Fig. 5 Comparison of oscillation frequency with the frequency of a fluid particle: (*a*) laminar flow; (*b*) turbulent flow

stability curves for different aspect ratios also show that the square loop ($A = 1$) has the lowest critical G_m. As the aspect ratio A decreases or increases from unity, the critical value of G_m increases. These results indicate that a square loop is least stable. Either a slender loop ($A < 1$) or a wide loop ($A > 1$) can suppress the onset of instability until a higher buoyancy drive across the loop is reached.

For G_m greater than the critical value, F is a double-value function on the neutral stability curves. The corresponding oscillation frequency for the higher F is higher than that for the lower F but the frequency difference between the higher and the lower F for each value of G_m is small especially for turbulent flows. The envelope of the unstable flows reduces to nearly a straight line in Fig. 4(*b*). Both the higher and the lower oscillation frequencies are slightly greater than the frequency of the steady flow. Thus, the thermal disturbance travels slightly faster than the fluid. The same conclusion has been made by Welander [2] in the study of rectangular loop with point heat source and sink. A comparison between the oscillation frequency and the frequency of the fluid is given in Figs. 5(*a*) and 5(*b*). The abscissa of these figures is the oscillation frequency divided by the cycles of the steady flow traveling along the loop per unit of time. It is shown in these figures that the oscillation frequency of the neutral disturbance corresponding to the lower F approaches the fluid frequency as G_m increases. On the other hand, the difference between the traveling speed of the disturbance corresponding to the higher F and the steady flow velocity increases as G_m increases.

In order to better understand the mechanism of this convection-induced instability, some typical results of the calculated disturbance temperature profiles are plotted in Figs. 6(*a–f*). In these figures, $\tilde{\theta}^\circ_R$, $\tilde{\theta}^\circ_I$, and $|\tilde{\theta}^\circ|$ are the real part, the imaginary part, and the absolute value of $\tilde{\theta}^\circ$. $\tilde{\theta}^\circ_I$ is needed for the determination of the propagation direction of the temperature disturbance. $|\tilde{\theta}^\circ|$ can be used to determine the variation in disturbance magnitude as the temperature disturbance travels along the loop. Since linear stability analysis cannot determine the magnitude of the disturbances, the phase and the magnitude of these temperature disturbances are compared to an arbitrarily chosen velocity disturbance $\tilde{V}^\circ = 1 + i0$. Thus, the temperature distributions shown in these figures are the real and imaginary parts, and the comparative magnitude of the temperature disturbance $\theta^\circ{}'$ along the loop when the flow rate is maximum. It was found that the effects of the variation in G_m and F on the temperature distributions for laminar flow are similar to that for turbulent flow. These two types of flow will not be separately discussed in this paper.

The length of the vertical branches in these figures is stretched by the factor $1/A$; otherwise both $\tilde{\theta}^\circ_R$ and $\tilde{\theta}^\circ_I$ would

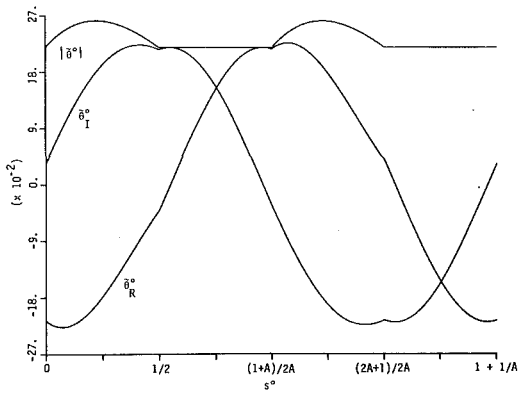

Fig. 6(*a*)

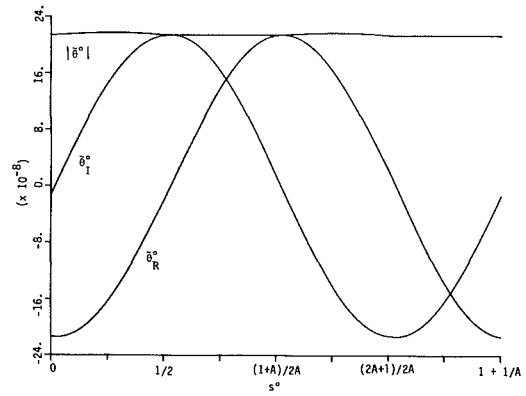

Fig. 6(*b*)

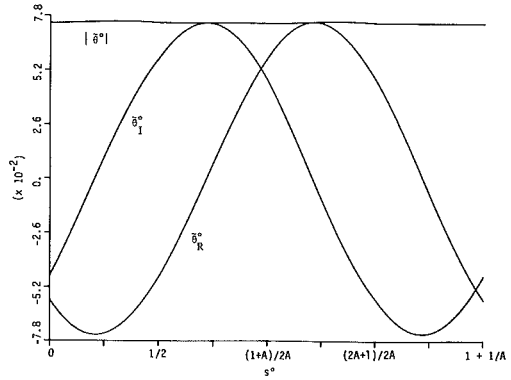

Fig. 6(*c*)

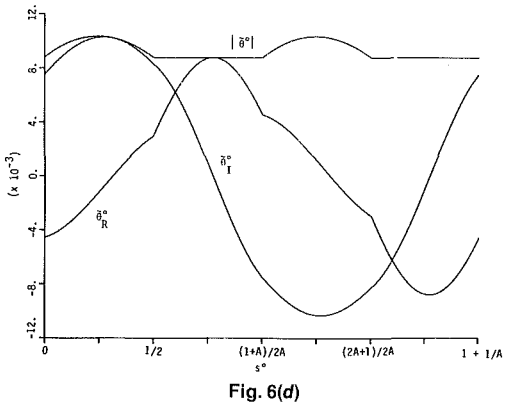

Fig. 6(*d*)

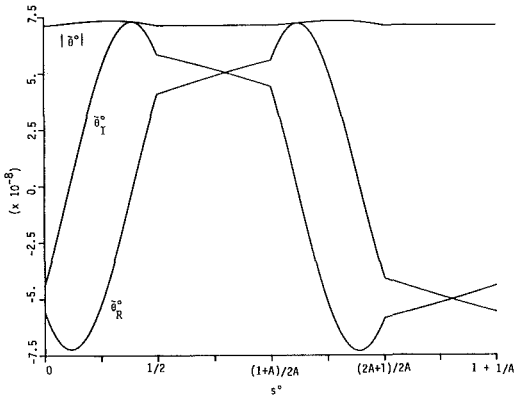

Fig. 6(*e*)

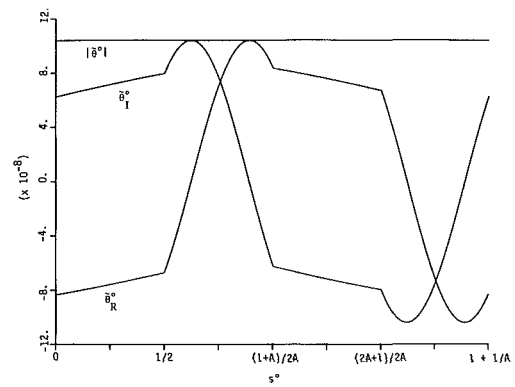

Fig. 6(*f*)

Fig. 6 Temperature disturbances along the loop: (*a*) laminar flow, A = 1, G_m = 7.634, F = 10.02; (*b*) turbulent flow, A = 1, G_m = 5.128 × 10^{12}, F = 2.738; (c) laminar flow, A = 1, G_m = 142.9, F = 3.959, (*d*) laminar flow, A = 1, G_m = 142.9, F = 525.8, (*e*) turbulent flow, A = 10, G_m = 2.857 × 10^{13}, F = 0.9995; (*f*) turbulent flow, A = 0.1, G_m = 2.857 × 10^{13}, F = 0.9995

resemble the sine wave. For neutral oscillations near the critical point (Figs. 6(*a*), 6(*b*), 6(*e*), and 6(*f*)), the highest value of the disturbed temperature $\tilde{\theta}^\circ_R$ reaches the cooling section (s° = (1 + A)/2A to (1 + 2A)/2A). Half a cycle later when the flow rate is minimum, the maximum point of $\tilde{\theta}^\circ_R$ will pass the heat source. Thus the residence time of the positive temperature disturbance is minimum along the heat sink and maximum along the heat source. Due to this heat regeneration (or overshooting), a small disturbance can easily be amplified and instability occurs. For G_m far above the critical point, the peak of the disturbed temperature $\tilde{\theta}^\circ_R$ corresponding to the higher F is in the right vertical branch as shown in Fig. 6(*d*). This represents a comparatively stable neutral oscillation since the temperature fluctuation spends equal time in the heating and the cooling sections. For the neutral stability state corresponding to the lower F (Fig. 6(*c*)), the magnitude of the temperature disturbance decreases as G_m increases. Although the phase lag between the velocity disturbance and the temperature disturbance remains unchanged, the variation in disturbance magnitude is too small in one cycle. These observations also explain why, for a fixed G_m, instability occurs only over a narrow range of F. In the limit of small F, equation (16) shows that the time variation of the flow rate V is small. Since the fluid has a large inertia, the gain in disturbance energy is infinitesimal in each cycle [2]. A large number of cycles is necessary for the growth of instability. On the other hand, in the limit of large F, the variation of buoyancy and the variation of flow rate are in phase and an

overshooting cannot occur, resulting in stable convection in the loop.

Acknowledgments

The author wishes to express his appreciation to the University of Utah Research Committee for their support, and to the staff of the Mechanical and Industrial Engineering office.

References

1 Keller, J. B., "Periodic Oscillations in a Model of Thermal Convection," *J. Fluid Mech.*, Vol. 26, Part 3, 1966, pp. 599–606.

2 Welander, P., "On the Oscillatory Instability of Differentially Heated Fluid Loop," *J. Fluid Mech.*, Vol. 29, Part 1, 1967, pp. 17–30.

3 Creveling, H. F., dePaz, J. F., Baladi, J. Y., and Schoenhals, R. J., "Stability Characteristics of a Single Phase Free Convection Loop," *J. Fluid mech.*, Vol. 67, Part 1, 1975, pp. 65–84.

4 Damerell, P. S., and Schoenhals, R. J., "Flow in a Toroidal Thermosyphon With Angular Displacement of Heated and Cooled Sections," ASME Paper No. 78-HT-44, 1978.

5 Greif, R., Zvirin, Y., and Mertol, A., "The Transient and Stability Behavior of a Natural Convection Loop," ASME JOURNAL OF HEAT TRANSFER, Vol. 101, 1979, pp. 684–688.

6 Mertol, A., Greif, R., and Zvirin, Y., "The Transient Steady State and Stability Behavior of a Thermosyphon With Throughflow," *Int. J. Heat Mass Transfer*, Vol. 24, No. 4, 1981, pp. 621–633.

7 Kaizerman, S., Wacholder, E., and Elias, E., "Stability and Transient Behavior of a Vertical Toroidal Thermosyphon," ASME Paper No. 81-WA/HT-11, 1981.

8 Bau, H. H., and Torrance, K. E., "On the Stability and Flow Reversal of an Asymmetrically Heated Open Convection Loop," *J. Fluid Mech.*, Vol. 106, 1981, pp. 417–433.

9 Zvirin, Y., Shitzer, A., and Bartal-Bornstein, A., "On the Stability of the Natural Circulation Solar Heater," in: *Proceedings 6th International Heat Transfer Conference*, Vol. II, Toronto, Canada, 1978, pp. 141–145.

10 Alstad, C. D., Isbin, H. S., Amundson, N. R., and Silvers, J. P., "The Transient Behavior of Single-Phase Natural Circulation Water Loop System," ANL-5409, Argonne National Laboratory, Lemont, IL, Mar. 1956.

11 Ong, K. S., "A Finite Difference Method to Evaluate the Thermal Performance of Solar Water Heater," *Solar Energy*, Vol. 16, 1974, pp. 137–147.

12 Chen, K., "The Influence of Loop Configuration on Closed-Loop Thermosyphons," ASME Paper No. 82-WA/HT-63, 1982.

Observations of Complex Oscillations in a Closed Thermosyphon

J. E. Hart

Department of Astrophysical, Planetary and Atmospheric Sciences, University of Colorado, Boulder, CO 80309

Observations have been made of thermal oscillations in a slightly inclined closed thermosyphon. The thermosyphon is made up of two isothermal tubes, capped at the outer ends, and joined along their axes by an insulating section. The tube assembly is filled with liquid and inclined slightly with respect to the vertical. The lower isothermal section is hotter than the upper one and convection is driven across the insulating region. Between the applied temperature difference at which simple steady convection occurs, and that required for persistent turbulent motions, there is a wide range over which thermal oscillations are observed. These oscillations reflect quasi-periodic flow as well as a type of periodic chaos.

1 Introduction

This paper discusses some observations of convective flow in a differentially heated tube of fluid. A schematic cross section of the apparatus is shown in Fig 1. Two stainless steel tubes of length H and inside diameter D each are closed at one end and joined together at the other end to a piece of plexiglass of height H_A. The steel tubes are surrounded by water jackets that maintain constant temperature boundary conditons $T = \pm\Delta T/2$ as shown in the figure. The plastic central section is insulated such that the outward heat flux at its surface is small. Thus this portion of the tube is called the adiabatic section. The finite-length cylindrical cavity is filled with a Boussinesq liquid, and the tube is oriented near the vertical in the gravitational field. Since the lower end is hotter one expects convection, and indeed it is the purpose of this note to discuss some rather bizarre oscillations measured in the laboratory.

The device shown in Fig. 1 is a version of the classic "closed thermosyphon" that has been much discussed in the heat transfer literature because of its relevance to problems in such diverse areas as crystal growth, geophysical flow, and turbine rotor blade cooling. Our version can also be thought of as a simplified form of a single-phase heat pipe. It is, however, distinct from the closed loop thermosyphon which is a differentially heated fully connected toroidal loop. However, in some loop systems the joints between sections of the loop can be modeled by the closed thermosyphon if the throughflow is small.

Japikse [1] provides an extensive review of both closed and open thermosyphons. Of particular interest here is the work of Bayley and Lock [2] who describe several flow regimes observed in a closed thermosyphon with $H_A \simeq 0$. In the "conduction regime" there is motion in each section since there is no pure zero-flow conductive solution. However, the parcel orbits do not cross the adiabatic section so the net vertical heat flux is by conduction. This regime occurs at small temperature difference ΔT. At a moderate difference convection *between* the isothermal tubes takes place so that there is a convective flux of heat across the adiabatic section. This convection can either be a simple cell with a single stream up and a single stream down, or a complicated multiple-stream steady flow (or in our case time-dependent flow) perhaps best visualized by clasping one's hands together with finger tips pointing horizontally and thinking that the convective flows go along each finger. Japikse et al. [3] provide photographs and sketches of typical fluid trajectories in the center section of a fairly large thermosyphon. In their discussion (especially pp. 874–875) they propose a classification of different convective modes based on the number of identifiable jets crossing the adiabatic section from the cool to the hot isothermal-wall regions and vice versa. Following their classification, if we have m convective upflows and n downflows we shall say there is (m, n)-stream convection. "Multiple-stream" motion has either m or n greater than 1. The multiple-stream flow can be impeded in the sense that the streams have to twist around each other to cross the adiabatic section.

In our very slightly inclined geometry, with the tube tipped a little over 1 deg off vertical, two modes of convection seem to dominate. In the first mode a single warm stream crosses the central section on the left (given that the top of the apparatus is tilted through a small angle to the right). It carries hot fluid from the lower section upward. Mass is conserved by a single cool plume flowing down through the adiabatic section on the right. The whole circulation thus consists of a single-celled loop in which the parcel orbits can be roughly described as vertically drawn-out ellipses in the plane defined by gravity and the axis of the tube.

In the second mode, the flow is impeded. There is a tendency for hot fluid which rises up the left side of the lower tube to encounter cool fluid sinking down the left side of the upper section. These two streams can meet head-on in the center section where they must turn. In doing so a strong and often remarkably stable thermal front, or thermal near-discontinuity, occurs in the adiabatic section. There is quasi-horizontal flow along the front over much of the cross section, but near the sidewall the hot plume must break free and move into the cold section. The sinking cold jet which flows across the upper side of the front similarly breaks free near the wall and moves into the lower hot tube. An identical process occurs on the right side. Thus, 2,2-stream impeded flow results. It is, however, the presence of the front and its attendant horizontal motions that distinguishes this latter mode from the first, for which near-vertical motions dominate the central section. It is shown below that for some conditions the front is stationary, but for the majority it oscillates in a complex manner.

Ultimately at large ΔT the flow becomes unstable and then turbulent. Japikse et al. [3] provide a summary of the heat transfer data and present some critical Rayleigh numbers for transition to turbulence in several different laboratory thermosyphons. Martin [4], Martin and Lockwood [5], and others (see [1]) mention observations of thermal oscillations

Contributed by the Heat Transfer Division for publication in the JOURNAL OF HEAT TRANSFER. Manuscript received by the Heat Transfer Division August 8, 1984.

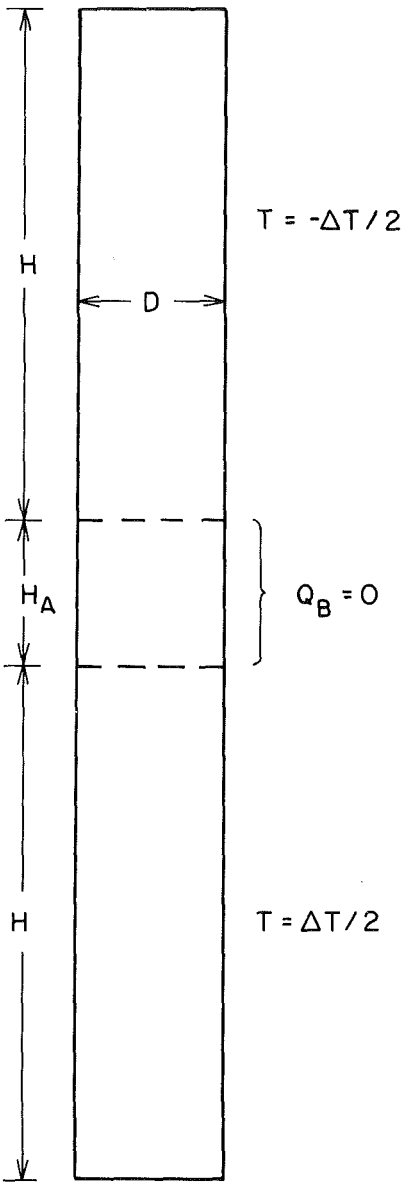

Fig. 1 Cross section of the tubular thermosyphon: H_A is the height of the plexiglass "adiabatic" region

between the region of laminar and turbulent flow, but say little about the character or prevalence of them. It is our purpose here to demonstrate that for a particular thermosyphon, oscillations, rather than steady motions, dominate the flow for most of the ΔT range between the breakdown of the conductive regime and what one might call high-dimensional turbulence involving many spatial structures.

2 Experimental Procedure

Previous experiments have been conducted in large cylinders (5 to 10 cm diameter) with what appear to be somewhat poorly controlled boundary conditions. The apparatus used here was designed so that there would be good control over the isothermal temperature sections, and with D small enough that the time scales for equilibration would be reasonably short. The isothermal tubes have inside diameter $D = 0.95$ cm. The length is $H = 12.4$ cm. The adiabatic section is made of insulated plexiglass and has $H_A = 1.25$ cm. The plexiglass annulus is 2 cm wide and is surrounded by urethane foam with an R value of about 6. It was felt that an adiabatic region would be necessary because if the two isothermal sections were in contact the boundary temperatures could not be maintained properly. An adiabatic section is crucial when closed thermal syphons are used in crystal growing applications where such thermosyphons are called Bridgman cells (Chang and Brown [6]).

The fluid is a 2-centistoke silicone fluid with a Prandtl number of 20.2. One can define a Rayleigh number based on D as $\mathrm{Ra} = g\alpha\Delta T D^3/\kappa\nu$, where ν is the kinematic viscosity, α the thermal expansion coefficient, and κ the thermal diffusivity. All parameters were held fixed except for ΔT. The results are presented in terms of ΔT (°C), with $\mathrm{Ra} = 4.96 \times 10^4 \Delta T$°C.

One crucial aspect of this study is that the tube is inclined 1.15 deg off vertical. This happened to be one of the first angles studied and the fluid response was so rich and varied that most measurements were made at this inclination. The inclination breaks the azimuthal symmetry of the purely vertical case and eliminates slow azimuthal drift modes. When the inclination is large ($> \simeq 10$ deg) many of oscillations described here are replaced by a simple steady 1,1-stream upslope-downslope unicell. This latter effect has been studied previously (see [3]).

The boundary temperatures were held constant to within 0.01°C by proportionally controlled thermal baths. The experiment was conducted by slowly increasing ΔT from zero to about 7° in 0.3° steps over a period of about 6 weeks. This significant experiment time was required because when crossing a bifurcation point the relaxation time becomes very long. In addition near a bifurcation of the flow from one state to another, smaller and sometimes reverse ΔT steps were taken. Measurements were made by two 0.002-cm NTC thermistors, one mounted flush with the wall of the adiabatic region at midheight, and one approximately at the center of the adiabatic cavity. The thermistor resistance was measured and digitized for further processing. Since we were interested in the existence and structure of oscillations, no attempt was made to measure the thermal offset of the probes. The temperature range was measured but not its mean level with respect to one of the wall temperatures. In the figures that follow, a temperature scale is given which indicates the amplitudes of the observed oscillations, but the mean value of the data presented (with respect to $T = 0$, say) is arbitrary. In

Nomenclature

D = diameter of convective region
S = gravitational acceleration
H = height of isothermal boundary sections
H_A = height of adiabatic boundary section
j = power law exponent for spiral (laminar) periods in periodic chaos
m = number of upflow streams
n = number of downflow streams
Pr = Prandtl number = ν/κ
Ra = Rayleigh number = $g\alpha\Delta T D^3/\kappa\nu = 4.96 \times 10^{+4}\Delta T$ (°C)
Q_A = boundary heat flux out of adiabatic section
T = temperature, °C
t = time, s
tau = lag time for projected attractors, s
α = coefficient of thermal expansion
ΔT = applied temperature difference
ΔT_c = critical applied temperature difference
κ = thermal diffusivity
ν = kinematic viscosity
ω = frequency, radians/s

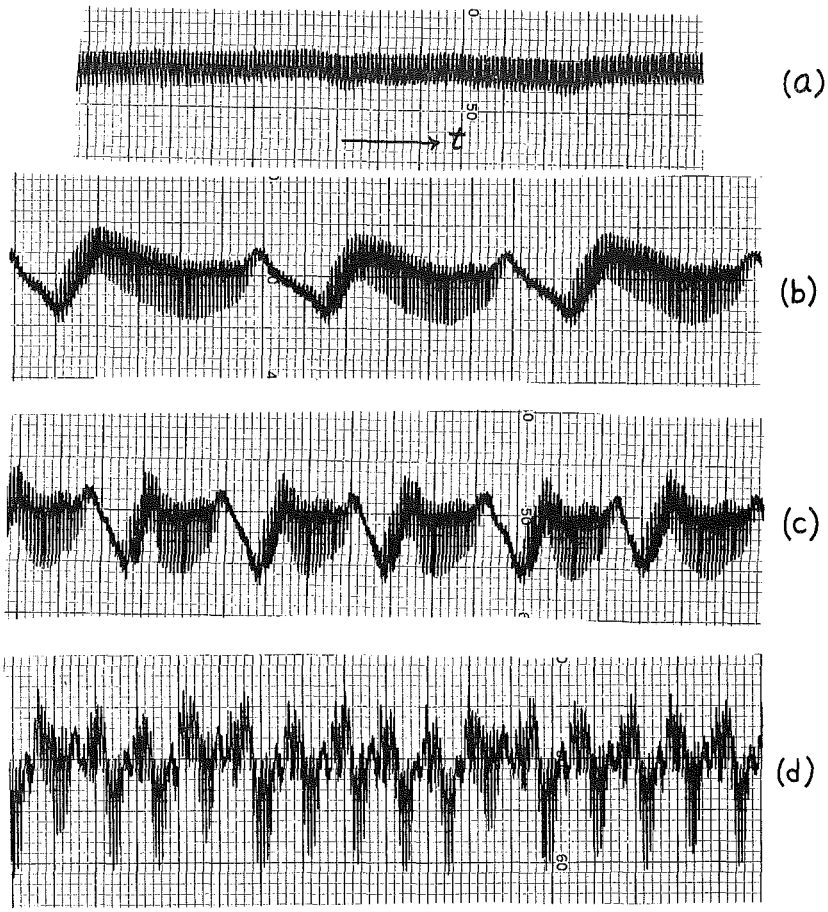

Fig. 2 Raw temperature data from the wall probe: (*a*) $\Delta T = 1.8°$; (*b*) $\Delta T = 3.1°$; (*c*) $\Delta T = 3.3°$, and (*d*) $\Delta T = 3.7°$; all temperature differences are in degrees Kelvin

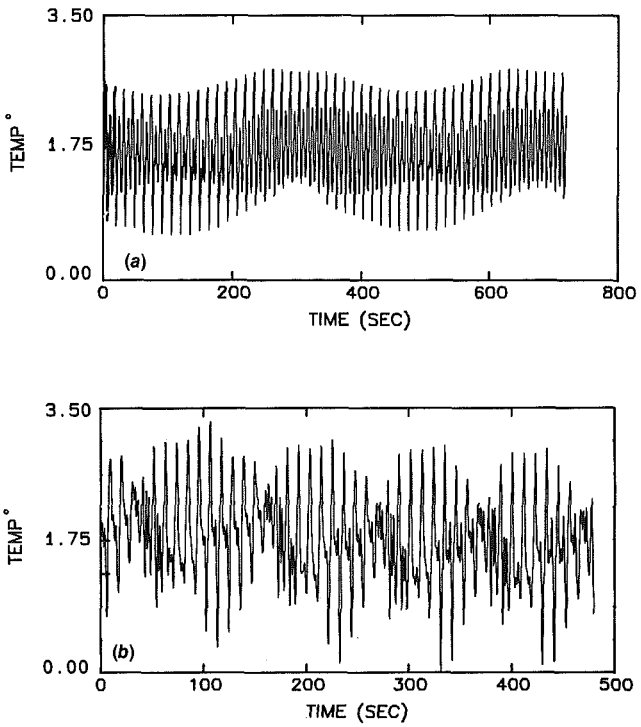

Fig. 3 Digitized temperature traces from the interior probe: (*a*) $\Delta T = 3.4°$; (*b*) $\Delta T = 3.7°$

addition it is useful to note that the precise amplitude and phase, but *not* the topological structure of the reported oscillations, are very dependent on the probe positions (as one would expect when making measurements in a thermal front).

3 Results

Weak but steady motions exist for ΔT less than 1.68°. Just above this the flow oscillates with a steady amplitude, although at applied ΔT less than 2° some weak modulation attributable to small drift in the controllers or room temperature was observed. Figure 2 shows some raw analog data from the wall probe. As ΔT is increased, the simple periodic oscillation becomes modulated. The modulation period itself decreases monotonically with increasing ΔT until at $\Delta T \simeq 3.63°$ the modulations become irregular in their amplitudes. The interior probe shows a similar behavior, although, as noted below, the amplitudes and phases of the various components in the signal are different. Figure 3 shows two traces from this probe. Figure 3(*b*) can be compared with 2(*d*), for example. In both measurements the qualitative or topological description of the signal is equivalent. Figures 2(*c*) and 3(*a*) can be described as a quasi-periodic modulation involving two incommensurate (irrationally related) frequencies.

In what follows we shall use data from the interior probe. The signal is larger and cleaner because, as discussed below, the thermal oscillations are a result of the tipping of a front that forms in the adiabatic region where there is impeded 2,2-

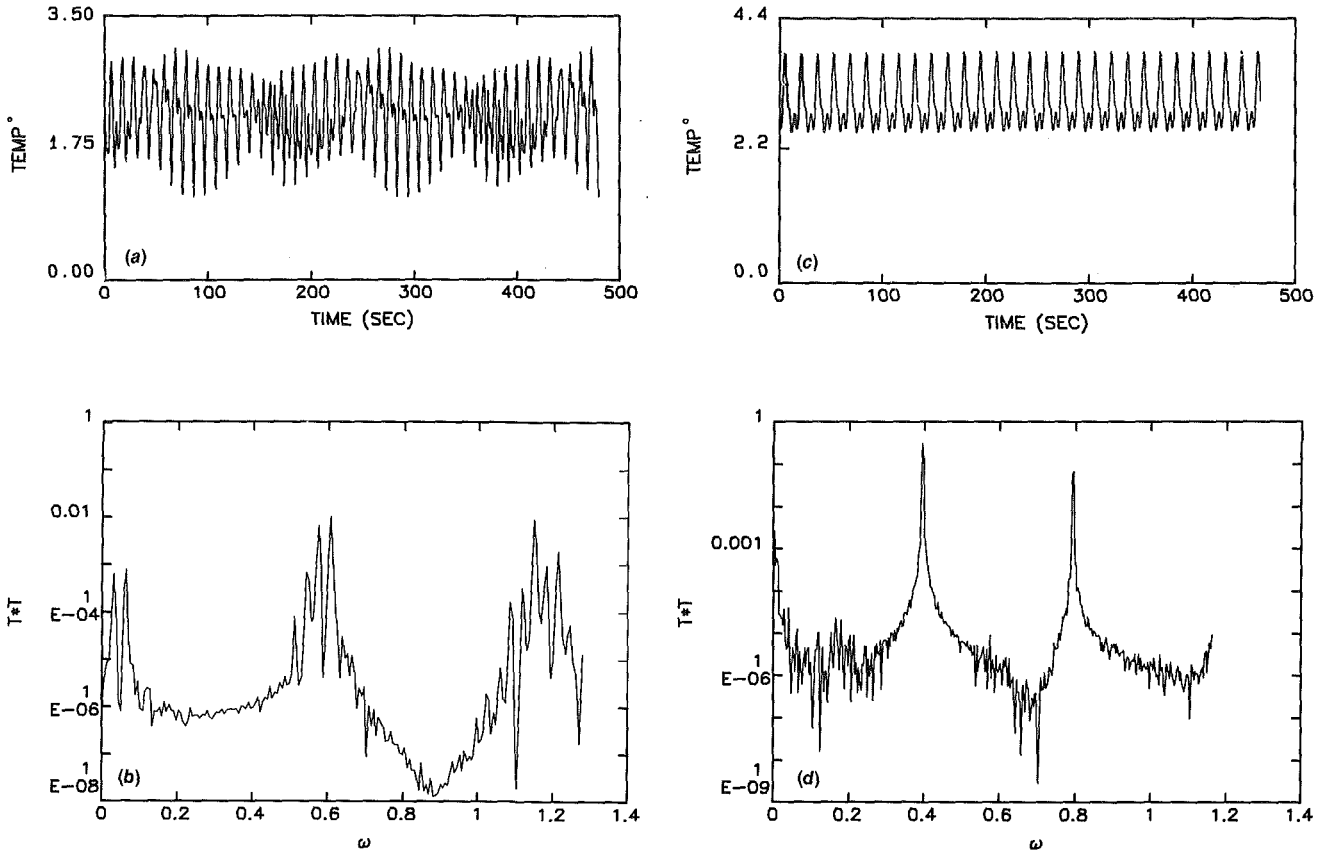

Fig. 4(*a*) Temperature trace for $\Delta T = 4.2°$; (*b*) spectrum of (*a*); (*c*) temperature trace for $\Delta T = 2.8°$; (*d*) spectrum of (*c*)

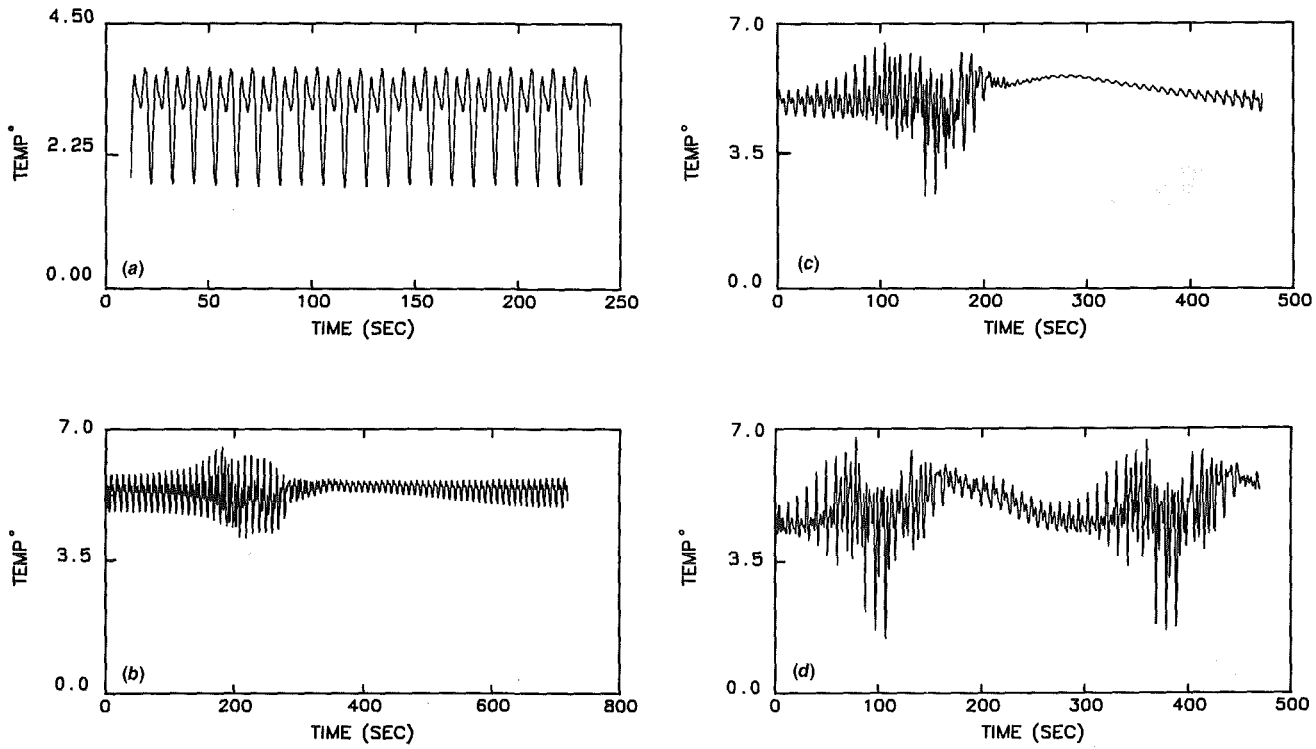

Fig. 5 Temperature traces for (*a*) $\Delta T = 5.00°$; (*b*) $\Delta T = 5.40°$; (*c*) $\Delta T = 5.60°$; (*d*) $\Delta T = 5.80°$

stream convection. This frontal oscillation is weak at the wall so we get better data from the interior probe.

The range of temperature $2.32° < \Delta T < 4.67°$ is characterized by quasi-periodic motion, with a very narrow window of irregularity of about 0.4° width around 3.7°. Figure 2 shows how this window is approached. While one might have expected the irregular or chaotic behavior of Fig. 2(*d*) to amplify as ΔT increases further, just the opposite happens. At 3.9° chaos ceases and regular quasi-periodic motion returns; however, now there is a subharmonic to the low-frequency modulation. This is shown in Fig. 4(*a*). The frequency spectrum in Fig. 4(*b*) shows that the low-frequency component of the motion is split into two peaks. The peaks are sharp and the continuum is very low, indicating a relative lack of chaotic or wide-band response. One can compare this signal and spectrum to that for the simple periodic motion observed at a lower ΔT and shown in Fig. 4(*c*, *d*).

As ΔT is further increased, the quasi-periodic amplitude modulated motion ceases and the flow becomes singly periodic again. This is shown in Fig. 5(*a*). Here the oscillation is composed of a steady fundamental frequency and a subharmonic. What happens next is truly bizarre. After a window of simple periodicity starting at 4.42°, at $\Delta T \simeq 5.35 \pm 0.025°$, another bifurcation occurs. The oscillations slowly amplify. They reach a point where they apparently become too large for the system to sustain them. But instead of slowly decreasing as in the quasi-periodic case, there are several large contortions of the flow after which the oscillations become quite weak. They start to build again, and the process repeats itself. Part of this relaxation oscillator is shown in Fig. 5(*b*). The surprising fact is that the short burst of activity before the oscillations die is never exactly the same, yet the time between the bursts varies by less than one cycle between consecutive bursts.

As ΔT increases, the period between bursts gets shorter, and the bursts themselves become larger and more chaotic. Figure 5(*c*) shows an example. The burst between 110 and 200 s on this graph (where the time origin is long after the transients due to changing ΔT have decayed) occurs precisely every 482 s, but the details within each successive burst are quite different. This is apparent in the two bursts shown in Fig. 5(*d*) at an applied ΔT 0.2° greater than that in 5(*c*).

Finally, Fig. 6 shows a frequency spectrum corresponding to the weak chaos at $\Delta T = 5.40°$. The broad peaks suggest the motion is irregular rather than quasi-periodic as in Fig. 4(*b*).

As ΔT is increased further, the bursts become closer together until at $\Delta T = 6.3°$ they occur without a "laminar" region involving simple growing oscillations in between. Beyond this applied gradient the flow appears to be fully turbulent.

It is of interest that between $\Delta T = 0$ and 6.3°, the upper 4.7° range is occupied by various types of oscillations. One is tempted to suggest that steady motion in this type of thermosyphon is the anomaly rather than the rule.

4 Interpretation

The complex oscillations described above apparently involve interactions between 1,1-stream and 2,2-stream convection modes. Particle visualization in the adiabatic section indicates that a wavering of the 2,2-stream mode is responsible for the basic oscillation. As illustrated in Japikse [3] an impeded flow results from the meeting and turning of upward and downward streams in the adiabatic section. Reiterating, such a head-on meeting results in the formation of a thermal front. This front appears to be unstable, tipping from side to side. If it tips far enough, the streams that were meeting head-on can pass by each other and 1,1-stream convection results. At low ΔT this does not appear to happen completely, and the front can rebuild, leading to the quasi-periodic oscillations.

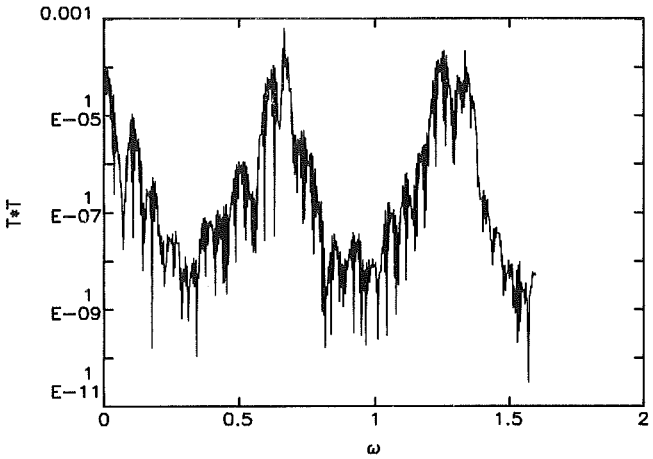

Fig. 6 Spectrum for an extended record (65,000 pts) corresponding to Fig. 5(*b*)

At large ΔT once 1,1-stream convection occurs, a larger heat flux is carried across the adiabatic region (as compared to that carried by the 2,2-stream impeded mode). This motion occurs at large Rayleigh number ($\simeq 2 \times 10^5$) and is irregular. However, the associated strong heat flux wipes out the mean thermal gradient in the adiabatic section. The 1,1-stream convection decreases in amplitude, and the front can reform.

Due to the high degree of spatial structure present in this flow a theoretical or numerical model of these oscillations will be difficult to construct. It is possible, however, that some connection can be made with other dynamic systems. If one views a dynamic system as being described by a finite-dimensional set of evolution equations (for example, a set of ordinary differential equations in time that describe the amplitudes and phases of a finite number of convective modes), then one standard way of analyzing solutions of this set is to look at the nature of trajectories in the phase space of the system. In a fluid experiment it is usually impossible to make enough measurements in space to isolate the spatial Fourier (or other) normal modes of the flow, thus enabling one to plot trajectories in a space spanned by their amplitudes. However, one can often reconstruct a consistent representation of the system phase space from a single time series as discussed and illustrated in Packard et al. [7] and Froehling et al. [8].

For example, a plot of the temperature at time t versus that at time $t+$tau (where tau is an arbitrary time delay) yields a trajectory representation of the thermal oscillations, somewhat akin to plotting a signal versus its derivative (e.g., position versus velocity). Figure 7(*a*) shows that the steady periodic signal at $\Delta T = 5.00°$ corresponds to a closed orbit or limit cycle in phase space. The loop is not as simple as the elliptical orbit one would get for a two-dimensional (velocity, position) phase space description of particle motion $X(t) = \sin(\omega t)$, say, but it is topologically equivalent. The inner twist in the upper right corner is a result of the secondary minima of Fig. 5(*a*) which are themselves related to the harmonic content of the temperature signal. The set of points on which the trajectories flow after initial transients have decayed is called an attractor. At larger ΔT, where the oscillations are more complex, the attractors become more complicated, respresenting objects of higher dimension than the simple curve of Fig. 7(*a*). Indeed the oscillations at $\Delta T = 5.4°$ yield an object that looks like a torus. For a long time the flow spirals around the inner funnel, then it loops around the outside portion during the "irregular bursts." At higher ΔT (Fig. 7*c*) less time is spent in the funnel and the outside loops are more erratic. At least just above the bifurcation point (5.35°) where the oscillations first start to amplify, the points

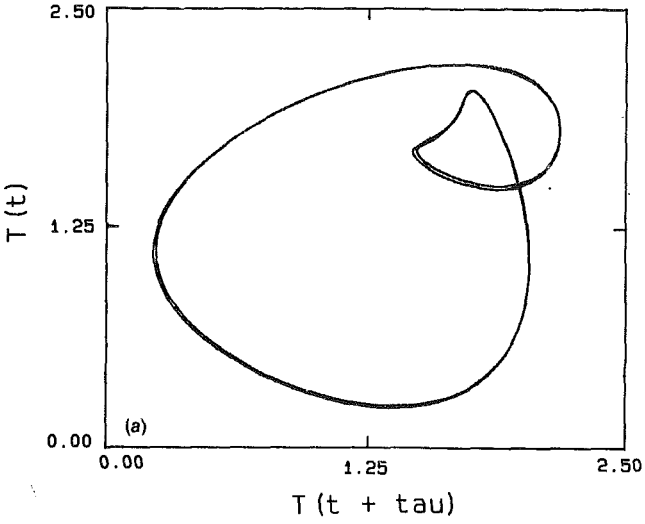

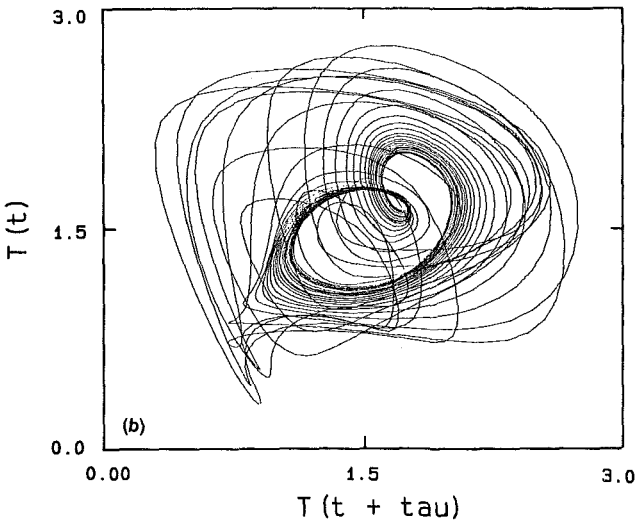

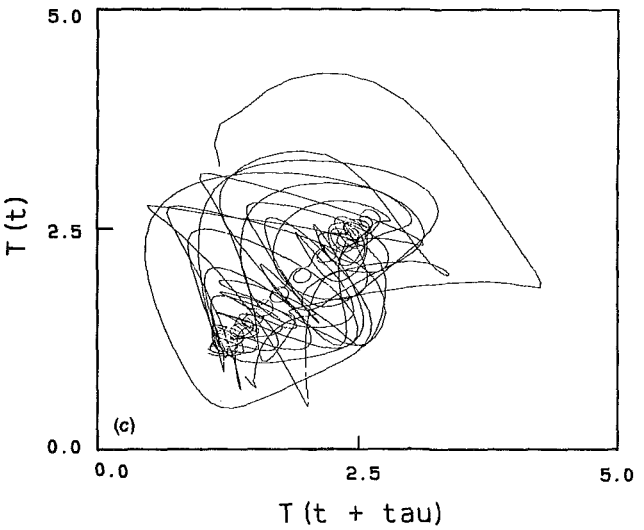

Fig. 7 Projected attractors of (a) $\Delta T = 5.00°$; $\Delta T = 5.40°$; (c) $\Delta T = 6.05°$; the value of tau used is 1.2 s

on the outside loops seem to lie near a well-defined surface. This is illustrated by passing a plane through a three-dimensional phase space reconstruction of the time series for $\Delta T = 5.4$ and marking where the orbits pierce the plane. This Poincare section is shown in Fig. 8. The funnel is clearly

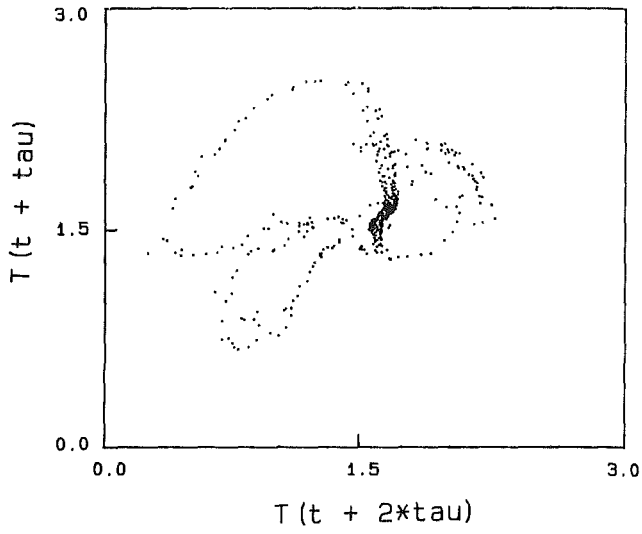

Fig. 8 Poincare section for $\Delta T = 5.40°$ (see Figs. 5*b* and 7*b*)

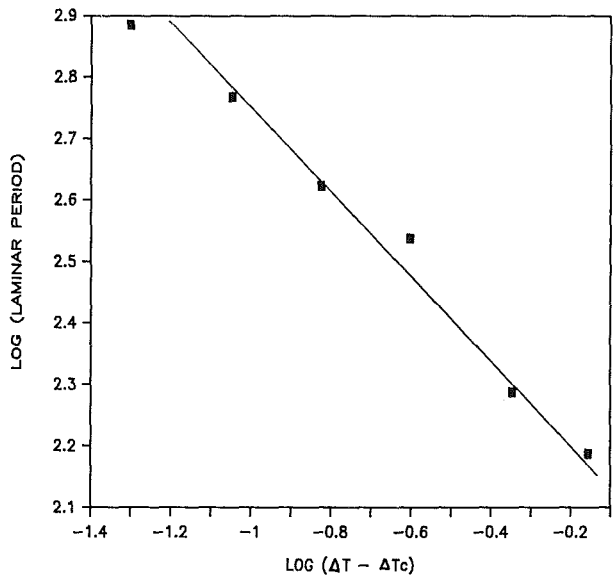

Fig. 9 Spiral period lengths versus supercriticality

visible. Afer some 40 complete periods of chaos it is seen that the outer points seem to be forming a surface. The object which was projected onto the plane in Fig. 7(*b*) thus appears to be a torus. Langford et al. [9] have shown theoretically that a torus can arise in the interaction between a stationary and an oscillatory mode of instability in typical weak-coupling problems that lead to nonlinear evolution equations for both modes. Their toroidal phase space motion is not chaotic. It is probable that data shown in Fig. 8 do not actually converge to a surface. The torus is fuzzy and the fuzziness is related to the irregular component in the bursts. The observation of a bifurcation directly from periodic motion to a noisy torus in a fluid system is new.

One last intriguing fact is that the highly predictable spiral regions of figures like 7(*b*) and 7(*c*), or the simple growing oscillations between the bursts in Fig. 5, have a length in time that correlates well with the supercriticality. Let $\Delta T_c = 5.35 \pm 0.025$ be the temperature difference at which steady oscillations bifurcate to separated bursts. We then measure the length of the funnel regions for various ΔT above ΔT_c. We call this the "laminar period" of the flow. Figure 9 shows that the laminar period scales with the supercriticality $(\Delta T - \Delta T_c)$ as $(\Delta T - \Delta T_c)^j$ where $j = 0.62 \pm 0.15$. The un-

Table 1 Regime summary for quasi-static runup

ΔT	Ra/10^4	System response
0 –1.68	0 – 8.33	steady convection
1.68–3.50	8.33–17.3	simply then quasi-periodic
3.50–3.91	17.3 –19.4	chaotic
3.91–4.40	19.4 –21.8	quasi-periodic
4.40–5.35	21.8 –26.5	simply periodic
5.35–6.2	26.8 –30.7	periodic chaos
6.2 –	30.7 –	fully chaotic

certainty in j is a result of the difficulty in measuring the bifurcation point ΔT_c more precisely. Such power laws are found in theories of intermittency in simple dynamic systems governed by almost one-dimensional mappings that undergo a tangent bifurcation (Hirsh et al. [10], Jeffries and Perez [11]). Maps produced from our time series by plotting successive maxima against previous ones, for example, do not appear to be one dimensional, nor like the logistic map used in [10]. Furthermore the intermittency discussed in [10, 11] usually involves one outer excursion from the funnel instead of an extended set of circuits. Nonetheless, the observed scaling behavior suggests an explanation. It may be that the growth rate of the frontal instability scales with the supercriticality. In Benard convection, for example, linear unstable modes have growth rates that follow the above scaling with $j = 0.5$. That the laminar periods decrease at roughly this power of the supercriticality suggests it is the time it takes the frontal oscillations to reach a critical amplitude for breakdown that governs the bizarre behavior of this system.

5 Conclusions

It has been shown that the flow in a very slightly inclined closed thermosyphon of aspect ratio $H/D = 13.05$ and with an adiabatic region of aspect ratio $H_A/D = 1.315$ has a propensity to oscillate. The oscillations occupy 3/4 of the Rayleigh parameter space between motion (at Ra > 0) and full turbulence at Ra $\simeq$ 300,000. Within the oscillation region there are windows of persistent chaos, regions of periodic bursts of chaos, as well as simply periodic and quasi-periodic motions. The data are summarized in Table 1. The oscillations seem to result from interactions between 1,1-stream and 2,2-stream modes, with the former representing direct convection across the central section of the thermosyphon, and the latter as impeded or frontal convection in that region.

All the transitions described above show considerable hysteresis. Steady motion was occasionally observed at $\Delta T =$ 6.5, for example if the system is started from rest and the thermal bath pumps turned on suddenly so that ΔT is established almost instantaneously. Apparently if just the right initial condition is set up, some m, n-stream modes can be stable at large ΔT. The behavior with no inclination is equally complex, although the breakdown to turbulence occurs at a slightly lower Ra after some quasi-periodic motion. This is probably a result of the absence of the stabilizing influence of tilt on the 1,1-stream mode. Indeed at even modest angles ($\simeq$ 10 deg) all time dependence disappears up to the limit of our temperature baths ($\Delta T = 30°$ or Ra $= 1.5 \times 10^6$).

Acknowledgments

This research was sponsored by NASA under contract NAS-8-31958.

References

1 Japikse, D., "Advances in Thermosyphon Technology," *Advances in Heat Transfer*, Vol. 9, 1973, pp. 1-111.

2 Bayley, F. J., and Lock, G. S. H., "Heat Transfer Characteristics of the Closed Thermosyphon," ASME JOURNAL OF HEAT TRANSFER, Vol. 87, 1965, pp. 30-40.

3 Japikse, D., Jallouk, P. A., and Winter, E. R. F., "Single-Phase Transport Processes in the Closed Thermosyphon," *Int. J. Heat and Mass Transfer*, Vol. 14, 1971, pp. 869-887.

4 Martin, B. W., "Free Convection in an Open Thermosyphon With Special Reference to Turbulent Flow," *Proc. Roy. Soc. A*, Vol. 230, 1955, pp. 502-530.

5 Martin, B. W., and Lockwood, F. C., "Entry Effects in the Open Thermosyphon," *J. Fluid Mech.*, Vol. 19, 1963, pp. 246-256.

6 Chang, C. J., and Brown. R., "Radial Segregation Induced by Natural Convection and Melt/Solid Interface Shape in Vertical Bridgman Growth," *J. Crystal Growth*, Vol. 63, 1983, pp. 343-364.

7 Packard, N., Crutchfield, J., Farmer, D., and Shaw, R., "Geometry From a Time Series," *Phys. Rev. Lett.*, Vol. 45, 1980, pp. 712-716.

8 Froehling, H., Crutchfield, J., Farmer, D., Packard, N., and Shaw, R., "On Determining the Dimension of Chaotic Flows," *Physica*, Vol. 3D, 1981, pp. 605-617.

9 Langford, W. F., Arneodo, A., Coullet, P., Tresser, C., and Coste, J., "A Mechanism for Soft Mode Instability," *Physics Letters*, Vol. 78A, 1980, pp. 11-14.

10 Hirsch, J. E., Huberman, B. A., and Scalapino, D. J., "Theory of Intermittency," *Phys. Rev. A*, Vol. 25, 1982, pp. 519-532.

11 Jeffries, C., and Perez, J., "Observation of a Pomeau-Manneville Intermittent Route to Chaos in a Non-Linear Oscillator," *Phys. Rev. A*, Vol. 26, 1982, pp. 2117-2122.

A Model of Flow in a Closed-Loop Thermosyphon Including the Soret Effect

J. E. Hart
Department of Astrophysical, Planetary and Atmospheric Sciences, University of Colorado, Boulder, CO 80309

This theoretical study addresses the nature of convective motions in a toroidal loop of binary fluid oriented in the vertical plane and heated from below. The boundaries of the loop are impermeable, but gradients of the solute can be set up by Soret diffusion in the direction around the loop. The existence and stability of steady solutions are discussed over the Rayleigh number–Soret coefficient parameter plane. When the Soret coefficient is negative, periodic and chaotic oscillations analogous to those of thermohaline convection are predicted. When the Soret coefficient is positive, relaxation oscillations and low Rayleigh number chaotic motions are found. Both sets of phenomena are predicted to occur for realistic thermosyphon parameters.

1 Introduction

There has recently been considerable interest in double diffusive convection phenomena. Much theoretical work has been done on motion between parallel plates maintained at different temperatures and solute concentrations. In practice it is very difficult to create a constant salinity boundary condition in the laboratory, so many of the theories using this assumed boundary condition cannot be checked. However, Soret diffusion, where a molecular flux of a solute is generated by an internal temperature gradient, can generate gradients of solute in a fluid, even with impermeable boundaries. The problem of Soret convection between isothermal plates has been investigated by a number of authors (e.g. [1, 2]) and the theoretically predicted double diffusive instability has been observed in experiments. The Soret-induced instabilities can be either monotonic or overstable. The oscillatory ones were found to compete with a direct thermally driven convection instability, and hysteresis effects have been observed and predicted [3].

This paper addresses the question of whether or not substantial Soret effects might occur in a closed-loop toroidal thermosyphon containing a two-component fluid mixture. Simple one-dimensional models have been proposed for motion in a fluid loop heated from below (Malkus [4]), in a fluid loop driven by thermal and solute boundary conditions (Seigmann and Rubenfeld [5]), and in a thermosyphon driven by angularly displaced nonvertical heating (Hart [6]). The fluid loop models derived in these papers are relatively simple, yet in some instances do very well in describing motions observed in the laboratory. For example, such models yield qualitatively favorable comparisons with the experiments of Creveling et al. [7] and Damerell and Schoenhals [8]. In addition, Gorman et al. [9] have observed chaotic oscillations in a laboratory thermosyphon that seem to be reasonably well described by the loop model even though the motion in the thermosyphon is highly supercritical (in the sense that the thermal stress far exceeds the critical level required for the onset of motion by instability.

Except for the Seigmann and Rubenfeld [5] model, previous work has dealt primarily with a one-component fluid. In [5] the boundary condition of specified solute concentration on the tube wall cannot be realized experimentally. However, since one might naturally want to run a thermosyphon with a two-component fluid (water and antifreeze for example), it seems of interest to ask the question of what double diffusive motions might occur in a system with impermeable walls such that there are no externally imposed solute conditions. A model is derived here for two-component one-dimensional flow in a fluid loop including the Soret effect, which will generate solute fluctuations internally. It is shown that interesting and complex motions are predicted for reasonable parameter values. The calculations suggest it might be possible to study these in the laboratory.

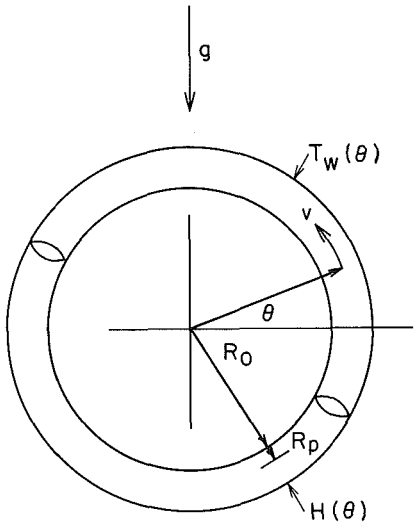

Fig. 1 Schematic of the toroidal thermosyphon

2 Formulation

Figure 1 shows a cross section of a model fluid loop. A tube of radius R_p is bent into a loop of radius R_0 and oriented in the vertical plane defined by the gravitational acceleration g. The boundary condition on the tube is either one of imposed temperature T_w or of imposed heat flux H, both of which can be functions of the angle around the torus θ. The tube wall is impermeable. The tube contains a two-component fluid with solute concentration S (%), which we will refer to as the "salinity" even though it could be any soluble substance. We assume the fluid has a kinematic viscosity ν, a thermal diffusivity κ, and a salt diffusivity D_s that are all constants. The equation of state is taken to be

$$\rho = \rho_0(1 - \alpha T + \beta S) \tag{1}$$

where T and S are the temperature and salinity relative to

Contributed by the Heat Transfer Division for publication in the JOURNAL OF HEAT TRANSFER. Manuscript received by the Heat Transfer Division August 8, 1984.

ambient values, α is the coefficient of thermal expansion, and β is the volumetric expansion coefficient (constant).

As discussed in Hurle and Jakeman [2] the molecular flux of salinity F_s in a nonisothermal fluid is given by

$$F_s = D_s[\Gamma^* S(1-S)\nabla T - \nabla S] \tag{2}$$

where Γ^* is the Soret coefficient for the fluid. Since the product $D_s\Gamma^*$ is small, the fluctuations of salinity will be small compared to the average value. It is thus customary to consider $\Gamma \equiv \Gamma^* S_0(1-S_0)$ a constant and write

$$F_s = D_s[\Gamma \nabla T - \nabla S] \tag{3}$$

where S_0 is now the ambient salinity and S the fluctuation from the mean.

The model equations are derived by averaging the azimuthal momentum equation, the thermodynamic (heat balance) equation, and the salt conservation equation over the diameter of the tube R_p. One assumption is used, that the variables can be replaced by their cross-sectional averages, and in particular that the terms describing the azimuthal advection of heat and salt can be replaced by the advection of the averaged quantities by the cross-sectional average velocity v. This assumption and the generation of one-dimensional models has been discussed in much detail previously (see the discussion and papers referenced in [6]). It is an ad hoc assumption at this point, justified in part by the success of previous models in describing experimental results. The momentum equation is further averaged around the loop (in θ) to form a circulation equation. One then obtains the following equations for the cross-sectionally averaged quantities, which we now call v, T, and S.

$$\rho \frac{dv}{dt} = \frac{g\rho\alpha}{2\pi}\int_{-\pi}^{\pi}\left(\cos(\theta)T - \frac{\beta}{\alpha}\cos(\theta)S\right)d\theta - \frac{2\mu}{R_p} \tag{4}$$

$$\rho C_p \frac{dT}{dt} \equiv \rho C_p\left(\frac{\partial T}{\partial t} + \frac{v}{R_0}\frac{\partial T}{\partial \theta}\right) = -2h(\theta)\frac{T-T_w}{R_p} + H(\theta) \tag{5}$$

$$\frac{dS}{dt} \equiv \frac{\partial S}{\partial t} + \frac{v}{R_o}\frac{\partial S}{\partial \theta} = \frac{D_s}{{R_0}^2}\frac{\partial^2 S}{\partial \theta^2} + \frac{D_s\Gamma}{{R_0}^2}\frac{\partial T}{\partial \theta^2} \tag{6}$$

Here C_p is the specific heat at constant pressure, t the time, h the heat transfer coefficient from the wall to the fluid, and μ the wall stress. In generating the right-hand side of (6) the boundary condition that $F_s = 0$ at the impermeable wall has been used. However, since there are no wall fluxes of solute, axial diffusion must be retained as the dominant molecular transport process for the solute. Equation (4) says that the average circulation is generated by the net buoyancy torque exerted by both salinity and temperature, and is retarded by viscous drag at the wall. In equation (5) heat is advected azimuthally by the velocity v, and diffuses in and out of the boundary with transfer coefficient h. As discussed below axial diffusion of heat can be lumped into h for the problem under consideration. Salinity varies along the wall, but there is no salt flux through it. In equation (6) a salt fluctuation is advected azimuthally, and can be generated by Soret diffusion and reduced by molecular diffusion in the azimuthal direction.

Hart [6] discusses various forms of equations (4) and (5) with applied boundary conditions that involve odd symmetry in θ and a general direction of gravity in the plane of the torus, as well as a heat transfer coefficient that varies in θ (although when h is not constant that model is only approximate). In order to focus on the Soret-driven component in this problem we will consider h to be constant, H to be zero, and $T_w(\theta)$ to be an odd function of θ, but even in each half plane $\theta \neq 0$ about $\theta = \pm\pi/2$. This last requirement means that it is possible to represent $T_w(\theta)$ as a sine series (as in equation (11)). In addition we take a linear drag law $\mu = C_d V v$ where C_d is the drag coefficient and $V = 2HR_0/\rho_0 R_p C_p$ is a velocity scale. We also use the scale $\Delta T = 2V^2 C_d/g\alpha R_p$ for temperature, the scale $\Delta T\alpha/\beta$ for salinity, and the scale R_0/V for time. With this nondimensionalization equations (4)–(6) become:

$$\frac{dv}{dt} = \mathrm{Pr}\left[-v + \frac{1}{\pi}\int_{-\pi}^{\pi}\cos(\theta)(T-S)d\theta\right] \tag{7}$$

$$\frac{\partial T}{\partial t} + v\frac{\partial T}{\partial \theta} = -T + \mathrm{Ra}T_d(\theta) \tag{8}$$

$$\frac{\partial S}{\partial t} + v\frac{\partial S}{\partial \theta} = -\tau\frac{\partial^2 S}{\partial \theta^2} + Q\mathrm{Ra}\frac{\partial^2 T}{\partial \theta^2} \tag{9}$$

Here we have introduced a nondimensional thermal driving function T_d with scale ΔT_d, such that $T_w = \Delta T_d \cdot T_d$. The parameter $\tau \equiv D_s/VR_0$ is a Lewis number. It is the ratio of the time for a signal to propagate around the loop by advection to the time it takes to do so by molecular diffusion. Pr = $R_0 C_d/R_p$ is essentially a Prandtl number, and Ra = $\Delta T_d/\Delta T$

Nomenclature

A = a stability region defined in Fig. 3
B = defined in Fig. 3
C = defined in Fig. 3
C_d = drag coefficient
C_p = specific heat at constant pressure
D = defined in Fig. 3
D_s = solute diffusivity
E = defined in Fig. 3
F_s = molecular solute flux, equation (2)
g = gravitational acceleration
h = wall heat transfer coefficient
H = wall or internal heating function, see Fig. 1
n = index for Fourier expansion
Pr = Prandtl number = $R_0 C_d/R_p$
Q = Soret parameter = $\Gamma\beta/\alpha$
Ra = Rayleigh number $\Delta T_d/\Delta T$
R_0 = radius of toroidal loop, Fig. 1
R_p = radius of fluid pipe, Fig. 1
S = solute or salinity fluctuation
S_0 = background or ambient salinity
t = time
T = temperature fluctuation
T_d = nondimensional thermal boundary forcing function
T_w = dimensional thermal forcing function, Fig. 1
U, U_n = salinity amplitude functions, equation (13)
v = azimuthal velocity
V = azimuthal velocity scale = $2hR_0/R_p C_p$
W, W_n = salinity amplitude functions, equation (13)
X = nondimensional circulation
Y, Y_n = temperature amplitude functions, equation (12)
Z, Z_n = temperature amplitude functions, equation (12)
α = coefficient of thermal expansion
β = volumetric expansivity
ΔT = temperature scale = $2V^2 C_d/g\alpha R_p$
ΔT_{dn} = thermal forcing amplitudes, equation (11), $\Delta T_d \equiv \Delta T_{d_1}$
Γ^* = Soret coefficient
Γ = $\Gamma^* S_0(1-S_0)$
κ = thermal conductivity
λ = growth rate for linear perturbations
μ = wall stress
ν = kinematic viscosity
ρ = density
ρ_0 = density at ambient conditions
θ = azimuthal angle, Fig. 1
τ = Lewis number = D_s/VR_0

is a Rayleigh number (Hart, [6]). The Soret effect enters through the parameter

$$Q \equiv \Gamma\beta/\alpha \tag{10}$$

With the symmetry arguments imposed on the driving function T_d, it can be represented as

$$T_d = \sum_{n=\text{odd}}^{\infty} -\Delta T_{dn} \sin(n\theta) \tag{11}$$

The problem can then be decomposed into Fourier harmonics. Writing

$$T = \sum_{n=1}^{\infty} Y_n \cos(n\theta) + Z_n \sin(n\theta) - \text{Ra} \sin(\theta) \tag{12}$$

$$S = \sum_{n=1}^{\infty} U_n \cos(n\theta) + W_n \sin(n\theta) + Q\text{Ra} \sin(\theta) \tag{13}$$

and setting $v \equiv X(t)$, and $\Delta T_d \equiv \Delta T_{d_1}$, equations (8)–(10) reduce to a five-component master problem for the modes $X = X_1$, $Y = Y_1$, $Z = Z_1$, $U = U_1$, $W = W_1$:

$$\frac{dX}{dt} = \text{Pr}[-X + Y - U] \tag{14}$$

$$\frac{dY}{dt} = -XZ - Y + \text{Ra}X \tag{15}$$

$$\frac{dZ}{dt} = XY - Z \tag{16}$$

$$\frac{dU}{dt} = -XW - \tau U - Q\text{Ra}X - \tau QY \tag{17}$$

$$\frac{dW}{dt} = XU - \tau W - \tau QZ \tag{18}$$

There is in addition, if ΔT_{dn} is nonzero for $n > 1$, an infinite set of slaved modes for $n > 1$ governed by:

$$\frac{dY_n}{dt} = -Y_n - nXZ_n \tag{19}$$

$$\frac{dZ_n}{dt} = -Z_n + nXY_n + \text{Ra}\frac{\Delta T_{dn}}{\Delta T_d} \tag{20}$$

and

$$\frac{dU_n}{dt} = -\tau U_n - XW - \tau QY_n \tag{21}$$

$$\frac{dW_n}{dt} = -\tau W_n + XU_n - \tau QZ_n \tag{22}$$

In what follows we shall concentrate on the master problem, since the motion $X(t)$ is completely determined by equations (14)–(18). If ΔT_{dn} is nonzero for $n > 1$, the slaved modes will contribute to the temperature and salinity fields in the loop, but will not affect the dynamics. It is worth mentioning here that as far as the dynamics are concerned, one can simply include axial diffusion of heat in this problem by rewriting $h \to h + \kappa R_p/2R_0^2$. Normally this correction will be of order $R_p^2/R_0^2 << 1$.

Note that if Ra is positive, the loop thermal boundary condition has an azimuthal wavenumber 1 component, and the bottom is hotter. Also, the dimensionless Soret parameter Q can be of either sign, since for some mixtures like isopropanol in water the Soret coefficient Γ^* is indeed multisigned depending on the percentage of alcohol in the mixture.

Before proceeding to analyze the master problem, it is useful to estimate the magnitude of the various nondimensional parameters for a typical physical realization of this problem. The following values are taken from Hurle and Jakeman [2] for an alcohol–water mixture: $D_s \simeq 10^{-5}\text{cm}^2\text{s}^{-1}$, $\alpha \simeq 2 \times 10^{-4}\,^\circ\text{C}^{-1}$, $\beta \simeq 0.1$, and $\Gamma^* \simeq 0.001\,^\circ\text{C}^{-1}$. Assuming the flows will be slow, an estimate of the transfer coefficient using thermal conduction as the dominant transfer mode gives $h/\rho C_p \simeq \kappa/R_p \simeq 0.001$ cm/s for a 1-cm pipe. $\text{Pr} = C_d V R_p/\kappa \simeq \nu/\kappa$ using viscous drag $C_d V \simeq \nu/R_p$. Thus Pr scales with the normal molecular Prandtl number for slow flow in the loop, and thus for typical liquid like water is about 7. The velocity scale V is then about $0.001 R_0/R_p \simeq 0.01$ cm/s for a 1-cm tube radius and a 10-cm loop radius. For this case the Lewis number τ is of order 10^{-4}. In many of the numerical integrations described below we use $\tau = 0.001$ to save com-

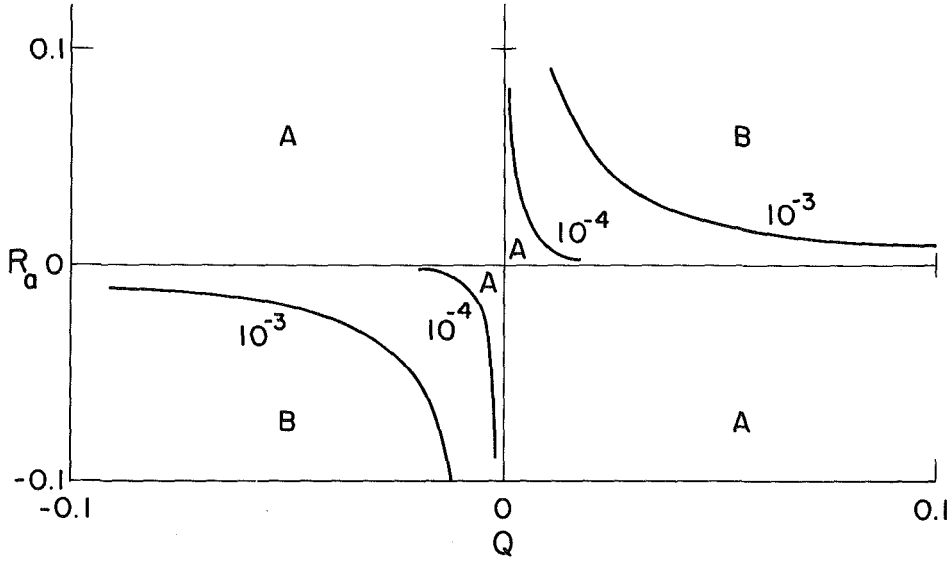

Fig. 2 Stability curves at small Ra and Q for values of τ as labeled; Pr = 6.7; (A) origin only real root and is stable; (B) origin monotonically unstable, Soret root exists and is stable

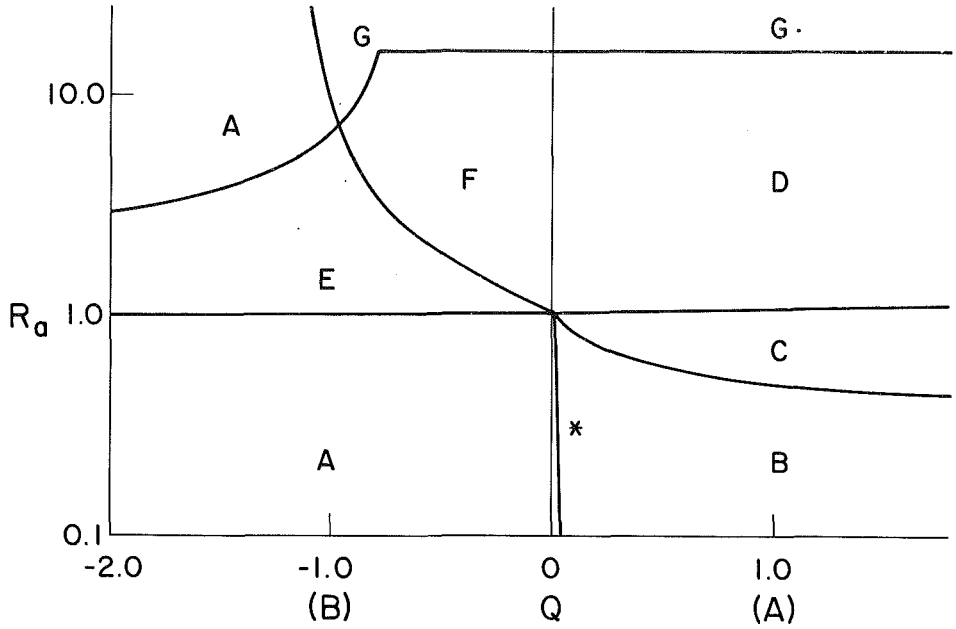

Fig. 3 Regime diagram for Pr = 6.7, $\tau = 0.001$; (*A*) and (*B*) as in Fig. 2; (*C*) origin monotonically unstable, Soret root exists but is unstable; (*D*) origin monotonically unstable, Lorenz root stable; (*E*) origin and Lorenz root stable, Soret root monotonically unstable; (*F*) origin overstable, Lorenz root stable, Soret root monotonically unstable; (*G*) all roots exist but are unstable; * curve's angle with vertical axis × 10

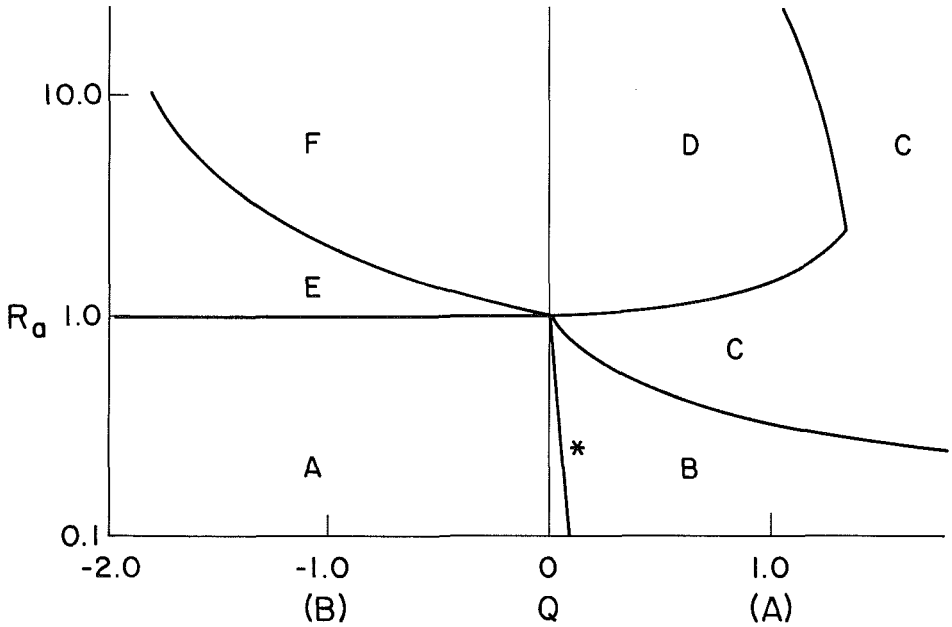

Fig. 4 Same as Fig. 3 except Pr = 1.0

puter time, as the structures of the motions are not significantly affected by this change. Finally, the Soret parameter Q ranges between 0 and about ± 0.5 depending on the background concentration S_0. Other fluids and geometries would give different values but these seem like a good starting point.

3 Steady Solutions and Stability

Steady (fixed-point) solutions are found from equations (14)–(18) by setting the time derivatives equal to zero. There is always one conductive steady solution at the origin in phase space, $X_0 = Y_0 = Z_0 = U_0 = W_0 = 0$. In addition there are finite-amplitude nontrivial steady roots given by:

$$Y_0 = \mathrm{Ra}\frac{X_0}{{X_0}^2+1} \tag{23}$$

$$Z_0 = X_0 Y_0 \tag{24}$$

$$U_0 = \mathrm{Ra}\frac{X_0}{{X_0}^2+1} - X_0 \tag{25}$$

$$W_0 = \frac{X_0 U_0}{\tau} - \mathrm{Ra}\frac{Q{X_0}^2}{{X_0}^2+1} \tag{26}$$

where X_0 is given by the real roots of

$${X_0}^2 = -\frac{1-\mathrm{Ra}+\tau}{2} \pm$$

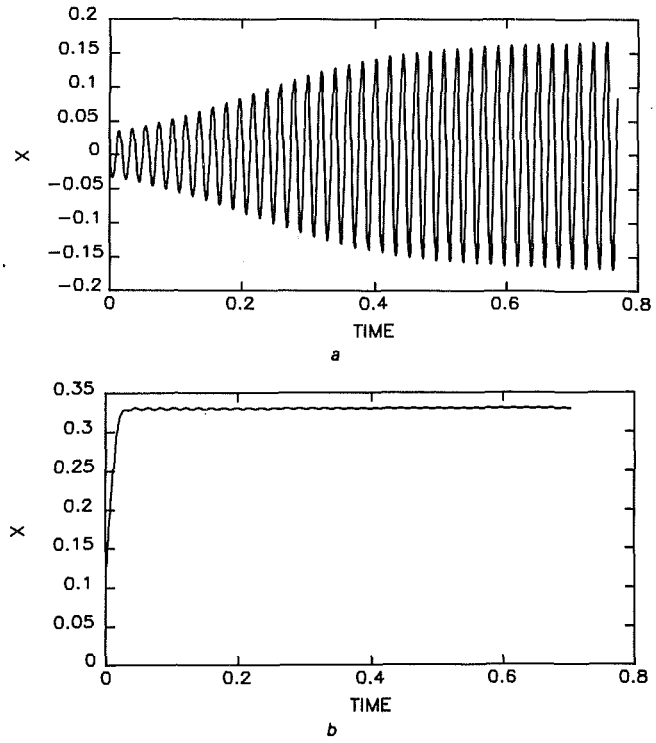

Fig. 5 Time traces for Pr = 6.7, $\tau = 0.001$, Q = −0.1, Ra = 0.11 in the F region of Fig. 3: (a) X(0) = 0.0001, (b) X(0) = 0.3; other starting values in this and subsequent figures are given by equations (23)-(26) using values of X(0) stated in the caption

$$\pm \frac{1}{2}\sqrt{(1-\mathrm{Ra}+\tau)^2+4(\tau \mathrm{Ra}Q(1+\tau)+\tau^2(\mathrm{Ra}-1)} \qquad (27)$$

Because the second term under the square root is of order τ when Ra and Q are order one, it is seen that there are two equal but opposite order one roots when Ra > 1, as well as a possible pair of smaller roots of order $\mathrm{Ra}Q\tau$. The former pair are the pure convection solutions discussed by Lorenz [10] in a different context. They arise when the driving is strong enough to overcome viscous and thermal diffusion and generate convection. Since the amplitude is strong, Soret diffusion is not effective, and Soret-induced salt gradients are stirred by the motion. The smaller pair of equal and opposite roots can occur when Ra < 1 depending on the sign of Q. We shall call the former pair of steady solutions the Lorenz root(s), and the latter the Soret root(s).

To investigate whether the steady solutions might be realized in an experiment one tests their stability by writing $X = X_0 + X'e^{\lambda t}$, etc., and linearizing equations (14)-(18). Solving the eigenvalue problem for λ provides information on instability ($\lambda_r > 0$) as well as whether the unstable perturbations grow monotonically ($\lambda_i = 0$) or as an overstable mode ($\lambda_i \neq 0$).

Figure 2 shows a stability diagram for small Ra and Q for two values of τ, 0.001 and 0.0001. In region A the conductive solution [the origin in the phase space of the differential system (14)-(18)] is stable. In region B the origin is unstable and orbits leave the origin monotonically and spiral into the stable Soret fixed point given by equations (23)-(27). In this narrow region of parameter space the orbits depend critically on τ. The quadrant with Ra < 0 (heated upper half of the loop) and $Q > 0$ (salt driven to the bottom) is always stable (conductive). The quadrant with Ra < 0 and $Q < 0$ always seems to approach a steady solution for Ra $\gtrsim -15$. Most of the interesting behavior occurs at positive Rayleigh numbers.

Figure 3 shows that over a wider Ra-Q space there is an extremely rich range of behavior possible. These curves

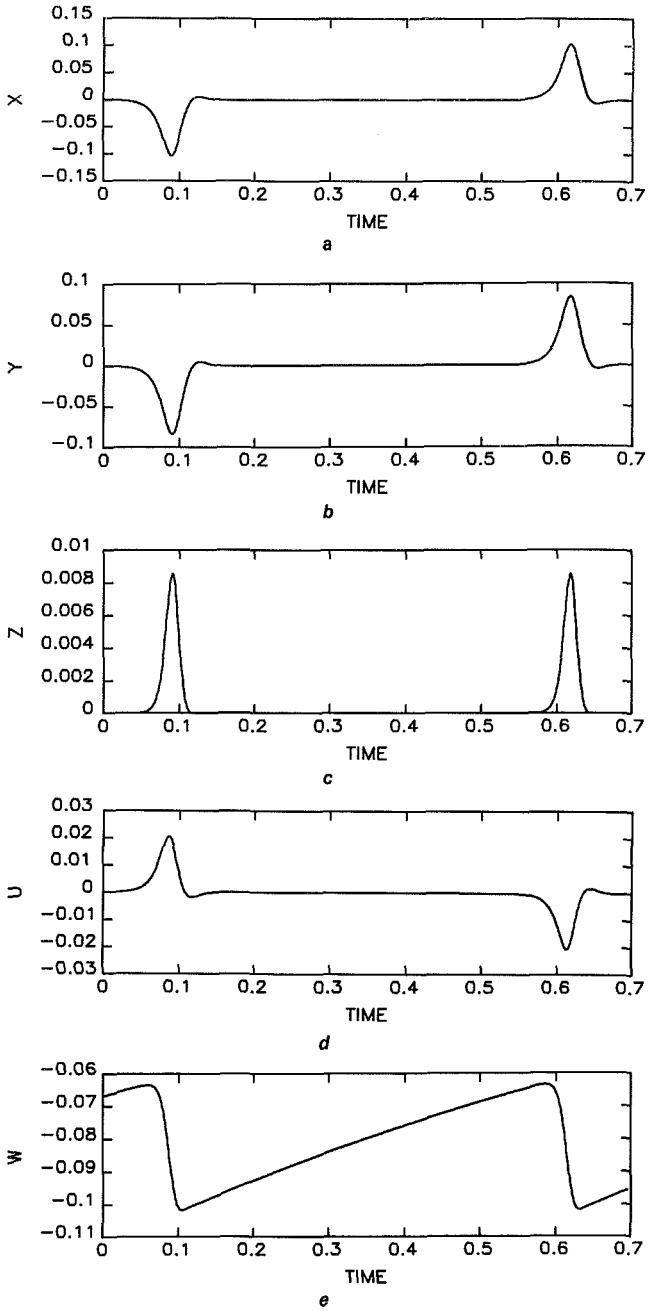

Fig. 6 A portion of the time trace of all variables for Pr = 6.7, $\tau = 0.001$, Q = 0.1, Ra = 0.825, X(0) = 0.01

depend somewhat on Prandtl number. But as Fig. 4 shows, most of the structure of Fig. 3 remains. Except for the range near the origin of Fig. 3, changing τ to 0.01 or 0.0001 makes little or no perceptible difference to these diagrams. The bifurcation line labeled with an asterisk represents an extension of the upper right-hand quadrant of Fig. 2. This line gives the boundary between the conductive state and monotonic convection. Since the "salt" diffusivity is very small, a weak Soret flux can reduce the critical Rayleigh number drastically below that for single-component thermal convection. This is reflected in the steep slopes of the starred lines.

The case $Q = 0$ has been studied by Lorenz [10], Malkus [4], and investigated experimentally by Gorman et al. [9]. In the D region steady solutions are indeed found in numerical integrations of the equations. In the G region where there are no stable fixed points, chaotic oscillations are found and observed.

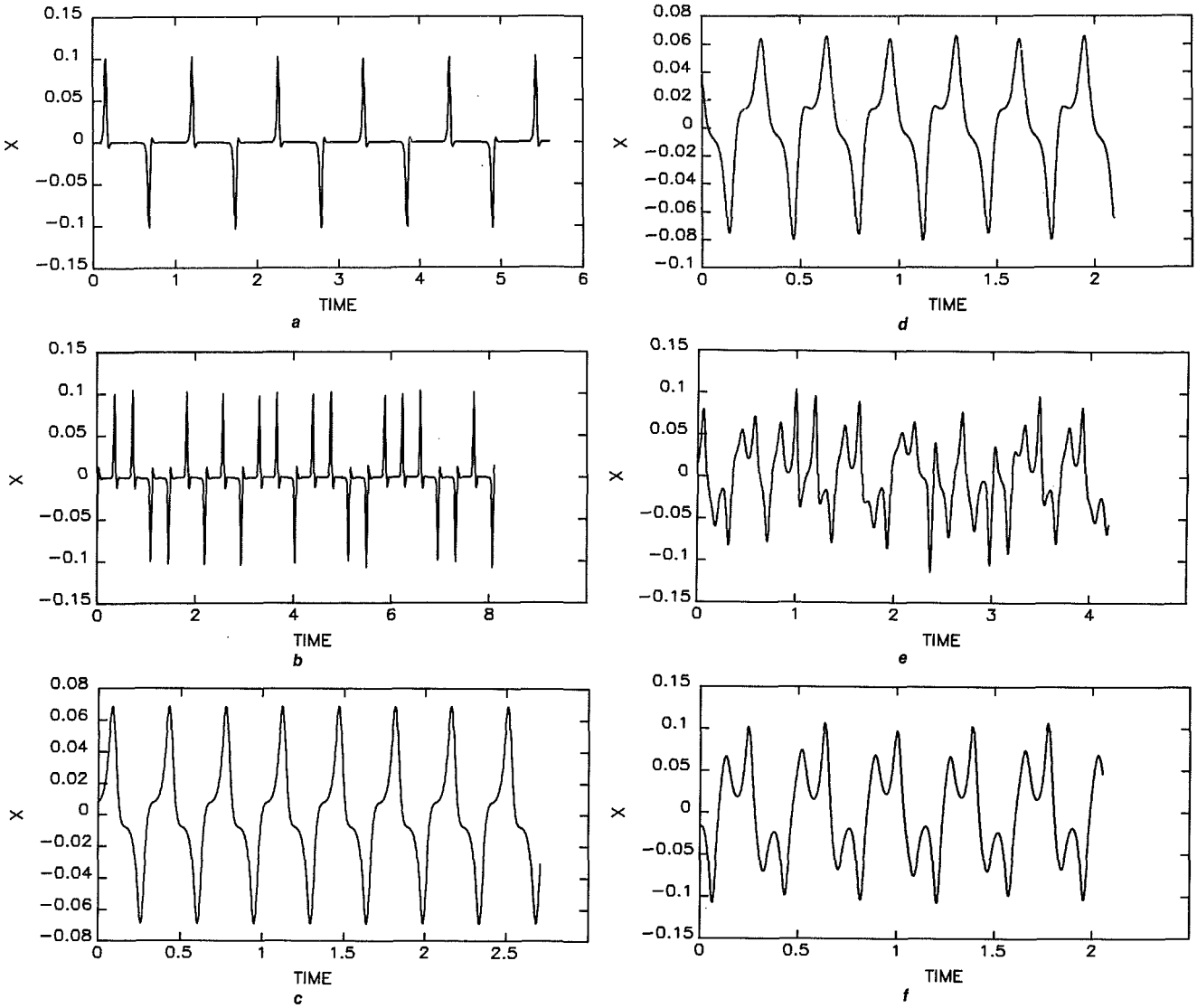

Fig. 7 Asymptotic time traces for Pr = 6.7, $\tau = 0.001$, $Q = 0.1$ in the C region of Fig. 3; $X(0) = 0.0001$: (*a*) Ra = 0.825; (*b*) Ra = 0.879; (*c*) Ra = 0.920; (*d*) Ra = 0.930; (*e*) Ra = 0.950; (*f*) Ra = 0.974

The $Q<0$ region of Fig. 3 has been studied in a parallel-plate single-wave convection model in [1, 3], as well as in Da Costa et al. [11]. Although the dimensionless parameters in the parallel-plate problems involve different parameters than for the thermosyphon, the equations are essentially the same. Knobloch [12] has also shown that the Soret problem can, apart from some difficulties at the boundaries, be transformed into the thermohaline problem where constant salinities are usually imposed at heated horizontal walls and the Soret effect ignored. At $Q=-0.5$, say, as Ra crosses 1.0 two steady states are possible. One has either no motion or convection depending on the initial disturbance. Upon crossing the curve bounding the F and E regions, the origin becomes overstable. If the initial perturbation is small the growing oscillations equilibrate to a limit cycle. These were seen by Hurle and Jakeman [2]. If the perturbation is large, the phase space orbit spirals into the Lorenz fixed point. This effect is illustrated in Fig. 5, which shows a pair of numerical integrations (the method is described in section 4). Each is started from the initial condition on X given in the caption, with the other starting values for Y through W being given by equations (23)–(26). As Ra is raised, when the envelope of the small amplitude oscillations meets the unstable branch of the Soret fixed point, the limit cycles cease to exist. Above this value, equilibration to steady convection is predicted. At larger values of $-Q$ chaotic oscillations can be found, not only where the G region dips down but near the F–E boundary as well. These notions are discussed in more detail in [3, 11].

4 Numerical Solutions for $Q > 0$

When $Q > 0$ and Ra $\lesssim$ 1.5 the motions are dominated by the thermal convective modes. Of interest here, though, is the region of positive Q where Ra is about 1. In particular it is natural to ask what will happen in the C region of Fig. 3 where there are no stable fixed points. This question is most easily addressed by numerically integrating equations (14)–(18) starting from an initial condition (i.c.) specified on X, using equations (23)–(26) to arbitrarily specify starting conditions on the other variables. A fourth-order variable-step Runge-Kutta scheme contained in the NCAR (National Center for Atmospheric Research) scientific subroutine package is used. Typically the time step is 0.1 (0.0001 in molecular diffusion units at $\tau=0.001$), and 65,000 points take about 30 s on a VAX 11-750.

Figure 6 shows the asymptotic character of a solution just above the B–C dividing line at $Q=0.1$. There is a stable relaxation oscillation of a rather different character than the buoyancy oscillations that occur for negative Q (e.g., Fig. 5*a*). Physically, the conductive state in the present situation is cold

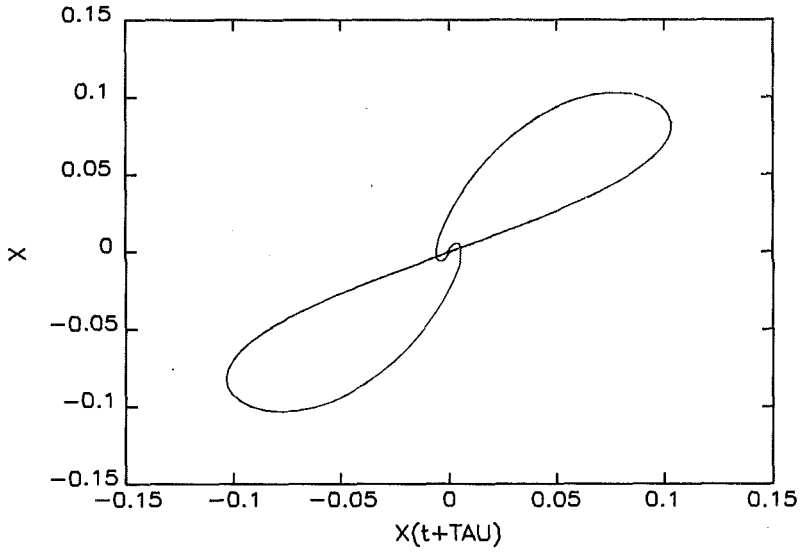

Fig. 8a

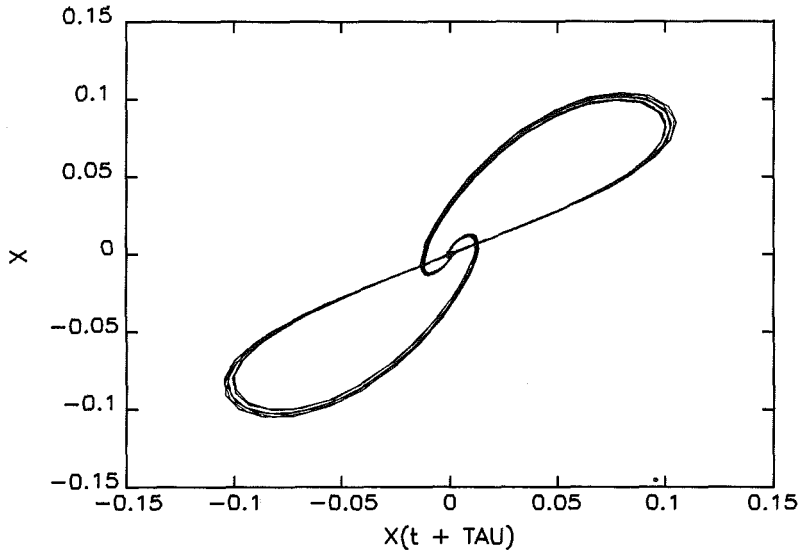

Fig. 8b

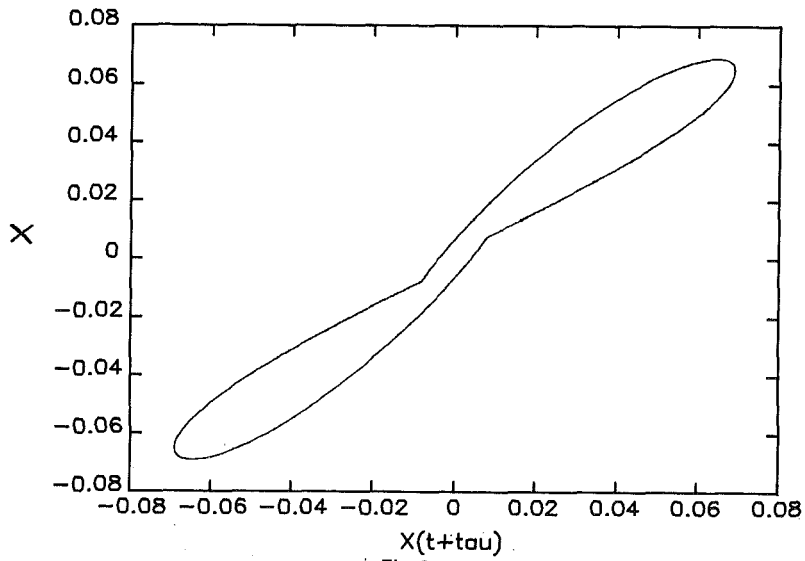

Fig. 8c

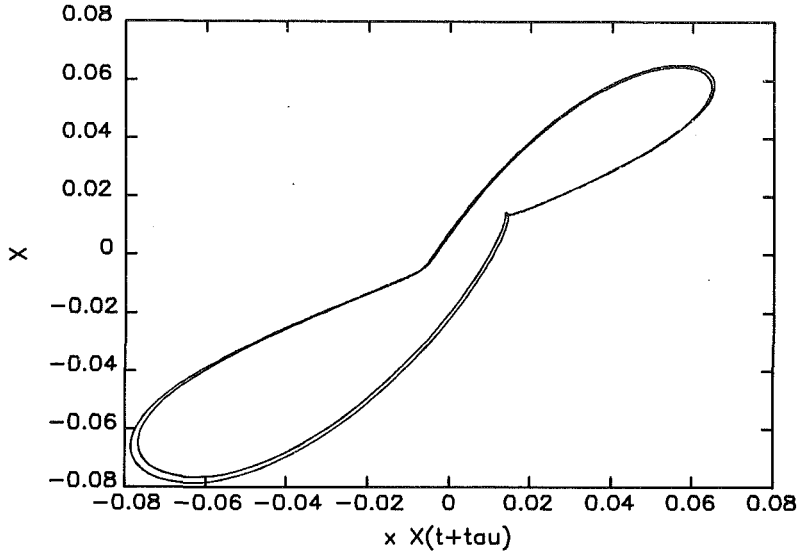

Fig. 8*d*

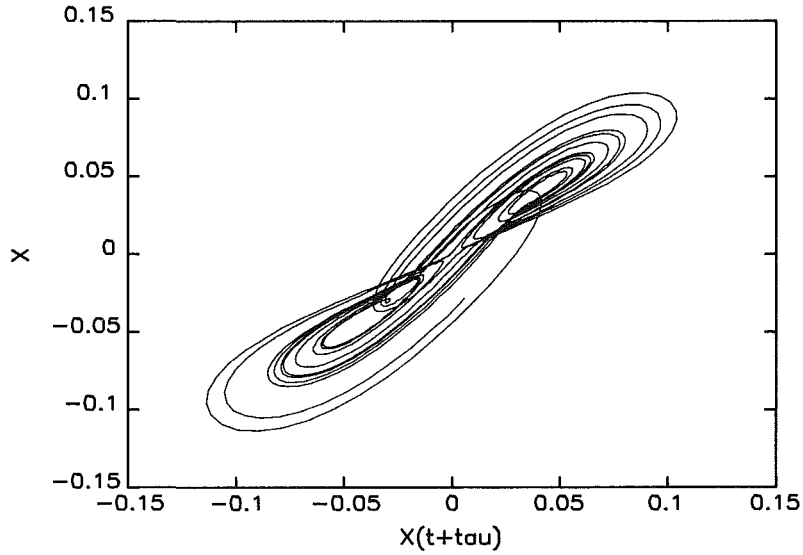

Fig. 8*e*

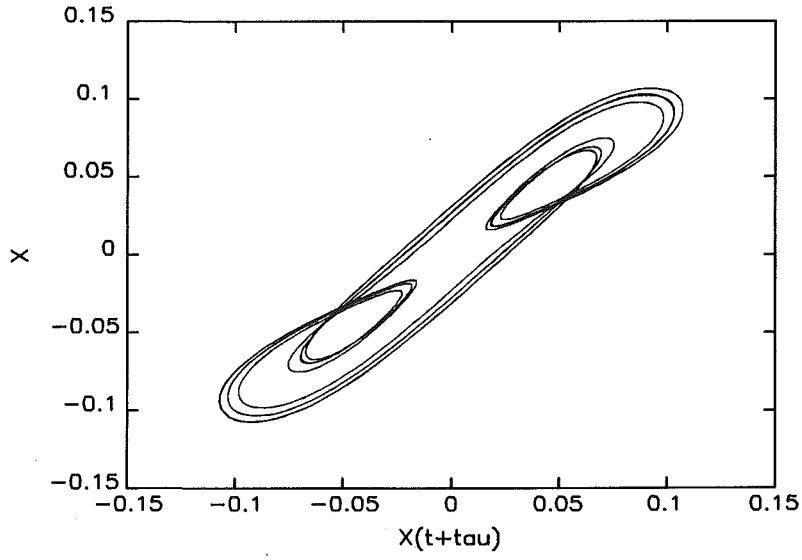

Fig. 8*f*

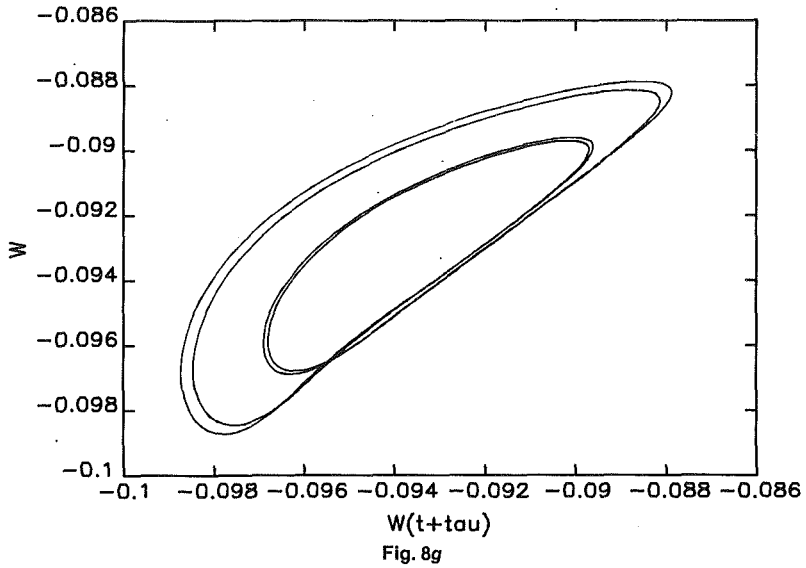

Fig. 8g

Fig. 8 Projected attractors for cases (a) through (f) of Fig. 7 respectively; Fig. 8(g) shows the W attractor for case 7(d) Ra = 0.930

near the top due to the imposed thermal boundary condition and salty on the top due to Soret diffusion. The oscillation mechanism is as follows. At $t \simeq 0.08$ a clockwise perturbation amplifies, and the cool-salty fluid starts to fall to the right. Imagine riding in the loop with this fluid. Y goes negative and U goes positive as the heat and salt maxima reach $\theta = 0$. At this time the buoyancy torque is large. However, as this pulse is propagating around the loop heat is diffusing in from the walls, raising the temperature and hence the component of buoyancy due to temperature. The motion is thermally stable (Ra < 1) so as the heat is added it slows down. Salt has a very low diffusivity compared to heat, so it is basically advected with the flow. By the time the initial cold-salty parcel reaches the bottom of the loop, its initial coldness has been removed by diffusion. Thus, at $t \simeq 0.12$, $X = Y = Z = U = 0$ but $W < 0$. The fluid comes to rest (with a slight buoyancy oscillation as the salty parcel overshoots its stable equilibrium at the bottom of the loop). The steady conductive fields in equations (12), (13) are not shown in Fig. 6, but when (QRa + W) < 0 the total salt distribution is bottom heavy (stable). That is, the stationary state at $t \simeq 0.12$ is statically stable because although thermal conduction has re-established hot fluid at the bottom, the stabilizing salt parcel is now also sitting at the bottom of the loop. However, Soret diffusion in the conductive temperature field will now proceed to drive the salt away from the bottom toward the top of the loop. This generates the upslope of the sawtooth of Fig. 6(e). When enough of the salt is driven to the top, instability sets in and another relaxation oscillation begins. Noting that Fig. 6 (and all subsequent figures) have a time axis rescaled by τ so that one time unit $= \tau^{-1}$ nondimensional time units, it is seen that the period of the relaxation oscillation is on the salt diffusion time scale.

Figure 7 illustrates what happens after transient decay for several Rayleigh numbers spanning the C region of Fig. 3. In Fig. 7(a) several cycles of the relaxation oscillation just described are shown. At a slightly higher Rayleigh number (Fig. 7b), the pulses start to occur in single signed bursts of unpredictable lengths. It appears that when Ra is larger, the system is extremely sensitive to the tails of the pulses (or, as can be verified in the numerical solutions, very sensitive to small changes in the initial conditions). When the Soret diffusion of salt just destabilizes the almost motionless system (e.g., at $t = 0.6$ in Fig. 6) any residual motion due to buoyancy oscillations will be amplified in its own direction. Indeed

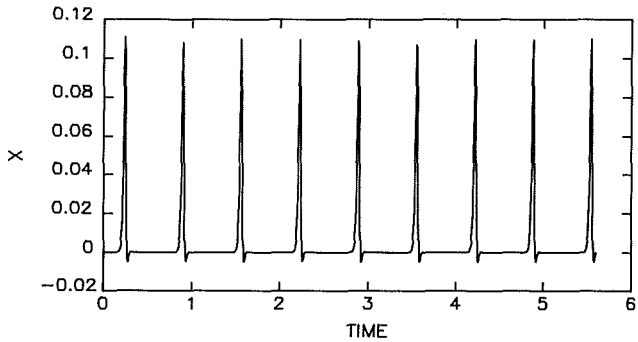

Fig. 9 Highly asymmetric oscillation; Pr = 6.7, $\tau = 0.001$, $Q = 0.1$, Ra = 0.825, $X(0) = 0.1$

when the Rayleigh number is increased further, the overshooting tails of the pulses, caused by the salt parcel sloshing past the bottom of the loop and then accelerating by buoyancy in the opposite direction, get large enough to communicate their sense of direction on the next cycle. Thus, as Fig. 7(c) shows, the unpredictable relaxation oscillations give way to a periodic oscillation. Note that this oscillation is symmetric about zero and every minimum has the same value, thus giving a period-1 response.

At still higher Rayleigh number the oscillation period-doubles, then period-doubles again. Figure 7(d) shows a typical time trace in such a period-doubling sequence. Compared with Fig. 7(c) it appears that the oscillation repeats itself every other cycle. In fact every fourth peak is now the same and there have been two period-doublings between Ra = 0.92 and 0.93. This is hard to see in the $X(t)$ trace where every other peak seems equivalent, but the period-4 response becomes obvious when one looks at either the Z or W variable (see Fig. 8g). The motion is also asymmetric. With an initial condition opposite in sign, one finds a solution with $X \rightarrow -X$. Indeed the equations (14)–(18) are invariant under the transformation $X \rightarrow -X$, $Y \rightarrow -Y$, $Z \rightarrow Z$, $U \rightarrow -U$, $W \rightarrow W$. As the inertial overshoots becomes larger (Ra↑) the oscillation period shortens because the stabilizing salt pool doesn't have to diffuse all the way from the bottom of the loop to the top. However, the system memory time is still associated with the salt diffusion. This leads to the periodicity over more than one cycle.

After a period-doubling sequence of bifurcations in which periodicity occurs over successively larger numbers (2^m, $m=1,2,3\ldots$.) of cycles, at Ra $=0.931\pm0.0005$ the motion becomes chaotic again. This time it is a result of a destabilization of the limit cycles. The physics here is more obscure, although mathematical descriptions in terms of heteroclinic bifurcations have been given [11] for $Q<0$. As the bifurcation line C-D is approached the motion becomes periodic again, with odd-cycle periodicity (Fig. 7*f*). As Ra is increased further, there are more bifurcations involving various periodic orbits, and thence to steady Lorenz convection.

These motions are conveniently illustrated using a phase space reconstruction. A projection of the phase space orbits of the solutions is shown in Fig. 8, where $X(t)$ is plotted versus $X(t+\tau)$, τ being an arbitrary constant. If sets thus produced attract nearby initial orbits they are called attractors. The trajectories show the subharmonic and chaotic motions discussed in the previous paragraphs. In particular, Fig. 8(*g*) shows the W attractor corresponding to Figs. 7(*d*) and 8(*d*). The reconnecting 4-loop signifies a period-4 limit cycle. The chaotic solutions that evolve out of the period-doubling sequence appear to be of a rather different character than those at lower Ra (e.g., compare Figs. 7*b* and 7*e*). Recall that since $\mathrm{Ra}=0.930<1$ the thermal conductive field by itself is stable. Because of the low salt diffusivity as soon as $(Q\mathrm{Ra}+W)>\tau(1-\mathrm{Ra}-Z)\simeq 0$ the static two-component conductive field will be unstable. Since Z is much less than one for these motions, one can see that the W orbits cycle around the neutral stability value QRa based on salt alone.

As is the case when $Q<0$, there are multiple branches of the solution topology for $Q>0$. Figure 9 shows a highly asymmetric oscillation which one gets when starting from a large initial condition. This should be compared with the symmetric mode in Fig. 7(*a*).

5 Conclusions

A fluid loop model of Soret convection has been constructed. For negative Soret coefficient the predicted flows are similar to previous thermohaline fluid loop or parallel-plate models. For positive Soret coefficient and Rayleigh number greater than one, the flows are primarily thermal, with solute diffusion playing little role. However, if Ra is somewhat less than one a wide variety of behavior is possible including steady flow, period-doubling cascades, and chaos. The fundamental oscillation mechanism is a relaxation mode in which a heavy statically stable solute pool in the lower (heated) section of the loop is driven toward the top by Soret diffusion, thereby giving rise to an unstable buoyant motion.

In view of the success of one-dimensional thermosyphon theory in qualitatively describing supercritical motions for a single component laboratory fluid, it is natural to suggest a two-component thermosyphon experiment. The predicted motions are very weak, so the usual condition that there be no negative temperatures or salinities should be satisfied. On the other hand the oscillation periods are long, scaling with D_s/V^2. In a small torus (e.g., $R_0=1$ cm, $R_p=0.2$ cm) V could be as large as 0.1 cm/s, giving periods of order 1000 s. In a larger apparatus of fixed aspect ratio R_0/R_p, the time increases with ${R_p}^2$. In a 1-cm pipe, the oscillations would probably show up as a slow drift (period $\simeq 10^5$ s), and could perhaps be misinterpreted as being externally caused.

Acknowledgments

This research was sponsored by NASA under contract NAS-8-31958.

References

1 Schecter, R. S., Velarde, M. G., and Platten, J. K., "The Two-Component Benard Problem," *Adv. Chemical Physics*, Vol. 26, 1974, pp. 265-301.

2 Hurle, D. T. J., and Jakeman, E., "Soret-Driven Thermosolutal Convection," *J. Fluid Mech.*, Vol. 47, 1971, pp. 667-687.

3 Platten, J. K., and Chavepeyer, G., "An Hysteresis Loop in the Two-Component Benard Problem," *Int. J. Heat and Mass Transfer*, Vol. 18, 1975, pp. 1071-1075.

4 Malkus, W. V. R., "Non-periodic Convection at High and Low Prandtl Number," *Mem. Soc. Roy. Sci. Liege*, Vol. 4, 1972, pp. 125-128.

5 Siegmann, W. L., and Rubenfeld, L. A., "A Non-linear Model for Double Diffusive Convection," *S.I.A.M. Applied Math.*, Vol. 29, 1975, pp. 540-557.

6 Hart, J. E., "A New Analysis of the Closed Loop Thermosyphon," *Int. J. Heat and Mass Transfer*, Vol. 27, 1984, pp. 125-136.

7 Creveling, H. F., DePaz, J. F., Baladir, J. Y., and Schoenhals, R. J., "Stability Characteristics of a Single-Phase Free Convection Loop," *J. Fluid Mech.*, Vol. 67, 1975, pp. 65-84.

8 Damerell, P. S., and Schoenhals, R. J., "Flow in a Toroidal Thermosyphon with Angular Displacements of Heated and Cooled Sections," *J. Heat Transfer*, Vol. 101, 1979, pp. 672-676.

9 Gorman, M., Widmann, P. J., and Robbins, K. A., "Chaotic Flow Regimes in a Convection Loop," *Physical Review Letters*, Vol. 52, No. 25, 1984, pp. 2241-2244.

10 Lorenz, E. N., "Deterministic Non-periodic Flow," *J. Atmos. Sci.*, Vol. 20, 1963, pp. 130-141.

11 Da Costa, L. N., Knobloch, E., and Weiss, N. O., "Oscillations in Double-Diffusive Convection," *J. Fluid Mech.*, Vol. 109, 1981, pp. 25-43.

12 Knobloch, E., "Convection in Binary Fluids," *Physics of Fluids*, Vol. 23, 1981, pp. 1918-1920.

Two-Dimensional Periodic Natural Convection in a Rectangular Enclosure of Aspect Ratio One

D. G. Briggs
Mem. ASME

D. N. Jones
Assoc. Mem. ASME

Department of Mechanical and Aerospace Engineering, Rutgers University, New Brunswick, NJ 08903

A two-dimensional rectangular cavity of aspect ratio one is studied experimentally using a laser-doppler velocimeter. The enclosure is air filled and consists of two vertical walls at unequal isothermal temperatures and two connecting horizontal walls with temperatures varying linearly between the two vertical surfaces. This study clearly defines the existence of periodic laminar flow regimes detectable at Ra numbers above 0.3×10^7. These periodic variations in velocity are induced by the upper and lower boundary conditions. The envelopes of vertical and horizontal velocity fluctuations are reported as a function of position for Rayleigh numbers of 0.25×10^7, 0.50×10^7, and 0.85×10^7. In addition, the effect of Ra number on frequency of flow is reported.

Introduction

Two-dimensional buoyancy-driven flows within rectangular cavities have received much attention because of the many practical heat transfer situations in which they arise and because their geometric simplicity makes numerical simulation attractive. Most of the studies have dealt with cavities which have high aspect ratios. Less attention has been directed to buoyancy flows taking place in cavities of low aspect ratio, i.e., aspect ratio less than or equal to one. Experimental work includes that of Sernas, Fletcher, and Rago [1], Lee and Sernas [2], Arnold, Catton, and Edwards [3] and more recently Kamotani, Wang, and Ostrach [4], and Wirtz, Righo, and Zirilli [5]. All of this work was conducted with either adiabatic upper and lower wall temperatures; or with upper and lower wall temperatures tending to stabilize the flow, i.e., cooled from below or heated from above. References [6-15] constitute a partial list of related numerical and analytical studies. Much of this work was limited to lower Rayleigh numbers due to numerical instabilities. Also, the upper and lower temperature boundary conditions were again chosen so as to induce stability in the fluid. An exception was the work of Fraiken et al. [6] who used a rectangular cavity of aspect ratio one and employed a $\kappa-\epsilon$ turbulence model. The cavity used the dynamically unstable boundary condition of linear temperature between the hot and the cold vertical walls. The numerical scheme employed was iterative and could only report on average steady state which their method described as turbulent at a Rayleigh number of 10^7.

The current work was prompted by attempts to predict the heat transfer numerically in cavities with aspect ratio of one or less and which have a destabilizing horizontal surface temperature, i.e., linear between vertical isothermal walls as shown in Fig. 1; and by experimental observations of Sernas [16]. The numerical solutions seemed to have no steady state at Rayleigh numbers around 10^7.

A schlieren study conducted by the authors (unpublished) for a cavity with aspect ratio of one and linearly varying upper and lower horizontal surface temperatures indicated the flow at Rayleigh numbers around 5×10^6 and higher was two dimensional, circulatory, and periodic. The slow period, around 0.5 Hz and the apparent large variation in temperature, heat transfer, and velocity motivated the work reported herein.

Apparatus

The air-filled enclosure is shown schematically in Fig. 2. The isothermal vertical walls were constructed from aluminum plates to form a cavity 15.0 cm high by 15.0 cm wide by 19.6 cm thick. A continuous convoluted channel was milled into the back of each vertical plate. This passage was sealed with a neoprene gasket and cover plate to produce a circulating water passage. The vertical plates were maintained at different fixed temperatures by water provided from constant temperature baths.

The horizontal 15.0 cm by 19.6 cm steel plates were bolted directly to the vertical end plates to ensure good thermal contact. They were insulated from the surroundings and an

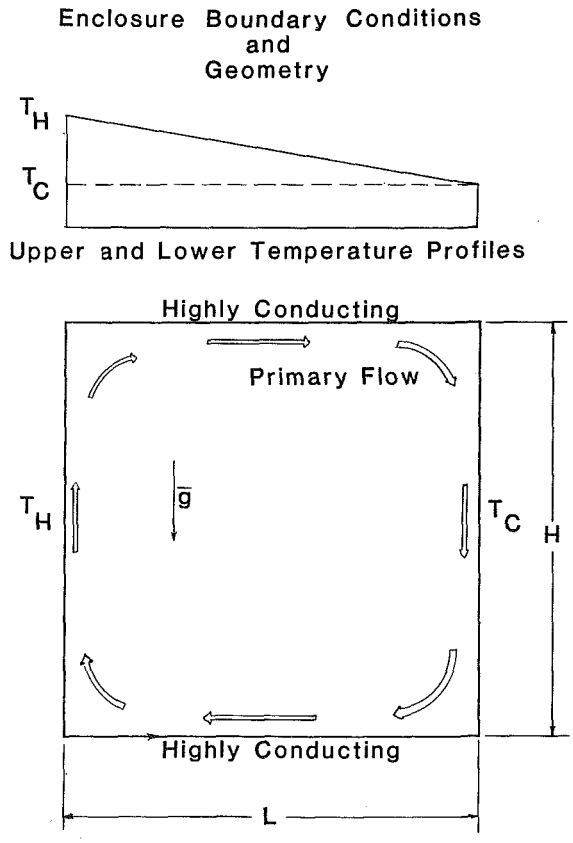

Fig. 1 Enclosure geometry and boundary conditions

Contributed by the Heat Transfer Division for publication in the JOURNAL OF HEAT TRANSFER. Manuscript received by the Heat Transfer Division March 6, 1984. Paper No. 82-WA/HT-64.

approximately linear temperature gradient was achieved by conduction through the steel plates.

Temperatures of both the horizontal and vertical walls were monitored by 16 judiciously located thermocouples which indicated uniformity within 0.3°C on the vertical walls and at successive intervals along the horizontal walls. The temperature difference between the two vertical plates was measured directly by a differential thermocouple mounted in the center of each vertical plate and recorded on a stripchart.

Double-paned glass windows were installed as the enclosure end plates. Initial trials with single glazing end plates and with one or the other of the vertical plate temperatures held close to ambient significantly altered the two dimensionality of the enclosure flow. Installation of the double-paned windows and operation of the system centered about the ambient temperature minimized experimental variations due to interaction with the surroundings.

The windows were separated from the enclosure walls by a

Cutaway View of Enclosure

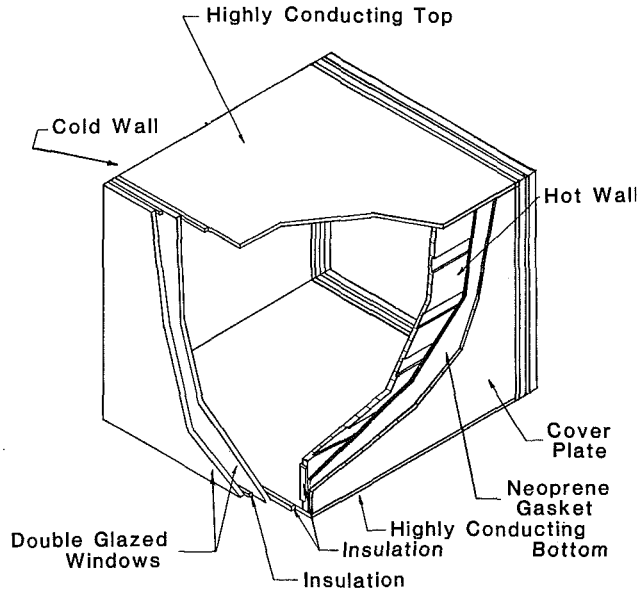

Fig. 2 Cutaway view of enclosure

Schematic of Apparatus

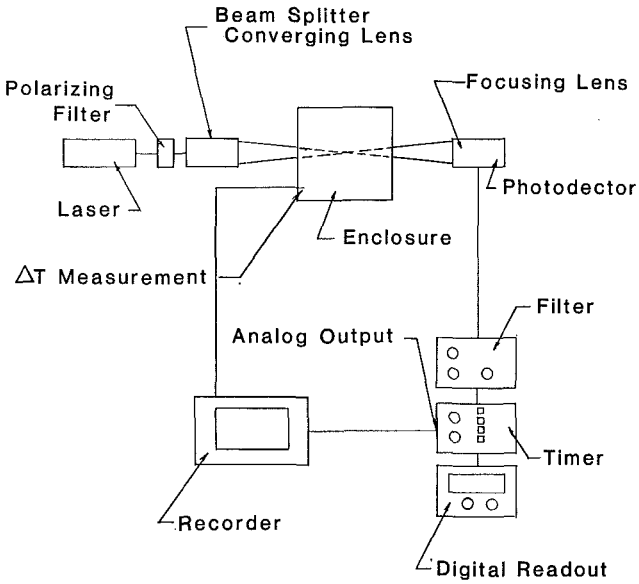

Fig. 3 Schematic of apparatus

Startup Trace

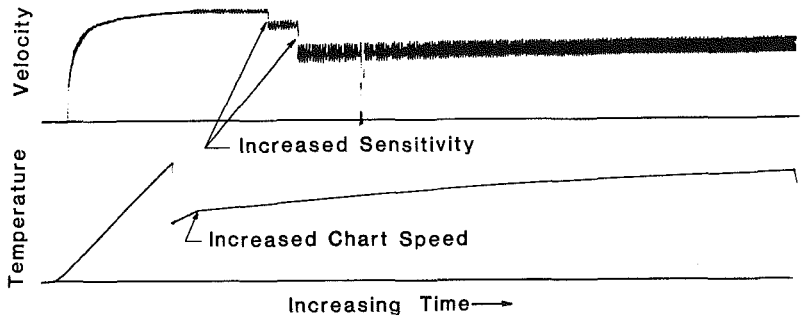

Fig. 4 Startup trace

Nomenclature

Ar = aspect ratio of the enclosures H/L
f = frequency in cycles per second
f_{ND} = normalized frequency = $fL/\sqrt{g\beta\Delta TH}$
g = gravitational constant
Gr = Grashof number based upon width = $g\beta\Delta TL^3/\nu^2$
H = height of the enclosure
K = thermal conductivity
L = width of the enclosure
Pr = Prandtl number = ν/α
Ra = Rayleigh number based upon width = $g\beta\Delta TL^3/\nu\alpha$
T_H = hot wall temperature
T_C = cold wall temperature
ΔT = temperature difference = $T_H - T_C$
U = horizontal velocity component
U_c = $\sqrt{g\beta\Delta TH}$
V = vertical velocity component
x = horizontal coordinate
y = vertical coordinate
α = thermal diffusivity
β = volumetric expansion coefficient
ν = kinematic viscosity = μ/ρ
μ = dynamic viscosity
ρ = density of air

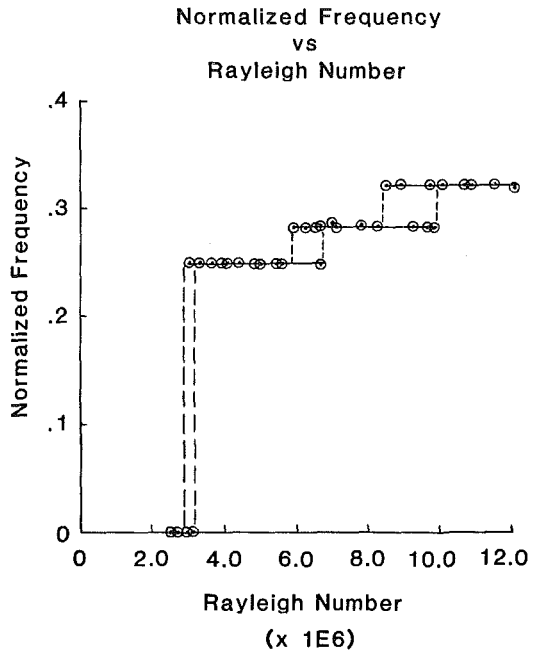

Fig. 5 Normalized frequency variation with Rayleigh numbers

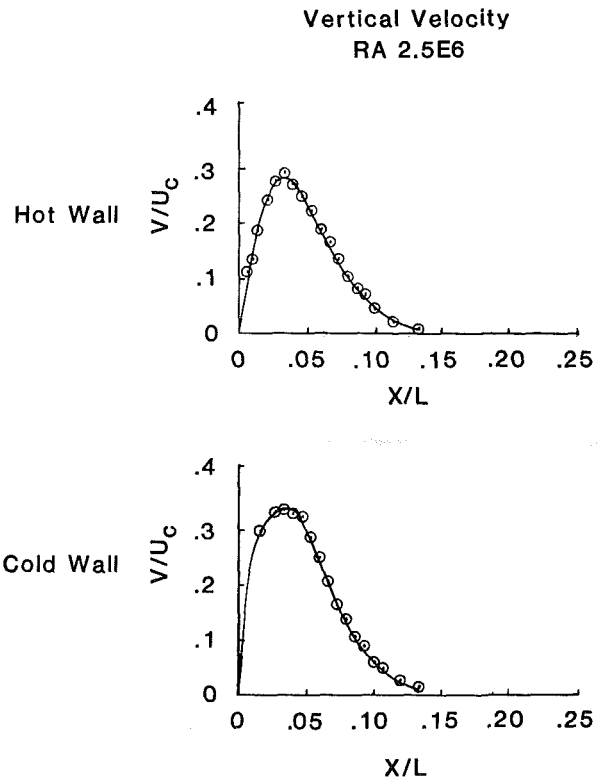

Fig. 6 Vertical velocities at Rayleigh number 2.5 × 10^6

thin strip of rubber insulation to minimize conduction from the metal walls to the glass windows.

The experimental setup is illustrated schematically in Fig. 3. It consisted of a Thermo-Systems single color Laser-Doppler Velocimeter (LDV) System, *x-y* traversing table, two-dimensional enclosure, and Gould recorder. The LDV was operated in forward scatter dual beam mode, with electronic pedestal removal. Flow reversals were not detectable with the system. An analog signal proportional to the flow velocity was provided by the LDV timer. The optical components were assembled on an optical bench, and the enclosure traversed

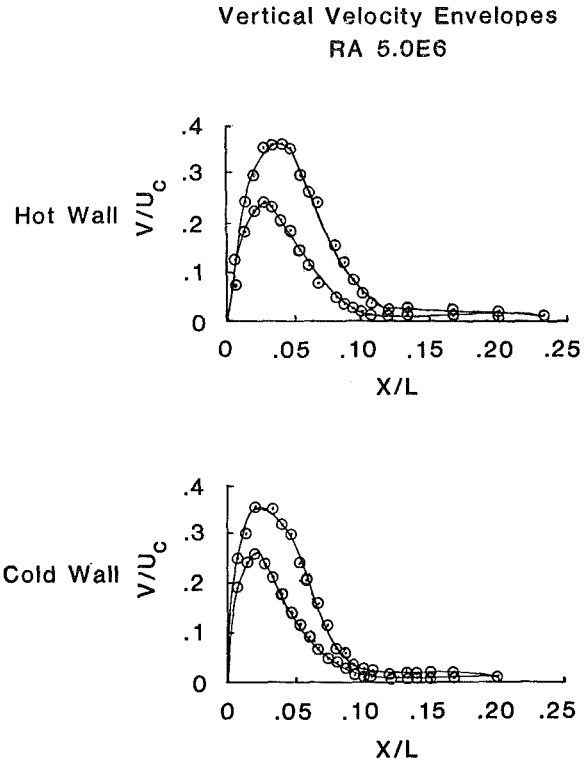

Fig. 7 Vertical velocity envelopes at Rayleigh number 5.0 × 10^6

relative to the beam in order to obtain velocity profile data. Moving the cavity in this manner did not result in any discernible pertubation of the flow. All profiles reported were taken at the center of the enclosure walls in order to minimize the effects of end boundary layers.

Experimental Procedure

The constant-temperature circulating baths were adjusted to provide the desired Rayleigh number and a small amount of cigarette smoke was introduced into the cavity. Steady-state operation was determined by monitoring all wall temperatures and the differential temperature between the vertical walls.

A side-by-side recording of the differential wall temperature and LDV analog output provided the time variation of the velocity at various Ra. The frequency of velocity fluctuations was determined by counting the number of cycles over a measured period of time on the strip chart.

An error analysis showed that the Rayleigh number could be determined within 1 percent. Physical properties of air were taken from [17] at 24°C.

The frequency of flow variation reported later was taken from measurements near the hot wall, but once periodic flow was initiated, the frequency of variation could be measured nearly anywhere within the wall boundary layer and determined within an error of 1 percent, as could the magnitudes of the flow velocities. The position at which measurements were taken could be determined within 0.20 mm.

A typical startup trace is shown in Fig. 4. The air within the cavity is initially at ambient temperature and stationary. At time t_0, the hot and cold water circulating baths were turned on. As the baths approach the set point temperature, the ΔT between the walls increased and a circulating flow was initiated. Depending on the Rayleigh number, periodic fluctuations in the velocity would appear and grow in amplitude until a quasi-steady state was reached.

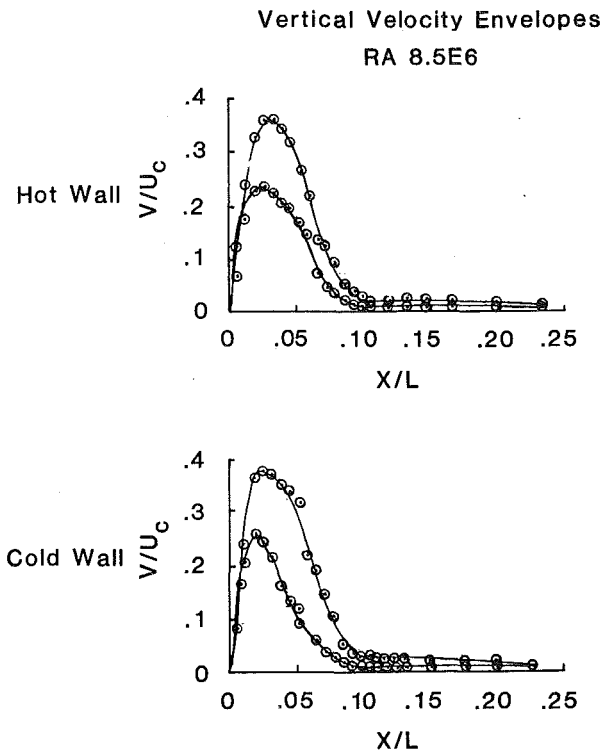

Fig. 8 Vertical velocity envelopes at Rayleigh number 8.5 × 10^6

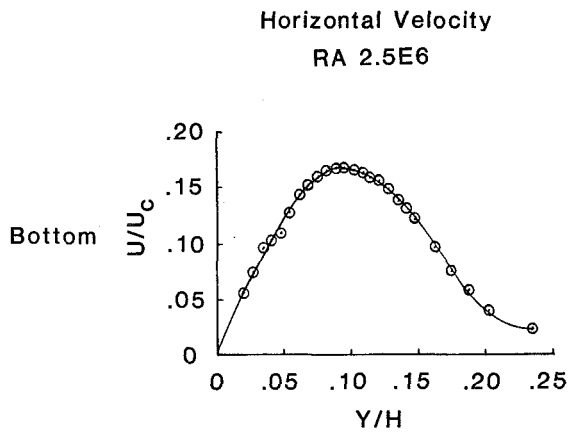

Fig. 9 Horizontal velocity at Rayleigh number 2.5 × 10^6

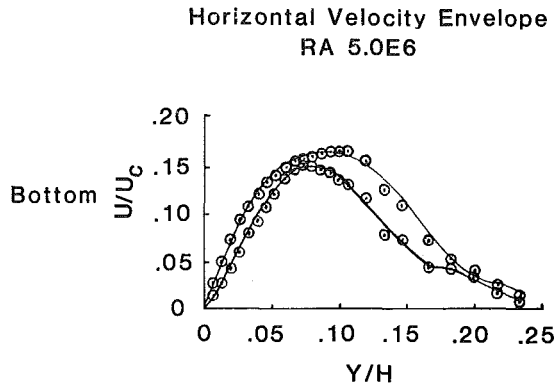

Fig. 10 Horizontal velocity envelope at Rayleigh number 5 × 10^6

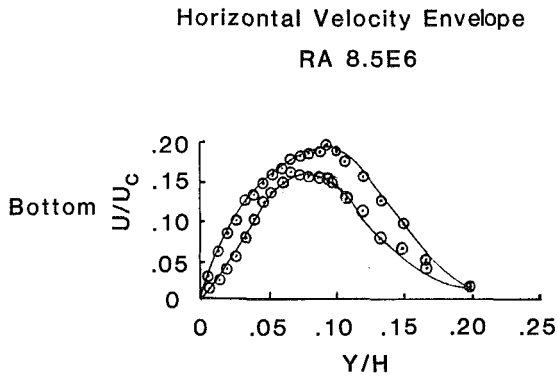

Fig. 11 Horizontal velocity envelope at Rayleigh number 8.5 × 10^6

Results and Discussion

Figure 5 shows the results of normalized frequency versus Rayleigh number at $Ar = 1.0$. The data indicate four distinct flow regimes over the modest change in Rayleigh number from 0.1 × 10^7 to 1.2 × 10^7. At Rayleigh numbers below 0.3 × 10^7, no periodic flow was detected. The flow was purely circulatory. Between 0.3 × 10^7 and 0.6 × 10^7 a very regular periodic flow was observed with constant normalized frequency.

Between 0.6 × 10^7 and 0.68 × 10^7 the flow seemed capable of two modes, one having a frequency about 16 percent larger than the other. This higher mode persisted to a Rayleigh number of approximately 0.84 × 10^7 where again two highly stable modes were observed. Both modes persisted until about 1.0 × 10^7, beyond which only the higher mode was observed. An hysteresis effect was quite pronounced in the regions marked by the vertical dashed lines in Fig. 5. Either the higher or lower frequency could be maintained for periods of at least thirty minutes depending on whether the Rayleigh number was reached from above or below. It is quite possible that the higher frequency mode would always occur if one waited a sufficient length of time, but in these experiments thirty to forty minutes after the temperature reached steady state was the time allowed.

The normalized cavity centerline vertical velocities are reported in Figs. 6, 7, and 8 at Rayleigh numbers of 0.25 × 10^7, 0.50 × 10^7, and 0.85 × 10^7, at selected distances above the cavity floor. These envelopes were obtained from the time-averaged maximum and minimum velocities at various distances from the wall.

The velocity profiles measured for the nonperiodic flow at a Rayleigh number of 0.25 × 10^7 showed a larger maximum velocity at the cold wall than at the hot vertical wall. This was unexpected from the standpoint of two-dimensional flow with fluid having a lower mean density near the hot wall than near the cold wall. Just the opposite variation in velocity had been expected.

A possible explanation is a slight three dimensionality to the flow which enhances mass flow down the center of the cold wall and depletes mass flow up the center of the hot wall. More measurements will be required to resolve this anomaly.

Figures 9, 10, and 11 show the horizontal velocity envelopes on the bottom wall for the same Rayleigh numbers. These velocity envelopes illustrate the very large velocity fluctuations which occur over a period of the order of two seconds for this experimental cavity. It may be seen that the velocity variation can be detected anywhere in the boundary layer of the cavity flow, but that the magnitude of variation is a strong function of position within the boundary layer. In general the largest variation in velocity is on the centerline side of the maximum velocity.

The cause of the periodicity is the linear temperature boundary condition between the hot and cold walls, as periodic flow has not been observed with similar flows bounded at top and bottom by adiabatic surfaces. It is inductively apparent that for extremely small Rayleigh numbers

($<10^3$) the thermal boundary conditions for the adiabatic wall and linearly conducting wall will be nearly identical.

As the Rayleigh number is increased and the flow velocities become more boundary layer oriented, the fluid passing over the horizontal surfaces becomes dynamically unstable, i.e., it is heated from below at the bottom and cooled from above at the top.

If the vertical gradient were strong enough, one might expect the additional buoyancy forces acting perpendicular to the horizontal surfaces to cause plumes or Benard-like convection cells to form and be discharged into the flow. The two dimensionality or wavelike character of the actual flow is somewhat unexpected but is probably due to the sweeping action of the flow induced at the two heated vertical walls.

It is hypothesized that the onset of the periodic flow at a Rayleigh number of 3×10^6 is a resonance phenomenon between traveling waves along the bottom and top of the container and the natural buoyant frequency of the stratified fluid in the interior region of the cavity. This natural or Brunt-Vaisala frequency is proportional to $\sqrt{g\beta\Delta T}$. This is consistent with a constant value of f_{ND} over a range of Rayleigh numbers.

The higher frequency modes seen in Fig. 5 could be a combination of the natural frequency and traveling waves. Further experimental investigation over a wider range of aspect ratio and use of Fourier decomposition must be conducted before these frequency variations can be fully understood.

Conclusions

The periodic flow reported in this work has several interesting aspects:

(*a*) It has a pronounced but as yet unmeasured effect on the heat transfer from a cavity of aspect ratio of order one.

(*b*) The difficulty in providing a truly adiabatic upper and lower surface for experimental measurements using air suggests that this phenomenon may have been present in previously published experimental results for cavities with "adiabatic" top and bottom surfaces.

(*c*) It has been suggested [18] that the cavity with aspect ratio one and adiabatic top and bottom provides a good comparison problem for two-dimensional steady-state Navier-Stokes solution schemes. We suggest this periodic flow phenomenon could act as an excellent test problem for transient two-dimensional Navier-Stokes schemes.

References

1 Sernas, V., Fletcher, L. S., and Rago, C., "An Interferometric Study of Natural Convection in Rectangular Enclosures of Aspect Ratios Less Than One," ASME Paper No. 75-HT-63, presented at the AIChE-ASME Heat Transfer Conference, Aug. 1975, San Francisco, CA.

2 Sernas, V., and Lee, E. I., "Heat Transfer in Air Enclosures of Aspect Ratio Less Than One," ASME Paper No. 78-WA/HT-7, presented at the Winter Annual Meeting, Dec. 1978, San Francisco, CA.

3 Arnold, J. N., Catton, I., and Edwards, D. K., "Experimental Investigation of Natural Convection in Inclined Rectangular Regions of Differing Aspect Ratios," ASME JOURNAL OF HEAT TRANSFER, Vol. 98, No. 1, Feb. 1976, pp. 67-71.

4 Kamotani, Y., Wang, L. W., and Ostrach, S., "Experiments on Natural Convection Heat Transfer in Low Aspect Ratio Enclosures," AIAA Paper No. 81-1066, presented at the AIAA 16th Thermophysics Conference, June 1981, Palo Alto, CA.

5 Wirtz, R. A., Righo, J., and Zirilli, F., "Measurements of Natural Convection Across Tilted Rectangular Enclosures of Aspect Ratios 0.1 and 0.2," AIAA Paper No. 81-1067, presented at the AIAA 16th Thermophysics Conference, June 1981, Palo Alto, CA.

6 Fraiken, M. P., Portier, J. J., and Fraiken, C. J., "Application of a K-ϵ Turbulence Model to an Enclosed Buoyancy Driven Recirculating Flow," ASME Paper No. 80-HT-68.

7 MacGregor, R. K., and Emery, A. F., "Free Convection Through Vertical Plane Layers-Moderate and High Prandtl Number Fluids," ASME JOURNAL OF HEAT TRANSFER, Vol. 91, No. 3, 1969, pp. 391-403.

8 Briggs, D. G., "A Finite Difference Scheme for the Incompressible Advection-Diffusion Equation," *Computer Methods in Applied Mathematics*, 1975, pp. 233-241.

9 Wilkes, J. V., and Churchill, S. W., "The Finite Difference Computation in a Rectangular Enclosure," *AIChE Journal*, Vol. 12, 1966, pp. 161-166.

10 deVahl Davis, G., "Laminar Natural Convection in an Enclosed Rectangular Cavity," *International Journal of Heat and Mass Transfer*, Vol. 11, 1968, pp. 1675-1693.

11 Boyack, B. E., and Kearny, D. W., "Heat Transfer by Laminar Natural Convection in Low Aspect Ratio Cavities," ASME Paper No. 72-HT-52, presented at the AIChE-ASME Heat Transfer Conference, Aug. 1972, Denver, CO.

12 Tseng, W., "Numerical Experiments on Free Convection in a Tilted Rectangular Enclosure of Aspect Ratio 0.5," M.S. thesis, Report #MIE-650, Clarkson College, Potsdam, NY, 1979.

13 Cormack, D. E., Leal, L. C., and Seinfeld, J. H., "Natural Convection in a Shallow Cavity with Differently Heated End Walls," *Journal of Fluid Mechanics*, Vol. 65, Part 2, 1974, pp. 231-246.

14 Lee, E. I., and Sernas, V., "Numerical Study of Heat Transfer in Rectangular Air Enclosures of Aspect Ratio Less Than One," ASME Paper No. 80-WA/HT-43, presented at the ASME Winter Annual Meeting, Nov. 1980, Chicago, IL.

15 Gill, A. E., "The Boundary Layer Regime for Convection in a Rectangular Cavity," *Journal of Fluid Mechanics*, Vol. 26, Part 3, 1966, pp. 515-536.

16 Sernas, V., private communication.

17 Hilsenrath, J., Beckett, C. W., Benedict, W. S., Fano, L., Hoge, H. M., Masi, J. F., Nuttall, R. L., Touloukian, Y. S., and Wooley, H. W., *Tables of the Thermal Properties of Gases*, National Bureau of Standards Circular 564, Washington, D.C., 1955.

18 deVahl Davis, G., Jones, I. P., and Roache, P. J., "Announcement," *Journal of Fluid Mechanics*, Vol. 95, Part 4, 1979, inside back page.

Natural Convection in an Externally Heated Vertical or Inclined Square Box Containing Internal Energy Sources

S. Acharya
Department of Mechanical Engineering,
Louisiana State University,
Baton Rouge, LA 70803
Assoc. Mem. ASME

R. J. Goldstein

Department of Mechanical Engineering,
University of Minnesota,
Minneapolis, MN 55455
Fellow ASME

A numerical investigation has been made of two-dimensional natural convection of air in an externally heated vertical or inclined square box containing uniformly distributed internal energy sources. Results have been obtained for Rayleigh numbers (both internal and external) up to 10^7 and inclination angles of 30, 60, and 90 deg from the horizontal. Two distinct flow pattern systems are observed: one, when the external Rayleigh number is larger than the internal Rayleigh number and the other, when the internal Rayleigh number is considerably greater than the external Rayleigh number. The average heat flux ratio (convective heat flux/corresponding conduction heat flux) along the hot surface is observed to undergo large variations in the external Rayleigh number range associated with the transition from one flow pattern to another. The average heat flux ratio along the cold plate is found to increase with increasing external Rayleigh number and decreasing internal Rayleigh number. The local heat flux ratio along a surface attains its maximum value in the vicinity of the region where the heated (or cooled) fluid from the opposite wall or from the interior encounters the surface.

Introduction

Considerable attention has been given to the study of natural convection in enclosures which are heated either externally or by internal energy sources. Natural convection induced by external heating is of importance in the estimation of heat loss from solar collectors [1] and across double-paned windows [2], in the design of energy efficient buildings, and in many other applications. Natural convection driven by volumetric energy sources is of importance in nuclear reactor design [3], geophysics [4], and astrophysics [5].

Natural convection induced simultaneously by external heating and internal energy sources has received very limited attention with investigations primarily for a horizontal fluid layer [6–10]. In this paper, a numerical study is made of natural convection in an inclined and vertical square enclosure containing internal energy sources and subjected to external heating.

The square enclosure considered is assumed to be very long in the third dimension. The flow is also assumed to be laminar, steady and two dimensional with the axes of the flow parallel to the third dimension. The assumption of steady, laminar flow in an externally heated square enclosure is expected to be valid for Rayleigh numbers as high as 10^6 (and possibly 10^7). This observation is corroborated by the experimental studies of Nansteel and Grief [11] and Linthorst, Schinkel, and Hoogendoorn [12]. The assumption of two-dimensional flow is also based on reported experimental and three-dimensional numerical studies for an externally heated enclosure. It is observed that as the enclosure is inclined from the horizontal to the vertical, at a certain critical angle θ_c, a transition in the flow pattern occurs from longitudinal rolls to a two-dimensional roll. A list of experimental (and three-dimensional numerical) studies that report the value of θ_c is given in Table 1. As may be seen, θ_c is a strong function of the aspect ratio and a weak function of the Rayleigh number. For an aspect ratio of 1, the experimental studies in [12–14] seem to indicate that beyond an inclination angle of 25 deg (from the horizontal) the flow is two dimensional with heated fluid moving up the hot wall and cooled fluid moving down the cold wall. In view of this, all angles considered in this work have been taken to be greater than 25 deg.

A Prandtl number of 0.7 has been used in this study and while this choice corresponds to air it also approximates the Prandtl number value for molten mixed-oxide nuclear fuel, $(U_{0.8}\ Pu_{0.2})O_2$. However, the influence of Prandtl number is not expected to be significant as shown by Jahn and Reineke [23] for a horizontal layer with internal energy sources.

Governing Equations

A schematic of the physical situation to be considered is shown in Fig. 1. The governing partial differential equations are the ones that express the conservation of mass, momentum and energy. By defining a modified pressure p^* as

$$p^* = p + \rho_0 g x \sin\theta + \rho_0 g y \cos\theta \tag{1}$$

and using the Boussinesq approximation

$$\rho = \rho_0\{1 - \beta(T - T_0)\} \tag{2}$$

the governing equations in dimensionless form become

$$\frac{\partial U}{\partial X} + \frac{\partial V}{\partial Y} = 0 \tag{3}$$

$$U\frac{\partial U}{\partial X} + V\frac{\partial U}{\partial Y} = -\frac{\partial P}{\partial X} + \frac{\partial^2 U}{\partial X^2} + \frac{\partial^2 U}{\partial Y^2} + \frac{\mathrm{Ra}_E}{\mathrm{Pr}}\phi\sin\theta \tag{4}$$

$$U\frac{\partial V}{\partial X} + V\frac{\partial V}{\partial Y} = -\frac{\partial P}{\partial Y} + \frac{\partial^2 V}{\partial X^2} + \frac{\partial^2 V}{\partial Y^2} + \frac{\mathrm{Ra}_E}{\mathrm{Pr}}\phi\cos\theta \tag{5}$$

$$U\frac{\partial \phi}{\partial X} + V\frac{\partial \phi}{\partial Y} = \frac{1}{\mathrm{Pr}}\left(\frac{\partial^2 \phi}{\partial X^2} + \frac{\partial^2 \phi}{\partial Y^2}\right) + \frac{\mathrm{Ra}_I}{\mathrm{Ra}_E \cdot \mathrm{Pr}} \tag{6}$$

Contributed by the Heat Transfer Division for publication in the JOURNAL OF HEAT TRANSFER. Manuscript received by the Heat Transfer Division November 16, 1983.

Table 1 Angle from the horizontal (θ_c) at which the transition from longitudinal rolls to a two-dimensional roll cell is observed when the enclosure is inclined from the horizontal to the vertical position

A	Ra	θ_c(deg)	Fluid	Reference
1	$5 \times 10^3 - 10^5$	15-20	air	Linthorst, Schinkel, and Hoogendoorn [12]
1	$10^5 - 10^6$	25	water to silicone oil	Arnold, Catton, and Edwards [13]
1	$3.3 \times 10^3 - 1.1 \times 10^4$	10	glycerol	Ozoe, Sayama, and Churchill [14]
2	4×10^3	7	water	Ozoe, Yamamoto, Sayama, and Churchill* [15]
2	1.2×10^4	7	glycerol	Ozoe, Sayama, and Churchill [16]
3	4.77×10^3	25	silicone oil	Ozoe, Yamamoto, Sayama, and Churchill [17]
7	5×10^3	55	air	Linthorst, Schinkel, and Hoogendoorn [12]
7	4×10^3	50	water	Ozoe, Fujii, Lior, and Churchill *[18]
6	$10^5 - 10^6$	60	water to silicone oil	Arnold, Catton, and Edwards [13]
9.25	$1.7 \times 10^3 - 4 \times 10^4$	57.5	water	Goldstein and Wang [19]
5–83	$1.2 \times 10^3 - 2 \times 10^6$	60	air	Inaba [20]
36.25	$10^3 - 10^6$	80	air, water	Hart [21]
44	near critical $(10^3 - 10^4)$	75	air	Hollands and Konicek [22]

*Numerical calculations (three-dimensional)

In obtaining the above equations, the following dimensionless variables have been used

$$X = x/L, \quad Y = y/L \tag{7a}$$

$$U = u/(\nu/L), \quad V = v/(\nu/L), \quad P = p^*/\rho(\nu/L)^2 \tag{7b}$$

$$\phi = (T - T_0)/(T_h - T_c) \text{ where } T_0 = (T_h + T_c)/2 \tag{7c}$$

Only rigid walls are considered, so that zero velocity boundary conditions may be assumed on all walls. The side walls are assumed to be adiabatic while the lower hot wall ($y/L = 0$) is maintained at a temperature $T_h(\phi = 0.5)$ and the upper cold wall ($y/L = 1$) has a temperature $T_c(\phi = -0.5)$.

The governing dimensionless parameters in the equations are the angle of inclination θ, the external Rayleigh number Ra_E, and the internal Rayleigh number Ra_I. Results have been obtained for inclination angles of 30, 60, and 90 deg and values of Ra_E and Ra_I up to 10^7.

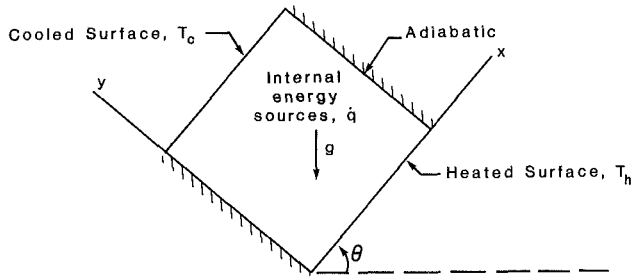

Fig. 1 Schematic of the physical situation

Nomenclature

g = gravitational force
G = uniform volumetric heat generation, energy/time/volume
k = thermal conductivity of the fluid
L = width and height of box
p, p^*, P = thermodynamic, modified and dimensionless pressures
Pr = Prandtl number
q_c = heat flux to cold wall from the fluid
q_h = heat flux from hot wall to fluid
$q_{c,\mathrm{cond}}, q_{h,\mathrm{cond}}$ = heat flux by pure conduction, to the cold wall and from the hot wall respectively
$q_{r,h}, q_{r,c}$ = heat flux ratio at the hot ($q_h/q_{h,\mathrm{cond}}$) and cold ($q_c/q_{c,\mathrm{cond}}$) surfaces
$\bar{q}_{r,h}, \bar{q}_{r,c}$ = average heat flux ratio along the hot and cold surfaces
$q_{r,\max}, q_{r,\min}$ = maximum and minimum values of $q_{r,h}$
R = overall energy residual
$\mathrm{Ra}_I, \mathrm{Ra}_E$ = internal Rayleigh number and the external Rayleigh number, $\mathrm{Ra}_I = g\beta GL^5/\nu\alpha k$, $\mathrm{Ra}_E = g\beta(T_h - T_c)L^3/\nu\alpha$
T = temperature
T_h, T_c = temperature of the hot and cold surfaces
T_0 = $(T_h + T_c)/2$
u, U = dimensional and dimensionless velocity in the x direction
$U_{\max}$ = maximum value of U
v, V = dimensional and dimensionless velocity in the y direction
$V_{\max}$ = maximum value of V
x, y = dimensional coordinates, x along hot and cold walls and y along adiabatic walls
$(x/L)_{V,\mathrm{mx}}$ = (x/L) location of $V_{\max}$
$(x/L)_{q,\mathrm{mx}}$ = (x/L) location of $q_{r,\max}$
$(x/L)_{q,\mathrm{mn}}$ = (x/L) location of $q_{r,\min}$
$(y/L)_{U,\mathrm{mx}}$ = (y/L) location of $U_{\max}$
X, Y = dimensionless coordinates = $x/L, y/L$
α = thermal diffusivity
β = thermal expansion coefficient
ν = kinematic viscosity
ρ = density
ρ_0 = reference density
ϕ = dimensionless temperature = $(T - T_0)/(T_h - T_c)$
$\phi_{\max}$ = maximum value of ϕ
$\phi_{\mathrm{cond,max}}$ = maximum value of ϕ due to conduction alone
θ = angle of inclination
$\psi, \psi_{\mathrm{mid}}$ = dimensionless stream function and its midpoint value

Table 2 Comparison of the present solutions with the bench-mark solution of de Vahl Davis [25] for natural convection in externally heated vertical layers

	$Ra_E = 10^3$		$Ra_E = 10^6$	
	de Vahl Davis [25] solution	Present solution	de Vahl Davis [25] solution	Present solution
ψ_{mid}	1.654	1.660	22.986	23.70
U_{max}	5.207	5.22	308.958	315.00
$(y/L)_{U,mx}$	0.178	0.177	0.0379	0.0345
V_{max}	5.139	5.140	91.028	92.20
$(x/L)_{V,mx}$	0.813	0.823	0.850	0.857
$\bar{q}_{r,h}$	1.117	1.119	8.817	8.859
$q_{r,max}$	1.505	1.51	17.925	18.07
$(x/L)_{q,mx}$	0.092	0.083	0.0378	0.0345
$q_{r,min}$	0.692	0.691	0.989	1.045
$(x/L)_{q,mn}$	1.0	1.0	1.0	1.0

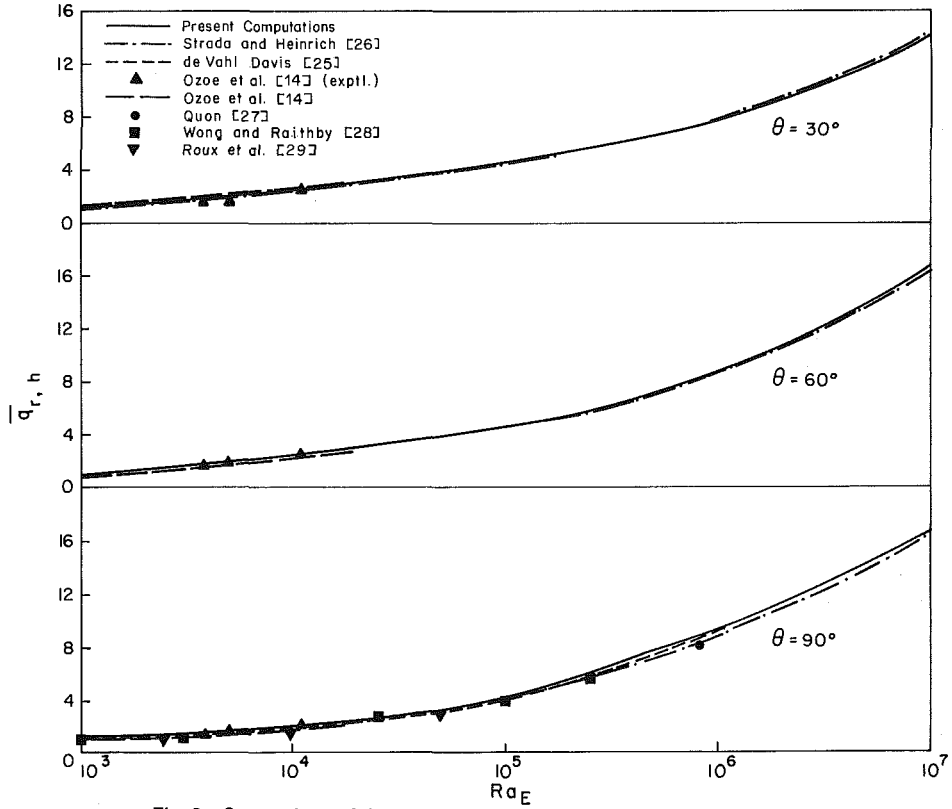

Fig. 2 Comparison of the published average heat flux ratio (along the hot surface) for an externally heated square enclosure

It should be pointed out that in equation (6), the Rayleigh numbers appear as a ratio and therefore this ratio could be used as the independent parameter instead of Ra_I. In fact, the ratio Ra_I/Ra_E can be expressed as $GL^2/k(T_h - T_c)$ which is a dimensionless quantity that is commonly employed as an independent parameter.

Solution Procedure

Equations (3)–(6) with the associated boundary conditions provide a complete mathematical specification of the problem. The equations are solved by a finite difference procedure called SIMPLER (Semi Implicit Method for Pressure Linked Equations Revised). In this method (described in detail by Patankar [24]), the domain is subdivided into a number of control volumes with a grid point at the center of each control volume. While the pressure and temperatures are stored at the grid points, the locations of the u and v velocities are staggered in the x and y directions, respectively. An exponential scheme which is based on the exact solution of the one-dimensional convection diffusion equation is used to describe the profile variation in each coordinate direction. This scheme reduces to the central difference scheme at low values of the Peclet number and the upwind scheme at high Peclet number values. The solution is obtained for the primitive variables and a predictor-corrector approach is used to obtain velocity and pressure fields that will satisfy both the continuity and momentum equations.

A 32 × 32 grid is used in the present calculations. The grid point distribution is carefully tailored to obtain numerically accurate results. This required a number of preliminary calculations, examination of the velocity and temperature profiles and clustering of grid points in regions of large gradients and curvature. For higher Rayleigh numbers the grid distribution is more nonuniform (compared to that at lower Rayleigh numbers) with a denser clustering in the boundary layer regions near the walls.

To demonstrate the adequacy of the grid used, four specific tests were made, as described below.

1 The overall energy balance should be satisfied. This requires

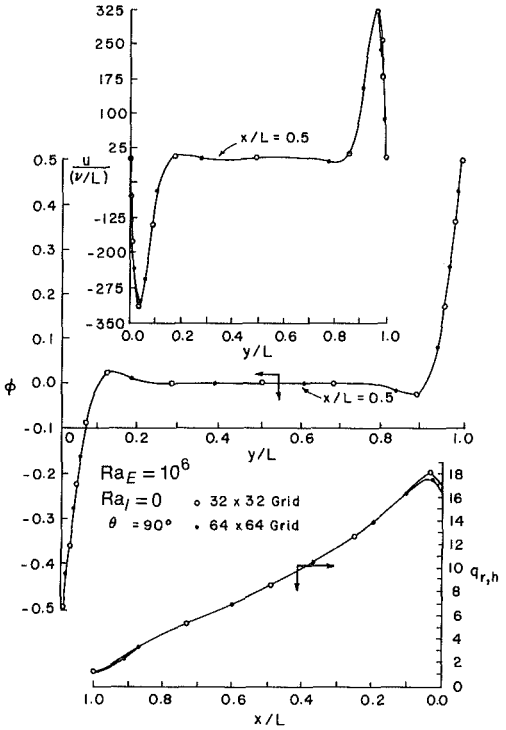

Fig. 3 Comparison of the results of a 32 × 32 grid with the corresponding results of a 64 × 64 grid

$$R=\int_{X=0}^{1}(-\partial\phi/\partial Y)_{Y=0}dX+(\mathrm{Ra}_I/\mathrm{Ra}_E)$$

$$-\int_{X=0}^{1}(-\partial\phi/\partial Y)_{Y=1}dX=0 \tag{8}$$

In all cases considered here, R differs from 0 in only the fourth significant digit after the decimal point.

2 The present results are compared with the benchmark solution of de Vahl Davis [25] for natural convection in an externally heated vertical ($\theta=90$ deg) enclosure. This comparison is shown in Table 2 for $\mathrm{Ra}_E=10^3$ and 10^6. As may be observed from this table, the two solutions agree well with each other.

3 The present results for an externally heated inclined enclosure ($\theta=30$, 60, and 90 deg) are compared with those in the published literature (Fig. 2). For all three inclination angles, the calculated value of the average Nusselt number along the hot surface $\bar{q}_{r,h}$ (called average heat flux ratio in this paper) compares well with the values reported by other investigators.

4 Results from the 32 × 32 grid presented in this paper are compared with the corresponding results of a 64 × 64 grid. This comparison at $\mathrm{Ra}_E=10^6$, $\mathrm{Ra}_I=0$, and $\theta=90$ deg is shown in Fig. 3. The midheight velocity ($u/\nu/L$) and temperature (ϕ) profiles obtained with the two grids are nearly identical to each other. Also the values of the local Nusselt number or heat flux ratio along the hot wall obtained using either grid are very close to each other. A similar comparison has been done for $\mathrm{Ra}_I=10^7$, $\mathrm{Ra}_E=10^3$, and $\theta=90$ deg (not shown). Again, the 32 × 32 grid results agree well with the 64 × 64 grid solutions.

Results and Discussion

Results presented will include the dimensionless streamline and isotherm contour plots and distributions of the average and local heat flux ratios along the hot and cold surfaces. The values of the maximum temperature and its corresponding location will also be presented.

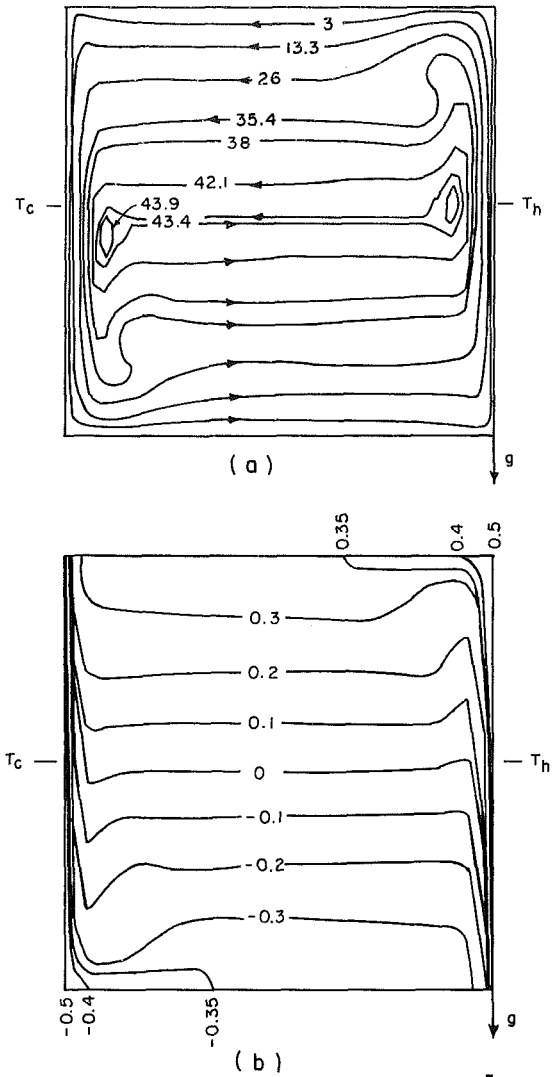

Fig. 4 Contour plots for a vertical enclosure at $\mathrm{Ra}_E=10^7$, $\mathrm{Ra}_I=0$; (a) streamline; (b) isotherm

Streamline and Isotherm Patterns

The stream function is obtained from the velocity field solution by evaluating the integral,

$$\psi=\int_0^Y UdY \tag{9}$$

along constant X lines with $\psi=0$ at $X=Y=0$.

The streamline and isotherms for a vertical enclosure ($\theta=90$ deg) will be presented first. For $\mathrm{Ra}_I=0$ (no internal heating) and $\mathrm{Ra}_E=10^3$ a unicellular flow pattern is observed with flow up the hot wall and down the cold one. At higher Rayleigh numbers, the inner core degenerates into a multicellular form (Fig. 4). Large velocity and temperature gradients characterize the region immediately adjacent to the thermally active walls while negligible gradients (normal to the hot surface) prevail in the rest of the enclosure. Such behavior, indicative of a boundary layer structure, has also been observed by a number of investigators [25, 26].

In the presence of internal heating ($\mathrm{Ra}_I>0$), the aforementioned trends in flow and heat transfer persist if $\mathrm{Ra}_I \leqq \mathrm{Ra}_E$. However, when the magnitude of Ra_I considerably exceeds that of Ra_E (e.g., $\mathrm{Ra}_E=10^3$, $\mathrm{Ra}_I=10^5$) the flow field takes on a different pattern (Fig. 5). It now consists of two counterrotating convective rolls spanning the entire length normal to the adiabatic boundaries. The maximum dimensionless temperature occurs between the hot and cold

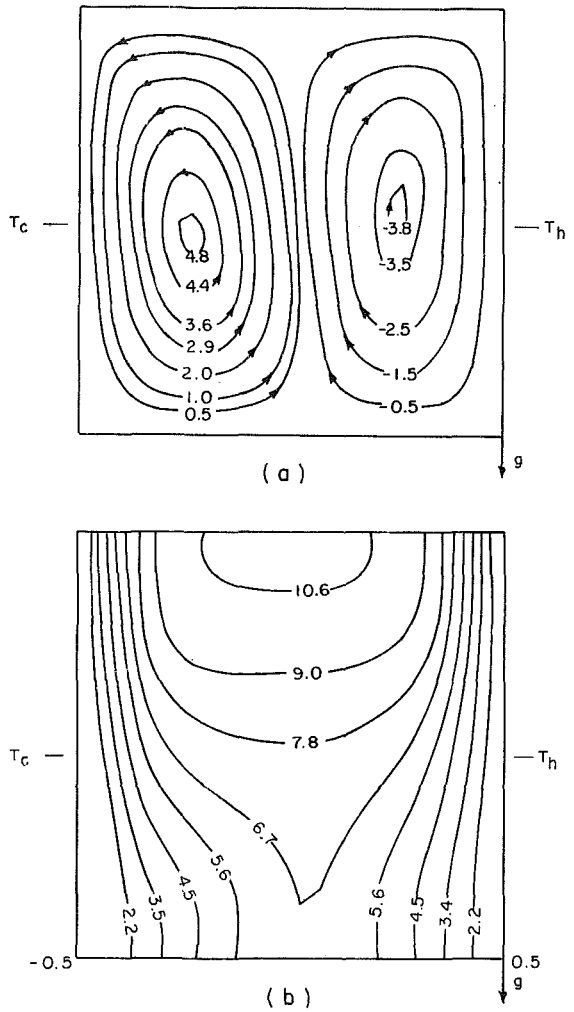

Fig. 5 Contour plots for a vertical enclosure at $Ra_E = 10^3$, $Ra_I = 10^5$; (a) streamline; (b) isotherm

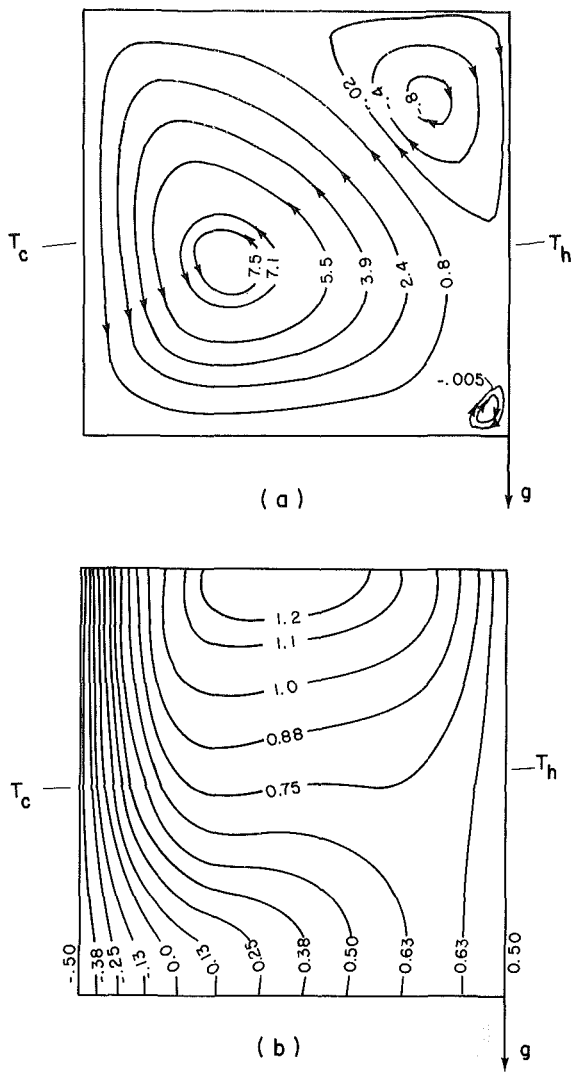

Fig. 6 Contour plots for a vertical enclosure at $Ra_E = 10^4$, $Ra_I = 10^5$; (a) streamline; (b) isotherm

surfaces which explains why the fluid rises in the central region of the enclosure and moves down both the hot and cold surfaces. The most notable difference between the aforementioned flow pattern and those predicted for $Ra_I \leq Ra_E$ is the direction of flow adjacent to the hot surface. It is upward with fluid being heated by the wall when $Ra_I \leq Ra_E$ and is downward with fluid being cooled when Ra_I is considerably greater than Ra_E.

With fixed Ra_I, as the magnitude of external heating (i.e., Ra_E) is increased the flow field undergoes a transition from a flow pattern resembling the one in Fig. 5 to the flow pattern predicted in Fig. 4 (with flow up the hot wall and down the cold one). This transition occurs through intermediate flow patterns, as illustrated in Figs. 6 and 7. In Fig. 6 ($Ra_I = 10^5$, $Ra_E = 10^4$), three eddies are present. The largest eddy is the counterclockwise flow moving downward along the cold surface and upward along the middle portion of the hot surface. The other two eddies are formed at the top-right and bottom-right corner of the box with the flow directed downward along the hot surface. The eddy at the top-right corner is faster than the one at the bottom although they are both sluggish relative to the downward flow along the cold surface. For $Ra_I = 10^7$ and $Ra_E = 10^6$ (Fig. 7), a weak counterrotating (to the main counterclockwise flow) eddy is present in the top right corner (adjacent to the adiabatic surface) of the square box. The isotherm plot indicates a localized region of high temperature (relative to the hot wall temperature) in the vicinity of the weak counterrotating eddy.

For an inclined enclosure ($\theta = 30$ and 60 deg) the body force has an additional component perpendicular to the thermally active surfaces. The Ra_E value at which the transition from a single-cell to a multi-cell inner core occurs is found to be higher when the enclosure is inclined than when it is vertical. This conclusion is substantiated by the flow patterns at $Ra_E = 10^5$ (not shown). For a vertical enclosure, a multi-cell inner core is predicted while the corresponding flow pattern for an inclined enclosure is still unicellular.

As at $\theta = 90$ deg, the presence of internal energy sources produces a change in the flow pattern when Ra_I is considerably greater than Ra_E. This is illustrated in Fig. 8 ($Ra_E = 10^3$, $Ra_I = 10^4$) where a weak clockwise flow occupies a small region adjacent to the hot surface (and moves downward along it) with the remaining space containing a stronger counterclockwise flow (which moves in a downward direction along the cold surface).

If the magnitude of internal heating is increased ($Ra_I = 10^5$) the clockwise flow along the hot surface grows in size and also becomes stronger (Fig. 9).

In the absence of internal heating (or when the effect of the external Rayleigh number is dominant) the flow at low Ra_E values is faster at 60 deg than at 30 or 90 deg. This behavior is consistent with earlier predictions [14]. At higher Ra_E values (i.e., 10^5 and 10^7) a comparison of the velocities at in-

clinations of 30, 60, and 90 deg indicates that the flow field is the fastest at 30 deg and the slowest at 90 deg. When the effect of internal Rayleigh number becomes significant (as in Figs. 5, 8, and 9), the speed of the clockwise flow (along the hot surface) increases and that of the counterclockwise flow (along the cold surface) decreases with increasing angle.

For an inclined enclosure a transitional flow pattern similar to that obtained for a vertical enclosure (Figs. 6 and 7) is observed. Such a flow pattern is shown (for $\theta = 60$ deg, $\mathrm{Ra}_I = 10^7$, $\mathrm{Ra}_E = 10^6$) in Fig. 10. As in Fig. 7, the weak counterrotating (to the main flow) eddy is adjacent to the adiabatic wall (at $x/L = 1$) but has now moved away from the hot surface. This is to be expected in view of the additional buoyancy component parallel to the adiabatic surface.

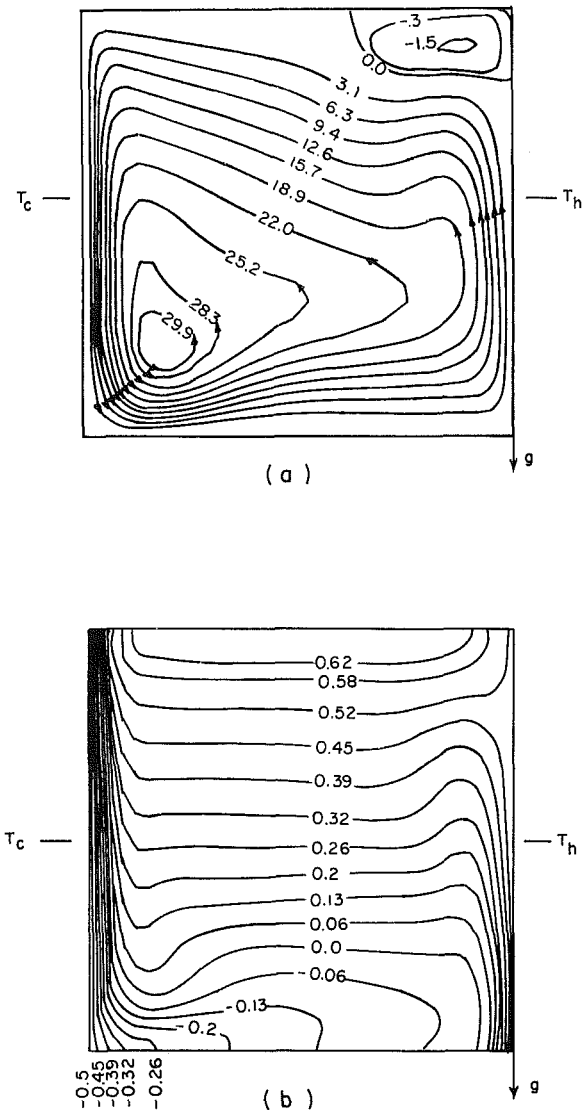

Fig. 7 Contour plots for a vertical enclosure at $\mathrm{Ra}_E = 10^6$, $\mathrm{Ra}_I = 10^7$; (*a*) streamline; (*b*) isotherm

Another transitional flow pattern for an inclined enclosure is shown in Fig. 11 ($\theta = 30$ deg, $\mathrm{Ra}_I = 10^5$, $\mathrm{Ra}_E = 10^4$). A comparison of this flow pattern with the corresponding one for a vertical enclosure (Fig. 6) indicates (as mentioned in the preceding paragraph) that the size and speed of the clockwise eddies (with flow moving downward along the heated surface) decrease with decreasing angle.

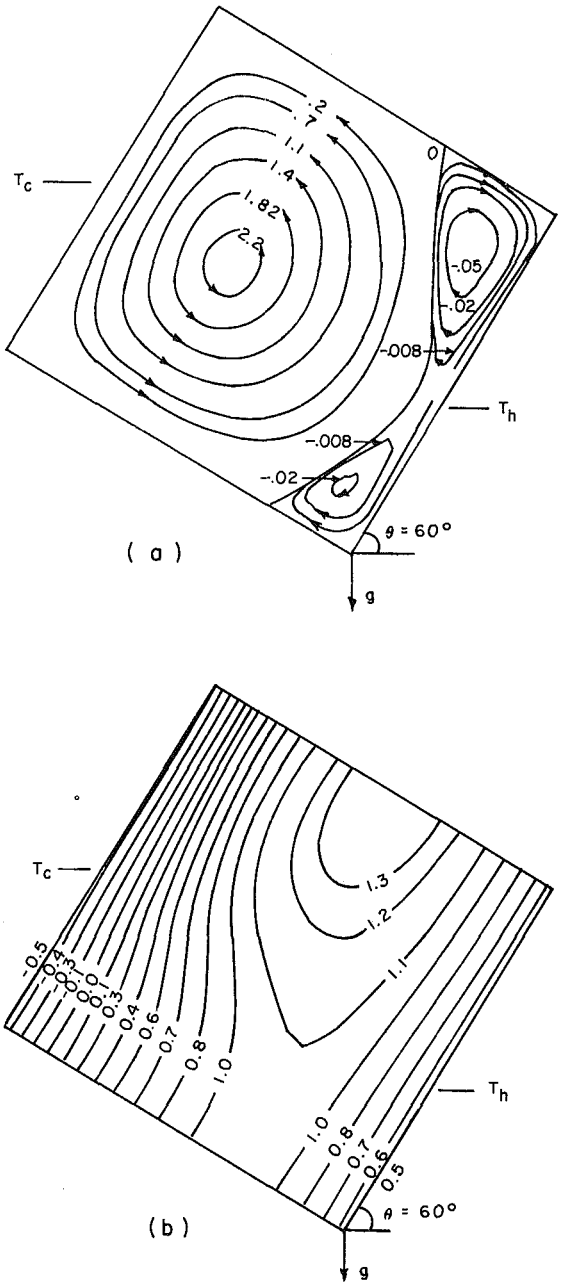

Fig. 8 Contour plots for an inclined enclosure ($\theta = 60$ deg) at $\mathrm{Ra}_E = 10^3$, $\mathrm{Ra}_I = 10^4$; (*a*) streamline; (*b*) isotherm

Table 3 Values of ϕ_{max} and $\phi_{cond,max}$ and the corresponding (y/L) values

			$\theta = 30$ deg		$\theta = 60$ deg		$\theta = 90$ deg	
Ra_I	Ra_E	$\phi_{cond,max}$	y/L	ϕ_{max}	y/L	ϕ_{max}	y/L	ϕ_{max}	y/L
10^4	10^3	1.30	0.40	1.39	0.45	1.41	0.48	1.40	0.45
10^5	10^3	12.51	0.49	11.80	0.62	11.80	0.60	11.20	0.53
10^5	10^4	1.30	0.40	1.09	0.62	1.16	0.62	1.25	0.53
10^7	10^3	1250.00	0.50	578.00	0.82	556.00	0.82	543.00	0.48
10^7	10^4	125.00	0.50	57.70	0.82	55.50	0.82	54.30	0.48
10^7	10^5	12.51	0.49	5.64	0.82	5.51	0.82	5.48	0.31
10^7	10^6	1.30	0.40	–	–	0.56	0.81	0.65	0.31

Note that for these Ra, ϕ_{max} occurs at $y/L = 1$ when convection is present.

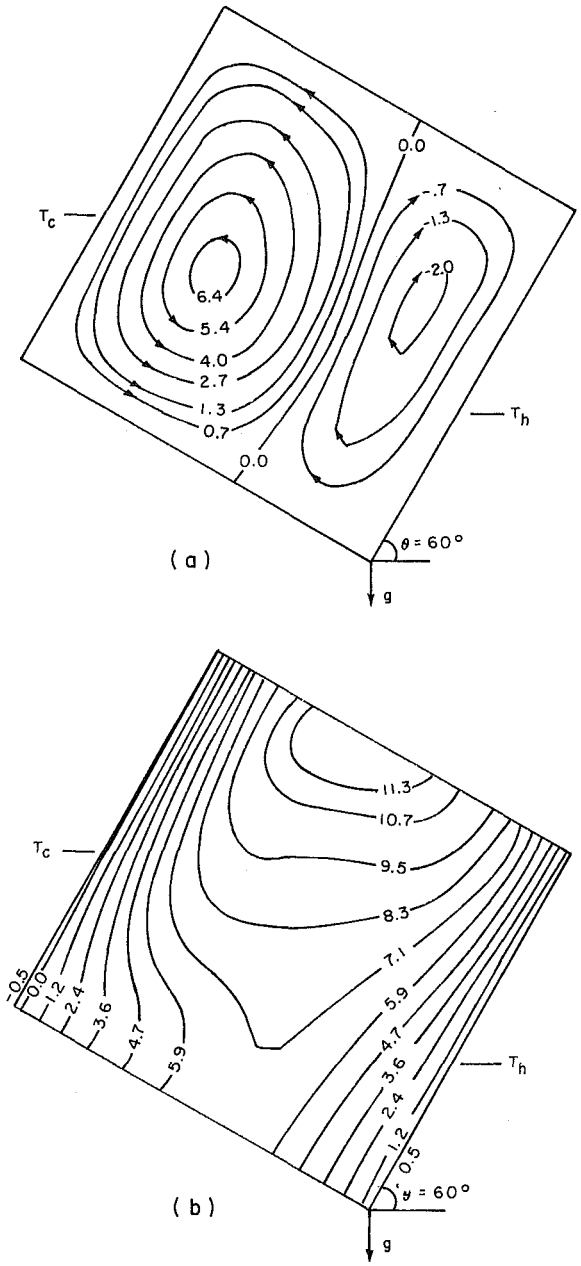

Fig. 9 Contour plots for an inclined enclosure ($\theta = 60$ deg) at $Ra_E = 10^3$, $Ra_I = 10^5$; (*a*) streamline; (*b*) isotherm

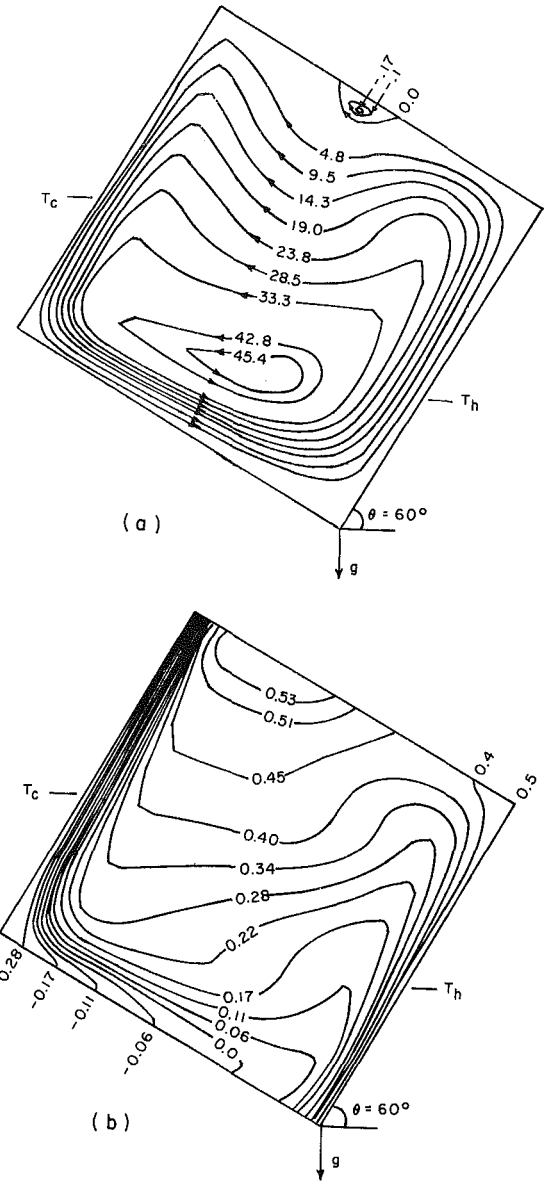

Fig. 10 Contour plots for an inclined enclosure ($\theta = 60$ deg) at $Ra_E = 10^6$, $Ra_I = 10^7$; (*a*) streamline; (*b*) isotherm

Average Heat Flux Ratios. The overall heat transfer characteristics of the enclosure will be described by an average heat flux ratio along the hot surface ($\bar{q}_{r,h}$) and along the cold surface ($\bar{q}_{r,c}$). The average value is computed from a local heat flux ratio

$$q_{r,h} = q_h / q_{h,\text{cond}} \tag{10a}$$

$$q_{r,c} = q_c / q_{c,\text{cond}} \tag{10b}$$

where q_h and q_c are the heat flux at the hot and cold surface and $q_{h,\text{cond}}$ and $q_{c,\text{cond}}$ are the heat flux at the hot and cold surface if conduction (at the same value of G and $(T_h - T_c)$) is the only mode of heat transfer. In dimensionless form, the local heat flux ratio along the hot ($q_{r,h}$) and along the cold ($q_{r,c}$) surfaces may be written as

$$q_{r,h} = -(\partial\phi/\partial Y)_{Y=0}/(1 - 0.5\text{Ra}_I/\text{Ra}_E) \tag{11}$$

and

$$q_{r,c} = -(\partial\phi/\partial Y)_{Y=1}/(1 + 0.5\text{Ra}_I/\text{Ra}_E) \tag{12}$$

The distribution of the average heat flux ratio along the hot surface of an inclined enclosure ($\theta = 60$ deg) is shown in Fig. 12. From equation (11) it can be seen that $q_{r,h}$ becomes singular at $\text{Ra}_E = 0.5\ \text{Ra}_I$. At this value, the theoretical conduction heat flux (at the hot wall) due to the externally imposed temperature difference and due to internal energy sources cancel each other. The location of the singularity for $\text{Ra}_I = 10^4$, 10^5, and 10^7 is indicated in Fig. 12 by a pair of short vertical lines. It should be noted that because of this singularity the behavior of the heat flux ratio as defined in equation (10) will be quite irregular in the neighborhood of $\text{Ra}_E = 0.5\ \text{Ra}_I$. Since results have not been obtained for a large number of Ra_E/Ra_I values in the neighborhood of the singularity, the $q_{r,h}$ plot has been intentionally omitted in the immediate vicinity of $\text{Ra}_E = 0.5\ \text{Ra}_I$. For $\text{Ra}_I = 10^3$, the singularity is beyond the range of Ra_E values shown and for $\text{Ra}_I = 0$, there is no singularity.

In the absence of internal energy sources ($\text{Ra}_I = 0$) the average heat flux ratio along the hot surface ($\bar{q}_{r,h}$) increases monotonically with Ra_E. In the presence of internal energy sources, the general nature of the ($\bar{q}_{r,h}$) plot is similar for all

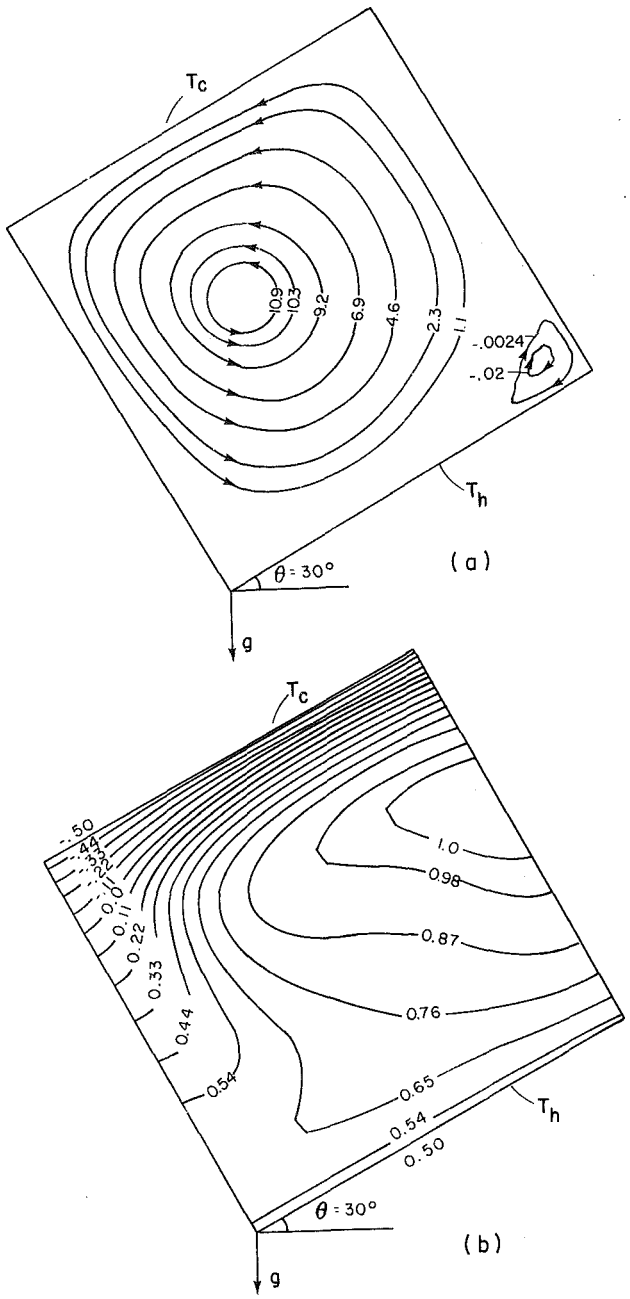

Fig. 11 Contour plots for an inclined enclosure ($\theta = 30$ deg) at $Ra_E = 10^4$, $Ra_I = 10^5$; (a) streamline; (b) isotherm

Ra_I values and is most clearly exemplified by the $Ra_I = 10^5$ curve. For this Ra_I, the magnitude of $\bar{q}_{r,h}$ for $Ra_E \leqq 10^4$ is smaller than the corresponding value at $Ra_I = 0$. Between Ra_E of 10^4 and 10^5 rapid changes in $\bar{q}_{r,h}$ occur and finally result in average heat flux ratios greater than that predicted for $Ra_I = 0$. Beyond Ra_E of 10^5, the rate of change of $\bar{q}_{r,h}$ is reduced and $\bar{q}_{r,h}$ approaches the value for zero Ra_I and the two curves more or less coincide for $Ra_E \geqq 10^6$.

The aforementioned behavior can be explained with reference to the calculated flow patterns and isotherms. At $Ra_I = 0$, the flow adjacent to the hot wall is always upward, with the hot surface washed by fluid cooled from the opposite wall as in Fig. 4. Thus, the dimensionless temperature gradient at the hot surface (and therefore $\bar{q}_{r,h}$) is higher than its conduction counterpart of unity (corresponding to a linear temperature profile). In the presence of internal heat sources the magnitude of $\bar{q}_{r,h}$ is governed by the direction and strength of the flow adjacent to the hot surface. At each Ra_I, there is (as shown earlier) a range of Ra_E values for which the hot interior fluid flows downward along both the hot and cold surfaces. In this range of Ra_E values, the magnitude of $\bar{q}_{r,h}$ is less than unity. To explain this it should be noted that in the presence of convection the interior fluid is cooled by the downward flow along cold wall and therefore the interior temperatures are lower than the corresponding conduction temperatures (see Table 3). In view of the lower interior temperatures, $\bar{q}_{r,h}$ drops below the corresponding conduction value.

If the Ra_E value is continuously increased, the flow pattern changes from one where the flow adjacent to the hot surface is downward (with heat being transferred from the fluid to the wall, i.e., q_h is negative) to one where the flow moves in an upward direction (with heat transferred from the wall to the fluid, i.e., q_h is positive) over the surface. Therefore, at some value of Ra_E (say Ra_E^*), the magnitude of q_h is zero. In general, Ra_E^* will not be equal to 0.5 Ra_I (which is the Ra_E value at which $q_{h,\text{cond}}$ is zero) and therefore both positive and negative values of $\bar{q}_{r,h}$ can be expected. As may be seen in Fig. 10, at $Ra_I = 10^7$ and $Ra_E = 10^6$, q_h is greater than zero, but since $Ra_E < 0.5\ Ra_I$, $q_{h,\text{cond}}$ is still less than zero. Therefore, a negative value for $\bar{q}_{r,h}$ is obtained in Fig. 12. The positive value for q_h is due to the readjustment of the flow field (Fig. 10) which carries fluid directly from the cold surface (in an anticlockwise direction) down to the hot surface. In general, for a given Ra_E and Ra_I, both positive and negative values of $q_{r,h}$ would occur (see Fig. 15).

As the singularity ($Ra_E = 0.5\ Ra_I$) is approached (and $q_{h,\text{cond}}$ approaches zero) the magnitude of $\bar{q}_{r,h}$ increases rapidly; after the singularity is crossed (and $q_{h,\text{cond}}$ becomes positive) the magnitude of $\bar{q}_{r,h}$ decreases rapidly. In the neighborhood of this singularity q_h also changes sign. As mentioned earlier, the rapid variation of $\bar{q}_{r,h}$ in the vicinity of the singularity has been intentionally omitted in Fig. 12.

For increasing Ra_E values, the influence of internal energy sources becomes progressively smaller. In particular, it may be seen that for $Ra_E/Ra_I \geqq 10$, the influence of internal heating on $\bar{q}_{r,h}$ is negligible.

Figure 13 shows the variation of the average heat flux ratio ($\bar{q}_{r,c}$) along the cold surface. For all values of Ra_I, the magnitude of $\bar{q}_{r,c}$ increases monotonically with Ra_E, irrespective of the nature of flow pattern. This is because the convective motion always carries heated fluid (either directly from the hot surface or from the central regions) to the cold surface, thereby augmenting the heat transfer at that surface. The heat transferred by convection q_c and by conduction $q_{c,\text{cond}}$ are always of the same sign. Therefore, unlike $\bar{q}_{r,h}$, the average heat flux ratio along the cold plate $\bar{q}_{r,c}$ is always greater than zero.

The nature of the flow pattern does however dictate the dependence of $\bar{q}_{r,c}$ on Ra_I. For $Ra_I >> Ra_E$ the hot interior fluid moves down both the hot and cold wall. As mentioned earlier and as shown in Table 3, the interior temperature in such situations is generally smaller than the corresponding conduction temperature. Thus, the increase in heat transfer at the cold surface due to the convective motion is offset by the lower interior temperatures and therefore, the corresponding $\bar{q}_{r,c}$ values are low. For $Ra_E > Ra_I$, the cold wall receives fluid directly from the hot wall and therefore the $\bar{q}_{r,c}$ values approach those for $Ra_I = 0$ (as seen in Fig. 13).

An idea of the influence of inclination angle on the average heat flux ratios can be obtained from the present results. In the absence of internal heat sources ($Ra_I = 0$) the average heat flux ratio for the lower Ra_E values (e.g., 10^3 and 10^5) is greater at $\theta = 60$ deg than at $\theta = 30$ or 90 deg. Such behavior has also been predicted by Ozoe, Sayama, and Churchill [14] and Strada and Heinrich [26]. For high Ra_E values (e.g., 10^7)

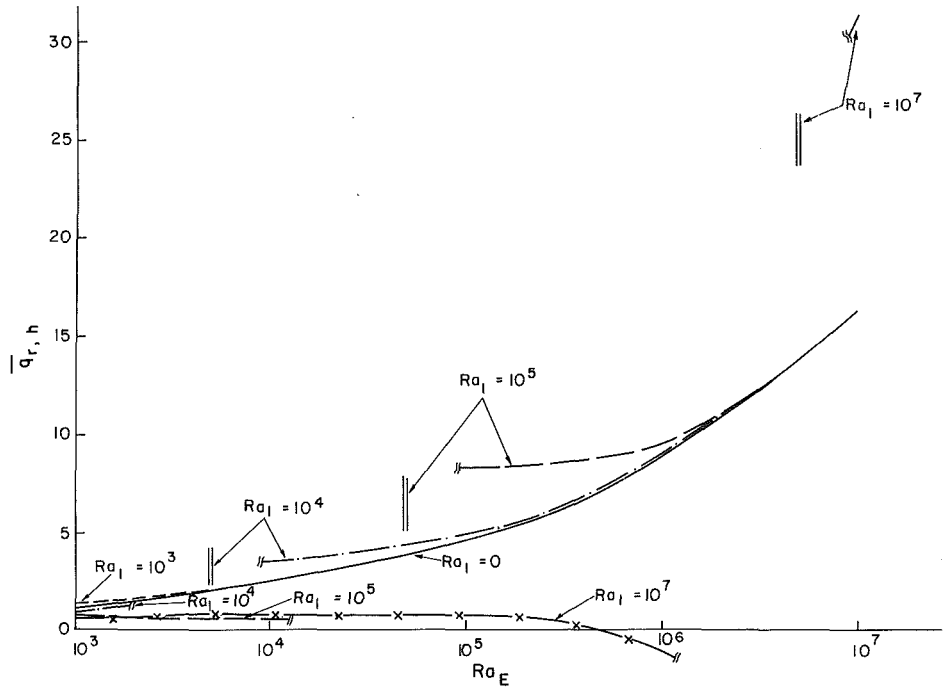

Fig. 12 Average heat flux ratio along the hot surface of the inclined enclosure ($\theta = 60$ deg)

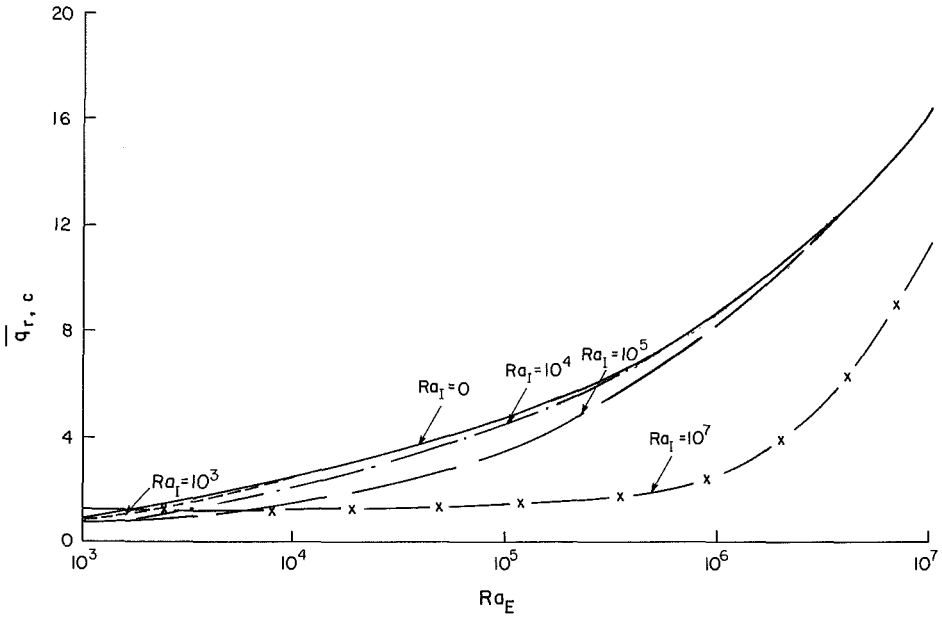

Fig. 13 Average heat flux ratio along the cold surface of the inclined enclosure ($\theta = 60$ deg)

the magnitude of the average heat flux ratio is higher at $\theta = 90$ deg than at 30 or 60 deg. The predictions of Strada and Heinrich [26] corroborate this trend.

In the presence of internal heat sources, the average heat flux ratio along the hot or cold surface is plotted against inclination angle for Ra_E values of 10^3, 10^5, and 10^7 (Fig. 14). Since only three inclination angles have been considered, the computed points have been joined by straight lines instead of a smooth curve. When Ra_E is greater than Ra_I, the trends are expectedly similar (since flow patterns are alike) to the trends in the absence of internal heat sources. If the internal Rayleigh number has a larger magnitude, the average heat flux ratio along the hot surface increases and that along the cold surface decreases with increasing angle. This behavior is linked to the fact that the strength of the clockwise flow moving downward on the hot surface increases and that of the counterclockwise flow moving down the cold surface decreases as the angle of inclination is increased.

Local Heat Flux Ratios. The distribution of local heat flux ratios ($q_{r,h}$ and $q_{r,c}$) as defined in equations (10)–(12) is plotted in Fig. 15 (for the hot surface) and Fig. 16 (for the cold surface). These distributions are shown only for $Ra_E = 10^5$ and for Ra_I values of 0, 10^5, and 10^7. For the smaller Ra_I values (of 0 and 10^5) the flow moves down the cold surface and up the hot surface. Thus, close to $x/L = 0$ (along the upper abscissa in Fig. 15) the hot surface is washed by fluid directly cooled from the top surface and therefore, high values of the local heat flux ratios are obtained in this region. As the fluid moves over the hot surface its tem-

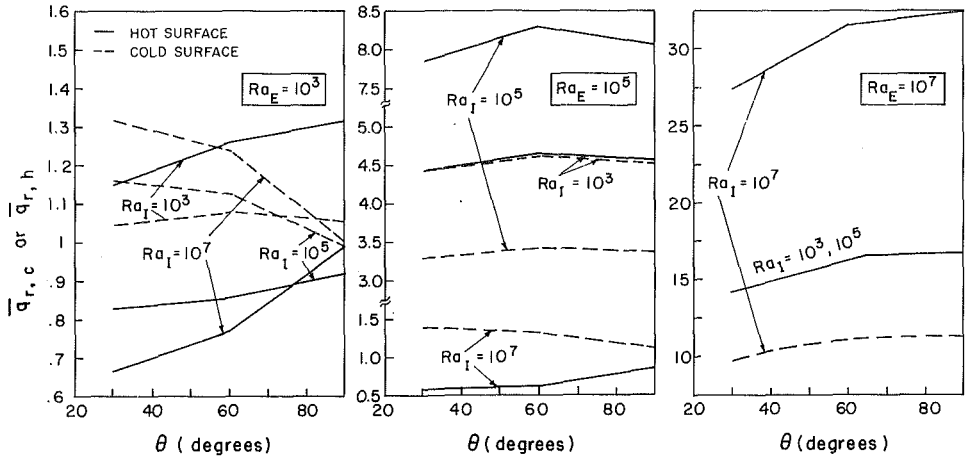

Fig. 14 Dependence of the average heat flux ratio on inclination angle

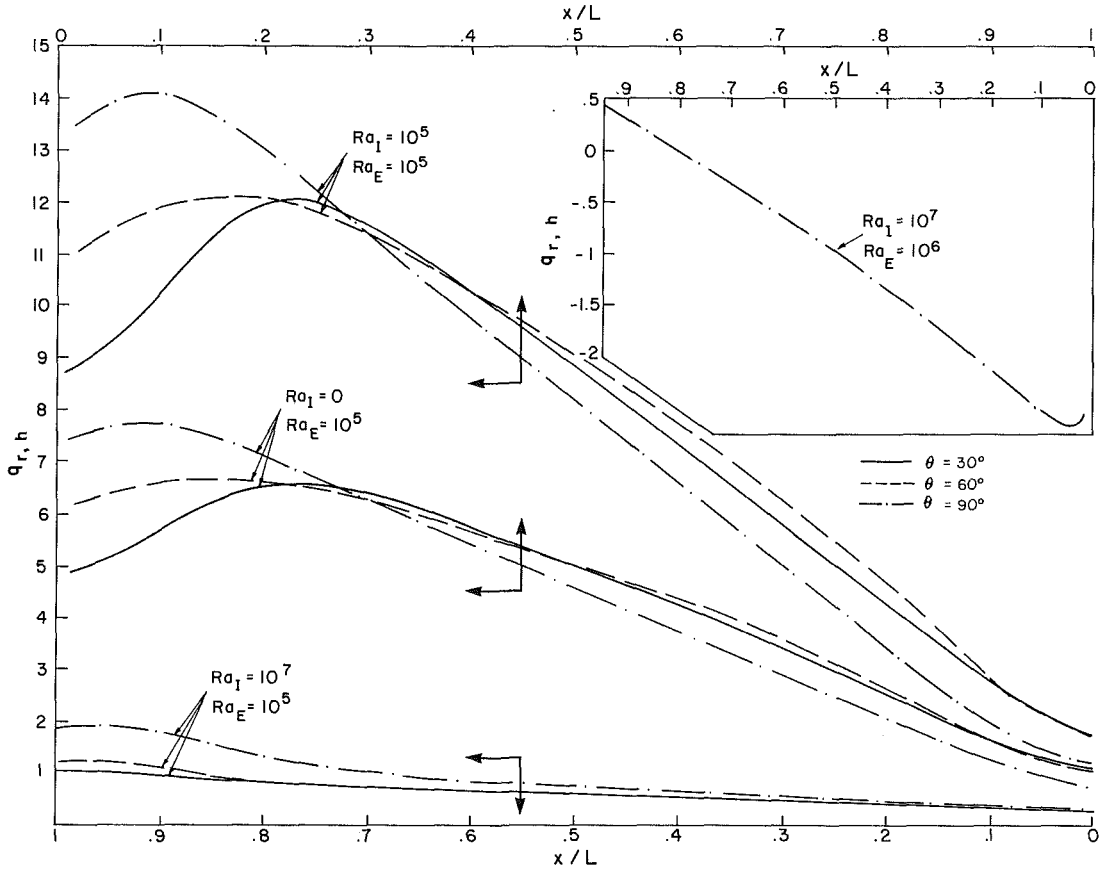

Fig. 15 Local heat flux ratios along the hot surface

perature rises and consequently, the heat flux ratio decreases. For large Ra_I values (e.g, 10^7) the hot interior fluid moves in a downward direction over the hot surface and therefore the maximum value of $q_{r,h}$ is obtained near $x/L = 1$. As before, the temperature of the flow increases and the heat flux ratio decreases in the direction of fluid motion.

The influence of inclination angle (Fig. 15) is particularly strong in the neighborhood of $x/L = 0$ when the flow over the hot surface is upward and in the neighborhood of $x/L = 1$ when the flow is downward along the hot surface. In these regions, the local heat flux ratio is the highest for a vertical enclosure and decreases with decreasing angle. This trend for downward flow along the hot surface ($Ra_I >> Ra_E$) is explained by the increasing strength of the downward flow with increasing angle. For upward flow along the hot surfaces ($Ra_E > Ra_I$) the isotherms become more oblique with decreasing angle and thus provide more uniform temperature distributions and heat transfer ratios.

The inset on Fig. 15 shows the local heat flux ratio along the hot surface for a vertical enclosure at $Ra_I = 10^7$ and $Ra_E = 10^6$. For this case, the conduction flux at the heated surface $q_{h,\text{cond}}$ is still negative while the actual heat flux, due to readjustment of the flow field (Fig. 7), is positive over most of the surface. However, in the vicinity of $x/L = 1$, the convective heat flux q_h is still negative due to the small clockwise eddy present in that corner. Thus, $q_{r,h}$ has both positive and negative values.

Along the cold surface, the flow is always downward. Thus, for all Ra_I, the local heat flux ratio (Fig. 16) is highest in the neighborhood of $x/L \simeq 1$ and decreases in the direction of fluid motion. The local heat flux ratio predictions of Marshall, Heinrich, and Zienkiewicz [30] for an externally heated

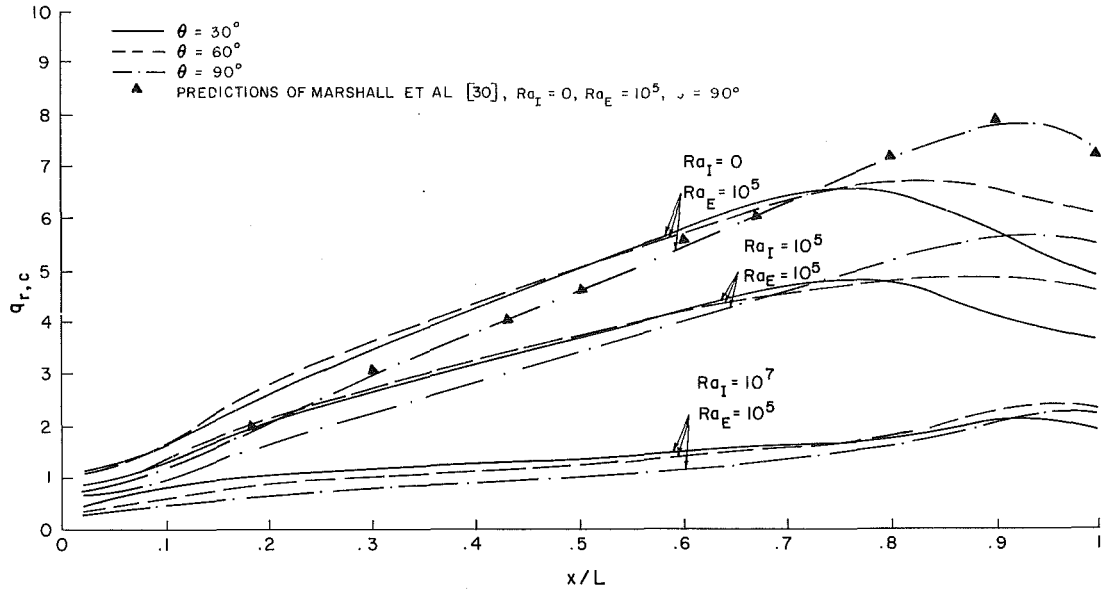

Fig. 16 Local heat flux ratios along the cold surface

vertical enclosure are shown in the figure. As may be seen, the comparison between the two predictions (at $Ra_E = 10^5$) is good.

Maximum Temperatures. The maximum temperature and the corresponding (y/L) location are listed in Table 3 for inclination angles of 30, 60, and 90 deg. Also listed are the maximum temperature values (and the corresponding y/L location) which would be obtained if conduction alone were responsible for the heat transfer behavior in the enclosure. The values are listed only for Rayleigh numbers for which the maximum temperature is observed to occur between the hot and cold surface. For all other values of Ra_E and Ra_I, the maximum temperature is attained at the hot surface.

The maximum temperature in the presence of conduction alone depends on the ratio (Ra_I/Ra_E) and therefore, for larger Ra_I/Ra_E, higher temperatures are obtained. In the presence of convection, hot interior fluid is convectively cooled by the hot and cold surface and therefore compared to $\phi_{cond,max}$, the values of ϕ_{max} are considerably smaller. For all Rayleigh numbers listed in Table 3, the highest temperature occurs along the elevated adiabatic wall (at $x/L = 1$). This is to be expected since heated fluid rises from the interior or from the hot surface and blankets the top adiabatic wall.

The y/L location at which ϕ_{max} occurs depends on the nature of the flow pattern. For a vertical enclosure, if Ra_I is much larger than Ra_E, the flow and isotherm patterns are approximately symmetric and therefore the y/L value corresponding to ϕ_{max} is in the neighborhood of 0.5. As the inclination angle is decreased, the symmetry in the temperature distribution is lost, with the counterclockwise flow along the cold surface increasing in size and strength and thus transporting more energy towards the cold wall. Therefore, for an inclined enclosure, the ϕ_{max} location is shifted toward the cold wall.

For a transitional flow pattern, the location of ϕ_{max} depends on the size, strength, and location of the clockwise eddy along the top adiabatic surface.

Concluding Remarks

The flow and heat transfer for two-dimensional natural convection in an externally heated vertical or inclined box containing internal energy sources have been solved by a finite-difference procedure. When Ra_E is greater than or equal to Ra_I, the flow is upward along the hot surface and downward along the cold surface. However, when Ra_I is considerably larger than Ra_E the flow is downward along the hot wall and also along the cold wall. The transition from one flow pattern to another occurs over a range of Ra_E which is approximately given by $0.1Ra_I \leqq Ra_E \leqq Ra_I$.

The average heat flux ratio along the cold surface increases monotonically with increasing Ra_E. However, the average heat flux ratio along the hot surface displays a nonmonotonic behavior for nonzero Ra_I. The local heat flux ratio at a surface attains its maximum value in the vicinity of the region where the heated (or cooled) fluid from the opposite wall or the interior encounters the surface.

Acknowledgments

The authors wish to express their appreciation for support from the National Science Foundation Heat Transfer Program.

References

1 Buchberg, H., Catton, I., and Edwards, D. K., "Natural Convection in Enclosed Spaces – A Review of Application to Solar Energy Collection," ASME JOURNAL OF HEAT TRANSFER, Vol. 98, 1976, p. 182.

2 Korpela, S. A., Lee, Y., and Drummond, J. E., "Heat Transfer Through a Double Pane Window," ASME JOURNAL OF HEAT TRANSFER, Vol. 104, 1982, p. 539.

3 Baker, L., Faw, R. E., and Kulacki, F. A., "Postaccident Heat Removal – Part 1: Heat Transfer Within an Internally Heated, Non-Boiling Liquid Layer," *Nuclear Science and Engineering*, Vol. 61, 1976, p. 222.

4 McKenzie, D. P., Roberts, J. M., and Weiss, N. O., "Convection in the Earth's Mantle: Towards a Numerical Simulation," *J. Fluid Mech.*, Vol. 62, 1974, p. 465.

5 Tritton, D. J., "Internally Driven Heat Convection in the Atmosphere of Venus and in the Laboratory," *Nature*, Vol. 257, 1975, p. 110.

6 Sua-Anttila, A. J., and Catton, I., "The Effect of a Stabilizing Temperature Gradient on Heat Transfer From a Molten Fuel Layer With Volumetric Heating," ASME JOURNAL OF HEAT TRANSFER, Vol. 97, 1975, p. 544.

7 Suo-Anttila, A. J., and Catton, I., "An Experimental Study of a Horizontal Layer of Fluid With Volumetric Heating and Unequal Surface Temperatures," Paper No. AICHE-5, *16th National Heat Transfer Conference*, St. Louis, 1976.

8 Cheung, F. B., "Correlation Equation for Turbulent Thermal Convection in a Horizontal Fluid Layer Heated Internally and From Below," ASME JOURNAL OF HEAT TRANSFER, Vol. 100, 1978, p. 416.

9 Boon-Long, P., Lester, T. W., and Faw, R. E., "Convective Heat Transfer in an Internally Heated Horizontal Fluid Layer With Unequal Boundary Temperatures," *Int. J. Heat Mass Transfer*, Vol. 22, 1979, p. 437.

10 Kikuchi, Y., Kawasaki, T., and Shioyama, T., "Thermal Convection in a Horizontal Fluid Layer Heated Internally and From Below," *Int. J. Heat Mass Transfer*, Vol. 25, 1982, p. 363.

11 Nansteel, M. W., and Grief, R., "Natural Convection in Undivided and Partially Divided Rectangular Enclosures," ASME JOURNAL OF HEAT TRANSFER, Vol. 103, 1981, p. 623.

12 Linthorst, S. J. M., Schinkel, W. M. M., and Hoogendoorn, C. J., "Flow Structure with Natural Convection in Inclined Air Filled Enclosures," ASME JOURNAL OF HEAT TRANSFER, Vol. 103, 1981, p. 535.

13 Arnold, J. N., Catton, I., and Edwards, D. K., "Experimental Investigations of Natural Convection in Inclined Rectangular Regions of Differing Aspect Ratios," ASME JOURNAL OF HEAT TRANSFER, Vol. 98, 1976, p. 67.

14 Ozoe, H., Sayama, H., and Churchill, S. W., "Natural Convection in an Inclined Square Channel," *Int. J. Heat Mass Transfer*, Vol. 17, 1974, p. 401.

15 Ozoe, H., Yamamoto, K., Sayama, H., and Churchill, S. W., "Natural Convection Patterns in a Long Inclined Rectangular Box Heated From Below: Part II. Three Dimensional Numerical Results," *Int. J. Heat Mass Transfer*, Vol. 20, 1977, p. 131.

16 Ozoe, H., Sayama, H., and Churchill, S. W., "Natural Convection Patterns in a Long Inclined Rectangular Box Heated From Below," *Int. J. Heat Mass Transfer*, Vol. 20, 1977, p. 123.

17 Ozoe, H., Yamamoto, K., Sayama, H., and Churchill, S. W., "Natural Circulation in an Inclined Rectangular Channel Heated on One Side and Cooled on the Opposing Side," *Int. J. Heat Mass Transfer*, Vol. 17, 1974, p. 1209.

18 Ozoe, H., Fujii, K., Lior, N., and Churchill, S. W., "Long Rolls Generated by Natural Convection in an Inclined Rectangular Enclosure," *Int. J. Heat Mass Transfer*, Vol. 26, 1983, p. 1427.

19 Goldstein, R. J., and Wang, Q. J., "An Interferometric Study of the Natural Convection in an Inclined Water Layer," *Int. J. Heat Mass Transfer*, Vol. 27, 1984, p. 1445.

20 Inaba, H., "Experimental Study of Natural Convection in an Inclined Air Layer," *Int. J. Heat Mass Transfer*, Vol. 27, 1984, p. 1127.

21 Hart, J. E., "Stability of the Flow in a Differentially Heated Inclined Box," *J. Fluid Mech.*, Vol. 47, 1971, p. 547.

22 Hollands, K. G. T., and Konicek, L., "Experimental Study of the Stability of Differentially Heated Inclined Air Layers," *Int. J. Heat Mass Transfer*, Vol. 16, 1973, p. 1467.

23 Jahn, M., and Reineke, H. H., "Free Convection Heat Transfer with Internal Heat Sources, Calculations and Measurements," Paper NC2.8, *5th Int. Heat Transfer Conf.*, Tokyo, Sept. 1974.

24 Patankar, S. V., *Numerical Heat Transfer and Fluid Flow*, Hemisphere Publishing, 1980.

25 de Vahl Davis, G., "Natural Convection of Air in a Square Cavity. A Bench Mark Solution," Report 1982/FMT/2, School of Mechanical and Industrial Engr., Univ. of New South Wales, Apr. 1982.

26 Strada, M., and Heinrich, J. C., "Heat Transfer Rates in Natural Convection at High Rayleigh Numbers in Rectangular Enclosures," *Numerical Heat Transfer*, Vol. 5, 1982, p. 81.

27 Quon, C., "High Rayleigh Number Convection in an Enclosure — A Numerical Study," *Physics of Fluids*, Vol. 15, 1972, p. 12.

28 Wong, H. H., and Raithby, G. D., "Improved Finite Difference Methods Based on a Critical Evaluation of the Approximation Errors," *Numerical Heat Transfer*, Vol. 2, 1979, p. 139.

29 Roux, B., Grondin, J. C., Bontoux, P., and Gilly, B., "On a High Order Accurate Method for the Numerical Study of Natural Convection in a Vertical Square Cavity," *Numerical Heat Transfer*, Vol. 1, 1978, p. 331.

30 Marshall, R. S., Heinrich, J. C., and Zienkiewicz, O. C., "Natural Convection in a Square Enclosure by a Finite-Element Penalty Function Method Using Primitive Fluid Variables," *Numerical Heat Transfer*, Vol. 1, 1978, p. 315.

Natural Convection in a Confined Fluid-Filled Space Driven by a Single Vertical Wall With Warm and Cold Regions

D. Poulikakos
Mechanical Engineering Department,
University of Illinois at Chicago,
Box 4348,
Chicago, IL 60680
Assoc. Mem. ASME

This paper reports heat and fluid flow results which describe the phenomenon of natural convection in an enclosure heated and cooled along a single vertical wall. In the first part of the paper, the case where the side-heating effect is positioned above the side-cooling effect is considered. Numerical simulations and scale analysis show that the temperature field in this configuration transforms from one of incomplete vertical penetration to one of incomplete horizontal penetration depending on the values of the Rayleigh number based on the enclosure height (Ra) and the height-to-length aspect ratio of the enclosure (H/L). *The heat transfer scales differ substantially from one type of penetrative convection to the other in agreement with the numerical findings. The parametric domain of validity of the conclusions of this part of the study is outlined on the* H/L–*Ra plane. When the heated portion of the driving side wall is positioned below the cooled portion the flow spreads throughout the cavity. This configuration results in an enhancement of the overall heat transfer through the enclosure.*

1 Introduction

The phenomenon of natural convection in a confined space filled with fluid has received a great deal of attention in recent years, primarily because this phenomenon often affects the thermal performance in many engineering applications. These applications are exemplified by energy conservation in building enclosures, solar collector spaces, thermal circulation in lakes and estuaries, and cooling of electronic equipment.

When the natural circulation is triggered by heating or cooling from the side, the popular model used by many fundamental studies of the problem frequently assumes isothermal vertical boundaries kept at different temperatures, and adiabatic horizontal boundaries. The heat and fluid flow characteristics for this configuration are well documented in the literature [1–3]. A common finding of these studies is that the natural circulation fills the entire enclosure and that the cooling and heating effect of the vertical boundaries is felt by the entire fluid body occupying the enclosure.

The object of this paper is to draw attention to a relatively unknown class of natural convection in enclosed spaces, namely, the thermal flows driven by heating and cooling a single vertical boundary (Fig. 1). From a practical standpoint this class of problems is relevant to all natural convection applications possessing vertical boundaries with hot and cold regions (building walls, for example, often contain differentially heated regions). From the point of view of fundamental research, this class of problems constitutes a first attempt toward a better understanding of the effect of more realistic (other than uniform temperature or heat flux) thermal boundary conditions on the net heat transfer through enclosed spaces. Related work with applications to solar collectors has been reported in [4] which focuses on natural convection on an inclined rectangular box with the top surface cold and the lower surface half heated and half insulated. The findings in [4] differ significantly from those for a uniformly heated lower surface, since the size and relative strength of the cells in the box depended on the size of the hot portion of the bottom wall. The authors in [4] concluded that "unintentional and undocumented deviations from isothermality and/or perfect insulation may produce significant and anomalous effects." Solutions for natural convection from a vertical flat plate in contact with an unbounded fluid reservoir, involving discontinuous changes in the plate temperature, have been reported in [5].

In this paper it is shown that when the flow is diven by a single differentially heated vertical wall, under certain circumstances the length scales of thermal penetration due to this wall differ from the dimensions of the enclosure in which the flow develops. This type of "incomplete thermal penetration" differs fundamentally from the classical problem [1–3] where the thermal flow occupies the entire enclosure. In this study it is also shown that under a different set of circumstances the thermal effect of the differentially heated driving wall is felt by the entire fluid body occupying the system. Thus, the class of natural convection flows driven by a single vertical boundary with hot and cold regions may or may not result in complete thermal penetration in the enclosure.

2 Mathematical Formulation

The system of interest is shown in Fig. 1. The left wall is differentially heated while the three remaining walls are insulated. All walls are impermeable. In the first part of the study we consider the case where the upper half of the left wall is heated and the lower half is cooled. The opposite situation will be considered at the end of this study. For the temperature distribution along the left wall we used the step function

$$T(0,y)=\begin{cases} T_0-\Delta T & 0<y<H/2 \\ T_0+\Delta T & H/2<y<H \end{cases} \tag{1}$$

where the subscript 0 denotes the reference temperature at midheight ($y=H/2$).

The usual Boussinesq-approximated equations governing the conservation of mass momentum and energy at each point in the system shown in Fig. 1 are

Contributed by the Heat Transfer Division for publication in the JOURNAL OF HEAT TRANSFER. Manuscript received by the Heat Transfer Division June 28, 1984.

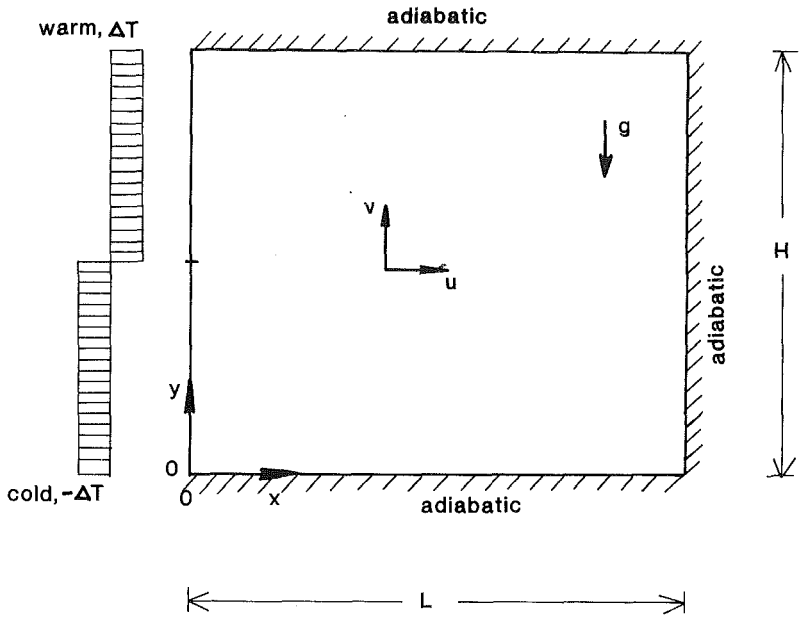

Fig. 1 Two-dimensional confined fluid layer differentially heated along a single vertical wall

$$\frac{\partial u}{\partial x}+\frac{\partial v}{\partial y}=0 \tag{2}$$

$$\frac{\partial u}{\partial t}+u\frac{\partial u}{\partial x}+v\frac{\partial u}{\partial y}=-\frac{1}{\rho_0}\frac{\partial P}{\partial x}+\nu\nabla^2 u \tag{3}$$

$$\frac{\partial v}{\partial t}+u\frac{\partial v}{\partial x}+v\frac{\partial v}{\partial y}=-\frac{1}{\rho_0}\frac{\partial P}{\partial y}+\nu\nabla^2 v-g[1-\beta(T-T_0)] \tag{4}$$

$$\frac{\partial T}{\partial t}+u\frac{\partial T}{\partial x}+v\frac{\partial T}{\partial y}=\alpha\nabla^2 T \tag{5}$$

In the above equations T is the temperature, P the pressure, x and y the Cartesian coordinates, u and v the horizontal and the vertical component of velocity, g the gravitational acceleration, and ρ, ν, β, α the fluid density, kinematic viscosity, coefficient of thermal expansion, and thermal diffusivity, respectively. Subscript zero refers to a reference state. Combining statements (3) and (4) to eliminate the pressure P yields a single momentum equation

$$\frac{\partial}{\partial t}\left(\frac{\partial u}{\partial y}-\frac{\partial v}{\partial x}\right)+\frac{\partial}{\partial y}\left(u\frac{\partial u}{\partial x}+v\frac{\partial u}{\partial y}\right)-\frac{\partial}{\partial x}\left(u\frac{\partial v}{\partial x}+v\frac{\partial v}{\partial y}\right)=\nu\left[\frac{\partial}{\partial y}(\nabla^2 u)-\frac{\partial}{\partial x}(\nabla^2 v)\right]-g\beta\frac{\partial T}{\partial x} \tag{6}$$

Relative to the Cartesian system shown in Fig. 1 the appropriate boundary conditions for solving equations (2), (5), and (6) are

$$\begin{aligned} &u=v=0, \quad T=\text{function given by equation (1) at } x=0\\ &u=v=0, \quad \frac{\partial T}{\partial x}=0 \text{ at } x=L\\ &u=v=0, \quad \frac{\partial T}{\partial y}=0 \text{ at } y=0, H \end{aligned} \tag{7}$$

In what follows we rely on numerical simulations and on scaling arguments to document the natural convection phenomena taking place in the fluid-filled cavity heated and cooled along the left vertical wall. Uniform initial conditions were assumed for all the numerical simulations reported in this paper, that is, the enclosure was initially isothermal and filled with motionless fluid ($u=v=0$, $T=T_0$). At $t=0$, the boundary condition under examination was imposed on the driving wall at $x=0$ (equation (7)). Two different sets of initial conditions were also considered to determine the effect of these conditions on the steady-state flow and temperature

Nomenclature

g = gravitational acceleration
H = enclosure height
h = vertical thermal penetration distance, Fig. 6
k = thermal conductivity of fluid
L = enclosure length
l = horizontal thermal penetration distance, Fig. 6
m = number of vertical grid lines
n = number of horizontal grid lines
Nu = Nusselt number, equation (18)
P = pressure
Pr = Prandtl number, equation (15)
Q = overall heat transfer rate
Ra = Rayleigh number based on H, equation (16)
T = temperature
T_0 = average temperature
ΔT = temperature step increment
u = horizontal velocity
v = vertical velocity
x = horizontal coordinate
y = vertical coordinate
α = fluid thermal diffusivity
β = coefficient of thermal expansion
δ_t = thermal boundary layer thickness
μ = viscosity
ν = kinematic viscosity = μ/ρ
ρ = density
ψ = streamfunction

Superscripts

$\hat{}$ = dimensionless variable

Table 1 Numerical results for natural convection in a fluid layer heated and cooled along one vertical wall, for Pr = 0.7, unless noted otherwise

H/L	Ra	Nu	Grid ($m \times n$)
	side heating located above side cooling		
4	10^4	1.284	21 × 81
4	3×10^4	1.372	21 × 81
4	6×10^4	1.455	21 × 81
4	10^5	1.527	21 × 81
2	10^5	2.046	21 × 41
1	10^2	1.455	41 × 41
1	10^3	1.52	41 × 41
1	10^4	1.951	41 × 41
1	10^5	2.583	21 × 21
1	10^5	2.693	33 × 33
1	10^5	2.698	41 × 41
1	10^5	2.7	53 × 53
1	10^5	(Pr = 6) 2.835	41 × 41
1/5	10^2	1.465	101 × 21
1/5	10^3	1.61	101 × 21
1/5	10^4	2.123	101 × 21
1/5	10^5	3.971	101 × 21
1/6	10^2	1.465	121 × 21
1/8	10^2	1.465	161 × 21
	side heating located below side cooling		
1	10^2	1.456	41 × 41
1	10^3	1.55	41 × 41
1	10^4	2.59	41 × 41
1	10^5	4.931	41 × 41
4	10^5	2.697	21 × 81

patterns: (*a*) The system was initially isothermal at the cold temperature ($u=v=0$, $T=T_0-\Delta T$) and at $t=0$, the temperature of the warm portion of the driving wall was raised to $T=T_0+\Delta T$. (*b*) The system was initially isothermal at the warm temperature ($u=v=0$, $T=T_0+\Delta T$) and at $t=0$, the temperature of the cold portion of the driving wall was lowered to $T_0-\Delta T$. These two alternative sets of initial conditions yielded identical steady states for a number of test runs.

3 Numerical Simulations

Before solving the problem numerically, it is convenient to nondimensionalize the governing equations and boundary conditions. Selecting H, ν/H, ΔT, and H^2/ν as reference quantities for length, velocity, temperature, and time we define the following group of dimensionless variables

$$\hat{x} = x/H,\ \hat{y}=y/H,\ \hat{t}=\frac{t}{H^2/\nu}$$
$$\hat{u} = \frac{u}{\nu/H},\ \hat{v}=\frac{v}{\nu/H},\ \hat{T}=\frac{T-T_0}{\Delta T} \tag{8}$$

Next, introducing the dimensionless stream function

$$\hat{u}=\frac{\partial\hat{\psi}}{\partial\hat{y}}, \tag{9}$$

$$\hat{v}=-\frac{\partial\hat{\psi}}{\partial\hat{x}} \tag{10}$$

and the dimensionless vorticity

$$\hat{\omega}=-\nabla^2\hat{\psi} \tag{11}$$

we recast the governing equations and boundary conditions (equations (5-7)) in the following form

$$\frac{\partial\hat{\omega}}{\partial\hat{t}}+\frac{\partial(\hat{u}\hat{\omega})}{\partial\hat{x}}+\frac{\partial(\hat{v}\hat{\omega})}{\partial\hat{y}}=\nabla^2\hat{\omega}+\frac{\mathrm{Ra}}{\mathrm{Pr}}\frac{\partial\hat{T}}{\partial\hat{x}} \tag{12}$$

$$\frac{\partial\hat{T}}{\partial\hat{t}}+\frac{\partial(\hat{u}\hat{T})}{\partial\hat{x}}+\frac{\partial(\hat{v}\hat{T})}{\partial\hat{y}}=\mathrm{Pr}^{-1}\nabla^2\hat{T} \tag{13}$$

at $\hat{x}=0$: $\hat{u}=\hat{v}=\hat{\psi}=0$, $\quad T=\begin{cases}-1 & \text{for } 0<\hat{y}<\frac{1}{2}\\ 1 & \text{for } \frac{1}{2}<\hat{y}<1\end{cases}$

at $\hat{x}=L/H$: $\hat{u}=\hat{v}=\hat{\psi}=0$, $\quad \dfrac{\partial\hat{T}}{\partial\hat{x}}=0$ (14)

at $\hat{y}=0,1$: $\hat{u}=\hat{v}=\hat{\psi}=0$, $\quad \dfrac{\partial\hat{T}}{\partial\hat{y}}=0$

where Pr and Ra are the Prandtl number and the Rayleigh number based on the enclosure height respectively,

$$\mathrm{Pr}=\frac{\nu}{\alpha}, \tag{15}$$

$$\mathrm{Ra}=\frac{g\beta H^3\Delta T}{\nu\alpha} \tag{16}$$

The above formulation shows that the dimensionless solution depends on the Prandtl number, the Rayleigh number, and the aspect ratio L/H. The present study is mainly concerned with the effect of the last two parameters on the thermal penetration characteristics of the natural convective flow in the cavity. Hence, the value of the Prandtl number is, unless noted otherwise, fixed at Pr = 0.7 typical of air.

The governing equations (9–13) were discretized using the control volume formulation [6]. The region of interest was covered with m vertical and n horizontal uniformly spaced grid lines. The numerical solution method was true-transient and fully implicit. At each time step the temperature and vorticity distributions were obtained from equations (12) and (13) respectively by using the power law scheme. This scheme was developed, tested, and recommended by Patankar [6] and it is well established in the literature. Briefly, the power law scheme exhibits the qualitative behavior of the exponential scheme (the exact solution for one-dimensional convection problems) while it is easier to compute. The power law scheme has also performed very well in enclosure natural convection studies exemplified by [7, 8]. Next, the streamfunction distribution was obtained from equation (11) by using successive relaxation [6, 9] and a known vorticity distribution. The above process was repeated in the next time step until steady state was reached. The grid fineness $m=n=41$ was used for the case $H/L=1$, $\mathrm{Ra}=10^5$, even though grids as coarse as $m=n=21$ yielded results accurate within 10 percent of the results of the chosen more refined grid. The grids used in other cases are listed in Table 1. When natural convection near a differentially heated vertical wall facing a semi-infinite space ($H/L \ll 1$) was simulated, the minimum number of vertical grid lines that lead to a solution satisfying the far-field boundary conditions $\hat{\psi}=0$ and $\partial\hat{T}/\partial\hat{x}=0$ within a prescribed error, was used. Table 1 shows that the largest number of vertical grid lines used was $m=161$ in the case $\mathrm{Ra}=100$, $H/L=1/8$. As an additional check on the numerical simulations in the shallow layer limit, we calculated the values of $\hat{T}$ at the insulated end ($\hat{x}=L/H$) and found that $\hat{T}$ is particularly zero (to the sixth decimal point). Hence, despite the fact that the domain of the numerical solution was finite in length, in order to simulate convection in the $H/L\to 0$ limit we used a long enough domain so that the fluid situated far from the driving wall remained unaffected by the heating and cooling effects provided by the driving wall. The dimensionless time step which yielded convergence for the majority of cases was $\hat{t}=0.1$.

An iterative process was employed to find the streamfunction, vorticity, and temperature fields. The process was repeated until the following criterion was satisfied

$$\frac{\sum_{i=1}^{m}\sum_{j=1}^{n}|\phi_{i,j}^{r+1}-\phi_{i,j}^{r}|}{\sum_{i=1}^{m}\sum_{j=1}^{n}|\phi_{i,j}^{r+1}|}<10^{-6} \tag{17}$$

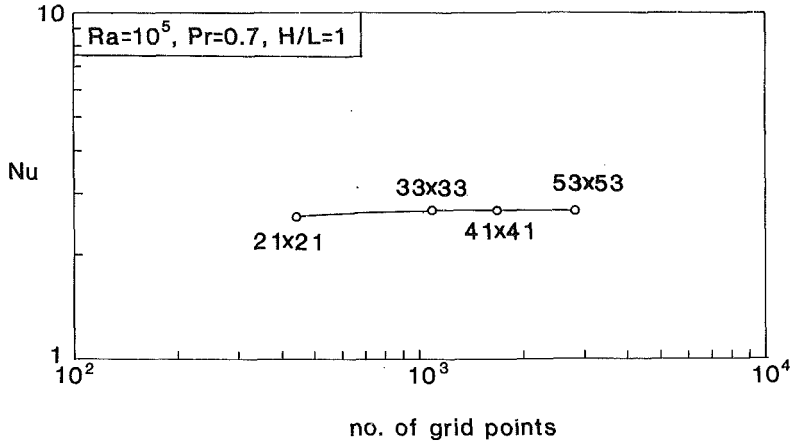

Fig. 2 An example on the adequacy of the grid fineness

In the above criterion, ϕ stands for $\hat{\psi}$, $\hat{T}$, or $\hat{\omega}$ and r denotes the number of time steps.

The effect of fluid motion on the net heat transfer rate Q entering the system through the heated portion of the driving wall was evaluated and cast in dimensionless form as a Nusselt number

$$\mathrm{Nu} = \frac{Q}{k\Delta T} = -\int_{1/2}^{1} \left(\frac{\partial \hat{T}}{\partial \hat{x}}\right)_{\hat{x}=0} d\hat{y} \tag{18}$$

The numerical integration of equation (18) was performed after the steady-state temperature field was obtained. A relation similar to equation (18) is obtained by integrating the heat flux along the cold portion of the driving wall. This second calculation was carried out in all cases in order to check the accuracy of the original estimate (equation (18)). Throughout the course of this study, the results agreed better than 2.5 percent. The above accuracy check is justified, for it assures that the total heat flux in the enclosure equals the total heat flux out of the enclosure at all times, since, according to the initial conditions used in this study, the numerically obtained temperature field in the cavity must be symmetric about the midheight at all times. As discussed at the end of Section 2, we also experimented with two different sets of initial conditions. For these initial conditions the transient temperature field in the cavity is nonsymmetric. Thus, showing that the Nusselt number of the bottom half of the wall equals the Nusselt number of the top half, while satisfying criterion (17), assures steady-state conditions. In addition, mass was conserved as integrating the velocity field along a vertical grid line for a number of test cases indicated.

The overall Nusselt number was also used to develop an understanding of what grid fineness is necessary for accurate numerical simulations. As shown in Fig. 2 and Table 1, in the case $\mathrm{Ra}=10^5$, $H/L=1$, a grid containing 41 vertical and 41 horizontal grid lines yields satisfactory results. The fineness of the grids used throughout this study is comparable with the case $m=41$, $n=41$ whose accuracy is illustrated in Fig. 2 and Table 1.

Since a step change in the temperature of the driving wall is imposed a question pertaining to the accuracy of the heat transfer calculations (Nu) might be raised due to the fact that the heat flux in y blows up mathematically at midheight ($y=H/2$, $x=0$) where the temperature changes from $\hat{T}=-1$ to $\hat{T}=1$ across zero distance (the hot and the cold portions make direct thermal contact). However, in a real situation, the fluid (and the wall) in the neighborhood of $x=0$, $y=H/2$ will reach an average temperature between $\hat{T}=1$ and $\hat{T}=-1$, thus removing the temperature discontinuity and its unrealistic implication. For the present numerical simulations the point at midheight on the left wall was assigned the value $\hat{T}=0$ (the average of the warm and cold temperatures).

4 Discussion of Numerical Results

The main characteristics of the natural convection pattern in a fluid space differentially heated along a single vertical wall are shown in Figs. 3 and 4. These figures show the effect of changing the Rayleigh number Ra and the effect of changing the height-to-length aspect ratio H/L.

In relatively tall spaces (Fig. 3*a*, *b*) increasing H/L while keeping Ra constant weakens the flow significantly. Note that in going from left to right in Fig. 3(*a*), the strength of each cell ($\hat{\psi}_{\max}$) decreases. The flow pattern consists of two counterrotating cells symmetric about the midheight. The upper cell rotates clockwise driven by the warm region of the left wall and by its contact with the lower cell. A similar argument holds for the lower cell.

The isotherm patterns shown in Fig. 3(*b*) show that increasing H/L transforms the temperature field in the enclosure from one of complete vertical thermal penetration to one of incomplete vertical thermal penetration. The upper and lower segments of a tall fluid layer are occupied by weakly moving almost isothermal fluid. The upper end of the $H/L=4$ system, for example, is filled with fluid almost as hot as the hot section of the left wall. This fluid is unable to feel the cooling effect existing near the $y=H/2$ plane and remains "trapped" at the highest altitude possible. The same argument holds for the cold fluid occupying the lower end of the slender layer. The trend shown in Fig. 3(*b*) implies that this "trapping" phenomenon becomes more dramatic as the height-to-length aspect ratio increases.

In relatively shallow layers (Fig. 4*a*, *b*) the flow field consists again of two counterrotating cells symmetric about the midheight. The cells fill the entire height of the enclosure. However, the length of the cells depends on the Rayleigh number, i.e., the higher Ra the longer the horizontal distance the fluid travels before being driven back into the left wall region. The isotherm maps in Fig. 4(*b*) show that when the horizontal dimension of the enclosure is longer than the horizontal thermal penetration length then the right end of the layer is filled with relatively motionless isothermal fluid that does not participate in the convection heat exchange between the hot and the cold regions of the left wall. This is the case shown in Fig. 4(*b*) for $\mathrm{Ra}=100$. It was observed that the temperature and flow fields for this case did not change significantly when we increased L while keeping H fixed. The "inactive" region located near the right wall increased in length leaving the "active" region near the left wall unaffected. Increasing the Rayleigh number however to $\mathrm{Ra}=10^5$

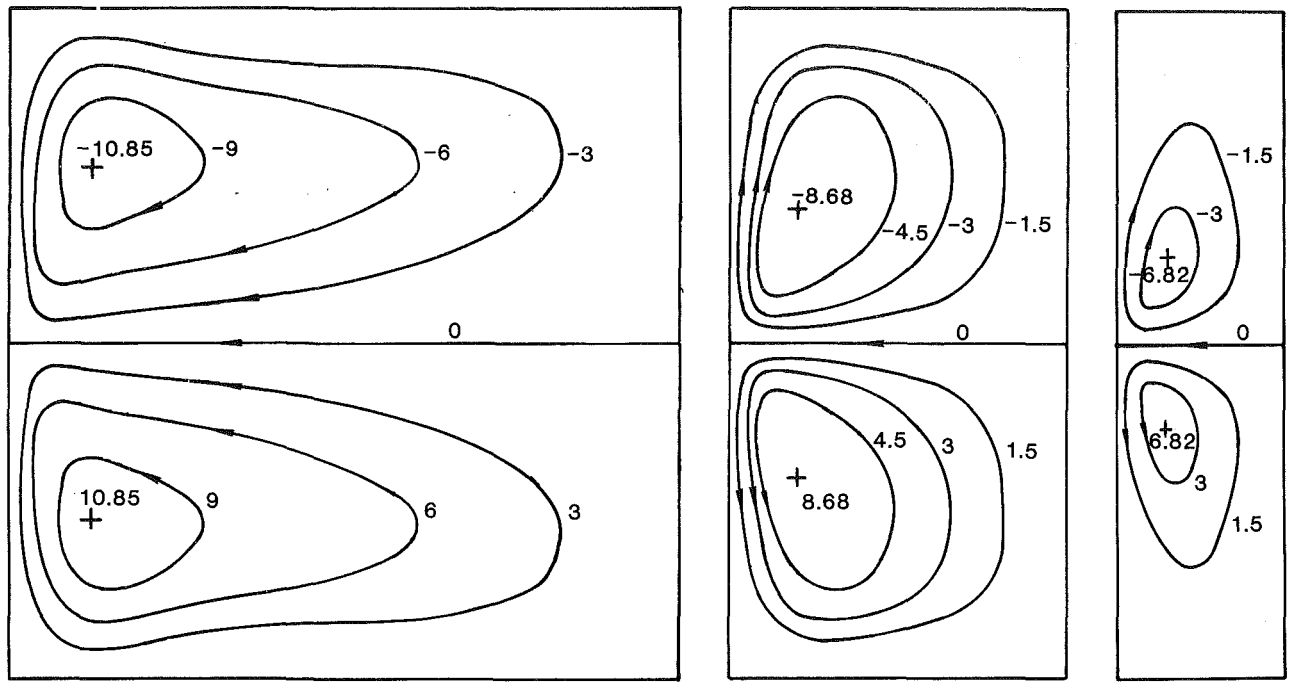

Fig. 3(*a*)

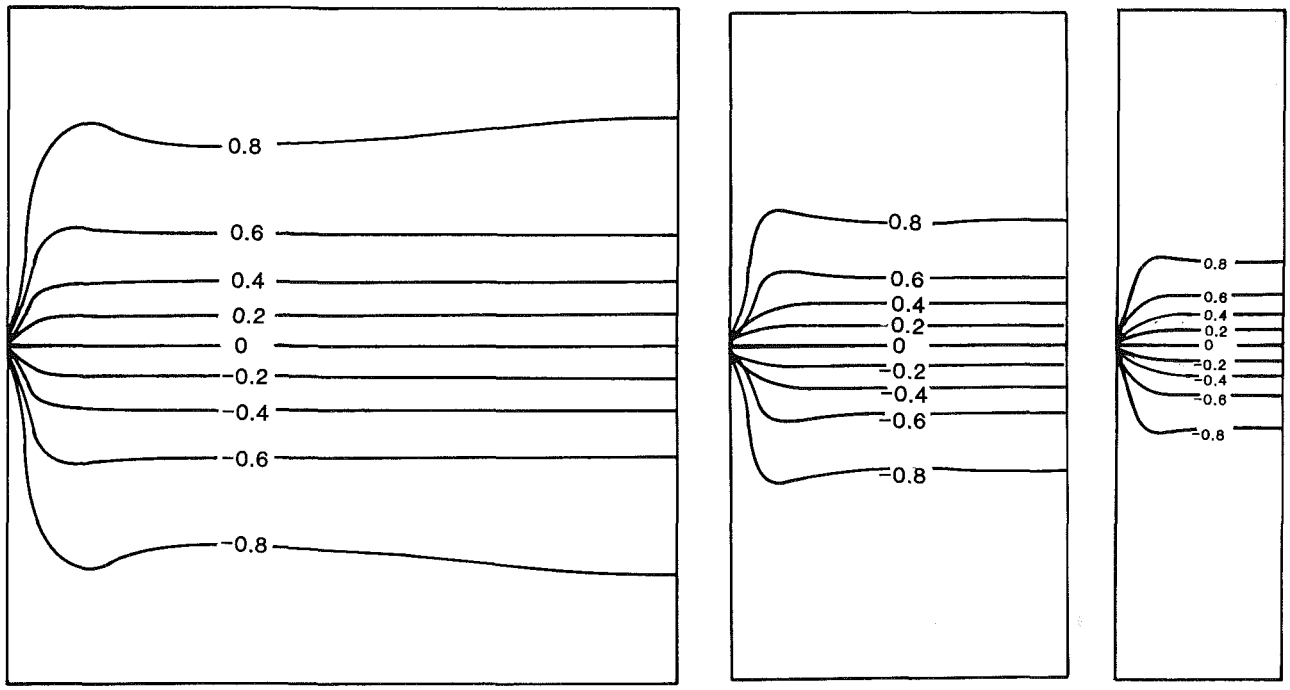

Fig. 3(*b*)

Fig. 3 Numerical results for Ra = 10^5 and *H/L* = 1, 2, 4 showing the phenomenon of incomplete vertical penetration: (*a*) streamlines; (*b*) isotherms

yields the complete horizontal penetration temperature and flow fields exhibited in Fig. 4(*a*, *b*).

With regard to heat transfer from the warm to the cold region of the driving wall, the Nu versus Ra results reported in Fig. 5 indicate that increasing Ra for fixed H/L enhances convection. In addition, in the high Ra regime, increasing the height-to-length ratio for fixed Ra drastically suppresses convection. Finally, increasing the value of Prandtl number to $\mathrm{Pr} = 6$ while keeping $H/L = 1$, $\mathrm{Ra} = 10^5$ increased the value of Nu without significant qualitative effects on the isotherm and streamline patterns. The results shown in Fig. 5 will also be discussed in the following two sections.

In summary, the main conclusion of Figs. 3 and 4 is that the natural convection pattern in the cavity can be one of complete horizontal and vertical penetration or one of complete horizontal and incomplete vertical penetration or one of complete vertical and incomplete horizontal penetration. As we will show in the next section, this phenomenon is governed by distinct scaling laws that govern the overall heat transfer between the differentially heated portions of the driving left

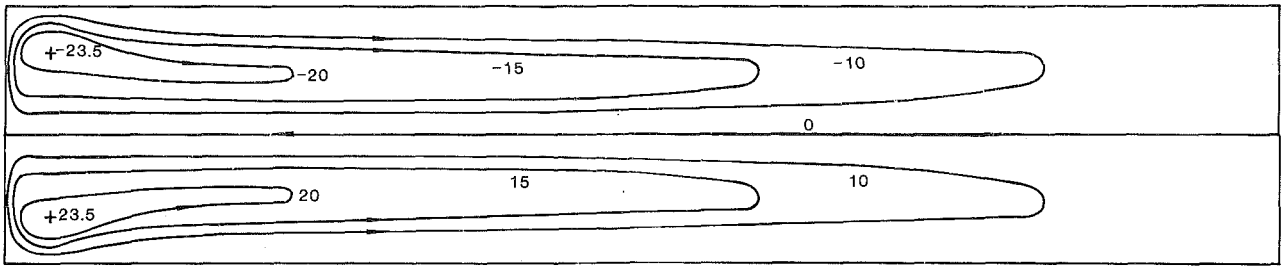

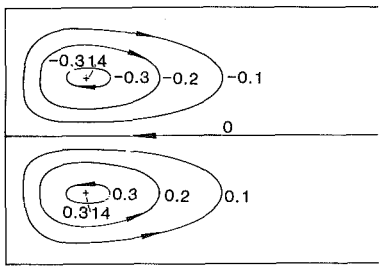

Fig. 4(*a*)

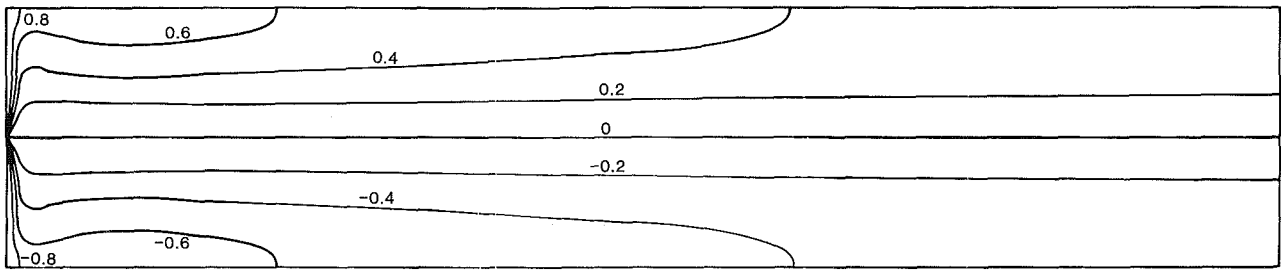

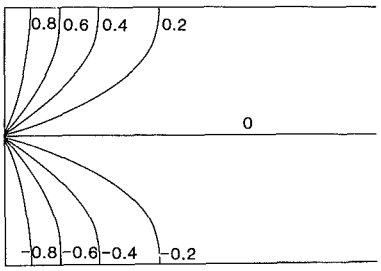

Fig. 4(*b*)

Fig. 4 Numerical results for *H/L* = 1/5 showing the phenomenon of incomplete and complete horizontal penetration: top Ra = 10^5; bottom Ra = 100: (*a*) streamlines; (*b*) isotherms

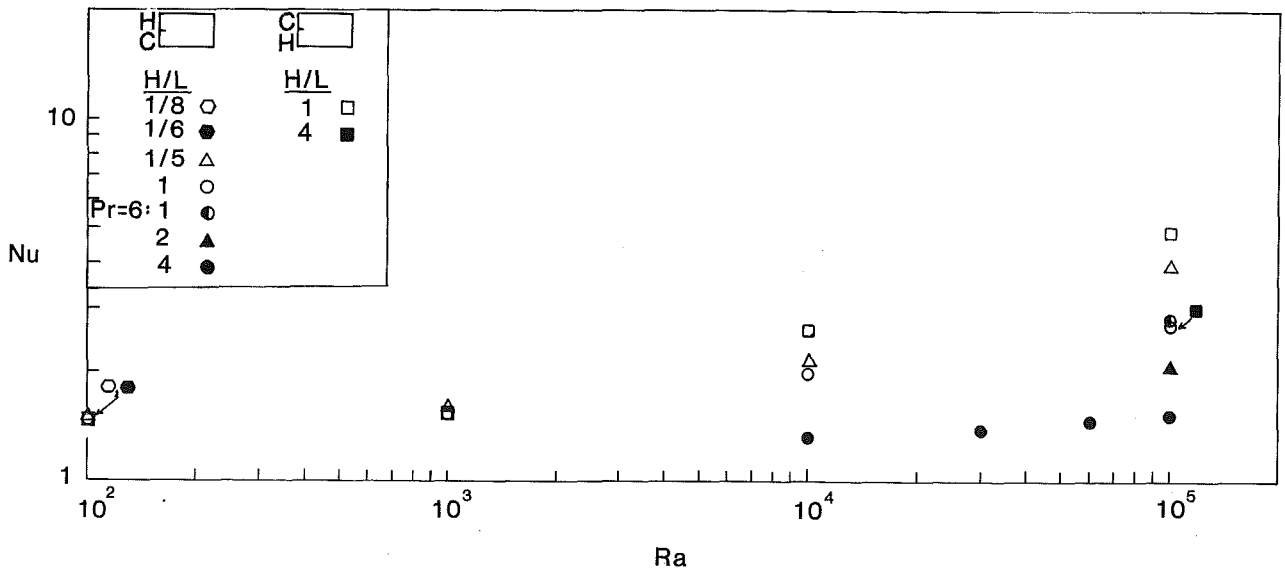

Fig. 5 Numerical results for the overall heat transfer rate through the system; note that since some of the points in this figure are located close to each other, they are difficult to distinguish; Table 1 reports accurate values for the Nusselt number in all runs

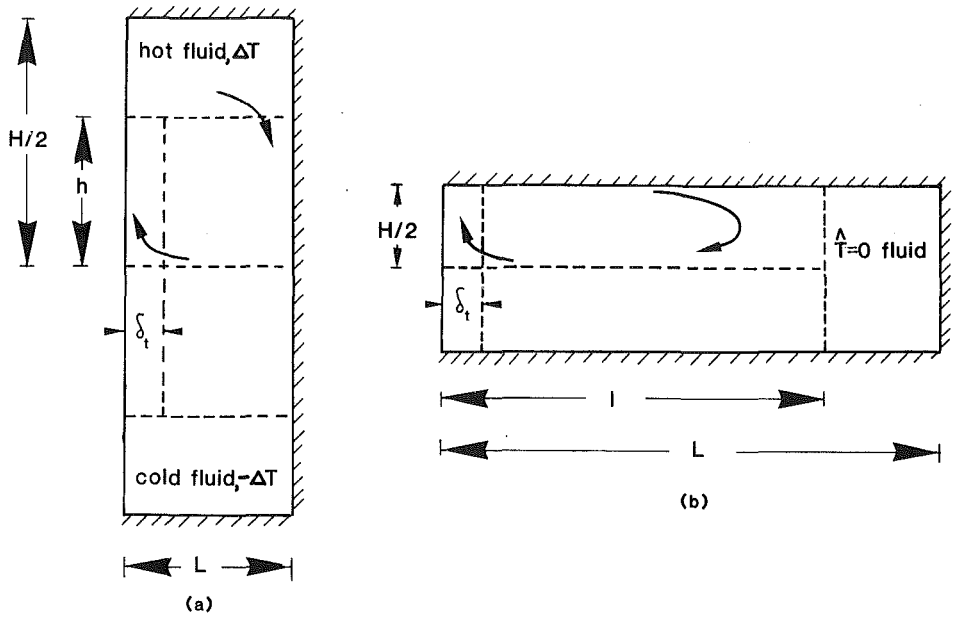

Fig. 6 The scales of thermal penetration in the configuration of Fig. 1: (*a*) incomplete vertical thermal penetration; (*b*) incomplete horizontal thermal penetration

wall. In our scaling analysis, for the sake of brevity, we will focus on the thermal penetration characteristics of the natural convection phenomenon. However, similar arguments can be applied to reveal the main features of the flow penetration in the cavity.

5 Scaling Analysis

(*a*) Vertical Thermal Penetration. Assume first that the thermal penetration height h (Fig. 6) is considerably shorter than the maximum height of the enclosure,

$$h << H/2 \tag{19}$$

Assume further that each cell makes thermal contact with the vertical wall through a slender vertical thermal boundary layer

$$\delta_t << h \tag{20}$$

In the thermal boundary layer region whose height is h and thickness δ_t, it can be easily shown [10, 11] that the correct balance in the momentum equation (6) for Prandtl numbers of order unity or greater is between friction and buoyancy terms

$$\frac{\nu v}{\delta_t^3} \sim g\beta\frac{\Delta T}{\delta_t} \tag{21}$$

In addition, the energy equation (5) at the same location requires

$$\frac{v\Delta T}{h} \sim \alpha\frac{\Delta T}{\delta_t^2} \tag{22}$$

Finally, the heat transfer rate from the left wall to the vertical thermal boundary layer must be the same as the thermal diffusion rate downward through the plane separating the two cells

$$Q \sim kh\frac{\Delta T}{\delta_t} \sim kL\frac{\Delta T}{h} \tag{23}$$

Equations (21–23) are sufficient to provide the unknown scales of the thermal penetration of Fig. 6(*a*), namely, the penetration height and the thickness of the thermal boundary layer

$$\frac{h}{H} \sim \left(\frac{L}{H}\right)^{4/7} \mathrm{Ra}^{-1/7} \tag{24}$$

$$\frac{\delta}{H} \sim \left(\frac{L}{H}\right)^{1/7} \mathrm{Ra}^{-2/7} \tag{25}$$

The Nusselt number defined by equation (18) is of order

$$\mathrm{Nu} \sim \frac{h}{\delta_t} \sim \mathrm{Ra}^{1/7}\left(\frac{L}{H}\right)^{3/7} \tag{26}$$

In a layer with H/L fixed, in the convection-dominated regime, the Nusselt number must vary as $\mathrm{Ra}^{1/7}$. This conclusion is supported by the $H/L=4$ data in Fig. 5 which, despite the still dominant effect of conduction, show that Nu indeed increases slowly with Ra.

The domain of validity of results (24–26) was defined via equations (19, 20). These equations yield

$$\mathrm{Ra}^{1/7}\left(\frac{H}{L}\right)^{4/7} >> 2 \tag{27}$$

$$\mathrm{Ra}^{2/7}\left(\frac{L}{H}\right)^{6/7} >> 1 \tag{28}$$

Equation (27) represents the criterion necessary for incomplete vertical thermal penetration, equation (19), and equation (28) represents the criterion necessary for the existence of boundary layer convection, equation (20). The above criteria are also reported graphically in Fig. 7 to illustrate how they divide the H/L, Ra domain.

(*b*) Horizontal Thermal Penetration. Consider the configuration shown in Fig. 6(*b*). The distance of the horizontal penetration l is shorter than the horizontal dimension of the cavity

$$l << L \tag{29}$$

In addition, if the thermal boundary layer along the left wall is slender,

$$\delta_t << H/2 \tag{30}$$

then, as before, for $\mathrm{Pr} \sim 0(1)$ or greater, equations (5, 6) yield the following balances

$$\nu\frac{v}{\delta_t^3} \sim g\beta\frac{\Delta T}{\delta_t} \tag{31}$$

$$v\frac{\Delta T}{H} \sim \alpha\frac{\Delta T}{\delta_t^2} \tag{32}$$

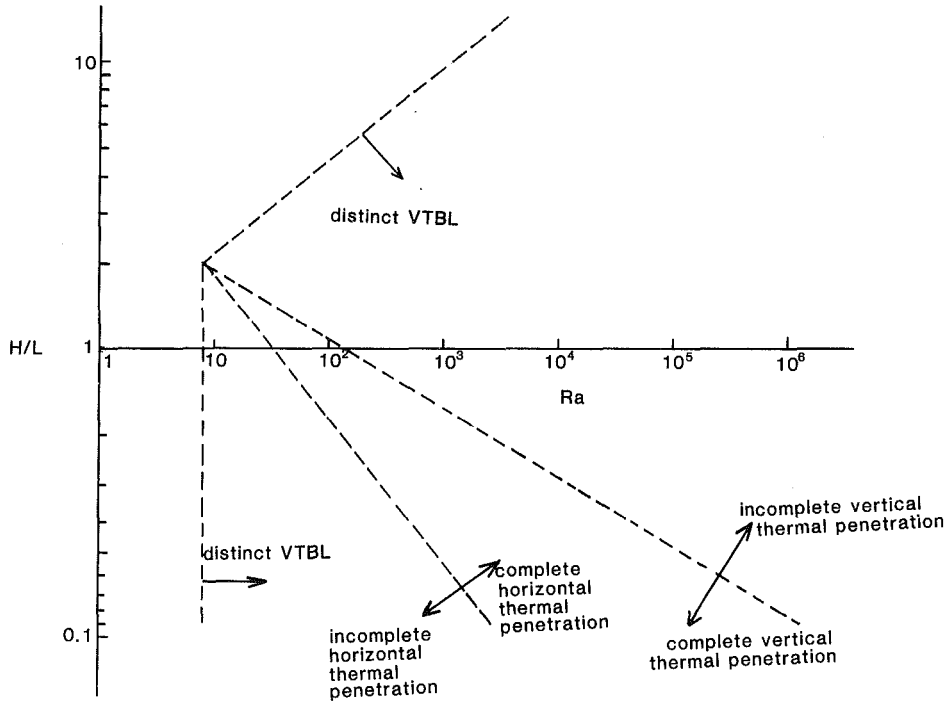

Fig. 7 Graphic summary of the regimes characterized by incomplete or complete thermal penetration

Combining equations (31, 32) yields

$$\frac{\delta_t}{H} \sim 2^{-1/4}\,\mathrm{Ra}^{-1/4} \tag{33}$$

The vertical thermal boundary layer scale also helps to determine the scale for the heat flux extracted from the vertical wall

$$\mathrm{Nu} = \frac{Q}{k\Delta T} \sim \frac{H/2}{\delta_t} \sim 2^{3/4}\mathrm{Ra}^{1/4} \tag{34}$$

Note that Nu increases with $\mathrm{Ra}^{1/4}$ in the same fashion as in natural convection from an isothermal vertical plate [12]. This result makes sense physically because, in the shallow enclosure limit, the presence of the adiabatic right vertical wall is not felt by the fluid near the driving differentially heated wall.

The conservation of momentum and energy in the region $l \times H/2$ requires

$$\nu\frac{u}{(H/2)^3} \sim g\beta\frac{\Delta T}{l} \tag{35}$$

$$u\frac{\Delta T}{l} \sim \alpha\frac{\Delta T}{(H/2)^2} \tag{36}$$

It is worth clarifying that equation (35) represents a balance between friction and buoyancy forces in equation (6), with the fact that the two velocity components are connected via the continuity equation (2), $u/l \sim v/(H/2)$, taken into account. This balance is justified for fluids with $\mathrm{Pr} \sim 0(1)$ or greater for it can be proved that [0(friction terms)/0(inertia terms)] $\sim$ Pr (see for example [10–12]). Eliminating u between equations (35, 36) yields the scale for the horizontal thermal penetration distance

$$\frac{l}{L} \sim 2^{-5/2}\frac{H}{L}\mathrm{Ra}^{1/2} \tag{37}$$

The above conclusion is verified qualitatively by the temperature fields in Fig. 4(*b*).

The domain of validity of the scale analysis constructed in this section is determined by rewriting conditions (29, 30) as

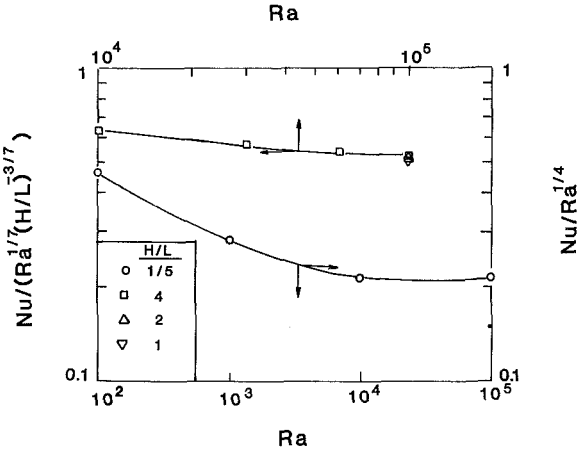

Fig. 8 Correlating the numerical results for Nu according to the scaling predictions

$$\frac{H}{L}\mathrm{Ra}^{1/2} << 2^{5/2} \tag{38}$$

$$\mathrm{Ra}^{1/4} >> 2^{3/4} \tag{39}$$

The above criteria are also sketched in Fig. 7 which now illustrates the various "families" of temperature distributions which may develop in the cavity. In this figure VTBL stands for "vertical thermal boundary layer."

The scaling arguments presented in this section are accurate in an order-of-magnitude sense. Comparisons of the scaling predictions to the numerical findings are shown in Fig. 8 which tests whether equations (26) and (34) predict the correct dependence of Nu on Ra and H/L. Indeed, the trends shown in Fig. 8 indicate that as Ra increases (boundary layer regime in which the scaling analysis is valid) scales (26) and (34) yield the correct exponents for Ra and H/L. Clearly, the heat transfer scales (equations (26, 34)) refer to the real heat flux in the cavity, i.e., after removing the unrealistic implications of the temperature discontinuity at midheight, of the driving wall. Finally, the scaling arguments presented in this section

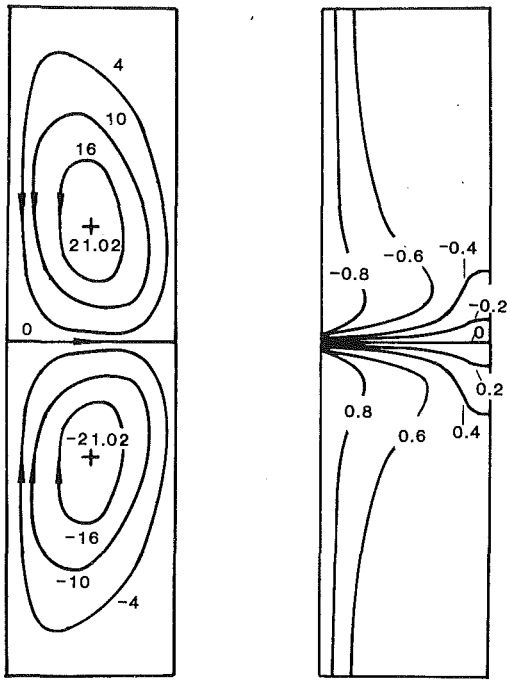

Fig. 9 Streamlines and isotherms for the case Ra = 10^5, H/L = 4 in a system with side heating positioned below side cooling

are based on the symmetry of the flow field about the midheight; hence, they are valid provided that the lengths of the warm and the cold portions of the driving wall do not differ significantly.

6 Heated Region Positioned Below Cooled Region

The preceding numerical simulations and scale analysis all focused on the arrangement shown in Fig. 1, where the heated portion of the driving wall is positioned above the cooled portion. In this section we will consider the opposite situation where the heated wall section is positioned below the cooled section, but briefly, due to space limitations. This situation is less complicated than the one analyzed so far because the incomplete penetration phenomenon is no longer a feature of the temperature and flow fields.

Figure 9 shows a sample numerical solution for a relatively tall cavity, $H/L=4$, at $\mathrm{Ra}=10^5$. Focusing on the upper half of the cavity we see that the temperature field consists of two thermal boundary layers connected through a core in which no steep temperature variations occur. One boundary layer coats the vertical wall section of temperature $\hat{T}=-1$, while the other is a horizontal jet of centerline temperature $\hat{T}=0$. In the high Rayleigh number regime, this boundary layer structure is not likely to be seriously affected by changes in the aspect ratio H/L. This is due to the fact that since the warm wall section is positioned below the cold wall section the warm fluid must sweep the entire height of the warm wall section and once at midheight the warm stream can only spread horizontally as far as possible ($x \sim L$). For this reason, in the high Rayleigh number regime, the flow triggered by side heating positioned below side cooling is not one of penetrative convection because the outer dimensions of the convection cell always coincide with the dimensions of the enclosure. Representative heat transfer results for this case are shown in Fig. 5. As in the previous case of side heating positioned above side cooling increasing Ra significantly enhances convection, and increasing H/L tends to reduce the convection effect on the overall heat transfer from the hot to the cold wall segments. In addition, Fig. 5 indicates that for the same values of Ra, Pr, and H/L, side heating positioned below side cooling enhances the net heat transfer through the enclosure compared to side heating positioned above side cooling. The reason for this result is twofold: (*a*) participation of the entire fluid body filling the enclosure in the convection motion and (*b*) contact of the hottest fluid with the coldest fluid in the enclosure which provides a large temperature gradient for conduction, since the two fluid streams act as if in a heat exchanger and do not mix.

Before closing this section, we should point out that the configuration shown in Fig. 9 is potentially unstable; hence, increasing the Rayleigh number sufficiently may lead to a Benard-type instability in the region of the horizontal jet which separates the upper cold cell from the lower warm cell. Kublbeck et al. [13] briefly discuss this problem for the case of a square cavity. Their findings for $\mathrm{Ra} = 5.6 \times 10^5$ reveal the existence of two convection rolls, one on top of the other, which grow and decay periodically with time. No oscillations were observed in the present study in the steady state; however, this may be due to the fact that there exist two significant differences between this study and the study in [13]:

1 The lowest Ra reported in [13] is $\mathrm{Ra} \approx 5 \times 10^5$ which is five times larger than the Rayleigh number in Fig. 9. In addition, the aspect ratio in [13] was $H/L=1$. The aspect ratio in Fig. 9 is $H/L=4$. Hence, the results in Fig. 9 are representative of a considerably "weaker" convective flow than the results in [13].

2 The study in [13] does not start from a stationary state, as the present study does; instead, at $t=0$, the driving left wall is set at the cold temperature. It then remains at the cold temperature during the first 500 s of the numerical experiment. During this time the enclosure is continuously cooled from the left side while the remaining three boundaries are adiabatic. At $t=500$ s, the temperature of the lower half of the left wall is suddenly raised to the warm temperature. Hence, by the time the "step" temperature boundary condition is imposed on the driving wall, a significant counterclockwise unicellular flow has already been established in the cavity.

The present study is limited to two-dimensional configurations. A three-dimensional study may reveal that, if Ra is high enough, Benard rolls in the direction perpendicular to the x-y plane (the axis of rotation of the rolls being parallel to the x axis) may appear. The results reported in this paper clearly do not provide information on such three-dimensional phenomena.

In view of the above discussion, it is felt that the results of the second part of this study (warm region below cold region) are representative of tall enclosures and low Rayleigh numbers. The reader should be aware of this fact and treat the findings of the second part of this study (especially the results for $H/L=1$, high Ra) with caution until experimental evidence becomes available.

7 Conclusions

This paper reported a study of buoyancy induced convection in a confined fluid-filled rectangular region differentially heated along the left vertical wall. The remaining walls were insulated. The first and main part of the study focused on the case where the side heating effect was positioned above the side cooling effect. Numerical simulations and scale analysis showed that the natural convection phenomenon in this configuration is one of complete horizontal and incomplete vertical penetration or one of complete vertical and incomplete horizontal penetration or one of complete vertical and complete horizontal penetration (Figs. 3–4). It was found that the heat transfer scales differ significantly from one type of penetrative convection to the other, in agreement with the trends revealed by numerical simulations (Fig. 8). The parametric domain of validity of the

scale analysis results was outlined on the H/L–Ra plane (Fig. 7). When the heated portion of the driving wall was positioned below the cooled portion, the flow spread throughout the enclosure. In this configuration an enhancement in the overall heat transfer through the enclosure was observed (Fig. 5). However, since this configuration is potentially unstable and hence "vulnerable" to three-dimensional phenomena, experimental evidence is needed to establish the credibility of the results in section 6.

In summary, the relatively simple geometry of a fluid layer with one differentially heated vertical wall and three adiabatic walls yields an interesting variety of natural convection flows which can result into complete or incomplete thermal penetration, depending on the relative position of the heated and cooled portions of the side wall and the dimensionless groups H/L and Ra.

References

1 Ostrach, S., "Natural Convection in Enclosures," *Advances in Heat Transfer*, Vol. 8, 1972, pp. 161–227.

2 Catton, I., and Torrance, K. E., eds., *Natural Convection in Enclosures*, ASME HTD, Vol. 8, 1980.

3 Ostrach, S., "Natural Convection Heat Transfer in Cavities and Cells," keynote paper at the Seventh Intl. Heat Transfer Conference, Munich, 1982.

4 Chao, P. K. B., Ozoe, H., Churchill, S. W., and Lior, N., "Laminar Natural Convection in an Inclined Rectangular Box With the Lower Surface Half-Insulated," ASME JOURNAL OF HEAT TRANSFER, Vol. 105, 1983, pp. 422–432.

5 Schetz, J. A., and Eichhorn, R., "Natural Convection With Discontinuous Wall-Temperature Variations," *J. Fluid Mechanics*, Vol. 18, Part 2, 1964, pp. 167–175.

6 Patankar, S., *Numerical Heat Transfer and Fluid Flow*, Hemisphere, New York, 1980.

7 Poulikakos, D., "Maximum Density Effects on Natural Convection in a Porous Layer Differentially Heated in the Horizontal Direction," *Intl. Journal Heat and Mass Transfer*, Vol. 27, 1984, pp. 2067–2075.

8 Blake, K. R., Poulikakos, D., and Bejan, A., "Natural Convection Near 4°C in a Horizontal Water Layer Heated From Below," *Physics of Fluids*, Vol. 27, 1984, pp. 2608–2616.

9 Roache, P. J., *Computational Fluid Dynamics*, Hermosa, Albuquerque, N.M., 1976.

10 Poulikakos, D., and Bejan, A., "The Fluid Dynamics of an Attic Space," *Journal of Fluid Mechanics*, Vol. 131, 1983, pp. 251–269.

11 Patterson, J., and Imberger, J., "Unsteady Natural Convection in a Rectangular Cavity," *Journal Fluid Mechanics*, Vol. 100, 1980, pp. 65–86.

12 Bejan, A., *Convection Heat Transfer*, Wiley, New York, 1984.

13 Kublbeck, K., Merker, G. P., and Straub, J., "Advanced Numerical Computation of Two-Dimensional Time-Depended Free Convection in Cavities," *Intl. J. Heat and Mass Transfer*, Vol. 23, 1980, pp. 203–217.

Y. Kamotani

J. K. Lin

S. Ostrach
Fellow ASME

Department of Mechanical and Aerospace Engineering, Case Western Reserve University, Cleveland, OH 44106

Effect of Destabilizing Heating on Görtler Vortices

Experimental investigations of the effect of destabilizing heating on the vortex instability in a laminar boundary-layer flow of air along a concave surface are reported. The ranges of the parameters studied herein are Gr (Grashof number) from 0 to 70 and G (Görtler number) from 0.46 to 9.0. The wavelength of the vortices remains unchanged with heating but the strength of the vortices is enhanced by heating. The amplitude of the vortices increases almost exponentially with the combined parameter $(G^2 + \mathrm{f}\,Gr)^{1/2}$, *where* f *is found to be between 0.3 and 0.4, until the nonlinear effects become important. In the nonlinear region the original sinusoidal wave form of the vortices becomes distorted and they meander in the lateral direction.*

Introduction

Thermal instability in boundary-layer flows over heated horizontal flat plates has been studied by several investigators in the last decade. The instability is caused by buoyancy forces and results in the appearance of longitudinal vortices in the flows [1, 2, 3]. Analogously, centrifugal forces in boundary-layer flows over concavely curved walls are also known to cause instability and longitudinal vortices called Görtler vortices [4]. The present work is concerned with the interaction of those instabilities in a laminar boundary-layer flow over a heated concave surface.

Kahawita and Meroney [5, 6] studied theoretically the effect of destabilizing heating on the Görtler instability. In their first work [5] they assumed parallel streamlines and isotherms for the basic flow, and showed that the effect of heating is to destabilize the flow. They later improved the work by including the effect of the boundary layer development [6]. They found that heating destabilized the flow at short lateral wavelengths but stabilized the flow at longer wavelengths. Moutsoglou et al. [3] showed in their work on the thermal instability of flat plate boundary layers that the buoyancy term in the basic flow equations has a strong destabilizing effect. McCormack et al. [7] have shown experimentally that Görtler vortices increase the rate of heat transfer through the boundary layer along a concave surface. Martin and Brown [8] and Mayle et al. [9] also showed experimentally the heat transfer augmentation by Görtler vortices. Except for the heat transfer aspect, the effect of heating on the Görtler instability has not been studied experimentally in the past.

It is known that the onset of vortex instability is very difficult to detect experimentally. For example, the critical Grashof numbers determined experimentally by Gilpin et al. [2] using a flow visualization technique in heated horizontal flat plate boundary layers are much larger than those predicted by Moutsoglou et al. [3]. In their study of the Görtler instability Bippes and Görtler [10] used an elaborate hydrogen-bubble technique to introduce longitudinal vortex disturbances and investigated how those vortices developed in the downstream region.

The present experimental investigation is not concerned with the onset of the instability but with the effect of destabilizing heating on the development of Görtler vortices in the postcritical regime. The data taken in the present experiment are given in [11], and only some pertinent data are presented herein.

Contributed by the Heat Transfer Division and presented at the 22nd National Heat Transfer Conference, Niagara Falls, New York, August 1984. Manuscript received by the Heat Transfer Division June 5, 1984.

Experimental Design

Important Parameters of Problem. In order to obtain the basis for the experiments, careful formulation of the problem is essential. The basic equations for a laminar boundary-layer flow over a curved heated plate with longitudinal vortex rolls are discussed in [11]. After dividing the flow field into the basic flow and the disturbance flow, Lin [11] has shown that the important dimensionless parameters for the basic flow field are the Reynolds number (Re), Grashof number (Gr), boundary-layer thickness to wall curvature ratio (K), and Prandtl number (Pr). The effect of buoyancy on the basic flow in the streamwise direction is represented by the parameter $\mathrm{Gr}\sin(x/R)/\mathrm{Re}$ and that in the direction normal to the wall by $\mathrm{Gr}\cos(x/R)/\mathrm{Re}^2$. If we confine ourselves to the region where those buoyancy parameters and K are much less than unity, and where the magnitudes of the disturbance quantities are much less than those of the basic flow quantities (the linear region), the equations for the basic flow become identical to those for a boundary-layer flow over a flat plate.

In the equations for the disturbance flow field, two forces are identified to be responsible for creating vortex rolls, one being the centrifugal force represented by the parameter Re^2K and the other being the buoyancy force in the direction normal to the wall represented by the parameter $\mathrm{Gr}\cos(x/R)$. The square root of the parameter Re^2K is commonly called Görtler number $\mathrm{G} = \mathrm{Re}\sqrt{K}$. Thus, the relative importance of buoyancy to centrifugal forces in the region $\cos(x/R) \approx 1$ is characterized by the parameter Gr/G^2. Kahawita and Meroney [5] used a similar parameter $\mathrm{Gr}\,\mathrm{Pr}/G^2$ to represent the relative importance in their work on the vortex instability over a curved heated surface. The effect of buoyancy on the disturbance flow field in the streamwise direction is represented by the parameter $\mathrm{Gr}\sin(x/R)/\mathrm{Re}$ as in the basic flow equations.

In summary, in the region where $K << 1$, $\mathrm{Gr}\sin(x/R)/\mathrm{Re} << 1$, and $\cos(x/R) \approx 1$, the important dimensionless parameters of the problem are G, Gr, $\mathrm{Gr}/\mathrm{Re}^2$, and Pr. Under isothermal conditions, G is the only parameter.

Experimental Apparatus and Procedure. The basic flow facility for the experiments is the wind tunnel shown in Fig. 2. A 1-hp motor with feedback speed control is used to drive the centrifugal blower. Air from the blower passes through a divergent section. A honeycomb is put inside the divergent section near the end to make the air flow uniform. The flow then goes through a rectangular channel with cross section of 41.5 cm × 41.5 cm and length of 32 cm, and arrives at a contracting nozzle. Four different size screens are used in the rectangular channel to reduce the disturbances in the air flow. The cross section at the end of the contracting nozzle is 10 cm × 26 cm.

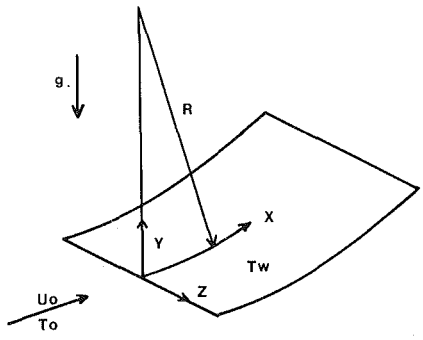

Fig. 1 Coordinate system

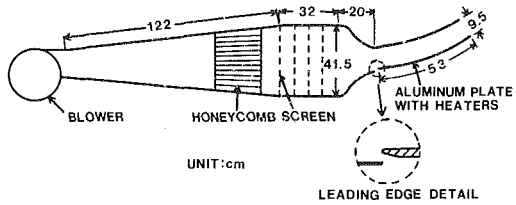

Fig. 2 Schematic of experimental apparatus

The test section (Fig. 2) is made of a 4.8-mm-thick plexiglass top plate and an aluminum bottom plate. The radius of curvature of the bottom aluminum plate is 75 cm. The distance between top and bottom plates is 9.5 cm. The top plate is connected to the contracting nozzle, but there is a gap of 0.5 cm between the aluminum bottom plate and the nozzle bottom plate (see Fig. 2) to make the boundary layer develop from the leading edge, as was done in the past investigations of the Görtler instability (e.g., Sonoda and Aihara [12]). The leading edge of the bottom plate is shaped to a chamfered tip to minimize the disturbances. The dimension of the test section is 53 cm × 26 cm, length by width.

In order to obtain a uniform temperature at the bottom plate, eleven major heaters and six guard heaters are bonded on the back of the aluminum plate. Copper-constantan thermocouples are imbedded into carefully drilled holes in the aluminum plate to monitor the local temperature. The heat input to each heater is adjusted by controlling the voltage applied to the heater with a variable transformer. The major heaters are arranged in such a manner as to meet the need of heat input adjustment according to the variation of local heat transfer rate along the direction of the flow. Guard heaters are utilized on both sides of the major heaters to minimize the edge effects.

The side walls of the test section are made of paper board and reinforced with insulation materials to reduce heat loss from the sides.

Probes are inserted into the test section through the four narrow slits of the upper plate, which span 22 cm in the lateral direction. The probes are mounted on a two-dimensional traversing positioning system. Since the experiments are mostly performed inside the boundary layers, accurate positioning normal to the bottom plate is important. A micrometer with accuracy to 0.002 cm is used for this purpose.

In the experiments without heating (isothermal case) the mean velocity and turbulence intensity of the flow are measured by a hot wire operated in constant-temperature mode. In the experiments with heating the same hot wire operated in constant-current mode is used to measure the mean temperature and temperature fuctuation level.

In order to obtain well-defined Görtler vortices under isothermal conditions we confine the Görtler number of the experiment to the range $0.46 \leq G < 9$, since the critical Görtler number is 0.46 according to Floryan and Saric [13] and $G = 9$ is approximately the limit beyond which nonlinear effects become important. For this reason the range of the free-stream velocity is chosen to be between 35 and 100 cm/s. As explained above, the effect of heating becomes important when the ratio Gr/G^2 becomes approximately equal to unity. With $\Delta T \leq 45°C$, the ratio Gr/G^2 can be made to be as large as 8.5.

The last measuring station is located at $x = 33$ cm. At that station $\cos x/R = 0.90$, $\sin x/R = 0.43$, and $K < 0.0052$ so that the conditions $K << 1$ and $\cos x/R \approx 1$ are satisfied. The ratio Gr/Re^2 is less than 0.05 so that the effect of buoyancy on the basic flow field is considered to be negligible. With $\Delta T = 45°C$ and $U_0 = 100$ cm/s the parameter $Gr \sin(x/R)/Re$ is considered to be small (0.21), but with $\Delta T = 45°C$ and $U_0 = 35$ cm/s the parameter becomes as large as 1.7 at $x = 33$ cm. Therefore, the effect of streamwise buoyancy cannot be neglected in the data taken near the last station in the low-speed, high ΔT experiments. It is noted, however, that the onsets of the instability have been found to occur around the first measuring station ($x = 6.5$ cm) in the ranges of the parameters studied herein so that the effect of streamwise buoyancy on the initial instability is considered to be negligible.

The experimental error in the velocity measurement is estimated to be ± 2.5 percent and that in the temperature measurement ± 3 percent. The nonuniformity of T_w over the plate surface is less than 5 percent. For $\Delta T = 45°C$ the variation of air kinematic viscosity across the boundary layer is about 25 percent, which needs to be considered in comparing the present results with theoretical results.

Experimental Results and Discussion

Free-Stream Conditions. At first, the free stream is in-

Nomenclature

C = combined parameter = $(G^2 + f\,Gr)^{1/2}$
f = constant
G = Görtler number = $Re K^{1/2}$
G_c = critical Görtler number
g = gravitational acceleration
Gr = Grashof number based on local boundary-layer thickness = $(g\beta\Delta T/\nu^2)\cdot(\nu x/Uo)^{3/2}$
K = ratio of boundary-layer thickness to wall radius of curvature = $(\nu x/Uo)^{1/2}/R$
Pr = Prandtl number = ν/α
R = wall radius of curvature
Re = Reynolds number based on local boundary-layer thickness = $(Uox/\nu)^{1/2}$
T = temperature
T' = temperature fluctuation
T_0 = free-stream temperature
T_w = wall temperature
U = velocity
U_0 = free-stream velocity
(x, y, z) = coordinate system defined in Fig. 1
α = thermal diffusivity
β = volumetric expansion coefficient
ΔT = temperature difference = $T_w - T_0$
δT_{max} = maximum peak-to-valley temperature variation at a given x location
δU_{max} = maximum peak-to-valley velocity variation at a given x location
η = boundary-layer coordinate = $y(Uo/\nu x)^{1/2}$
ν = kinematic viscosity

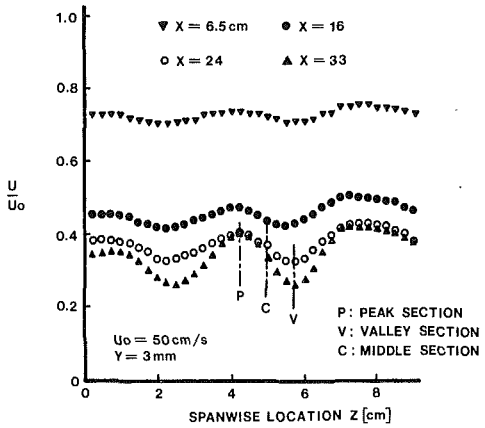

Fig. 3 Spanwise velocity distributions at various streamwise locations

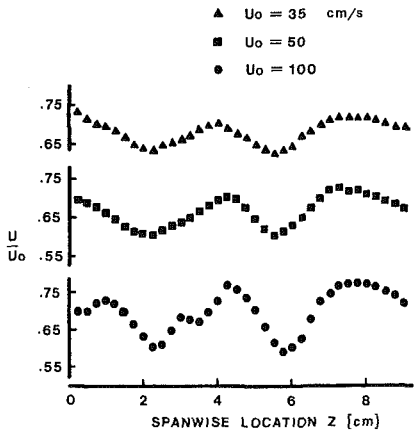

Fig. 4 Spanwise velocity distributions for various free-stream velocities at $x = 24$ cm and $\eta = 2.0$

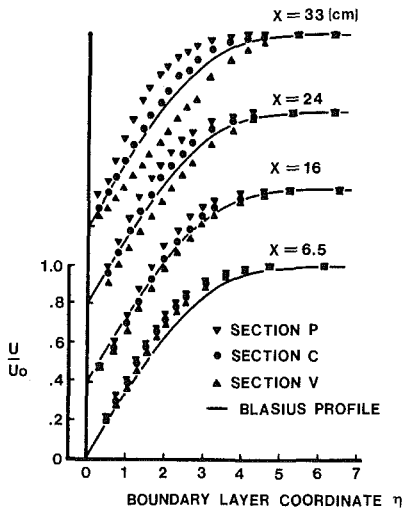

Fig. 5 Velocity profiles across boundary layer at various streamwise locations for $U_0 = 100$ cm/s

vestigated to check its two dimensionality and turbulence level in the test section. It is found [11] that the flow is very uniform in the spanwise direction. The free-stream turbulence level is 0.45 percent at $U_0 = 35$ cm/s and 0.3 percent at $U_0 = 100$ cm/s. Since the main purpose of this study is to investigate the effect of heating on Görtler vortices rather than its effect on the onset of the instability, such turbulence levels are considered to be low enough for the present investigation.

In the present experimental system the gap between the top and bottom plates is fixed at 9.5 cm. Therefore, as the boundary layer thickness increases with x, the free stream accelerates and the pressure decreases in the streamwise direction. To show overall pressure variations, the pressure coefficient is calculated based on the difference between the static pressure near the leading edge and that at the most downstream measuring station. The pressure coefficient is defined as $C_p = (P_1 - P_2)/\rho U_1^2$, where the subscripts 1 and 2 refer to the quantities at the location $x = 6.5$ cm and 33 cm, respectively, and ρ is the air density. C_p is found to be equal to -0.17 for $U_o = 35$ cm/s and -0.11 for $U_0 = 100$ cm/s. The corresponding values to a Falkner-Skan parameter of β are 0.09 for the former and 0.06 for the latter. It was shown by Smith [14] that the pressure gradient is distinctly minor factor compared with other major terms in the Görtler instability problem. The experimental results obtained by Sonoda and Aihara [12] showed that only in the region where Görtler vortices behave very nonlinearly is the behavior influenced by the pressure gradient. For these reasons no attempt was made in the present work to adjust the gap in the x direction to minimize the pressure gradient.

Characteristics of Görtler Vortices for Isothermal Case. Before investigating the heating effect on Görtler vortices, it is important to obtain basic information on the characteristics of the vortices without heating. To visualize the vortices smoke is put into the test section. Görtler vortices are clearly visible over the ranges of the parameters studied herein. The method used previously by McCormack et al. [7] is also used. The concave surface is sprayed with a solution of methyl alcohol saturated with naphthalene. When it is dry, the surface is covered with white fluffy naphthalene layer. The material is removed faster where the velocity is larger so that distinct longitudinal streaks appear after some time [11]. The average wavelength of the vortices is measured to be about 3.5 cm. The wavelength does not change with the free-stream velocity.

To show the effect of Görtler vortices on velocity distributions, spanwise velocity distributions are measured by a hot wire. Figure 3 shows the spanwise distributions measured at four different downstream locations at $U_o = 50$ cm/s. The periodic spanwise variation of velocity is regarded as produced by a system of alternating vortices superposed on the basic flow near the wall. Note in Fig. 3 that the average velocity at a given height decreases with x because of the development of a boundary layer. As seen in Fig. 3, the peak and valley positions of the distributions remain the same at different stations, that is, the wavelength of the vortices is conserved in the flow direction, which agrees with the aforementioned streak pattern observations. The spanwise velocity distributions measured at the same dimensionless distance from the wall surface $\eta = 2.0$ (η is the boundary-layer coordinate) are presented in Fig. 4 at the station $x = 24$ cm for three different free-stream velocities. As Fig. 4 shows, the wavelength of the vortices does not change appreciably with U_0; only the amplitude increases with U_0. The facts that the wavelength does not change with the free-stream velocity in the present experiment and that different wavelengths were obtained in different setups in the past investigations seem to indicate, as suggested by Tani and Sakagami [15], that the wavelength observed is the one inherent to a particular experimental arrangement.

Figure 5 shows the distributions across the boundary layer of the mean velocity at various distances from the leading edge in the spanwise sections P, V, and C defined in Fig. 3. Sections P and V correspond to a peak and a valley, respectively, of the spanwise velocity distribution, and section C is located at the middle of sections P and V. The average profiles (over one wavelength) at all locations are close to the Blasius profile for the flat plate boundary layer.

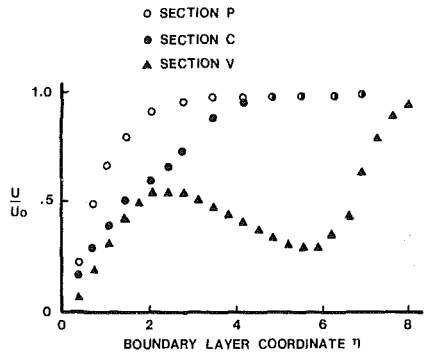

Fig. 6 Velocity profiles across boundary layer at $x = 43$ cm and $U_0 = 275$ cm/s ($G = 12.8$)

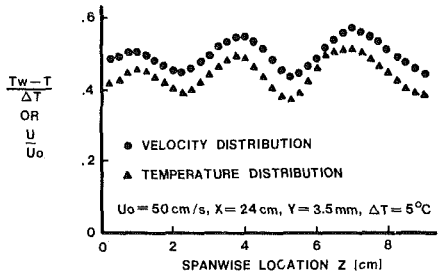

Fig. 7 Comparison of velocity and temperature distributions at small ΔT

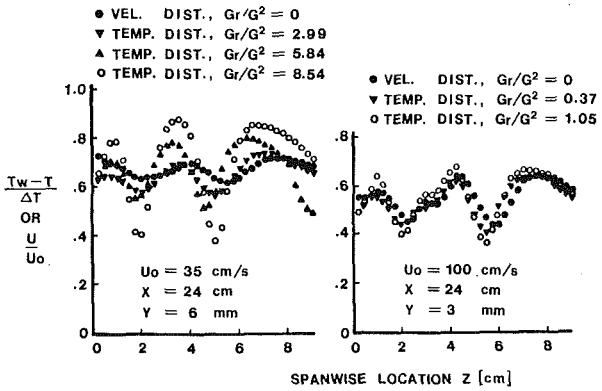

Fig. 8 Spanwise distributions of velocity and temperature

As the distance from the leading edge increases, the strength of the vortices increases and the velocity profiles become more distorted. The very distorted profiles shown in Fig. 6 are obtained at $x = 43$ cm and $U_0 = 275$ cm/s ($G = 12.8$). The profile at section V indicates that the flow is strongly decelerated in the region where the vortices have upward motion. This, according to Sonoda and Aihara [12], is caused by the nonlinear behavior of Görtler vortices. The nonlinear effect changes the spanwise periodic spacing so that the vortices at both sides of each decelerated section make a pair by approaching each other. Such a change causes a strong upwash in the decelerated section, resulting in a velocity profile like the one shown in Fig. 6. Sonoda and Aihara [12] suggested that such unstable profiles cause the secondary instability of Görtler vortices, resulting in a formation of horseshoe type vortices. We also observed the horseshoe type vortices in our flow visualization experiments, but our main isothermal experiments are conducted in the range before the nonlinear effect sets in. The above process, though, is important in the heated case, as described below.

Effect of Heating on Görtler Vortices. In a heated flow the measurement of velocity distributions by hot wire becomes less accurate than in an isothermal flow due to variations in the fluid properties (mainly density and viscosity) in the flow as well as due to the variation in the wire overheating, although those errors can be corrected to some extent by knowing the temperature field. For this reason only the temperature fields are studied in the present heated experiments, it is useful to know, then, how the measured temperature fields are related to the velocity fields, since only the latter can be studied in the isothermal experiment and it is interesting to see how the velocity fields change with heating. Their relations were checked in the tests in which ΔT was less than 5°C so that the velocity measurement error of the hot wire was relatively small. One comparison is presented in Fig. 7. The figure shows that the spanwise variations of the velocity and temperature follow a nearly identical trend – they do not coincide because of the difference in the velocity and temperature boundary-layer thickness for Pr = 0.7. Both fields were also found to develop nearly identically in the streamwise direction for small ΔT. The above observations together with the fact that the spanwise temperature variation pattern remains very similar with increasing ΔT in the linear region, as shown below, imply that the above similarity between the velocity and temperature distributions in the spanwise direction is nearly preserved at larger ΔT. In any case, the temperature information itself is useful in studying the heat transfer aspects of the flow.

Typical spanwise temperature distributions are presented in Fig. 8. The velocity distributions for the isothermal case also shown for comparison. Some important observations can be made from the results. The wavelength of the vortices does not change appreciably with heating even when the ratio Gr/G^2 is as large as 8.5. The amplitude of the spanwise variation increases with ΔT, but the effect becomes smaller as U_0 increases. In terms of the dimensionless parameters of the problem, the amplitude (or strength) of the vortices increases with Gr and G, and the relative effect of heating on the amplitude increases with the ratio Gr/G^2. It is noted in Fig. 8 that as the strength of the vortices is amplified by heating, the temperature distribution in the warm region (upwash region) becomes spiky, which means that the upwash region tends to be concentrated in a narrow region, but the temperature distribution in the cold region (downwash region) suggests that the downwash region tends to be more spread out. This is the nonlinear effect described by Sonoda and Aihara [12] for the isothermal case. Therefore, it can be said that heating Görtler vortices from below augments their strength and enhances the nonlinear effect.

The temperature distributions across the boundary layers measured for various values of ΔT and U_0 are shown in Fig. 9. The theoretical temperature profile for a flat plate boundary layer is shown for each figure. The section P is in the downwash region and cooler, and the section V is in the upwash region and warmer. Due to the nonlinear behavior of the vortices, the temperature profile at section V has an inflection point, and the distortion increases with increasing Gr/G^2 for a fixed G.

The temperature profiles for $Gr/G^2 = 8.5$ ($U_0 = 35$ cm/s, $\Delta T = 45$°C, $x = 33$ cm) are very similar to the velocity distributions shown in Fig. 6. As mentioned above, the effect of buoyancy in the streamwise direction cannot be neglected for that condition. Although the effect is mainly to accelerate the flow in the streamwise direction, whether it can enhance the nonlinear behavior of the vortices, and thereby distort the temperature distribution, is not presently known.

To represent the strength of the vortices the amplitude of the spanwise temperature variation is calculated. The amplitude is defined as the difference in the temperatures at sections P and V. It is found [11] that at a given x location the amplitude becomes maximum around $\eta = 2$ in the ranges of the parameters studied herein. The maximum value at a

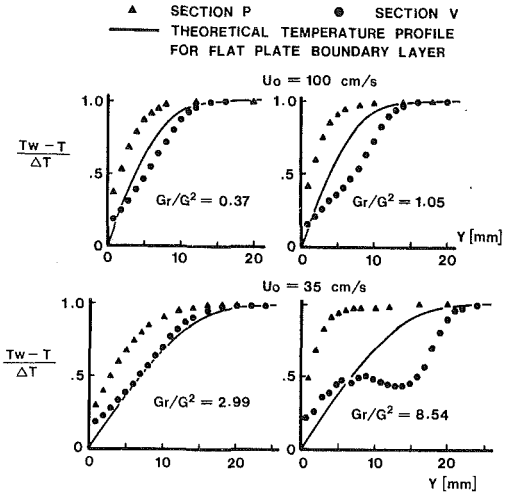

Fig. 9 Temperature profiles across boundary layer at $x = 33$ cm

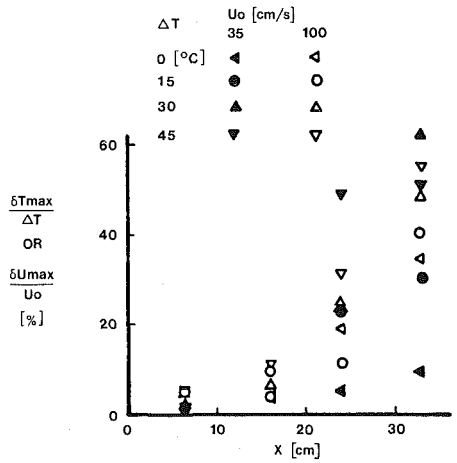

Fig. 10 Variations of maximum disturbance amplitude along streamwise direction

given x location (δT_{max}) is used herein to represent the strength of the vortices at the location. The values of $\Delta T_{max}/\Delta T$ are plotted against x in Fig. 10 for various values of ΔT and U_0. The maximum amplitudes of the spanwise velocity distributions for the isothermal case δU_{max} (defined similarly to ΔT_{max}) are also shown for comparison. As seen in Fig. 10, the effect of heating on the vortices is very small at the first measuring station ($x = 6.5$ cm) in all cases. The location where the heating effect becomes important depends on the parameter Gr/G^2. According to the theoretical analysis by Floryan and Saric [13] for the Görtler instability (isothermal case), for a given dimensionless wavelength parameter $\Lambda = (U_0\ \lambda/\nu)\ (\lambda/R)$ (λ=wavelength) Görtler vortices grow nearly exponentially with G after the onset of the instability. Based on this, an attempt is made to correlate the values of δU_{max} obtained in the present experiment by the form $A/A_0 = \exp[a(G-G_c)]$, where A and A_0 are the maximum amplitudes (of velocity) at the specific G and critical Gortler number G_c, respectively. G_c is taken to be 0.46 according to Floryan and Saric [13], and A_0 is considered to be the asymptotic value of δU_{max} for small x in Fig. 10. The coefficient a is considered to be a function of Λ (or U_0 in the present experiment since λ is fixed). The correlation is shown in Fig. 11. The values of δU_{max} seem to correlate very well with $a = 0.40$ for $U_0 = 35$ cm/s ($\Lambda = 180$), and $a = 0.33$ for $U_0 = 100$ cm/s ($\Lambda = 512$). It is noted that the data taken by Aihara [16] also show the exponential growth with $a = 0.40$ for $\Lambda = 774$ [11]. Analogously, in order to express the effect of destabilizing heating on the vortices a correlation of the

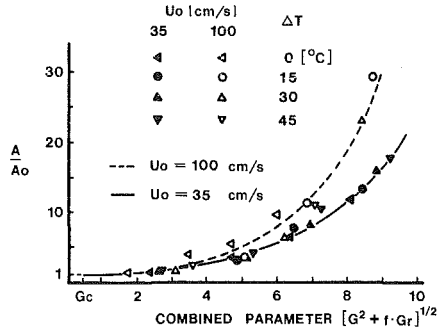

Fig. 11 Correlation of maximum disturbance amplitude with combined parameter C

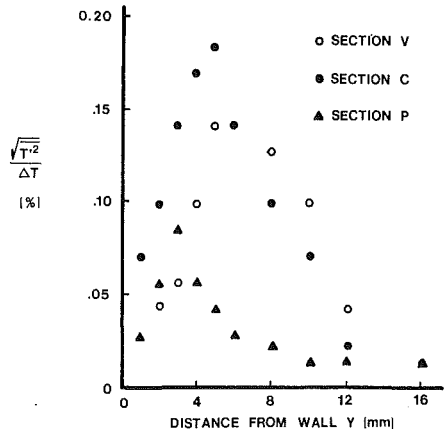

Fig. 12 Temperature fluctuation levels across boundary layer at $x = 24$ cm, $U_0 = 50$ cm/s, and $\Delta T = 45°C$

values of δT_{max} by a similar exponential form is attempted. Following the work of Kahawita and Meroney [5], it is assumed that the critical condition of the combined instability is reached when the combined parameter $(G^2 + f\,Gr)^{1/2}$ (f = a constant) becomes equal to the critical value for the isothermal case G_c. Therefore, we try to correlate the data of δT_{max} by the expression of $A/A_0 \exp[a(C-G_c)]$, where $C = (G^2 + f\,Gr)^{1/2}$ and A and A_0 are the values of δT_{max} at C and G_c, respectively. The result is shown in Fig. 11 together with the isothermal case. The values of a and f for the best correlation coefficients are $a = 0.37, f = 0.4$ for $U_0 = 100$ cm/s and $a = 0.44, f = 0.3$ for $U_0 = 35$ cm/s. Within the errors of the experimental data and the approximations made herein the values of a are nearly the same as those for the isothermal case with corresponding velocities. Thus, a is considered to be nearly independent of the parameter Gr/G^2 within the ranges of the parameters studied herein. f is considered to be in the range $0.3 < f < 0.4$ in the present experiment. In the work by Kahawita and Meroney [5] for the critical condition of the combined instability f is found to be 0.43, which is close to that of the present experimental value describing the postcritical vortex behavior.

Since the above exponential growth concept is based on the linear theory by Floyan and Saric [13], it is expected that the nonlinear effects change the trend beyond certain downstream locations. Aihara [16] states that "the vortices seem to approach the finite amplitude continued from linear region associated with some distortion of wave form from the original simusoidal pattern in the lateral direction" for the isothermal case. The same trend can be seen in the present data of δT_{max} given in Fig. 10. For $\Delta T = 45°C$ and $U_0 = 35$ cm/s, δT_{max} seems to become nearly constant beyond $x = 25$ cm.

The root-mean-square temperature fluctuation levels $(\overline{T'^2})^{1/2}$ are measured under various conditions. Some results

are presented in Fig. 12, in which the fluctuation levels are shown at three spanwise locations P, V, C at a fixed x location. As Fig. 12 shows, the fluctuation level is smallest at section P. According to Aihara [16], as the nonlinear effect becomes important, the vortices start to meander. As shown in Fig. 8, the spanwise temperature distribution develops in such a way that in the cooler region (seciton P) it becomes wide and flat and in the warmer region (section V) narrow and sharp. If there is an unsteady meandering motion of the vortices in the spanwise direction, the temperature fluctuation should be large near sections C and V and relatively small near section P, which is the case with the data in Fig. 12. The typical frequency of the fluctuation is found to be rather small (of the order of 1 Hz), which suggests that the temperature fluctuation is mainly caused by the slow meandering motion of the vortices. The data given in [11] show that the fluctuating level increases with the parameter $G^2 + f\,Gr$ as well as with the parameter Gr/G^2.

From the above temperature field study it can be said that an important effect of destabilizing heating is to enhance the nonlinear process described by Sonada and Aihara [12] (although the process with heating may not be exactly the same), which is expected to lead to earlier transition to turbulence.

Conclusions

Experiments have been performed to study the effect of destabilizing heating on Görtler vortices in a laminar boundary-layer flow of air along a concave surface.

The following conclusions are drawn from the experiments.

1 Within the range of the parameter Gr/G^2 studied herein ($0 \leq Gr/G^2 \leq 8.5$) the wavelength of the vortices remains unchanged.

2 The amplitude of the vortices increases almost exponentially with the combined parameter $(G^2 + f\,Gr)^{1/2}$ where f is found to be $0.3 < f < 0.4$, until the nonlinear effects become important.

3 Heating enhances the nonlinear process. The warm upwash region of the vortices tends to be concentrated in a narrow region and the cold downwash region tends to spread out as Gr is increased while G is fixed, and the vortex rolls meander, which causes temperature fluctuations with time at a given point.

4 The nonlinear effects become noticeable at a smaller value of the parameter $G^2 + f\,Gr$ as the value of the parameter Gr/G^2 is increased.

References

1 Wu, R. C., and Cheng, K. C., "Thermal Instability of Blasius Flow Along Horizontal Plates," *International Journal of Heat and Mass Transfer*, Vol. 19, 1976, pp. 907-913.

2 Gilpin, R. R., Imura, H., and Cheng, K. C., "Experiments on the Onset of Longitudinal Vortices in Horizontal Blasius Flow Heated From Below," ASME JOURNAL OF HEAT TRANSFER, Vol. 100, 1978, pp. 71-77.

3 Moutsoglou, A., Chen, S. T., and Cheng, K. C., "Vortex Instability of Mixed Convection Flow Over a Horizontal Flat Plate," ASME JOURNAL OF HEAT TRANSFER, Vol. 103, 1981, pp. 257-261.

4 Görtler, H., "Instabilität laminarer Grenzschichten an konkaven Wänden gegenüber gewissen dreidimensionalen Störungen," *Z.A.M.M.*, Vol. 21, 1941, pp. 250-252.

5 Kahawita, R. A., and Meroney, R. N., "Longitudinal Vortex Instabilities in Laminar Boundary Layers Over Curved Heated Surfaces," *The Physics of Fluids*, Vol. 17, No. 9, 1974, pp. 1661-1666.

6 Kahawita, R. A., and Meroney, R. N., "The Influence of Heating on the Stability of Laminar Boundary Layers Along Concave Walls," ASME *Journal of Applied Mechanics*, Vol. 44, 1977, pp. 11-17.

7 McCormack, P. P., Welke, H., and Kelleher, M., "Taylor-Görtler Vortices and Their Effect on Heat Transfer," ASME JOURNAL OF HEAT TRANSFER, Vol. 92, 1970, pp. 101-112.

8 Martin, B. W., and Brown, A., "Factors Influencing Heat Transfer to the Pressure Surfaces of Gas Turbine Blades," *International Journal of Heat and Fluid Flow*, Vol. 1, 1979, pp. 107-114.

9 Mayle, R. E., Blair, M. F., and Kopper, F. C., "Turbulent Boundary Layer Heat Transfer on Curved Surfaces," ASME JOURNAL OF HEAT TRANSFER, Vol. 101, 1979, pp. 521-525.

10 Bippes, H., and Görtler, H., "Dreidimensionale Störungen in der Grenzschicht an einer konkaven Wand," *Acta Mechanica*, Vol. 14, 1972, pp. 251-267.

11 Lin, J. K., "Effect of Heating on Görtler Instability," Ph.D. thesis, Department of Mechanical and Aerospace Engineering, Case Western Reserve University, 1982.

12 Sonoda, T., and Aihara, Y., "Effects of Pressure Gradient on the Secondary Instability of Görtler Vortices," AIAA Paper No. 80-0197, presented at the 19th AIAA Aerospace Sciences Meeting, St. Louis, MO, Jan. 12-15, 1981.

13 Floryan, J. M., and Saric, W. S., "Wavelength Selection and Growth of Görtler Vortices," AIAA Paper No. 80-1376, presented at the 13th AIAA Fluid and Plasma Dynamics Conference, Snowmass, CO, July 14-16, 1980.

14 Smith, A. M. O., "On the Growth of Taylor-Görtler Vortices Along Highly Concave Walls," *Quart. J. Math.*, Vol. 13, 1955, pp. 233-262.

15 Tani, I., and Sakagami, J., "Boundary Layer Instability at Subsonic Speeds," *Proc. Int. Council Aero. Sci.*, Third Congress, Stockholm, 1962, pp. 391-403 (published by Spartan, Washington, D.C., 1964).

16 Aihara, Y., "Transition in an Incompressible Boundary Layer Along a Concave Wall," *Bull. Aeronautical Research Inst.*, Univ. of Tokyo, 1962, pp. 195-240.

Interaction of Natural Convection Wakes Arising From Thermal Sources on a Vertical Surface

Y. Jaluria
Mechanical and Aerospace Engineering Department, Rutgers University, New Brunswick, NJ 08903
Mem. ASME

A numerical study of the interacting natural convection flows generated by isolated thermal energy sources, such as electronic components, located on a vertical adiabatic surface is carried out. Of particular interest were the effects of the wake on the heat transfer from and the flow over a downstream heat source and the nature of the wall plume far from the sources. This consideration is related to the positioning of finite-sized electronic components and the relevant heat removal process. A two-dimensional flow is considered, without making the boundary-layer assumptions. The full elliptic equations governing the flow are solved numerically, employing finite-difference methods. The results are compared with the boundary layer solutions, obtained in earlier studies, in order to determine the nonboundary-layer effects. This is an important consideration in several practical circumstances that involve small heat inputs, sources of relatively small heights, and small separation distances between the sources. It is found that the flow downstream rapidly approaches the characteristics of an idealized wall plume due to a line source. A boundary-layer flow arises far from the heat sources and this flow provides the boundary conditions for the elliptic problem. The nature of the velocity and temperature fields is studied in detail for a wide range of governing parameters and the heat transfer coefficients for the heated elements determined. The relevance of the results obtained to practical systems is outlined, particularly for small Grashof numbers which necessitate a solution of the full equations.

Introduction

Natural convection wakes generated by isolated thermal sources in an extensive ambient medium are of interest in several practical problems, such as the cooling of electronic equipment by natural convection. The energy dissipated by an electronic component results, in the absence of an externally induced flow, in a buoyancy-driven flow that rises above the energy source as a wake or plume [1-3]. The interaction of such a wake with the flows arising from other thermal sources is an important consideration in the positioning of components, since the heat transfer from an element is strongly affected by the flow generated adjacent to it by wakes in its neighborhood [4, 5]. Depending on the physical conditions, the heat transfer from a heated body may be increased or decreased by locating it in the wake of an upstream heat source [6, 7]. Therefore, in the design of electronic equipment, where cooling is often by natural convection and is a crucial consideration due to the temperature sensitive nature of the components, it is important to study the interaction of natural convection wakes generated by isolated thermal sources.

The natural convection flow due to isolated thermal sources on a vertical surface has received some attention in the literature. For a line heat source located at the leading edge of a vertical adiabatic surface, similarity arises and numerical results on the wall plume thus generated have been obtained [8]. The wall plumes due to finite-sized sources have also been studied numerically and experimentally [9-11]. The wake above a heated isothermal vertical plate has been investigated [12, 13]. The interaction of the natural convection wakes arising from multiple sources has been studied numerically, employing boundary layer approximations [7, 14]. Some work has also been done on the conjugate heat transfer problem, considering conductive heat loss from the sources to the plate on which they are located [11, 15]. Again, boundary layer approximations were employed for the natural convection flow.

The present study considers the interaction of the natural convection wakes arising from multiple thermal sources, of finite height, located on a vertical adiabatic surface. A uniform surface heat flux input is assumed at the heated elements. This results in a constant energy input into the natural convection flow, which is taken as the only transport mechanism. As considered in [11], other independent or conjugate mechanisms may need to be included in many practical cases. A horizontal isothermal surface is taken at the leading edge of the vertical surface, in order to simulate a practical circumstance relevant to electronic equipment. In most physical applications, the vertical surface would be positioned on a horizontal isothermal, or adiabatic, surface [16]. Since boundary-layer assumptions are not made in this study, the boundary condition at the leading edge is an important consideration. The full governing equations are solved numerically by finite-difference methods, the boundary conditions far downstream being obtained from the boundary-layer solution.

Of particular interest in this work was the nature of the flow at low values of the Grashof number Gr, which is based on the height of the heated element L and the surface heat flux q. The results obtained are of particular importance in several circumstances of practical interest and are compared with the corresponding boundary-layer solutions, indicating several interesting differences. The effect of the horizontal surface on the flow is examined for a wide range of the Grashof number. The heat transfer coefficient for the downstream element is determined and the effect of the interaction of the wakes on the transport mechanisms studied. The approach of the interacting flow to the characteristics of the wall plume generated by an idealized line source is studied and a rapid decay of the nonboundary-layer effects is found to arise. Several other interesting and important features are obtained

Contributed by the Heat Transfer Division and presented at the 22nd National Heat Transfer Conference, Niagara Falls, New York, August 5-8, 1984. Manuscript received by the Heat Transfer Division May 9, 1984.

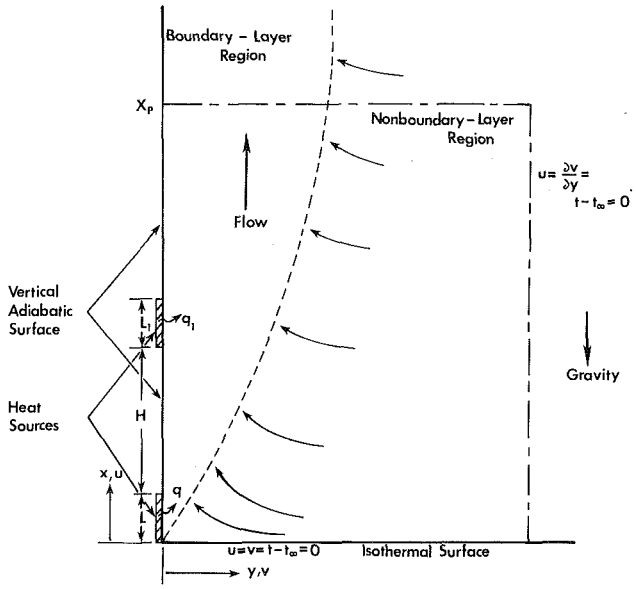

Fig. 1 Flow configuration and the coordinate system

in this flow and related to the underlying physical processes. The relevance of the study to the design of practical systems is discussed.

Analysis

The flow under consideration is shown in Fig. 1, along with the coordinate system employed. Two heat sources of heights L and L_1 are positioned on a vertical adiabatic surface, at a separation distance H. The transverse dimension is taken large enough that a two-dimensional flow may be assumed. The sources have uniform heat flux inputs q and q_1 at the surface. At the leading edge, $x = 0$, a horizontal surface at temperature t_∞, the temperature of the extensive ambient medium, is considered. As mentioned earlier, this boundary condition is relevant to most practical electronic systems, where the bottom surface is often close to isothermal. Of course, the problem is actually a conjugate one, with conductive loss to the bottom plate. However, that requires a consideration of the elliptic equations governing conductive transport in the plate and, therefore, considerably increases the complexity of the analysis. In this study, other boundary conditions, particularly that resulting from the assumption of an extensive medium below the leading edge, with no impediment to entrainment from below, were also considered for comparison, as discussed later. The presence of a horizontal surface at the leading edge does not affect the boundary layer results, which are obtained with a zero vertical velocity and the fluid temperature equal to the ambient temperature as boundary conditions at the leading edge [3, 13]. The solution of the full equations, however, would indicate the effect of the boundary condition imposed at the leading edge [17, 18].

The buoyancy-induced boundary-layer flow arising from a line source on an adiabatic vertical surface may be studied by employing the similarity analysis, which gives the following similarity variables [8]

$$\eta=\frac{yG}{4x},\quad \psi=\nu G f,\quad \tilde{\theta}=\frac{t-t_\infty}{t_0-t_\infty} \tag{1}$$

with

$$u=\frac{\partial\psi}{\partial y},\quad v=-\frac{\partial\psi}{\partial x},$$

$$G=4\left[\frac{g\beta x^3(t_0-t_\infty)}{4\nu^2}\right]^{1/4},\quad t_0-t_\infty=Nx^{-3/5} \tag{2}$$

Nomenclature

f = dimensionless stream function for similarity analysis
f' = dimensionless vertical velocity from similarity analysis
g = gravitational acceleration
G = Grashof number parameter, defined in equation (2)
Gr = Grashof number, defined in equation (16)
Gr_x = local Grashof number for a uniform heat flux surface, defined in equation (20)
H = distance between two heat sources, Fig. 1
k = thermal conductivity of the fluid
L, L_1 = heights of heated elements, Fig. 1
N = constant, defined in equation (2)
Nu = average Nusselt number $= \dfrac{q}{(t_0-t_\infty)_{\mathrm{avg}}}\dfrac{L}{k}$
p = local pressure
P = dimensionless pressure, defined in equation (16)
Pr = Prandtl number of the fluid
q, q_1 = heat flux input at the heated surfaces
Q = total convective thermal energy input into the flow
R = ratio of the Nusselt number for the upper source to that for the lower one
t = local temperature
t_0 = surface temperature
t_∞ = ambient temperature
u = vertical velocity component
U = dimensionless vertical velocity component, defined in equation (16)
U_c = convection velocity, defined in equation (16)
v = horizontal velocity component normal to the surface
V = dimensionless horizontal velocity component
$\bar{V}$ = local velocity vector
x = vertical coordinate distance
X = dimensionless vertical coordinate distance, defined in equation (16)
x_p = downstream vertical location beyond which boundary-layer assumptions are employed
y = horizontal coordinate distance normal to the surface
Y = dimensionless horizontal coordinate distance, defined in equation (16)
α = thermal diffusivity of the fluid
β = coefficient of thermal expansion of the fluid
η = similarity variable, defined in equations (1) and (20)
ν = kinematic viscosity of the fluid
ω = local vorticity in the flow, defined in equation (16)
Ω = dimensionless vorticity, defined in equation (16)
ρ = fluid density
ψ = stream function, defined in equation (2)
Ψ = dimensionless stream function, defined in equation (16)
τ' = physical time
τ = dimensionless time $= U_c\tau'/L$
θ = dimensionless temperature, defined in equation (16)
$\tilde{\theta}$ = dimensionless temperature, defined in equation (1)
θ_0 = dimensionless surface temperature

Subscripts

p = boundary-layer solution
e = solution of full governing equations
u = upper heat source
l = lower heat source

Here, t_0 is the surface temperature downstream of the source and N is a constant determined by the rate of energy input into the flow. A solution of the resulting ordinary differential equations yields the velocity and the temperature fields, which are employed here for a comparison with the results obtained for a finite-sized source.

The full governing equations for the vertical natural convection flow being studied may be written for laminar, two-dimensional flow, employing the Boussinesq approximations for the density variation, assuming the remaining properties to be constant and neglecting viscous dissipation and pressure work, as [3, 13]

$$\frac{\partial u}{\partial x}+\frac{\partial v}{\partial y}=0 \tag{3}$$

$$u\frac{\partial u}{\partial x}+v\frac{\partial u}{\partial y}=-\frac{1}{\rho}\frac{\partial p}{\partial x}+\nu\left(\frac{\partial^2 u}{\partial x^2}+\frac{\partial^2 u}{\partial y^2}\right)+g\beta(t-t_\infty) \tag{4}$$

$$u\frac{\partial v}{\partial x}+v\frac{\partial v}{\partial y}=-\frac{1}{\rho}\frac{\partial p}{\partial y}+\nu\left(\frac{\partial^2 v}{\partial x^2}+\frac{\partial^2 v}{\partial y^2}\right) \tag{5}$$

$$u\frac{\partial t}{\partial x}+v\frac{\partial t}{\partial y}=\alpha\left(\frac{\partial^2 t}{\partial x^2}+\frac{\partial^2 t}{\partial y^2}\right) \tag{6}$$

The boundary-layer equations that apply far downstream may be obtained from the above as [3]

$$\frac{\partial u}{\partial x}+\frac{\partial v}{\partial y}=0 \tag{7}$$

$$u\frac{\partial u}{\partial x}+v\frac{\partial u}{\partial y}=\nu\frac{\partial^2 u}{\partial y^2}+g\beta(t-t_\infty) \tag{8}$$

$$u\frac{\partial t}{\partial x}+v\frac{\partial t}{\partial y}=\alpha\frac{\partial^2 t}{\partial y^2} \tag{9}$$

The boundary-layer solutions have been obtained by employing finite-difference methods [7, 14]. References [11, 15] retained the axial conduction in the energy equation, with the boundary-layer formulation, in order to consider the effect of steep axial temperature gradients in the flow.

The boundary conditions employed for the flow are also shown in Fig. 1. The conditions at the wall are the same as those in [7] and may be written as

at $y=0$:

$$u=v=0, \text{ for } x\geq 0$$

$$q=-k\frac{\partial t}{\partial y}, \text{ for } 0\leq x\leq L$$

$$q_1=-k\frac{\partial t}{\partial y}, \text{ for } (H+L)\leq x\leq (H+L+L_1)$$

$$\frac{\partial t}{\partial y}=0, \text{ for } L<x<(H+L), \text{ and } x>(H+L+L_1) \tag{10}$$

Similarly, other heated elements located on the surface may be treated. For a horizontal, isothermal, surface at the leading edge, the conditions are

at $x=0$:

$$u=v=t-t_\infty=0, \text{ for } y>0 \tag{11}$$

The conditions in the ambient medium far from the surface are:

as $y\to\infty$:

$$u=\frac{\partial v}{\partial y}=t-t_\infty=0, \text{ for } x>0 \tag{12}$$

which implies only a horizontal flow at temperature t_∞ far from the flow region. The boundary conditions at the downstream location x_p beyond which the flow may be treated as a boundary-layer flow, governed by equations (7–9), are obtained numerically, as outlined below. These may be specified as

at $x=x_p$:

$$u=u_p, \quad v=v_p, \quad t=t_p, \quad \text{for } y>0 \tag{13}$$

where the subscript p refers to the solution of the parabolic boundary layer equations.

In the absence of the horizontal surface, the boundary conditions for the region below the leading edge are:

at $y=0$:

$$\frac{\partial u}{\partial y}=v=\frac{\partial t}{\partial y}=0, \quad \text{for } x<0 \tag{14}$$

as $x\to-\infty$:

$$\frac{\partial u}{\partial x}=v=t-t_\infty=0, \quad \text{for } y>0 \tag{15}$$

The conditions in equation (14) arise from the assumption of symmetry around the vertical surface and those in equation (15) from entrainment far from the leading edge. The numerical treatment of the boundary conditions is discussed later in this section.

The governing equations are nondimensionalized with L and q as the characteristic quantities. The dimensionless variables employed are given by

$$X=x/L, \quad Y=y/L, \quad U=u/U_c, \quad V=v/U_c, \quad \Psi=\psi/U_cL,$$
$$\Omega=\omega/(U_c/L), \qquad \theta=(t-t_\infty)/(qL/K) \qquad P=p/\rho U_c^2 \tag{16}$$

where

$$U_c=\sqrt{g\beta qL^2/k}, \quad \mathrm{Gr}=g\beta qL^4/k\nu^2, \quad \omega=\frac{\partial v}{\partial x}-\frac{\partial u}{\partial y}$$

Here, ω is the vorticity, U_c the convection velocity, and Gr the Grashof number based on qL/k as the characteristic temperature difference. The full equations are obtained in the vorticity-stream function formulation by eliminating pressure from equations (4) and (5). The resulting equations, in the conservative formulation, for a time-dependent flow, are [3, 13]

$$\frac{\partial\Omega}{\partial\tau}+\nabla\cdot(\bar{V}\Omega)=\frac{1}{\sqrt{\mathrm{Gr}}}\nabla^2\Omega-\frac{\partial\theta}{\partial Y} \tag{17}$$

$$\nabla^2\Psi=-\Omega \tag{18}$$

$$\frac{\partial\theta}{\partial\tau}+\nabla\cdot(\bar{V}\theta)=\frac{1}{\mathrm{Pr}\sqrt{\mathrm{Gr}}}\nabla^2\theta \tag{19}$$

where the dimensionless time τ is obtained by employing (L/U_c) as the characteristic time for nondimensionalization. Similarly, the boundary conditions are obtained in terms of the dimensionless quantities and the problem is solved numerically.

The boundary conditions at the downstream location $x=x_p$ may be obtained by first solving the boundary-layer equations (7–9) and then using the results obtained for specifying the velocity and temperature at $x=x_p$. The location x_p is determined numerically by moving this boundary downstream until a further movement has a negligible effect on the solution of the full equations. For the values of H/L considered here, ranging from 0 to 10, an x_p of around three times the value of H was usually found to be adequate since the downstream flow rapidly approaches the characteristics of the wall plume due to a single line source and the non-boundary-layer effects decay sharply. A similar procedure for generating the boundary conditions for the elliptic problem was employed in [13]. Another method employed here was the simultaneous solution of the equations for the two regions, starting with an initial no-flow condition and allowing the

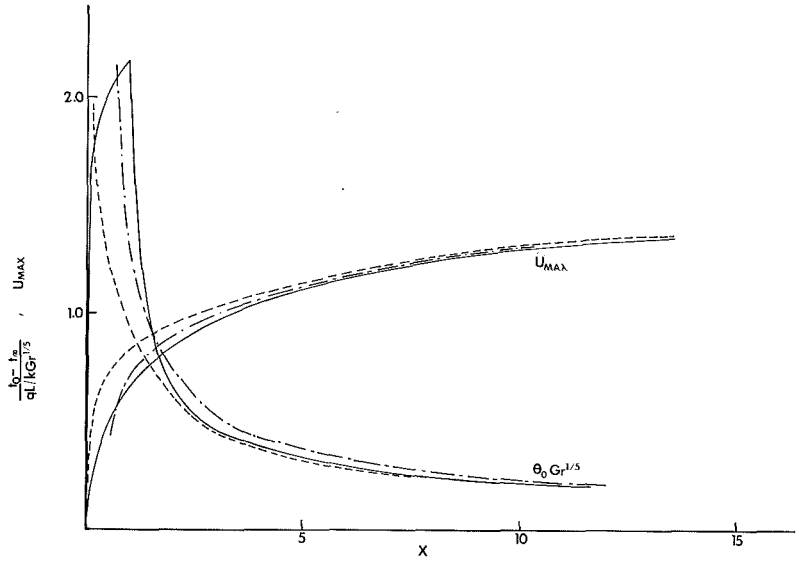

Fig. 2 Variation of the surface temperature θ_0 and the local maximum vertical velocity U_{max} with height X for a single isolated source on a vertical adiabatic surface; also shown are the results from the similarity analysis for the wall plume due to a line source [8]: ——, finite-sized source; — — —, representative line source at $x = 0$; —•—, representative line source at $x = L/2$

conditions at x_p to develop with time. The convergence by this method was slightly more rapid and the numerical results obtained by both the methods were very close in magnitude. Thus, both methods were used for the solution. The lower boundary for the case in which a horizontal surface is not present at the leading edge was also determined in a similar way to specify the boundary conditions given in equation (15). Also, the conditions in the ambient medium, equation (12), were imposed at a distance far from the surface, this distance again being varied to ensure a negligible dependence of the results on the location.

The governing full equations (17–19) were solved numerically by employing finite-difference methods. The time-dependent solution was obtained by marching in time, using the alternating direction implicit (ADI) method [19], or an explicit procedure, with the hybrid scheme [20] for the vorticity and the temperature equations. The elliptic stream function equation (18) was solved by successive overrelaxation or by employing the false transient method [21], which converts this equation also into a transient one so that it may be solved by the method adopted for the other equations to obtain the steady state. For the boundary layer region, equations (7–9) were employed and the boundary-layer solution provides the boundary conditions at x_p for the full equations. The initial condition was generally taken as no flow and the convergence of the transient solution to steady state at long times was determined. The grid spacing, convergence criterion, and initial conditions were varied so as to make sure that their effect on the converged steady-state results is negligible. The computation was performed on the IBM 370/168 computer and wide ranges of the governing parameters, particularly Gr and H/L, were considered. The value of the Prandtl number Pr was held constant at 0.7, which applies for air at temperatures generally encountered. For brevity, only the results for equal source heights and heat flux inputs are presented. Trends similar to those discussed in [7] were obtained for nonequal values.

Some of the important and characteristic results obtained are presented and discussed in the following section. The grid for these results employed 10 points over the heights of each thermal source and 30–40 points across the flow region. This grid spacing was found to be quite adequate both by studying the effect of a reduction in size on the results and by comparison with far downstream results for a wall plume and with boundary layer results for a heated vertical surface. A convergence criterion of 10^{-4} on the temperature field was found to be satisfactory for indicating steady-state conditions. As mentioned above, the convergence criterion was varied to ensure that the results were essentially independent of the value chosen. Near the leading edge, a finer mesh was employed in a few cases to study the effect on the results. It was found that $\Delta x = 0.1$ gave satisfactory results for the solution of the boundary layer equations [7], as well as of the full equations.

Numerical Results and Discussion

The study first considered a single, isolated, finite-sized thermal source on a vertical adiabatic surface. The finite-difference solution of the boundary-layer equations were obtained and compared with the corresponding results from the similarity analysis of the wall plume arising from a line source [8]. Figure 2 shows the finite-difference results for the downstream variation of the surface temperature θ_0 and the local maximum vertical velocity U_{max} in the flow. The temperature initially increases from zero at the leading edge due to the surface heat flux input and then decays downstream due to entrainment. The maximum velocity increases downstream due to the effect of buoyancy in the flow. The results are close to those obtained earlier in [7]. Also shown in Fig. 2 are the variations obtained from the similarity analysis of the wall plume due to a line source, with the variables converted to those of the present study. Two circumstances are considered. The first refers to the case when the corresponding line source, with the same total energy input Q as the finite-sized source, is located at the leading edge and the other to when it is located at midheight of the source.

It is clearly seen from Fig. 2 that the flow far downstream of the thermal source approaches the characteristics of the wall plume due to a line source. In fact the approach is quite rapid, as seen for other flows [13, 22]. Near the leading edge, however, the results are quite different, as expected from the difference in the nature and location of heat input. Since the velocity is zero at the leading edge, for the boundary-layer solution, locating the idealized line source at the leading edge is seen to be more appropriate, though far downstream the

effect of a difference in the location of the line source is negligible. This figure, therefore, lends support to the boundary-layer solution and also indicates the decay of leading edge effects that arise due to differences in the heat input mechanisms, as long as the total input is the same. This being a boundary-layer solution, the results are independent of the location of the finite-sized source on the vertical surface.

Before proceeding to the solution of the full governing equations for multiple sources, the flow over a uniform heat flux surface was considered, assuming an extensive ambient medium all around the surface, i.e., without the imposition of a horizontal surface at the leading edge. This solution of the full equations was obtained to check the numerical scheme and also to study the behavior of the flow near the leading edge. The results obtained were compared with those from the similarity analysis [3, 23], as shown in Fig. 3. The finite-difference results are presented in terms of the similarity variables. The local Grashof number Gr_x and velocity u are given by

$$\mathrm{Gr}_x = \frac{g\beta q x^4}{k\nu^2}, \quad u = 5\frac{\nu}{x}\left(\frac{\mathrm{Gr}_x}{5}\right)^{2/5} f'(\eta)$$

where

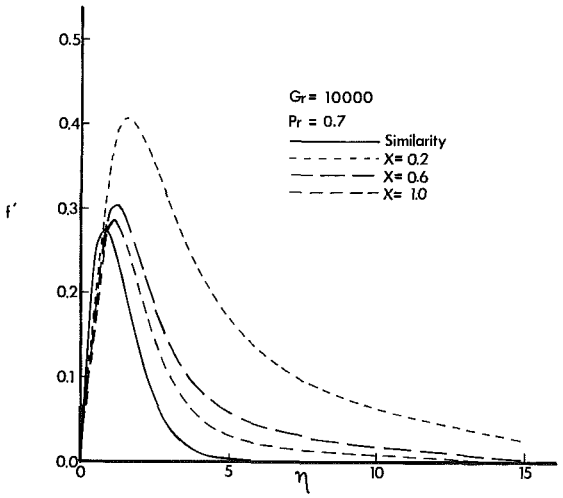

Fig. 3 Comparison of velocity profiles obtained from a solution of the *full governing equations for a vertical uniform heat flux surface with* those from similarity analysis [23], at Gr = 10^4 and three downstream locations

$$\eta = \frac{y}{x}\left(\frac{\mathrm{Gr}_x}{5}\right)^{1/5} \tag{20}$$

The results are shown in Fig. 3 at three downstream locations x/L = 0.2, 0.6, and 1.0, where Gr_x at $x = L$ is denoted by Gr, as given before, and is 10^4. For a semi-infinite vertical plate, L may be chosen as any convenient height in the parabolic region and for a plate of finite height L, the wake must be analyzed to provide boundary conditions for the upstream elliptic region [13, 18]. Figure 3 shows the considerable difference between the boundary-layer similarity results and the solution of the full equations. This is due to the nonzero flow from below the leading edge in the latter case. However, as the flow proceeds downstream, the velocity field rapidly approaches the similarity solution. This behavior was also seen in the temperature results. The flow from below gives rise to a thicker flow region and larger velocities near the leading edge. This, in turn, results in a larger heat transfer coefficient in the region downstream of the leading edge and lower temperature levels, as observed in other studies of the higher order effects [2, 18]. Therefore, this figure lends support to the numerical scheme employed and also indicates the downstream approach to boundary-layer characteristics. Similar trends have been observed in earlier studies [24].

The flow configuration of Fig. 1 is now considered. The surface temperature variation with height X is obtained from a solution of the full equations and is shown in Fig. 4 at Gr = 500 and in Fig. 5 at Gr = 10^4. In both cases, the corresponding boundary-layer solution is also shown. Several interesting features are observed in these figures. The non-boundary layer, or higher-order, effects are quite small at the larger Gr, as expected, though the basic trends are similar at the two values. As seen in Fig. 4, the maximum temperature levels decrease mainly due to axial conduction and the sharp drop at the trailing ends of the heat sources also becomes much more gradual. Far downstream, the solutions for both values of H/L approach the boundary-layer results asymptotically. It is interesting to note that the temperatures at the lower heat source drop more than that at the upper one. This is mainly because of the presence of an isothermal surface at the leading edge. Energy is lost by axial conduction to this surface, resulting in a lower thermal energy input Q into the flow. As a consequence, the temperature levels are lower and so is the buoyancy, which drives the flow. The effect on the velocity field is seen later. But it is clear from Figs. 4 and 5 that axial conduction is important in the flow and that its importance increases as the Grashof number Gr decreases.

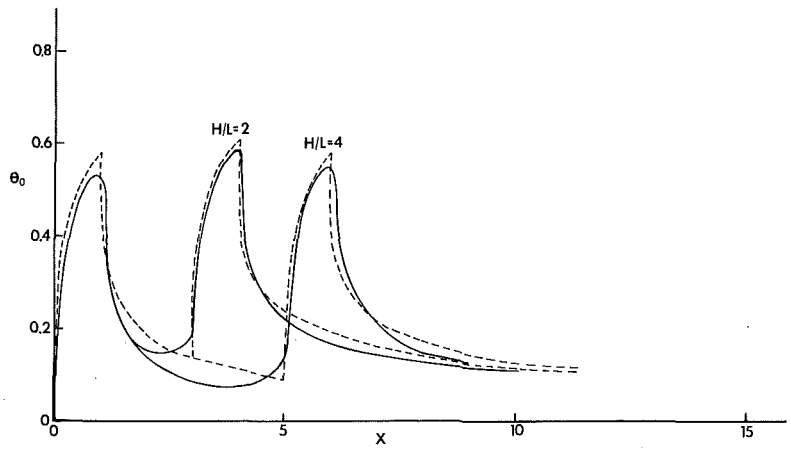

Fig. 4 Surface temperature variation with height X at Gr = 500 for H/L = 2.0 and 4.0: ——, solution of full equations; — — —, boundary-layer solution

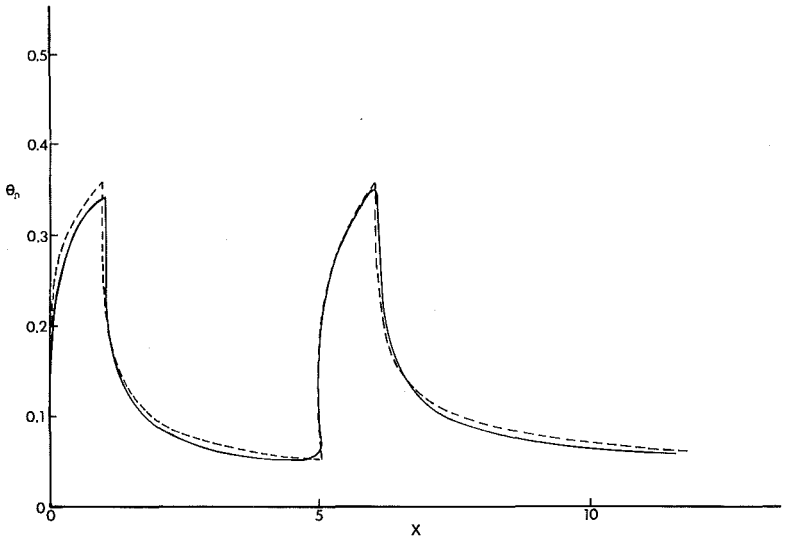

Fig. 5 Surface temperature variation with height X at Gr = 10^4 for H/L = 4.0: ——, solution of full equations; — — —, boundary-layer solution

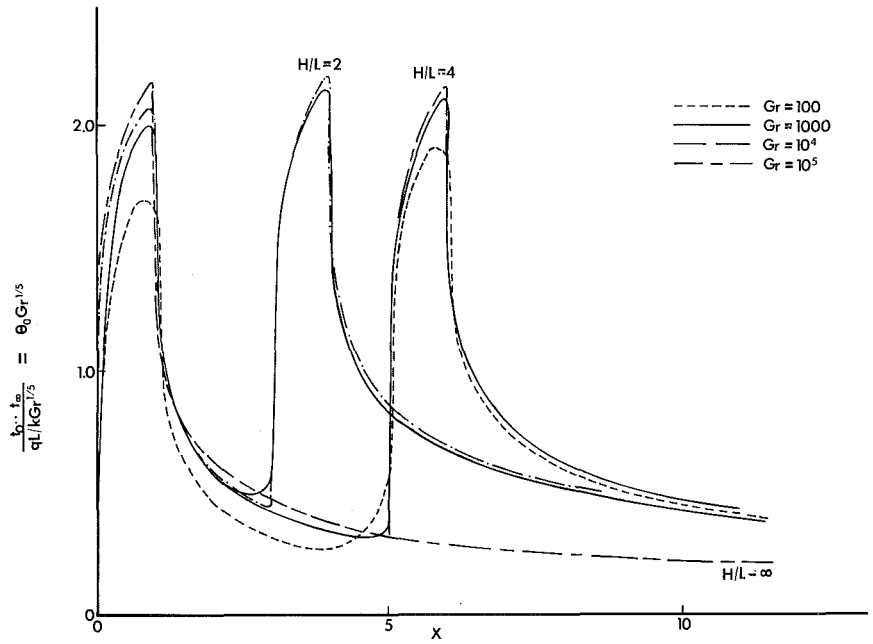

Fig. 6 Downstream surface temperature variation at various values of Gr and H/L

In several electronic systems, small heat inputs and small heights of the thermal sources would give rise to small values of Gr and, therefore, require the solution of the full governing equations for an accurate representation of the transport processes. Since an essentially isothermal base is usually present in these systems, it is necessary to study the effect of this surface on the flow and thermal fields. The conjugate problem, involving conduction loss to the vertical plate, as well as to the horizontal base, would, therefore, be important in the numerical modeling of these flows. At large values of the Grashof number, the boundary-layer formulation is seen to be adequate, since the axial diffusion terms in the energy and the momentum equations are small. Similar effects have been observed in earlier studies [17, 18]. Also, if the lower source is located away from the leading edge, the effect was found to be less. It must be noted from Figs. 4 and 5 that the decrease in the energy input Q into the flow, particularly at lower Gr, also results in lower temperature levels in the flow far downstream. The temperature rises sharply as the flow approaches the upper source and the effect is felt upstream of the source, again because of axial conduction. The change in the surface temperature due to these higher-order effects, therefore, indicates the need to employ the full equations at Gr values of around 10^3 and less. The corresponding heat transfer results are discussed later.

The surface temperature variations obtained for various values of Gr and H/L are shown in Fig. 6. The surface temperature θ_0 is multiplied by $Gr^{1/5}$ to obtain the corresponding nondimensional temperature for the boundary-layer solution [7]. Therefore, as Gr increases, the results obtained are expected to asymptotically approach a single curve which would be close to that obtained from the boundary-layer solution. This trend is clearly seen in Fig. 6. Again, all the results approach the characteristics of a wall plume far downstream. Thus, for large Gr values, the problem may be treated as a boundary-layer flow and for low

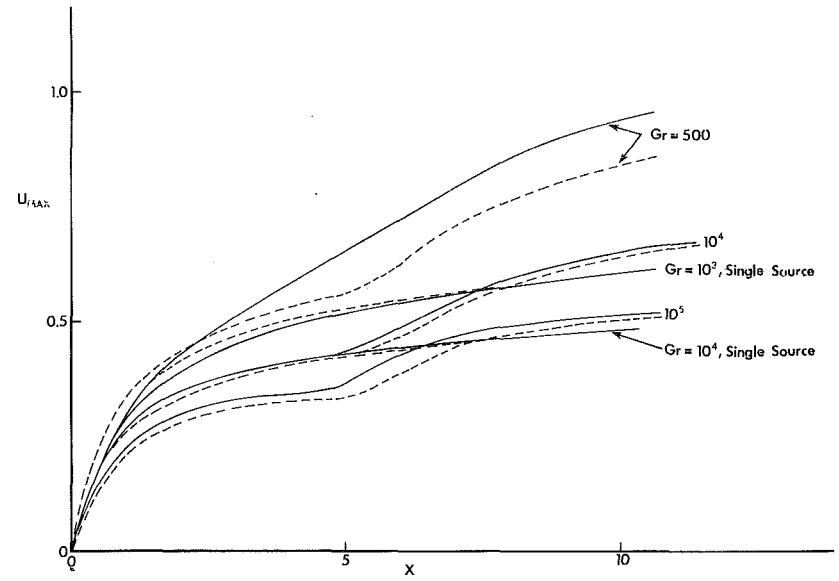

Fig. 7 Downstream variation of the local maximum vertical velocity for H/L = 4.0 and ∞ (single source): ——, solution of full equation; — — —, boundary-layer solution

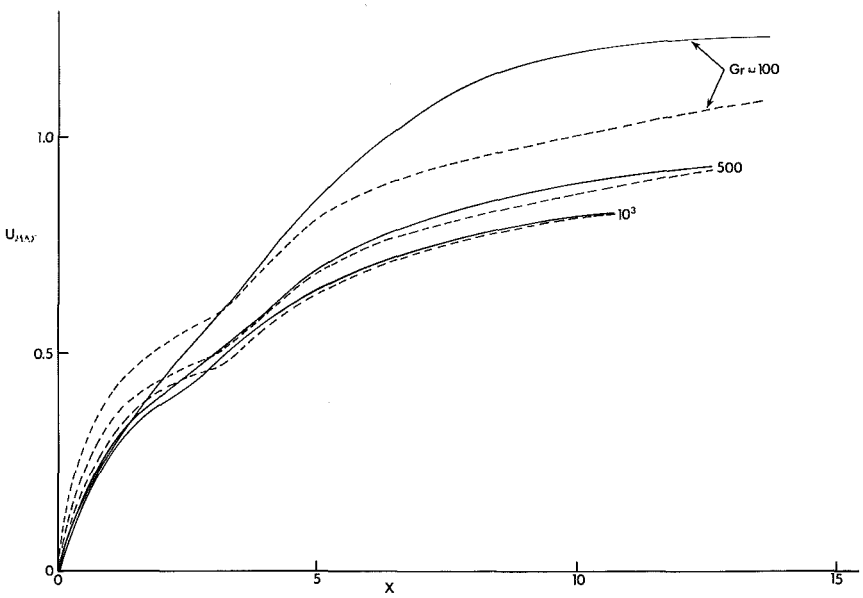

Fig. 8 Downstream variation of the local maximum vertical velocity for H/L = 2.0: ——, solution of full equations; — — —, boundary-layer solution

values, the full equations must be solved with the relevant boundary conditions at the leading edge.

As seen above, the temperature level in the region near the leading edge decreases due to axial conduction. This results in a lowering of buoyancy which would, in turn, tend to lower the velocity. However, the effect of pressure and of the axial diffusion in the full governing momentum equations must also be considered. The resulting velocity level is shown, in terms of the downstream variation of U_{max}, at two values of H/L in Figs. 7 and 8. Similar trends are observed at these two separation distances, as well as at larger values. Also shown is the variation for a single source at Gr = 10^3 and 10^4. It is interesting to observe the initial rapid increase of velocity, followed by another sharp increase at the upper source due to the buoyancy input there. In the case of a single source, the velocity increase monotonically at a decreasing rate, as predicted by the analysis of a wall plume [8, 9]. Far downstream, the flow is found to approach the characteristics of the boundary-layer solution, though the approach is much more gradual at smaller Gr, which, therefore, also required larger values of the numerically determined downstream location x_p of the parabolic region.

It is seen in Figs. 7 and 8 that the computed maximum velocity U_{max} is less than the corresponding value from the boundary-layer solution near the leading edge for smaller values of Gr. However, for larger Gr, Gr ≥ 10^4, the velocity level was found to be slightly larger than the boundary-layer results. This is an interesting result since it indicates the resulting effect on the flow due to axial conduction, which decreases the energy input into the flow, and the pressure effect, which tends to increase the velocity and which arises due to the downstream energy input. The nonboundary-layer

effects in the absence of the horizontal surface lead to a larger velocity level, along with a lower temperature level due to the higher heat transfer coefficient for a uniform heat flux input, as seen earlier in Fig. 3. However, in the present problem, axial conduction leads to an energy loss to the horizontal surface. For low Gr, this is a large effect and is seen in a lower velocity level. However, the pressure effects dominate downstream, leading to a increased velocity level near the upper source. This increased velocity level is expected to increase the heat transfer coefficient, thus lowering the downstream temperature level, as observed in Figs. 4 and 5. Obviously, the mechanisms are coupled and very complex. The trends observed may be explained in terms of the underlying physical processes; but a detailed experimental study is needed to lend further support to the predictions.

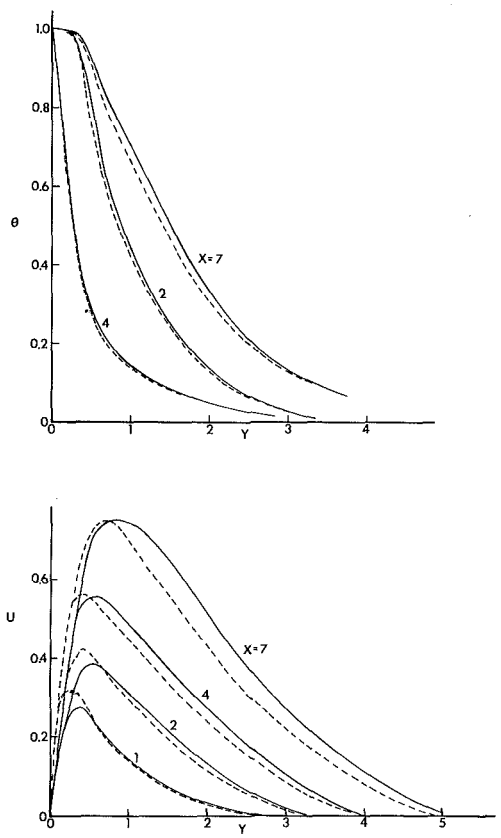

Fig. 9 Temperature and velocity profiles at Gr = 10^3 and H/L = 2.0: ——, solution of full equations; — — —, boundary-layer solution

The temperature and velocity profiles in the flow were also determined. Some of these are shown in Fig. 9 at Gr = 10^3. A significant difference is seen between the boundary-layer solution and the results obtained from a solution of the full equations. The flow is thicker in the latter case due to the nonboundary-layer realignment of the flow near the leading edge. The no-slip condition at the horizontal surface also tends to lower the velocity level, along with a similar effect due to energy loss by axial conduction. However, as the flow proceeds downstream, the flow accelerates rapidly to give rise to larger velocity levels, in the elliptic solution, and a thicker flow region. These effects lead to a thicker thermal region and lower temperature levels, as compared to the boundary-layer results.

The effect on the heat transfer results due to the inclusion of the nonboundary-layer effects is seen in Fig. 10. The ratio of the average Nusselt number Nu_u for the upper element to the Nusselt number Nu_l for the lower element, where Nu is based on the average temperature excess over the ambient temperature t_∞ and the height of the element, is denoted by R. The elliptic solution result is denoted by R_e and the parabolic, boundary-layer one by R_p. Figure 10 shows the percentage decrease in this ratio, $[(R_p - R_e)/R_p] \times 100$, as a function of the Grashof number for two values of H/L, 2.0 and 4.0. In all cases, the inclusion of the nonboundary-layer effects decreases the ratio. This may be explained from the results of Figs. 4 and 5. Due to axial conduction, the temperature of the lower element suffers a greater decrease than the upper element temperature, which remains essentially unchanged in several cases. This implies a greater decrease in the average surface temperature for the lower source. Since, for a uniform heat flux condition, the heat transfer coefficient varies inversely as the surface temperature excess over the ambient, the above effect results in a greater increase in the heat transfer coefficient at the lower element and, thus, a lower value of the

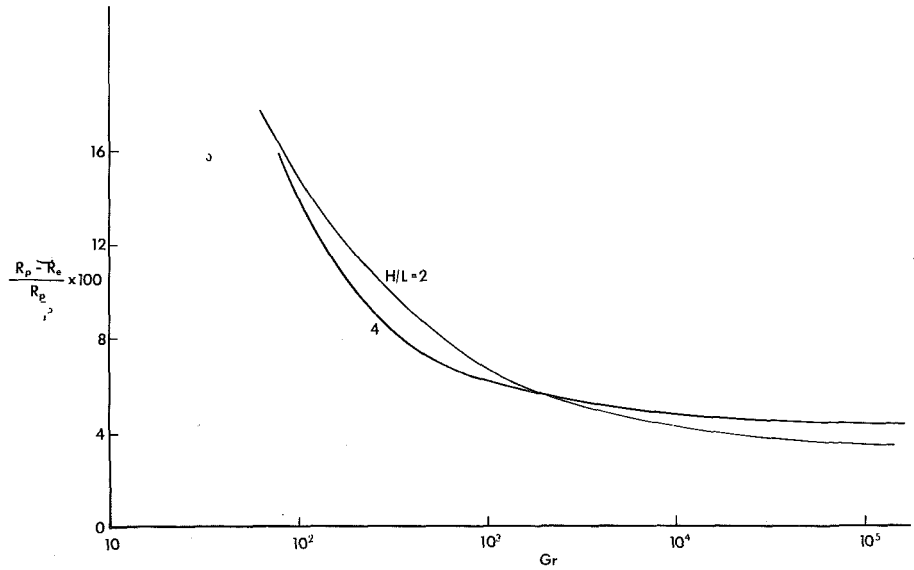

Fig. 10 Percentage decrease in the ratio R of the average Nusselt number for the upper element to that of the lower element due to the inclusion of nonboundary-layer effects, as a function of Gr

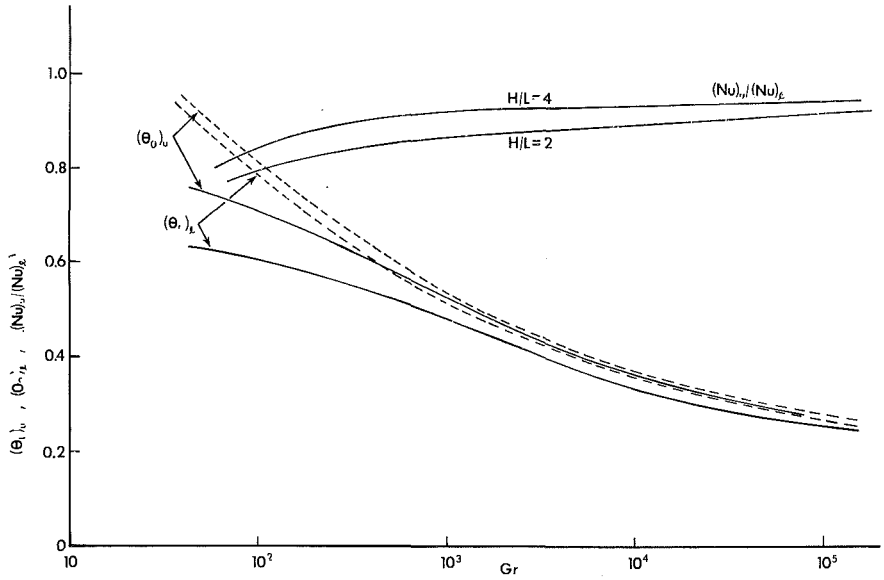

Fig. 11 Variation of $(Nu)_u/(Nu)_l$ and of the surface temperatures $(\theta_0)_u$ and $(\theta_0)_l$ at the trailing ends of the upper and lower heated elements respectively with Gr: ——, solution of full equations; — — —, boundary-layer solution

ratio R. Therefore, the positioning of the upper element in the wake of the lower element results in a lower heat transfer coefficient. The inclusion of the nonboundary layer effects gives a still lower value, indicating the importance of this consideration at small Gr. As Gr increases, the effect is seen to decrease. The trends are similar at the two separation distances. A smaller separation was found to have a stronger effect at small Gr values.

The ratio $[(Nu)_u/(Nu)_l]$ is also shown as a function of Gr in Fig. 11, along with the corresponding maximum surface temperatures at the two heat surfaces. The features discussed earlier are, thus, summarized in this figure for the heat transfer results. Again, at large Gr, the boundary-layer solution is satisfactory and the ratio R asymptotically approaches a constant value. A larger separation distance leads to a larger value of R and thus a more effective heat removal from the upper element. A larger heat transfer coefficient was also obtained at the upper element, as compared to that at the lower element, for still larger separation distances. Thus, as seen in [7], the heat transfer coefficient of the upper element may be increased or decreased, depending on H/L. These results are of particular interest in the design of electronic systems, where adequate cooling of such isolated thermal sources is of considerable importance. The results obtained here, along with those of [7], would provide the necessary inputs over most of the Gr range expected in laminar flow. It may be noted here that, though the presence of the horizontal surface at the leading edge accentuates the above effects in the heat transfer results, the trends are quite similar if the surface is absent.

Conclusions

A numerical study of the interaction of natural convection wakes arising from isolated, finite-sized, thermal sources located on a vertical adiabatic surface, with a horizontal, isothermal surface at the leading edge has been carried out. This flow configuration is of particular interest in the cooling of electronic equipment. The full governing equations are solved by finite-difference methods and the results obtained are compared with the boundary-layer solutions obtained earlier, in order to determine the higher-order effects in the flow. Also of interest was the effect of the horizontal surface at the leading edge on the flow, since, in practical circumstances, such a horizontal boundary is often present.

Several interesting and important results are obtained, particularly for low values of the Grashof number, $Gr \leq 10^4$. Such low values are frequently encountered in practical systems that employ thermal sources of small heights and/or small energy inputs. It is found that nonboundary-layer effects are quite substantial at small Gr, with these effects becoming negligible in the flow and temperature fields obtained for large values. The flow is also found to be significantly affected by the presence of the horizontal, isothermal surface at the leading edge. Again, the effect is largely due to axial conduction and is, therefore, important mainly at small Gr. The decrease in the energy input into the flow due to this conductive energy loss leads to a lower velocity level near the leading edge. However, the flow accelerates rapidly downstream and the boundary-layer characteristics are approached asymptotically far downstream. A comparison of the results obtained for a single source, with and without the horizontal boundary, with the similarity results also indicates the rapid approach of the flow to the boundary-layer solution far from the heated elements. The effect of the inclusion of axial diffusion and pressure terms in the governing equations on the flow and temperature fields and also on the heat transfer coefficients for the heated elements is studied in detail. The observed trends are related to the underlying physical processes and the importance of the results obtained in the design of electronic systems outlined.

Acknowledgments

The author acknowledges the support of the National Science Foundation through Grant No. MEA-82-14325 for this study and the help of Mr. R. Agarwal with some of the computational work.

References

1 Fujii, T., "Theory of the Steady Laminar Natural Convection Above a Horizontal Line Source and a Point Heat Source," *Int. J. Heat Mass Transfer*, Vol. 6, 1963, pp. 597–606.

2 Jaluria, Y., and Gebhart, B., "On the Buoyancy-Induced Flow Arising From a Heated Hemisphere," *Int. J. Heat Mass Transfer*, Vol. 18, 1975, pp. 415–431.

3 Jaluria, Y., *Natural Convection Heat and Mass Transfer*, Pergamon Press, Oxford, U.K., 1980.

4 Lieberman, A., and Gebhart, B., "Interactions in Natural Convection from an Array of Heated Elements," *Int. J. Heat Mass Transfer*, Vol. 12, 1969, pp. 1385–1396.

5 Pera, L., and Gebhart, B., "Laminar Plume Interactions," *J. Fluid Mech.*, Vol. 68, 1975, pp. 259–271.

6 Jaluria, Y., "Natural Convection Flow Due to Line Thermal Sources on a Vertical Adiabatic Surface," *Proc. 7th Int. Heat Transfer Conf.*, Vol. 2, Hemisphere, N.Y., 1982, pp. 147–152.

7 Jaluria, Y., "Buoyancy-Induced Flow Due to Isolated Thermal Sources on a Vertical Surface," ASME JOURNAL OF HEAT TRANSFER, Vol. 104, 1982, pp. 223–227.

8 Jaluria, Y., and Gebhart, B., "Buoyancy-Induced Flow Arising From a Line Thermal Source on an Adiabatic Vertical Surface," *Int. J. Heat Mass Transfer*, Vol. 20, 1977, pp. 153–157.

9 Sparrow, E. M., Patankar, S. V., and Abdel-Wahed, R. M., "Development of Wall and Free Plumes Above a Heated Vertical Plate," ASME JOURNAL OF HEAT TRANSFER, Vol. 100, 1978, pp. 184–190.

10 Carey, V. P., and Mollendorf, J. C., "The Temperature Field Above a Concentrated Heat Source on a Vertical Adiabatic Surface," *Int. J. Heat Mass Transfer*, Vol. 20, 1977, pp. 1059–1067.

11 Kishinami, K., and Seki, N., "Natural Convective Heat Transfer on an Unheated Vertical Plate Attached to an Upstream Isothermal Plate," ASME JOURNAL OF HEAT TRANSFER, Vol. 105, 1983, pp. 759–766.

12 Yang, K. T., "Laminar Free Convection Wake Above a Heated Vertical Plate," ASME JOURNAL OF HEAT TRANSFER, Vol. 86, 1964, pp. 131–138.

13 Hardwick, N. E., and Levy, E. K., "Study of the Laminar Free Convection Wake Above an Isothermal Vertical Plate," ASME JOURNAL OF HEAT TRANSFER, Vol. 95, 1973, pp. 289–294.

14 Sparrow, E. M., and Faghri, M., "Natural Convection Heat Transfer From the Upper Plate of a Collinear, Separated Pair of Vertical Plates," ASME JOURNAL OF HEAT TRANSFER, Vol. 102, 1980, pp. 623–629.

15 Zinnes, A. E., "The Coupling of Conduction With Laminar Natural Convection From a Vertical Plate With Arbitrary Surface Heating," ASME JOURNAL OF HEAT TRANSFER, Vol. 92, 1970, pp. 528–535.

16 Kraus, A. D., and Bar-Cohen, A., *Thermal Analysis and Control of Electronic Equipment*, Hemisphere, N.Y., 1983.

17 Yang, K. T., and Jerger, E. W., "First-Order Perturbations of Laminar Free-Convection Boundary Layer on a Vertical Plate," ASME JOURNAL OF HEAT TRANSFER, Vol. 86, 1964, pp. 107–115.

18 Hieber, C. A., "Natural Convection Around a Semi-Infinite Vertical Plate: Higher-Order Effects," *Int. J. Heat Mass Transfer*, Vol. 17, 1974, pp. 785–791.

19 Peaceman, D. W., and Rachford, H. H., "The Numerical Solution of Parabolic and Elliptic Differential Equations," *J. Soc. Ind. Appl. Math.*, Vol. 3, 1955, pp. 28–41.

20 Spalding, D. B., "A Novel Finite-Difference Formulation for Differential Expressions Involving Both First and Second Derivatives," *Int. J. Num. Methods Eng.*, Vol. 4, 1972, pp. 551–559.

21 Mallinson, G. D., and de Vahl Davis, G., "The Method of False Transient for the Solution of Coupled Elliptic Equations," *J. Comp. Phys.*, Vol. 12, 1973, pp. 435–461.

22 Jaluria, Y., "Natural Convection Flow Interaction Above a Heated Body," *Letters Heat Mass Transfer*, Vol. 3, 1976, pp. 457–466.

23 Sparrow, E. M., and Gregg, J. L., "Laminar Free Convection From a Vertical Plate With Uniform Surface Heat Flux," *Trans. ASME*, Vol. 78, 1956, pp. 435–440.

24 Mahajan, R. L., and Gebhart, B., "Higher Order Approximations to the Natural Convection Flow Over a Uniform Heat Flux Vertical Surface," *Int. J. Heat Mass Transfer*, Vol. 21, 1978, pp. 549–556.

Natural Convection in Open-Ended Inclined Channels

L. F. A. Azevedo

E. M. Sparrow
Fellow ASME

Department of Mechanical Engineering,
University of Minnesota,
Minneapolis, MN 55455

Heat transfer and flow visualization experiments were carried out in water to investigate the effect of inclination on natural convection in a parallel-walled channel. Parametric variations were also made of the dimensionless interwall spacing S/H, *the mode of heating, and the wall-to-ambient temperature difference (i.e., the Rayleigh number* Ra_s*). The heating modes included: (I) both walls heated and maintained at the same uniform temperature, (II) heating only from above, and (III) heating only from below. The Nusselt number results for top-heated channels inclined at an angle* θ *and for the vertical one-sided heated channel were perfectly correlated by the single parameter* $(S/H)Ra_s\cos\theta$. *On the other hand, the results for bottom-heated channels displayed a separate dependence on* S/H, Ra_s, *and* θ. *The Nusselt numbers for two-sided heating exceeded those for one-sided heating for vertical and moderately inclined channels, with a mixed trend at high inclinations. The global correlation* $Nu_s = 0.645[(S/H)\,Ra_s]^{1/4}$ *represented all the results within* ± 10 *percent. Recirculation zones were present adjacent to the unheated wall of top-heated and one-sided heated channels. In the presence of heating from below, secondary flows in the form of longitudinal vortices existed above a threshold Rayleigh number.*

Introduction

Laminar natural convection in parallel-walled channels open to ambient at top and bottom has been extensively investigated for the vertical orientation of the channel for both symmetric and asymmetric heating (e.g., [1–5]). However, there has been relatively little work on the effects of inclining an open-ended channel with respect to the gravitational field. The objective of the present research is to provide definitive information on the response of both the natural convection heat transfer and patterns of fluid flow to channel inclination. In addition to the inclination, three other parameters were varied during the course of the experiments. These included the mode of heating, the spacing between the principal walls of the channel, and the wall-to-ambient temperature difference as expressed by the Rayleigh number. The experiments were performed in water ($Pr \cong 5$).

The two principal walls of the channel were independently heated so as to allow the investigation of both symmetric and asymmetric heating boundary conditions. For the symmetric heating condition, both walls were maintained at the same uniform temperature, elevated with respect to the ambient. The asymmetric condition was achieved by isothermally heating one wall while the other wall was unheated. Due to the inclination of the channel, the asymmetric heating condition allowed two heating possibilities, namely, heating from above and heating from below.

In order to provide baseline results for the inclined configurations, Nusselt numbers for the vertical one-sided and two-sided heated channels were first obtained. Then, the inclined channel heat transfer results were obtained for two different inclinations (30 and 45 deg). For each inclination, the three heating modes described earlier were investigated. Correlations of the heat transfer results were sought which encompassed all of the four investigated parameters. In particular, the effectiveness of the streamwise gravity component in correlating the inclination effects was examined in detail.

Flow visualization experiments were performed utilizing the thymol blue method, which is an electrochemical technique whereby a neutrally buoyant tracer fluid is produced by local changes in pH. Secondary motions in the form of longitudinal vortices were observed above a critical value of the Rayleigh number. Both the critical Rayleigh number and the spatial distribution of the vortices were determined and documented. Also documented in the case of one-sided heated channels were the fractions of the channel length occupied by pockets of recirculating flow adjacent to the top part of the unheated wall.

Experiments

Test Section. The experiments were performed in water with an apparatus whose main components are schematically portrayed in Fig. 1. In part (*a*) of the figure, the apparatus is shown in a pictorial view, while the (*b*) part serves to define the inclined orientation of the channel.

The active components of the apparatus were two identical 0.635-cm-thick copper plates with a height H of 14.52 cm and a width W of 9.67 cm. To achieve temperature uniformity, each plate was electrically heated by means of three independently controlled heating circuits. Twenty equally spaced horizontal grooves were machined into the rear face of each plate to accommodate the Teflon-coated electrical resistance wire (0.0127-cm-dia chromel). The heater wires

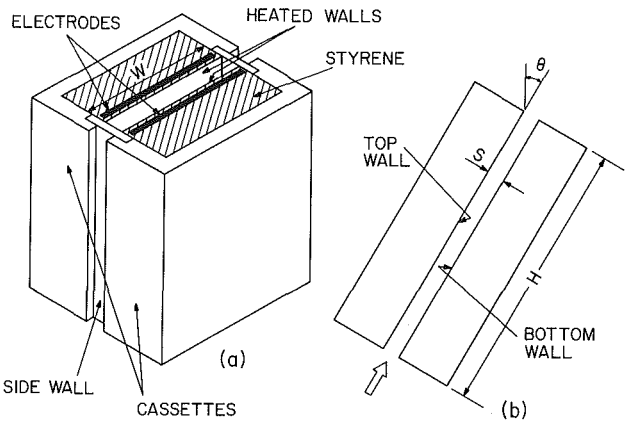

Fig. 1 Experimental apparatus

Contributed by the Heat Transfer Division for publication in the JOURNAL OF HEAT TRANSFER. Manuscript received by the Heat Transfer Division August 24, 1984.

were fixed in place with a water-resistant cement which filled the grooves. Additional watertight sealing was provided by the application of two coats of waterproof epoxy paint on the entire rear face of each plate.

Each of the circuits provided heat to a preselected portion of the plate, respectively, to the lowermost four grooves, to the middle six grooves, and to the uppermost ten grooves. This nonuniform heating-circuit layout was prompted by the expectation that the rate of heat transfer would decrease along the height of the channel.

Depending on whether the channel was to be symmetrically or asymmetrically heated, power from a regulated a-c source was supplied to either one or both of the plates. The voltage drop across each of the three heaters of each active plate was carefully adjusted with the objective of attaining temperature uniformity in each plate and, when both were active, temperature equality between the plates. In this adjustment process, guidance was taken from the readings of eight thermocouples distributed in each plate. In the overwhelming majority of the runs performed, local deviations from the mean plate temperature were less than 1.5 percent of the plate-to-ambient temperature difference. The thermocouples were made of 0.0254-cm chromel and constantan wire that had been precalibrated to 1 μV before installation. The junctions were positioned about 0.05 cm from the front surface of the plate. A digital voltmeter with an accuracy of 1 μV was used for the readings of the thermocouples.

In order to minimize extraneous heat losses, a 3.2-cm-thick block of water-tolerant, closed-pore polystyrene was affixed to the rear face of each plate. The lower and upper edges of the plates were specially shaped and covered with insulation to avoid direct contact with the water (i.e., only the front face of each plate was in contact with water). Each plate and its polystyrene backing were housed in a C-shaped plexiglass container, hereafter referred to as a cassette. The cassettes were mounted, with the copper plates facing each other, on a plexiglass supporting frame (not shown in Fig. 1). The supporting frame was designed so as not to obstruct or deflect the flow passing in or out of the channel openings. The parallel channel configuration was completed with the addition of two plexiglass side walls. Plexiglass was chosen to facilitate the observation of a tracer fluid inside the channel.

The two cassettes could be moved horizontally in order to enable different interplate spacings S to be set. Once a spacing had been set, it was locked in place. The spacing was verified by a dial-gage-equipped caliper with an accuracy of better than 0.0025 cm.

The inclination angle θ between the symmetry axis of the channel and the vertical (shown in Fig. 1*b*) was set and verified by a bubble-level-equipped protractor head capable of resolving 0.5 deg.

The Test Environment. The test environment was designed to be free of extraneous fluid motions which might otherwise affect the fluid flow and heat transfer characteristics of the channel. To this end, a system of two water-filled chambers was employed, one within the other. The inner chamber served as the fluid environment for the test section, while the outer chamber provided thermal control.

Both chambers were rectangular plexiglass tanks, with respective dimensions 73.1 × 43.2 × 45.3 cm and 101.6 × 66.0 × 48.3 cm (length × width × height). Both the inner chamber and the space between the inner and outer chambers (i.e., the interchamber space) were filled with distilled water.

The assembly shown in Fig. 1(*a*) was positioned in the inner chamber so that the channel inlet was situated about 12.7 cm above the floor of the chamber, and the exit was 12.7 cm below the water surface.

A temperature control and water circulating unit was installed in the interchamber space. The outer chamber was insulated with 2.54-cm-thick polystyrene sheets. The two chambers were capped with a polystyrene cover sheet to avoid heat and water losses due to evaporation. The polystyrene cover was made impermeable to water by applying several coats of latex paint.

The temperature of the water inside the test chamber was measured by three precalibrated thermocouples (0.0254-cm chromel and constantan) located approximately 30 cm away from the test channel. The three thermocouples were situated along a vertical line at, respectively, 7.6, 17, and 24 cm above the floor of the test chamber.

A 0.1°C ASTM-certified thermometer was installed in each tank. As will be explained shortly, the readings of these thermometers were used to indicate that thermal conditions prevailed which were appropriate for the initiation of a data run.

Experimental Procedure for Heat Transfer Runs. The experiments consisted of several sequences of data runs. Each sequence was characterized by a preselected value of the spacing S between the bounding surfaces of the channel, the angle of inclination θ of the channel, and the nature of the heating (either one-sided or two-sided). During each sequence, the heating rate (i.e., the wall-to-ambient temperature difference) was varied parametrically.

As described earlier in this section, the experiments were performed in a test environment consisting of two chambers, one within the other. This arrangement was employed to avoid extraneous buoyancy-induced flows in the inner chamber. To achieve this goal, it is necessary that the water in the inner chamber and the water in the interchamber space be at the same temperature. The attainment of this condition was a necessary prerequisite for the initiation of a data run and was verified by reading the thermometers situated in the inner chamber and in the interchamber space. Another condition imposed for the initiation of a data run was that temperature uniformity prevailed throughout the water of the inner chamber.

Once temperature equality between the inner-chamber water and the interchamber water was established, the voltage settings of the six heating circuits (three for each plate) were dialed in. In the case of asymmetric heating, only the voltages for one plate were set. The relationships among the voltage

Nomenclature

A = surface area
g = acceleration of gravity
H = channel height, Fig. 1
h = heat transfer coefficient, equation (1)
k = thermal conductivity
Nu_s = Nusselt number = hS/k
Pr = Prandtl number
Q = heat transfer rate
Ra_s = Rayleigh number = $[g\beta(T_w - T_\infty)S^3/\nu^2]\mathrm{Pr}$
$\mathrm{Ra}_{s,T}$ = Rayleigh number at the onset of secondary flow
S = interplace spacing, Fig. 1
T_w = plate surface temperature
T_∞ = fluid environment temperature
W = plate width, Fig. 1
β = coefficient of thermal expansion
Δ = penetration depth
θ = inclination angle, Fig. 1
λ = wavelength of a vortex pair, Fig. 8
ν = kinematic viscosity
ρ = density

settings that would yield uniform wall temperature were known from experience gained in previous runs. Once the voltage settings were made, the power was then switched off (but the settings maintained). Then, the water in the inner chamber was manually stirred to obtain temperature uniformity throughout the chamber. After stirring, a period of one hour was allowed to guarantee that all motions generated by the stirring operation had died away.

After the waiting period, power was applied to the heating circuits, and the attainment of the steady-state condition was verified by monitoring selected plate thermocouples. In all cases, ten to fifteen minutes were sufficient for the achievement of steady state. After an additional five-minute waiting period, the wall and fluid temperatures and the heater voltages and currents were read and recorded. Then, the new voltage settings for the next run were dialed in and the power switched off. The water in the inner chamber was stirred and, after an hour's wait, a new data run was consummated.

Even for the high power runs, it was observed that the amount of energy added to the water in the inner chamber produced a negligible rise in its temperature after the stirring operation was completed. This characteristic enabled the data for all of the power settings corresponding to a given sequence to be taken during the same day.

In the event that a temperature imbalance occurred between the inner and outer tank water environments, an overnight waiting period was sufficient to restore the equilibrium.

Experimental Procedure for Flow Visualization. Visualizations of flow patterns were performed in runs separate from those for heat transfer, using the thymol blue method [6]. This is an electrochemical technique in which a change in the fluid color is produced by changes in pH brought about by an imposed d-c voltage. The tracer fluid generated is neutrally buoyant and precisely follows the natural-convection-induced motions.

Three substances were added to the water in the test chamber in order to enable the desired changes in color to take place. They are: an acid (hydrochloric acid), a base (sodium hydroxide), and a pH indicator (thymol blue).

The thymol blue was the first substance to be added to the water, and it was dissolved by vigorous stirring. This solution was then titrated to the end point with the addition of sodium hydroxide. The color of the solution at this stage is deep blue. The solution is next made slightly acidic by the addition of hydrochloric acid. A red-yellow color results from this operation.

If a small d-c voltage (less than 6 V) from an adjustable supply is applied across two electrodes situated in the solution, an electrochemical reaction will take place and the pH of the solution in the neighborhood of the negative electrode will change from the acidic to the basic side. This change in pH is accompanied by a change in the color of the fluid, from red-yellow to blue. By placing the negative electrode in a suitable location, various aspects of the flow pattern are revealed.

The location and type of the negative electrode used in the present experiments were dictated by the particular flow pattern being studied. The positive electrode used in the experiments was a copper sheet (8.75 × 8.75 cm) situated at the floor of the test chamber.

Two main sets of flow visualization experiments were conducted. In the first, the effect of the angle of inclination on a pocket of recirculating flow situated adjacent to the top of the unheated wall was studied. Since an inclined unheated wall may face either upward or downward, a tracer-producing electrode was provided for each of the principal walls of the channel. As seen in Fig. 1(*a*), a 0.0024-cm-thick copper foil was cemented atop each wall adjacent to the exit cross section. To avoid possible disturbances of the flow by the formation of hydrogen bubbles at the negative electrode, voltage was applied to the electrochemical circuit in pulses.

A slit was cut in the insulation of the outer chamber to allow observation of the motion of the tracer fluid. Another slit in the insulation of the opposite wall enabled light from a photo floodlight to pass through the test section. This light was diffused by a milk-white plastic plate.

The other set of flow visualization experiments was intended to reveal secondary motions inside the channel. These secondary motions, in the form of longitudinal vortices, were visualized by letting one or the other bounding copper wall of the channel act as the tracer-producing negative electrode for the electrochemical reaction. For this purpose, the plate was electrically connected to the d-c voltage supply. Also, as before, the voltage was applied in an intermittent manner to avoid hydrogen bubble formation. It should be noted that due to the high electrical resistance of the electrochemical circuit (water is the main resistance), the electrical currents involved were very small. This low current level, taken together with the small d-c voltages applied, resulted in a negligible heating of the copper plates compared to the heat generated by the embedded heaters.

The blue dye is generated at the surface of the plate and is carried out of the channel by the flow. The flow patterns were observed at the exit of the channel from a point of view situated in a plane containing the exit cross section. These observations were made by looking through the water surface (with the top cover of the chambers removed).

The preparatory procedures for a flow visualization run were the same as those for the heat transfer runs, i.e., temperature equilibrium, stirring, one hour waiting period, and ten to fifteen minutes heating period allowed for the attainment of steady state. For the visualization run proper, voltage was intermittently applied to the electrochemical circuit. The motion of the tracer fluid was tracked until a steady pattern was achieved. In the case of the recirculating flow studies, a cathetometer was used to determine how far the recirculation bubble had penetrated into the channel.

In the case of the longitudinal vortices, it was noted that the boundary between vortex pairs was delineated by a longitudinal streak of tracer fluid. An array of such streaks was distributed across the span of the channel. The number of interstreak spaces which filled the span was visually counted and from this, the space between vortex pairs was deduced.

Data Reduction. The objectives of the data reduction were to calculate the Nusselt and Rayleigh numbers for the channel. The Nusselt number was evaluated by

$$\mathrm{Nu}_s = hS/k, \quad h = Q/A\,(T_w - T_\infty) \tag{1}$$

In this equation, Q is the sum of the rates of convective heat transfer at the two walls (when only one wall was heated, Q was the heat transfer rate for that wall). In addition, A is the surface area of one or both plates, respectively for one-sided or two-sided heating.

The fluid environment temperature T_∞ was obtained by averaging the readings of the three thermocouples vertically distributed in the chamber. Almost without exception, the readings of the three thermocouples were identical, within the resolving power of the instrumentation (the extreme deviation of any thermocouple from the average was about 0.25 percent of the wall-to-ambient temperature difference). When one plate was heated, the wall temperature T_w was computed by averaging the readings of the eight thermocouples embedded in that plate. In the case of both plates being heated, the readings of all sixteen thermocouples were averaged (eight in each plate). The range of $(T_w - T_\infty)$ for the entirety of the runs extended from 1 to 10°C, and this was also the range of the temperature difference between the plates when one was heated and the other was unheated.

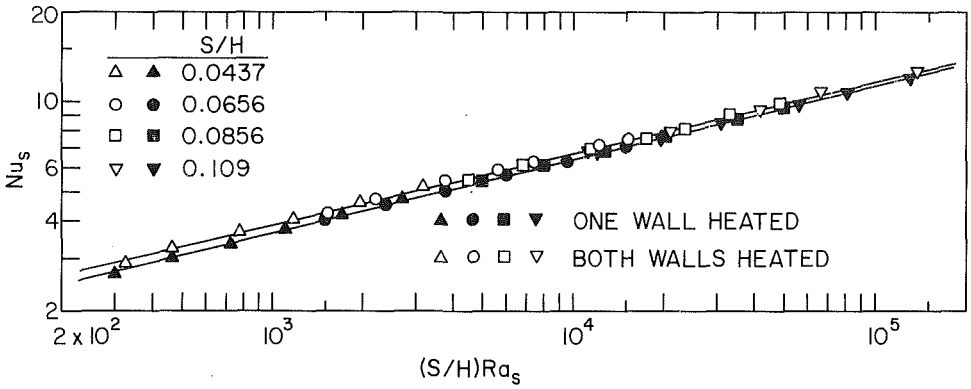

Fig. 2 Nusselt number results for the vertical channel

The rate of convective heat transfer Q was calculated from the electric power delivered to the heaters. From a one-dimensional heat conduction model it was found that the conduction losses through the back side of the cassettes were negligible when compared to the total heat input to the plates.

The Nusselt number results will be correlated by the dimensionless group $(S/H)\,\mathrm{Ra}_s$, which is suggested by theory [2], where

$$\mathrm{Ra}_s = [g\beta(T_w - T_\infty)S^3/\nu^2]\mathrm{Pr} \tag{2}$$

The thermophysical properties in the Nusselt and Rayleigh numbers were all evaluated at the film temperature $\frac{1}{2}(T_w + T_\infty)$.

Results and Discussion

As described earlier, experiments were performed at three different angles of inclination θ with respect to the vertical (θ = 0, 30, and 45 deg). For each inclination, four dimensionless spacings S/H were utilized (S/H = 0.0437, 0.0656, 0.0856, and 0.109). Three heating modes were studied for each geometry defined by θ and S/H. To facilitate future reference in the text, they will be designated as heating modes I, II, and III and are described as follows:

I Both walls heated
II Top wall heated with bottom wall unheated
III Top wall unheated with bottom wall heated

The designations top wall and bottom wall refer to the relative positions of the walls as illustrated in Fig. 1(b). In the case of the vertical channel (θ = 0 deg), there is neither a top wall nor a bottom wall, so that heating modes II and III merge into a single heating condition IV:

IV One wall heated with other wall unheated

For each θ, S/H, and heating mode, the power input to the plate(s) was varied in order to achieve an order of magnitude variation in the Rayleigh number Ra_s. The temperature level was controlled so that the Prandtl number Pr was approximately equal to 5 throughout all the experiments.

The presentation which follows will be structured to highlight the effect of the inclination of the channel on the heat transfer results for each of the previously identified heating modes. Since the results for the vertical channel will be used as base cases for the evaluation of the inclination effects, they will be presented first. Next, in sequence, the heating modes I, II, and III are individually examined, and the inclination effects are identified. A global summary of all Nusselt number results of this investigation is then presented. The heat transfer results are followed by the flow visualization results. These include the identification of flow patterns and the quantitative characteristics of certain of their features.

Vertical Channel Results. Nusselt number results for the vertical channel (θ = 0 deg) are plotted in Fig. 2 as a function of $(S/H)\mathrm{Ra}_s$ for heating modes I and IV. The data for the respective heating modes are represented in the figure by open and black symbols, while the four dimensionless interwall spacings S/H are denoted by symbols identified in the figure. The solid lines passing through each set of data are least-squares fits having the following equations

$$\mathrm{Nu}_s = 0.740[(S/H)\mathrm{Ra}_s]^{0.240}, \quad \text{Mode I} \tag{3}$$

$$\mathrm{Nu}_s = 0.661[(S/H)\mathrm{Ra}_s]^{0.247}, \quad \text{Mode IV} \tag{4}$$

In view of the fact that the exponents appearing in equations (3) and (4) are very close to the traditional 0.25 power, alternative fits utilizing this exponent were worked out, yielding

$$\mathrm{Nu}_s = 0.675[(S/H)\mathrm{Ra}_s]^{0.25}, \quad \text{Mode I} \tag{3a}$$

$$\mathrm{Nu}_s = 0.642[(S/H)\mathrm{Ra}_s]^{0.25}, \quad \text{Mode IV} \tag{4a}$$

It can be seen that for both heating modes, the data are perfectly correlated by the parameter $(S/H)\mathrm{Ra}_s$, so there is no separate dependence on the interplate spacing. This can be verified by noting that there are several regions along both curves where data corresponding to different S/H values overlap and are in agreement.

The fact that the data for Nu_s correlate very well when plotted against the single group $(S/H)\mathrm{Ra}_s$ will now be explored in greater detail. A nondimensionalization of the two-dimensional conservation equations governing the problem under study (continuity, momentum, and energy) shows that the Nusselt number will depend on three separate parameters: $\mathrm{Nu}_s = \mathrm{Nu}_s(S/H, \mathrm{Ra}_s, \mathrm{Pr})$. If, however, the streamwise second derivatives are neglected and the pressure within the channel is taken to be a function only of the streamwise coordinate (i.e., the standard boundary layer approximations), the Nusselt number dependence collapses to $\mathrm{Nu}_s = \mathrm{Nu}_s((S/H)\mathrm{Ra}_s, \mathrm{Pr})$. As already noted, a functional relationship of this form is in evidence in Fig. 2.

The solution of the conservation equations incorporating the boundary layer assumptions does not allow for the existence of recirculating flow inside the channel. However, as will be documented by the flow visualization results, in mode IV, there are pockets of recirculating flow within the channel adjacent to the upper portion of the unheated wall beyond certain critical values of $(S/H)\mathrm{Ra}_s$. The fact that the Nu_s data for mode IV are well correlated by $(S/H)\mathrm{Ra}_s$ demonstrates that the existence of the recirculating flow does not affect the average Nusselt number results. This outcome was rationalized in [7], whose scope was confined to heating mode IV.

From Fig. 2 it can also be noted that the Nusselt numbers for mode I are higher than those for mode IV. This observation implies that the heat transfer rate for the channel

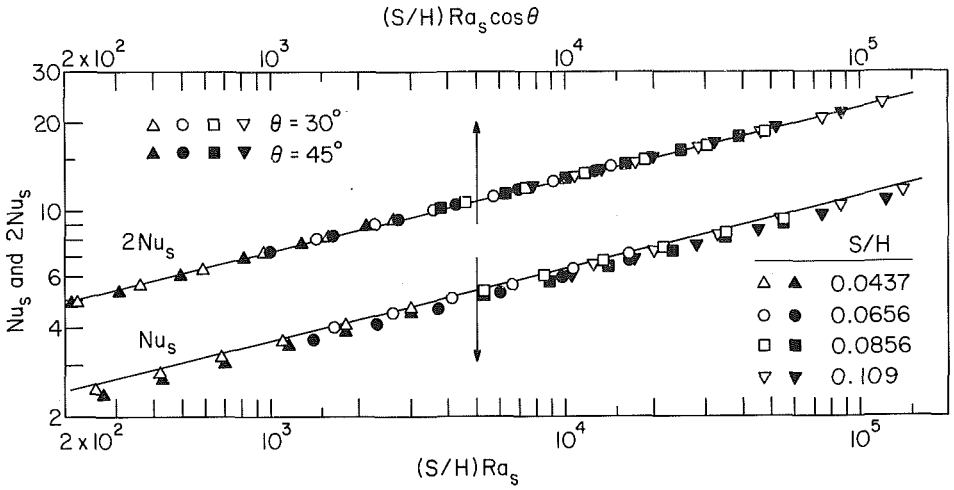

Fig. 3 Nusselt numbers for inclined channels with top wall heated and bottom wall unheated

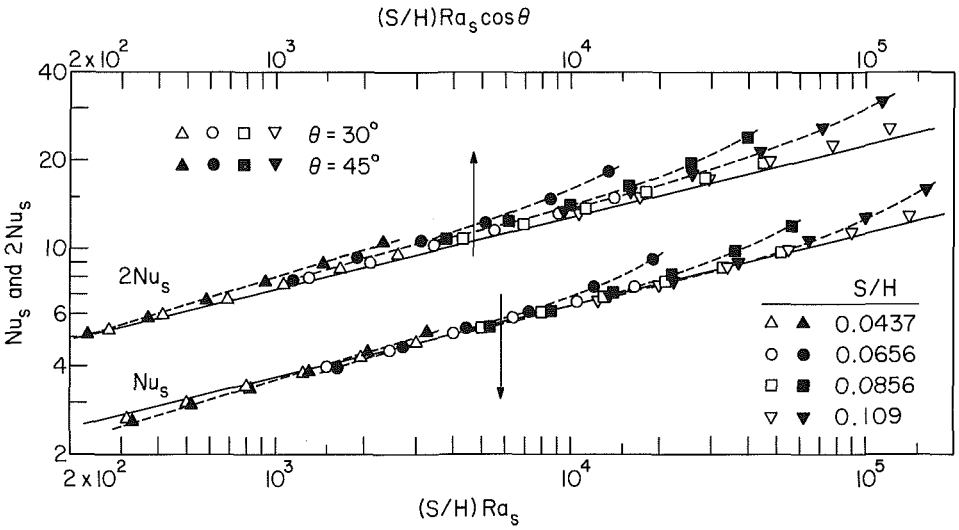

Fig. 4 Nusselt numbers for inclined channels with bottom wall heated and top wall unheated

with both walls heated is greater than twice the heat transfer rate for the one-sided heated channel. This finding can be attributed to an increase in mass throughflow associated with the greater buoyancy induced by the two-sided heating.

Inclined Channel Results. Attention will now be turned to Fig. 3, where the Nusselt number for heating mode II (top wall heated with bottom wall unheated) is plotted both as a function of $(S/H)\mathrm{Ra}_s$ and its cos θ modification $(S/H)\mathrm{Ra}_s\cos\theta$. The use of $(S/H)\mathrm{Ra}_s\cos\theta$ as an alternative correlating group represents an adoption of an already widely used practice for inclined plates which was first suggested by Rich [8]. The data that are plotted against $(S/H)\mathrm{Ra}_s$ are referred to the lower abscissa, while those plotted against $(S/H)\mathrm{Ra}_s\cos\theta$ are referred to the upper abscissa. Both abscissas span three orders of magnitude. In addition, to avoid overlap between the two sets of data, the latter is plotted as $2\mathrm{Nu}_s$ and the former as Nu_s. Open symbols in the figure correspond to $\theta = 30$ deg, while the black symbols represent data for $\theta = 45$ deg. The different data symbols are keyed to the four interplate spacings S/H. The solid lines in the figure are representations of equation (4), the least-squares fit of the data for the vertical, one-sided heated channel.

The most striking feature of the figure is the virtually perfect correlation of the results for all inclinations (including the vertical case) and all interplate spacings which is achieved by use of $(S/H)\mathrm{Ra}_s\cos\theta$ as the independent variable. Thus, for heating mode II, the cos θ factor takes full account of inclination effects, and equation (4) can be generalized to include mode II inclined channels.

$$\mathrm{Nu}_s = 0.657[(S/H)\mathrm{Ra}_s\cos\theta]^{0.247}, \quad \text{Modes II and IV} \tag{5}$$

or, alternatively,

$$\mathrm{Nu}_s = 0.644[(S/H)\mathrm{Ra}_s\cos\theta]^{0.25} \tag{5a}$$

Equation (5*a*) shows that for a fixed geometry $h \sim (\cos\theta)^{0.25}$, i.e., h decreases with inclination.

Both of the representations set forth in Fig. 3 concur in demonstrating that for any fixed inclination, the effects of interplate spacing are totally accommodated by $(S/H)\mathrm{Ra}_s$ (i.e., there is no separate effect of spacing). This finding is especially noteworthy because, in common with the vertical case, there are pockets of recirculating flow adjacent to the unheated wall in inclined channels.

Attention is now directed to the results for heating mode III, which corresponds to the bottom wall heated and the top wall unheated. The Nusselt number results for this case are presented in Fig. 4, whose format is identical to Fig. 3. The solid lines passing through the data are representations of equation (4), which is the very same line that appeared in Fig. 3.

An overall inspection of the figure indicates that neither $(S/H)\mathrm{Ra}_s$ nor $(S/H)\mathrm{Ra}_s\cos\theta$ are successful in bringing the data together. In particular, the data maintain their separate

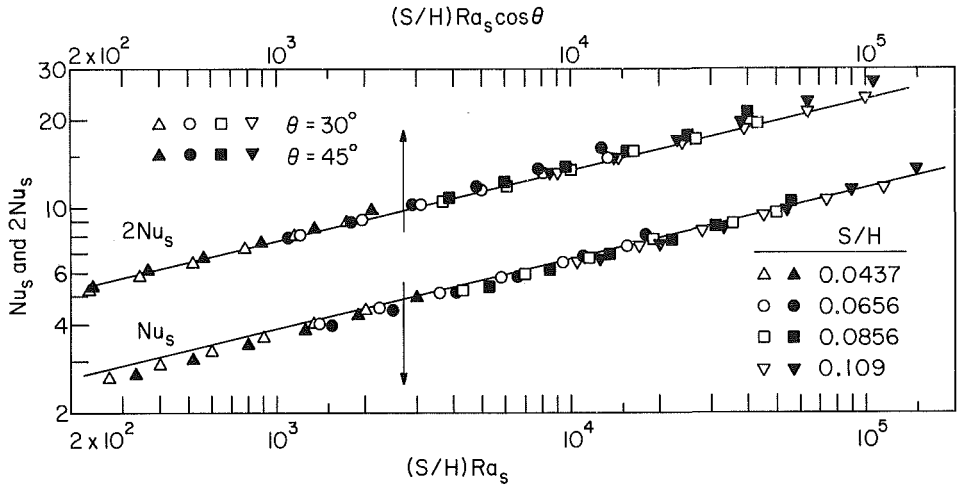

Fig. 5 Nusselt numbers for inclined channels heated at both walls

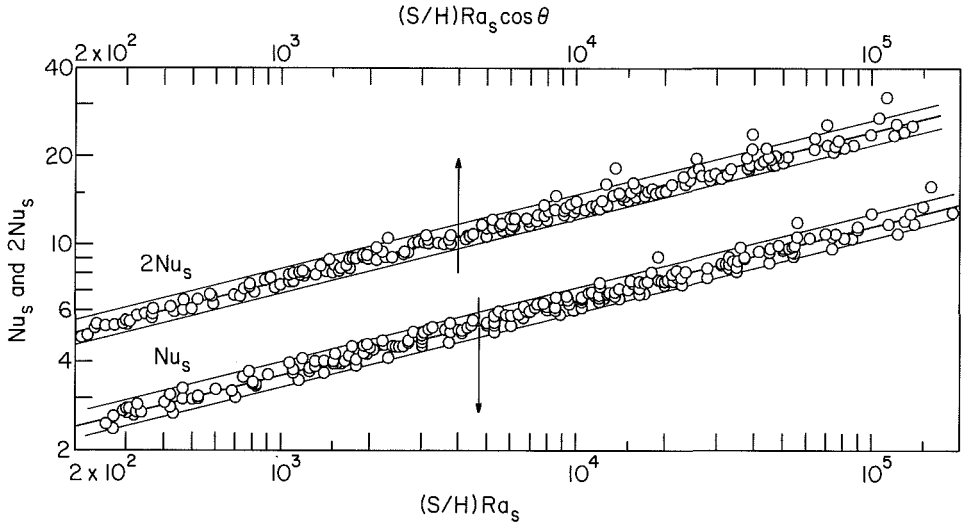

Fig. 6 Nusselt numbers for all investigated cases

identities with respect to both inclination and interplate spacing. These separate identities are accentuated at the 45 deg inclination and, for this reason, individual dashed lines have been used to connect the data for each S/H. At any fixed S/H, the data tend to progressively lift off the vertical channel correlation (i.e., the solid line) as Ra increases. This liftoff is caused by a change in flow regime associated with the instability brought about by the heating from below, as will be demonstrated in the presentation of the flow visualization results. The maximum deviations of the $(S/H)\mathrm{Ra}_s$ and $(S/H)\mathrm{Ra}_s\cos\theta$ versions of the data from the correlation are 12 and 17 percent, respectively.

Overall, the spread of the data is somewhat less for the $(S/H)\mathrm{Ra}_s$ format than for the $(S/H)\mathrm{Ra}_s\cos\theta$ format. The aforementioned inability of cos θ to correlate the inclination effect for the bottom heated case is reminiscent of similar observations by Lloyd [9] and by Fujii [10] for the case of an upward-facing, inclined plate.

The behavior displayed by the Nu_s data for heating mode III will now be rationalized. In experiments performed with an upward-facing, inclined plate [11], heating from below was shown to generate three-dimensional cells of fluid periodically distributed across the span of the plate (longitudinal vortices). The basic mechanism responsible for this behavior of the flow field for the flat plate is also present for the bottom-heated inclined channel. The component of the buoyancy force normal to the upfacing heated surface tends to drive fluid away from the surface. In order to satisfy mass conservation (i.e., to replace the departed fluid), relatively colder fluid moves toward the heated surface, generating the cellular pattern. The secondary motions just described promote mixing of the fluid within the channel which will, in turn, enhance the heat transfer from the heating surface. From the data presented in Fig. 4, it can be seen that at 30 deg there is only a slight effect of the secondary motions on Nu_s. On the other hand, significant effects are present for the 45 deg inclination.

The heat transfer results for the inclined channel with both walls heated (mode I) are presented in Fig. 5 using the same format as that of the two preceding figures. However, the solid lines appearing in the figure now represent equation (3), the least-squares fit for the two-sided heated vertical channel.

From the figure, it is evident that the data spread for the two-sided heated channel is substantially less than that for the bottom-heated channel. This is to be expected, since the two-sided Nusselt number includes contributions from both the top and bottom walls, one of which tends to promote liftoff (i.e., data spread) while the other promotes tightly grouped data. By comparing Fig. 5 with Figs. 3 and 4, the Nusselt numbers for two-sided heating are seen to exceed those for one-sided heating for vertical and moderately inclined channels, with a mixed trend at high inclinations.

If inclinations between 0 and 30 deg are being considered, it is clear that $(S/H)\mathrm{Ra}_s\cos\theta$ format provides a better

correlation than does the $(S/H)\mathrm{Ra}_s$ format. However, if all the angles are considered, the $(S/H)\mathrm{Ra}_s\cos\theta$ format works best up to an abscissa of 10^4, beyond which the $(S/H)\mathrm{Ra}_s$ format appears to be better.

Global Presentation. A global summary of all the heat transfer results of this investigation is presented in Fig. 6. The data displayed in this figure encompass all three inclinations, four interplate spacings, four heating modes, and all heating rates. The Nusselt number results are plotted against both $(S/H)\mathrm{Ra}_s$ and $(S/H)\mathrm{Ra}_s\cos\theta$ and should be referred, respectively, to the lower and upper abscissas of the graph. Again, as in the previous graphs, the overlap of the two data sets was avoided by plotting Nu_s and $2\mathrm{Nu}_s$ as indicated in the figure.

The straight line passing through the body of each set of data is a least-squares fit. The equations of the fitted lines are

$$\mathrm{Nu}_s = 0.645[(S/H)\mathrm{Ra}_s]^{0.25} \tag{6}$$

and

$$\mathrm{Nu}_s = 0.673[(S/H)\mathrm{Ra}_s\cos\theta]^{0.25} \tag{7}$$

Overall, it appears that the data are better correlated when plotted against $(S/H)\mathrm{Ra}_s$. In fact, with the exception of only three points, all the data fall within the ± 10 percent band defined by the lines which flank the least-squares representation. This is a remarkable result, since not only are the investigated ranges of inclination and channel spacing significant, but also the different heating modes give rise to distinct flow patterns within the channel.

The information contained in Fig. 6 is especially convenient for design purposes because of its generality. If ± 10 percent is an acceptable level of uncertainty in a particular design, a single correlation, equation (6), having the traditional flat-plate 0.25 exponent, can be used for a wide range of channel spacings, inclinations, and heating modes and levels. It should also be noted that the involvement of Ra in the correlation moderates the influence of the Prandtl number (see Fig. 7 of [7]).

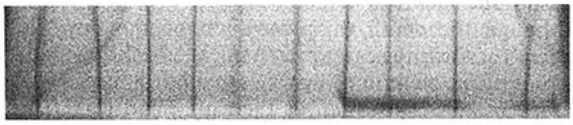

Fig. 7 Photograph of a typical streak pattern

In Fig. 6, the three points that lie above the ± 10 percent band of the lower data set, as well as the ten points which lie above the band for the upper data set, do not represent scatter in the experimental results. They all belong to the same physical situation (θ = 45 deg, heating mode III) which, as already mentioned in connection with Fig. 4, displays secondary motions within the channel in the form of longitudinal vortices.

Flow Visualization Results. The flow visualization experiments had two main objectives, namely, the investigation of the existence and nature of the secondary flow within the channel and the identification of the pockets of recirculating flow.

Secondary Flow Observations. The flow visualizations that will now be presented were motivated by the unique behavior displayed by the Nusselt number results when the channel was inclined at 45 deg. The visualization experiments were conducted by using each one of the bounding walls of the channel, one at a time, as the tracer-producing electrode. Flow visualization runs were made for all of the heating modes I–III at the 45 deg inclination for the same range of $(S/H)\mathrm{Ra}_s$ as in the heat transfer experiments.

When the electrochemical circuit is activated, the blue fluid generated covers the tracer-producing wall. If the fluid flow adjacent to the wall is strictly in the streamwise direction, the tracer fluid will move upward as a sheet along the wall. This pattern was observed for the 45 deg inclined channel with its top wall heated and bottom wall unheated (heating mode II), regardless of which wall was used as the tracer-producing electrode. The tracer fluid moved along the tracer-producing wall and did not cross the channel to the opposite wall. There was no evidence of any secondary motions.

The 45 deg inclined channel heated from below and unheated from above (heating mode III) was investigated next. When the top wall was used as the tracer-producing electrode, a continuous layer of blue fluid, similar to the one described for the mode II case, was observed for all the spacings investigated and for the entire range of $(S/H)\mathrm{Ra}_s$. However, when the tracer fluid was generated at the bottom wall, a distinct fluid flow pattern was observed. Up to a critical value of $(S/H)\mathrm{Ra}_s$, which depended on S/H, the continuous layer pattern of the tracer fluid prevailed. Beyond the critical value, this pattern was replaced by an array of

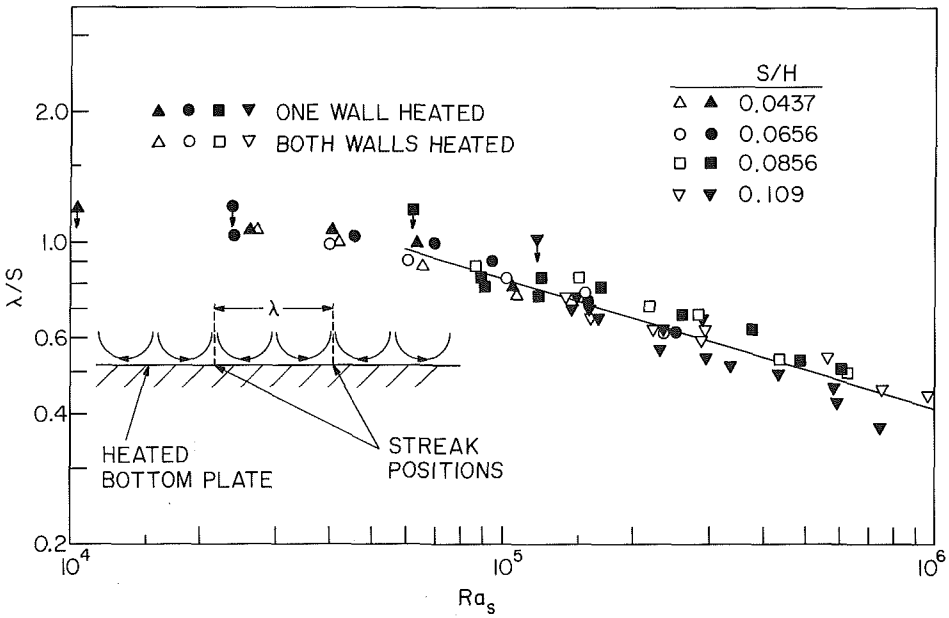

Fig. 8 Wavelength for pairs of secondary flow vortices

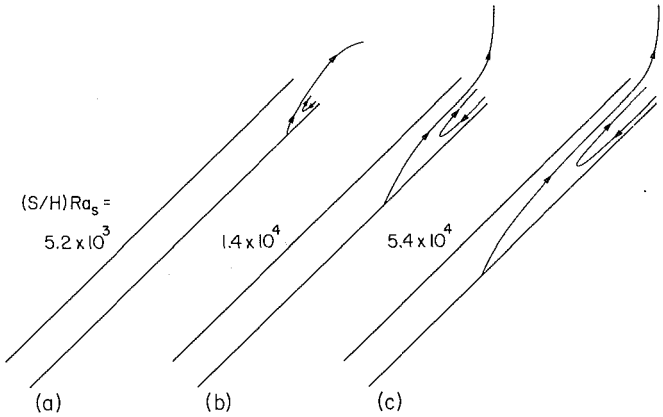

Fig. 9 Illustration of backflow adjacent to the unheated wall of the channel

more or less regularly spaced longitudinal streaks adjacent to the bottom wall. Figure 7 is a photograph of a typical streak pattern, taken at the exit of the channel with the camera situated in a plane containing the exit cross section (Fig. 7 corresponds to $S/H = 0.0656$ and $(S/H)\mathrm{Ra}_s = 6000$).

The formation of the longitudinal streaks is illustrated in the inset of Fig. 8. As seen there, a streak is formed when a pair of neighboring, counterrotating, longitudinal vortices sweeps the layer of blue fluid across the plate in the transverse direction, accumulating it at the boundary line between the two vortices. Since the streaks were not present when the top wall was used as the tracer-producing electrode for this heating mode (mode III), it can be concluded that the longitudinal vortex system described does not occupy the entire cross section of the channel.

The flow structure in the channel inclined at 45 deg with both walls heated (heating mode I) was observed to be qualitatively similar to that just described for the channel of the same inclination and heated only from below (heating mode III).

The wavelength characterizing a vortex pair is defined as the distance λ between two observed longitudinal streaks, as shown in the inset in Fig. 8. As stated earlier in the paper, for a given run, the wavelength λ was obtained by dividing the width of the channel by the number of interstreak spaces, which was visually counted. In Fig. 8, the nondimensional wavelength λ/S is plotted as a function of Ra_s for heating modes I and III which are represented, respectively, by open and black symbols. The different data symbols are related to the four interplate spacings investigated. All the data points presented in the figure correspond to an inclination of 45 deg.

Overall, it can be observed that, within scatter that is acceptable for this type of experiment, the data for the two heating modes are intermingled. Furthermore, it appears that the λ/S versus Ra_s distribution does not display a separate dependence on the dimensionless interplate spacing S/H. The data for $\mathrm{Ra}_s > 6 \times 10^4$ have been fit with a least-squares straight line whose equation is

$$\lambda/S = 26.2\mathrm{Ra}_s^{-0.300} \tag{8}$$

so that in this range, λ is virtually independent of S. Both from equation (8) and from Fig. 8, it is evident that λ/S decreases with Ra_s. In particular, at a fixed interplate spacing S, an increase in Ra_s corresponds to a larger number of longitudinal vortices in the channel (i.e., smaller λ). This observation reinforces the previously suggested rationalization of the behavior displayed by the Nusselt number results for $\theta = 45$ deg in Figs. 4 and 5. In the discussion of those results, the enhancement of Nu_s with $(S/H)\mathrm{Ra}_s$ for a fixed S/H was attributed to the mixing associated with the longitudinal vortices. This increased mixing can now be related to an increase in the number of vortices in the channel.

The visualization experiments also provided information on the transition of the flow from a pure streamwise motion to one in which secondary flow (longitudinal vortices) is present. The procedure for determining the transition point for a particular S/H spacing was to carefully vary the power setting to the plate(s) until the tracer fluid exiting the channel first displayed unsteadiness. This unsteady behavior was characterized by an alternation from the continuous layer regime to the longitudinal streak regime. The Rayleigh number corresponding to this condition was recorded and taken as the transition Rayleigh number $\mathrm{Ra}_{s,T}$ for the specific S/H being studied.

The transition values $\mathrm{Ra}_{s,T}$ for each dimensionless interwall spacing S/H and for heating mode III are shown in Fig. 8 by the arrow-attached symbols. The following equation is a least-squares fit of the transition Rayleigh numbers

$$\mathrm{Ra}_{s,T} = 5.93 \times 10^7 (S/H)^{2.80} \tag{9}$$

This correlation is based on observations for the 45 deg inclination. Flow visualization was not performed for the 30 deg inclination because the effect of the secondary flow on the heat transfer was modest, as seen in Fig. 4.

Backflow Observations. Additional flow visualization experiments were conducted in order to investigate the existence of pockets of recirculating flow adjacent to the unheated wall of inclined channels. Those recirculation zones were documented in [7] for one-sided heated vertical channels, where they were shown to be located at the top portion of the unheated wall.

The first configuration studied was the channel subjected to heating mode II (top wall heated and bottom wall unheated) for inclinations of 30 and 45 deg. To this end, the electrode positioned atop the bottom wall (unheated wall for this case) was used as the tracer-fluid generator. Sketches reproducing the observations of the motions of the tracer fluid for an inclination of 45 deg and heating mode II are presented in Fig. 9(*a–c*) for three values of $(S/H)\mathrm{Ra}_s$ (for $\theta = 30$ deg the pattern of the backflow is similar).

Although the depth of penetration of the downflow is different for the three cases presented, the backflow pattern is the same. The backflow region is bounded by a **V**-shaped envelope (note that the wall is the right-hand leg of the envelope). The tracer fluid generated at the electrode penetrates the channel along the unheated wall. After reaching a maximum penetration, the downflowing fluid reverses direction and rises toward the exit of the channel, forming the left leg of the **V**. It is seen from Fig. 9(*a*) that the exiting plume bends toward the right, while in the other two sketches it rises vertically. This behavior is related to the temperature difference between the plume and the ambient fluid, which determines the plume's buoyancy. In the case of Fig. 9(*a*), which is characterized by a very small temperature difference, the plume cools to a nonbuoyant state relatively near the exit and, therefore, arcs over.

The maximum depths of penetration of the downflow for the top-heated channel (mode II) were recorded for inclinations of 30 and 45 deg. These results are presented in Fig. 10, where the dimensionless depth of penetration Δ/H is plotted as a function of $(S/H)\mathrm{Ra}_s$. The open and black symbols correspond to inclinations of 30 and 45 deg, respectively, while the different symbols are related to the four dimensionless interplate spacings.

The data for the two inclinations are intermingled. Furthermore, owing to data scatter, no clear trend with S/H can be identified. However, it is clear that there is a trend toward deeper penetration with increasing $(S/H)\mathrm{Ra}_s$, with a penetration of about half the channel height being encountered at the largest investigated values of $(S/H)\mathrm{Ra}_s$. The points corresponding to $\Delta/H = 0$ (i.e., no penetration)

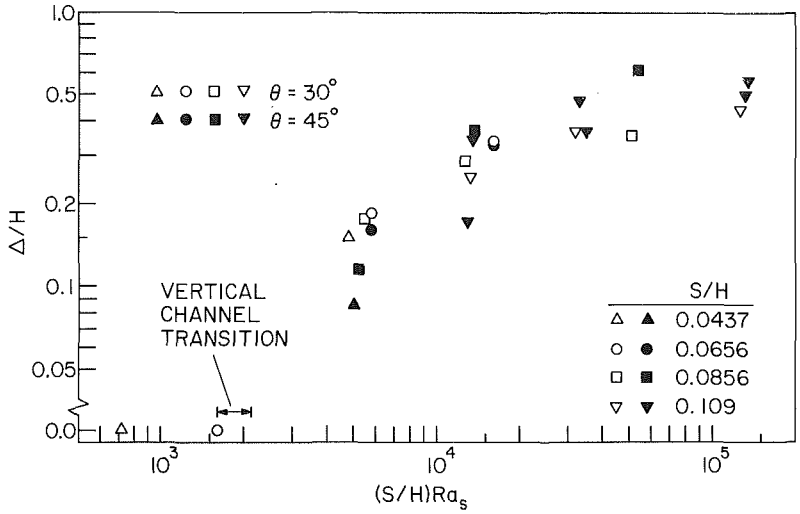

Fig. 10 *Maximum penetration depths of downflow in top-heated inclined channels*

presented in the figure are in reasonable agreement with the transition values obtained in [7] for the vertical case (represented by the horizontal band in the figure). The trend toward increased penetration with increasing $(S/H)\mathrm{Ra}_s$ is explained in detail in [7].

The experiments were then focused on the bottom-heated channel (mode III) for inclinations of 30 and 45 deg. The tracer-producing electrode used for these experiments was situated atop the top wall (now the unheated wall). For all the interplate spacings and for the range of $(S/H)\mathrm{Ra}_s$ investigated, no backflow was observed.

Concluding Remarks

The effect of inclination on natural convection in a parallel-walled channel was investigated for angles of 0, 30, and 45 deg relative to the vertical and for dimensionless interwall spacings S/H of 0.0437, 0.0656, 0.0856, and 0.109. For each inclination and spacing, three heating modes were employed: (I) both walls heated and maintained at the same temperature level, (II) top wall heated and bottom wall unheated, and (III) bottom wall heated and top wall unheated. As a base case, one-sided heated and two-sided heated vertical channels were also investigated. In all cases, the heated wall(s) were maintained isothermal. The experiments were performed in water at a nominal Prandtl number equal to 5 and included measurements of the Nusselt number Nu_s and flow visualization. The wall-to-ambient temperature difference was varied by an order of magnitude.

The Nu_s results for top-heated channels (mode II) inclined at 30 and 45 deg and for the vertical one-sided heated channel were perfectly correlated when plotted against the single parameter $(S/H)\mathrm{Ra}_s\cos\theta$, despite the existence of pockets of recirculating flow adjacent to the top part of the unheated wall. The depth of penetration of the recirculation zone into the channel was determined by flow visualization experiments, which revealed a trend toward deeper penetration (up to half the channel height) with increasing $(S/H)\mathrm{Ra}_s$.

When the inclined channel was heated only from below (mode III), neither $(S/H)\mathrm{Ra}_s$ nor $(S/H)\mathrm{Ra}_s\cos\theta$ succeeded in bringing together the Nusselt number data. At any fixed interplate spacing S/H, Nu_s progressively lifted off the vertical channel correlation as the Rayleigh number Ra_s was increased. Flow visualization revealed the existence of a system of longitudinal vortices within the channel. The number of such vortices was found to increase with Ra_s, resulting in greater mixing of the fluid and consequent enhancement of Nu_s, thereby accounting for the aforementioned liftoff. The onset of the longitudinal vortex regime was determined and correlated.

The heat transfer results for the two-sided heated channel (mode I) were affected by the longitudinal vortices only at the 45 deg inclination and to a lesser extent than the bottom-heated channel.

A global correlation of the heat transfer results for all the investigated heating modes, inclinations, interplate spacings, and Rayleigh numbers (i.e., $(S/H)\mathrm{Ra}_s$ between 200 and 2×10^5 and θ between 0 and 45 deg) yielded the compact expression $\mathrm{Nu}_s = 0.645[(S/H)\mathrm{Ra}_s]^{0.25}$, with a spread of ± 10 percent. The tightness of the correlation suggests an insensitivity of the heat transfer results to inclination and heating mode.

Acknowledgments

Support accorded to L. F. A. Azevedo by Conselho Nacional de Desenvolvimento Cientifico e Tecnologico (CNPq) of Brazil is gratefully acknowledged.

References

1 Elenbaas, W., "Heat Dissipation of Parallel Plates by Free Convection," *Physica*, Vol. 9, 1942, pp. 1-28.

2 Bodoia, J. R., and Osterle, J. F., "The Development of Free Convection Between Heated Vertical Plates," ASME JOURNAL OF HEAT TRANSFER, Vol. 84, 1962, pp. 40-44.

3 Aung, W., Fletcher, L. S., and Sernas, V., "Developing Laminar Free Convection Between Vertical Flat Plates With Asymmetric Heating," *International Journal of Heat and Mass Transfer*, Vol. 15, 1972, pp. 2293-2308.

4 Sparrow, E. M., Shah, S., and Prakash, C., "Natural Convection in a Vertical Channel: I. Interacting Convection and Radiation. II. The Vertical Plate With and Without Shrouding," *Numerical Heat Transfer*, Vol. 3, 1980, pp. 297-314.

5 Wirtz, R. A., and Stutzman, R. J., "Experiments on Free Convection Between Vertical Plates With Symmetric Heating," ASME JOURNAL OF HEAT TRANSFER, Vol. 104, 1982, pp. 501-507.

6 Baker, D. J., "A Technique for the Precise Measurement of Small Fluid Velocities," *Journal of Fluid Mechanics*, Vol. 26, 1966, pp. 573-575.

7 Sparrow, E. M., Chrysler, G. M., and Azevedo, L. F., "Observed Flow Reversals and Measured-Predicted Nusselt Numbers for Natural Convection in a One-Sided Heated Vertical Channel," ASME JOURNAL OF HEAT TRANSFER, Vol. 106, 1984, pp. 325-332.

8 Rich, B. R., "An Investigation of Heat Transfer From an Inclined Flat Plate in Free Convection," *Transactions of ASME*, Vol. 75, 1953, pp. 489-498.

9 Lloyd, J. R., Sparrow, E. M., and Eckert, E. R. G., "Laminar, Transition, and Turbulent Natural Convection Adjacent to Inclined and Vertical Surfaces," *International Journal of Heat and Mass Transfer*, Vol. 15, 1972, pp. 457-473.

10 Fujii, T., and Imura, H., "Natural-Convection Heat Transfer From a Plate With Arbitrary Inclination," *International Journal of Heat and Mass Transfer*, Vol. 15, 1972, pp. 755-767.

11 Sparrow, E. M., and Husar, R. B., "Longitudinal Vortices in Natural Convection Flow on Inclined Plates," *Journal of Fluid Mechanics*, Vol. 37, 1969, pp. 251-255.

Laminar Mixed Convection in a Concentric Annulus With Horizontal Axis

A. O. Nieckele

S. V. Patankar
Mem. ASME

Department of Mechanical Engineering,
University of Minnesota,
Minneapolis, MN 55455

Axial laminar flow in a horizontal annular pipe is influenced by the presence of buoyancy-induced secondary flows that are caused by the heat flow from the inner cylinder. A numerical study is presented for the fully developed region of the buoyancy-affected flow. The distributions of the axial and cross-sectional velocities are calculated along with the temperature variation in the cross section. Results are presented for a range of values of the Rayleigh number, the Prandtl number, and the radius ratio of the annulus. The Nusselt number increases significantly with the Rayleigh number; yet the corresponding increase in the friction factor is found to be rather small. Distributions of secondary flow and isotherms over the cross section are presented for different values of the parameters. In each half of the annulus on either side of the vertical centerline, the secondary flow displays a single-eddy pattern at low Rayleigh numbers and changes to a double-eddy pattern at high values.

Introduction

Forced convection in duct flows is often significantly influenced by body forces, which tend to produce secondary flows in the duct cross section. A common example is that of a laminar horizontal pipe flow, in which the nonuniformities of temperature in the cross section lead to the buoyancy-induced secondary currents. The present paper describes a study of the laminar mixed convection in a horizontal annular duct flow subjected to heating from the inner cylinder. The situation is encountered in practice when the fluid in a pipe is heated by passing it over a central heater rod or electrical resistor. Similarly, gas-cooled electrical cables require the consideration of mixed convection in an annular flow. Double-pipe heat exchangers and the cooling of nuclear fuel rods present additional examples where the results for the buoyancy-influenced convection in an annulus are useful.

Laminar mixed convection in *circular* horizontal tubes has been analyzed in a number of papers [1-11]. Similarly, there are several studies that examine the *natural* convection between two horizontal concentric cylinders maintained at two different temperatures. These include the numerical work reported in [12-20] and the experimental investigation in [21-24]. The situation where a prescribed temperature is maintained at one cylinder, while there is a uniform heat flux at the other, is treated in [25-26]. Mixed convection between two isothermal concentric cylinders is presented in [27-28]. The analysis of the fully developed *forced* convection in annular ducts is well established and has been summarized in [29].

The purpose of this paper is to present a numerical study of the fully developed laminar flow and heat transfer in a concentric annulus, in which the heating from the inner cylinder leads to significant buoyancy-induced secondary motion.

Analysis

The cross section of the annular duct under consideration is shown in Fig. 1. In the fully developed region of the flow, the velocity components u, v, and w in the θ, r, and z coordinates become independent of the axial distance z. As to the thermal boundary conditions, the outer cylinder is considered to be adiabatic, while the inner cylinder has a circumferentially uniform surface temperature and an axially uniform heat transfer rate. This heat flow can originate from electrical or nuclear heat generation within the material of the inner cylinder. Alternatively, the inner cylinder can be a tube, as in a double-pipe heat exchanger, and provide a uniform heat flow from the hot fluid flowing within it provided equal capacity flow rates are maintained for the hot fluid and the fluid in the annular duct. In any case, the solid material forming the inner cylinder is considered to have sufficiently high conductivity so that in any given cross section a uniform temperature T_w prevails on the surface of the cylinder. In the thermally developed region, the temperature T_w and any local temperature T of the fluid in the annulus vary linearly with z at the same constant rate determined by Q', the rate of heat flow per unit axial length.

It may be noted that the thermal boundary condition employed here is not identical to that of uniform heat flux at the inner cylinder. If the local heat flux were maintained as uniform, circumferential variations of the wall temperature would result. In practice, whenever the inner cylinder is made of metal, it would be very difficult to maintain a perfect uniformity of the local heat flux. The condition of cir-

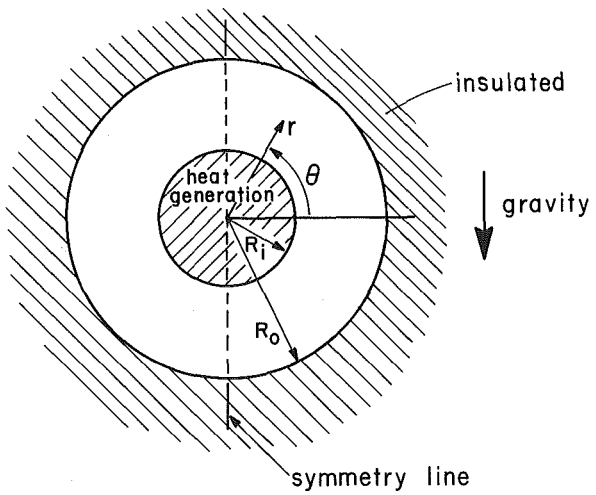

Fig. 1 Cross section of the annulus

Contributed by the Heat Transfer Division for publication in the JOURNAL OF HEAT TRANSFER. Manuscript received by the Heat Transfer Division February 3, 1983. Paper No. 83-HT-74.

cumferentially uniform wall temperature is more likely to be encountered in practical applications.

The constant rate of rise of the fluid temperature T in the axial direction will be denoted by a. It can be related to the heat flow rate Q' by means of the overall heat balance. Thus,

$$a=\partial T/\partial z=dT_w/dz=dT_b/dz=Q'/[\rho c_p \bar{w}\pi(R_o^2-R_i^2)] \quad (1)$$

If the inner cylinder is solid and S represents the rate of internal heat generation per unit volume within the cylinder, then Q' and S are related by

$$Q'=\pi R_i^2 S \quad (2)$$

The average heat flux $\bar{q}$ at the surface of the inner cylinder is given by

$$\bar{q}=Q'/(2\pi R_i)=SR_i/2 \quad (3)$$

The problem is analyzed for uniform fluid properties. The variation of the density ρ is, according to the Boussinesq approximation, included only in the calculation of the buoyancy terms. The pressure gradient and body force terms in the momentum equation for the radial direction are

$$-\partial p/\partial r-\rho g \sin\theta \quad (4)$$

where θ is measured as shown in Fig. 1. The density is given by

$$\rho=\rho_{w0}[1-\beta(T-T_{w0})] \quad (5)$$

where T_{w0} is the wall temperature at a reference location in the thermally developed region and ρ_{w0} is the fluid density at that temperature. Since, as given by equation (1), dT_w/dz equals the constant a, the density variation can be written as

$$\rho=\rho_{w0}[1-\beta az-\beta(T-T_w)] \quad (6)$$

where z is measured from the reference location and T_w is the local wall temperature.

Now it is convenient to define a modified pressure p^* by

$$p^*=p+\rho_{w0}(1-\beta az)gr\sin\theta \quad (7)$$

so that the equation (4) can be written as

$$-\partial p^*/\partial r+\rho_{w0}g\beta(T-T_w)\sin\theta \quad (8)$$

The corresponding terms in the θ direction can be similarly written as

$$-(1/r)(\partial p^*/\partial\theta)+\rho_{w0}g\beta(T-T_w)\cos\theta \quad (9)$$

If $\overline{p^*}$ denotes the mean value of p^* over a cross section, then it can be shown from equation (7) that $\overline{p^*}$ equals $\bar{p}$, which is the mean cross-sectional pressure. Further, $(p^*-\bar{p})$ represents the local pressure variation over a cross section and it depends, for the fully developed flow, only on r and θ and not on z. Therefore,

$$\partial(p^*-\bar{p})/\partial z=0 \quad (10)$$

This, along with equation (7), enables the calculation of the pressure gradient $\partial p/\partial z$ appearing in the axial momentum equation. The result is

$$\partial p/\partial z=d\bar{p}/dz+\rho_{w0}\beta agr\sin\theta \quad (11)$$

At this stage, the subscript $w0$ in ρ_{w0} will be dropped to conform to the constant density assumption.

Appropriate dimensionless variables for this problem can be defined as

$$\eta=r/d, \quad U=ud/\alpha, \quad V=vd/\alpha \quad (12)$$

$$W=w/[(-d\bar{p}/dz)(d^2/\mu)], \quad P=(p^*/\rho)/(\nu\alpha/d^2) \quad (13)$$

$$\phi=(T-T_w)/(\bar{q}d/k), \quad \mathrm{Gr}=g\beta\bar{q}d^4/(\nu^2 k), \quad \mathrm{Pr}=\nu/\alpha \quad (14)$$

$$\mathrm{Ra}=\mathrm{Gr}\,\mathrm{Pr}, \quad \mathrm{Re}=\bar{w}d/\nu \quad (15)$$

where d is the hydraulic diameter given by

$$d=2(R_o-R_i) \quad (16)$$

The geometry is characterized by the radius ratio RR of the annulus defined as

$$RR=R_o/R_i \quad (17)$$

In terms of these dimensionless quantities, the axial pressure gradient $\partial p/\partial z$ can be written as

$$\frac{\partial p}{\partial z}=\frac{d\bar{p}}{dz}\left[1-\frac{4\bar{W}}{(RR+1)}\frac{\mathrm{Ra}}{(\mathrm{Re}\,\mathrm{Pr})^2}\eta\sin\theta\right] \quad (18)$$

where $\bar{W}$ denotes the cross-sectional average of W. It seems that most published analyses of thermally developed mixed convection [1-4, 6, 8-11] neglect the second term in the square brackets and thus assume that $\partial p/\partial z$ equals $d\bar{p}/dz$. This is

Nomenclature

a = axial temperature gradient = $\partial T/\partial z$, equation (1)
c_p = specific heat at constant pressure
d = hydraulic diameter, equation (16)
f = friction factor, equation (30)
Gr = Grashof number = $g\beta\bar{q}d^4/(\nu^2 k)$
g = acceleration due to gravity
k = thermal conductivity
Nu = local Nusselt number, equation (26)
$\overline{\mathrm{Nu}}$ = average Nusselt number, equation (27)
$\overline{\mathrm{Nu}}_0$ = forced convection value of $\overline{\mathrm{Nu}}$
P = dimensionless pressure, equation (13)
Pr = Prandtl number
p = pressure
$\bar{p}$ = mean cross-sectional pressure
p^* = modified pressure, equation (7)
Q' = rate of heat transfer per unit length
q = local rate of heat transfer per unit area
$\bar{q}$ = average rate of heat transfer per unit area
Ra = Rayleigh number = Pr Gr
Re = Reynolds number = $\rho\bar{w}d/\mu$
R_i = radius of inner cylinder, Fig. 1
R_o = radius of outer cylinder, Fig. 1
RR = radius ratio = R_o/R_i
r = radial coordinate
S = rate of internal heat generation per unit volume
T = temperature
T_b = bulk temperature
T_w = wall temperature
T_{w0} = wall temperature at a reference location
U, V, W = dimensionless velocities, equations (12) and (13)
u, v, w = velocity components in θ, r, z coordinates
$\bar{W}$ = mean value of W
$\bar{w}$ = mean axial velocity
z = axial coordinate
α = thermal diffusivity
β = thermal expansion coefficient
η = dimensionless radial coordinate = r/d
θ = angular coordinate
μ = viscosity
ν = kinematic viscosity
ρ = density
ϕ = dimensionless temperature = $(T-T_w)/(\bar{q}d/k)$
ψ = dimensionless stream function, equation (25)
ψ_m = maximum value of ψ

consistent with the usual treatment of duct flows, in which the axial velocity is taken to be influenced by only the mean pressure gradient $d\bar{p}/dp$. Only the perturbation analysis in [5, 7] has attempted to include the effect of the nonuniform pressure gradient over the cross section. The extra term is mentioned in [9] but is subsequently omitted.

The multiplier of $\mathrm{Ra}/(\mathrm{Re\ Pr})^2$ in the extra term in equation (18) has a magnitude of about 0.03 for forced convection and is expected to be even lower for mixed convection. Thus, the extra term is negligible for values of $\mathrm{Ra}/(\mathrm{Re\ Pr})^2$ less than unity. This condition is easily satisfied for large Prandtl numbers. For moderate Prandtl numbers, neglect of the extra term is justified only for small values of $\mathrm{Ra}/\mathrm{Re}^2$.

The present analysis is also based on the use of $d\bar{p}/dz$ in the place of $\partial p/\partial z$. From the foregoing discussion, it can be concluded that the results presented here are applicable when $\mathrm{Ra}/(\mathrm{Re\ Pr})^2$ is less than unity.

The equations expressing the conservation of the mass, momentum and energy can now be written as

$$\partial U/\partial\theta + \partial(\eta V)/\partial\eta = 0 \tag{19}$$

$$\frac{1}{\mathrm{Pr}}\left[\frac{U}{\eta}\frac{\partial U}{\partial\theta} + V\frac{\partial U}{\partial\eta} + \frac{UV}{\eta}\right] = -\frac{1}{\eta}\frac{\partial P}{\partial\theta} + \nabla^2 U + \frac{2}{\eta^2}\frac{\partial V}{\partial\theta} - \frac{U}{\eta^2} + \mathrm{Ra}\,\phi\cos\theta \tag{20}$$

$$\frac{1}{\mathrm{Pr}}\left[\frac{U}{\eta}\frac{\partial V}{\partial\theta} + V\frac{\partial V}{\partial\eta} - \frac{U^2}{\eta}\right] = -\frac{\partial P}{\partial\eta} + \nabla^2 V - \frac{2}{\eta^2}\frac{\partial U}{\partial\theta} - \frac{V}{\eta^2} + \mathrm{Ra}\,\phi\sin\phi \tag{21}$$

$$\frac{1}{\mathrm{Pr}}\left[\frac{U}{\eta}\frac{\partial W}{\partial\theta} + V\frac{\partial W}{\partial\eta}\right] = \nabla^2 W + 1 \tag{22}$$

$$\frac{U}{\eta}\frac{\partial\phi}{\partial\theta} + V\frac{\partial\phi}{\partial\eta} + \frac{W}{\bar{W}}\frac{4}{(RR+1)} = \nabla^2\phi \tag{23}$$

where ∇^2 is the Laplacian operator defined by

$$\nabla^2 = \frac{1}{\eta^2}\frac{\partial^2}{\partial\theta^2} + \frac{1}{\eta}\frac{\partial}{\partial\eta}\left(\eta\frac{\partial}{\partial\eta}\right) \tag{24}$$

The equations (19)–(23) include three independent parameters: Ra, Pr, and RR.

Because of the symmetry about the vertical center line shown in Fig. 1, it is sufficient to solve the equations over only the right half of the annulus. The boundary conditions for this domain are given by

inner cylinder: $U = V = W = \phi = 0$

outer cylinder: $U = V = W = 0, \quad \partial\phi/\partial\eta = 0$

symmetry line: $U = 0, \quad \partial V/\partial\theta = \partial W/\partial\theta = \partial\phi/\partial\theta = 0$

The set of equations (19)–(23) was solved numerically by the method described in [30]. The coupling between the momentum and continuity equations was handled by the SIMPLER algorithm. A 29 × 22 grid in θ–r coordinates was used for the calculation domain forming the right half of the annulus. In the θ direction, a uniform grid spacing was chosen. On the other hand, the r direction spacing was nonuniform, the grid lines being more close packed near the cylinder walls. Also, in general, the grid spacing was made finer near the inner cylinder than near the outer one. Further, as the Rayleigh number increased, the grid was made more nonuniform to properly resolve the correspondingly thin boundary layers. Exploratory calculations on coarser grids were employed to provide guidance for the design of the appropriate nonuniform grid.

Initial computational experiments on finer grids and on grids of different nonuniformity indicated that the present results at high Rayleigh numbers are accurate to at least 0.5 percent for the Nusselt number and 1 percent for the friction factor. The accuracy is, of course, much better at low Rayleigh numbers.

Results and Discussion

The numerical solutions were obtained for four values of the radius ratio: RR = 1.5, 2, 3, and 5. The Rayleigh number was varied from 10^4 to 10^7. Although a weak secondary flow is formed for any nonzero Rayleigh number, the distributions of the axial velocity and the temperature for $\mathrm{Ra} \le 10^4$ turn out to be virtually indistinguishable from the pure forced convection situation. Four values of the Prandtl number were used: Pr = 0.7 (for air), Pr = 5 and 10 (for water), and Pr = ∞.

From the wealth of information generated by the numerical solution, only a selection can be presented here in the available space. The results to be presented include, in addition to the overall results useful for design, some local details of the flow and temperature fields, which give insight into the interacting physical processes.

Isotherms and Streamlines. Figures 2–5 display the temperature distribution and the secondary flow pattern in the cross section of the duct. Because of the symmetry about the vertical diameter, the isotherms are plotted in the left half and the streamlines in the right half. The value of ψ_m listed below each pattern is a measure of the strength of the secondary flow; ψ_m is the maximum value of the dimensionless stream function ψ, which may be calculated from

$$\psi = \int_{\eta_i}^{\eta} U\,d\eta \tag{25}$$

where η_i is the value of η at the inner cylinder.

Figure 2 shows, for Pr = 0.7, the effect of the Rayleigh number on the temperature and streamline patterns. For Ra = 10^5, the secondary flow is weak and forms a symmetrical eddy rotating in the clockwise direction. The isotherms are nearly circular and thus little affected by the secondary currents. As the Rayleigh number increases, the secondary motion becomes stronger as evidenced by the higher values of ψ_m. At Ra = 10^6, a small second eddy is seen to have formed below the main eddy, which is pushed upward and rendered unsymmetrical. The isotherms tend to become horizontal, especially in the regions away from and under the inner cylinder, approximating the temperature distribution in a stably stratified fluid. The isotherm pattern for Ra = 10^7 shows a rather clear distinction between the thin thermal boundary layer near the heated inner cylinder and the stably stratified region elsewhere.

Figure 3 is similar to Fig. 2 but pertains to Pr = 5. In both figures, the same isotherms and streamlines are presented for the same Rayleigh number. It is interesting to note that the patterns in Fig. 3 are almost identical to those for the same Rayleigh number in Fig. 2. As judged from the thickness of the thermal boundary layers, the heat transfer coefficient is larger at the higher Prandtl number for the same Rayleigh number.

The similarity between the behavior for different Prandtl numbers is shown again in Fig. 4 for a larger radius ratio. It can, in general, be concluded that, when the Rayleigh number is used as the buoyancy parameter, the influence of the Prandtl number is quite weak. On the other hand, the use of Grashof number as the buoyancy parameter would have shown a rather strong effect of the Prandtl number, as seen for example in [11].

Figure 5 is intended to show the influence of the radius ratio. The evidence in this figure, supplemented by the ap-

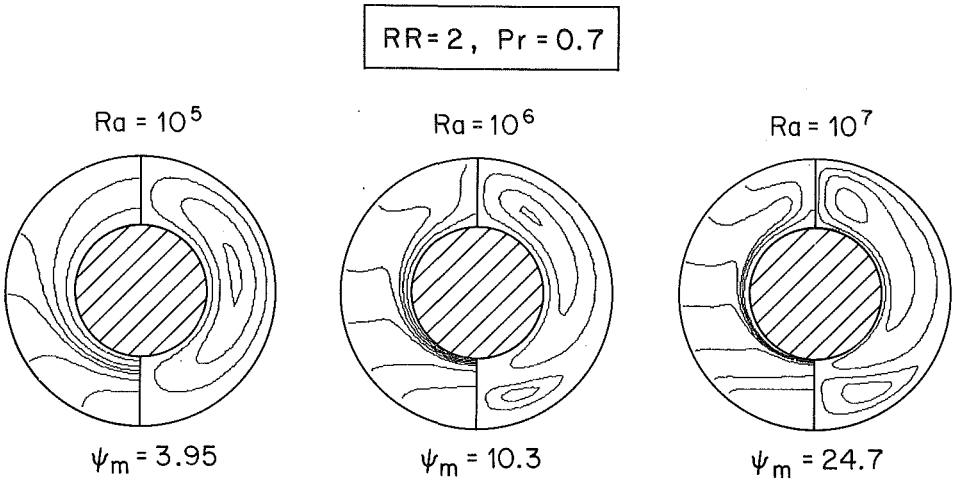

Fig. 2 Isotherms and streamlines for $RR = 2$, Pr = 0.7 at different Rayleigh numbers

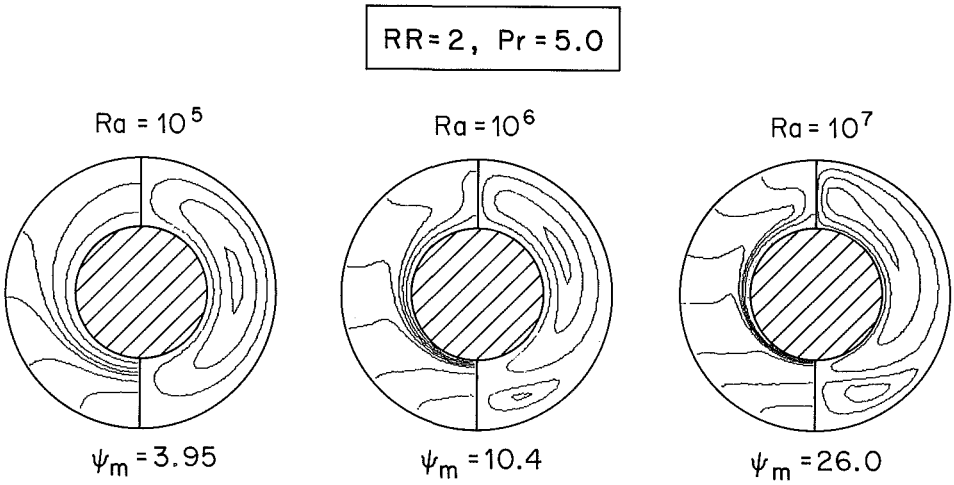

Fig. 3 Isotherms and streamlines for $RR = 2$, Pr = 5 at different Rayleigh numbers

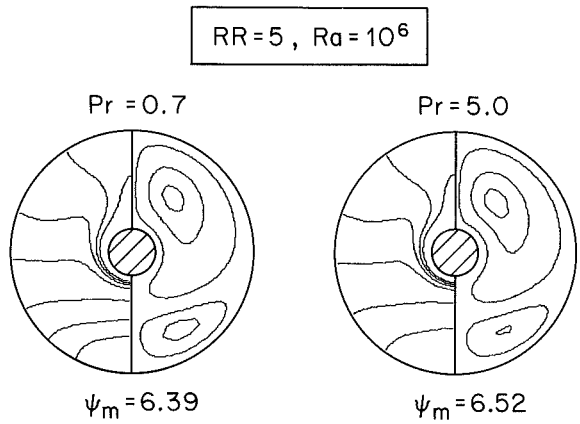

Fig. 4 Effect of the Prandtl number on the isotherms and streamlines for $RR = 5$, $Ra = 10^6$

propriate plots in Figs. 3 and 4, indicates that the radius ratio does not alter the qualitative features of the isotherm and streamline patterns. The strength of the secondary flow is seen to decrease with the increase of the radius ratio. When RR is large, the heated surface of the inner cylinder, near which the buoyancy force is the greatest, forms a relatively small portion of the boundary of the calculation domain, thus reducing the driving force for the secondary motion.

For all the radius ratio and the Prandtl numbers investigated, the transition from the single-eddy pattern to the double-eddy pattern appears to occur at Ra between 10^5 and 10^6.

Axial Velocity. It can be concluded from equation (22) that, for large Prandtl numbers, the distribution of the axial velocity remains virtually unaffected by the secondary flow. In the present computations, any significant influence on velocity was obtained only for Pr = 0.7.

Figure 6 presents the influence of the Rayleigh number on the axial velocity profile; it shows the variation of the axial velocity with the radial position at three different angles, i.e., top, center, and bottom, for Pr = 0.7 and $RR = 2$. The axial velocity profile for pure forced convection (Ra = 0) is also presented as a reference. At Ra = 10^5, the axial velocity profile is very similar to the forced convection curve. As the Rayleigh number increases, the maximum velocity at the top (θ = 90 deg) reduces substantially, while the opposite occurs at the bottom (θ = −90 deg). The distortion of the axial flow is more pronounced near the inner walls, resulting in a higher shear stress there.

Local Heat Transfer Coefficient. Since the velocity and

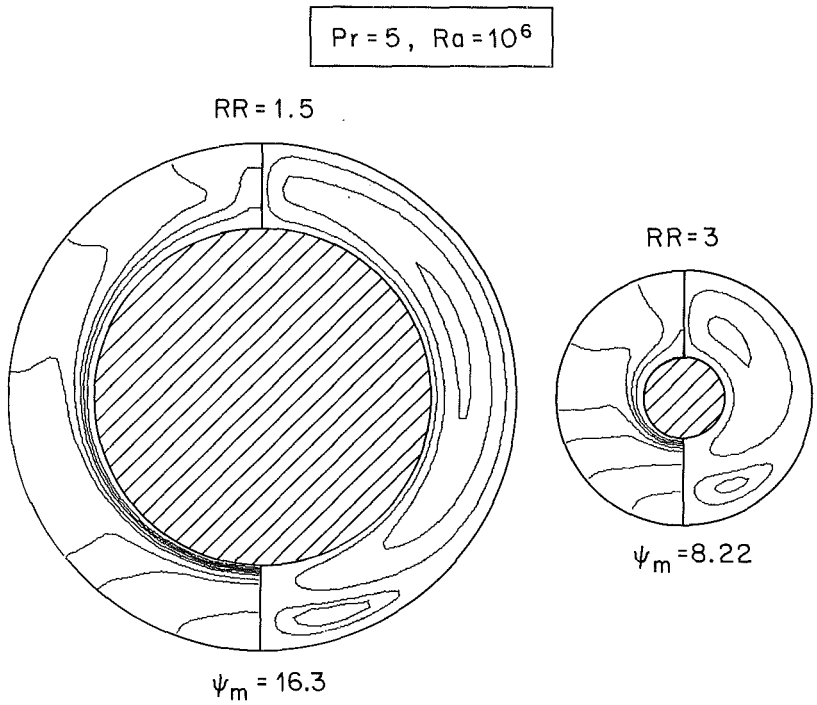

Fig. 5 Effect of the radius ratio on the isotherms and streamlines for Pr = 5, Ra = 10^6

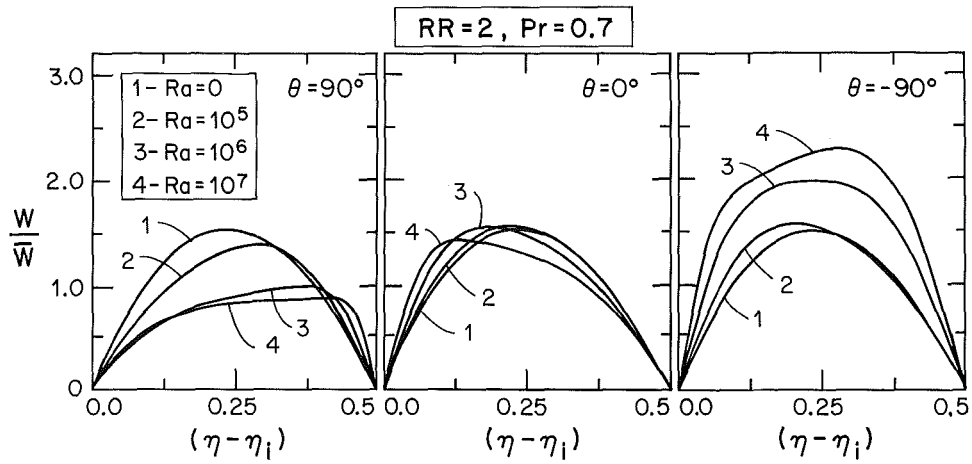

Fig. 6 Effect of the Rayleigh number on the axial velocity profile for RR = 2, Pr = 0.7

temperature patterns encountered in mixed convection are far from being axisymmetrical, it follows that the local heat transfer coefficient along the circumference of the inner cylinder will be highly nonuniform. Here the local and average Nusselt numbers are defined as

$$\mathrm{Nu} = qd/[k(T_w - T_b)] \tag{26}$$

$$\overline{\mathrm{Nu}} = \bar{q}d/[k(T_w - T_b)] \tag{27}$$

where q is the local heat flux at the inner cylinder and T_b is the bulk temperature of the fluid. T_b is calculated from

$$T_b = \iint Twrdrd\theta / \iint wrdrd\theta \tag{28}$$

where the integrals are to be evaluated over the duct cross section. Equation (27) can be rewritten by the use of equation (14) to yield

$$\overline{\mathrm{Nu}} = -1/\phi_b \tag{29}$$

where ϕ_b is the dimensionless form of T_b.

Figures 7 and 8 show the variation of $\mathrm{Nu}/\overline{\mathrm{Nu}}$ with the circumferential position around the inner cylinder. In general, since colder fluid tends to collect below the inner cylinder and hotter fluid above it, large temperature gradients and higher local Nusselt numbers are to be expected at the bottom. This is clearly seen for the case of Ra = 10^6 in Figs. 7 and 8. On the other hand, the case of Ra = 10^4 shown in Fig. 7 displays little nonuniformity as the effect of buoyancy is weak. Also, the influence of the Prandtl number on the variation of $\mathrm{Nu}/\overline{\mathrm{Nu}}$ does not appear very strong. The influence of the radius ratio is shown in Fig. 8 for Pr = 5. Whereas no influence of RR is detectable at Ra = 10^4, some spread in the curves is seen at Ra = 10^6, the nonuniformity being more pronounced at smaller radius ratios. This behavior is attributed to the stronger secondary flows associated with the smaller values of RR.

Overall Heat Transfer Coefficient. The main focus of this paper is to study the enhancement of the overall heat transfer coefficient caused by the buoyancy forces. It is, therefore, useful to plot the ratio $\overline{\mathrm{Nu}}/\overline{\mathrm{Nu}}_0$, where $\overline{\mathrm{Nu}}_0$ represents the

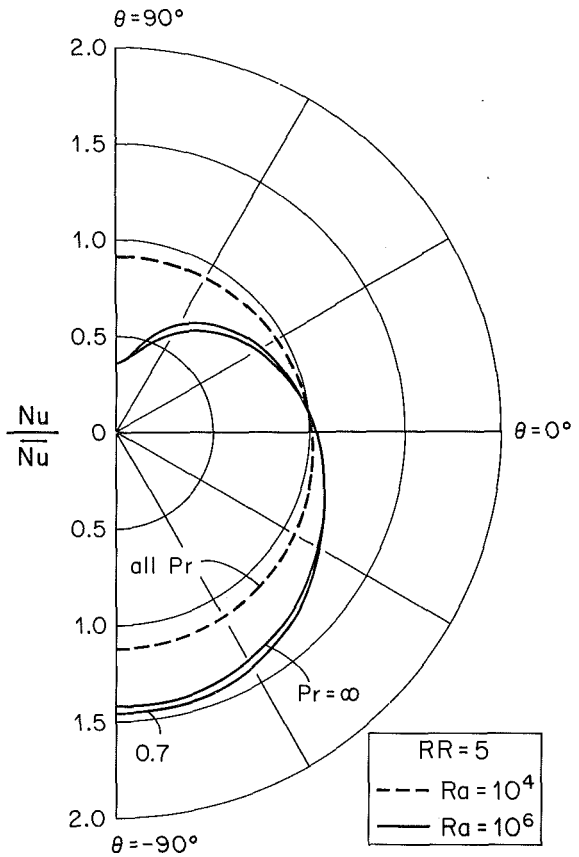

Fig. 7 Circumferential variation of the local Nusselt number for *RR* = 5: the influence of the Prandtl number

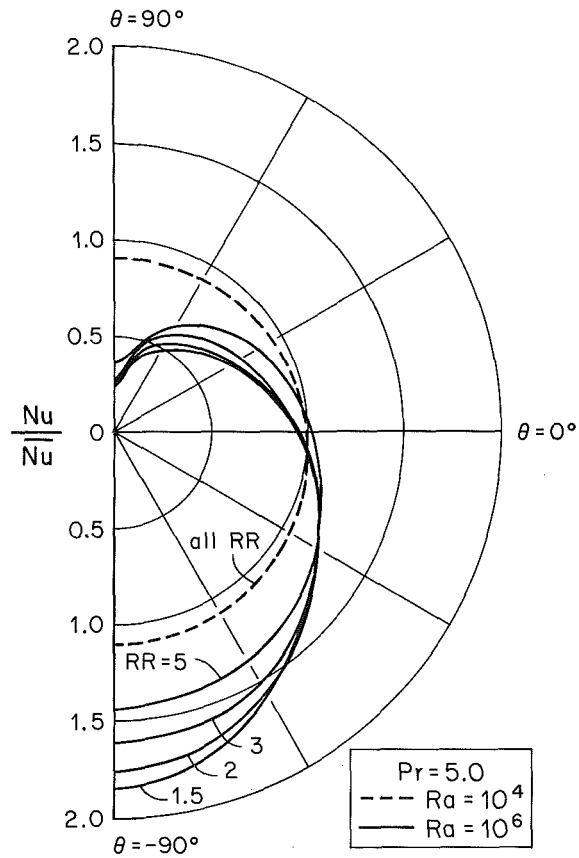

Fig. 8 Circumferential variation of the local Nusselt number for Pr = 5: the influence of the radius ratio

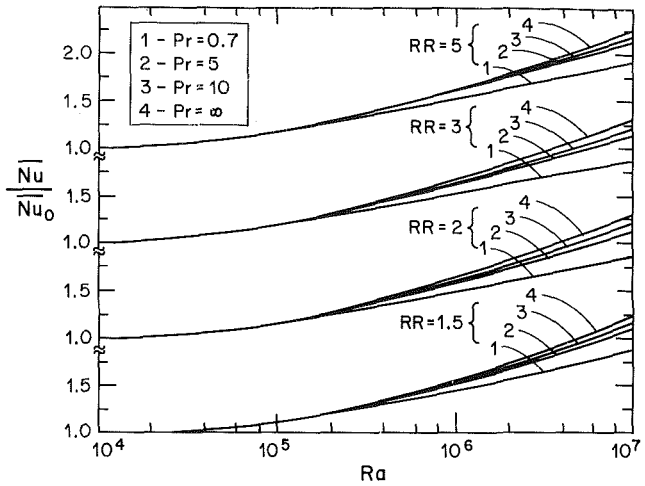

Fig. 9 Overall Nusselt number

Table 1 Values of $\overline{Nu}_0$ and $(f\,Re)_0$

RR	1.5	2.0	3.0	5.0
$\overline{Nu}_0$	5.78	6.18	6.98	8.50
$(f\,Re)_0$	95.7	95.3	94.2	92.4

pure forced convection value of $\overline{Nu}$. Further, $\overline{Nu}_0$ is independent of Pr and depends only on *RR*. The exact analytical values of $\overline{Nu}_0$ are available in [29] and are listed in Table 1. Incidentally, the results of the present numerical solutions at very small Ra were found to be in excellent agreement with the values in Table 1.

The variation of $\overline{Nu}/\overline{Nu}_0$ with Ra is shown in Fig. 9 for various Prandtl numbers and radius ratios. The graph is divided in four parts, each *RR* having different origins. The influence of buoyancy is to increase $\overline{Nu}$; but this becomes noticeable only after a threshold value of Ra equal to 10^4 is exceeded. Further, the higher the Prandtl number, the higher the value of $\overline{Nu}$. The radius ratio does not seem to have much effect on $\overline{Nu}/\overline{Nu}_0$, the curves for all *RR* being very similar. This behavior is consistent with the earlier observation that the *patterns* of isotherms and streamlines depend little on the radius ratio.

Friction Factor. The increased heat transfer in mixed convection does not come without a penalty. The pressure gradient required for a given mass flow rate through the duct also increases in magnitude. A common measure of the pressure gradient is the friction factor defined as

$$f = (-d\bar{p}/dz)\,d/[(1/2)\rho\bar{w}^2] \tag{30}$$

Further, it can be shown that

$$f\,\mathrm{Re} = 2/\bar{W} \tag{31}$$

where $\bar{W}$ is the cross-sectional average of the dimensionless velocity W and Re is the duct Reynolds number.

In the absence of buoyancy, the product f Re is a constant, which depends only on the geometry. This value is here denoted by $(f\,\mathrm{Re})_0$. The exact analytical values of $(f\,\mathrm{Re})_0$ are available in [29] and are listed here in Table 1 for the different values of *RR*.

Figure 10 shows the ratio $(f\,\mathrm{Re})/(f\,\mathrm{Re})_0$ plotted as a function of Ra for different values of Pr and *RR*. In general, the increase in f Re is substantially smaller than the corresponding increase in $\overline{Nu}$. This is because Nu reflects the changes in the temperature field caused by both the secondary flow and the associated distortion of the axial flow. The quantity f Re, on the other hand, is simply a measure of the

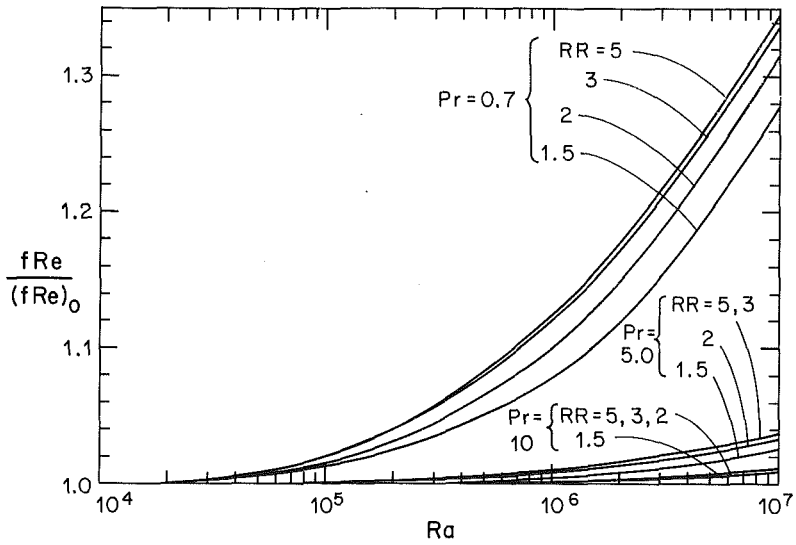

Fig. 10 Friction factor

influence of the secondary flow on the axial velocity distribution. An examination of equation (22) indicates that this influence of the secondary flow diminishes with the increase of the Prandtl number. Thus, the effect of buoyancy on fRe is seen to be quite small for Pr = 5 and 10. Only for the case of Pr = 0.7 does the ratio $(f\text{Re})/(f\text{Re})_0$ noticeably depart from unity.

The ratio $(f\ \text{Re})/(f\ \text{Re})_0$ increases with the radius ratio for given values of Ra and Pr. This is somewhat surprising in view of the fact that the secondary flow is actually stronger for the smaller values of *RR*. What happens is that when *RR* is small, the annular duct resembles a long thin channel in which the axial flow is predominately controlled by the shear stress at the duct walls; even a strong secondary flow is then unable to appreciably alter the axial velocity profiles.

Concluding Remarks

The present numerical study shows the significant effect that the buoyancy forces exert on heat transfer in an annulus. In each half of the annulus divided by the vertical center line, the secondary flow generated by buoyancy has a single-eddy pattern for low Rayleigh numbers and a double-eddy pattern for higher values. At a given Rayleigh number, the effect of buoyancy on the heat transfer coefficient is stronger at higher Prandtl numbers. The buoyancy forces tend to create thin thermal boundary layers on the heated inner cylinder and a stable stratification of the fluid elsewhere. The local heat transfer coefficients on the inner cylinder become highly nonuniform at high Rayleigh numbers, the lowest value being at the top of the cylinder.

Acknowledgments

This research was supported in part by the National Science Foundation. Ms. Nieckele received a scholarship from Brazil from the National Council for Scientific and Technological Development (CNPq).

References

1 Cheng, K. C., and Hong, S. W., "Combined Free and Forced Laminar Convection in Inclined Tubes," *Applied Scientific Research*, Vol. 27, 1972, pp. 19–38.

2 Hwang, G. J., and Cheng, K. C., "Boundary Vorticity Method for Convective Heat Transfer With Secondary Flow—Application to the Combined Free and Forced Laminar Convection in Horizontal Tubes," *Heat Transfer*, Vol. 4, 1970, Paper No. NC 3.5, Elsevier, Amsterdam, 1970.

3 Newell, P. H., and Bergles, A. E., "Analysis of Combined Free and Forced Convection for Fully Developed Laminar Flow in Horizontal Tubes," ASME JOURNAL OF HEAT TRANSFER, Vol. 92, 1970, pp. 83–93.

4 Faris, G. N., and Viskanta, R., "An Analysis of Laminar Combined Forced and Free Convection Heat Transfer in a Horizontal Tube," *International Journal of Heat and Mass Transfer*, Vol. 12, 1969, pp. 1295–1309.

5 Iqbal, M., and Stachiewicz, J. W., "Variable Density Effects in Combined Free and Forced Convection in Inclined Tubes," *International Journal of Heat and Mass Transfer*, Vol. 10, 1967, pp. 1625–1629.

6 Iqbal, M., and Stachiewicz, J. W., "Influence of Tube Orientation on Combined Free and Forced Laminar Convection Heat Transfer," ASME JOURNAL OF HEAT TRANSFER, Vol. 88, 1966, pp. 109–116.

7 Del Casal, E., and Gill, W. N., "A Note on Natural Convection Effects in Fully Developed Horizontal Tube Flow," *AIChE Journal*, Vol. 8, 1962, pp. 570–574.

8 Morton, B. R., "Laminar Convection in Uniformly Heated Horizontal Pipes at Low Rayleigh Numbers," *Quarterly Journal of Mechanics and Applied Mathematics*, Vol. 12, 1959, pp. 410–420.

9 Siegwarth, D. P., Mikesell, R. D., Readal, T. C., and Hanratty, T. J., "Effect of Secondary Flow on the Temperature Field and Primary Flow in a Heated Horizontal Tube," *International Journal of Heat and Mass Transfer*, Vol. 12, 1969, pp. 1535–1552.

10 Mori, Y., and Futagami, K., "Forced Convective Heat Transfer in Uniformly Heated Horizontal Tubes," *International Journal of Heat and Mass Transfer*, Vol. 10, 1967, pp. 1801–1813.

11 Patankar, S. V., Ramadhyani, S., and Sparrow, E. M., "Effect of Circumferentially Nonuniform Heating on Laminar Combined Convection in a Horizontal Tube," ASME JOURNAL OF HEAT TRANSFER, Vol. 100, 1978, pp. 63–70.

12 Charrier-Mojtabi, M. C., Mojtabi, A., and Caltagirone, J. P., "Numerical Solution of a Flow Due to Natural Convection in Horizontal Cylindrical Annulus," ASME JOURNAL OF HEAT TRANSFER, Vol. 101, 1979, pp. 171–173.

13 Kuehn, T. H., and Goldstein, R. J., "A Parametric Study of Prandtl Number and Diameter Ratio Effects on Natural Convection Heat Transfer in Horizontal Cylindrical Annuli," ASME JOURNAL OF HEAT TRANSFER, Vol. 102, 1980, pp. 768–770.

14 Walton, I. C., "The Stability of Free Convection in a Horizontal Cylindrical Annulus," *Quarterly Journal of Mechanics and Applied Mathematics*, Vol. 33, 1980, pp. 125–139.

15 Seki, N., Fukusaka, S., and Nakaoka, M., "An Analysis of Free Convective Heat Transfer Between Two Horizontal Concentric Cylinders Shows the Effect of a Density Inversion," ASME JOURNAL OF HEAT TRANSFER, Vol. 98, 1976, pp. 670–692.

16 Mack, L. R., and Bishop, E. H., "Natural Convection Between Horizontal Concentric Cylinder for Low Rayleigh Numbers," *Quarterly Journal of Mechanics and Applied Mathematics*, Vol. 21, 1968, pp. 223–241.

17 Custer, J. R., and Shaughnessy, E. J., "Thermoconvective Motion of Low Prandtl Number Fluids Within a Horizontal Cylindrical Annulus," ASME JOURNAL OF HEAT TRANSFER, Vol. 99, 1977, pp. 596–602.

18 Hung Nguyen, T., Vasseur, P., and Robillard, L., "Natural Convection of Cold Water in Concentric Annular Spaces: Effect of the Maximum Density," *Proceedings of the Seventh International Heat Transfer Conference*, Vol. 2, Munich, Germany, 1982, pp. 251–256.

19 Projahn, U., Rieger, H., and Beer, H., "Numerical Analysis of Laminar Natural Convection Between Concentric and Eccentric Cylinders," *Numerical Heat Transfer*, Vol. 4, 1981, pp. 131–146.

20 Cho, C. H., Chang, K. S., and Park, K. H., "Numerical Simulation of Natural Convection in Concentric and Eccentric Horizontal Cylindrical Annuli," ASME JOURNAL OF HEAT TRANSFER, Vol. 104, 1982, pp. 624–630.

21 Kuehn, T. H., and Goldstein, R. J., "An Experimental and Theoretical Study of Natural Convection in the Annulus Between Horizontal Concentric Cylinders," *Journal of Fluid Mechanics*, Vol. 74, 1976, pp. 695–719.

22 Seki, N., Fukusaka, S., and Nakaoka, M., "Experimental Study on Natural Convection Heat Transfer With Density Inversion of Water Between Two Horizontal Concentric Cylinders," ASME JOURNAL OF HEAT TRANSFER, Vol. 97, 1975, pp. 556–561.

23 Powe, R. E., Carley, C. T., and Bishop, E. H., "Free Convective Flow Patterns in Cylindrical Annuli," ASME JOURNAL OF HEAT TRANSFER, Vol. 91, 1969, pp. 310–314.

24 Kuehn, T. H., and Goldstein, R. J., "An Experimental Study of Natural Convection Heat Transfer in Concentric and Eccentric Horizontal Annuli," ASME JOURNAL OF HEAT TRANSFER, Vol. 100, 1978, pp. 635–640.

25 Huetz, J., and Petit, J. P., "Natural and Mixed Convection in Concentric Annular Spaces—Experimental and Theoretical Results for Liquid Metals," *Proceedings of the Fifth International Heat Transfer Conference*, Vol. 3, Tokyo, Japan, 1974, pp. 169–172.

26 van de Sande, E., and Hamer, B. J. G., "Steady and Transient Natural Convection in Enclosures Between Horizontal Circular Cylinders (Constant Heat Flux)," *International Journal of Heat and Mass Transfer*, Vol. 22, 1979, pp. 361–370.

27 Hung Nguyen, T., Vasseur, P., Robillard, L., and Chandra Shekar, B., "Combined Free and Forced Convection of Water Between Horizontal Concentric Cylinders," ASME JOURNAL OF HEAT TRANSFER, Vol. 105, 1983, pp. 498–504.

28 Mojtabi, A., and Caltagirone, J. P., "Analyse du transfert de chaleur en convection mixte laminaire entre deux cylindres coaxiaux horizontaux," *International Journal of Heat and Mass Transfer*, Vol. 23, 1980, pp. 1369–1375.

29 Shah, R. K., and London, A. L., *Laminar Flow Forced Convection in Ducts*, Academic Press, New York, 1978.

30 Patankar, S. V., *Numerical Heat Transfer and Fluid Flow*, McGraw-Hill, New York, 1980.

B. R. Hollworth
Associate Professor.
Mechanical and Industrial Engineering Department,
Clarkson University,
Potsdam, NY 13676
Mem. ASME

L. R. Gero
Research Assistant.
Mechanical Engineering Department,
Rensselaer Poytechnic Institute,
Troy, NY 12181
Assoc. Mem. ASME

Entrainment Effects on Impingement Heat Transfer: Part II—Local Heat Transfer Measurements

Convective heat transfer was measured for a heated axisymmetric air jet impinging on a flat surface. It was found that the local heat transfer coefficient does not depend explicitly upon the temperature mismatch between the jet fluid and the ambient fluid if the convection coefficient is defined in terms of the difference between the local recovery temperature and target surface temperature. In fact, profiles of local heat transfer coefficients defined in this manner were found to be identical to those measured for isothermal impinging jets.

Introduction

Systems of impinging fluid jets are frequently used to produce high rates of convective heat or mass transfer. For example, heat fluxes approaching 500 W/cm^2 are obtained when arrays of small high-velocity air jets are used to cool hot section components in modern gas turbine aircraft engines. For such configurations, heat transfer rates depend upon coolant flow, coolant properties, and system geometry. A number of experiments have been conducted to generate heat transfer correlations for impingement systems which involve these parameters, and Martin [1] has recently reviewed much of this work.

In most impingement cooling schemes, the fluid jets are discharged (see Fig. 1) into a fairly confined space between the orifice plate from which the jets originate and the target plate at which they are aimed. In this space also circulates the spent fluid whose (mean) temperature is between the initial jet temperature and that of the target surface. The distribution of spent fluid temperature and the pattern of flow in this region depend upon the means by which spent fluid is vented. The entrainment of such fluid into the jets reduces the effective fluid-to-surface temperature difference and causes a corresponding reduction in heat transfer at the target surface.

Gas turbine cooling is an especially important application. The design or specification of a turbine cooling system requires accurate and comprehensive heat transfer data for both the hotside and coolant side surfaces of the component in question; and emphasis appears currently to be upon better understanding the heat transfer associated with external (i.e., hotside) flows. The fact remains, however, that an engine performance penalty results directly when air is diverted for cooling purposes. Entrainment tends to degrade the performance of impingement systems, so that the coolant flow required to contend with a fixed heat load is increased. There is, then, an apparent need to understand this process (as it relates to impingement heat transfer) so that its effect can be minimized in future designs.

To date, relatively little work has been done to quantify this effect. Schauer and Eustis [2] and Striegl and Diller [3, 4] proposed analytical models to predict heat transfer from impinging turbulent slot jets, with temperature different from that of the surrounding fluid, and generated supporting experimental data. Vlachapoulos and Tomich [5] calculated heat transfer for a single heated air jet impinging on a flat surface and compared their prediction to test data; however, the thermal boundary conditions for the experiment were unspecified. Finally, Florschuetz et al. [6] measured heat transfer distributions for an array of jets with an initial crossflow whose temperature differed from that of the jets.

The work reported here is an experimental study whose objective is to isolate and measure the effect of entrainment upon impingement heat transfer. The case considered is that of a single heated air jet, submerged in quiescent air (at room temperature and prevailing barometric pressure), and impinging normal to an isothermal flat surface. Jet air is heated so that its initial total temperature T_p is above the ambient air temperature T_a; measurements are made also for the isothermal jet ($T_p = T_a$) to serve as a reference case. The target plate is cooled so that its surface temperature T_s is below ambient temperature. The experiment was conducted in this manner because it is generally more convenient to heat the jet fluid than the entrained fluid. Thus, it represents the inverse of a conventional impingement cooling situation.

Independent test variables included jet orifice diameter d, jet Reynolds number Re, temperature mismatch $\Delta T (\equiv T_p - T_a)$ between jets and entrained fluid, and standoff $\bar{Z}$ between orifice exit plane and target surface. Table 1 sum-

Table 1 Test program

ΔT(°C)	d(mm)	10				2.5	
	$\bar{Z}$	1	5	10	15	10	15
	Re x 10^{-3}						
0	5	X	X	X	X	X	X
	10		X				
	20	X	X	X	X	X	X
	40	X	X				
	60	X	X	X	X		
30	5	X	X	X	X		
	20	X	X	X	X	X	X
	40	X	X				
	60	X	X	X	X		
60	20	X	X	X	X		
	60	X	X	X			

Notes: X indicates test run, $\Delta T \equiv T_p - T_a$

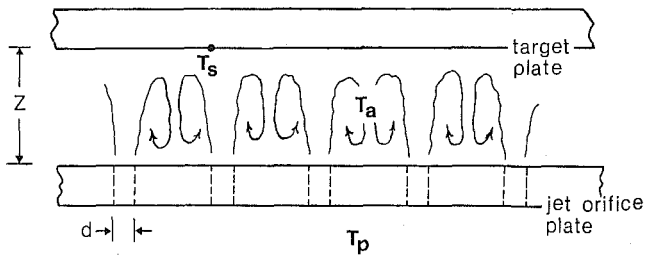

Fig. 1 Multiple jet cooling configuration

Contributed by the Heat Transfer Division for publication in the JOURNAL OF HEAT TRANSFER. Manuscript received by the Heat Transfer Division May 21, 1984.

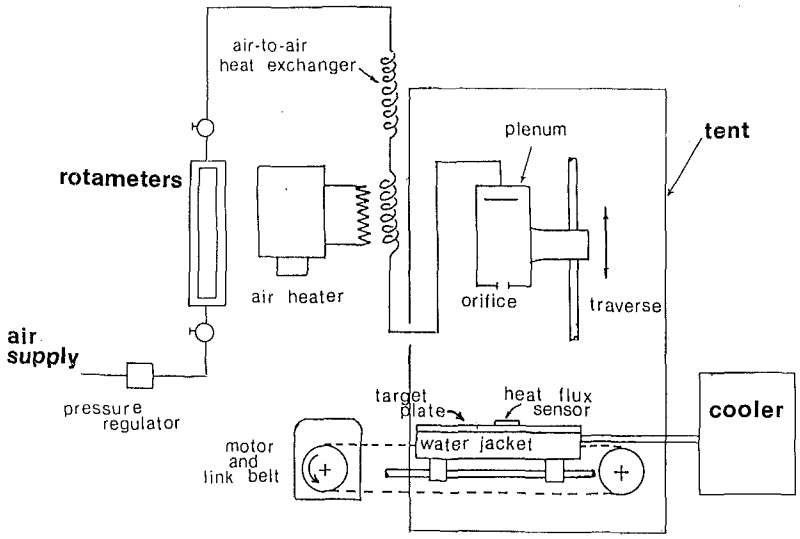

Fig. 2 Experimental apparatus

marizes the test program. The range of Re corresponds to those commonly encountered in gas turbine cooling; and the values of $\bar{Z}$ (especially those at the low end of our range) are likewise relevant. Finally, the jet orifice design (discussed below) is typical of the microdrilled holes used in impingement cooling designs for gas turbines.

Preliminary experiments were previously conducted to fully characterize the jet for which heat transfer was to be measured. The work included making detailed measurements of velocity and total temperature within the jet, and of recovery temperature on an adiabatic flat surface normal to the jet. Such tests were conducted for the same test conditions (see Table 1) as those used for heat transfer measurements, and the results are presented in an earlier paper [7].

Test Apparatus and Methods

Figure 2 is a diagram of the test rig used for this work. It consists essentially of an air delivery circuit, a jet plenum with interchangeable orifice plates, a movable target plate, and a cooling system for the impingement surface. The apparatus and test methods are discussed briefly below, and in more detail in [8], on which this paper is based.

Test air is supplied by a compressor located in the basement of the building and piped to the Forced Convection Lab, where it passes through a filter and pressure regulator. The mass flow is controlled with manually operated valves and measured with a bank of precision (±1 percent f.s.) rotameters. An air-to-air heat exchanger is used to bring the supply air into thermal equilibrium with room air for the isothermal ($T_p = T_a$) tests. For the nonisothermal tests a 6-kW air heater, with proportional controller, was used to heat the air. The jet plenum is an insulated airtight aluminum box, fabricated from 9-mm aluminum plate. Outside dimensions are 102 mm × 102 mm × 216 mm parallel to the jet axis. The orifice plate serves as one end wall of the plenum; there are two such interchangeable plates, one for each ($d = 10$ mm, $d = 2.5$ mm) of the orifices tested. The orifices which form the jets are square edged with length/diameter = unity. Both were calibrated and found to have discharge coefficients in the range 0.75–0.77 for the range of flows used here. The plenum contains two sets of screens, as well as thermocouples and pressure taps for determination of stagnation conditions. The plenum is attached to a traverse, which allows vertical motion so that the standoff $\bar{Z}$ may be varied.

The impingement surface is a copper plate 6.4 mm thick × 406 mm wide × 610 mm long. Attached near the center of the airside face is a small (sensing area = 2.6 mm × 1.5 mm) microfoil HFS (heat flux sensor) which directly measures local heat flux q. The stick-on sensor also contains an integral TC (thermocouple) which produces an output indicative of the surface temperature T_s at the same point. The remainder of the test surface is masked with sheet Kapton having the same thickness (≈0.1 mm) and thermal impedance as the sensor itself. The masking is "butted" against the edges of the HFS, so that the latter does not actually protrude into the flow as Fig. 2 shows. In addition to producing an

Nomenclature

d = jet orifice diameter
h = heat transfer coefficient based on temperature difference ($T_r - T_s$)
h' = heat transfer coefficient based on temperature difference ($T_p - T_s$)
k = thermal conductivity of air
$\dot{m}$ = mass flow rate of jet air
Nu = Nusselt number = hd/k
Nu′ = Nusselt number = $h'd/k$
Pr = Prandtl number
q = heat flux
q_c = convective heat flux
q_r = radiative heat flux
r = radial distance from jet axis
$r_{1/2}$ = jet half-width
$\bar{r}$ = r/d
Re = jet Reynolds number
T_a = temperature of entrained (ambient) air
T_p = jet plenum temperature
T_r = jet recovery temperature
T_{rm} = stagnation point recovery temperature
T_s = target surface temperature
Z = standoff, normal distance from jet orifice exit plane to target surface
$\bar{Z}$ = Z/d
α = dimensionless stagnation point recovery temperature = $(T_{rm} - T_a)/(T_p - T_a)$
β = dimensionless local recovery temperature = $(T_r - T_a)/(T_{rm} - T_a)$
ΔT = temperature mismatch = $T_p - T_a$
ΔT_1 = temperature difference = $T_a - T_s$
γ = h'/h
μ = dynamic viscosity of air
ϕ = $\alpha \cdot \beta$

aerodynamically smooth surface, the masking tends to eliminate surface temperature discontinuities which would otherwise exist at the sensor site. Also, there were three TC's imbedded in the copper plate at distances varying between 5 and 11 cm from the HFS. These could be used as a rough check on the reading provided by the TC in the heat sensor; however, they could not be used to give a direct indication of the surface temperature because there is, in general, a fairly significant temperature difference across the sensor itself or the surrounding Kapton. In fact, the HFS is a thermopile device which produces an output emf proportional to the heat flux through (hence the temperature drop across) the sensor itself. The manufacturer of these devices (RdF, Inc.) furnishes a calibration with each unit. These have been checked by a researcher making similar measurements [9] and found to be as accurate (±5 percent) as claimed by the manufacturer.

The target plate was cooled to a nominal temperature of 7–8°C using an ethylene glycol solution, which was chilled in a circulating refrigeration unit. The liquid was pumped through small (0.8 mm × 2.0 mm) passages between the back face of the target plate and a ribbed baffle plate pressed tightly against it. Both plates were mounted to a plexiglas jacket which collected coolant after it had cooled the target. This entire assembly rode on two parallel horizontal rails which passed through pillow block bearings attached to the bottom surface of the jacket. It could be drawn at constant speed along the tracks by a variable speed electric motor, to which it was connected with a link belt.

Measurements of local heat transfer versus radial position were made as the target plate was traversed slowly past the stationary air jet. Prior to each run, the jet plenum was carefully aligned so that the jet axis was normal to the impingement surface and so that the jet axis would intercept the centroid of the heat flux sensor. Preliminary tests were conducted to determine how slowly the traverses must be made to yield heat transfer profiles which did not differ from those obtained from steady-state tests. Voltages representing local heat flux q and surface temperature T_s were recorded in analog fashion on a two-channel chart recorder during each traverse.

It was found that, because T_s was well below room temperature, there was a tendency for water vapor to condense on the target plate. The test air was dried by passing it through a cooler at the compressor exhaust. However, the air flowing across the target surface was a mixture of the dry jet flow and (depending upon the relative humidity at the time of the test) the considerably more moist room air. This is one entrainment effect which we did not care to examine. The condensation problem was alleviated by enclosing the plenum and target assembly within a "tent" made from sheet polyethylene plastic. Prior to each test run, dry jet air was allowed to flow into the enclosure long enough to completely displace all of the moist air which originally occupied it. The tent was sufficiently large (1.7 m high × 1.5 m deep × 2.0 m long) so that no appreciable air currents existed within it, and it was sufficiently vented so that there was no detectable difference between the internal pressure and prevailing atmospheric pressure. A TC probe was used to traverse the region within the tent between the jet orifice and the impingement plate, and the "ambient" air temperature T_a was found to be quite uniform. It was thereafter measured with a TC located in the same horizontal plane as the jet orifice, 20 cm from the jet axis. No significant temporal change in T_a was observed during any of the test runs.

Results and Discussion

Local heat transfer was measured by traversing the target past the impinging jet as described in the previous section. Figure 3 shows typical ($\bar{Z}=5$, $d=10$ mm) distributions of heat

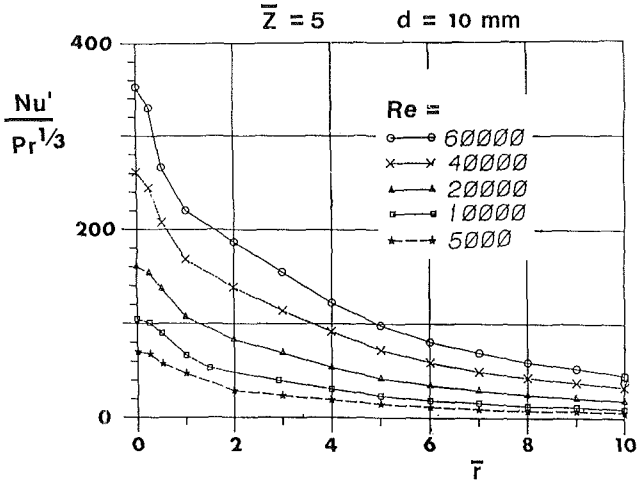

Fig. 3 Effect of Re on heat transfer profiles for isothermal jet

transfer for the isothermal case, $\Delta T=0$. Local heat flux is expressed in terms of a Nusselt number defined by

$$\mathrm{Nu}' = \frac{h'd}{k} = \frac{q_c}{T_p - T_s} \cdot \frac{d}{k} \tag{1}$$

where the local convective heat flux q_c is obtained by subtracting a small radiation correction from the flux q measured by the sensor. The jet flow rate $\dot{m}$ is incorporated into a Reynolds number given by

$$\mathrm{Re} = \frac{4}{\pi} \frac{\dot{m}}{\mu d} \tag{2}$$

It was assumed that $\mathrm{Nu} \sim \mathrm{Pr}^{1/3}$, where the Prandtl number was essentially fixed at $\mathrm{Pr}=0.71$ for this study.

Data reduction was performed on Clarkson's mainframe digital computer. Values of emf corresponding to q and T_s were read from the strip chart at discrete points and input to the Fortran program which carried out the required calculations and generated plots (such as Fig. 3) of the results. The symbols on the figure indicate locations at which data were discretized, and the somewhat "choppy" appearance of the curves results because the plotting routine connects adjacent points with straight line segments. The actual distributions of heat transfer are, of course, smooth curves.

The literature contains considerable data on heat transfer from isolated isothermal jets, and the behavior represented by Fig. 3 is consistent with that observed by others. The boundary layer on the impingement surface is essentially laminar near the stagnation point ($\bar{r}=0$), but becomes turbulent when the stabilizing effect of the favorable pressure gradient within the so-called impingement region vanishes near $\bar{r} \cong 1.5$–2.0. If the data of Fig. 3 are used to generate plots of log Nu versus log Re at several $\bar{r}$ the resulting curves are essentially linear, which implies that $\mathrm{Nu} \sim \mathrm{Re}^n$ at fixed $\bar{r}$ and $\bar{Z}$. The exponent is often taken as an indication of whether the boundary layer is locally laminar or turbulent: $n \simeq 0.5$ corresponds to purely laminar flow and $n \simeq 0.8$ corresponds to turbulent. The least-squares method was used to find values of n to determine if the heat transfer profiles of Fig. 3 behaved in the manner described above. This procedure yielded $n=0.65$ at $r=0$, 0.76 at $\bar{r}=3$, 0.79 at $\bar{r}=6$, and 0.80 at $r=9$. Similar results were obtained for cases with different $\bar{Z}$ and d. Thus, the data behave as expected in the region (large $\bar{r}$) where flow is turbulent. It is also accepted that, near the stagnation point, turbulence in the approaching jet may penetrate the otherwise laminar boundary layer. This yields heat transfer which exceeds that predicted by laminar theory, and leads to exponent values (such as our own) which exceed the value ($n=0.5$) associated with a laminar boundary layer flow.

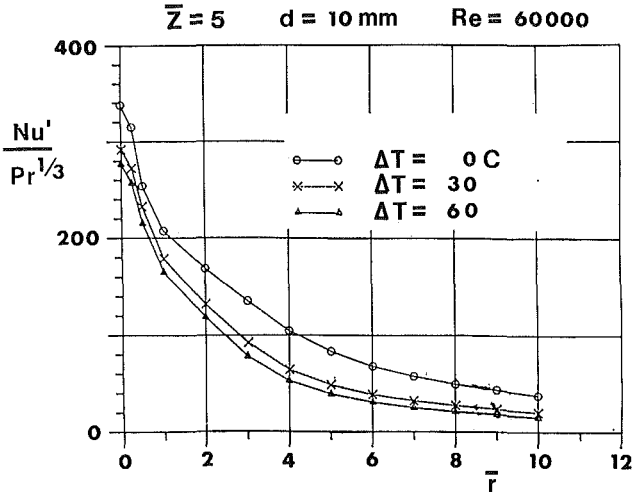

Fig. 4 Effect of entrainment on heat transfer profiles for $\bar{Z}=5$, Re = 60,000

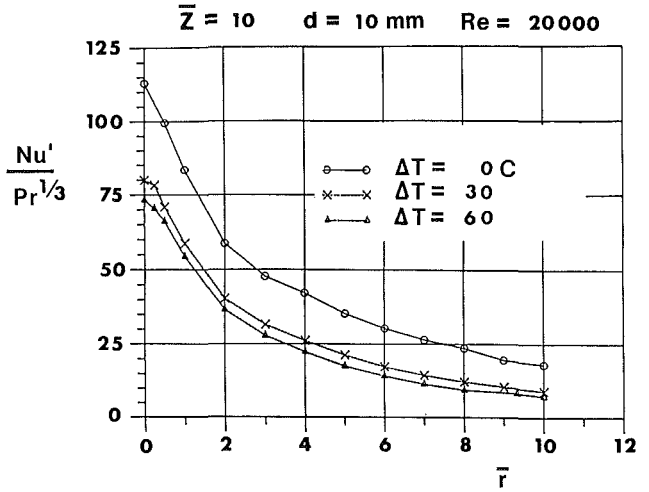

Fig. 5 Effect of entrainment on heat transfer profiles for $\bar{Z}=10$, Re = 20,000

Figures 4 and 5 show typical comparisons between heat transfer profiles for isothermal ($T_p=T_a$) jets and heated ($T_p>T_a$) jets. The heat transfer coefficient Nu′ is again defined as in equation (1), and all fluid properties are evaluated at a film temperature halfway between T_{rm} and T_s using tables in [10]. The curves $\Delta T=30°C$ and 60°C represent situations where the ambient temperature lies between the initial jet temperature and the target temperature, as would occur within a multiple jet array. Both figures show the negative effect of entrainment of ambient fluid (having T_a between T_p and T_s) upon impingement heat transfer. This is apparent if one observes that the vertical coordinate of Figs. 4 and 5 is proportional to local q_c for fixed (T_p-T_s). The isothermal jet produces significantly higher heat transfer than the heated jets. Heat transfer near the stagnation point is reduced, for the latter, by entrainment of surrounding fluids as they flow between the orifice and the target, and the effect becomes more pronounced as $\bar{Z}$ is increased. Additional entrainment occurs as the wall jet spreads radially over the impingement surface, which causes further degradation of the heated jets' performance relative to that of the isothermal jet.

The effect of the temperature mismatch ΔT upon impingement heat transfer is strongly dependent upon the standoff $\bar{Z}$. Figure 6 shows typical variations of Nu′ with $\bar{Z}$ at the stagnation point and at an intermediate ($\bar{r}=4$) radial position. The profiles for an isothermal jet show only the effects of velocity variations upon heat transfer, while those for the heated jet ($\Delta T=30$ K) show the combined effects of

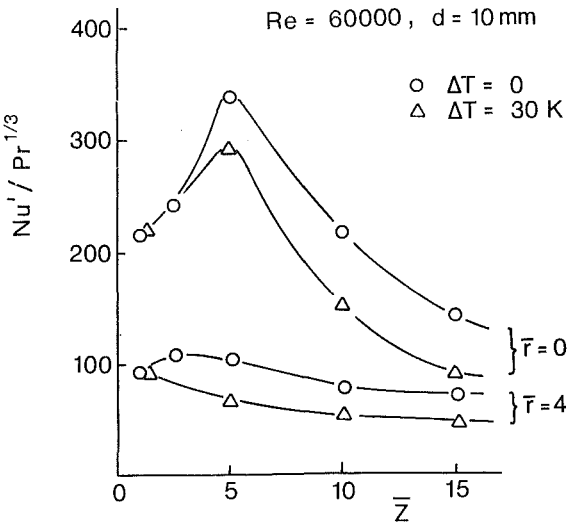

Fig. 6 Effect of standoff

velocity variation and thermal entrainment. The latter effect depends more strongly upon $\bar{Z}$ at $\bar{r}=0$ becauses it is due entirely to thermal mixing which occurs in the free jet en route to the target surface. At $\bar{r}=4$, a significant portion of the thermal entrainment occurs as the jet spreads radially on the surface, and the dependence upon $\bar{Z}$ diminishes.

In the companion paper [7] to this one, we discussed the resemblance between the process considered here (i.e., impingement of a nonisothermal jet) and film cooling. It was noted that heat fluxes to film-cooled surfaces can be calculated from

$$q_c=h(T_r-T_s) \tag{3}$$

where T_r is local recovery temperature. The recovery temperature (usually embodied in the nondimensional film cooling effectiveness) is typically measured or predicted on an adiabatic surface for a given set of conditions (i.e, geometry, crossflow, injected flow) and subsquently applied in calculating heat transfer rates for nonadiabatic surfaces using equation (3). While there is no rigorous basis for this procedure, it has generally given satisfactory results.

Earlier work [11] dealing with an impinging jet in a crosswind suggests that this same approach should be applicable to the problem considered here. Heat transfer to isothermal or nonisothermal jets should correlate according to

$$\mathrm{Nu}/\mathrm{Pr}^{1/3}=f_1(\mathrm{Re},\bar{Z}) \tag{4}$$

where the appropriate fluid-to-surface temperature difference in Nu is (T_r-T_s) and local T_r is measured on an adiabatic surface. Thus the local heat transfer coefficient (unprimed Nu) of equation (4) is given by

$$\mathrm{Nu}=\frac{q_c}{T_r-T_s}\,\frac{d}{k}\,. \tag{5}$$

The resulting correlation, then, does not explicitly contain the temperature mismatch ΔT or a corresponding temperature ratio such as $\Delta T/(T_p-T_s)$. Instead, it is buried in the recovery temperature and appears implicitly.

The results of detailed measurements of recovery temperature (made on the same test rig) were reported in [7]. Data representing the decay of stagnation point recovery temperature T_{rm} were found to fall on a curve of the form

$$\alpha\equiv(T_{rm}-T_a)/(T_p-T_a)=f_2(\bar{Z}) \tag{6}$$

where $\alpha=1$ for $\bar{Z}\le 3$ and subsequently decays monotonically toward zero with increasing $\bar{Z}$. The radial distribution of T_r was found to be

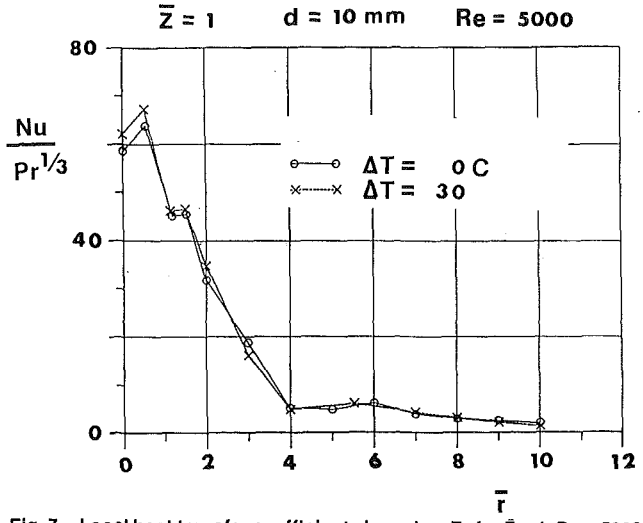

Fig. 7 Local heat transfer coefficients based on T_r for $\bar{Z}=1$, Re = 5000

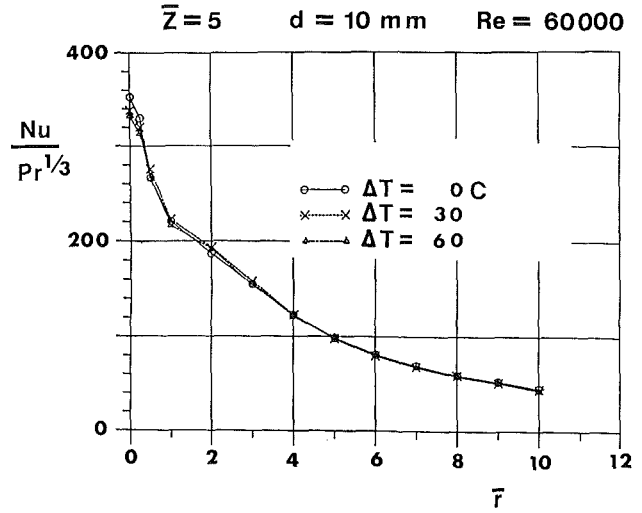

Fig. 8 Local heat transfer coefficients based on T_r for $\bar{Z}=5$, Re = 60,000

$$\beta \equiv (T_r - T_a)/(T_{rm} - T_a) = f_3(r/r_{1/2}, \bar{Z}) \quad (7)$$

where $r_{1/2}$ is the half-width of the jet measured at axial location $\bar{Z}$ in the absence of the target. In fact, such data collapsed onto a single curve $\beta=\beta(r/r_{1/2})$ for all $\bar{Z}\geq 5$. For lack of space, these curves are not reproduced here. However, α and β are given by Figs. 8 and 9, respectively, of [7] and the rate of jet spreading $r_{1/2}$ versus $\bar{Z}$ is given by Fig. 6 of the same reference.

Figures 7–10 show typical heat transfer distributions for both isothermal and heated jets having $d=10$ mm. The local Nusselt number is defined by equation (5), and we used $T_r=T_p=T_a$ for the isothermal cases. As discussed in the companion paper [7], this assumption is not acceptable for jet velocities higher than those used for the experiment reported here. As the figures clearly show, the curves of $Nu/Pr^{1/3}$ versus $\bar{r}$ for various ΔT are virtually coincident at fixed Re and $\bar{Z}$. Even the largest discrepancies observed fall well within our experimental uncertainty, which was estimated [8] to be ±9.6 percent. Thus, it appears that by choosing local T_r (as measured on an adiabatic target) as the effective fluid temperature, values of Nu are obtained which are independent of the temperature mismatch ΔT—except through the dependence of T_r on the ambient temperature. Furthermore, the data indicate that heat transfer coefficients measured for isothermal jets can be used to calculate heat transfer rates for nonisothermal jets provided that, in all cases, one uses $(T_r - T_s)$ as the driving potential for convective heat transfer. Also

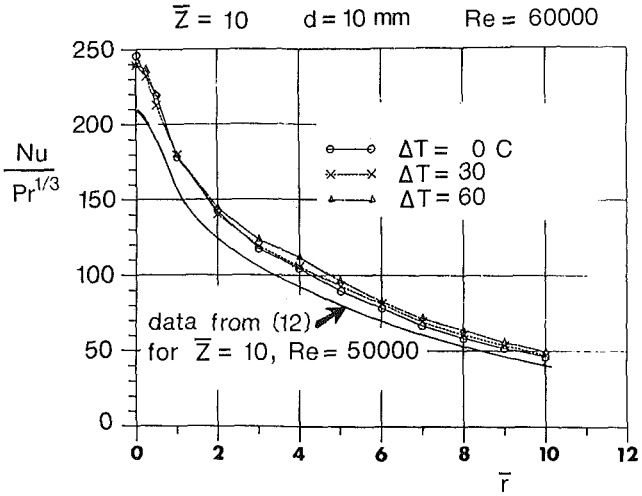

Fig. 9 Local heat transfer coefficients based on T_r for $\bar{Z}=10$, Re = 60,000

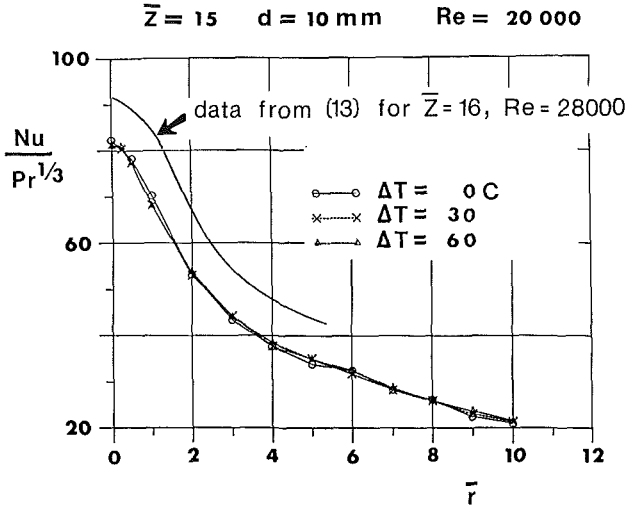

Fig. 10 Local heat transfer coefficients based on T_r for $\bar{Z}=15$, Re = 20,000

shown on these figures are heat transfer profiles measured by others [12, 13] for the isothermal case at test conditions close to our own. Results are quite consistent.

The shapes of the various heat transfer profiles of Figs. 7–10 require only a brief explanation here, as this topic has been addressed thoroughly in earlier papers related to isothermal jets. Heat transfer is high near the stagnation point and drops off as the impingement surface boundary layer thickness grows with r. Heat transfer coefficients tend, in general, to increase with increasing Re. There is, however, a tendency for the profiles to flatten with increasing Re because $h\sim \mathrm{Re}^{0.5}$ for small $\bar{r}$ and $h\sim \mathrm{Re}^{0.8}$ at large $\bar{r}$. For large $\bar{Z}$ (Figs. 8–10) profiles are bell shaped; and as Z is increased the stagnation point Nu decreases and profiles become relatively wider. For small $\bar{Z}$ (Fig. 7) profiles exhibit off-center peaks near $\bar{r}=0.5$ and $\bar{r}=1.5$–2.0, which have been observed in a number of previous isothermal jet experiments. The inner one coincides to a local maximum of turbulence near the center of the mixing region of the approaching jet and the outer one occurs at the laminar/turbulent transition point of the impingement surface boundary layer.

Local heat transfer was measured also for jets formed by smaller ($d=2.5$ mm) but geometrically similar orifices, and the results are given in [8]. Such measurements were limited, however, to $\bar{Z}\geq 10$ because the size of the sensor (1.5 × 2.6 mm) was such that it could not adequately resolve the steeper q versus r profiles associated with small $\bar{Z}$. All of the available data (see Table 1) indicate that there is no diameter depen-

dence: For the same Re and $\bar{Z}$, jets formed by orifices of both sizes yield profiles of Nu versus $\bar{r}$ which are, within our experimental certainty, identical.

It is worthwhile, at this point, to re-examine Figs. 4 and 5. In these figures, the local heat transfer coefficient h' is defined in terms of the temperature difference $(T_p - T_s)$, and is therefore dependent upon the mismatch $(T_p - T_a)$. In Figs. 7 through 10, however, the heat transfer coefficient h is defined in terms of $(T_r - T_s)$. The ratio of these quantities is

$$\gamma \equiv h'/h = (T_r - T_s)/(T_p - T_s) \tag{8}$$

so that $\gamma = 1$ for an isothermal jet. For the nonisothermal cases the ratio is ≤ 1, and γ also represents the ratio of local heat flux q_c to the heat flux which would occur for the same conditions but with $T_a = T_p$. Equation (8) can be recast as

$$\gamma = (1 + \phi \Delta T/\Delta T_1)/(1 + \Delta T/\Delta T_1) \tag{9}$$

where ϕ was defined in the Nomenclature and $\Delta T_1 \equiv (T_a - T_s)$. For our experiments, T_a and T_s were essentially constant, and a typical value of their difference is $\Delta T_1 = 17°C$. Figure 5 indicates that for a fairly large $\bar{Z}$ ($\bar{Z} = 10$), both nonisothermal jets ($\Delta T = 30$, 60°C) give heat transfer considerably lower than that produced by the isothermal jet. However, the difference between q_c (i.e., Nu′) for $\Delta T = 30$ and 60°C is relatively slight. Consider a typical location (say $\bar{r} = 2$): The recovery temperature data of [7] indicate that the local ϕ is 0.43. With $\Delta T_1 = 17°C$ and $\phi = 0.43$, equation (9) predicts $\gamma = 0.64$ for $\Delta T = 30°C$ and $\gamma = 0.56$ for $\Delta T = 60°C$. Both values agree well with those that one reads from Fig. 5. Figure 4 ($\bar{Z} = 5$) shows, except for the region near the stagnation point, the same trend. For smaller $\bar{Z}$, the effect of entrainment upon T_{rm} is reduced so that q_c values for nonisothermal jets are closer to those obtained with $\Delta T = 0$. This behavior is likewise predictable from equation (9).

Equation (9) leads to other useful conclusions. If ΔT_1 is fixed and ΔT is increased (say by increasing T_p) then γ will approach a lower limit of ϕ. Thus, local γ will lie between unity and $\phi(\bar{r}, \bar{Z})$ with its actual value depending upon $\Delta T/\Delta T_1$. Furthermore, the heat flux can be written as

$$q_c = h\Delta T_1 + h\phi\Delta T \tag{10}$$

where h depends only upon Re, $\bar{Z}$, and $\bar{r}$. It is apparent that, for fixed ΔT_1, increasing ΔT does cause q_c to increase; but its rate of increase depends upon ϕ. For large ϕ (small $\bar{Z}$ and $\bar{r}$) a given increase in T_p causes a significant corresponding increase in q_c. However for small ϕ (large $\bar{Z}$ and/or $\bar{r}$) q_c is not strongly influenced by changes in T_p. This is due to the fact that, under these conditions, the jet has $T_r \cong T_a$ regardless of the initial jet temperature T_p.

Conclusions

Measurements of local convective heat transfer were made for a nonisothermal turbulent air jet impinging upon a flat isothermal plate. The data show that the entrainment of surrounding fluid, with temperature different from that of the jet, has a considerable effect upon impingement heat transfer rates.

A correlation was developed which accounts for the temperature mismatch between the jet fluid and the ambient fluid. The basis of this correlation is that the local jet recovery temperature (measured on an adiabatic surface under the same test conditions as pertain to the heat transfer measurement) is taken as the effective fluid temperature. The ambient temperature enters the correlation in that it determines, along with other system parameters, the distribution of the recovery temperature. If the fluid temperature is chosen in this manner, then the local heat transfer coefficient Nu is independent of the temperature mismatch and is, in fact, equal to the value for an isothermal jet at the same Re and $\bar{Z}$.

The experiment described here must be considered as a first step toward addressing a rather complex problem: the determination of the adverse effect of the entrainment of spent fluid within jet arrays. Accordingly, we selected the simplest possible physical model (i.e., a single isolated jet in infinite surroundings) for which the thermal entrainment effect could be examined. In multiple jet configurations the surrounding fluid is not quiescent, nor does it have uniform temperature. Obviously, additional work is required to determine the distributions of spent fluid velocity and temperature in these systems, and the manner in which heat transfer is influenced by them.

Furthermore, this experiment was limited to relatively modest temperature differences, so that the jet-to-ambient density ratio was never significantly different from unity. In typical impingement cooling situations related to gas turbines, the (initial) jet density may approach twice that of the surrounding fluid. At the opposite extreme, systems involving combusting gas jets or high-temperature jets used to simulate re-entry environments are characterized by ambient densities which may be several times that of the jet fluid. The density ratio effects the entrainment process in the free jet approaching the target surface and the growth of the surface boundary layer. It is apparent, then, that the effects of large density difference (with jets both warmer and cooler than the entrained fluid) need to be ascertained in future studies.

References

1 Martin, H., "Heat and Mass Transfer Between Impinging Jets and Solid Surfaces," *Advances in Heat Transfer*, Vol. 13, 1977, pp. 1–60.

2 Schauer, J. J., and Eustis, R. H., "The Flow Development and Heat Transfer Characteristics of Plane Turbulent Impinging Jets," Stanford University, Department of Mechanical Engineering, Technical Report No. 3, 1963.

3 Striegl, S. A., and Diller, T. E., "An Analysis of the Thermal Entrainment Effect on Impingement Heat Transfer," ASME Paper No. 82-WA/HT-54, 1982.

4 Striegl, S. A., and Diller, T. E., "The Effect of Entrainment Temperature on Jet Impingement Heat Transfer," accepted for publication in ASME JOURNAL OF HEAT TRANSFER.

5 Vlachopoulos, J., and Tomich, J. F., "Heat Transfer From a Turbulent Hot Air Jet Impinging Normally on a Flat Plate," *Canadian Journal of Chemical Engineering*, Vol. 49, 1971, pp. 462–466.

6 Florschuetz, L. W., Metzger, D. E., and Su, C. C., "Heat Transfer Characteristics for Jet Array Impingement With Initial Crossflow," ASME Paper No. 83-GT-28, 1983.

7 Hollworth, B. R., and Wilson, S. I., "Entrainment Effects on Impingement Heat Transfer. Part I: Measurements of Heated Jet Velocity and Temperature Distributions, and Recovery Temperatures on Target Surface," ASME Paper No. 83-HT-8, 1983.

8 Gero, L. R., "Heat Transfer From a Nonisothermal Impinging Jet," M.S. Thesis, Clarkson College of Technology, Mechanical and Industrial Engineering Department, Oct. 1983.

9 Metzger, D. E., personal communication, 22nd National Heat Transfer Conference, Niagara Falls, NY, Aug. 5–8, 1984.

10 Gebhart, B., *Heat Transfer*, 2nd edn., McGraw-Hill, New York, p. 563.

11 Bouchez, J.-P., and Goldstein, R. J., "Impingement Cooling From a Circular Jet in a Crossflow," *International Journal of Heat and Mass Transfer*, Vol. 13, 1975, pp. 719–730.

12 Donaldson, C. D., Snedeker, R. S., and Margolis, D. P., "A Study of Free Jet Impingement. Part 2. Free Jet Turbulent Structure and Impingement Heat Transfer," *J. Fluid Mech.*, Vol. 45, Part 3, 1971, pp. 477–512.

13 Gardon, R., and Cobonpue, J., "Heat Transfer Between a Flat Plate and Jets of Air Impinging on It," *International Developments in Heat Transfer, Proc. of 2nd International Heat Transfer Conference*, ASME, New York, NY, 1962, pp. 454–460.

Heat Transfer Around a Circular Cylinder Near a Plane Surface

S. Aiba
Professor.
Department of Mechanical Engineering,
Akita Technical College,
Akita 011, Japan

An experimental study has been conducted on the effect of the clearance (c) *between a circular cylinder and a plane surface on the heat transfer from the cylinder to a cross flow of air. The test cylinder diameters* (d) *were 10.1, 15.2, and 25.2 mm. The turbulent boundary layer thickness* (δ) *along the wall with no cylinder present was varied from 15 to 19 mm. The Reynolds number* (*Re*) *based on the undisturbed uniform flow velocity above the wall ranged from* 10^4 *to* 6.6×10^4. *Variations of the characteristic features of the local and mean Nusselt numbers are discussed in relation to the values* c/d, δ/d, *and Re investigated.*

Introduction

Although a large number of studies of heat transfer have been devoted to a circular cylinder mounted transversely in a uniform stream, there have been few investigations of what occurs near a plane surface even though this is important in many engineering applications, such as the design of a shell and tube type heat exchanger or pipe lines of a thermal plant. Flow around the circular cylinder near a plane surface has been investigated by Bearman and Zdravkovich [1] and Fujita et al. [2]. Bearman et al. measured the distributions of mean pressure around the cylinder at a Reynolds number of 4.5×10^4. The thickness of turbulent boundary layer δ on the plate in the absence of the cylinder at the cylinder position was equal to 0.8 of the cylinder diameter d. They found that regular vortex shedding was suppressed for clearances between the cylinder and the plate less than about 0.3 of a cylinder diameter and that the nondimensional vortex shedding frequency St is almost equal to 0.20. The results of Fujita et al. differed from those obtained by Bearman et al., but were for a cylinder diameter that was smaller than the thickness of the turbulent boundary layer. That is, St varied with the cylinder diameter, the clearance, and was not always equal to 0.20.

Heat transfer characteristics around the circular cylinder above the plane surface will be related to the cylinder diameter d, the boundary layer thickness δ, the clearance c, and fluid properties. Furthermore the undisturbed flow velocity U_∞ above the plate will have an important role. The present study was undertaken to determine quantitative information about the effects of these variables. Data on the local pressure and heat transfer distributions were obtained for ranges of δ/d of $0.62\sim1.84$, c/d of $0\sim6$, and Re of $10^4\sim6.6\times10^4$.

Experimental Apparatus and Procedures

Experiments were carried out in an open wind tunnel with a rectangular test section 225 mm wide and 325 mm high. The side walls of the test section were made of plexiglass to permit observation of surface oil flow patterns. The test cylinders spanned the wind tunnel horizontally. The working section was divided by a horizontal partition plate mounted in the middle of the tunnel. The plate was 1 m long and 5 mm thick and had a round leading edge as shown in Fig. 1 (which also shows the coordinate system employed). Trip wires of diameter 1.4 mm were fixed across the plate 100 mm from the leading edge. The free-stream turbulence of the upstream uniform flow $\sqrt{\overline{u'^2}}/U_\infty$ was about 0.7 percent throughout the experiments. A constant-temperature hot-wire anemometer with a single tungsten wire of 0.005 mm diameter as the sensing element was used for measuring the distribution of the velocity and turbulence intensity in the flow field above the plane wall. The test cylinders were placed at 500 mm and 700 mm downstream of the leading edge of the plate. Thicknesses of the turbulent boundary layer at the cylinder positions (but with the cylinders removed from the tunnel) were equal to $15\sim16$ mm and $18\sim19$ mm, respectively. The boundary layer velocity distribution obtained agreed with that shown by Schubauer and Klebanoff [3]. It was also confirmed that the distribution of turbulence intensity on the wall at the cylinder positions was almost identical with that presented by Klebanoff [4].

Test cylinders with diameters of 10.1, 15.2, and 25.2 mm were used for the measurements of the heat transfer around the cylinder. Cylinders used for the measurements for the pressure distribution were smaller by 0.1 mm to 0.2 mm. The ratio of the thickness of the boundary layer δ to the cylinder diameters d ranged from 0.62 to 1.84. The clearance c between the cylinder and the plate was varied from 0 to 60 mm. In order to measure the clearance c accurately a block gauge was used for all experiments.

Reynolds number Re, based on d and U_∞, ranged from 10^4 to 6.6×10^4. The largest diameter cylinder occupied 16 percent of the total height of the tunnel. Therefore, blockage corrections for the flow characteristics were applied as recommended by Pope [5]. The result of corrections recommended by Pope agree with the one reported by Hiwada et al. [6] quite well up to blockage of 20 percent.

For the heat transfer measurements, a stainless steel ribbon wound helically around the center section of a plexiglass tube was electrically heated. The inside of the tube was filled with rigid urethane foam in order to minimize the heat loss by conduction. The wall temperatures were measured with 0.065 mm copper-constantan thermocouples affixed to the back of the stainless steel sheet at intervals of 20°. In addition, the maximum temperature of the cylinder surface was kept under 38°C to reduce the radiative heat loss as much as possible. The heat loss by radiation from the cylinder surface was

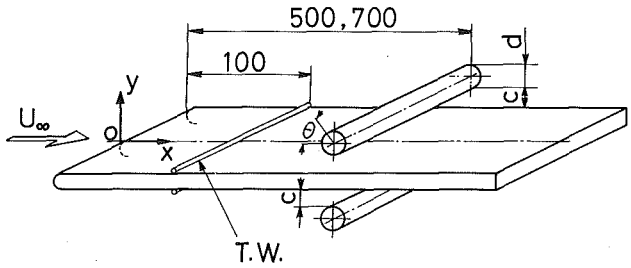

Fig. 1 Arrangement of cylinder and coordinate system

Contributed by the Heat Transfer Division for publication in the JOURNAL OF HEAT TRANSFER. Manuscript received by the Heat Transfer Division May 30, 1984.

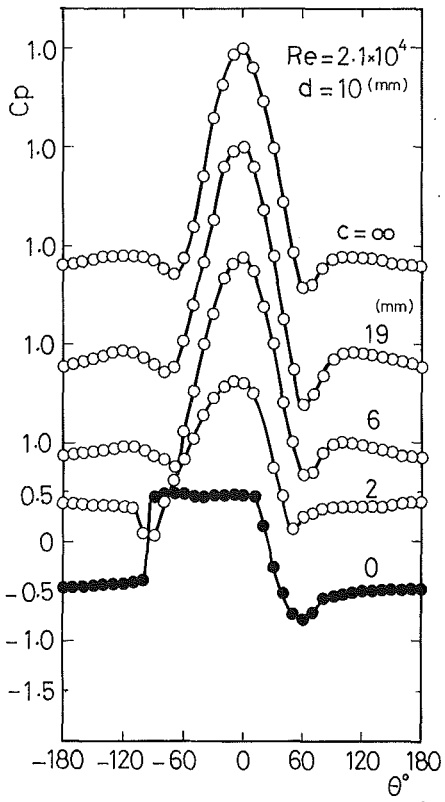

Fig. 2(a) $d = 10$ mm, $\delta = 19$ mm, $\mathrm{Re} = 2.1 \times 10^4$

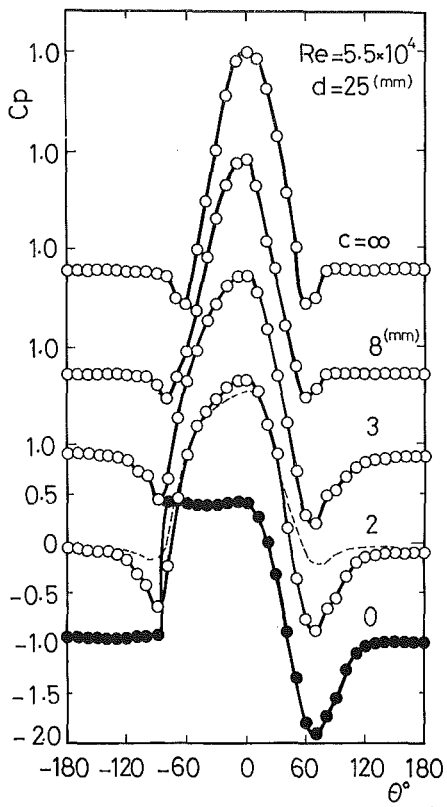

Fig. 2(b) $d = 25$ mm, $\delta = 16$ mm, $\mathrm{Re} = 5.5 \times 10^4$

Fig. 2 Variation of local static pressure coefficient with clearance

estimated to be about 0.6 percent of the heat supplied to the tube. Thus the present data were obtained under the condition of constant heat flux. The local heat transfer coefficient and the corresponding Nusselt number are defined, respectively, as follows: $h_\theta = Q/S(T_w - T_\infty)$; $\mathrm{Nu}_\theta = h_\theta d/\lambda$. The apparatus and technique for the heat transfer measurements are almost the same as those used in previous studies by the present author [7-9]. The correction of the loss by conduction in the radial direction amount to less than 1 percent of the electric power input.

The surface pressure was measured at intervals of 10° with an unheated cylinder having a static pressure hole of 0.5 mm in diameter. Oil flow patterns showed the flow field to be two dimensional.

Experimental Results and Discussion

Flow Characteristics. The distributions of the local static pressure coefficients C_p are presented in Fig. 2(*a*) and 2(*b*). The results for $\delta > d$ ($d = 10$ mm, $\delta = 19$ mm, $\mathrm{Re} = 2.1 \times 10^4$) are shown in Fig. 2(*a*). Although the cylinder is immersed in the boundary layer when $c/d = 0.6$, the pressure distribution on the cylinder is nearly symmetric about the geometric front stagnation point θ_f, and similar to the distribution in a uniform flow ($c/d = \infty$). In the range of $c/d < 0.5$, the front stagnation static pressure coefficient C_{pf} decreases rapidly with decreasing clearance c/d. Furthermore, with decreasing c/d the rear stagnation static pressure coefficient C_{pb} increases and the pressure distribution around the cylinder becomes asymmetric about θ_f (see the case for $c/d = 0.2$). The separation point, which is determined using the wake angle defined by Niemann [10], on the upper surface of the cylinder ($\theta = 0 \sim +180$ deg) shifts upstream as shown by Bearman et al. [1]. Another separation point on the lower surface ($\theta = 0 \sim -180$ deg) is located at about $\theta = -110$ deg.

In the case of $c/d = 0$, the pressure coefficient behavior

Nomenclature

c = distance between the cylinder and the plane wall
C_p = $(p - p_\infty)/(1/2)\rho U_\infty^2$ = static pressure coefficient
d = cylinder diameter
Nu = Nusselt number
p = static pressure
Q = supplied heat flow rate
Re = $U_\infty d/\nu$ = Reynolds number
S = heated surface area
St = Strouhal number
T = temperature
$\sqrt{\overline{u'^2}}/U_\infty$ = stream turbulence intensity
U = flow velocity
u' = streamwise turbulent fluctuating velocity
δ = thickness of the boundary layer
θ = circumferential angle from geometric forward stagnation point
λ, ν, ρ = thermal conductivity, kinematic viscosity, and density of air at T_∞

Subscripts

f = geometric forward stagnation point
m = mean
max = maximum
min = minimum
r = geometric rear stagnation point
w = wall
∞ = undisturbed uniform stream

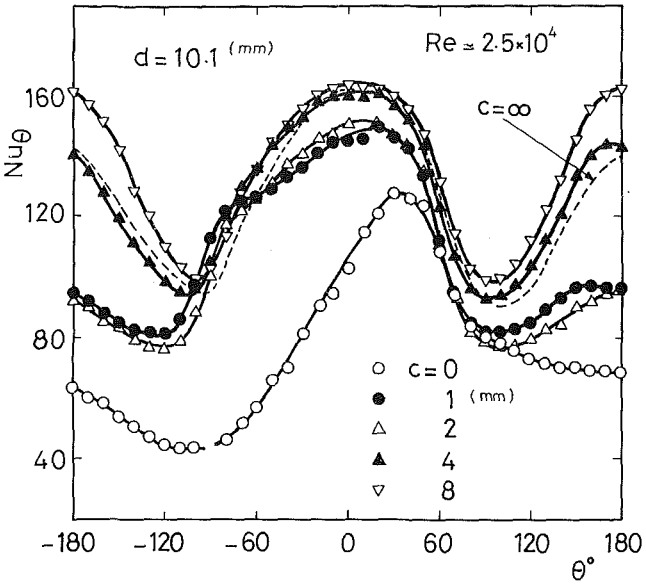

Fig. 3 Distribution of local Nusselt number for $d = 10.1$ mm, $\delta = 19$ mm, $Re = 2.5 \times 10^4$

suggests that the flow around the cylinder surface in the neighborhoods of $\theta = 0 \sim -90$ deg and $\theta = -90 \sim -180$ deg is very stagnant.

The results for $\delta < d$ ($d = 25$ mm, $\delta = 16$ mm, $Re = 5.5 \times 10^4$) are presented in Fig. 2(*b*). For $c/d = 0.32$, the distribution of the local pressure coefficient is similar to that for $c/d = \infty$, although the minimum pressure coefficient $C_{p\min}$ is located farther downstream. In the range of $c/d < 0.16$, the distribution of C_p about θ_f is no longer symmetric, and it appears that the separation points shift downstream. For example, for $c/d = 0.08$, it can be observed that $C_{p\min}$ located in the vicinity of $\theta = 70$ deg has an extremely low value of about -2.0 and the separation point on the upper surface of the cylinder is located at about $\theta = 120$ deg. This suggests that the flow on the surface downstream of $\theta = 70$ deg may be accelerated in comparison with the flow for $c/d = \infty$.

It is well known that the laminar separation points on the circular cylinder situated in the uniform flow occur in the vicinity of $\theta = \pm 80$ deg independent of Reynolds number in the range of $Re = 10^4 \sim 10^5$. When the free-stream turbulence intensity increases, the separation points shift downstream in that Reynolds number range.

In Fig. 2(*b*), the result for $Re = 1.54 \times 10^4$, $c/d = 0.08$, is shown also by the dotted line. The locations of the separation points are different from those for the case of $Re = 5.5 \times 10^4$, $c/d = 0.08$. This fact shows that the flow characteristics for $\delta < d$ depend on the Reynolds number.

Results of Local Heat Transfer. Figure 3 shows an example of the variation of the Nusselt number around the cylinder for $\delta > d$ ($d = 10.1$ mm, $\delta = 19$ mm, and $Re \cong 2.5 \times 10^4$). For $c/d = 0$ the local Nusselt number around the cylinder is lower than that for the other clearances, especially on the side next to the wall. The distribution of Nu_θ is quite asymmetric about $\theta = 0$ and the maximum Nusselt number, Nu_{max}, occurs around $\theta = 30$ deg. These results are consistent with the stagnant flow indicated by the C_p distribution shown in Fig. 2(*a*). On the other hand it was found that the local Nusselt number increases significantly for even quite small clearances ($c/d = 0.1 \sim 0.2$) compared with that for $c/d = 0$. Moreover, although the velocity of the oncoming flow to the cylinder is smaller than that of the undisturbed flow, Nu_θ in the vicinity of $\theta = -90$ deg is not less than that for $c/d = \infty$, because of the acceleration of flow between the cylinder and the plane wall. The regular vortex shedding from the cylinder was suppressed

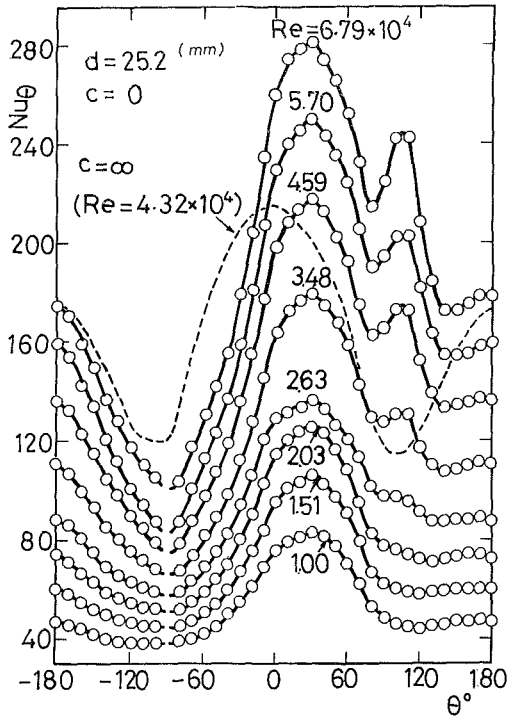

Fig. 4 Variation of local Nusselt number for $d = 25.2$ mm, $\delta = 15 \sim 16$ mm, $c = 0$

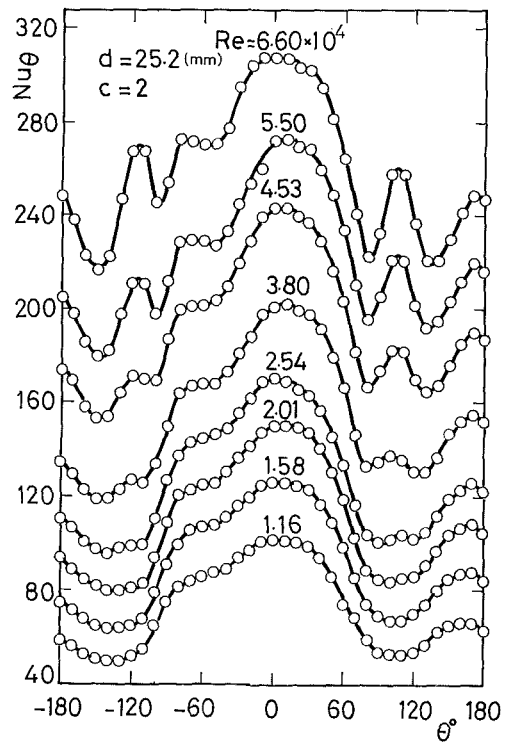

Fig. 5 Variation of local Nusselt number for $d = 25.2$ mm, $\delta = 15 \sim 16$ mm, $c = 2$ mm

for all clearances less than about 0.3 of a cylinder diameter for $Re \sim 10^4$ [1, 11, 12]. As a result, values of Nu_θ behind the cylinder are lower than for $c/d \geqq 0.4$ as shown in the figure.

It was confirmed that the distribution of Nu_θ for $\delta > d$ did not depend on the Reynolds number for values up to $Re \cong 2.5 \times 10^4$, differing from the case of $\delta < d$ as shown later.

Figures 4 and 5 present the results of Nu_θ for $\delta < d$. The distributions of Nu_θ shown in Fig. 4 are for $d = 25.2$ mm, $\delta \approx 15 \sim 16$ mm, and $c = 0$. For values of $Re \leqq 2.03 \times 10^4$, the distribution is similar to that for $\delta > d$ as shown in Fig. 3 for

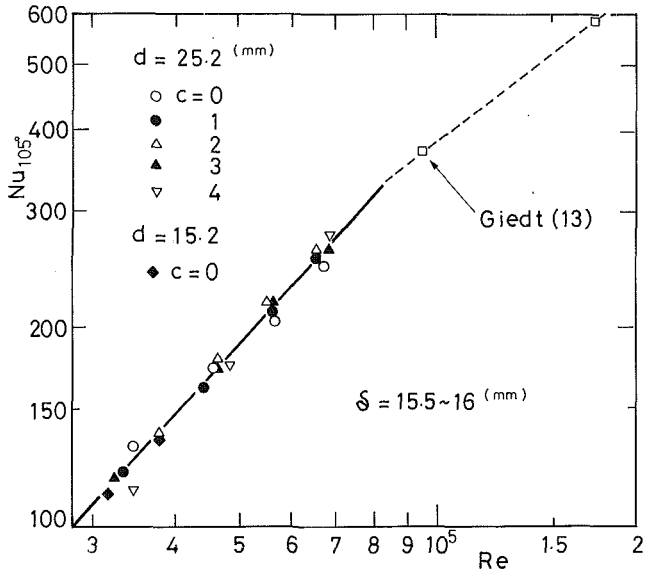

Fig. 6 Variation of Nusselt number at angular position of $\theta = 105$ deg for $\delta = 15.5 \sim 16$ mm with Reynolds number

$c/d = 0$. However a peak at around the angular position of $\theta = 105$ deg for $\mathrm{Re} > 2.03 \times 10^4$ can be seen, and it becomes well defined with increasing Reynolds number. Figure 5 presents the results for $c/d = 0.079$ which is the most complicated in this study. Heat transfer variation around the upper surface of the cylinder ($\theta = 0 \sim +180$ deg) is similar to that for the case of $c/d = 0$. On the other hand, on the lower surface ($\theta = 0 \sim -180$ deg) the Nusselt number peaks appear in the neighborhoods of $\theta = -80$ deg and -115 deg. The high values of Nu_θ at around $\theta = -80$ deg may be due to the acceleration of the flow. Second maxima at around $\theta = -115$ deg can be seen clearly for $\mathrm{Re} \geqq 2.54 \times 10^4$. These were not observed in the uniform flow field at Reynolds numbers around 10^5. They occur downstream of the small separation bubble in the neighborhood of $\theta = -100$ deg which probably causes the lower values of Nu_θ in this region. It appears that the laminar boundary layer separates at about $\theta = -95$ deg and reattaches at an angular position of about $\theta = -115$ deg.

Although these maxima occurring at angular positions of $\theta = 105$ deg and -115 deg have increased with increased Reynolds number, they were not observed, even with increased Reynolds number, when $c > 8$ mm (where the distribution of Nu_θ approaches that for $c/d = \infty$).

It is well known that a maximum in Nu_θ occurs in the vicinity of $\theta = 110$ deg at high Reynolds number (say, near the critical Reynolds number, $\mathrm{Re} = 4 \times 10^5$) [13-15]. Also, it has been made clear that when the oncoming flow has a high turbulence level, even if $\mathrm{Re} \leqq 4 \times 10^5$, a similar peak of Nu_θ can be recognized [16].

In this investigation, the oncoming flow structure may be different from that in the studies referenced above. The velocity distribution of the oncoming flow was not always uniform and the flow itself may have been deflected by a separation bubble which formed upstream of the cylinder along the plate when the clearance c is very small [1]. It is therefore remarkable that a maximum in Nu_θ occurs at about the same location as for the critical flow region, namely around $\theta = 105$ deg.

Figure 6 illustrates the variations of Nu_θ at around $\theta = 105$ deg with Reynolds number including the results of Giedt [16]. It is quite interesting that the data are brought into a single correlation independently of the nondimensional clearance c/d. At high Reynolds number in this study, the data are almost the same as those determined by Giedt in a uniform flow field. However, it seems that the slope of the curve of Nu_{105} versus Re is very large compared with that of Giedt.

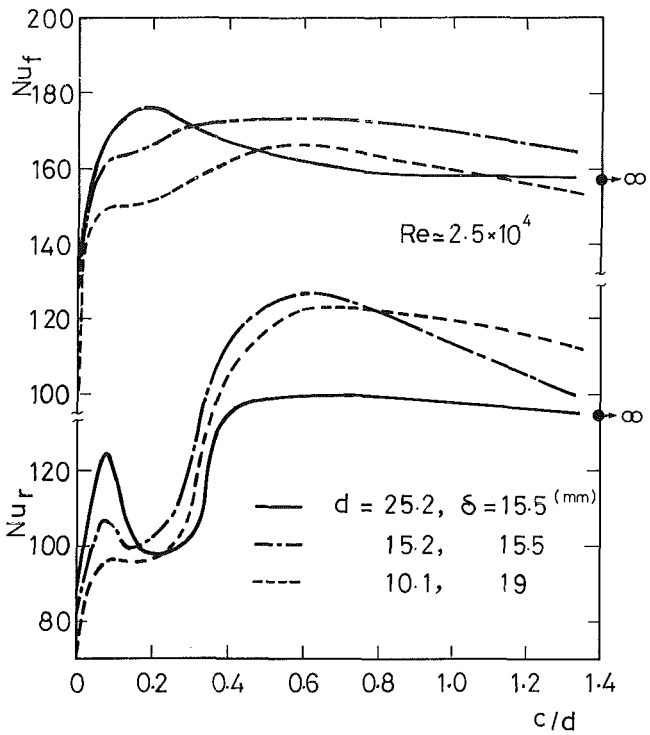

Fig. 7 Variation of Nu_f, Nu_r for c/d at $\mathrm{Re} = 2.5 \times 10^4$

From this it can be concluded that in the lower range of Re, the free shear layer which separates laminarly from the cylinder does not develop into a fully turbulent layer. Therefore, the maximum cannot be seen so clearly in the range of $\mathrm{Re} < 3.48 \times 10^4$ as shown in Figs. 4 and 5. The transition from a laminar to a turbulent shear layer is more pronounced with increasing Reynolds number, and the maximum value increases. Also, note that when $\delta \sim d$, the maximum of Nu_θ at around $\theta = 105$ deg is difficult to identify within the ranges $c/d \leqq 0.067$ and $\mathrm{Re} < 2 \times 10^4$ [11].

In Fig. 7 the variations of Nu_f with c/d at a $\mathrm{Re} \cong 2.5 \times 10^4$ are shown for different values of δ/d. When $\delta < d$ ($d = 25.2$ mm, $\delta = 15.5$ mm), a maximum in Nu_f occurs around $c/d = 0.16$. However, the maximum values of Nu_f are not so clearly evident for $\delta \sim d$ and $\delta > d$ and tend to occur at larger values of c/d with increasing δ/d.

In Fig. 7, the variations of Nu_r (Nusselt number at the rear stagnation point) are also shown. It may be noted that Nu_r varies dramatically with c/d, compared with Nu_f. For $\delta/d = 1.88$ and 1.02, a maximum in Nu_r occurs in the neighborhood of $c/d = 0.6$, and all results for Nu_r tend to decrease in the vicinity of $c/d \cong 0.3$, at which the regular vortex shedding from the cylinder does not occur. However, some peaks in Nu_r can be seen near $c/d = 0.08$, and they increase with decreasing δ/d. This suggests that the flow in the gap between the plane surface and the cylinder is deflected by a separation bubble which is formed on the plane surface downstream of the cylinder. Consequently, the Nusselt number behind the cylinder is increased by this deflected flow near $c/d = 0.08$. In the small clearance region, $c/d < 0.05$, however, the momentum of the flow through the gap probably decreases, and consequently Nu_r decreases.

Results of Mean Heat Transfer. Figure 8 shows the results for mean Nusselt number for $\delta/d > 1$ with c/d ($\delta = 18 \sim 19$ mm, $d = 10.1$ mm and 15.2 mm). From this figure it can be seen that the mean Nusselt number is approximately proportional to $\mathrm{Re}^{2/3}$ in the range of $c/d < 1.6$, though the data for $\delta/d \cong 1.22$ scatter some in the range $c/d < 0.4$.

It is well known that the average Nusselt number in the turbulent wake region is proportional to $\mathrm{Re}^{2/3}$. Results ob-

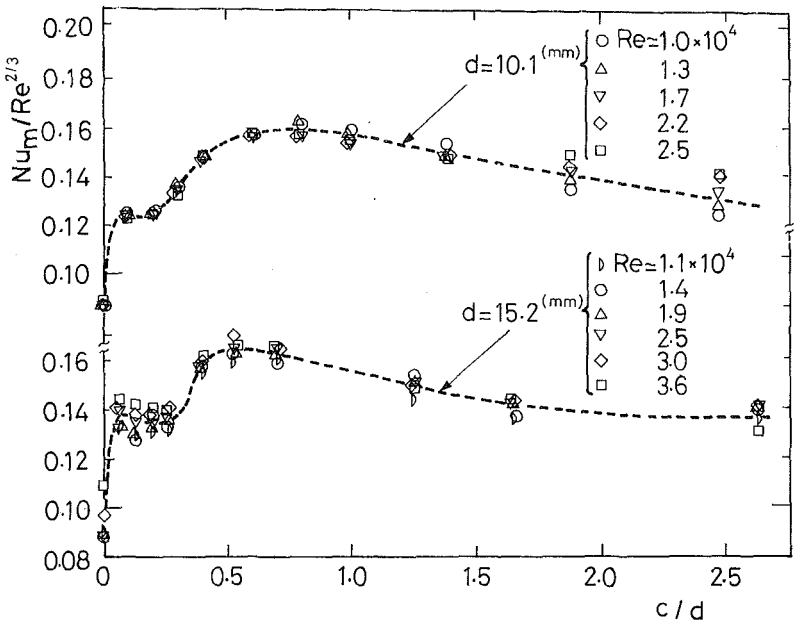

Fig. 8 Mean Nusselt number results for $d = 10.1$ mm, 15.2 mm, $\delta = 18 \sim 19$ mm

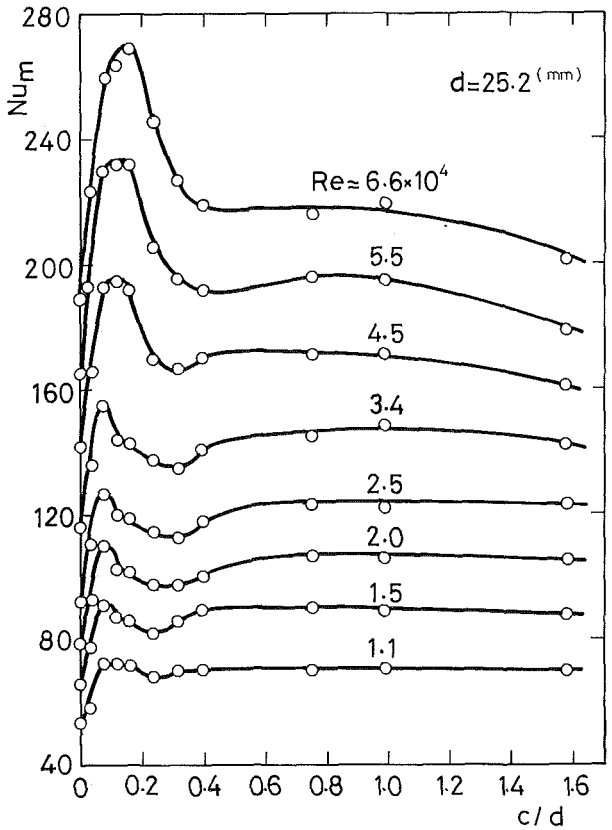

Fig. 9 Mean Nusselt number results for $d = 25.2$ mm, $\delta = 15 \sim 16$ mm with c/d

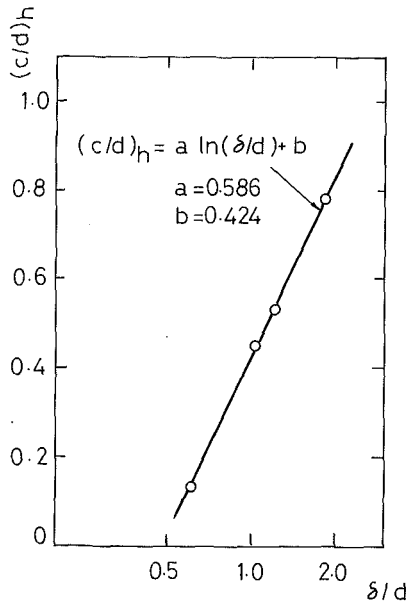

Fig. 10 Relationship between $(c/d)_h$ and δ/d for the maximum mean Nusselt number

tained in this study where the cylinder is placed near the plane surface show the same variation with Re. Maximum Nusselt numbers occur at about $c/d = 0.78$ for $\delta/d \cong 1.83$ and about $c/d = 0.54$ for $\delta/d \cong 1.22$ independent of Reynolds number. The values of maximum Nusselt number are $20 \sim 30$ percent larger than that for $c/d = \infty$. It can be assumed that for these clearances, the velocity of the oncoming flow onto the cylinder is nearly equal to that of the undisturbed flow and the flow has a high turbulence intensity, which may shorten the length of the vortex formation region [17] and entrain the oncoming flow behind the cylinder. Subsequently, the total heat transfer around the cylinder increases. In addition, for $c/d = 0$ (this case is very important in relation to various engineering aspects) the Nusselt number becomes about 2/3 to 3/4 that for $c/d = \infty$.

On the other hand, for $\delta/d < 1$, the mean Nusselt number results are quite different from those for $\delta/d > 1$. Figure 9 gives the mean Nusselt number for $\delta/d \cong 0.615$. The results show that the data cannot be arranged by relations such as $Nu_m/Re^{2/3}$. Nu_m has a relatively large maximum value for the small clearances compared with the case for $\delta/d > 1$ and the maximum values of Nu_m increase markedly with increasing Re. Such results are due to the following. The heat transfer on the front face of the cylinder increases because of the turbulence of the oncoming flow in the range of small c/d. Because of the turbulence, the oncoming flow is entrained behind the cylinder. Consequently, the heat transfer on the rear face does not decrease for values of $c/d \cong 0.08$. Fur-

thermore, in the range of $c/d<0.16$ the laminar boundary layer around the cylinder undergoes transition to turbulence at higher Reynolds numbers.

A plot of $(c/d)_h$ at which the mean Nusselt number reaches a maximum value against δ/d is shown in Fig. 10. The correlation is independent of Re and can be expressed by

$$(c/d)_h = 0.586 \ln (\delta/d) + 0.424 \quad (1)$$

where $0<c/d<0.8$, $0.6<\delta/d<2.0$.

Note that since $(c/d)_h$ for $\delta/d<1$ depends somewhat on the Reynolds number as shown in Fig. 9, a conservative lower value was specified. This result may be important for engineering applications.

Conclusions

In the present experiments, the heat transfer characteristics around a cylinder placed near a plane surface have been examined. It was found that the variation of Nu_f with c/d is not as large at a given Re as that of Nu_r. Nu_r decreases in the range of $c/d \lesssim 0.3$ where regular vortex shedding is suppressed. However, a maximum value of Nu_r occurs in the vicinity of $c/d=0.08$ and it increases with decreasing δ/d, where the gap flow is deflected toward the rear face by a separation bubble formed on the plane surface downstream of the cylinder.

For $c/d=0$, the Nusselt number at the lower and the rear faces of the cylinder decreases because of the stagnation of the flow, and the mean Nusselt number is from 10 to 30 percent less than that with $c/d=\infty$.

When $\delta/d>1$, results of mean Nusselt number can be represented approximately by a single curve independent of Reynolds number in the range $Re=10^4 \sim 3.6\times10^4$ provided that $c/d<1.6$.

The clearance $(c/d)_h$ which gives the maximum mean Nusselt number increases with increasing δ/d as shown in equation (1). The maximum mean Nusselt number values are above the mean Nusselt number for $c/d=\infty$.

Acknowledgments

The author is grateful to Professor N. Seki, of Hokkaido University, Japan, for his valuable suggestions, and to the former students Mr. S. Okubo and Mr. Y. Konda for their assistance in the experiment.

References

1 Bearman, P. W., and Zdravkovich, M. M., "Flow Around a Circular Cylinder Near a Plane Boundary," *J. Fluid Mech.*, Vol. 89, 1978, pp. 33–47.

2 Fujita, H., Takahama, H., and Oishi, T., "Effect of a Circular Cylinder Installed in the Boundary Layer on Heat Transfer From a Flat Plate (Vortex Shedding From the Cylinder)," *20th National Heat Transfer Symposium of Japan*, 1983, pp. 82–84.

3 Schubauer, G. B., and Klebanoff, P. S., "Contributions on the Mechanism of Boundary Layer Transition," NACA TR No. 1289, 1956.

4 Klebanoff, P. S., "Characteristics of Turbulence in a Boundary Layer With Zero Pressure Gradient," NACA TR No. 1247, 1955.

5 Pope, A., *Wind Tunnel Testing*, 2nd ed., Wiley, 1954.

6 Hiwada, M., et al., "Effects of Tunnel Blockage on Local Mass Transfer From a Column Cylinder in Cross Flow," *Trans. JSME*, Vol. 42, 1976, pp. 2481–2491.

7 Aiba, S., and Yamazaki, Y., "An Experimental Investigation of Heat Transfer Around a Tube in a Bank," ASME JOURNAL OF HEAT TRANSFER, Vol. 98, 1976, pp. 503–508.

8 Aiba, S., Ota, T., and Tsuchida, H., "Heat Transfer and Flow Around a Circular Cylinder With Tripping-Wires," *Wärme- und Stöffubertragung*, Vol. 12, 1979, pp. 221–231.

9 Aiba, S., Ota, T., and Tsuchida, H., "Heat Transfer of Tubes Closely Spaced in an In-line Bank," *Int. J. Heat Mass Transfer*, Vol. 23, 1980, pp. 311–319.

10 Niemann, H. J., "On the Stationary Wind Loading of Axisymmetric Structures in the Transcritical Reynolds Number Region," Inst. Konstruktiven Ingenieurbau, Ruhr-Univ. Bochum, Rep. No. 71-2.

11 Aiba, S., et al., "Heat Transfer Around a Circular Cylinder Near a Plane Boundary," *20th National Heat Transfer Symposium of Japan*, 1983, pp. 67–69.

12 Kamemoto, K., Oda, Y., and Aizawa, M., "Characteristics of the Flow Around a Bluff Body Near a Plane Surface," *Trans. JSME*, Vol. 49, 1982, pp. 2929–2936.

13 Schmidt, E., and Wenner, K., "Wärmeabgabe über den Umfang eines Angeblasenen Geheizten Zylinders," *Forsh. Geb. IngWes.*, Vol. 12, 1941, pp. 65–73.

14 Giedt, W. H., "Investigation of Variation of Point Unit-Heat Transfer Coefficient Around a Circular Cylinder Normal to an Airstream," *Trans. ASME*, Vol. 71, 1949, pp. 375–381.

15 Achenbach, E., "Total and Local Heat Transfer From a Smooth Circular Cylinder in Cross-Flow at High Reynolds Number," *Int. J. Heat Mass Transfer*, Vol. 18, 1975, pp. 1387–1396.

16 Giedt, W. H., "Effect of Turbulence Level of Incident Air Stream on Local Heat Transfer and Skin Friction on a Cylinder," *J. Aero. Sci.*, Vol. 18, 1951, pp. 725–731.

17 Gerrard, J. H., "The Mechanics of the Formation Region of Vortices Behind Bluff Bodies," *J. Fluid Mech.*, Vol. 25, 1966, pp. 401–413.

Combined Heat Transfer and Fluid Dynamic Measurements Downstream of a Backward-Facing Step

J. C. Vogel[1]
Research Assistant.

J. K. Eaton
Assistant Professor.
Mem. ASME

Mechanical Engineering Department,
Stanford University,
Stanford, CA 94305

Combined heat transfer and fluid dynamic measurements in a separated and reattaching boundary layer, with emphasis on the near-wall region, are presented. A constant heat-flux surface behind a single-sided sudden expansion is used to obtain Stanton number profiles as a function of Reynolds number and boundary-layer thickness at separation. Fluctuating skin-friction and temperature profiles demonstrate the importance of the near-wall region in controlling the heat transfer rate. The fluctuating skin friction controls the heat transfer rate near reattachment, while the conventional Reynolds analogy applies in the redeveloping boundary layer beginning two or three step heights downstream of reattachment.

Introduction

In many flows of practical interest, separation of a boundary layer and subsequent reattachment of the separated layer to a solid surface is unavoidable. Such flows occur in nuclear reactors, gas turbines, electronic circuitry, and heat transfer devices. Reattaching flows are a serious problem for the heat transfer engineer, because they can cause large variations of the local heat transfer coefficient as well as substantial overall heat transfer augmentation. A design method is needed to predict thermal loads caused by reattachment.

When a predictive design method is developed, it will most probably be based on computational fluid mechanics. Several calculation techniques have been developed which can adequately reproduce the gross fluid mechanical features of separated flow fields (see the detailed review of the results of 18 methods in Eaton [1]). Efforts are now under way to extend the models to predict heat transfer. Experimental work is needed to gain a physical understanding of the flow and to provide detailed information for comparison with models.

Most of the previous work on reattachment involved study of the hydrodynamics of backward-facing step flows. Eaton and Johnston [2] and Watkins and Gooray [3] reviewed the literature in this area. A large number of early studies served to delineate the basic characteristics of reattaching flows, but could not provide quantitative data. More recently, experimenters have used the pulsed-wire anemometer (e.g., Eaton and Johnston [4]) and the laser-doppler anemometer (LDA) (e.g., Durst and Tropea [5]) to supply quantitative data in the highly turbulent reattaching flow. Near-wall velocity data have only recently become available with the advent of the thermal tuft (Eaton et al. [6]), the pulsed wall probe (Westphal et al. [7]), and specially configured LDA systems.

There have been fewer studies of heat transfer in reattaching flows. Fletcher et al. [8], Aung and Watkins [9], and Watkins and Gooray [3] have all recently reviewed the literature in this area. Most of the experiments cited in the reviews contained only mean heat transfer rates and very little fluid dynamic data. The data sets show the same general features for a variety of geometries: a drop in the heat transfer coefficient at separation followed by a sharp rise in the reattachment zone.

Aung and Goldstein [10] used a Mach-Zehnder interferometer to measure temperature profiles and heat transfer coefficients in the back-step geometry. There was a significant temperature gradient across the free shear layer just downstream of separation, but they concluded that the heat transfer resistance is concentrated in the near-wall region for most of the flow.

Generally, it has been assumed that the point of maximum heat transfer coefficient corresponds to the mean reattachment point. However, Kang et al. [11] and Suzuki et al. [12] contradicted this assumption after a series of experiments on confined coaxial jets. They measured the Nusselt number using a constant heat-flux surface and collected mean-velocity and turbulence data with a laser-doppler anemometer. They showed clearly that the peak heat transfer coefficient occurs well upstream of reattachment. They also showed that the Nusselt number correlates well with the turbulence intensity measured at $y = 4$ mm, their point nearest to the wall.

Armaly et al. [13] presented heat transfer, mass-transfer, and fluid-dynamic data for a sudden expansion at relatively low Reynolds numbers. The peak in the Sherwood number was clearly upstream of reattachment for turbulent flows, but both the Sherwood and Nusselt number data showed a double peak for laminar flows. Heat transfer data were not presented for the higher Reynolds numbers.

Recently Chieng and Launder [14] applied the k–ϵ model of turbulence to the prediction of separated-flow heat transfer. Their model assumes that the length scale in the near-wall region depends only on the normal distance from the wall and that the viscous sublayer thickness adjusts itself as a specified function of the external turbulence energy. No separated-flow data are available to check these assumptions, and recent experiments reported by Simpson et al. [15], Eaton and Johnston [4], and Westphal et al. [7] suggest that the near-wall region of separated flow is substantially different from the corresponding region in an ordinary boundary layer.

The objective of the present experiment was to provide detailed heat transfer data coupled with temperature and velocity profiles. These data will provide a well-documented test case and physical insight into the mechanisms controlling the heat transfer rate in reattaching flows. The emphasis is placed on the near-wall region, which controls the heat transfer rate.

The measurements presented here are a subset of data presented in a full report (Vogel and Eaton [16]). Some of the fluid-dynamic measurements are drawn from the report of Adams et al. [17].

[1]Present address: Contour Medical Systems, Mountain View, CA

Contributed by the Heat Transfer Division for publication in the JOURNAL OF HEAT TRANSFER. Manuscript received by the Heat Transfer Division January 19, 1984. Paper No. 83-WA/HT-11.

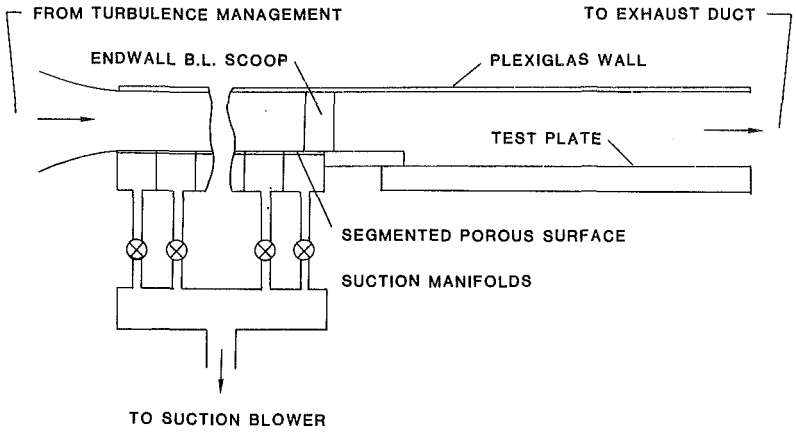

Fig. 1 Test section schematic

Experimental Apparatus

The facility (see Fig. 1) is an open-circuit, two-dimensional, sudden-expansion wind tunnel. It consists of a blower and turbulence management section, a boundary-layer development section, and a sudden-expansion test section.

After the air is filtered upstream of the blower, mineral-oil smoke (particle size 1/2 μ) is added to provide seeding for the laser-doppler anemometry. The flow is provided by an airfoil-bladed blower driven by a computer-controlled AC motor. Turbulence management consists of a honeycomb, four screens, and a 4:1 two-dimensional contraction. The free-stream turbulence level in the test section is less than 0.2 percent, and total pressure nonuniformity as documented by spanwise traverses was less than 1 percent.

The test boundary layer develops on the bottom surface of the 15 cm × 51 cm development section, which is 2.5 m long. The bottom wall is porous, and transpiration may be used to vary the boundary-layer thickness at the test-section entrance from 0.3 to 6 cm.

The sidewall boundary layers are removed by scoops upstream of the test section to reduce the strength of any secondary flows. The scoops narrow the test section to a width of 45 cm. After the scoops, there is a 0.2-m-long flat section before the boundary layer flows over the 3.8-cm-high backward-facing step (expansion ratio = 1.25).

Mass and momentum balances were performed on the test section using pitot-tube profiles at the inlet reference station and exit plane and skin-friction measurements on both the top and bottom walls of the tunnel. Both balanced within 3 percent of the inlet flux, indicating that the flow is two dimensional within the uncertainty of the measurements.

Two test surfaces were used, one a clear Plexiglas plate with

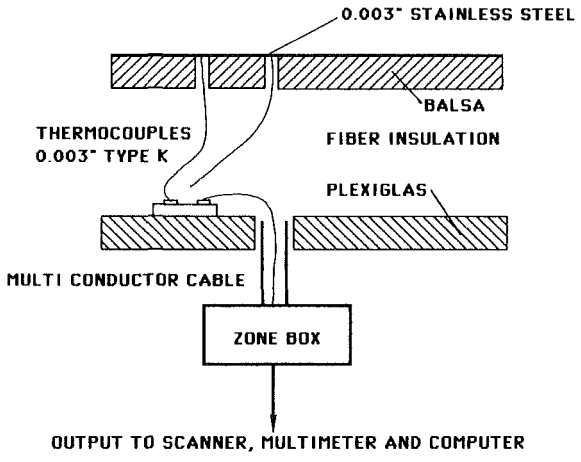

Fig. 2 Cross section of the heat transfer measurement surface

instrument ports for near-wall measurements. The thermal tuft and pulsed-wall probe are mounted in this surface for obtaining forward-flow fraction and skin-friction data, respectively. The other is a constant-heat-flux heat transfer measurement surface. The two are easily interchanged.

The heat transfer measurement plate consists of a thin (0.003 in.), stainless steel foil glued smoothly to a balsa-wood backing (Fig. 2). Forty type-K, 0.003-in.-dia thermocouples are welded to the back surface, for temperature measurement. The thermocouples were placed in grooves cut in the balsa parallel to the surface. Conduction along the fine thermocouples was therefore negligible. Alternating current is supplied to the busbars through a large stepdown transformer, to provide a constant heat flux from the surface.

Nomenclature

AR = area ratio, upstream height/downstream height
C_f = instantaneous skin-friction coefficient $= \tau_0 \Big/ \frac{1}{2}\rho_\infty U_{\text{ref}}^2$
$\bar{C}_f$ = time mean skin-friction coefficient
C_f' = fluctuating component of C_f
c_∞ = free-stream specific heat
h = heat transfer coefficient $= \dot{q}_0''/(T_w - T_\infty)$
H = step height
$\dot{q}_0''$ = wall heat transfer rate per unit area
Re_H = step-height Reynolds number $= U_{\text{ref}}H/\nu$
St = Stanton number $= h/U_{\text{ref}}\rho_\infty c_\infty$
$\bar{T}$ = local mean temperature
T_∞ = free-stream temperature
T_w = local wall temperature
$\bar{U}$ = mean streamwise velocity
u' = fluctuating component of streamwise velocity
u^+ = nondimensional velocity $= U/\sqrt{\tau_0/\rho}$
U_{ref} = reference free-stream velocity measured at $x/H = -3$
x = streamwise coordinate measured from step edge
x_R = reattachment length
y = coordinate normal to wall
y^+ = nondimensional distance from wall $= y\sqrt{\tau_w/\rho}/\nu$
γ = forward-flow fraction
ν = freestream kinematic viscosity
ρ_∞ = freestream density
τ_0 = local wall shear stress

Conduction through the back insulation accounts for less than 1 percent of the total heat transfer from the foil, while conduction along the surface accounts for a smaller fraction, even in regions of high temperature gradient. At these current densities in the surface, the Hall effect can be expected to introduce approximately a 1 percent uncertainty in the centerline heat-flux measurements (Tarasuk and Castle [18]). The heat flux from the surface is uniform within this limitation, and the heat transfer coefficient can be determined simply by measuring the difference between the surface and free-stream temperatures.

The heat transfer surface was qualified by lifting it into position flush with the upstream boundary-layer development section thereby providing an unheated starting-length flat plate. The deviation between the data and flat-plate correlations was less than 2 percent. Four spanwise rows of thermocouples were placed in the surface to check on the two dimensionality of the heat transfer data. For all measurements, the scatter in the spanwise direction was less than 5 percent about the mean.

Mean temperature profiles are measured using a traversing thin-wire thermocouple probe. This probe is similar in appearance to a hot-wire probe but has an 0.003-in.-dia butt-welded thermocouple junction at the center of the wire with an aspect ratio of 100:1.

A pulsed wall probe was used to measure the time-averaged and fluctuating skin friction. This probe, which is described in detail in Eaton et al. [6], is capable of measuring the velocity very near the wall in highly unsteady flow. Eaton et al. [6] and Westphal et al. [7] have demonstrated that the probe can be used to accurately measure the skin friction when the wires are placed in the viscous sublayer. In practice, the wires were set to a fixed height (0.13 mm) and the probe was calibrated in a laminar channel flow of known skin friction.

The thermal tuft (Eaton et al. [6]) measures the instantaneous sign of the velocity at a height of about 1 mm above the surface. At a given location the fraction of time that the flow is in the downstream direction is measured. Eaton et al. [6] showed that the point of 50 percent forward-flow fraction corresponds to the mean reattachment point ($C_f = 0$) with an uncertainty of less than 0.1 step heights.

Velocity measurements are made in the flow using a single-component, forward-scattering LDA system. A 2-W, argon-ion laser is used with T.S.I. optics and a counter type processor. A beam expander was used to give a large beam intersection angle of 15 deg. A number of different sampling schemes were used to ensure minimal velocity bias (see Adams et al. [19]). Generally, direct time averaging proved very satisfactory.

Results

This paper presents the detailed heat transfer and relevant fluid-dynamic data for the investigation of the near-wall region. Complete details of the flow measurements, including velocity and turbulent transport, are contained in Adams et al. [17] and Vogel and Eaton [16]. The reference free-stream velocity for the measurements presented here is 11.3 m/s, which corresponds to a step-height Reynolds number of 28,000. The expansion ratio is held constant at 1.25, and the aspect ratio of the tunnel is 12. The heat flux through the heat transfer surface is 270 W/m^2, corresponding to a maximum temperature of 15°C above ambient. A low-overheat ratio was used to minimize variable-properties effects. Table 1 presents estimates of the errors for each of the measurands. The uncertainty in most of the measurands was calculated by estimating the calibration and reading uncertainties for each instrument. The component uncertainties were then combined using the method of Kline and McClintock [20]. The un-

Table 1 Uncertainties

St	0.00025
C_f	0.0002
C_f'	0.00015
$\dot{q}_0''$	2 W
u^+	1
$T - T_{inf}$	0.1°C
U/U_{ref}	0.01
u'/U_{ref}	0.02

Table 2 Parameters describing inlet boundary layer for reference case

Reference conditions: $U_{ref} = 11.3$ m/s	
$Re_H = 28{,}000$	
Boundary-layer parameters (measured at $x/H = -3.8$)	
Boundary-layer thickness	$\delta_{99} = 4.05$ cm
Momentum thickness	$\theta = 0.468$ cm
Momentum-thickness Reynolds number	$Re_\theta = 3370$
Shape factor	$H = 1.389$
Skin friction (log-law fit)	$C_f = 0.00312$

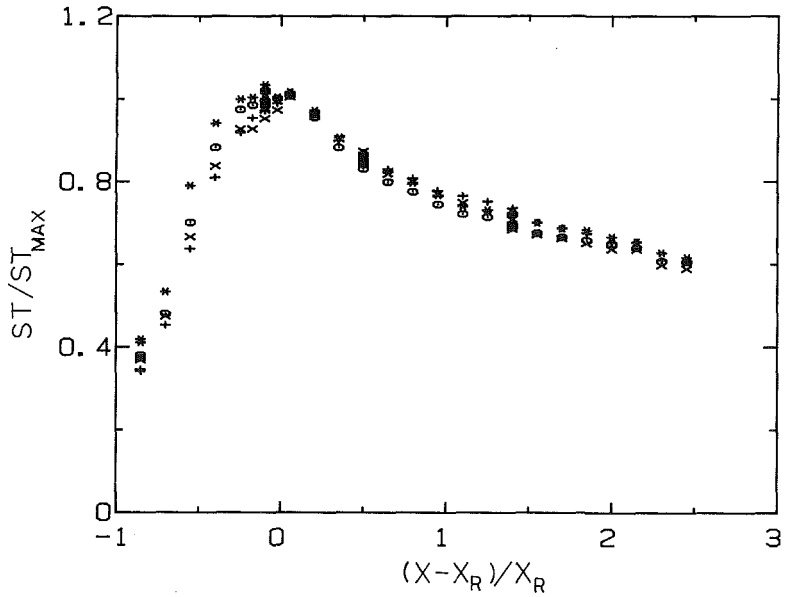

Fig. 3 Normalized Stanton number profiles for δ/h = 1.1: * Re_H = 13,000; o Re_H = 20,000; × Re_H = 28.000; + Re_H = 42,000

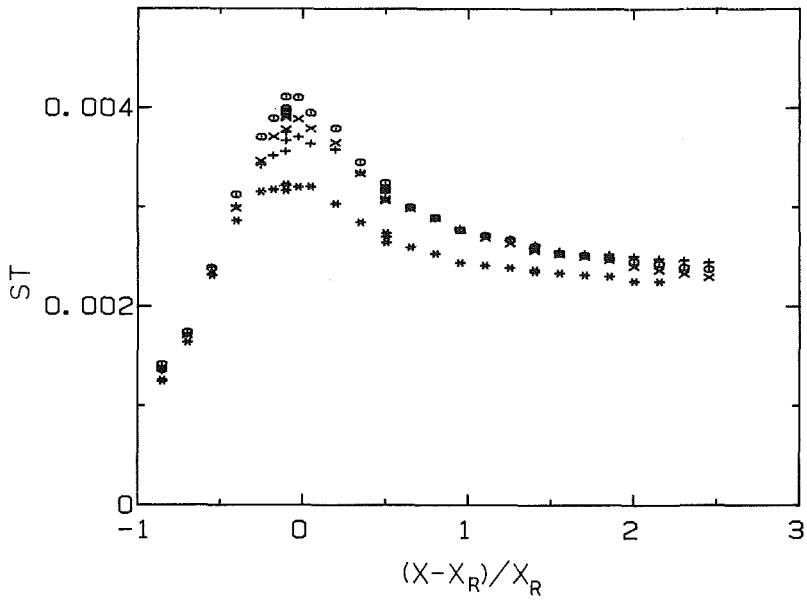

Fig. 4 Stanton number profiles with varying upstream boundary-layer thickness at a Reynolds number of 28,000: ○ $\delta/h = 0.15$; × $\delta/h = 0.19$; + $\delta/h = 0.7$; * $\delta/h = 1.1$

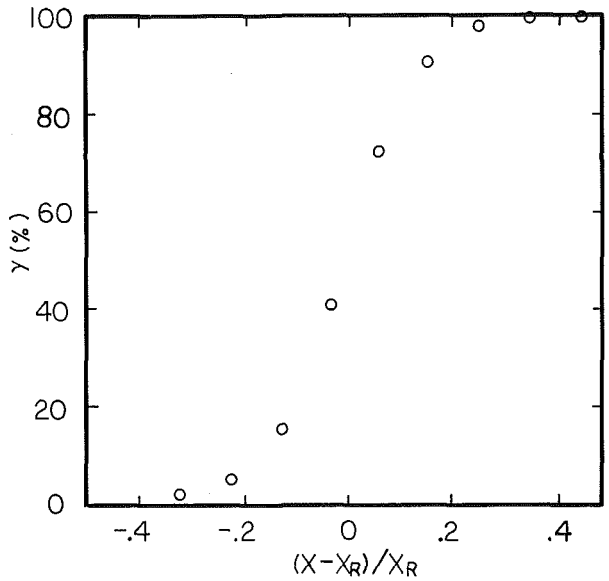

Fig. 5 Profiles of γ (fraction of time flow is in downstream direction) for reference case

certainties in the LDA data were calculated statistically, because the calibration and reading uncertainties were virtually zero.

The inlet velocity profile was measured at a station 3.8 step heights upstream of the step. The profile agreed well with conventional log-law plots. Profile parameters are tabulated in Table 2.

Stanton-number profiles were obtained at four different step-height Reynolds numbers ranging from 13,000 to 42,000. These data are presented in Fig. 3 in terms of the Stanton number normalized on the maximum value plotted against a nondimensional streamwise coordinate ($x^* = (x - x_R)/x_R$), where x_R is the reattachment length. This nondimensionalization has been shown by Westphal and Johnston [21] to collapse the fluid-dynamic data for single backward-facing steps. In the present experiments, the reattachment point is located 6-2/3 step heights downstream of separation.

All the Stanton-number profiles show the same general features. There is a low heat transfer rate in the recirculation region, followed by a steep rise to the maximum near the reattachment point. Previous work showed the maximum heat transfer point anywhere from three to five step heights from the backstep. The peak heat transfer rate in the present experiment occurs slightly upstream of reattachment, as measured by the thermal tuft. The apparent maximum is on the order of 0.1 reattachment lengths (x^*) upstream of mean reattachment, corresponding to 2/3 of a step height for this flow. The actual peak Stanton number varies inversely with the Reynolds number (see below).

Downstream of reattachment, the Stanton number recovers toward that found under a normal turbulent boundary layer. The recovering boundary layer behaves much like a boundary layer with an unheated starting length upstream of the heated section. The effective origin of the redeveloping thermal boundary layer lies approximately two step heights downstream of reattachment for all Reynolds numbers.

In Fig. 4, the dependence of the Stanton number profile on boundary-layer thickness at separation is shown. The upstream boundary layer is turbulent in all cases presented here. It is apparent that the upstream shear layer thickness has a significant effect near reattachment but very little effect either up or downstream of reattachment. Figure 5 shows the forward-flow fraction as measured with the thermal tuft. The region of reversing flow corresponds roughly to the region where the upstream boundary-layer thickness has a significant effect on the Stanton number.

In Fig. 6, the maximum Stanton number is plotted for each value of boundary-layer thickness and Reynolds number. The maximum was measured by hand from the Stanton-number profiles. For all boundary layers and Reynolds numbers, the curves are smooth and monotonic in shape. This behavior suggests that a correlation for the maximum heat transfer rate as a function of these two parameters would be possible. However, such a correlation would obscure the different behavior of the profiles when the two parameters are varied independently (see Figs. 3 and 4).

Mean velocity and streamwise turbulence intensity profiles for the reference case are presented in Figs. 7 and 8. These profiles show the typical features that have been observed in other backward-facing step experiments. It is noteworthy that the peak value of the turbulence intensity occurs slightly

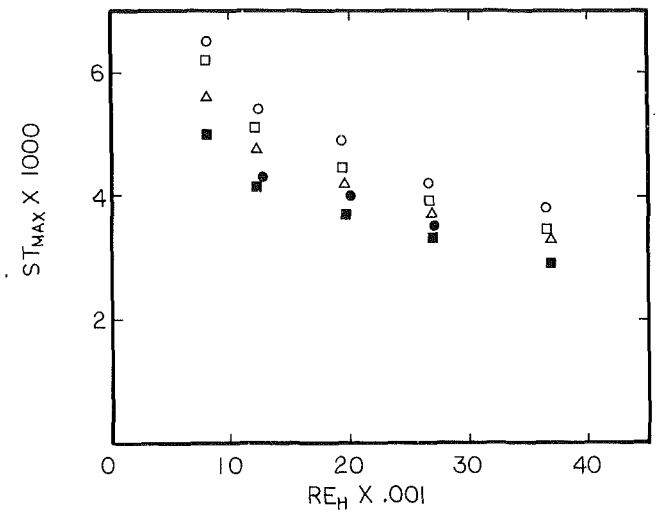

Fig. 6 Peak Stanton number as a function of Reynolds number and upstream boundary-layer thickness: ○ δ/h = 0.15; □ δ/h = 0.19; △ δ/h = 0.7; ● δ/h = 1.1; ■ δ/h = 1.6

upstream of the mean reattachment point near the location of the peak Stanton number.

Eight temperature profiles (Fig. 9) were taken at various distances downstream of the backstep using the thermocouple probe. These compare very well with the results of Aung and Goldstein [10], obtained using interferometry. As can be seen from these profiles, most of the thermal resistance is in the region very close to the wall, which is conduction dominated. In only one of the profiles, that closest to the step, is there a considerable temperature gradient in the flow far from the wall. Convective mixing effects everywhere else are great enough to flatten any temperature gradients. The near-step recirculation-region velocities are very small compared to the free-stream, producing more nearly stagnant air.

The temperature profiles show that the heat transfer resistance is dominated by the near-wall region. Clearly the fluid mechanics of the near wall region must be very important in determining the local Stanton number. The behavior of the near-wall flow is most simply quantified by the mean and fluctuating skin friction. In Fig. 10, the mean skin friction coefficient ($\bar{C}_f$) along the lower wall is plotted for the reference inlet conditions. The skin friction follows the

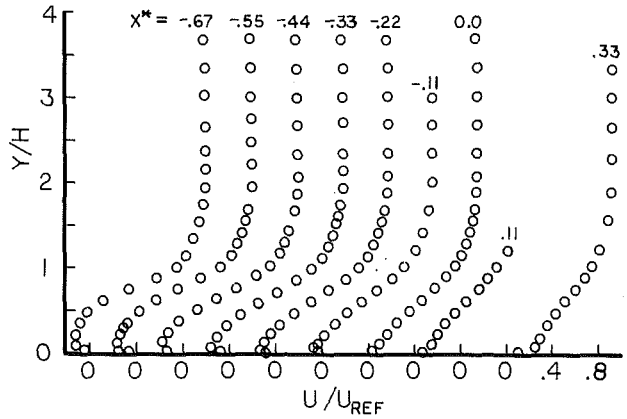

Fig. 7 Mean velocity profiles for reference conditions; most of points near the wall omitted for clarity

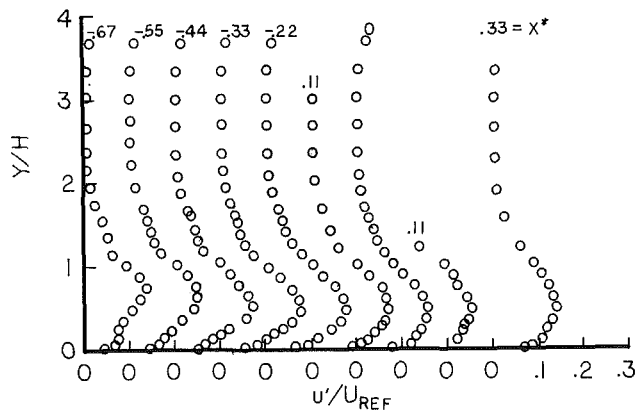

Fig. 8 Streamwise turbulence intensity (u') profiles for reference conditions; most of points near the wall omitted for clarity

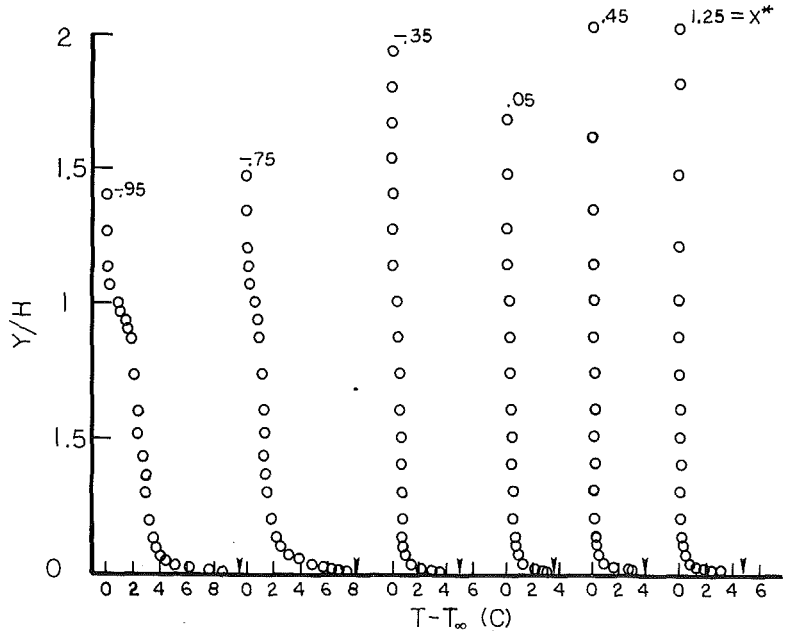

Fig. 9 Temperature profiles for the reference case; arrow indicates the local wall temperature

usual behavior for backstep flow. It is negative in the backflow region of recirculation, passes through zero at reattachment, and then increases downstream. The skin-friction coefficient is slightly positive close to the step edge, indicating the corner eddy. In the recirculation region, the negative skin friction is fairly large, about 50 percent of the far-downstream value.

The fluctuating component of the skin friction is shown in Fig. 11 for the reference Reynolds number and two different boundary-layer thicknesses. Near the backstep, the velocities are low and the flow is not very turbulent. Moving toward reattachment, the flow is very unsteady close to the wall, with the maximum fluctuations in the vicinity of reattachment. The maximum fluctuating component of the skin friction is more than 40 percent of the maximum mean skin friction. Both profiles then relax toward a far-downstream value. The fluctuating skin-friction variation with boundary-layer thickness is discussed in the next section.

Discussion

The peak in the Stanton number around reattachment varies as the -0.4 power of the Reynolds number, while the flat-plate flow Stanton number varies as the -0.2 power of Reynolds number. The exponent for the reattaching flow is similar to that of experiments on impinging jet flows, which show Stanton-number dependence on Reynolds number of -0.42 for a wide range of impingement angles (Kumada et al. [22]). The fairly good collapse of these profiles suggests that the Stanton number scales everywhere on Reynolds number.

In contrast, the Stanton-number profiles changing with the initial thickness of the separated shear layer do not collapse to a single profile when normalized on the maximum value. The Stanton number is nearly independent of boundary-layer thickness in the recirculating flow region and redeveloping boundary layer but varies significantly within the reattachment region. The change in the reattachment length was small for the same thickness variation so the mean flow is probably not substantially changed. The variation in the Stanton number with boundary-layer thickness must therefore be attributed to variations in the turbulent structure.

The question remains: What controls the heat transfer

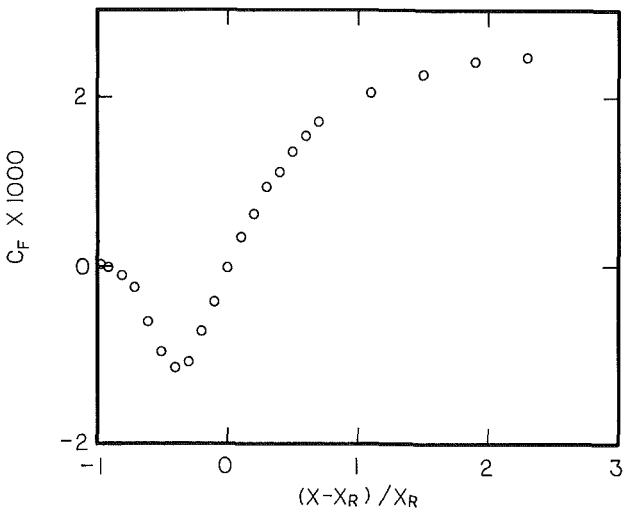

Fig. 10 Mean skin-friction coefficient downstream of the step

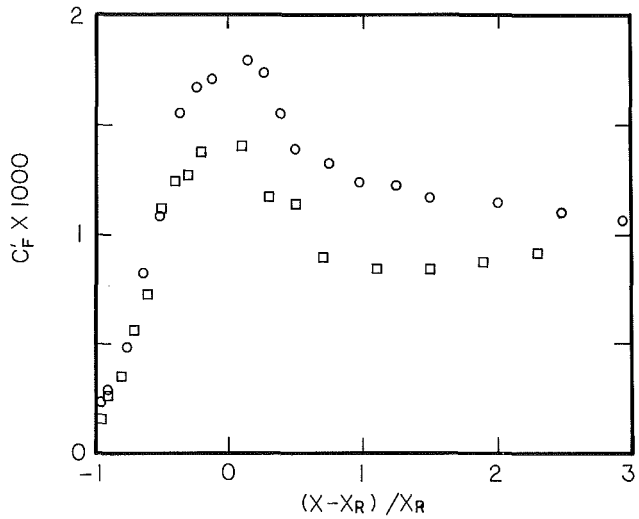

Fig. 11 RMS skin-friction fluctuations for a Reynolds number of 28,000: ○ $\delta/h = 0.15$; □ $\delta/h = 1.1$

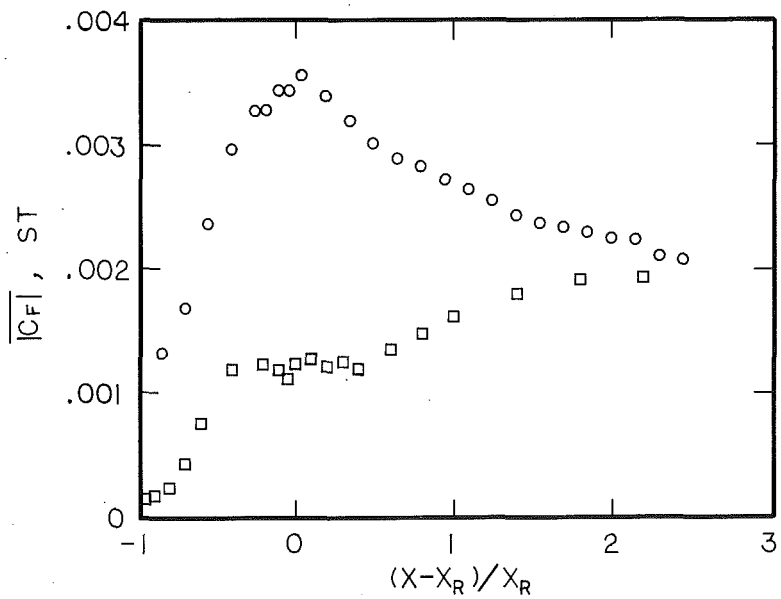

Fig. 12 Comparison of Stanton number and time average of the absolute value of the skin friction for the reference case: ○ St; □ $\overline{|C_f|}$

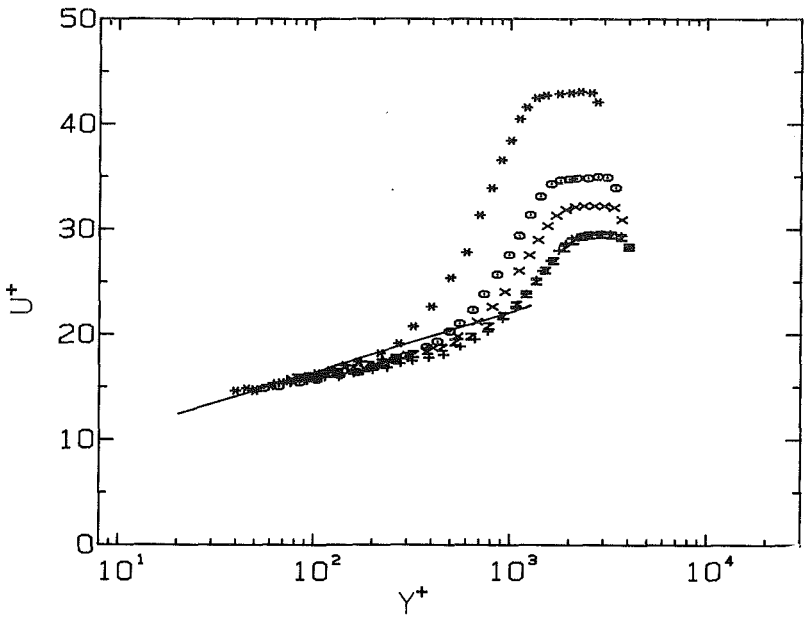

Fig. 13 Mean velocity downstream of reattachment for the reference case: *x/H = 10; ○ x/H = 12; × x/H = 14; z x/H = 16; + x/H = 18

coefficient in the reattachment zone? Obviously, the Stanton number is not determined by the mean flow. The Reynolds analogy fails entirely, since the skin friction passes through zero near the point of maximum Stanton number. It has been suggested that the Reynolds analogy may apply instantaneously in reattaching flows. If that is the case, one would expect the Stanton number to be related to the time average of the absolute value of the skin friction ($\overline{|C_f|}$). This quantity is estimated from the measured mean and fluctuating skin friction by assuming a Gaussian probability distribution for the skin friction. Eaton and Johnston [4] have shown that the probability distribution can be reasonably approximated by a Gaussian distribution near reattachment.

Figure 12 shows the time average of the absolute value of the skin friction and the Stanton-number profile. The agreement between the two curves is poor except well downstream of reattachment, where the thermal boundary layer behaves like that on a flat plate. Downstream of the reattachment zone there are no flow reversals and $\overline{|C_f|}$ is just equal to the mean skin friction. Therefore the data show that the Reynolds analogy does hold in the recovering boundary layer.

The Stanton number can be related to the thickness of the thermal (or hydrodynamic) sublayer. The sublayer is very thin in the reattachment region corresponding to the high Stanton number. The region of high temperature gradient is two to three times thicker in the recirculation region corresponding to the lower Stanton number. Adams, Johnston, and Eaton [17] have shown that the near-wall layer below the recirculating flow grows as a laminar boundary layer for the moderate Reynolds number of this experiment. Such laminar boundary layer growth corresponds to a decrease in the Stanton number moving away from reattachment. Downstream of reattachment the sublayer grows as it would under an unheated starting-length boundary layer. Again, the thickening of the sublayer accounts for the reduction in the Stanton number.

Within the reattachment zone, the Stanton number is apparently controlled by the turbulence level near the wall. The fluctuating skin friction is much higher than under an ordinary boundary layer, because very energetic free-shear-layer eddies are impinging on the wall. The RMS level of the skin-friction fluctuations is determined by the structure of the impinging shear layer. When the upstream layer is thin, the shear-layer turbulence is more energetic and the skin-friction fluctuations are large relative to a thick boundary layer case. The larger skin-friction fluctuations result in a proportionally larger Stanton number.

It is frequently observed that the recovering boundary layer remains disturbed for a long distance downstream of reattachment (cf. Bradshaw and Wong [23]). This observation seems in conflict with the fact that the Stanton number returns quickly to a flat-plate profile. Log plots of the mean-velocity profiles downstream of reattachment (Fig. 13) show that the disturbance in the boundary layer is primarily in the outer part of the log region. The inner part of the boundary layer which controls the heat-transfer resistance is largely undisturbed.

Summary and Conclusions

The present heat transfer measurements are in general agreement with previous experiments; reattachment causes a local augmentation of the heat transfer coefficient by a factor of about two. The maximum heat transfer coefficient occurs slightly upstream of reattachment, where the peak values of the turbulence intensity are measured. The heat transfer coefficient recovers fairly rapidly to flat-plate behavior downstream of reattachment.

As in other turbulent flows the majority of the heat transfer resistance occurs in the near-wall region. Turbulent mixing in the separated free-shear layer is very strong except close to the step. Downstream of $x/h = 2$, there is virtually no temperature gradient across the separated shear layer. The large temperature gradients in the near-wall region point out the importance of understanding this zone if the heat transfer is to be predicted accurately.

In the various regions of the flow, different physical mechanisms act to control the heat transfer coefficient. For example, moving upstream from reattachment, the near-wall layer grows as a laminar boundary layer, thickening as it approaches the center of the recirculation bubble. The thickening of this layer causes the heat transfer coefficient to drop rapidly. Well downstream of reattachment, the near-wall layer behaves like that under an ordinary turbulent boundary layer. The heat transfer coefficient is determined by the local skin friction, and the Reynolds analogy applies.

Within the reattachment region there is essentially no mean

flow in the near-wall region and the effective conductivity of the near wall zone is determined by the intensity of turbulence fluctuations. Variations in the Stanton number correlate well with variations in the rms level of skin friction fluctuations.

Acknowledgments

We thank the Heat Transfer Program of the National Science Foundation for supporting this work (Grant #MEA-8108189). Dr. Win Aung is the responsible program manager.

References

1 Eaton, J. K., "Summary of Computations for Cases 0421, 0431, P2, and P3, Separated Internal Flows," *Proceedings 1980=81 AFOSR-HTTM-Stanford Conference on Complex Turbulent Flows:* Vol. III, *Comparison of Computation and Experiment*, 1982.

2 Eaton, J. K., and Johnston, J. P., "A Review of Research on Subsonic Turbulent Flow Reattachment," *AIAA J.*, Vol. 19, No. 9, Sept. 1981, pp. 1093-1100.

3 Watkins, C. M., and Gooray, A. M., "Numerical Calculations of Turbulent Recirculating Heat Transfer Beyond Two-Dimensional Backsteps and Sudden Pipe Expansions," Dept. of Mech. Engrg., Howard University, Washington, D.C., Aug. 1982.

4 Eaton, J. K., and Johnston, J. P., "Turbulent Flow Reattachment: An Experimental Study of the Flow and Structure Behind a Backward-Facing Step," Rept. MD-39, Dept. of Mech. Engrg., Stanford University, June 1980.

5 Durst, R., and Tropea, C., "Turbulent, Backward-Facing Step Flows in Two-Dimensional Ducts and Channels," *Proceedings of the 3rd International Symposium on Turbulent Shear Flows*, Davis, CA, 1981.

6 Eaton, J. K., Westphal, R. V., and Johnston, J. P., "Two New Instruments for Flow-Direction and Skin-Friction Measurements in Separated Flows," *ISA Transactions*, Vol. 21, No. 1, 1982, pp. 69-78.

7 Westphal, R. V., Eaton, J. K., and Johnston, J. P., "A New Probe for Measurement of Velocity and Wall Shear Stress in Unsteady, Reversing Flow," *J. Fluids Engrg.*, Vol. 102, No. 2, 1981, pp. 478-482.

8 Fletcher, L. S., Briggs, D. G., and Page, R. H., "Heat Transfer in Separated and Reattaching Flows: An Annotated Review," *Israel J. of Tech.*, Vol. 12, 1974, pp. 236-261.

9 Aung, W., and Watkins, C. B., "Heat Transfer Mechanisms in Separated Forced Convection," *Proceedings of the NATO Institute on Turbulent Forced Convection in Channels and Bundles: Theory and Applications to Heat Exchangers*, Turkey, June 20-Aug. 2, 1978.

10 Aung, W., and Goldstein, R. J., "Heat Transfer in Turbulent Separated Flow Downstream of a Rearward-Facing Step," *Israel J. of Tech.*, Vol. 10, 1972, pp. 35-41.

11 Kang, Y., Nishino, J., Suzuki, K., and Sato, T., "Application of Flow Surface-Temperature Visualization Techniques to a Study of Heat Transfer in Recirculating Flow Regions," *Flow Visualization II*, ed. W. Merzkirch, Hemisphere, 1982, pp. 77-81.

12 Suzuki, K., Ida, S., and Sato, T., "Turbulence Measurements Related to Heat Transfer in an Axisymmetric Confined Jet with Laser-Doppler Anemometer," *Proceedings of 4th Symposium on Turbulent Shear Flows*, Karlsruhe, Germany, Sept. 1983, pp. 18.1-18.6.

13 Armaly, B. F., Durst, F., and Kottke, V., "Momentum, Heat and Mass Transfer in Backward-Facing Step Flows," *Proceedings of 3rd Symposium on Turbulent Shear Flows*, Davis, CA, Sept. 1981, pp. 16.1-16.4.

14 Chieng, C. C., and Launder, B. E., "On the Calculation of Turbulent Heat Transport Downstream From an Abrupt Pipe Expansion," *Numerical Heat Transfer*, Vol. 3, 1980, pp. 189-207.

15 Simpson, R. L., "A Model for the Backflow Mean Velocity Profile," *AIAA J.*, Vol. 21, No. 1, 1983, pp. 142-143.

16 Vogel, J. C., and Eaton, J. K., "Heat Transfer and Fluid-Mechanics Measurements in the Turbulent Reattaching Flow Behind a Backward-Facing Step," Report MD-44, Thermosciences Division, Dept. of Mech. Engrg., Stanford University, July 1984.

17 Adams, E. W., Johnston, J. P., and Eaton, J. K., "Experiments on the Structure of Turbulent Reattaching Flow," Report MD-43, Thermosciences Division, Dept. of Mech. Engrg., Stanford University, May 1984.

18 Tarasuk, J. D., and Castle, G. S. P., "Temperature Distribution in an Electrically Heated, Wide, Metallic Foil," ASME JOURNAL OF HEAT TRANSFER, Vol. 105, Feb., 1983, pp. 210-212.

19 Adams, E. W., Eaton, J. K., and Johnston, J. P., "An Examination of Velocity Bias in a Highly Turbulent Separated and Reattaching Flow," *Proceedings of the 2nd Int'l. Symposium on Applications of Laser Anemometry to Fluid Mechanics*, Lisbon, Portugal, July 1984.

20 Kline, S. J., and McClintock, F. A., "Analysis of Uncertainty in Single-Sample Experiments," *Mechanical Engineering*, Jan. 1952.

21 Westphal, R. V., and Johnston, J. P., "Effect of Initial Conditions on Turbulent Reattachment Downstream of a Backward-Facing Step," *AIAA J.*, Vol. 22, No. 12, 1984, pp. 1727-1732.

22 Kumada, M., Mabuchi, I., and Oyakawa, K., "General Correlation of Mass Transfer by Reattached Jet at Stagnation Point on a Plate," *Heat Transfer—Japanese Research*, Vol. 3, Jan. 1974, pp. 93-103.

23 Bradshaw, P., and Wong, F. Y. F., "The Reattachment and Relaxation of a Turbulent Shear Layer," *J. Fluid Mechanics*, Vol. 152, Part 1, 1972, pp. 113-135.

Augmentation of Laminar Flow Heat Transfer in Tubes by Means of Wire Coil Inserts

S. B. Uttarwar

M. Raja Rao

Department of Chemical Engineering,
Indian Institute of Technology,
Bombay 400076, India

Experimental studies have been carried out on isothermal pressure drop and convective heat transfer to servotherm medium grade oil in laminar flow in one smooth tube and seven wire coil-inserted tubes of varying wire diameter and pitch of wire coil. The performance of these wire coil inserted tubes has been evaluated by two different criteria based on the objective of either maximizing heat transfer rate or minimizing exchanger size. The results indicated that as much as fourfold improvement can be obtained in laminar flow heat transfer coefficient using these tubes.

Introduction

Laminar flow heat transfer occurs in a variety of engineering applications and is of particular importance where viscous liquids are heated or cooled. Since the heat transfer coefficients in this type of flow are generally low, there is a need for augmentation. However, as most of the flow problems in industrial exchangers involve turbulent flow region, attention has been directed mainly towards turbulent flow heat transfer augmentation. A very limited amount of literature is however available on laminar flow heat transfer enhancement [1–4], and a review of the published results in this field was recently reported by Bergles and Joshi [8].

Hong and Bergles [1] studied the performance of twisted tape inserted tubes for laminar flow heat transfer and found that the Nusselt number depends on the Reynolds number, Prandtl number, and tape twist ratio. They observed as much as threefold improvement in heat transfer rates using twisted tape insert tubes. Marner and Bergles [2] studied twisted tape insert tubes and internally finned tubes, and observed that both friction factor and heat transfer coefficient increased substantially beyond a particular Reynolds number, at which secondary swirl flow and turbulence were induced in the flowing fluid. Van Rooyen and Kroger [3] studied internally finned tubes with twisted tape inserts and observed fourfold improvement in heat transfer coefficient for cooling runs and threefold improvement for heating runs. Geiger and Mandal [4] conducted an experimental investigation on the effect of roughness on heat transfer and pressure drop for laminar flow of transformer oil in an horizontal annulus. The roughness consisted of conductive and nonconductive fins of varying height and pitch. Their results indicated that conductive fins transfer more heat than nonconductive fins. Furthermore, closely spaced fins transfer more heat than widely spaced fins.

It was observed from the literature that devices which establish swirl in the flowing fluid are particularly attractive augmentative schemes for forced convective systems [1, 2, 5, 6]. Full-length twisted tape as an insert was found to improve heat transfer by 200 percent under the conditions of constant pumping power and fixed basic geometry. Wire coil inserts are also one of the augmentation devices that establish mild swirl flow in the flowing fluid. These have not been studied previously for augmentation of laminar flow heat transfer. The present study was therefore undertaken:

(*i*) To obtain laminar flow heat transfer and friction results for wire coil-insert tubes and to develop correlation for predicting heat transfer coefficients

(*ii*) To compare the heat transfer performance of wire coil-insert tubes with the performance of the smooth tube under similar operating conditions, and thus ascertain effectiveness of these tubes in augmenting laminar flow heat transfer to viscous liquids.

Experimental Work

Tube Configuration. In the present experimental study seven wire coil-insert tubes and one smooth tube were used. The smooth tube was used for calibrating the experimental setup and also to compare the enhancement obtained both in heat transfer and friction factor. All tubes were made of copper material, their dimensions are given in Table 1 and the sketch is presented in Fig. 1.

The coils are prepared to fit tightly inside the copper tubes. The wire coil-inserted copper tube of 25.2 mm i.d. and 28.0 mm o.d. formed the inner tube of a double pipe heat exchanger, with a steel jacket of 52.2 mm i.d. forming the outer tube. The flow diagram of the experimental setup is shown in Fig. 2, and the equipment used includes a coolant liquid pump, a hot water pump, calibrated rotameters for coolant liquid and hot water flow measurement, a U-tube manometer for measurement of pressure drop, thermocouples for measuring temperatures of the tube wall along the length of the heat exchanger tube, and also precision 0.1°C accurate thermometers for measuring inlet and outlet temperatures of coolant liquid and hot water. The test section was insulated heavily to minimize heat losses to the surroundings.

Servotherm oil, a medium grade oil of Hindustan Petroleum Corporation, India, having the properties given in Table 2, was used as a test liquid.

Experimental Procedure. The isothermal friction studies were conducted at 30°C in 1500-mm-long tubes of dimensions listed in Table 1, for laminar flow of servotherm oil inside the inner tube.

Heat transfer studies were conducted for heating of the servotherm oil inside the inner tube ($L = 1500$ mm) of the concentric pipe heat exchanger, using hot water (as heating

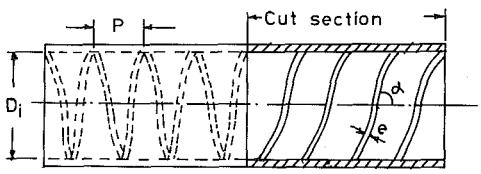

Fig. 1 Characteristic parameters of the wire coil-insert tubes

Contributed by the Heat Transfer Division for publication in the JOURNAL OF HEAT TRANSFER. Manuscript received by the Heat Transfer Division September 2, 1983.

Table 1 Characteristic dimensions of wire coil insert tubes

Tube no.	D_i mm	D_o mm	e mm	p mm	D_e mm	L mm	(L/D_e)	α deg
0	25.2	28.0	0	∞	25.2	1500	59.5	—
1	25.2	28.0	2.0	66.0	22.3	1500	67.3	32
2	25.2	28.0	2.0	38.0	21.3	1500	70.4	46
3	25.2	28.0	2.0	22.0	19.8	1500	75.8	61
4	25.2	28.0	2.0	10.0	16.0	1500	93.8	76
5	25.2	28.0	3.4	66.0	20.2	1500	74.3	32
6	25.2	28.0	3.4	38.0	18.6	1500	80.7	46
7	25.2	28.0	3.4	22.0	15.8	1500	94.9	61

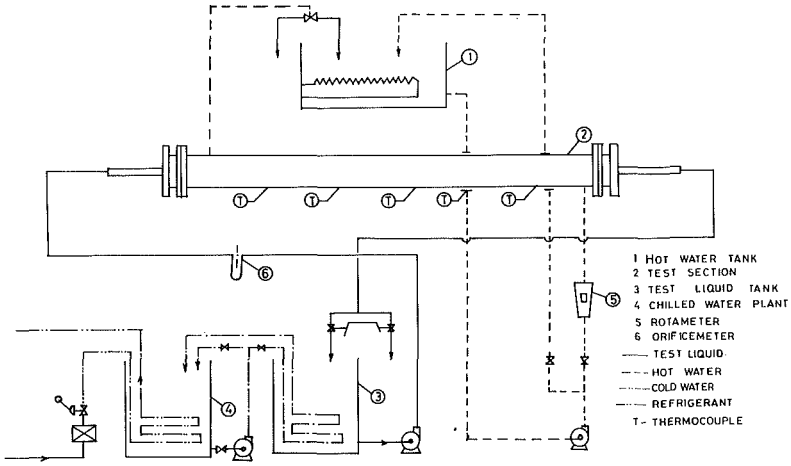

Fig. 2 Schematic diagram of experimental setup

medium) flowing in highly turbulent flow (at essentially constant temperature) in the annulus of the heat exchanger so as to give constant metal wall temperature. Besides the measurement of temperatures of all the incoming and outgoing hot and cold fluids, wall temperature was also measured with a view to evaluate the individual inside film heat transfer coefficient of the test liquid. The uncertainties in the measured friction factor f and h_i are ± 3 percent and ± 6 percent, respectively.

Results and Discussion

Friction Factor. The Fanning friction factor was calculated from the equation

$$f = \frac{D\Delta P g_c}{2\rho L V^2} \tag{1}$$

The smooth tube laminar flow friction factors were well correlated by the equation

$$f = \frac{16}{\mathrm{Re}} \tag{2}$$

for the range studied, $30 < \mathrm{Re} < 2000$, with a standard deviation of 2.7 percent, and this served the purpose of calibration of the experimental setup.

The laminar flow friction factors for the wire coil-inserted tubes were found to increase substantially when these tubes replaced the smooth tube. Figure 3 shows the variation of f

Nomenclature

A = area, m^2
C_p = specific heat, KJ/kg K
D_i = tube inside diameter, m
D_e = equivalent diameter, $\left(\frac{4 \times \text{volume of free space for flow}}{\text{Total wetted surface}}\right)$
e = roughness height, wire diameter, m
f = friction factor, $2\tau_w g_c/\rho v^2$
Gz = Graetz number, WC_p/KL
h_i = tube inside heat transfer coefficient, W/m^2 K
K = thermal conductivity, W/mK
L = length, m
Nu = Nusselt number, $h_i D_i/K$
P = pitch of wire coil insert
Pr = Prandtl number, $C_p\mu/K$
ΔP = pressure drop, Pa
Q = heat load W
Re, Re_{De} = Reynolds number, $D_i V\rho/\mu$, $DeV\rho/\mu$
U = overall heat transfer coefficient, W/m^2 K
V = bulk average velocity, m/s
W = mass flow rate kg/s

Greek Letters

α = helix angle, deg
μ = viscosity, Pa•s
ρ = fluid density, kg/m^3
τ = shear stress, Pa

Subscripts

a = augmented tube
c = cold stream
h = hot stream
o = smooth tube
w = wall
x = cross section

Table 2 Properties of servotherm medium oil

Property	Temperature			
	30°C	40°C	50°C	60°C
Viscosity, Pa•s	0.040	0.027	0.0192	0.0155
Sp. heat, $\frac{kJ}{kg\ K}$	1.865	1.907	1.943	1.964
Thermal cond, $\frac{W}{mk}$	0.1329	0.1322	0.1317	0.1311
Density kg/m^3	866.5	847.0	827.0	807.0

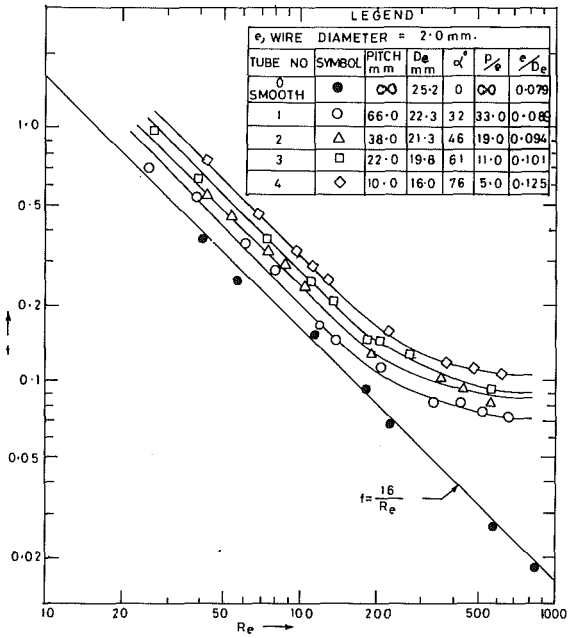

Fig. 3 Variation of friction factor with Reynolds number for isothermal laminar flow of servotherm oil inside one smooth and four wire coil inserted tubes

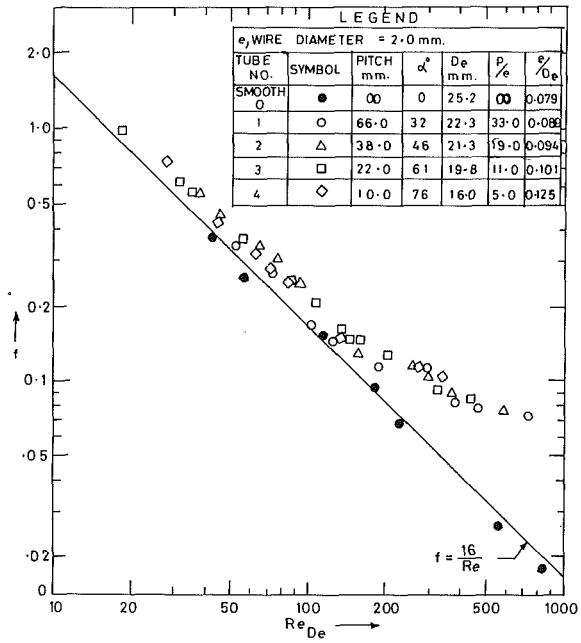

Fig. 4 Variation of friction factor with Reynolds number based on equivalent diameter for isothermal laminar flow of servotherm oil inside one smooth and four wire coil inserted tubes

with Re for four wire coil-inserted tubes (i.e., tubes 1, 2, 3, and 4) and the smooth tube. It is clear from the figure that at lower Re, increase in the friction factors is comparatively low, and at higher values of Re, it is very large. This can be explained by the fact that at lower values of Reynolds number corresponding to lower flow rates, liquid just passes over the wire coil and the increase in the friction factor is due to the presence of small vortices behind the wire.

However, as the flow rate (and hence Re) is increased, a secondary flow and hence some turbulence is induced in the flowing fluid due to the presence of wire coil, which gives rise to higher increase in the friction factors. A similar trend was also observed in the case of tubes 5, 6, and 7. The foregoing observation was similar to the one Marner and Bergles [2] made earlier for twisted tape insert tube and internally finned tubes, and of Hong and Bergles [1] for twisted tape insert tubes.

When plotted against Re_{De}, the friction factor values were found to lie closer to the smooth tube line, $f = 16/Re$, (showing only 5–8 percent increase) up to $Re_{De} = 180$ (Fig. 4). This clearly suggests that on using equivalent diameter in Re, wire coil-insert tubes behaved essentially like a smooth tube at lower flow rates. The equivalent diameter De in the present work is calculated as four times the ratio of volume of free space available for flow to the total wetted surface of tube wall and the insert.

Transition from laminar to turbulent flow occurs at a lower Reynolds number in the wire coil-insert tube than in a smooth one. The presently observed critical Reynolds number of 200 for wire coil-insert tubes can be compared to a value of 1000 observed by Blumenkrantz and Taborek for Turbotech spirally grooved tube.

Heat Transfer. The tube side heat transfer coefficient was calculated by the following equation

$$Q_c = h_i A_i (T_w - T_c)_{im} \tag{3}$$

and an average of inlet and outlet bulk temperatures was used to calculate the property values of the test liquid.

The inside heat transfer coefficient h_i, calculated in terms of Nusselt number $(h_i D_i/K)$, was plotted against Re_{De} in Fig. 5 for tubes 1, 2, 3, and 4 and for the smooth tube, for laminar flow of servotherm oil. Experimental values of Nusselt number for laminar flow of water and servotherm oil agreed closely within 4 percent of the values predicted by Sieder–Tate equation

$$\mathrm{Nu} = \left(\frac{h_i D_i}{K}\right) = 2{\cdot}0\left(\frac{WC_p}{KL}\right)^{1/3}\left(\frac{\mu_b}{\mu_w}\right)^{0.14} \tag{4}$$

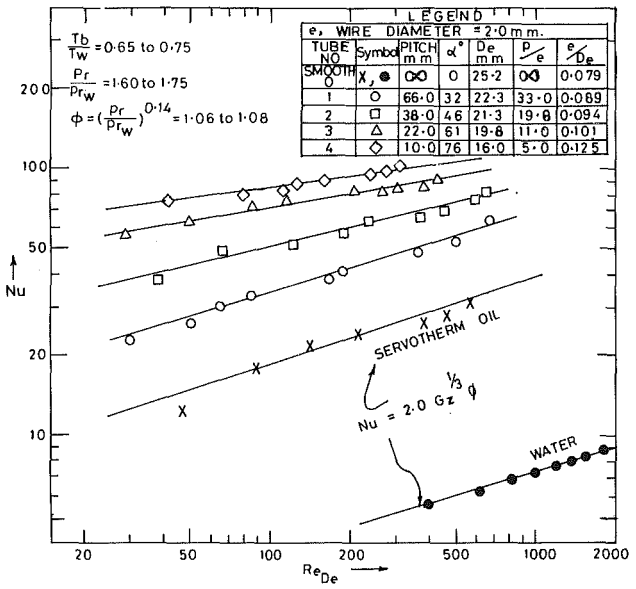

Fig. 5 Variation of Nusselt number with Reynolds number based on equivalent diameter for laminar flow heating of servotherm oil inside one smooth tube and four wire coil inserted tubes

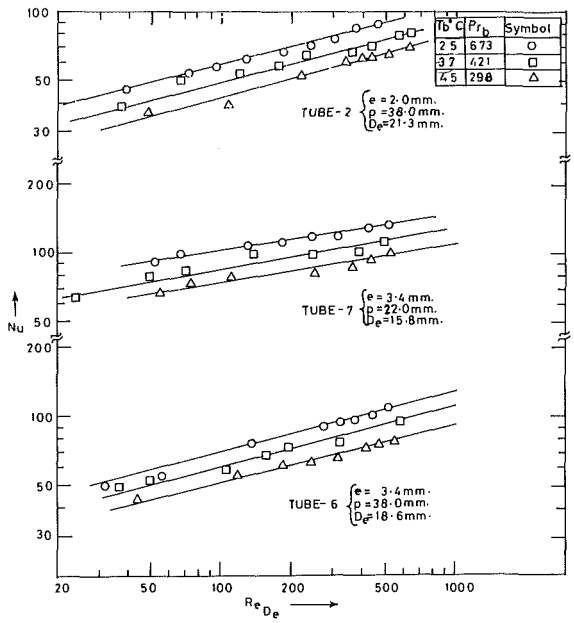

Fig. 6 Variation of Nusselt number with Reynolds number based on equivalent diameter for heating of servotherm oil in three wire oil insert tubes for three different Prandtl numbers

From Fig. 5, it can be seen that the enhancement in Nusselt number for servotherm oil was as high as 350–400 percent for tube 4 and about 100 percent for tube 1. Similarly, the enhancement was about 300 to 350 percent for tube 7 (figure not shown) and about 150 percent for tube 5.

The increase in heat transfer coefficient in wire coil-insert tubes between 150 to 400 percent, depending on the wire coil insert, cannot be accounted for by the increase in heat transfer surface, which was only of the order of 10 to 40 percent. Temperature profile effects in the wall region may be responsible for the marked enhancement in the heat transfer coefficient.

Analysis of the experimental results indicates that the natural convection contribution to heat transfer was negligible due to the high oil viscosities and low Grashof numbers.

Because the value of μ_b/μ_w is around 1.60 to 1.75 in the present work, the viscosity correction factor $\phi[=(\mu_b/\mu_w)^{0.14}]$ is close to 1.0 (=1.06 to 1.08 only), assuming 0.14 as exponent of (μ_b/μ_w) for the rough tubes.

In order to study the effect of Prandtl number, servotherm oil was heated in the test exchanger tube for three different inlet temperatures of 25, 35, and 45°C so as to obtain bulk mean temperatures, corresponding to Prandtl numbers in the range of 300 to 675. Figure 6 shows the variation of Nusselt number with Re_{De} for the three tubes 2, 6 and 7 and for the three different Prandtl numbers of 298, 421, and 673. An analysis of these results showed that Nu varied with 0.35 power of Pr.

It is evident from Figs. 5 and 6 that the Nusselt number for the wire-coil-insert tube is a function of Reynolds number Re_{DE} coil helix angle α and Prandtl number Pr as given by the equation.

$$\mathrm{Nu} = C\mathrm{Re}^{m}\mathrm{Pr}^{0.35},\phi \tag{5}$$

The slopes of the straight lines m obtained on Nu-Re_{De} logarithmic plots were determined and it was found possible to correlate m with helix angle of the wire coil insert as given below

$$m = 0.25\,(\tan\alpha)^{-0.38} \tag{6}$$

The coefficient C was plotted against $\tan\alpha$ in Fig. 7 and the variation of C with $\tan\alpha$ is represented by

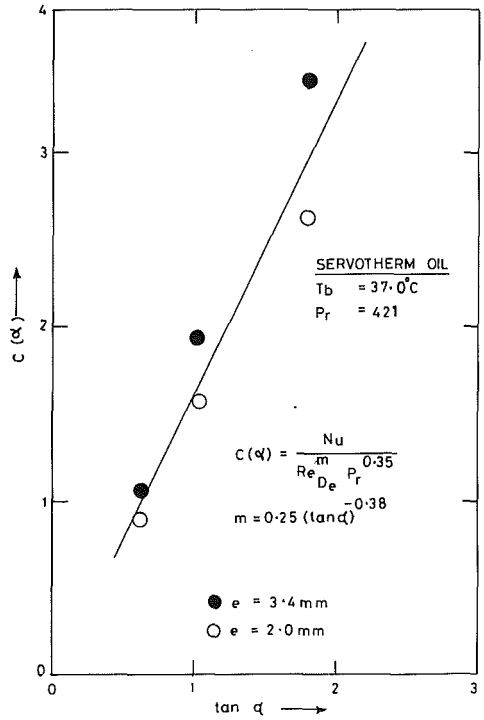

Fig. 7 Variation of $C(\alpha)$ with tan α for two sets of wire coil inserted tubes

$$C(\alpha) = 1.65\tan\alpha \tag{7}$$

The final correlation was obtained for the Nusselt number in wire coil-insert tubes

$$\mathrm{Nu} = 1.65\tan\alpha(\mathrm{Re}_{De})^{[0.25(\tan\alpha)^{-0.38}]}(\mathrm{Pr})^{0.35}\phi \tag{8}$$

The Nusselt numbers predicted from equation (8) agreed with the experimental values with a standard deviation of 7.5 percent for all the tubes except for tube 4 with $\alpha = 76$ deg.

Equation (8) is applicable for the following limits of the variables and it cannot be used for α greater than 61 deg, as for tube 4 with $\alpha = 76$ deg

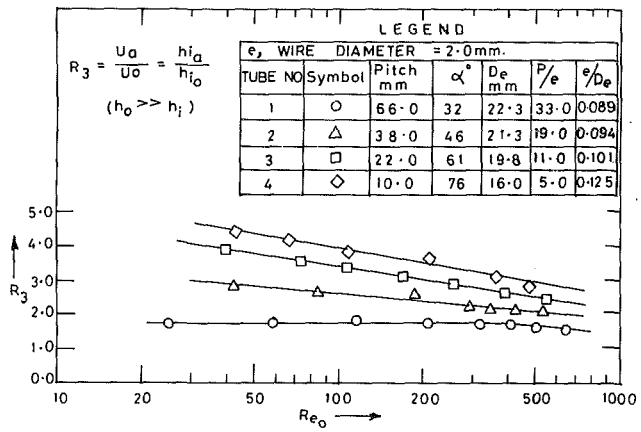

Fig. 8 Thermal performance of four wire coil insert tubes compared with smooth tube, based on criterion 3, for laminar flow heating of servotherm oil

$$2.0\text{ mm} < e < 3.4\text{ mm}.$$

$$32 < \alpha < 61\text{ deg}$$

$$300 < \text{Pr} < 675$$

$$30 < \text{Re} < 700$$

$$15.8\text{ mm} < De < 25.2\text{ mm}$$

$$59.5 < L/De < 95.0$$

Overall Tube Performance. Bergles et al. [7] outlined several practical criteria for evaluation of the performance of augmented tubes, relative to a smooth tube, and performance ratios based on all the criteria have been worked out for turbulent flow of the tube side fluid. No published information is available on the application of these criteria for laminar flow heating and cooling of fluids in enhanced tubes. In the present work, expressions for the performance ratios R_3 and R_5 have been developed for criteria 3 and 5. Criterion 3 aims at improving the heat duty for the case of constant pumping power and for constant basic geometry of the exchanger, and R_3 was evaluated as (h_{ia}/h_{io}) instead of (U_a/U_o) in view of the fact that the ratio γ of combined outside film and metal wall resistance to the inside film resistance is insignificant. This is because of the outside water film coefficient ($h_o = 3500$ to 4000 W/m^{2}K) is 10 to 15 times greater than the inside oil film coefficient ($h_i = 150$ to 450 W/M^{2}K), and the combined outside film and metal wall resistance is negligibly small, compared to the inside oil film resistance.

Criterion 3. The performance ratio R_3 is given by

$$R_3 = \left(\frac{U_a}{U_o}\right) Di, L, N, P, Ti, \Delta T_{im}. \tag{9}$$

For equal pumping power in smooth and augmented tubes

$$A_{xo}\, f_o \text{Re}_o{}^3 = A_{xa}\, f_a \text{Re}_a{}^3 \tag{10}$$

For laminar flow, the friction factor f_o in a smooth tube is given by,

$$f_o = \frac{16}{\text{Re}_o} \tag{11}$$

On substitution for f_o in equation (10), and on simplification, we get

$$\text{Re}_o = \left[\frac{f_a \text{Re}_a{}^3 A x_a}{16 A x_o}\right]^{1/2} \tag{12}$$

Knowing Re_o, the corresponding U_o for the smooth tube is obtained. R_3 then becomes

$$R_3 = \frac{U_a \text{ at } \text{Re}_a}{U_o \text{ at } \text{Re}_o} \tag{13}$$

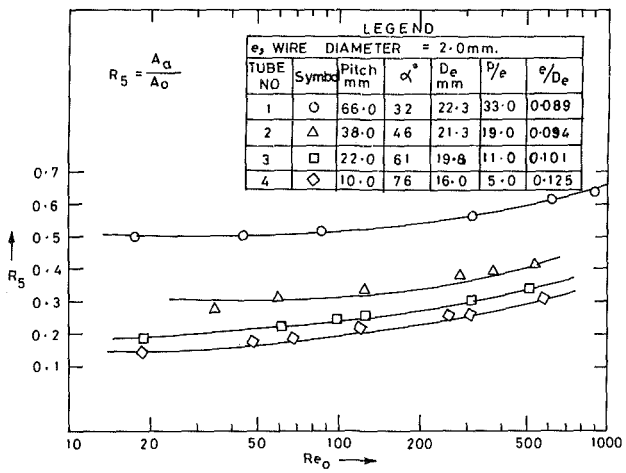

Fig. 9 Thermal performance of four wire coil insert tubes compared with smooth tube, based on criterion 5, for laminar flow heating of servotherm oil

Criterion 5. This criterion aims at reducing the heat transfer area under the constraints of fixed heat duty and fixed pumping power. The performance ratio R_5 is given by

$$R_5 = \left(\frac{A_a}{A_o}\right)_{q,P,Di,Ti,\Delta T_{im}} \tag{14}$$

For equal pumping power

$$\frac{A_{xa}}{A_{xo}} = \frac{f_o \text{Re}_o^3}{f_a \text{Re}_a^3} \quad \text{Also} \quad \frac{A_{xa}}{A_{xo}} = \frac{\frac{\pi}{4} D_e^2}{\frac{\pi}{4} D_i{}^2} = \frac{A_a \cdot D_e}{A_o \cdot D_i} \tag{15}$$

$$\frac{A_a}{A_o} = \frac{f_o \text{Re}_o^3 D_i}{f_a \text{Re}_a^3 D_e} = \frac{16}{\text{Re}_o} \frac{\text{Re}_o^3 D_i}{f_a \text{Re}_a^3 D_e} \tag{16}$$

For equal heat duty

$$\frac{A_a}{A_o} = \frac{hi_o}{hi_a} = \frac{\text{Nu}_o}{\text{Nu}_a} = 2.(\text{Gz})^{1/3} (\mu_b/\mu_w)^{0.14} \tag{17}$$

Equating (16) and (17),

$$\frac{16}{\text{Re}_o} \cdot \frac{\text{Re}_o^3 D_i}{f_a \text{Re}_a^3 D_e} = 2(\text{Re}_o)^{1/3} \text{Pr}^{1/3} \left(\frac{\pi}{4}\right)^{1/3} \left(\frac{D_i}{L}\right)^{1/3} \frac{(\mu_b)^{0.14}}{\mu_w} \tag{18}$$

Rearranging, we get

$$\text{Re}_o = \left[\frac{0.114 f_a \text{Re}_a^3 \cdot \text{Pr}^{1/3} De (\mu_b/\mu_w)^{0.14}}{(L)^{1/3} \cdot D_i^{2/3} \cdot \text{Nu}_a}\right]^{0.60} \tag{19}$$

Knowing the values of f_a, Re_a, and Nu_a, the equivalent smooth tube Reynolds number Re_o can be calculated. Knowing hi_o at this value of Re_o, and hi_a at Re_a, the performance ration R_5 can be found as follows

$$R_5 = \frac{A_a}{A_o} = \frac{hi_o \text{ at } \text{Re}_o}{hi_a \text{ at } \text{Re}_a} \tag{20}$$

R_5 can be taken as U_o/U_a, if h_o is very very large, compared to h_i, as observed in the present work.

Figure 8 shows the variation of the performance ratio R_3 with equivalent smooth tube Reynolds number Re_o. Amongst tubes 1, 2, 3, and 4 which are all made up of wire coil of wire diameter 2.0 mm, tube 4 shows an improvement of 350 percent in heat transfer coefficient at lower values of Re_o, compared to 200 percent only at higher Re_o values, while tube 1 shows the least improvement of only 50 to 70 percent, over the entire Re_o range. An important observation about these tubes is that R_3 values improve greatly as the helix angle (α) is

increased or the pitch of the wire coil is reduced. A similar trend is also observed for tubes 5, 6, and 7, which are inserted with wire coils of wire diameter 3.4 mm. Tube 7, with a helix angle of 61 deg for the wire coil, shows an improvement of 150 to 340 percent, while tube 5 shows an improvement of only 50 to 90 percent. It was found that wire diameter has insignificant effect on R_3 values; wire coil inserted tube of the same helix angle but of higher wire diameter gave only 5 to 15 percent more improvement. For all the wire coil-insert tubes studied, performance ratio based on the criterion 3 was generally found to decrease with an increase in Re_o. This trend was also observed earlier by Marner and Bergles [2].

The performance ratio based on criterion 5 is plotted in Fig. 9 for tubes 1, 2, 3, and 4. This figure shows that a reduction as high as 70 to 80 percent can be obtained in heat transfer area using tube 4, while the reduction is only about 50 percent for tube 1. Again the reduction was found to be more pronounced at lower Re_o values and that too for the tubes with wire coil inserts of higher helix angle. Here again the effect of wire diameter was found to be insignificant for tubes of the same helix angles but of the two different wire diameters studied. When compared with each other, coils of the higher wire diameter showed only 5 to 10 percent more reduction in heat transfer area.

In general, it was observed that tubes with a higher helix angle of wire coil insert perform better than the tubes with a lower helix angle. Thus these tubes are better suited for laminar flow heating of viscous liquids at lower flow rates.

Conclusions

An experimental study has been conducted to investigate heat transfer augmentation by means of wire coil-insert tubes. The heat transfer results indicate that Nusselt number is a function of the helix angle, Reynolds number, and Prandtl number. The final correlation is given by equation (8).

The pressure drop results indicate that the friction factor increase is somewhat low at lower flow rates, but at higher flow rates swirl flow increases the friction factor to a much greater extent. The friction factor correlation $f = 16/\mathrm{Re}_{Dc}$ is useful for estimating pressure drop for Re_{De} values less than 200.

When compared with a smooth tube at constant pumping power and constant basic geometry, an improvement as high as 350 percent was obtained in heat capacity and a reduction in heat exchanger area of about 70 to 80 percent can be achieved using wire coil-insert tubes. Also the performance of these tubes is better at lower flow rates, indicating that they are better suited for laminar flow heating of viscous liquids at low Reynolds number Re_{De} less than 200.

An important feature observed in the case of laminar flow heat transfer augmentation is that the net improvement in the heat transfer coefficient is much higher than that observed for turbulent flow heat transfer. This is clear from the fact that the earlier work of Sethumadhavan [6] on wire coil-insert tubes for turbulent flow showed only 30 to 50 percent improvement in heat transfer coefficient as compared to the presently reported improvement of 350 percent for laminar flow heat transfer in wire coil-insert tubes, based on criterion 3.

References

1 Hong, S. W., and Bergles, A. E., "Augmentation of Laminar Flow Heat Transfer by Means of Twisted Tape Inserts," ASME JOURNAL OF HEAT TRANSFER, Vol. 98, 1978, pp. 251–256.

2 Marner, W. J., and Bergles, A. E., "Augmentation of Tube Side Laminar Flow Heat Transfer by Means of Twisted Tape Inserts, Static Mixer Inserts and Internally Finned Tubes," *Proc. of Sixth Int. Heat Transfer Conference* (Toronto), Vol. 2, Hemisphere Publishing, Washington, D.C., 1978, pp. 583–588.

3 Van Rooyen, R. S., and Kroger, D. G., "Laminar Flow Heat Transfer Augmentation in Internally Finned Tubes With Twisted Tape Inserts," *Proc. of Sixth Int. Heat Transfer Conference* (Toronto), Vol. 2, Hemisphere Publishing, Washington, D.C., 1978, pp. 578–581.

4 Geiger, G. E., and Mandal, S. K., "Heat Transfer and Friction Factors of High Prandtl Number Laminar Flow Through an Annulus With Circumferential Fins," *Proc. of Sixth Int. Heat Transfer Conference* (Toronto), Vol. 2, Hemisphere Publishing, Washington, D.C., 1978, pp. 607–611.

5 Gupta, R. K., and Raja Rao, M., "Heat Transfer and Friction Characteristics of Newtonian and Power Law Fluids in Smooth and Spirally Corrugated Tubes," *Advances in Enhanced Heat Transfer*," ASME/AIChE, New York, 1979, pp. 103–113.

6 Sethumadhavan, R., "Studies in High-Performance Heat Exchange Surfaces," Ph.D. dissertation, 1982, I.I.T., Bombay, India.

7 Bergles, A. E., Blumenkrantz, A. R., Taborek, J., "Performance Evaluation Criteria for Enhanced Heat Transfer Surfaces," *Proc. of Fifth Int. Heat Transfer Conference* (Tokyo), Vol. 2, 1974, pp. 239–243.

8 Bergles, A. E., and Joshi, S. D., "Augmentation Techniques for Low Re in Tube Flow," *Low-Reynolds Number Flow Heat Exchangers*, edited by S. Kakac, R. K. Shah and A. E. Bergles, Hemisphere, Washington, D.C. 1983.

The Exchange Factor Method: An Alternative Basis for Zonal Analysis of Radiating Enclosures[1]

M. E. Larsen
Fluid Mechanics and Heat Transfer Division 1513, Sandia National Laboratories, Albuquerque, NM 87185

J. R. Howell
Mechanical Engineering Department, The University of Texas at Austin, Austin, TX 78712
Fellow ASME

In zonal analysis of an enclosure containing a radiatively participating medium, the volume and bounding surface are divided into volume and area elements which are assumed to be isothermal. For a system of M *elements consisting of* N *surfaces and* Γ *volume elements* ($M = N + \Gamma$), M^2 *relationships (direct- or total-exchange areas of conventional zonal analysis) define all possible radiant interchange between element pairs. Due to reciprocity there are at most* $M(M + 1)/2$ *unique direct-exchange areas. The use of symmetry may greatly reduce the number of unique exchange areas. In the alternative form presented, exchange factors are defined such that a gray medium's gas-to-gas exchange factors describe only the redistribution of radiative source terms. Only surface-to-surface and surface-to-gas (gas-to-surface) relationships are required to wholly define the system in radiative equilibrium. That is, a system in radiative equilibrium may be characterized by as many as* $\Gamma(\Gamma + 1)/2$ *fewer factors. These same exchange factors may be augmented by gas-to-gas exchange factors to analyze media not in radiative equilibrium. In an isotropically scattering, gray medium, exchange factors are functions of system geometry and total extinction only. The degree of extinction due to scattering does not affect exchange factors. Transformations between direct-exchange areas and exchange factors are developed.*

Introduction

Earliest references to the zone method are usually credited to Hottel [1]. However, the first description of a zonal analysis which resolves temperature distributions in the region being analyzed was given by Hottel and Cohen [2]. The method is extended to the treatment of isotropically scattering media in [3]. A most useful and comprehensive description of zonal analysis is given in [4]. Zonal modeling results in the reduction of the governing integral radiant exchange equations to algebraic equations, the coefficients of which embody the opticogeometric properties of the system. References [2–4] discuss direct-exchange areas, their use to construct total-exchange areas, and finally, temperature-dependent weighting of total-exchange areas to effect nongray gas modeling.

The present work briefly summarizes past work in zonal analysis and identifies an alternative basis by which zonal analysis of gray media may be accomplished. Exchange factors are defined and related to direct-exchange areas. The motivation of the present work is the difficulty in evaluating direct-exchange areas in systems of arbitrary geometry. Current methods which treat multidimensional radiation in participating media are difficult to apply to arbitrary geometries. The invariance of exchange factors with scattering albedo, for a system of specified total extinction, suggests the possibility of measuring exchange factors. Such measurements and the difficulties and expected accuracy in carrying them through have been reported in [5]. The exchange factors of a system containing an absorbing/emitting, gray medium are the same as those of its scale model containing an isotropically scattering medium of the same total extinction. The present contribution relates exchange factors to conventional zonal exchange areas, develops analogous reciprocity and conservation relations, and discusses the physical interrelationships between the methods.

[1]A portion of this work was completed at Sandia National Laboratories, supported by the U.S. Department of Energy under contract number DE-AC04-76DP00789.

Contributed by the Heat Transfer Division for publication in the JOURNAL OF HEAT TRANSFER. Manuscript received by the Heat Transfer Division June 5, 1984.

Conventional Zonal Analysis

The basic building blocks of zonal analysis are direct-exchange areas which are defined for a gray, isotropically scattering gas as follows

$$s_i s_j = \frac{1}{\pi}\int_{A_j}\int_{A_i} \frac{\tau(S_{ij})\,\cos(\theta_i)\,\cos(\theta_j)}{S_{ij}^2}\,dA_i dA_j \tag{1}$$

$$s_i g_\gamma = \frac{K_t}{\pi}\int_{V_\gamma}\int_{A_i} \frac{\tau(S_{i\gamma})\,\cos(\theta_i)}{S_{i\gamma}^2}\,dA_i dV_\gamma \tag{2}$$

and

$$g_\mu g_\gamma = \frac{K_t^2}{\pi}\int_{V_\mu}\int_{V_\gamma} \frac{\tau(S_{\mu\gamma})}{S_{\mu\gamma}^2}\,dV_\gamma dV_\mu \tag{3}$$

Symbol definitions are given in the nomenclature. The physical dimension of equations (1–3) is area and each direct-exchange area defines the relative "connectedness" of one element to another. For a gray, isotropically scattering medium $\tau = \exp(-K_t S)$, $K_t = a + \sigma$, and reciprocity requires:

$$s_i s_j = s_j s_i \tag{4}$$

$$s_i g_\gamma = g_\gamma s_i \tag{5}$$

and

$$g_\gamma g_\mu = g_\mu g_\gamma \tag{6}$$

Given the direct-exchange areas of a system, energy balances may be written for surface and volume elements of the system as:

Surface elements:

$$[AI]\bar{W} = [\epsilon AI]\overline{E_s} + [\rho I]\{[ss]^T\bar{W} + [gs]^T\overline{E_g}\} \tag{7}$$

Note that the energy balances represented by equation (7) are not true energy balances, but a statement that surface radiosity is composed of emitted and reflected radiation, because these balances hold regardless of whether other heat transfer mechanisms are present.

Volume elements:

$$[4aVI]\overline{E_g} = [sg]^T\bar{W} + [gg]^T\overline{E_g} + \bar{Q} \tag{8}$$

The energy emitted by a volume element must equal that

absorbed from surfaces and other volume elements (and itself, i.e., $g_\gamma g_\gamma \neq 0$), plus radiant sources from other heat transfer modes or generation. Equations (7) and (8) represent M linear (given $\bar{Q}$) equations and they may be solved for $\bar{W}$ and $\overline{E_g}$. If $Q = f(T)$, as is ordinarily the case, we have nonlinear algebraic equations. When $\bar{W}$ and $\overline{E_g}$ are known, the surface element net radiant heat fluxes may be found from

$$[AI]\overline{q_s''} = \{[ss]^T - [AI]\}\bar{W} + [gs]^T\overline{E_g} \tag{9}$$

Equations (7–9) illustrate the assembly of direct-exchange areas to perform zonal analysis of a nonscattering, gray gas. Consideration of equations (8) and (9) for an isothermal, black-walled enclosure leads to the conservation constraints

$$\overline{4aV} = [sg]^T\,\bar{1} + [gg]^T\,\bar{1} \tag{10}$$

and

$$\bar{A} = [ss]^T\,\bar{1} + [gs]^T\,\bar{1} \tag{11}$$

Direct-exchange areas for systems composed of cubic volume elements are presented in graphic form by Hottel and Cohen [2]. Those for a system of cylindrical coordinates are tabulated in [4]. Becker [6] has contributed a technique for the evaluation of equation (2) for rectangular parallelepiped volume elements. Edwards and Balakrishnan [7] have documented a simplified technique for the evaluation of equation (3) between cube-shaped volume elements which incorporates transmittance models other than Beer's law. The evaluation of equations (1-3) poses little problem with modern computational equipment if the system elements are readily defined by an orthogonal coordinate system. However, it can become computationally expensive. For enclosures of arbitrary geometry the challenge increases substantially and for these cases Monte Carlo techniques are often required. As outlined in [8] all the direct-exchange areas of a system can be found from the definition for $s_i s_j$ by repeatedly placing fictitious surfaces about volume elements of the system and using the conservation requirements. An alternative form of equation (1) is the product of the sending element's area, the conventional view-factor between the sending and receiving area elements, and a mean geometric transmittance. Such an approach allows use of transmission models other than Beer's Law in zonal analysis as suggested in [8]. The works of [7] and [8] consider nongrayness in the evaluation of direct-exchange areas, an alternative to weighting total-exchange areas of multiple gray gases.

In practice it is convenient to analyze nonlinear systems with total-exchange areas. As described in [2–4] radiosities may be eliminated from the balances when direct-exchange areas are converted to total-exchange areas which incorporate the direct and reflected paths between system elements. Noble [9] has documented matrix operations to perform the transformations from direct-exchange areas to total-exchange areas which account for isotropic scatter as discussed in [3–4]. When some of the enclosure surface elements are black, corresponding reductions of the order of the matrices handled in Noble's transformations are realized. Hottel and Sarofim [4] accomplish the same transformations by physical arguments in which the enclosure problem is solved repeatedly (using direct-exchange areas) with each surface or volume element in turn serving as the system's sole emitter. The transformation to total-exchange areas serves to eliminate radiosities from equations (7) and (8) and they are replaced by

$$(1-\omega_0)[4K_t VI]\overline{E_g} = [GG]^T\overline{E_g} + [SG]^T\overline{E_s} + \bar{Q} \tag{12}$$

and,

$$[AI]\overline{q_s''} = [SS]^T\overline{E_s} + [GS]^T\overline{E_g} - [\epsilon AI]\overline{E_s} \tag{13}$$

Conservation constraints analogous to those of equations (10) and (11) are apparent when equations (12) and (13) are considered for an isothermal enclosure. Note that for the case of the black-walled enclosure and no scattering, total-exchange areas and direct-exchange areas are identical since no reflection paths are present.

The Exchange Factor Method

The exchange factor method defines an alternative basis for zonal analysis of gray media which is effectively a complement to total-exchange areas. While total-exchange areas allow for transmission of energy which travels unabsorbed along direct and reflected (including scatter) paths between elements, exchange factors account for direct paths and paths created by absorption and re-emission, and/or isotropic scattering, but do not include paths created by reflections at the system boundary. Perlmutter and Howell [10, 11] used a similar concept when they found solutions for geometries bounded by two black surfaces and extended them to gray-walled enclosures of the same geometry. We begin by stating definitions of exchange factors

Nomenclature

a = absorptivity, m^{-1}
A = area, m^2
E = emissive power
$\overline{FSS}, \overline{FSG}, \overline{FGS}, \overline{FGG}$ = exchange factors defined in text
gg, gs, sg, ss = direct-exchange areas (equations (1-3)), m^2
GG, GS, SG, SS = total-exchange areas, m^2
$[I]$ = indentity matrix
$[\_I]$ = diagonal matrix of quantity preceding "I", arbitrary units
$[\_\_\_]$ = full matrix of enclosed quantity, arbitrary units
$\bar{1}$ = vector of 1's
k = thermal conductivity, W/m/K
K_t = total extinction, m^{-1}
M = number of area and volume elements
N = number of area elements
N_s = Stark number = $kK_t/(4\sigma T_{ref}^3)$
q_γ''', Q_γ = volumetric or total heating rate of volume V_γ, W/m^3, W
q_i'' = heat flux of A_i, W/m^2
S = path length between elements, m
V_γ = volume element γ, m^3
W_i = radiosity of A_i, W/m^2
ϵ_i = emissivity of A_i
θ = angle from surface normal
κ = optical thickness = $K_t S$
Γ = number of volume elements
ρ_i = reflectivity of A_i
σ = scattering extinction coefficient, m^{-1}
$\tau(S)$ = transmittance along path S
ω_0 = scattering albedo = $\sigma/(\sigma + a)$

Subscripts

i, j = denotes association with A_i, A_j
γ, μ = denotes association with V_γ, V_μ
s = surface quantity
g = gas quantity
w = denotes wall location

$\overline{FS_iS_j}$ = Fraction of energy leaving surface A_i and incident on A_j by any path excluding wall reflections.

$\overline{FS_iG_\gamma}$ = Number of times a quantity of energy leaving surface A_i is absorbed in or scattered by V_γ prior to reaching any surface of the enclosure.

$\overline{FG_\gamma S_i}$ = Fraction of energy originating as a radiation source at V_γ, emitted, and incident on A_i by any path excluding wall reflections.

$\overline{FG_\gamma G_\mu}$ = Number of times energy originating as a radiation source at V_γ is absorbed in or scattered by V_μ prior to reaching any surface of the enclosure.

Using the exchange factors of the preceding definitions, we can write energy balances for surface and volume elements of a zoned system. In the following section transformations between direct-exchange areas and exchange factors will be established by considering special cases and requiring energy balances of both methods of analysis to hold simultaneously. These transformations will then be used to examine the exchange factors for a simple enclosure to clarify the exchange factor definitions.

For clarity the energy balances using exchange factors will be written first using index notation and then using the corresponding matrix notation. The radiant flux balances for the surfaces of the system may be written as

$$(AW)_i = (\epsilon AE_s)_i + \rho_i \left\{ \sum_{j=1}^{N} A_j \overline{FS_jS_i} W_j + \sum_{\gamma=1}^{\Gamma} \overline{FG_\gamma S_i} Q_\gamma \right\} \tag{14a}$$

or

$$[AI]\bar{W} = [\epsilon AI]\overline{E_s} + [\rho I]\{[FSS]^T[AI]\bar{W} + [FGS]^T\bar{Q}\} \tag{14b}$$

The first summation (equation (14*a*)) accounts for energy arriving at A_i from all other surfaces, including emission or scattering from gas elements of energy which leaves surface elements of the system. The latter summation accounts for energy which originated as a radiation source within the medium such as conduction sources or sinks or internal generation.

The balances for the system's volume elements are given by

$$(4aV)_\gamma E_\gamma = (1-\omega_0)\left\{ \sum_{i=1}^{N} A_i \overline{FS_iG_\gamma} W_i + \sum_{\mu=1}^{\Gamma} \overline{FG_\mu G_\gamma} Q_\mu \right\} + Q_\gamma \tag{15a}$$

or

$$[4aVI]\overline{E_g} = (1-\omega_0)\{[FSG]^T[AI]\bar{W} + [FGG]^T\bar{Q}\} + \bar{Q} \tag{15b}$$

The first summation of the right-hand side of equation (15*a*) again accounts for energy which arrives from the system's boundaries and the second summation accounts for energy originating (as a radiation source) in the medium and arriving by radiative means. Notice that the left-hand side uses the absorptivity of the medium ($a = (1 - \omega_0)K_t$) while the exchange factors include scattering paths. Only the energy absorbed by V_γ alters its temperature and $(1 - \omega_0)$ is the fraction of energy arriving along exchange factor paths which is absorbed. Equations (14) and (15) may be solved for $\bar{W}$ and $\overline{E_g}$ and the heat flux at surface A_i is given by:

$$(Aq_s'')_i = \sum_{j=1}^{N} A_j \overline{FS_jS_i} W_j + \sum_{\gamma=1}^{\Gamma} \overline{FG_\gamma S_i} Q_\gamma - (WA)_i \tag{16a}$$

or

$$[AI]\overline{q_s''} = \{[FSS]^T - [I]\}[AI]\bar{W} + [FGS]^T\bar{Q} \tag{16b}$$

In equation (15) the emissive power of V_γ is given explicitly as a function of the source terms for the system. In the presence of other modes of heat transfer $\overline{E_g}$ is present on the right-hand side as well through these source terms.

Reciprocity relations for exchange factors are derived in the following section, but will be stated here and used to write alternate forms of equations (14–16). These are

$$A_i\overline{FS_iS_j} = A_j\overline{FS_jS_i} \tag{17a}$$

or

$$[FSS]^T[AI] = [AI][FSS] \tag{17b}$$

($[FSS]^T[AI]$ is symmetric.)

$$A_i\overline{FS_iG_\gamma} = (4K_tV)_\gamma\overline{FG_\gamma S_i} \tag{18a}$$

or

$$[FSG]^T[AI] = [4K_tVI][FGS] \tag{18b}$$

and

$$(4K_tV)_\gamma\overline{FG_\gamma G_\mu} = (4K_tV)_\mu\overline{FG_\mu G_\gamma} \tag{19a}$$

or

$$[FGG]^T[4K_tVI] = [4K_tVI][FGG] \tag{19b}$$

($[FGG]^T[4K_tVI]$ is symmetric.)

Using these relations, equations (14–16) may be written as follows

$$\bar{W} = \overline{\epsilon E_s} + [\rho I]\left\{[FSS]\bar{W} + \frac{1}{4K_t}[FSG]\overline{q'''}\right\} \tag{14c}$$

$$\overline{E_g} = [FGS]\bar{W} + \frac{1}{4K_t}[FGG]\overline{q'''} + \frac{1}{4a}\overline{q'''} \tag{15c}$$

and

$$\overline{q_s''} = \{[FSS] - [I]\}\bar{W} + \frac{1}{4K_t}[FSG]\overline{q'''} \tag{16c}$$

Now, referring to equations (15*c*) and (16*c*), the conservation relations of the exchange factor method may be seen by considering an isothermal, black-walled enclosure in radiative equilibrium, which are

$$\sum_{i=1}^{N} \overline{FG_\gamma S_i} = 1 \quad (\gamma = 1,2 \ldots \Gamma) \tag{20a}$$

or

$$[FGS]\,\bar{1} = \bar{1} \tag{20b}$$

and

$$\sum_{j=1}^{N} \overline{FS_iS_j} = 1 \quad (i = 1,2, \ldots N) \tag{21a}$$

or

$$[FSS]\,\bar{1} = \bar{1} \tag{21b}$$

Equations (20) and (21) state that energy leaving a volume element eventually strikes a surface, and that energy leaving a surface eventually returns to a surface.

Change of Basis Relationships

The previous section presents algebraic equations obtained by interpreting the exchange factor definitions. In this section relationships between exchange factors and direct-exchange areas are found by considering various special cases and requiring energy balances written with direct-exchange areas and those with exchange factors to be simultaneously valid. For the sake of brevity they are first developed for a gray, nonscattering medium. In the process, the reciprocity relationships of equations (17–19) are proven for the nonscattering medium. Extension to isotropically scattering media will be discussed at the end of the section.

FGG:

Consider an enclosure with cold (negligible emissive

power), black walls and any prescribed $\bar{Q}$. Equation (8) simplifies to

$$[4aVI]\overline{E_g} = [gg]^T\overline{E_g} + \bar{Q} \tag{22}$$

and the complementary exchange factor method energy balance is

$$[4aVI]\overline{E_g} = [FGG]^T\bar{Q} + \bar{Q} \tag{23}$$

Solving for $\overline{E_g}$ from equation (22), substituting into equation (23), and requiring the result to hold for arbitrary $\bar{Q}$ yields

$$[FGG]^T = [4aVI]\{[4aVI] - [gg]^T\}^{-1} - [I] \tag{24}$$

Examining equation (24) it is apparent that $[FGG] \to 0$ as $a \to 0$. Postmultiplying equation (24) by $[4aVI]$, the right-hand side must be symmetric (it is composed only of diagonal matrices and the symmetric matrix $[gg]$) which leads to the reciprocity condition

$$(4aV)_\gamma\overline{FG_\gamma G_\mu} = (4aV)_\mu\overline{FG_\mu G_\gamma} \tag{19c}$$

FSG and FGS:

Consider a black-walled enclosure in radiative equilibrium with bounding walls of any prescribed temperature distribution. Volume energy balances written using direct-exchange areas and exchange factors give:

$$[4aVI]\overline{E_g} = [sg]^T\overline{E_s} + [gg]^T\overline{E_g} \tag{25}$$

and

$$[4aVI]\overline{E_g} = [FSG]^T[AI]\overline{E_s} \tag{26}$$

Solving for the gas emissive power distribution from equation (25), substituting into equation (26), using equation (24), and requiring the result to be valid for arbitrary $\overline{E_s}$ leads to the condition

$$[FSG]^T = \{[FGG]^T + [I]\}[sg]^T[AI]^{-1} \tag{27}$$

To arrive at the relationship between direct-exchange areas and $[FGS]$, consider an enclosure with cold, black walls with a specified distribution of sources $\bar{Q}$. Using direct-exchange areas we may write

$$[AI]\overline{q_s''} = [gs]^T\overline{E_g} \tag{28}$$

but from equation (15)

$$\overline{E_g} = [4aVI]^{-1}\{[FGG]^T + [I]\}\bar{Q} \tag{29}$$

From the exchange factor method we may write

$$[AI]\overline{q_s''} = [FGS]^T\bar{Q} \tag{30}$$

Substituting equation (29) into (28) leads to the condition

$$[AI]\overline{q_s''} = [gs]^T[4aVI]^{-1}\{[FGG]^T + [I]\}\bar{Q} = [FGS]^T\bar{Q} \tag{31}$$

Requiring equation (31) to be valid for arbitrary $\bar{Q}$ leads to the condition

$$[FGS]^T = [gs]^T[4aVI]^{-1}\{[FGG]^T + [I]\} \tag{32}$$

Examining equations (27) and (32), it is apparent that, in the optically thin limit (where $[FGG] \to 0$), $[FGS]$ and $[FSG]$ are the same as their direct-exchange counterparts (normalized by the sending element's "area"). Using the reciprocity relations of equations (5) and (19), and equations (27) and (32) it may be shown that:

$$[FSG]^T[AI] = [4aVI][FGS] \tag{18c}$$

FSS:

The net radiative heat fluxes for a black-walled enclosure in radiative equilibrium are given by:

$$[AI]\overline{q_s''} = \{[ss]^T - [AI]\}\overline{E_s} + [gs]^T\overline{E_g} \tag{9}$$

and

$$[AI]\overline{q_s''} = \{[FSS]^T - [I]\}[AI]\overline{E_s} \tag{33}$$

using direct-exchange areas and exchange factors respectively. Now comparing equations (9) and (33) requires

$$[FSS]^T[AI]\overline{E_s} = [ss]^T\overline{E_s} + [gs]^T\overline{E_g} \tag{34}$$

Solving for $\overline{E_g}$ from equation (15*c*), substituting into equation (34), and requiring the result to be valid for all $\overline{E_s}$ leads to the condition:

$$[FSS]^T = \{[ss]^T + [gs]^T[FGS]\}[AI]^{-1} \tag{35}$$

In the optically thin limit, $[FSS]$ is the matrix of conventional configuration factors for the transparent enclosure. Using the foregoing reciprocity it may be shown that

$$[FSS]^T[AI] = [AI][FSS] \tag{17b}$$

The transformations and reciprocity relationships are valid for isotropically scattering as well as nonscattering media when exchange factors and direct-exchange areas are evaluated using the total extinction coefficient. The transformations are independent of the scattering albedo because exchange factors are composed of direct paths and those which are created by exchange among volume elements in equilibrium. Either isotropic scattering or absorption and re-emission from gray gas elements in radiative equilibrium have the effect of distributing re-emitted or scattered energy uniformly into all directions.

The mathematical proof that exchange factors depend only on total extinction, and not albedo, utilizes results from Noble [9]. Consider the same four cases that were used previously, but assume that $0 < \omega_0 < 1$. Using the same procedure, writing energy balances using both total-exchange areas and exchange factors, equations analogous to equations (24), (27), (32), and (35) are

$$[FGG]^T = [4K_tVI]\{[4K_tVI] - [GG]^T\}^{-1} - \frac{1}{1-\omega_0}[I] \tag{36}$$

$$[FSG]^T = [4K_tVI]\{(1-\omega_0)[4K_tVI] - [GG]^T\}^{-1}[SG]^T[AI]^{-1} \tag{37}$$

$$[FGS]^T = [GS]^T[(1-\omega_0)4K_tVI]^{-1}\{(1-\omega_0)[FGG]^T + [I]\} \tag{38}$$

and

$$[FSS]^T = \{[SS]^T + [GS]^T[FGS]\}[AI]^{-1} \tag{39}$$

From [9], the total-exchange areas for a black-walled enclosure containing an isotropic scatterer are

$$[SS]^T = [ss]^T + \omega_0[sg]\{[4K_tVI] - \omega_0[gg]^T\}^{-1}[gs] \tag{40}$$

$$[SG] = (1-\omega_0)[sg]\{[4K_tVI] - \omega_0[gg]^T\}^{-1}[4K_tVI] \tag{41}$$

$$[GS]^T = [SG] \tag{42}$$

$$[GG]^T = (1-\omega_0)^2[4K_tVI]\{[4K_tVI] - \omega_0[gg]^T\}^{-1}[gg]^T \tag{43}$$

Substitution of equations (40–43) into equations (36–39) to eliminate the total-exchange areas also results in the elimination of ω_0 and the resulting equations are equations (24), (27), (32), and (35) with the absorptivity a replaced by the total extinction coefficient K_t.

Now let us consider the exchange factors for a cube containing a gray, isotropically scattering medium. The system has six surface elements ($N = 6$), the cube's faces, and a single volume element ($\Gamma = 1$). There is only one FGG-type factor and it is given by equation 24 as: $FGG = gg/(4K_tV - gg)$. It is apparent from equation (3) that in the optically thin limit gg is proportional to K_t^2. Then, as noted previously, FGG must go to zero in the optically thin limit. FGG is unbounded in the optically thick limit as energy emitted somewhere within the cube is absorbed and re-emitted countless times without reaching a surface. However, zonal analysis is not useful in the optically thick limit since the volume cannot be isothermal

Table 1 Comparison of zonal analysis results with the exact formulation of Crosbie [13]

X or Y	Q_{side} zone	Q_{side} [13]	Q_{top} zone	Q_{top} [13]	Q_{bottom} zone	Q_{bottom} [13]	$E_{centerplane}$ zone	$E_{centerplane}$ [13]
0.1	0.524	0.518(1.2)	0.832	0.827(0.6)	0.189	0.190(0.5)	0.521	0.519(0.4)
0.2	0.437	0.431(1.4)	0.798	0.796(0.3)	0.212	0.213(0.5)	0.434	0.433(0.2)
0.3	0.368	0.366(0.5)	0.778	0.777(0.1)	0.229	0.230(0.4)	0.361	0.361(0.0)
0.4	0.310	0.308(0.6)	0.768	0.767(0.1)	0.240	0.240(0.0)	0.300	0.299(0.3)
0.5	0.260	0.259(0.4)	0.764	0.764(0.0)	0.243	0.244(0.4)	0.250	0.250(0.0)
0.6	0.218	0.217(0.5)	0.768	0.767(0.1)	0.240	0.240(0.0)	0.208	0.208(0.0)
0.7	0.182	0.181(0.6)	0.778	0.777(0.1)	0.229	0.230(0.4)	0.173	0.173(0.0)
0.8	0.149	0.149(0.0)	0.798	0.796(0.3)	0.212	0.213(0.5)	0.142	0.142(0.0)
0.9	0.119	0.119(0.0)	0.832	0.827(0.6)	0.189	0.190(0.5)	0.114	0.115(0.9)

Note: Numbers in parentheses are percentage differences.

Table 2 Three-dimensional zonal analysis results, pure radiation

k	j	Emissive power $i=1$	Emissive power $i=3$	Emissive power $i=5$	Heat flux #	Heat flux Q
5	5	0.105	0.177	0.368	1	0.499
5	3	0.177	0.298	0.500	2	0.695
5	1	0.368	0.500	0.632	3	0.821
					4	0.292
3	5	0.177	0.298	0.500	5	0.483
3	3	0.298	0.500	0.702	6	0.177
3	1	0.500	0.702	0.823		
1	5	0.368	0.500	0.632		
1	3	0.500	0.702	0.823		
1	1	0.632	0.823	0.895		

Note: Surfaces for which $z = 0$, $y = 0$, or $x = 1$ have unit emissive power, others are cold. All walls are black, and $\bar{Q} = \bar{0}$.

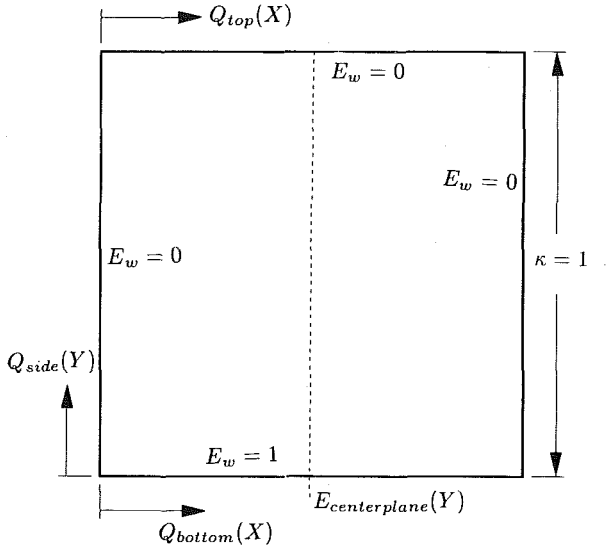

Fig. 1 Infinitely long, black-walled enclosure of square cross section

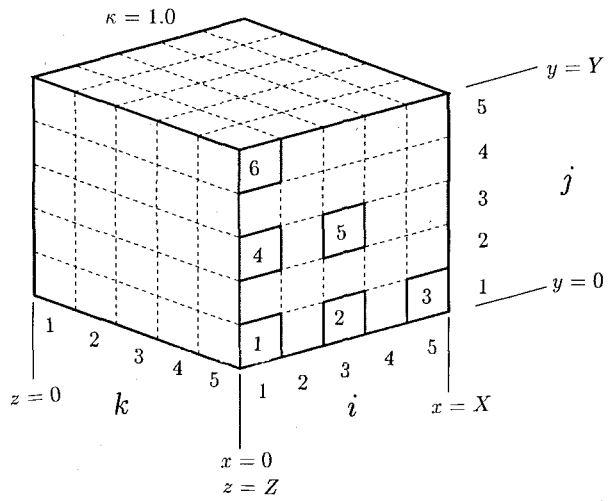

Fig. 2 Black-walled cube with five zones in each direction

as assumed. Energy leaves the cube volume without directional preference so all *FGS* must be 1/6 (without regard for the optical thickness). This can also be demonstrated using equations (10), (24), and (32). The *FSG* can be related to the optical thickness by equation (18*c*), and for the current case they are larger than unity for the case in which the cube optical thickness (based on an edge length) is greater than 1.5. There are only three unique values in [*FSS*] and [*ss*]. In the optically thin limit the *FSS* are just the conventional configuration (or view) factors between the surfaces. In the other extreme, $\kappa \to \infty$, all of the *FSS* are 1/6. Actually, since energy leaving a surface is absorbed within a gas layer immediately adjacent to the surface (for $\kappa \to \infty$), and subsequent emissions are equally likely to be directed toward or away from the surface, half of the energy leaving a surface must return. However, our model does not discern between locations within the volume and assumes energy leaving the volume has equal probability of hitting any given surface.

Numerical Verification

As described in [12], two- and three-dimensional enclosures were analyzed using the foregoing zonal formulation. Figure 1 and Table 1 are included to indicate the accuracy that can be achieved using zonal analysis. Crosbie [13] has recently contributed an exact formulation of the two-dimensional enclosure shown in Fig. 1 and zonal analysis results are compared to those of [13] for the case of a gray medium enclosed by three cold walls and one hot wall. The zonal analysis was performed using 11 zones of equal size per side. The tabulated information in [13] is at irregularly spaced intervals. The results of Table 1 were adjusted to the uniformly spaced locations by linear interpolation. The agreement is excellent for both heat flux predictions and centerplane emissive power. The present zonal analysis conserves energy identically (to within machine accuracy) since direct-exchange areas were smoothed as described in [14]. This same geometry was also analyzed [12] (using the

Table 3 Three-dimensional zonal analysis results, combined radiation and conduction

		Emissive power				Heat flux
k	j	$i=1$	$i=3$	$i=5$	#	Q
5	5	0.069	0.181	0.479	1	0.663
5	3	0.181	0.431	0.679	2	0.959
5	1	0.479	0.679	0.779	3	1.165
					4	0.298
3	5	0.181	0.431	0.679	5	0.589
3	3	0.431	0.807	0.917	6	0.158
3	1	0.679	0.917	0.960		
1	5	0.479	0.679	0.779		
1	3	0.679	0.917	0.960		
1	1	0.779	0.960	0.980		

Note: Surface conditions are as in Table 2; $N_s = 0.01$.

present formulation) for conducting/radiating media of varying scattering albedo and results showed excellent agreement with those of Ratzel [15].

In the process of numerically verifying the foregoing formulation of the exchange factor method three-dimensional enclosures of variable aspect ratios were analyzed. Here we include results for the analysis of a cube (Fig. 2) in the interest of documenting three-dimensional analyses which may be of interest to other investigators. Table 2 gives conditions and results for the cube for a case in which it is in radiative equilibrium. The lack of three-dimensional results reported in the literature precludes reliable estimation of the error of the present analysis. De Marco and Lockwood [16] report results (credited to Jenner [17] and referred to as exact) for heat flux prediction in a cube of specified boundary conditions and containing a gray medium with uniform volumetric heat generation. For that case zonal analysis [12] results varied from Jenner's [17] Monte Carlo results by as much as 6 and 11 percent for enclosures with optical thicknesses (based on cube edge length) of 0.5 and 2.0, respectively. In that comparison the zonal analysis used an enclosure evenly divided into 64 (4 × 4 × 4) cubic elements. Based on that information, it appears that the heat flux results reported in Table 2 are accurate within 5 percent.

Table 3 includes results for the cube geometry of Fig. 2 for the case in which the medium conducts and radiates. The Stark number, $N_s = kK_t/(4\sigma T_{ref}^3)$, for the results of Table 3 is 0.01. In this study, as in [19], conduction into a volume element adjacent to a bounding surface is computed based on the wall temperature gradient given by

$$\left(\frac{\partial T}{\partial x}\right)_w = \frac{9T_\gamma - 8T_w + T_{\gamma+\Delta x}}{3\Delta x} \tag{44}$$

T_w, T_γ, and $T_{\gamma+\Delta x}$ are the wall temperature, and the center point temperatures of the two adjacent volume elements, in the order of their occurrence (spatially) on a normal located at the surface element's midpoint. Equation (44) results from fitting a quadratic function $T(x)$ to T_w, T_γ, and $T_{\gamma+\Delta x}$ and evaluating its derivative at $x = 0$. Simple central difference operators were used to estimate temperature gradients at surfaces between adjacent volume elements. As in other combined-mode zonal analysis, the zonal analysis limits the practical number of system elements and using the same grid for radiation and conduction calculations compromises the accuracy of the conduction portion of the solution.

Applications of the Exchange Factor Method

The present formulation was developed in pursuit of a zonal basis which may be measured from a scale model of the system to be analyzed. The principal achievement of the present work is identification of a basis of zonal analysis which characterizes a gray/isotropically scattering system's opticogeometric properties in a manner which does not depend on the system's scattering albedo. As a result, measurements can be attempted in a purely scattering ($\omega_0 \simeq 1$) medium using monochromatic sources and detectors. A limited discussion of the practical problems anticipated in making the suggested measurements is included in [12] and actual measurements are reported in [5].

The exchange factor formulation also has practical value in comparison with conventional zonal formulation in studies of enclosures in radiative equilibrium, with black walls, or in which scattering albedo is to be varied, because of the simplifications of the element energy balance equations which result for these conditions.

In the weighted sum of gray gases technique, directed-flux areas are formed from total-exchange areas. Energy of a given spectral region (corresponding to one of the gray gases being considered) traveling from one system element to another along total-exchange area paths is not absorbed and its spectral distribution is not altered. As a result, total-exchange areas can be weighted in a useful, temperature-dependent fashion. The definitions of exchange factors explicitly include absorption and re-emission (hence spectral redistribution) and their direct use in a weighted-gray-gas technique is not reasonable. However, if exchange factors of a given system geometry can be obtained (through measurement) for multiple gray gases their conversion to direct-exchange areas is straightforward.

Conclusions

An alternate, physically meaningful basis for zonal analysis has been formulated and related to that of conventional direct-exchange areas. Gas-to-surface and gas-to-gas exchange factors are proportionality constants operating on the volume element source strength (departure from radiative equilibrium) rather than on emissive power. Many practical problems are inevitable in measuring exchange factors. However, the formulation presented here offers advantages over conventional zonal analysis for measurement of a system's opticogeometric properties. These include the use of monochromatic sources and detectors and the measurement of factors which express transfer in proportion to source strength rather than local emissive power.

References

1 Hottel, H. C., "Radiant Heat Transmission," in: *Heat Transmission*, ed. W. H. McAdams, 3rd ed., Chap. 4, McGraw-Hill, 1954,.

2 Hottel, H. C., and Cohen, E. S., "Radiant Heat Exchange in a Gas-Filled Enclosure: Allowance for Non-Uniformity of Gas Temperature," *AIChE Journal*, Vol. 4, No. 1, 1958, pp. 3–14.

3 Hottel, H. C., and Sarofim, A. F., "Gaseous Radiation with Temperature Gradients—Allowance for Isotropic Scatter," in: *Research in Heat Transfer*, Pergamon Press, Oxford, 1963, pp. 139–150.

4 Hottel, H. C., and Sarofim, A. F., *Radiative Transfer*, McGraw-Hill, 1967.

5 Liu, Hsing-Pang, and Howell, J. R., "Measurement of Radiative Exchange Factors," submitted to the AIChE/ASME National Heat Transfer Conference, Denver, Aug. 1985.

6 Becker, H. B., "A Mathematical Solution for Gas-to-Surface Radiative

Exchange Area for Rectangular Parallelepiped Enclosure Containing a Gray Medium," ASME JOURNAL OF HEAT TRANSFER, Vol. 99, May 1977, pp. 203-207.

7 Edwards, D. K., and Balakrishnan, A., "Volume Interchange Factors for Nonhomogeneous Gases," ASME JOURNAL OF HEAT TRANSFER, Vol. 94, May 1972, pp. 181-187.

8 Vercammen, H. A. J., and Froment, G. F., "An Improved Zone Method Using Monte Carlo Techniques for the Simulation of Radiation in Industrial Furnaces," *International Journal of Heat and Mass Transfer*, Vol. 23, No. 3, Mar. 1980, pp. 329-336.

9 Noble, J. J., "The Zone Method: Explicit Matrix Relations for Total Exchange Areas," *International Journal of Heat and Mass Transfer*, Vol. 18, No. 2, Feb. 1975, pp. 261-269.

10 Perlmutter, M., and Howell, J. R., "Radiant Transfer Through a Gray Gas Between Concentric Cylinders Using Monte Carlo," ASME JOURNAL OF HEAT TRANSFER, Vol. 86, No. 2, 1964, pp. 169-179.

11 Howell, J. R., "Determination of Combined Conduction and Radiation of Heat Through Absorbing Media by the Exchange Factor Approximation," *Chemical Engineering Progress Symposium Series*, Vol. 61, No. 59, 1965, pp. 162-171.

12 Larsen, M. E., "The Exchange Factor Method: an Alternative Zonal Formulation for Analysis of Radiating Enclosures Containing Participating Media," Ph.D. dissertation, The University of Texas at Austin, 1983.

13 Crosbie, A. L., and Schrenker, R. G., "Radiative Transfer in a Two-Dimensional Rectangular Medium Exposed to Diffuse Radiation," *Journal of Quantitative Spectroscopy and Radiative Transfer*, Vol. 31, No. 4, pp. 339-372.

14 Larsen, M. E., and Howell, J. R., "Least-Squares Smoothing of Direct-Exchange Areas in Zonal Analysis," ASME Paper No. 84-HT-40.

15 Ratzel, A. C., "P-N Differential Approximation for Solution of One- and Two-Dimensional Radiation and Conduction Energy Transfer in Gray Participating Media," Ph.D. dissertation, The University of Texas at Austin, 1981.

16 De Marco, A. G., and Lockwood, F. C., "A New Flux Model for the Calculation of Radiation in Furnaces," *La Rivista dei Combustibili*, Vol. 29, 1975, pp. 184-196.

17 Jenner, R., Numerical results using FURDEC program described in [18].

18 Gibb, J., and Jenner, R., "Preliminary Note on the Radiant Heat Transfer Program FURDEC," Central Electricity Generating Board Report MS/C/N646.

19 Einstein, T. H., "Radiant Heat Transfer to Absorbing Gases Enclosed Between Parallel Flat Plates with Flow and Conduction," NASA Technical Report R-154, 1963.

Thermal Radiation Properties of Acetylene

M. A. Brosmer
Assoc. Mem. ASME

C. L. Tien
Fellow ASME

Department of Mechanical Engineering,
University of California,
Berkeley, CA 94720

The spectral absorptivities of the ν_3 and ν_5 fundamental and the $\nu_4 + \nu_5$ combination bands of acetylene have been measured at low resolution for temperatures between 290 and 600 K. These measurements allow the determination of spectral-mean (narrow-band) parameters for the three bands based on the Elsasser and Goody models and the correlation of the band absorptance data using the Edwards exponential wide-band model. Charts for the total emissivity and Planck mean absorption coefficient have been developed for acetylene based on the wide-band parameters.

Introduction

Acetylene is one of the primary decomposition products which result from the pyrolysis of petroleum-based solid and liquid substances. During the combustion of such fuels, the flame temperature reaches 1200 to 1700 K while the fuel surface may be maintained near 300 K [1, 2]. Throughout this temperature range, the absorption by the decomposition gases of the infrared energy radiated by the flame becomes important in the analysis of the combustion process [3, 4]. The important infrared absorption bands of acetylene are the ν_5 fundamental located at 729 cm^{-1} (13.7 μ), the ν_3 fundamental at 3287 cm^{-1} (3.04 μ), and the $\nu_4 + \nu_5$ combination band located at 1328 cm^{-1} (7.53 μ) [5].

A relatively comprehensive list of information exists for the infrared bands of acetylene. The integrated intensities of the bands have been well defined [6-8] as have the spectral line positions [9, 10] and line widths [11, 12]. These high-resolution spectroscopic studies are useful in the analysis of planetary atmospheric radiation and other low absorber concentration studies, as well as the determination of detailed quantum mechanical calculations. For large absorber concentration, high-temperature applications such as combustion or flame radiation problems, low-resolution data are more applicable [4, 13, 14]. The use of spectral-mean or narrow-band models has been shown to represent accurately the spectral emissivity of gases, as well as to correlate low-resolution experimental absorptivity data without requiring rigorous, line-by-line determination of the various spectral parameters [13]. The total band absorptance models have been shown to be useful in engineering calculations, as they are able to yield accurate band and total gas emissivities, and are applicable to problems dealing with nongrey, nonisothermal conditions [13, 14]. It is in this area where a deficiency of data and analysis is present.

The purpose of the present work is to improve the existing knowledge of the infrared absorption of acetylene through the measurement and correlation of low-resolution data. The focus is on the spectral-mean and total-band properties, as well as the total gas properties—emissivity, absorptivity and mean absorption coefficients—of C_2H_2.

Apparatus and Measurements

The present study, similar to an earlier study for SO_2 [15], utilized a furnace-absorption cell apparatus to observe the spectral absorptivity of C_2H_2 under various thermodynamic and optical conditions. A high-temperature, high-pressure furnace equipped with movable optical windows is used to maintain the experimental conditions of temperature, pressure, and path length. The optical path is confined to the central region of the furnace and is defined by the position of the optical windows. Due to transmission limitations, BaF_2 windows were used for wavelengths up to 9 μ, while KBr windows were used for longer-wavelength data. The physical path length was varied between 0.7 and 22 cm, while the partial pressure of the absorbing gas was varied between 0.05 and 1.75 atm. The optical (pressure) path length ranged from 0.035 to 30 atm-cm. The acetylene was diluted with dry nitrogen such that the total pressure of the test gas ranged between 0.35 and 2.0 atm. The gas temperature ranged from room temperature ($\approx$ 290 K) to the spontaneous combustion temperature of acetylene ($\approx$ 600 K) [16]. A carbon globar served as the infrared source. The infrared signal was detected by a Perkin-Elmer model 99 double pass monochromater fitted with a potassium bromide thermocouple detector. For short-wavelength data ($\lambda < 9\ \mu$), a sodium chloride prism was installed in the monochromator, while a potassium bromide prism was used for longer wavelengths. For total absorptivity measurements, a potassium bromide thermocouple detector was placed in the optical path ahead of the monochromator. The output signal was amplified by a lock-in voltmeter and recorded by a PDP 1134A digital computer.

Acetylene was purchased from Matheson Co., which specifies a minimum purity of 99.6 mole percent. The primary contaminants are oxygen and nitrogen, with a combined composition less than 0.4 percent.

Experimental Analysis

The present analysis is directed at determining the various spectral-mean or narrow-band, wide-band, and total radiative properties from the experimentally obtained spectral absorptivity data. The spectral-mean absorption data can be correlated using several well-known narrow-band models, and the total band absorption data will be correlated using Edwards exponential wide-band model [13, 14]. The wide-band properties will be used to calculate the total emissivity and the Planck mean absorption coefficient for acetylene.

Narrow-Band Analysis. The spectral evaluation of the band absorptivity is characterized by two narrow-band parameters: the mean spectral line intensity to spacing ratio S_ω/δ_ω and the line width to spacing ratio $\gamma_\omega/\delta_\omega$; S_ω is the mean spectral line intensity, γ_ω is the line half-width, and δ_ω is the line spacing. Two narrow-band models, the Elsasser and Goody models [13], are used to correlate the two parameters in terms of wavenumber and temperature.

The Elsasser model, which assumes a uniform distribution of uniformly intense lines, gives the spectral-mean absorptivity as

$$A_\omega = 1 - \frac{1}{2\pi}\int_{-\pi}^{\pi} \exp\frac{-2\beta_\omega\chi_\omega \sinh 2\beta_\omega}{\cosh 2\beta_\omega - \cos z_\omega} dz_\omega, \qquad (1)$$

where

$$\beta_\omega = \pi\gamma_\omega/\delta_\omega, \quad \chi_\omega = S_\omega X/2\pi\gamma_\omega, \quad z_\omega = 2\pi\omega/\delta_\omega,$$

Contributed by the Heat Transfer Division for publication in the JOURNAL OF HEAT TRANSFER. Manuscript received by the Heat Transfer Division November 19, 1984.

with $X(=Py)$ defined as the pressure path length. The Elsasser function, when combined with the Godson equation and an approximation of the Ladenburg-Reiche function, can be approximated as

$$A_\omega = \mathrm{erf}[\pi^{1/2}\beta_\omega\chi_\omega[1+(\pi\chi_\omega/2)]^{-1/2}] \quad (2)$$

The Goody model, which assumes a statistically random spacing of randomly intense lines, defines the spectral-mean absorptivity as

$$A_\omega = 1-\exp[-2\beta_\omega\chi_\omega(1+2\chi_\omega)^{-1/2}] \quad (3)$$

Equations (2) and (3) may be rearranged to specify the line intensity parameter S_ω/δ_ω as

$$S_\omega/\delta_\omega = \frac{(\mathrm{erf}^{-1}A_\omega)^2}{2\pi X\left(\frac{\gamma_\omega}{\delta_\omega}\right)}\left\{1+\left[1+\left(\frac{\gamma_\omega}{\delta_\omega}\right)^2\frac{16\pi}{(\mathrm{erf}^{-1}A_\omega)^2}\right]^{1/2}\right\} \quad (4)$$

and

$$S_\omega/\delta_\omega = \frac{\{\ln(1-A_\omega)\}^2}{2\pi X\left(\frac{\gamma_\omega}{\delta_\omega}\right)}\left\{1+\left[1+\left(\frac{\gamma_\omega}{\delta_\omega}\right)^2\frac{4\pi^2}{\{\ln(1-A_\omega)\}^2}\right]^{1/2}\right\} \quad (5)$$

For the present analysis, $\gamma_\omega/\delta_\omega$ will be assumed to be constant across the entire band. Its value is adjusted iteratively and S_ω/δ_ω is recalculated until the integrated band intensity, defined as

$$\alpha(T) = \int_{\Delta\omega} S_\omega/\delta_\omega d\omega, \quad (6)$$

is obtained. A knowledge of $\alpha(T)$ is thus required for each absorption band. It can be expressed as

$$\alpha(T) = \alpha_0(T_0/T)[\psi(T)/\psi(T_0)], \quad (7)$$

where α_0 is the value of α at temperature T_0. For the present analysis, the values of α_0 are taken to be 294, 87, and 729 $\mathrm{atm}^{-1}\ \mathrm{cm}^{-2}$ [6] for the 3287, 1328, and 729 cm^{-1} bands, respectively, with $T_0 = 300$ K. For fundamental bands, $\psi(T)/\psi(T_0) = 1$. For the combination band at 1328 cm^{-1}, $\psi(T)$ may be expressed as [14]

$$\psi(T) = (1-e^{-u_4-u_5})/(1-e^{-u_4})(1-e^{-u_5}) \quad (8)$$

where

$$u_i = hc\nu_i/kT, \quad hc/k = 1.4388 \text{ cm-K}$$

Based on this analysis, the spectral absorptivity data were correlated for the three bands. The Goody model was found, based on the scatter of the calculated values of γ/δ for various path lengths, to accurately correlate the data for the 3287 cm^{-1} band. The Elsasser model was likewise determined to be more accurate for the 1328 and 729 cm^{-1}, bands. In general, the variation of γ/δ with pressure and temperature can be expressed as

$$\gamma/\delta = (\gamma/\delta)_0 P_e^n (T_0/T)^{1/2}\psi(T)/\psi(T_0).$$

Over the present range of data, the low-temperature $T^{-1/2}$ response was not observable. This observed response was determined to be

$$\gamma/\delta = 0.0426\, P_e^{0.6}(T/T_0)^{1.4} \quad (3287\ \mathrm{cm}^{-1}) \quad (9)$$

$$\gamma/\delta = 0.0695\, P_e^{0.5}(T/T_0)^{0.35} \quad (1328\ \mathrm{cm}^{-1}) \quad (10)$$

$$\gamma/\delta = 0.0280\, P_e^{0.6}(T/T_0)^{0.8} \quad (729\ \mathrm{cm}^{-1}) \quad (11)$$

A normalized effective pressure P_e is used in this analysis and is defined as

$$P_e = (P_T + (B-1)P_a)/P_0 \quad (12)$$

where P_T is the total pressure of the gas mixture, P_a is the partial pressure of the absorbing gas, and B is the self-broadening coefficient. The value of B has not been reported in the literature for C_2H_2-N_2 mixtures, and was therefore determined experimentally to be 1.3 (cf. next section).

The results for the line intensity parameter S_ω/δ_ω are shown in Figs. 1-3 for temperatures of 295, 450, and 600 K. Spectral room temperature data, based on the calculated values of γ/δ, are also presented to give an indication of the scatter in the data. Since S_ω/δ_ω is solely a function of temperature, any variation with path length should be attributed to inaccuracies in the experimental measurements. The assumption of a constant value of γ/δ may also contribute to any fluctuations.

The values of γ and δ can also be obtained independently through high-resolution spectroscopic studies. Varanasi et al. [11, 12] have experimentally determined the collision broadened half-widths for the 729 and 1328 cm^{-1} bands at low temperatures ($T \leq 296$ K). An average, nitrogen broadened value, based on the first 20 lines in the P and R branches at 296 K, can be computed to be approximately 0.093 $\mathrm{cm}^{-1}\ \mathrm{atm}^{-1}$ for each band. Line positions of acetylene have been reported by Palmer et al. [9] and Heitanen and Kaupinen [10]. The average values of line spacing can be calculated from their data to be approximately 2.36 cm^{-1} for the ν_3 and ν_5 fundamentals, and 2.39 cm^{-1} for the $\nu_4 + \nu_5$ combination band. These values do not include the lines of the various weak, overlapping bands in each of the spectral regions. If it is assumed that the line widths of the ν_3 band are equal to those of the ν_5 band, the average line width parameter γ/δ can be seen to be approximately 0.039 for all three bands. The low-resolution results for the two fundamental bands are in good agreement with the high-resolution data. The results for the combination band located at 1328 cm^{-1} are approximately 70 percent greater than the

Nomenclature

A = absorptivity, absorption
B = pressure broadening coefficient
C_2 = empirical wide-band parameter
c = speed of light
h = Planck constant
I = radiant intensity
k = Boltzmann constant
L = physical path length
n = pressure broadening exponent
P = pressure
S = spectral line intensity
T = temperature
X = optical path length ($=P_aL$)
α = integrated intensity, total gas absorptivity
β = wide-band line shape parameter
γ = spectral line width
δ = spectral line spacing
ϵ = emissivity
κ = absorption coefficient
σ = Stefan-Boltzmann constant
ϕ = line shape parameter temperature correction
ψ = integrated intensity temperature correction
ω = wavenumber

Subscripts

a = absorbing gas
b = blackbody
e = effective
g = gas
0 = reference
s = source
T = total
ω = wavenumber

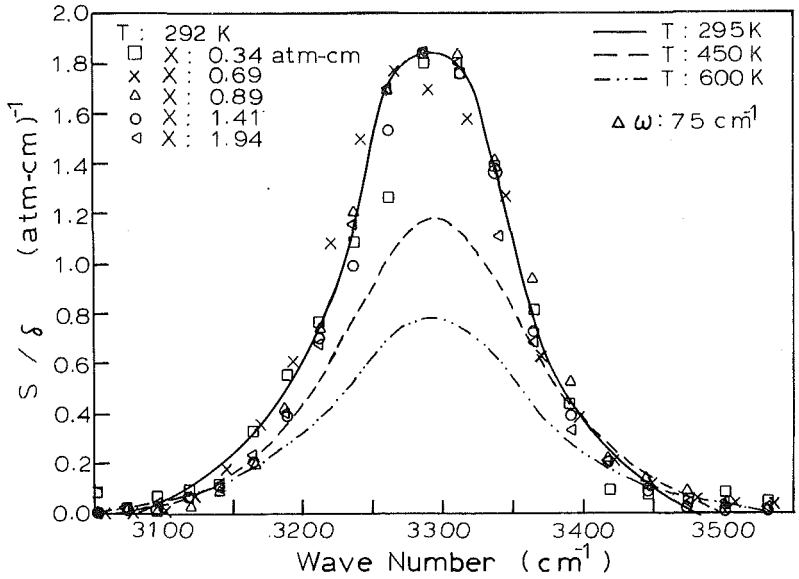

Fig. 1 Spectral data correlation for the ν_3 band at 295, 450, and 600 K

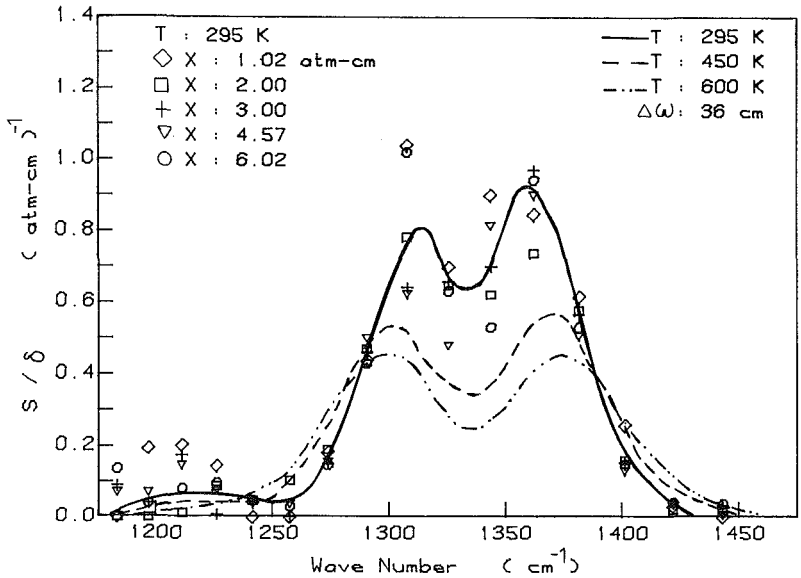

Fig. 2 Spectral data correlation for the $\nu_4 + \nu_5$ band at 295, 450, and 600 K

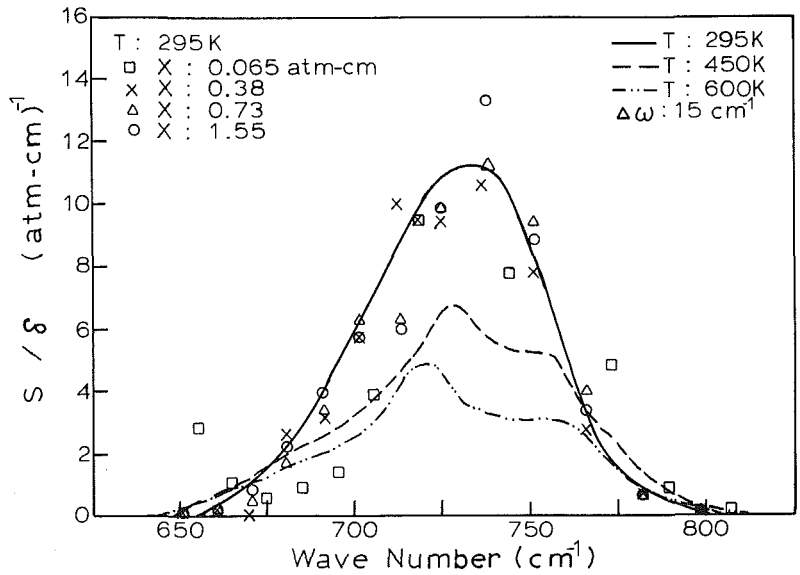

Fig. 3 Spectral data correlation for the ν_5 band at 295, 450, and 600 K

high-resolution studies would predict. Even with this discrepancy, the Elsasser model is considered more accurate than the Goody model for this band, as the value of γ/δ calculated by the Goody model is approximately twice that of the Elsasser model. This value would then be 2.5 times larger than the high-resolution results.

Table 1 Wide-band correlation parameters

Band (cm^{-1})	α_o ($atm^{-1}cm^{-2}$)	β	ω (cm^{-1})	C_2 ($atm^{-3/2}cm^{-1/2}$)
3287	294	$0.185\left\|\frac{T}{T_o}\right\|^{1.04}$	$39.8\left\|\frac{T}{T_o}\right\|^{0.5}$	$93.3\left\|\frac{T}{T_o}\right\|^{0.27}$
1328	87	$0.181\left\|\frac{T}{T_o}\right\|^{0.8}\frac{\psi(T_o)}{\psi(T)}$	$54.3\left\|\frac{T}{T_o}\right\|^{0.17}$	$57.9\left\|\frac{T}{T_o}\right\|^{0.19}$
729	729	$0.0958\left\|\frac{T}{T_o}\right\|^{0.81}$	$27.9\left\|\frac{T}{T_o}\right\|^{0.41}$	$88.3\left\|\frac{T}{T_o}\right\|^{0.11}$

T_o = 300 K

The quantity γ/δ can be related to the line shape parameter $\beta(=\pi\gamma/\delta)$ of the exponential wide-band model (cf. next section). From the wide-band analysis, values of γ/δ, at 300 K, were determined to be 0.0589, 0.0576, and 0.0305 for the 3287, 1328, and 729 cm^{-1} bands, respectively. These values, which were obtained from the same spectral data, are also in good agreement with the narrow-band results (within 26 percent) and further support the narrow-band analysis.

Wide-Band Analysis. The total band absorptance is defined as

$$A(T,P_aL,P_e)=\int_{\text{band}} A_\omega(T,P_aL,P_e,\omega)\,d\omega \tag{13}$$

and was calculated from the spectral absorption data. The exponential wide-band model [14] was used to correlate the absorption data in terms of three wide-band parameters. The first coefficient is defined as the integrated intensity of the band α, while the third parameter is defined as the effective exponential decay half-width of the band ω. An empirical coefficient C_2 is used to relate the wide-band parameters to the narrow-band line width-to-spacing ratio through the relation

$$\beta=\pi\gamma/\delta=C_2^2P_e^n/4\alpha\omega \tag{14}$$

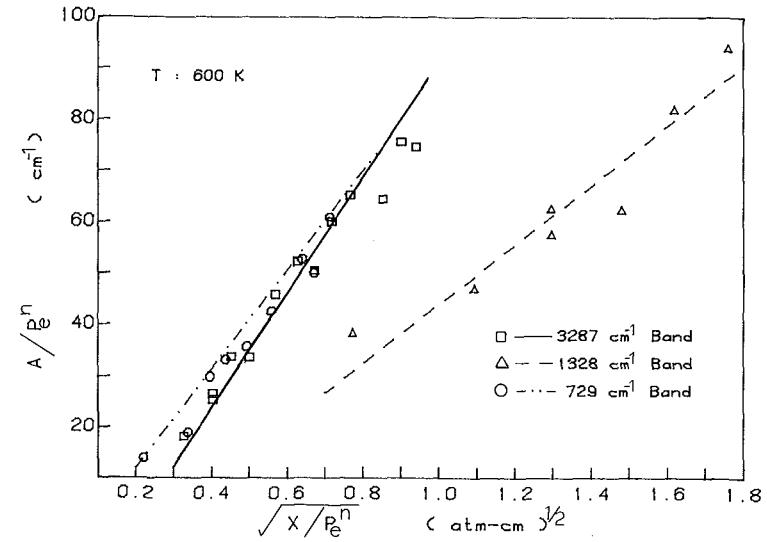

Fig. 4 Square-root band absorptance correlation for the ν_3, ν_4 + ν_5, and ν_5 bands at 600 K

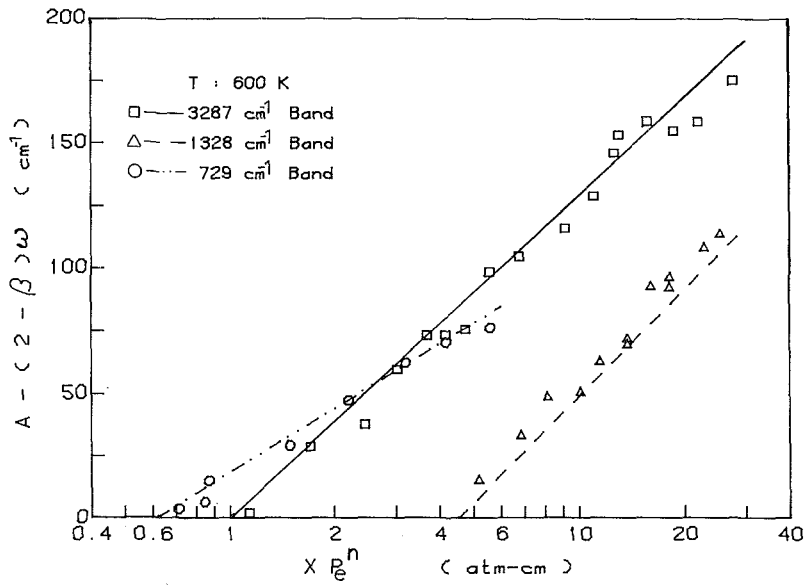

Fig. 5 Logarithmic band absorptance for the ν_3, ν_4 + ν_5, and ν_5 bands at 600 K

where β is the second wide-band parameter often referred to as the line shape parameter. C_2 is used in the analysis rather than β since it is directly obtained from the square-root region of the wide-band model. The effective pressure P_e in equation (14) is equivalent to the effective pressure defined for the narrow-band analysis.

The values of α for the three bands are obtained from the literature and have been reported in the narrow-band analysis. The values of C_2 and ω are determined experimentally by observing the square-root and logarithmic responses of the band absorption.

Edwards indicated that the band-width parameter ω should vary as $T^{1/2}$. The actual response was seen to deviate slightly from this theory for the 1328 and 729 cm^{-1} bands, and empirical correlations have been developed. The theoretical response of C_2 can be expressed as

$$C_2 \sim (T/T_0)^{1/2}[\phi(T)/\phi(T_0)]^{1/2} \tag{15}$$

The functional form has been empirically approximated in the analysis based on the present data in conjunction with equation (14). The three wide-band coefficients, α, β, and ω, along with the empirical coefficient C_2 are presented in Table 1.

The values of B and n have also been determined for the three bands, based on the present data. From the square-root region, the band absorption is given as

$$A = C_2(XP_e^n)^{1/2} - \beta\omega \tag{16}$$

The slope of this correlation, with respect to $X^{1/2}$, is given as $C_2P_e^{n/2}$. Thus from the definition of the effective pressure, if the pressure ratio P_a/P_T is varied, the resulting slopes of the absorption curves may be compared and the values of B and n determined. In the present analysis, absorption data were taken for pressure ratios between 0.05 and 1.4 with total pressures in the range of 0.35 to 2.0. The value of B was found to be approximately 1.3 for all three bands, while the value of n was found to be 0.6 for the fundamental bands and 0.5 for the combination band. The accuracy of this method is adequate, over the present range of data, for the accurate correlation of the total (integrated) band data as well as the spectral-mean (narrow-band) data as seen in the previous section. Representative total band data for the three bands are presented in Figs. 4 and 5 along with the wide-band correlations for a temperature of 600 K. Figure 4 displays the data which exhibit a square-root response to path length, while Fig. 5 presents the logarithmic region. It may readily be seen from these figures, that the wide-band model provides a good correlation of the experimental, total band data. In each case, the rms error is less than 9 percent and as low as 5 percent for the 1328 cm^{-1} band.

Total Radiative Properties. In many engineering applications, total radiative properties are of interest rather than the spectral or band properties. These properties include the total gas absorptivity and emissivity as well as various mean absorption coefficients [4, 13]. The total absorptivity and emissivity of a gas are defined as

$$\alpha(T_g,T_s,X,P_e) = \frac{\pi}{\sigma T_s^4}\int_0^\infty I_{b\omega}[1-\exp(-\kappa_\omega X)]d\omega$$

$$\approx \sum_j \pi I_{b\omega_j} A_j/\sigma T_s^4 \tag{17}$$

and

$$\epsilon(T_g,X,P_e) = \frac{\pi}{\sigma T_g^4}\int_0^\infty I_{b\omega}[1-\exp(-\kappa_\omega X)]d\omega$$

$$\approx \sum_j \pi I_{b\omega_j} A_j/\sigma T_g^4 \tag{18}$$

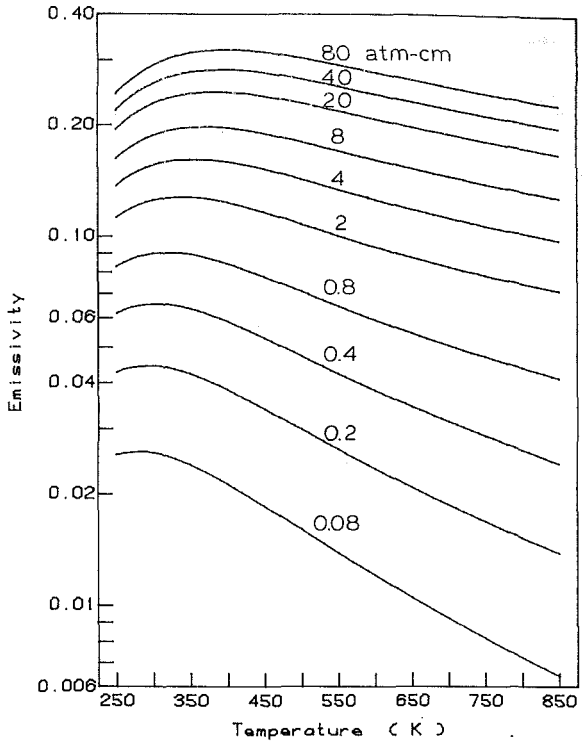

Fig.6 Total emissivity of acetylene for $P_T = P_{C_2H_2} \approx 1$

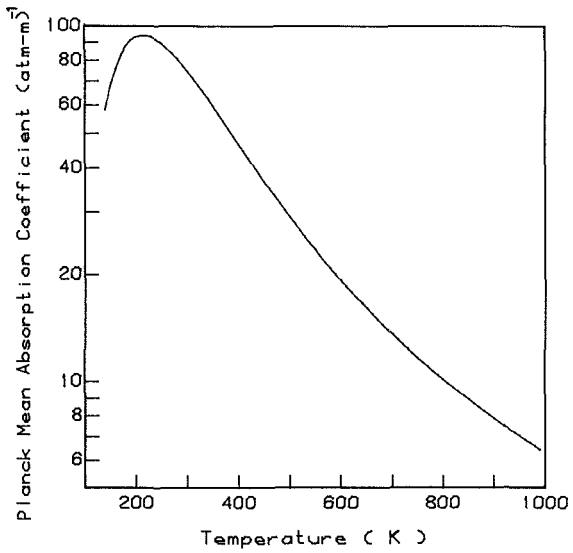

Fig. 7 Planck mean absorption coefficient for acetylene

where $I_{b\omega_j}$ is the blackbody intensity evaluated at the source temperature T_s for absorptivity or the gas temperature T_g for the emissivity, and the band center of the jth band. A_j is the total band absorption of the band, evaluated at T_g. For optically thin transport analyses, it is beneficial to use the Planck mean absorption coefficient, defined as

$$\kappa(T_g) = \frac{\pi}{\sigma T_g^4}\int_0^\infty \kappa_\omega I_{b\omega} d\omega \approx \sum_j \pi I_{b\omega_j}\alpha_j/\sigma T_g^4 \tag{19}$$

$I_{b\omega_j}$ and α_j, the integrated intensity of the jth band, are evaluated at the gas temperature T_g. Since it is based on the gas temperature, it is essentially an emission coefficient rather than an absorption coefficient. The modified Planck mean absorption coefficient is the true absorption coefficient and is expressed as

$$\kappa(T_g, T_s) = \frac{\pi}{\sigma T_s^4} \int_0^\infty \kappa_\omega I_{b\omega} d\omega \approx \sum_j \pi I_{b\omega_j} \alpha_j / \sigma T_s^4 \qquad (20)$$

where $I_{b\omega_j}$ is based on the source temperature and α_j is based on the gas temperature.

Calculations of the total absorptivity have been performed based on the present wide-band parameters and compared to experimentally obtained total absorptivity data. They were found to be in good agreement. This indicates that the other combination and overtone bands do not contribute significantly to the total absorptivity or emissivity of acetylene.

Total emissivity calculations have also been performed. The strong ν_5 fundamental band located at 729 cm^{-1} is important for the accurate determination of the total emissivity throughout the present temperature and path length range. At low temperatures, $T < 600$ K, and short path lengths, $X <$ 0.1 atm-cm, it is the most dominant band in the calculations, contributing up to 90 percent of the emissivity. The weak $\nu_4 + \nu_5$ combination band cannot be neglected, however, as it contributes up to 50 percent of the emissivity over most of the present range of path length and temperature. The strong ν_3 fundamental band located at 3287 cm^{-1} only becomes important for temperatures about 550 K. The results of the total emissivity calculations are presented in Fig. 6 for $P_T = P_a =$ 1atm. The Planck mean absorption coefficient has also been calculated and is presented in Fig. 7 for gas temperatures up to 1000 K.

Acknowledgments

The authors wish to express their appreciation to the National Bureau of Standards, Center for Fire Research for their support of this research.

References

1 Seshandri, K., and Williams, F. A., "Structure and Extinction of Counterflow Diffusion Flames Above Condensed Fuels: Comparison Between Poly(methyl-Methacrylate) and Its Liquid Monomer, Both Burning in Nitrogen-Air Mixtures," *Journal of Polymer Science: Polymer Chemistry Edition*, Vol. 16, 1978, pp. 1755-1778.

2 De Ris, J., "Fire Radiation—A Review," *Seventeenth Symposium (International) on Combustion*, The Combustion Institute, 1979, pp. 1003-1016.

3 Lee, K. Y., Zhong, Z. Y., and Tien, C. L., "Blockage of Thermal Radiation by the Soot Layer in Combustion of Condensed Fuels," *Proceedings of the Twentieth Symposium (International) on Combustion*, The Combustion Institute, in press.

4 Tien, C. L., and Lee, S. C., "Flame Radiation," *Progress in Energy and Combustion Science*, Vol. 8, 1982, p. 41-59.

5 Herzberg, G., *Molecular Spectra and Molecular Structure, Vol. II, Infrared and Raman Spectra of Polyatomic Molecules*, van Nostrand, New York, 1964.

6 Varanasi, P., and Bangaru, B. R. P., "Measurement of Integrated Intensities of Acetylene Bands at 3.04, 7.53, and 13.7 μm," *Journal of Quantitative Spectroscopy and Radiative Transfer*, Vol. 14, 1974, pp. 839-844.

7 Smit, W. M. A., van Straten, A. J., and Visser, T., "Measurement and Interpretation of the Integrated Infrared Intensities of C_2H_2 and C_2D_2," *Journal of Molecular Structure*, Vol. 48, 1978, pp. 177-189.

8 Kim, K., and King, W. T., "Integrated Infrared Intensities in HCCH, DCCD, HCCD," *Journal of Molecular Structure*, Vol. 57, 1979, pp. 201-207.

9 Palmer, K. F., Michelson, M. E., and Rao, K. N., "Investigation of Several Infrared Bands of $^{12}C_2H_2$ and Studies of the Effects of Vibrational Rotational Interactions," *Journal of Molecular Spectroscopy*, Vol. 44, 1972, pp. 131-144.

10 Heitanen, J., and Kauppinen, J., "High-Resolution Infrared Spectrum of Acetylene in the Region of the Bending Fundamental ν_5," *Molecular Physics*, Vol. 42, 1977, pp. 411-423.

11 Varanasi, P., Giver, L. P., and Valero, F. P. J., "Infrared Absorption of Acetylene in the 12-14 μm Region at Low Temperatures," *Journal of Quantitative Spectroscopy and Radiative Transfer*, Vol. 30, 1983, pp. 497-504.

12 Varanasi, P., Giver, L P., and Valero, F. P. J., "Measurements of Nitrogen-Broadened Line Widths of Acetylene at Low Temperatures," *Journal of Quantitative Spectroscopy and Radiative Transfer*, Vol. 30, 1983, pp. 505-509.

13 Tien, C. L., "Thermal Radiation Properties of Gases," *Advances in Heat Transfer*, eds. J. P. Hartnett and T. F. Irvine, Vol. 5, Academic Press, New York, 1968, pp. 253-324.

14 Edwards, D. K., "Molecular Gas Band Radiation," *Advances in Heat Transfer*, eds. T. F. Irvine and J. P. Hartnett, Vol. 12, Academic Press, New York, 1976, pp. 115-193.

15 Chan, S. H., and Tien, C. L., "Infrared Radiative Properties of Sulfur Dioxide," ASME JOURNAL OF HEAT TRANSFER, Vol. 93, 1971, pp. 172-178.

16 Kanury, A. M. *Introduction to Combustion Phenomena*, Gordon and Breach Science Publishers, New York, 1975.

M. M. Tunç
Assistant Professor.
Assoc. Member ASME

A. Karakaş
Assistant Professor.

Technical University of Istanbul,
Mechanical Engineering Faculty,
Gümüşsuyu,
Istanbul, Turkey

Three-Dimensional Formulation of the Radiant Heat Flux Variation on a Cylinder Engulfed in Flames

A three-dimensional formulation is used to determine the incident radiant heat flux on a cylinder surface which is engulfed in flames. For an axisymmetric horizontal pool fire of a specified flame shape, effective flame radiation temperature and a gray flame absorption coefficient, this analysis computes the variation of the incident radiant heat flux along the length and around the circumference of the tank portrayed as a cylinder, engulfed in flames. The radiant flux density from the flame to the cylinder becomes maximum toward the center of the pool and decreases markedly toward the edges. The points which are receiving the maximum amount of radiation heat flux around the circumference of the cylinder are also determined.

Introduction

Under certain accident conditions, cylindrical tanks containing liquefied gases, in particular LPG, may be exposed to enveloping pool fires. The primary objective of this paper is to determine the variation of the incident radiant heat flux along the length and around the circumference of the tank, portrayed as a cylinder, engulfed in flames.

There are numerous studies concerned with the properties of pool fires and the resulting radiant heat flux to external targets and to the pool surface. A mathematical model was developed by Masliyah and Steward [1] to calculate the radiative emission from the flame. The radiative interchange between the flame and the plane surrounding its base was determined by assuming the flame to be a gray emitter. To compute the radiative heat flux from a luminous pool fire to an arbitrarily located target surface, either within or external to the fire, a general calculation procedure has been presented by Modak [2]. Recently Birk and Oosthuizen [3] estimated the radiant heat transfer to a long horizontal cylinder engulfed in flames. In their two-dimensional analysis, the cylinder is considered to be of infinite length and the combustion gases which surround the cylinder occupy a space which can be represented by a rectangle. The walls of this rectangle are represented by an infinite but stagnant medium. The model estimates the various surface-to-surface and surface-to-volume exchange factors as a function of position around the circumference of the cylinder. This method is not able to determine the radiant heat flux variation along the length of the cylinder.

The present study presents a three-dimensional formulation to determine the variation of incident radiant heat flux along the length and around the circumference of the tank, portrayed as a cylinder, engulfed in flames. The influence of the effective flame temperature and the absorption coefficient on the incident radiant heat flux are investigated.

Calculation of the Incident Radiant Heat Flux Along the Length and Around the Circumference of the Cylinder

The radiation interchange between an elemental volume dV_i of radiating gas in the flame and an arbitrary surface element dA_j on the cylinder surface is depicted in Fig. 1.

The following assumptions are made in the present analysis.

(*a*) The effect of scattering is negligible [4].
(*b*) The effect of convective heat transfer is neglected [2].
(*c*) The flame shape is an important parameter and controls the radiative heat flux coming to the cylinder surface. This analysis avoids arbitrary assumptions regarding shapes (such as conical, rectangular or cylindrical flames, etc.) and instead characterizes the flame shape by means of axisymmetric flame contours obtained from actual photographs and other experimental evidence from large ($W \geq 4.5$ m) JP-4 jet fuel pool fires [5]. In this work a fourth-order polynomial is fitted to the contours of the flame to describe the radius of the flame as a function of height

$$R(z) = a_0 + a_1 z + a_2 z^2 + a_3 z^3 + a_4 z^4 \quad (1)$$

Table 1 Geometric parameters of the pool fire and the cylindrical tank: dimensions of the 1/5 scale rail tank car and a typical pool fire

Quantity	Value
a_0 (m)	2.24
a_1	-0.3806
a_2 (m^{-1})	$0.6202 \cdot 10^{-1}$
a_3 (m^{-2})	$0.1219 \cdot 10^{-1}$
a_4 (m^{-3})	$-0.3706 \cdot 10^{-2}$
D (m)	0.61
H (m)	6
h (m)	0.31
L (m)	3.66
W (m)	4.5

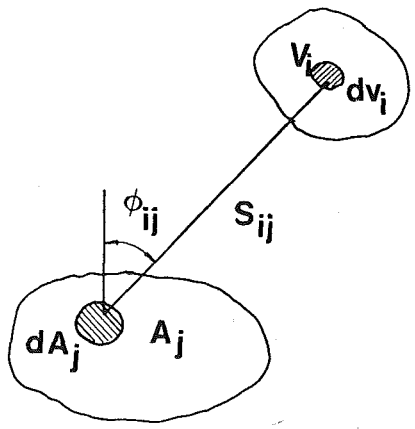

Fig. 1 Exchange between gas volume V_i and surface A_j

Contributed by the Heat Transfer Division for publication in the JOURNAL OF HEAT TRANSFER. Manuscript received by the Heat Transfer Division March 16, 1984.

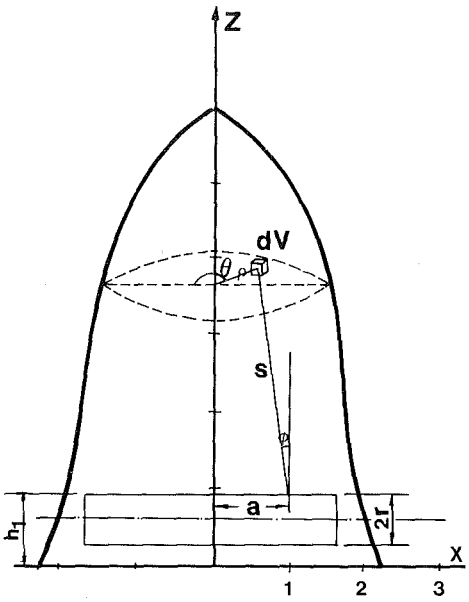

Fig. 2(*a*) Geometry of gas radiation interchange between a flame volume and an element of area located on the top plane of the cylinder

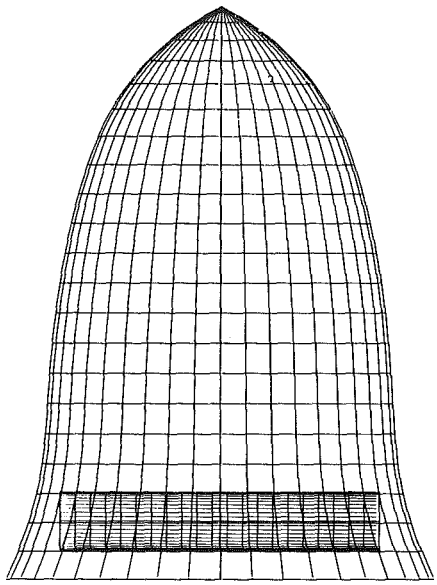

Fig. 3 A three-dimensional computer model for the pool fire and the cylinder

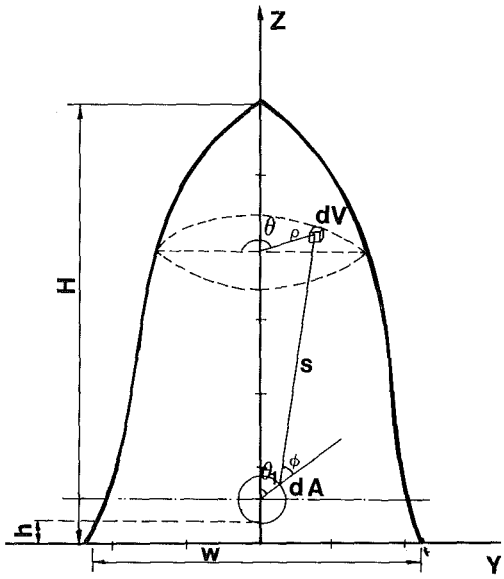

Fig. 2(*b*) Geometry of gas radiation interchange between a flame volume and element of area located by the θ_1 angle on the circumference of the cylinder

The flame shape corresponding to equation (1) is shown in Fig. 2. A three-dimensional computer model for the pool fire and the cylinder is shown in Fig. 3.

(*d*) The cylinder surface is a black body. The dimensions of the pool fire and the cylindrical tank and a_0, a_1, a_2, a_3, a_4 are given in Table 1.

(*e*) Finally, as a first step, we assume that the flame is an isothermal gas having a constant absorption coefficient.

Under these assumptions, the rate of radiative heat transfer between any arbitrary volume V_i and surface element of the tank A_j is given by the following expression [4]

$$Q=(K\sigma T^4/\pi)\int_{V_i}\int_{A_j}(\cos(\phi_{ij})\exp(-KS_{ij})/S_{ij}^2)dV_i dA_j \qquad (2)$$

(*a*) The Longitudinal Radiant Heat Flux Variation. The radiation interchange between an elemental volume dV of radiating gas in the flame and an arbitrary surface element dA on the top line of the cylinder ($h_l - h = 2r$), is depicted in Fig. 2(*a*). From the same figure the following relationships may be obtained

$$dV = \rho d\theta d\rho dz \qquad (3a)$$

$$\cos\phi = (z-h_1)/S \qquad (3b)$$

$$S^2 = a^2+(z-h_l)^2+\rho^2+2a\rho\cos\theta \qquad (3c)$$

Nomenclature

A = surface area, m^2
a = distance between the point under consideration and the top center point on the cylinder
a_i = flame shape constants, equation (1)
D = diameter of the cylinder, m
H = height of the combustion zone, m
h_l = distance between the top of the cylinder and the ground, m
h = distance between the bottom of the cylinder and ground, m
K = mean absorption coefficient of the combustion gases, m^{-1}
L = length of the cylinder, m
Q = rate of radiant heat transfer between an element of volume and a surface element, W
q = radiative flux density on a surface received from a finite source, W/m^2
r = radius of the cylinder, m
$R(z)$ = flame radius, m
S = absorbing path length, m
T = temperature, K
V = volume, m^3
W = width of the pool fire, m
T_f = flame temperature, K
x = horizontal axis
z = vertical axis
θ = angular coordinate, rad
θ_1 = angle between the vertical vector and the vector between the center of the cylinder and the point of interest on the circumference of the cylinder, rad
ρ = radial coordinate, m
σ = Stefan-Boltzmann constant, 5.66×10^{-8} W/m^2K^4
ϕ = angle between the connecting vector and the vector normal to the surface element, rad

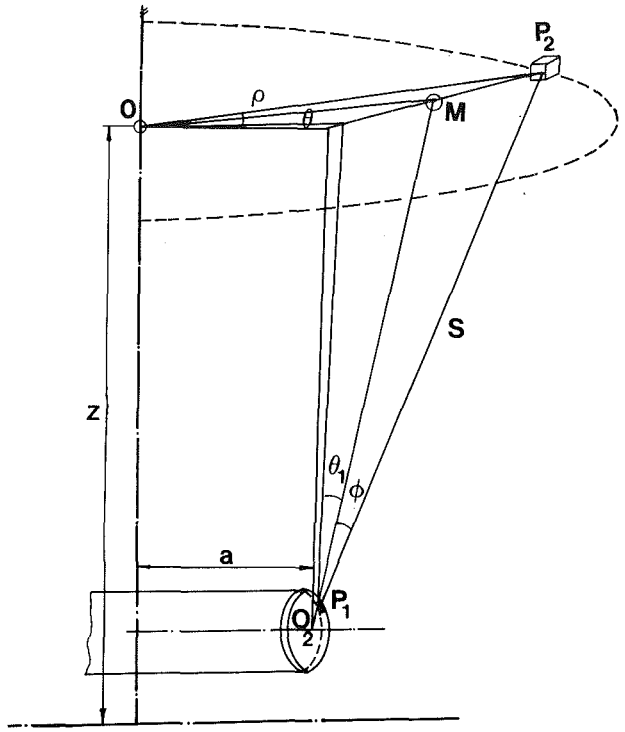

Fig. 4 Geometry for determining the absorbing path length s and cos ϕ

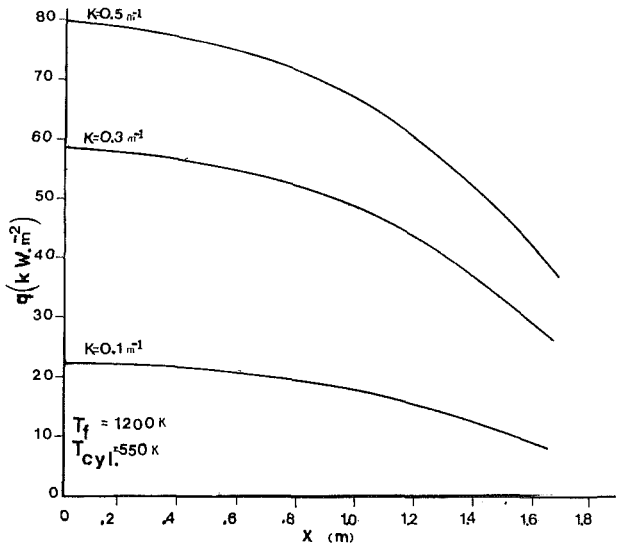

Fig. 5 The variation of the incident radiation heat flux longitudinally of the cylinder

Substituting the above quantities into equation (2) and integrating over proper limits yields the total flux density received by the area element dA from the flame

$$q=\int_{h_l}^{H}\int_{0}^{R(z)}\int_{0}^{\pi}\frac{2\sigma KT^4\rho(z-h_l)\exp(-KS)}{\pi S^3}\,d\theta d\rho dz \tag{4}$$

The triple integral above was solved numerically using Simpson's rule.

(*b*) The Circumferential Radiant Heat Flux Variation. The radiation interchange between an elemental volume dV of the radiating gas and the surface element dA located on the yz plane with an arbitrary angle θ_1 is shown in Fig. 2(*b*). For $0<\theta_1<\pi$ and $\theta_1\neq\pi/2$

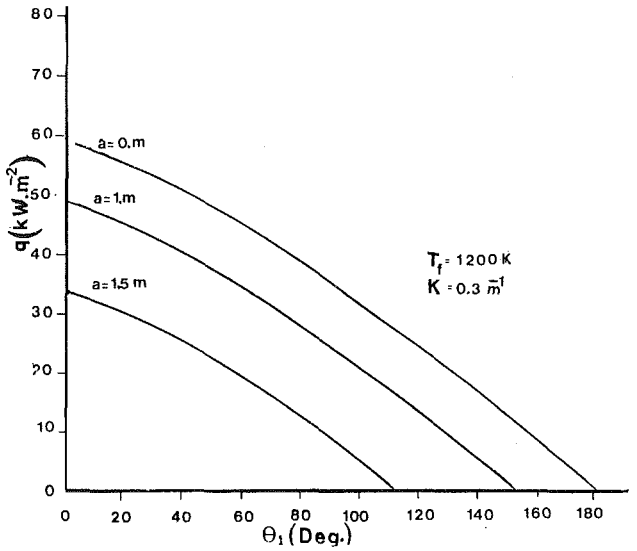

Fig. 6 Circumferential variation of the incident radiant heat flux for three different locations

$$\cos\phi=\frac{\cos\theta_1}{2S(z-(h+r+r\cos\theta_1))}\cdot\left(\left\{\frac{(z-(h+r+r\cos\theta_1))}{\cos\theta_1}\right\}^2+S^2-\rho^2-a^2-\{r\sin\theta_1+\tan\theta_1\cdot(z-(h+r+r\cos\theta_1))\}^2+2\rho\{a^2+\{r\sin\theta_1+\tan\theta_1\cdot(z-(h+r+r\cos\theta_1))\}^2\}^{1/2}\cdot\cos\left\{\theta-\tan^{-1}\left[\frac{\{r\sin\theta_1+\tan\theta_1\cdot(z-(h+r+r\cos\theta_1))\}}{a}\right]\right\}\right) \tag{5}$$

$$S^2=[z-(h+r+r\cos\theta_1)]^2+\rho^2+a^2+r^2\sin^2\theta_1-2\cdot\rho\cdot(a^2+r^2\sin^2\theta_1)^{1/2}\cdot\cos\left\{\theta-\tan^{-1}\left(\frac{r\sin\theta_1}{a}\right)\right\} \tag{6}$$

The calculation procedure for the above equations is illustrated in Fig. 4. During evaluation of the heat flux integral, the calculation of $\cos\phi_{ij}$ with the independent variables θ_1, ρ, θ, z has a singular value for $\theta_1=\pi/2$.

For $\theta_1=\pi/2$, the following equations were used

$$\cos\phi=\frac{(a^2+\rho^2-2a\rho\cos\theta)^{1/2}\cdot\sin\theta-r}{S} \tag{7}$$

$$S^2=(z-(h+r))^2+\rho^2+r^2+a^2-2\rho r\sin\theta-2a\rho\cos\theta \tag{8}$$

Substituting the above into equation (2) and integrating over proper limits yields the total heat flux density received by the area element dA_j on the circumference of the cylinder, located by the θ_1 angle

$$q=\int_{h/6}^{H}\int_{0}^{R(z)}\int_{0}^{2\pi}\frac{\sigma KT^4\rho\exp(-KS)\cos\phi}{\pi S^2}\,d\theta d\rho dz \tag{9}$$

Only the portion of the pool fire which is above a plane tangent to the point of interest on the circumference of the cylinder has to be considered in the above integration, so it is always true that $\phi<\pi/2$.

Results

Figure 5 shows the variation of incident radiant heat flux along the top surface of the cylinder for different K values. The flame temperature and the wall temperature are assumed to be 1200 K and 550 K respectively. The surface temperature

of the cylinder varies circumferentially. However, due to the intense heat flow from the surface of the cylinder to the LPG within it, 550 K is taken as an average circumferential value [5]. It is clear from Fig. 5 that the radiant heat flux from the flame to the cylinder is maximum at the center of the pool and decreases markedly toward the edges.

The circumferential variation of the incident radiant heat flux is shown in Fig. 6. The flame temperature and the wall temperature are assumed to be 1200 K and 550 K, respectively. The circumferential heat flux variation is depicted for three different locations along the length of the cylinder. From this figure it is clearly seen that the top of the cylinder receives the maximum amount of radiation, and that the incident heat flux varies considerably around the circumference of the cylinder near the center of the pool fire. Toward the edges of the cylinder the circumferential heat flux variation is smaller. The estimated accuracy of the numerical closure in the above computations is around 6 percent.

Acknowledgments

Professor J. E. S. Venart and Professor F. R. Steward of the University of New Brunswick provided many helpful suggestions. The assistance of the Mechanical Engineering Department of the University of New Brunswick, Canada is gratefully acknowledged.

References

1 Masliyah, J. H., and Steward, F. R., "Radiative Heat Transfer From a Turbulent Diffusion Buoyant Flame With Mixing Controlled Combustion," *Combustion and Flame*, Vol. 13, 1969, pp. 613–625.

2 Modak, A. T., "Thermal Radiation From Pool Fires," *Combustion and Flame*, Vol. 29, 1977, pp. 177–192.

3 Birk, A. M., and Oosthhuizen, P. H., "Model for the Prediction of Radiant Heat Transfer to a Horizontal Cylinder Engulfed in Flames," ASME Paper No. 82-WA/HI-52, 1982.

4 Siegel, R., and Howell, J. R., *Thermal Radiation Heat Transfer*, McGraw-Hill, New York, 1972.

5 Appleyard, R. D., "Testing and Evaluation of EXPLOSAGE System as a Method of Controlling the Boiling Liquid Expanding Vapour Explosion," Transport Canada Report No. TP 2740, 1980.

6 Ömer, A. D., and Cedomir, M. S., "Effect of Wind on Buoyant Diffusion Flames," *I & EC Fundamentals*, Vol. 3, No. 2, 1964, pp. 147–154.

7 Charles, A., "The Effects of a Fire Environment and Rail Tank Car Filled With LPG," U.S. Department of Transportation, PB-241358, 1974.

8 Hottel, H. C., and Sarofim, A. D., *Radiative Transfer*, McGraw-Hill, New York, 1967.

9 Steward, F. R., Private communication, 1984.

J. W. Baughn
Professor.
University of California,
Davis, CA
Mem. ASME

R. K. Takahashi
Aerospace Engineer.
Ames Research Center,
Moffett Field, CA

M. A. Hoffman
Professor.

A. A. McKillop
Professor.
Mem. ASME

University of California,
Davis, CA

Local Heat Transfer Measurements Using an Electrically Heated Thin Gold-Coated Plastic Sheet

This paper describes an experimental technique for measuring the local heat transfer coefficient in complex flows. The technique employs a gold-coated plastic sheet to generate a nearly uniform wall heat flux. The sheet is mounted on an insulated substrate of the desired shape and heating is achieved by passing an electrical current through the gold coating. Three applications of this technique are described: heat transfer downstream of an abrupt expansion, heat transfer from a cylinder in crossflow, and nonuniform circumferential heating in a pipe. For each of these applications the effect of the wall conduction on the surface heat flux is evaluated and found to be small. The effect of nonuniformities in the gold coating, and of the resistance temperature coefficient, are also evaluated and likewise are found to be quite small. Methods of correcting for each of these small effects are presented for the above applications.

Introduction

In many different heat transfer experiments, the determination of local convective heat transfer coefficients for a constant wall heat flux boundary condition is often complicated by wall conduction effects. This is especially true in two- and three-dimensional flows with significant spatial variations of the heat transfer coefficient. Evaluation of the local heat transfer coefficients may also be difficult in simple flows if nonuniform thermal boundary conditions are present (for example, a circumferential variation in surface heat flux or temperature even with fully developed flow in a circular pipe).

This paper describes a technique employing a thin gold-coated plastic sheet to generate a nearly uniform wall heat flux. The plastic sheet is mounted on test sections of the desired geometry made of low-thermal-conductivity materials; the combination thereby helps to reduce the effects of wall conduction. The nearly uniform coating of gold acts as an electrical conductor and when a current is passed through, it provides a nearly uniform and constant wall heat flux. The local temperatures are measured with fine-gage thermocouples attached to the back of the plastic sheet, from which the local heat transfer coefficients can then be calculated. A brief description of the thermal and electrical characteristics of this gold-coated sheet is given, and the corrections required for the calculation of the local heat flux due to the following effects are described:

(1) wall conduction effects
(2) nonuniformities in the gold-coating resistance due to nonuniform coating thickness, density, etc.
(3) effect of temperature on the resistance of the gold coating

The emphasis in this paper is on the gold-coated sheet technique and on the evaluation of the above corrections for each of three different applications. These corrections are shown to be small in all three cases. The detailed descriptions of each of the three experimental apparatus and the extensive results for the three experiments are beyond the scope of this paper; however, they are given in [1, 2, 3].

The most common technique for achieving a uniform wall heat flux has been the use of an electrically heated metal wall. This technique fixes the wall heat flux, within limits set by the uniformity of the wall and wall conduction corrections, and then the local wall temperature is measured. An early example of this technique is the study by Ede et al. of flow in a pipe [4]. The most diverse use of this technique, no doubt, has been that by Sparrow and his students whose work over many years has included heat transfer in circular pipes with orifices [5], with tee's [6], with a segmental orifice plate [7], and with slat blockage [8]. Another example of this technique is the study of heat transfer downstream of an abrupt expansion in a circular tube by Zemanick and Dougall [9]. This technique has proven to be a powerful approach, when the wall conduction is not too significant or when accurate corrections for the wall conduction can be made. However, when the heat transfer coefficient is low, as it often is with air, the wall conduction may overwhelm the results in some regions, making the use of a metal wall with any appreciable thickness subject to unacceptable uncertainties in the wall conduction correction.

There are two ways to help reduce the wall conduction effect: (1) make the wall very thin; (2) use a wall material which has a low thermal conductivity. If the wall is to be electrically heated, however, it must be metal, which conflicts with condition (2) above. One way to handle this dilemma is to use a metal heating element, like Nichrome, wrapped around a body with thin walls of low thermal conductivity of the desired shape. An early example of this method is the study by Seban et al. [10, 11] of heat transfer downstream of a backward-facing surface step. This technique was also used by Giedt [12] for a cylinder normal to an air stream. In both of these cases Nichrome ribbon was attached to a plastic (bakelite and lucite, respectively) substrate. A more recent example is the study by Petri and Simpson [13] of the effect of free-stream turbulence on local heat transfer from a cylinder in crossflow. They used a thin stainless steel foil rolled into cylindrical shape and filled with epoxy resin.

In the limit, the thin electrical heating element on the surface can be reduced to a coating applied to the surface. This is the approach described in this paper. A good example of this approach is the glass tube with an electrically conducting coating used by Morcos and Bergles [14]. Unfortunately, in this case, the glass substrate was not a suf-

Contributed by the Heat Transfer Division and presented at the National Heat Transfer Conference, Niagara Falls, New York, August 1984. Manuscript received by the Heat Transfer Division February 21, 1984.

ficiently good thermal insulator, and hence it was necessary to make conduction corrections. A number of investigators have used a plastic substrate with a copper coating, an example being the experiments in a flat duct by Hatton and Woolley [15]. In two recent investigations, a gold-coated sheet, similar to the one described in this paper, has been used as the heater. Simonich and Moffat [16] and Hippensteele et al. [17] used such a heater in conjunction with liquid crystals for thermal visualization of heat transfer.

In summary, the thin, gold-coated plastic sheet technique described next seeks to achieve a constant wall heat flux while avoiding the often large conduction corrections associated with metal walls.

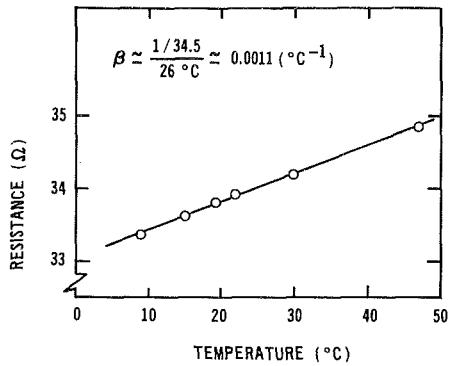

Fig. 1 Temperature coefficient of resistance of the gold coating (nominal 6 Ω/sq)

Description of Gold-Coated Sheet Technique

The technique we have employed makes use of a transparent thin polyester sheet on which a gold coating has been vacuum deposited. This coating of gold is thin enough to be somewhat transparent and has negligible conduction along the surface. The wall conduction is then determined essentially by the substrate on which the thin polyester sheet with the gold coating is mounted. The gold layer is overcoated with a very thin transparent and electrically conducting protective coating in the manufacturing process and is stable to approximately 90°C. However, we have only used it to 60°C. The sheet is manufactured by Sierracin/Sylmar (Sylmar, CA) and is called Intrex. The sheets used in each of the three applications described in this paper were 0.13 mm thick and can be purchased with gold-coating resistances ranging from 3 to 26 Ω/sq. This thickness of sheet is flexible, but remains smooth when glued or otherwise attached to a substrate. The gold coating is electrically heated and the wall temperature is measured with fine-gauge thermocouples mounted on the back of the sheet. The heat flux is determined by the electrical current and the local resistance, which is slightly temperature dependent.

Electrical contact with the gold coating was attained by gluing, with an electrically conducting adhesive, 0.09-mm-thick metal electrodes to the Intrex surface. It is important that these electrodes lie flat so as not to disturb the flow. Our early experiments used silver-loaded epoxy sandwiched between the Intrex and aluminum foil electrodes. Later experiments used copper foil with adhesive backing and a silver-loaded paint, called Electrodag (Acheson Industries, Inc., Port Huron, Michigan), which provided a more durable and stable connection. The method of attaching the copper foil electrode to the Intrex was as follows. A stripe was painted on the gold coating with the Electrodag and allowed to dry. The length of the stripe was the same as that of the electrode but the width was about 1-2 mm wider, or typically 4-5 mm wide. A copper wire was soldered to the copper foil and the junction peened flat and placed, adhesive side down, on the silver stripe such that one edge along the length of the electrode was flush with one edge of the stripe. An identical Electrodag stripe was painted over the original stripe and the electrode. This ensured good electrical contact between the copper electrode and the gold coating.

To allow various heating patterns (for example, in application (*c*) below) the Intrex surface was scribed with electrical isolation lines such that only the area between selected lines was heated. The isolation lines were drawn by using a sharp blade and cutting through the gold coating but not through the polyester sheet. Electrical isolation could be ensured by applying an appropriate voltage across the line such that any stray electrical connection would be burned open. This burning was usually accompanied by a visible spark and an audible crackling noise.

Of particular interest was the uniformity of resistance of the gold coating. Measurements of the resistance uniformity were made by applying a known voltage and current between the ends of a narrow strip of Intrex and measuring the voltage drop between two probes in contact with the conducting surface and a fixed distance apart. Measurements at many positions showed that the resistance varied by only 4–5 percent from a mean value throughout the central portion of the sheet (typically the central 40 percent of an 86-cm-wide roll). The resistance increased as the edges of the sheet were approached. As a result, we have always used only the central portion.

Measurements were also made of the temperature coefficient of resistivity of the gold coating, β. Tests strips of the Intrex were placed in a constant temperature water bath, accurate to ± 0.01°C, and the coating resistance was measured using a four-wire resistance measurement technique. The results for these test strips (shown in Fig. 1) yielded a value of $\beta = 0.0011\ (°C)^{-1}$. (Note that the resistivity and its temperature sensitivity are different for this thin coating than for the bulk material.)

Nomenclature

d = entrance diameter to abrupt expansion
D = diameter of test section
F = correction factor
h = heat transfer coefficient
I = electrical current
k = thermal conductivity
L = length
Nu = Nusselt number
q''_a = actual surface heat flux
q''_e = local electrical power per unit area
q''_L = local heat loss
$\overline{q''}$ = average heat flux
R = electrical resistance, Ω
R_0 = resistance measured at T_0, Ω
R'' = electrical resistance per square, Ω/sq
$\overline{R''}$ = average resistance per square, Ω/sq
Re = Reynolds number, UD/ν
r = radial coordinate
$\bar{r}$ = radius to center of pipewall
T = wall temperature
T_f = fluid static temperature
T_0 = reference (or room) temperature
U = fluid velocity
V = voltage
w = local width of gold strip
$\bar{w}$ = averaged width of gold strip
z = axial coordinate
β = temperature coefficient of gold-coating resistance
δ_w = wall thickness
θ = circumferential coordinate
ν = kinematic viscosity

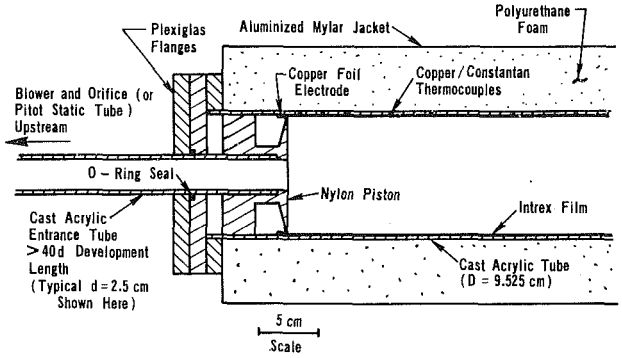

Fig. 2 Diagram of the abrupt expansion region showing the design details

The local R'' varies with temperature according to the relation:

$$R'' = R_0''(T_0)[1+\beta(T-T_0)] \tag{1}$$

where R'' is defined as the resistance per square (Ω/sq) of the coating, a common measure of coating resistance. [Note: the resistance is proportional to the length and inversely proportional to the width and therefore is independent of the size for a square.] The nominal value of R_0'' at $T_0 = 20°C$ for these test strips was 6 Ω/sq.

This sheet has been used in three applications which are described below. The next section describes the typical magnitudes of the wall conduction effects for these applications. Then following this, the data reduction methods accounting for the gold coating nonuniformity and temperature coefficient of resistance of the coating are described.

Wall Conduction Effects

General. A convenient dimensionless measure of wall conduction effects (following [18]) is:

$$N_c \equiv \frac{q_e''-q_a''}{q_e''} = \frac{q_L''}{q_e''} \tag{2}$$

where q_e'' is the local electrical power per unit surface area, q_a'' is the actual surface heat flux into the flow, and q_L'' is the local heat loss due to wall conduction. Physically, N_c is the fractional change in the wall heat flux into the flow due to wall conduction.

In order to determine q_a'' for most constant-wall-heat-flux experiments, some estimate of the wall conduction heat loss q_L'' must first be made. Once q_L'' is known, a value of the local heat transfer coefficient corrected for wall conduction can be calculated from:

$$h = (q_e''-q_L'')/(T_w-T_f) = q_a''/(T_w-T_f) \tag{3}$$

where T_w is the local wall temperature and T_f is a local fluid temperature. However, in most cases, the estimation of the wall conduction corrections (and consequently, also of N_c) depends on h. As a result, an iterative correction process is generally required to find accurate values of h and N_c, and there are always some residual uncertainties in this correction process. Therefore it can be seen that, in general, the smaller the wall conduction effects (i.e., N_c), the smaller will be the final uncertainties in h. In this section we will show that the gold-coated sheet technique leads to very small values of N_c in the three applications considered. As a result, the corrections for wall conduction effects are very small and even unnecessary in some cases.

(*a*) *Abrupt Expansion in a Pipe.* In this application, the thin gold-coated sheet technique was used to study heat transfer at the inner surface of the large tube downstream of an abrupt expansion [1]. A detailed drawing of the abrupt expansion region with the gold-coated sheet is shown in Fig. 2. On the downstream end of each of the small diameter tubes was a nylon "piston"; this defined the abrupt expansion into the heated region which had a fixed diameter of $D = 9.525$ cm. Five different values of d (2.54, 3.81, 5.08, 6.35, and 7.62 cm) were used to obtain a range of d/D values between 0.267 and 0.800.

The heated tube had a heated length of 171 cm (18 dia) and a wall thickness of 3.2 mm (1/8 in.). The tube material, cast acrylic, was chosen for its low thermal conductivity. The gold-coated sheet was glued to the tube while being tightly pressed against the tube inner surface by an inflated rubber tube. Weld-On-3 (Industrial Polychemical Service, Gardena, CA) capillary cement injected with a hypodermic syringe through small holes in the tube wall was used to ensure a permanent bond between the sheet and the tube wall.

The copper electrodes at each end were connected to a variable transformer in series with a 120 V a-c regulator, allowing an adjustable, but stable, a-c voltage to be set. Voltages used in the experiments ranged from 42 to 125 V a-c, providing a total power to the heated tube of 42 to 370 W. This, in turn, gave heat fluxes of 80 to 720 W/m^2. These low heat fluxes and the corresponding low wall temperatures (typically 5–20°C above the bulk temperature) result in negligible buoyancy effects.

To minimize axial conduction in the area near the corner of the abrupt expansion, the copper foil electrode was located about 5 cm upstream of the abrupt expansion, away from the tube flanges. To further reduce axial conduction, the abrupt expansion piston was designed of low-thermal-conductivity nylon. To minimize radial conduction losses to the ambient air, the tube was covered with 5.1 cm of polyurethane foam and, to minimize radiation losses to the room, the foam was wrapped with an aluminized mylar jacket.

The local tube wall temperatures were measured with thermocouples (0.08 mm type T) epoxied to the back side of the Intrex through small holes in the tube wall. The thermocouples were calibrated against a platinum resistance thermometer using a constant temperature bath. A typical axial profile for the inner wall temperature is shown in Fig. 3(*a*). A 2-D conduction analysis for the radial and axial heat flows in the acrylic tube wall was performed using these measured inner wall temperatures as the inner boundary condition. The outer boundary condition used the value of the free convection heat transfer coefficient on the outside of the polyurethane foam; the results were found to be insensitive to this outer boundary condition.

The local values of q_e'' shown in Fig. 3(*b*) were evaluated next by correcting the reference R_0'' for the effects of the local wall temperature using the β of Fig. 1. This is described in detail in the next section. The actual heat flux q_a'' shown in Fig. 3(*b*) was then calculated by subtracting the local q_L'' calculated in the 2-D conduction analysis from q_e''. Finally, the local N_c shown in Fig. 3(*b*) was calculated from equation (2).

From Fig. 3(*b*) we see that this design does indeed have a reasonably low N_c in most positions. The relatively low values of N_c in the vicinity of the piston ($0.1 < z/D < 1.0$) allowed heat transfer coefficients in that region to be accurately determined from temperature measurements, such as Fig. 3(*a*). These measurements revealed that, in many cases, there was a peak in the temperature distribution at the abrupt expansion which was attributed to a secondary recirculation region (see [1] for full details). This feature was not clearly evident in other similar experiments using metal tube heating sections.

(*b*) *Cylinder in Crossflow.* In this application, the gold-coated sheet was used in the study of heat transfer from a heated cylinder to air in an external crossflow. A cylindrical test section was constructed by chemically bonding the gold-coated sheet to a solid polyurethane cylinder with brass end fittings (Fig. 4). As in the other experiments, calibrated type T thermocouples (40 gauge) were mounted on the inside surface

of the plastic sheet to measure the wall temperatures. This cylinder was also used to study heat transfer in tube banks [2].

Electrical connections between the brass fittings and the gold surface were achieved by use of Electrodag conducting paint. Two wires were attached to each of the brass fittings; one set of wires served as the power leads during runs while the other served as leads for the cylinder voltage measurements. When no power was supplied to the tube, the wires could be used to make a four-wire resistance measurement. In the calibration phase of the program, the resistance of the gold coating was compared to the total resistance measured by the four-wire method. It was found that the resistance of the electrodes was less than 1 percent of the total resistance. In the data reduction, therefore, this electrode resistance was subtracted from the total cylinder resistance.

An analytical evaluation of the wall conduction was made using a two-dimensional (radial and circumferential) numerical conduction analysis with an impressed heat flux of 1.24 kW/m^2. As a surface boundary condition we used a previously determined experimental heat transfer coefficient shown in Fig. 5(*a*). The free-stream air temperature was assumed constant. The calculated heat flux distribution q_a'' and N_c obtained from this analysis are shown in Fig. 5(*b*). The maximum wall conduction effect occurs near the point of minimum heat transfer, as would be anticipated. The maximum correction as shown in Fig. 5(*b*) is approximately 2.5 percent. This value depends, of course, on the knowledge of h at separation, which is the region where its value might be most suspect. However, the analysis shows that the correction is small and that this design achieved its goal of small wall conduction effects.

(*c*) *Nonuniform Circumferential Heating in a Pipe.* In this application, the thin gold-coated sheet technique was used to study heat transfer in a pipe with nonuniform circumferential heating [3]. To accomplish this, the gold coating was scribed to provide a series of electrically independent axial strips. With the Intrex sheet glued to the inside of an acrylic tube using the same method as in the abrupt expansion experiment, these axial strips provided a means for producing different circumferential heat flux profiles.

Three to five tubes, each of L/D = 19.2, were used upstream of the heated section to obtain hydrodynamically fully developed flow. The heated sections used acrylic tubes identical to the entry-length tubes except that the gold-coated sheet was glued on the inside as shown in Fig. 6. The electrical isolation lines were scribed at 30 deg (circumferential) intervals and individual electrodes at the flanges made it possible to individually heat the strips in any programmed fashion.

The a-c electrical power to each strip in this case was individually controlled with a standard dimmer switch. Type T (0.08 mm) thermocouples were mounted with epoxy cement on the back of the polyester sheet (next to the inner surface of the tube) through holes in the tube wall at various axial and circumferential positions, and 5 cm of urethane foam insulation was mounted on the outside of the tubes. The entire apparatus was wrapped with an aluminized mylar jacket to minimize radiation heat loss.

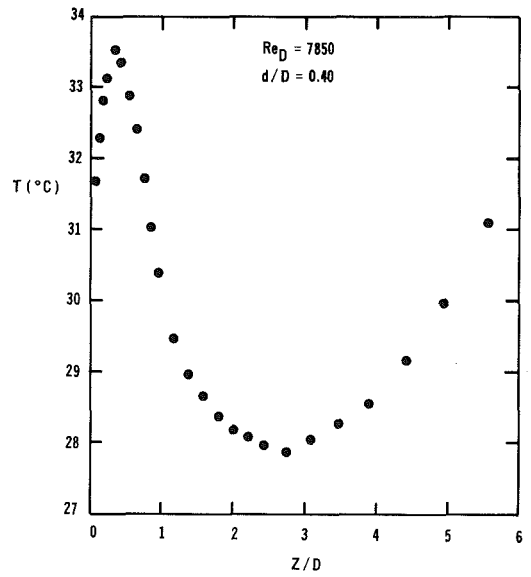

Fig. 3(*a*) Typical measured temperature distribution in the abrupt expansion region

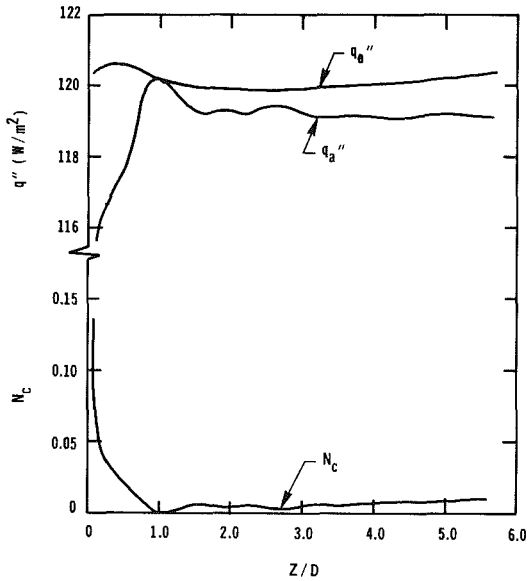

Fig. 3(*b*) Calculated conduction effects in the abrupt expansion region

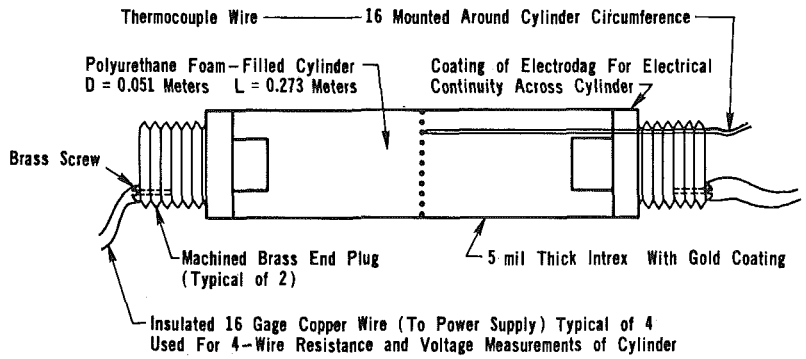

Fig. 4 Diagram of the constant-wall-heat-flux design for the cylinder in crossflow

A 2-D (radial and circumferential) conduction analysis of the acrylic tube and urethane foam for this apparatus was made using the measured wall temperatures as a boundary condition (the axial conduction was negligible). A typical experimental inner wall temperature profile for a Reynolds number of about 50,000 for the case of top-half heating is shown in Fig. 7(*a*). Using this temperature profile as the inner boundary condition for the 2-D conduction calculation, the resulting heat flux to the air flow q_a'' shown in Fig. 7(*b*) was calculated. The outer-wall boundary condition was the sum of a circumferentially varying free convection heat transfer coefficient and an effective heat transfer coefficient for radiation.

Local heat losses due to radiant exchange between the heated and unheated surfaces of the inner wall were also included in the analysis. A radiation analysis using the emissivity value $\epsilon = 0.15$ (the manufacturer recommended 0.10 to 0.20) showed that the maximum local radiation heat loss was about 0.014 q_e'' for the case of top-half heating.

From Fig. 7(*b*) we see that even for the extreme case of top-half heating, the circumferential heat flux pattern q_a'' is quite close to the ideal step value represented by q_e'' everywhere except very close to 90 deg. This is reflected in the values of $N_c(\theta)$ which are less than 0.05 for all angles up to about 80 deg.

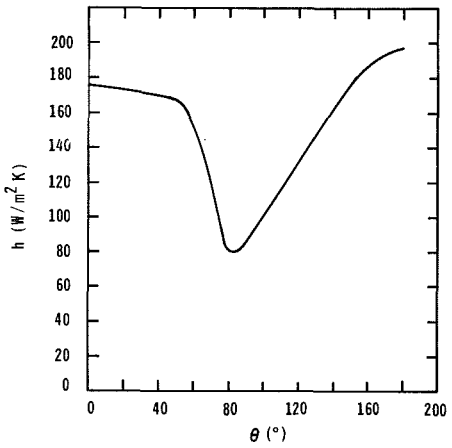

Fig. 5(*a*) Thermal boundary condition used for the conduction analysis of a cylinder in crossflow

Corrections for Coating Nonuniformity and Temperature Effects

General. The primary measurements in the three experiments described above are the heat flux and the wall temperature distributions (circumferential and/or axial) from which local Nusselt numbers can be determined by

$$\mathrm{Nu} = \frac{q_a''}{T_w - T_f}\frac{D}{k} \tag{4}$$

where q_a'' is the actual heat flux from the wall into the fluid, T_w is the measured wall temperature, k is the local thermal conductivity of the fluid at the film temperature, and D is the crossflow cylinder outer diameter or pipe inner diameter. The fluid temperature T_f is the adiabatic wall temperature for the crossflow experiment, and the local bulk temperature for the pipe flow experiments.

A discussion of the methods used in each of the three applications to correct for the effects of gold-coating nonuniformities and the temperature coefficient of resistance of the coating (both normally small effects) follows.

(*a*) *Abrupt Expansion in a Pipe.* In the abrupt expansion experiment the primary interest was the axial

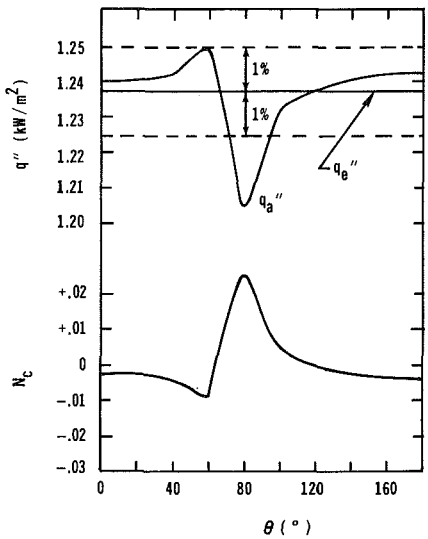

Fig. 5(*b*) Calculated conduction effects for a cylinder in crossflow

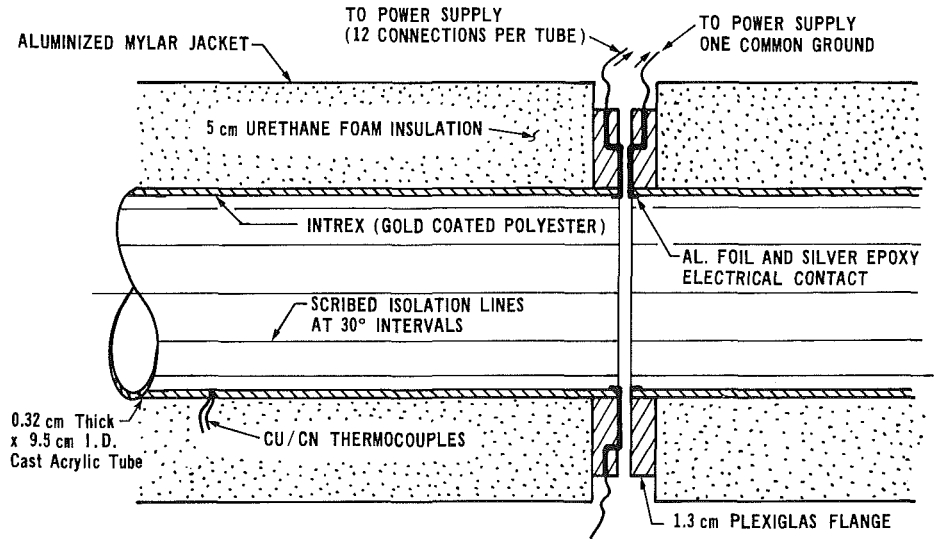

Fig. 6 Cross section of a portion of the tubes used in the nonuniform circumferential heating experiments showing the electrical connections at the flange between two tube sections

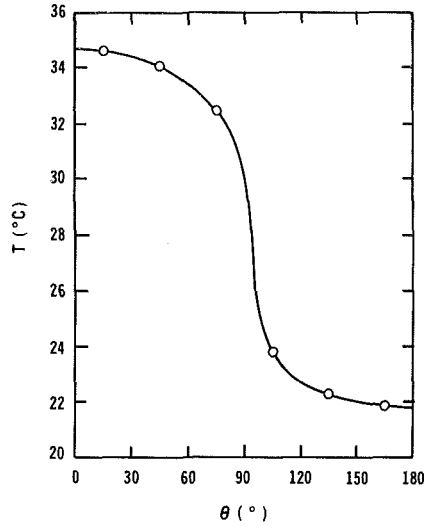

Fig. 7(*a*) Measured temperature distribution for the tube with nonuniform circumferential heating

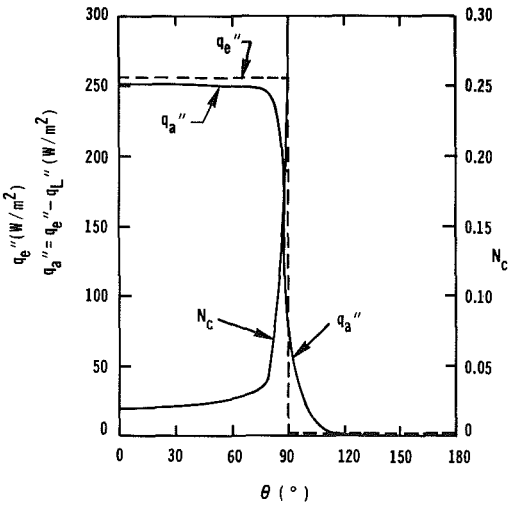

Fig. 7(*b*) Calculated conduction effects for the tube with nonuniform circumferential heating

variation of heat flux and wall temperature downstream of the expansion. The actual local heat flux into the flow was calculated as

$$q_a''(z) = q_e''(z) - q_L''(z) \tag{5}$$

where $q_e''(z)$ is the local electrical power per unit area and $q_L''(z)$ is the local heat loss due to conduction to the outside of the tube and axially in the tube wall. In this experiment the axial variations in Nu were large, so the small effects of the nonuniformity in the gold-coating thickness and hence resistance could be neglected, and the local heat flux was calculated as

$$q_e'' = \frac{I^2}{\pi D}\left(\frac{dR(z)}{dz}\right) \tag{6}$$

where I is the electrical current, and $dR(z)$ is the electrical resistance of the infinitesimal element of axial length dz. Introducing the gold coating resistance per square R'' we obtain

$$dR(z) = R''(z)\,\frac{dz}{\pi D} \tag{7}$$

$I = V/R(\bar{T})$, where V is the voltage across the Intrex and $R(\bar{T}) = R_0\,[1 + \beta(\bar{T} - T_0)]$ is the average resistance across the entire Intrex sheet at an average temperature $\bar{T}$. (T_0 is the temperature at which R_0 was measured.)

The local temperature affects the local resistivity as

$$R''(T,z) = \frac{\pi D}{L}[1 + \beta(T(z) - T_0)]R_0 \tag{8}$$

where L is the length of the Intrex sheet. Equation (6) finally becomes

$$q_e''(z) = \frac{V^2}{\pi D L R_0}\,\frac{[1 + \beta(T(z) - T_0)]}{[1 + \beta(\bar{T} - T_0)]^2} \tag{9}$$

The value of T_f used in the Nusselt number expression was that of the local bulk temperature, defined as

$$T_b(z) = \frac{\pi D}{\dot{m} c_p}\int_0^x [q_e''(z) - q_L''(z)]dz + T_{bi} \tag{10}$$

where T_{bi} was the inlet bulk temperature at the abrupt expansion, and $q_L''(z)$ was determined from the 2-D conduction analysis described in the preceding section. A check on this data reduction method was made by using the instrumented tube with straight flow (no expansion) and with nearly thermally developed conditions. For this application, the uncertainty in the Nusselt number, estimated with odds of 20:1 using the method of [19], ranged from ±2 percent at the lowest Nusselt number to ± 6.6 percent at the peak Nusselt number (which had smaller temperature differences). Details on the method of estimating the uncertainties are given in [20].

(*b*) *Cylinder in Crossflow.* In the crossflow experiment only the *circumferential* variations of heat flux and temperature were considered (axial wall conduction was neglected since the axial variations in h were found to be negligible). As shown earlier, the very small effect of wall conduction could be neglected in this experiment, and the actual heat flux into the fluid was expressed as

$$q_a''(\theta) = \frac{V^2 F_1}{R_0[1 + \beta(T(\theta) - T_0)]\pi D L} \tag{11}$$

where V is the voltage applied to the gold film and R_0 is the gold film resistance between the voltage connections measured at T_0. F_1 is the local correction factor for the nonuniformity of the gold coating and πDL is the gold-coated sheet surface area. The correction factor F_1 for nonuniformity of the gold coating was found by rotating the cylinder so that each thermocouple was at the stagnation point under nearly identical conditions. For the forward stagnation point in air the analytical and experimentally verified value of $\mathrm{Nu}/\sqrt{\mathrm{Re}}$ is 0.95. The correction factor, F_1, is the $\mathrm{Nu}/\sqrt{\mathrm{Re}}$ measured at the stagnation point divided by 0.95. The estimated uncertainty in the Nusselt number in this experiment was approximately 1–2 percent. The values of F_1 were found to be between 0.975 and 1.025. The detailed procedures used and the results are given in [21].

(*c*) *Nonuniform Circumferential Heating in a Pipe.* For the experiment with the circumferentially varying heat flux both circumferential and axial distributions of heat flux and temperature were important. The actual net heat flux into the fluid from a particular narrow strip at a mean angle θ (assumed uniform across its width) is expressed as

$$q_a''(z) = q_e''(z) - q_L''(z) \tag{12}$$

where $q_e''(z)$ is again the local electrical resistive heating per unit area and $q_L''(z)$ is the net local heat flux conducted radially and circumferentially in the tube wall and insulation.

Using a method analogous to that shown above for the abrupt expansion, the following expression for $q_e''(z)$ has been obtained [3]

$$q_e''(z) = \frac{V^2 R''(T,z)}{R_0^2[1 + \beta(\bar{T} - T_0)]^2 w^2} \tag{13}$$

where V is the voltage imposed on the strip, R_0 is the total resistance of the strip at T_0, $\bar{T}$ is the average temperature along the length and $R''(T,z)$ is the resistance per square at a particular position. For this case we defined a nonuniformity factor F_2 as

$$F_2 = \frac{R''(T_0,z)\bar{w}^2}{\bar{R}_0''[w(z)]^2} \tag{14}$$

where $\bar{w}$ is the average width of the strip and w is the width at a particular z. $\bar{R}_0''(z)$ is the average resistance per square measured at T_0. Since

$$R''(T,z) = [1 + \beta(T(z) - T_0)]R''(T_0,z) \tag{15}$$

and

$$\bar{R}_0'' = \bar{R}_0 w/L \tag{16}$$

then equation (13) becomes

$$q_e''(z) = \frac{V^2 F_2[1 + \beta(T(z) - T_0)]}{R_0 L \bar{w}[1 + \beta(\bar{T} - T_0)]^2} \tag{17}$$

This can be seen to be very similar to equation (9) for the abrupt expression, except that F_2 includes the effects of local variations in the gold film resistance and the strip width, and $\bar{w}$ appears in place of πD.

F_2 was determined from experimental data from runs with uniform heating in the fully developed flow region (for $z/D >$ 40). In this region where the true h is uniform, F_2 was evaluated at each thermocouple location by taking the ratio of the measured h to the average h in this fully developed region (the average h was assumed to be a valid measure of the true fully developed h). This "in situ" calibration technique of the gold coating using the fully developed region of the uniformly heated pipe allowed us to obtain high accuracy results for the local $h(\theta)$ in the subsequent nonuniform heating runs even with the nonuniformities present in the commercially available Intrex sheet. Typical values of F_2 for this experiment ranged between 0.96 and 1.04.

The value used for T_f in the Nusselt number expression was that of the local bulk temperature evaluated from equation (10). The estimated uncertainty in the Nusselt number in this application was ±4.5 percent [3].

Summary and Conclusions

The thin gold-coated sheet technique described in this paper for direct local measurements of the heat transfer coefficient has been shown to allow designs in which the effect of wall conduction is kept very low. In three different applications the analysis of wall conduction showed that it was essentially negligible in the regions of interest. This technique is a powerful approach since many different geometries can be studied as shown by the three applications described here.

Two additional corrections to the data required for this technique involve the nonuniformity of the gold coating and the temperature effect on the coating resistance. These are generally small corrections on the order of ±2–4 percent for nonuniformity and ±1 percent for the temperature effect. The methods for making these corrections have been described. In general, the methods for correction are dependent on the geometry and design used and are somewhat different for each of the three applications described in this paper. It should be noted that in many applications of this technique it is necessary to devise a means of calibration if the effect of the small nonuniformities in coating resistance is to be corrected.

Acknowledgments

The authors gratefully acknowledge the support of the National Science Foundation for much of this research under Grant CME-27613 and Grant MEA-8102657.

References

1 Baughn, J. W., Hoffman, M. A., Launder, B. E., and Takahashi, R. K., "Local Heat Transfer Downstream of an Abrupt Expansion," ASME JOURNAL OF HEAT TRANSFER, Vol. 106, Nov. 1984, pp. 789–796.

2 Baughn, J. W., Elderkin, M. J., and McKillop, A. A., "Measurements of the Local Heat Transfer to Air in Staggered and In-Line Tube Banks," submitted to the ASME JOURNAL OF HEAT TRANSFER.

3 Baughn, J. W., Hoffman, M. A., Launder, B. E., and Takahashi, R. K., "Turbulent Heat Transport in Circular Ducts with Circumferentially Varying Heat Flux," ASME JOURNAL OF HEAT TRANSFER, Vol. 106, Feb. 1984, pp. 64–70.

4 Ede, A. J., Hislop, C. I., and Morris, R., "Effect on the Local Heat-Transfer Coefficient in a Pipe of an Abrupt Disturbance of the Fluid Flow: Abrupt Convergence and Divergence of Diameter Ratio 2/1," *Proc. Inst. Mech. Eng. London*, Vol. 170, 1956, pp. 1113–1126.

5 Krall, K. M., and Sparrow, E. M., "Turbulent Heat Transfer in the Separated, Reattached, and Redevelopment Regions of a Circular Tube," ASME JOURNAL OF HEAT TRANSFER, Vol. 88, No. 1, Feb. 1966, pp. 131–136.

6 Sparrow, E. M., and Kemink, R. G., "Heat Transfer Downstream of a Fluid Withdrawal Branch in a Tube," ASME JOURNAL OF HEAT TRANSFER, Vol. 101, 1979, pp. 23–28.

7 Koram, K. K., and Sparrow, E. M., "Turbulent Heat Transfer Downstream of an Unsymmetric Blockage in a Tube," ASME JOURNAL OF HEAT TRANSFER, Vol. 100, 1978, pp. 588–594.

8 Sparrow, E. M., Koram, K. K., and Charmchi, M., "Heat Transfer and Pressure Drop Characteristics Induced by a Slat Blockage in a Circular Tube," ASME JOURNAL OF HEAT TRANSFER, Vol. 102, 1980, pp. 64–70.

9 Zemanick, P. P., and Dougall, R. S., "Local Heat Transfer Downstream of Abrupt Circular Channel Expansion," ASME JOURNAL OF HEAT TRANSFER, Vol. 92, 1970, pp. 53–60.

10 Seban, R. A., "Heat Transfer to the Turbulent Separated Flow of Air Downstream of a Step in the Surface of a Plate," ASME JOURNAL OF HEAT TRANSFER, Vol. 86, 1964, pp. 259–263.

11 Seban, R. A., Emery, A., and Levy, A., "Heat Transfer to Separated and Reattached Subsonic Turbulent Flows Obtained Downstream of a Surface Step," *J. Aerosp. Sci.*, Vol. 26, 1959, pp. 809–814.

12 Giedt, W. H., "Investigation of Variations of Point Unit Heat-Transfer Coefficient Around a Cylinder Normal to an Air Stream," *Transactions of ASME*, Vol. 71, 1949.

13 Petri, A. M., and Simpson, H. C., "An Experimental Study of the Sensitivity to Freestream Turbulence of Heat Transfer in Crossflow," *Int. J. Heat Mass Trans.*, Vol. 15, 1972, pp. 1497–1513.

14 Morcos, S. M., and Bergles, A. E., "Experimental Investigation of Combined Forced and Free Laminar Convection in Horizontal Tubes," ASME JOURNAL OF HEAT TRANSFER, May 1975, pp. 212–219.

15 Hatton, A. P., and Woolley, N. H., "Heated Transfer in Two-Dimensional Turbulent Confined Flows," *Proc. of the Institution of Mechanical Engineers*, Vol. 186, pp. 625–633, 1972.

16 Simonich, J. C., and Moffat, R. J., "New Technique for Mapping Heat-Transfer Coefficient Contours," *Rev. Sci. Instrum.*, Vol. 53, No. 5, 1982, pp. 678–683.

17 Hippensteele, S. A., Russell, L. M., and Stepka, F. S., "Evaluation of a Method for Heat Transfer Measurements and Thermal Visualization Using a Composite of a Heater Element and Liquid Crystals," ASME JOURNAL OF HEAT TRANSFER, Vol. 105, Feb. 1983, pp. 184–189.

18 Baughn, J. W., "Effect of Circumferential Wall Heat Conduction on Boundary Conditions for Heat Transfer in a Circular Tube," ASME JOURNAL OF HEAT TRANSFER, Vol. 100, 1978, pp. 537–539.

19 Kline, S. J., and McKlintock, F. A., "Describing Uncertainties in Single Sample Experiments," *Mechanical Engineering*, Vol. 75, No. 1, 1953, pp. 3–8.

20 Lee, D., "Measurements of the Turbulent Heat Transport Downstream of an Abrupt Expansion in a Circular Duct with a Constant Wall Temperature," M.S. thesis, University of California, Davis, 1984.

21 Kaul, S., "Experimental Study of the Local Heat Transfer from a Cylinder to Air in a Channel with Blockage," M.S. thesis, University of California, Davis, 1984.

Journal of Heat Transfer

Technical Notes

This section contains shorter technical papers. These shorter papers will be subjected to the same review process as that for full papers.

Effect of Circumferential Conduction on the Critical Radius of Insulation for Forced Convection Crossflow

E. M. Sparrow[1,2] and A. T. Prata[1]

Nomenclature

d_i = diameter of core
d_o = outer diameter of sheath
$h(\theta)$ = local heat transfer coefficient at θ
k_{air} = thermal conductivity of air
k_{ins} = thermal conductivity of insulation
Q' = heat transfer rate per unit length
Re_i = Reynolds number = $U_\infty d_i/\nu$
r_i = radius of core
r_o = outer radius of sheath
T_i = uniform temperature of core
T_∞ = free-stream temperature
U_∞ = free-stream velocity
θ = angular coordinate
ν = kinematic viscosity

Introduction

The critical radius gives rise to a maximum radial heat flow for a given overall temperature difference or to a minimum overall temperature difference for a given radial heat flow. The standard theory of the critical radius, as set forth in all heat transfer textbooks, contains numerous simplifying assumptions. Among these, the most significant is the assumption that the heat transfer coefficient at the outer surface of the body is independent of the body radius and is circumferentially uniform. The accounting of the radial dependence decreases the critical radius [1]. Circumferential variations of the heat transfer coefficient are a reality of nature. The effect of such variations will be assessed here with the aid of numerical solutions of the differential equation of energy conservation. The physical situation to be considered is the cylinder in crossflow.

Before proceeding with the analysis, it may be noted that the critical radius has little relevance in connection with the insulation of a fluid-carrying pipe situated in crossflow. This is because the critical radius is, typically, smaller than the outer radius of the pipe, as can be affirmed by evaluating the critical radius using equation (3) of [1] in conjunction with a standard Nusselt number correlation for a cylinder in crossflow.

On the other hand, since the radius of a heat-dissipating, electric-current-carrying conductor is normally smaller than that of a fluid-carrying pipe, critical radius considerations are relevant to the insulation layer surrounding the conductor. The analysis and results to be described here are couched in terms of the heat-dissipating conductor, although, if desired, they can be reinterpreted in terms of the fluid-carrying pipe.

Analysis

The description of the physical problem is facilitated by reference to Fig. 1. A cylindrical conductor of radius r_i dissipates energy at the rate Q' per unit axial length. Owing to its high thermal conductivity, the temperature of the conductor is cross-sectionally uniform and equal to T_i. Surrounding the conductor is an annulus ($r_i \le r \le r_o$) of electrical insulating material whose thermal conductivity is k_{ins}. The sheathed conductor is situated in an airflow whose free-stream velocity and temperature are U_∞ and T_∞, respectively.

The forced convection heat transfer coefficient h at the outer surface of the insulation sheath varies circumferentially as a function of the angle θ. As a consequence, $T = T(r, \theta)$ in the insulation annulus. The $h(\theta)$ inputs needed to solve for $T(r, \theta)$ were taken from available experimental data for isothermal-walled cylinders in crossflow [2]. These inputs serve as a first approximation whose refinement would require solving the momentum and energy equations for the airflow simultaneously with the energy equation for the insulation sheath. This computational undertaking is complex, costly, and subject to possible errors because of the separated region adjacent to the aft surface of the cylinder. The results obtained here using the $h(\theta)$ distribution for isothermal-walled cylinders will provide guidance as to whether it is worthwhile to undertake such a refinement.

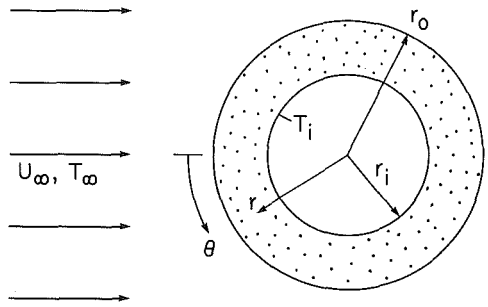

Fig. 1 Schematic representation of the physical problem

[1]Department of Mechanical Engineering, University of Minnesota, Minneapolis, MN 55455
[2]Fellow ASME

Contributed by the Heat Transfer Division for publication in the JOURNAL OF HEAT TRANSFER. Manuscript received by the Heat Transfer Division November 2, 1984.

Before describing the analysis, the overall approach will be outlined. Consider a physical situation characterized by a fixed dissipation Q' and conductor radius r_i along with an airstream of fixed U_∞ and T_∞. An insulating material having thermal conductivity k_{ins} is used to sheath the conductor. For these fixed parameters, the outer radius r_o of the insulation will be varied, and the corresponding variation of $(T_i - T_\infty)$ with r_o will be calculated, with special concern about a possible minimum.

In dimensionless terms, the fixed parameters are

$$\mathrm{Re}_i = U_\infty d_i/\nu \text{ and } k_{ins}/k_{air} \tag{1}$$

and the variation of $(T_i - T_\infty)/(Q'/k_{ins})$ with r_o/r_i will be calculated. These results will be obtained using two methods: (1) finite-difference solutions incorporating $h(\theta)$ and (2) algebraic solutions based on purely radial heat flow in the insulation and on circumferential-average heat transfer coefficients $\bar{h}$.

Governing Equations and Solutions. To facilitate the solution of $T(r, \theta)$ in the insulation sheath, let

$$\Phi = (T - T_\infty)/(Q'/k_{ins}), \qquad R = r/r_i \tag{2}$$

so that in the region $1 \le R \le r_o/r_i$

$$\nabla^2 \Phi = 0 \tag{3}$$

where ∇^2 is the Laplace operator in R, θ polar coordinates. At the inner surface of the insulation sheath ($r = r_i$ and $R = 1$), $T = T_i$ independent of θ, so that

$$\Phi = \Phi_i = (T_i - T_\infty)/(Q'/k_{ins}) \tag{4}$$

At the outer surface of the sheath ($r = r_o$ and $R = r_o/r_i$), the convective boundary condition has to be applied at each angular position θ, taking account of $h = h(\theta)$

$$-k_{ins}(\partial T/\partial r) = h(\theta)(T - T_\infty) \tag{5}$$

or

$$\partial \Phi/\partial R = -\mathrm{Bi}_\theta \Phi \tag{6}$$

where Bi_θ is an angle-dependent Biot number

$$\mathrm{Bi}_\theta = h(\theta) r_i/k_{ins} \tag{7}$$

The Biot number can be expressed in terms of the angular Nusselt number Nu_θ

$$\mathrm{Bi}_\theta = \tfrac{1}{2}\mathrm{Nu}_\theta/[(r_o/r_i)(k_{ins}/k_{air})] \tag{8}$$

in which

$$\mathrm{Nu}_\theta = h(\theta) d_o/k_{air} \tag{9}$$

In turn, Nu_θ is a function of both the Reynolds number Re_o ($= U_\infty d_o/\nu$) and θ, where

$$\mathrm{Re}_o = (d_o/d_i)\mathrm{Re}_i \tag{10}$$

In [2], Nu_θ is plotted versus θ for eight discrete values of Re_o in the range between $\mathrm{Re}_o = 23$ and 597, and interpolations and extrapolations were made as needed. The circumferential-average Nusselt numbers $\overline{\mathrm{Nu}}$ corresponding to the Nu_θ distributions of [2] are expressed by

$$\overline{\mathrm{Nu}}_o = \bar{h} d_o/k_{air} = 0.43 + 0.48\sqrt{\mathrm{Re}_o} \tag{11}$$

The computational task is to solve equation (3) subject to the boundary conditions (4) and (6), where, as just described, Bi_θ is a known function of position. This problem is not completely straightforward, since Φ_i is unknown (actually, the objective of the computation is to find Φ_i). The following approach avoids the use of trial and error. Let Φ_i be chosen arbitrarily and the solution for $\Phi(R, \theta)$ determined numerically. Then, at $r = r_o$

$$Q_o' = \int_0^{2\pi} [-k_{ins}(\partial T/\partial r)] r_o d\theta \tag{12}$$

or

$$Q_o'/Q' = -\int_0^{2\pi} (\partial \Phi/\partial R)(r_o/r_i) d\theta \tag{13}$$

If the chosen value of Φ_i were to be the proper one for the given values of Re_i, k_{ins}/k_{air}, and r_o/r_i, then $Q_o'/Q' = 1$; otherwise, $Q_o'/Q' \neq 1$.

Let $Q_o'/Q' = \Omega$ correspond to an arbitrarily chosen value of Φ_i, for instance, $\Phi_i = 1$. By defining a new temperature variable $\phi = \Phi/\Omega$, it is readily seen that the solution of the equations

$$\phi_i = 1/\Omega, \quad \nabla^2 \phi = 0, \quad \partial \phi/\partial \mathrm{R} = -\mathrm{Bi}_\theta \phi \tag{14}$$

yields $Q_o'/Q' = 1$.

In summary, the solution method consists of fixing Re_i and k_{ins}/k_{air}, specifying r_o/r_i as a parameter and determining Bi_θ via equations (7) to (10) and the accompanying text. Then, with $\Phi_i = 1$, equation (3) is solved subject to the boundary conditions (4) and (6), and equation (13) is evaluated to yield $\Omega = Q_o'/Q'$. It then follows that

$$(T_i - T_\infty)/(Q'/k_{ins}) = 1/\Omega \tag{15}$$

The finite-difference solutions were carried out with a uniform grid of 30 × 30 points (radial × circumferential). Owing to symmetry, it was necessary to work only in the region between $\theta = 0$ and 180 deg.

For the algebraic model based on pure radial conduction in the insulation sheath and on the circumferential-average heat transfer coefficient $\bar{h}$, the conventional series resistance analysis yields

$$(T_i - T_\infty)/(Q'/k_{ins}) = [\ln(r_o/r_i) + (k_{ins}/\bar{h} r_o)]/2\pi \tag{16}$$

where $\bar{h} r_o/k_{ins} = \tfrac{1}{2}(k_{air}/k_{ins})\overline{\mathrm{Nu}}_o$, and $\overline{\mathrm{Nu}}_o$ is obtained from equation (11).

Results and Discussion

In the presentation of the results, $(T_i - T_\infty)/(Q'/k_{ins})$ will be plotted as a function of r_o/r_i for fixed parametric values of k_{ins}/k_{air} and Re_i. This information is conveyed in Figs. 2-5, with each figure corresponding to a specific value of k_{ins}/k_{air}, respectively 2, 5, 10, and 15. Each figure consists of four graphs, which are respectively parameterized by Re_i values of 10, 25, 75, and 150. In each graph, results are given both for the model which takes account of circumferential variations (labeled $h = h(\theta)$) and for the model which neglects circumferential variations (labeled $h \neq h(\theta)$).

The values of r_o/r_i appearing on the abscissa of each graph were chosen to encompass the range where $(T_i - T_\infty)/(Q'/k_{ins})$ attains a minimum. In those cases where there is no minimum, r_o/r_i extends from one to four or five.

The critical radius corresponds to the value of r_o/r_i at which $(T_i - T_\infty)/(Q'/k_{ins})$ attains a minimum and, hereafter, this value will be denoted by $(r_o/r_i)^*$. From the figures, it is seen that there is no critical radius for good thermal insulators such as $k_{ins}/k_{air} = 2$. For a lesser thermal insulator, $k_{ins}/k_{air} = 5$, the critical radius exists for low Reynolds numbers such as $\mathrm{Re}_i = 10$ and 25 but not for higher Reynolds numbers. At still larger thermal conductivities of the insulating sheath, $k_{ins}/k_{air} = 10$ and 15, there is a critical radius for each of the investigated Reynolds numbers.

In general, $(r_o/r_i)^*$ increases with increasing thermal conductivity k_{ins}/k_{air} at a fixed value of the Reynolds number Re_i. For a fixed thermal conductivity, $(r_o/r_i)^*$ increases as the Reynolds number decreases. These characteristics are consistent with the general rule that the critical radius increases when the ratio of the external thermal resistance to the internal thermal resistance increases.

The values of $(r_o/r_i)^*$ corresponding to the $h = h(\theta)$ and $h \neq h(\theta)$ models will now be compared. For all of the investigated cases, the value of $(r_o/r_i)^*$ for the $h = h(\theta)$ model is smaller than or equal to that for the $h \neq h(\theta)$ model. Although the difference in the $(r_o/r_i)^*$ values for the two models is appreciable in some cases, the minima are sufficiently flat so that $(T_i - T_\infty)/(Q'/k_{ins})$ is not sensitive to the difference. For

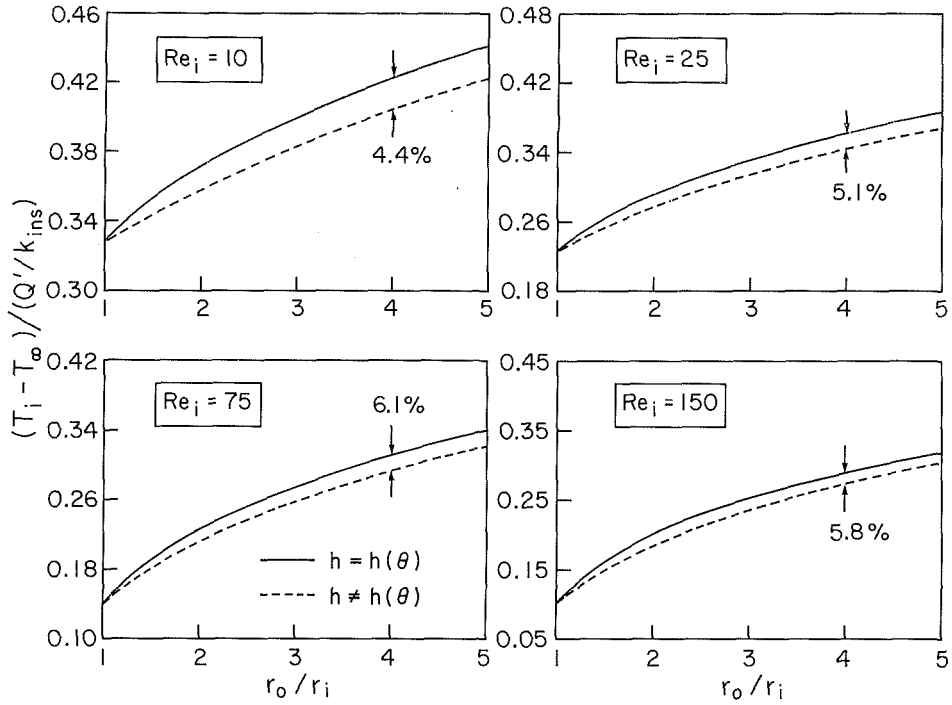

Fig. 2 Response of $(T_i - T_\infty)/(Q'/k_{ins})$ to the outer radius of the insulation sheath, $k_{ins}/k_{air} = 2$

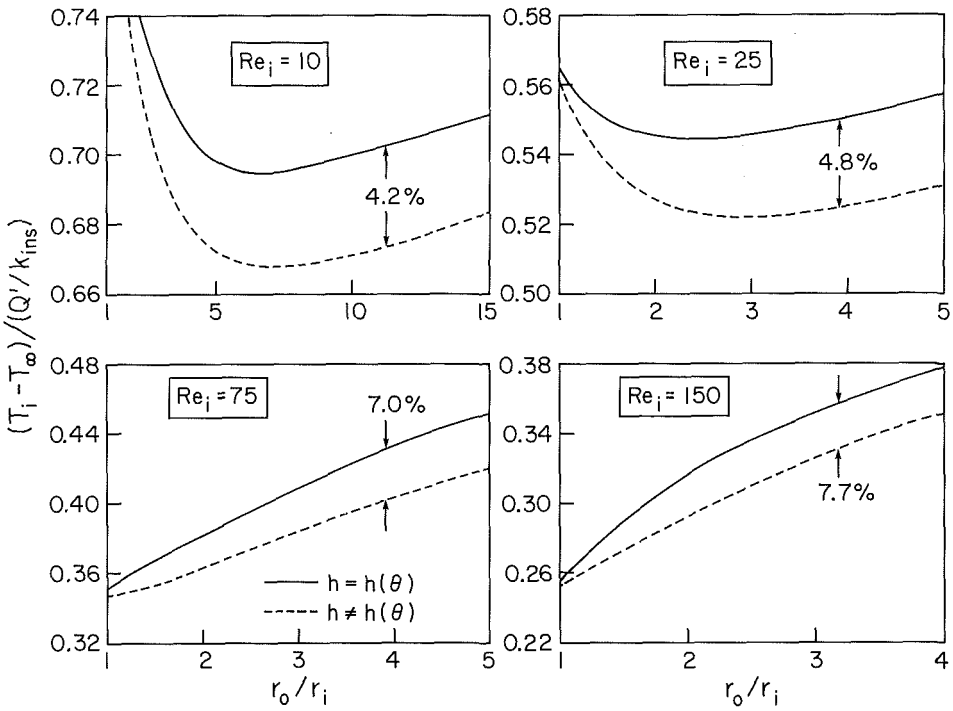

Fig. 3 Response of $(T_i - T_\infty)/(Q'/k_{ins})$ to the outer radius of the insulation sheath, $k_{ins}/k_{air} = 5$

example, for $k_{ins}/k_{air} = 10$ and $Re_i = 10$ (Fig. 4), $(r_o/r_i)^* = 26$ for the $h = h(\theta)$ model and 36 for the $h \neq h(\theta)$ model. From the $h = h(\theta)$ solutions, the values of $(T_i - T_\infty)/(Q'/k_{ins})$ at $r_o/r_i = 26$ and 36 are 0.956 and 0.963, a deviation of slightly less than 1 percent. Similarly, for the $h \neq h(\theta)$ solution, the $(T_i - T_\infty)/(Q'/k_{ins})$ values at $r_o/r_i = 26$ and 36 are 0.908 and 0.904, which is a deviation of less than 1/2 percent.

This example shows that it is not necessary to know the precise value of $(r_o/r_i)^*$ in order to obtain a value of $(T_i - T_\infty)/(Q'/k_{ins})$ very near the minimum. As a consequence, an approximate model, such as $h \neq h(\theta)$, is adequate for determining $(r_o/r_i)^*$.

What is more to the point is how $(T_i - T_\infty)/(Q'/k_{ins})$ is affected by taking $h = h(\theta)$ into account. The gap between the solid and dashed lines in each of the graphs shows the difference between the $(T_i - T_\infty)/(Q'/k_{ins})$ values for the $h = h(\theta)$ and the $h \neq h(\theta)$ models. To aid in quantifying the difference, percentage deviations between the lines have been indicated in each graph. An overall inspection of all the

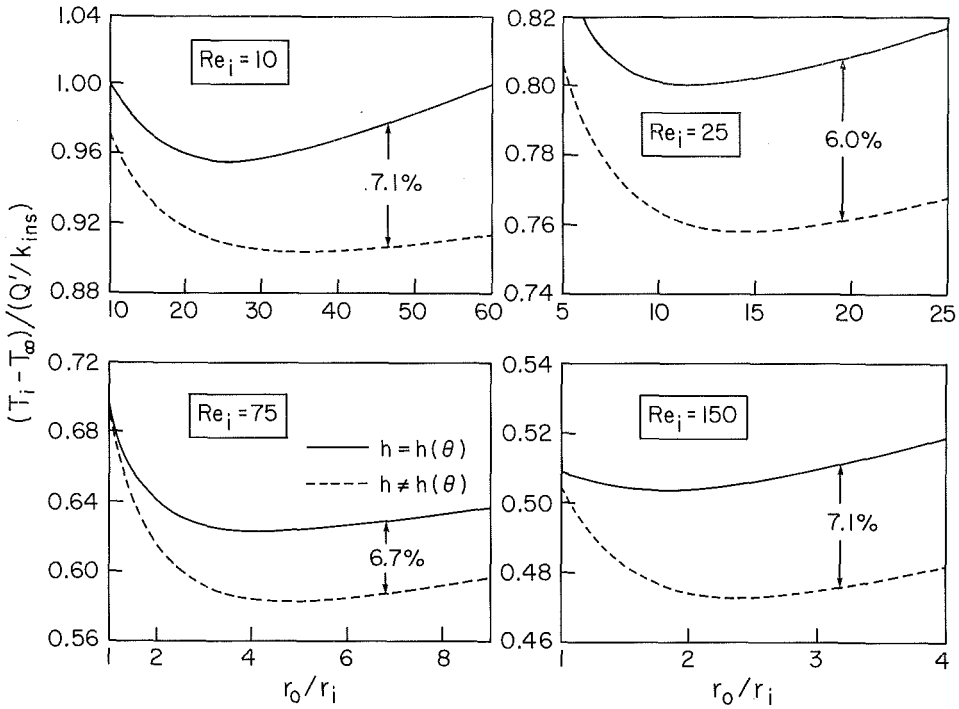

Fig. 4 Response of $(T_i - T_\infty)/(Q'/k_{ins})$ to the outer radius of the insulation sheath, $k_{ins}/k_{air} = 10$

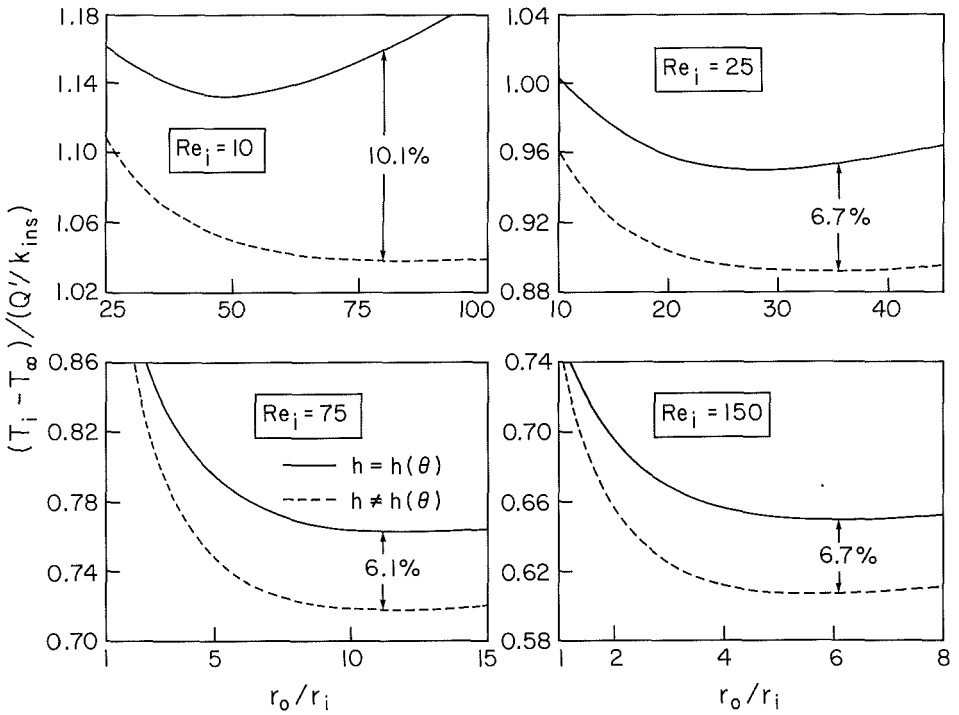

Fig. 5 Response of $(T_i - T_\infty)/(Q'/k_{ins})$ to the outer radius of the insulation sheath, $k_{ins}/k_{air} = 15$

graphs shows that, for the most part, the deviations are in the 4–8 percent range, with the $h = h(\theta)$ model consistently yielding higher values of $(T_i - T_\infty)/(Q'/k_{ins})$. If $(T_i - T_\infty)$ is to be minimized for a given Q', the conventional $h \neq h(\theta)$ model gives optimistic results.

The aforementioned deviations in the values of $(T_i - T_\infty)/(Q'/k_{ins})$ from the two models are moderate and are within the accuracy tolerance of many engineering design calculations. In view of this, the refinement of the $h(\theta)$ distribution to take account of the circumferential variation of the surface temperature appears warranted only when a precise design is necessary.

References

1 Sparrow, E. M., "Reexamination and Correction of the Critical Radius for Radial Heat Conduction," *AIChE Journal*, Vol. 16, 1970, p. 149.

2 Eckert, E. R. G., and Soehngen, E., "Distribution of Heat Transfer Coefficients Around Circular Cylinders in Crossflow at Reynolds Numbers From 20 to 500," *Trans. ASME*, Vol. 74, 1952, pp. 343–347.

Solidification of Binary Mixture in a Finite Planar Medium: Saline Water

H. Kehtarnavaz[1] and Y. Bayazitoglu[2]

Nomenclature

C = concentration, g solute/kg solvent
D = diffusion coefficient, cm^2/s
k = thermal conductivity, cal/cm s °C
L = latent heat of fusion, cal/g
l = depth of the planar layer
p = concentration at the nonpermeable surface for the second domain solution
q = heat flux, W/m^2
s = location of the interface, cm
T = temperature, K
t = time, s
z = spatial coordinate
α = thermal diffusivity, cm^2/s
δ_c = concentration boundary layer, cm
ρ = density, g/cm^3

Subscripts

c = concentration
0 = initial state
i = phase change state
l = liquid phase
s = solid phase
w = wall

Superscripts

$\dot{}$ = first derivative with respect to time
$\ddot{}$ = second derivative with respect to time

Introduction

There are many problems in engineering which require the study of solidification processes, and in some of these problems the liquid phase is a binary mixture that is undergoing the solidification transformation. Problems of this kind may be encountered in oceanography, geology, medicine, freezing of sea water, etc.

The problem of solidification of a binary mixture is coupled with a mass transfer problem at the interface. The buildup of the solute from the mixture at the interface causes a freezing point depression. This means that the interface temperature is a function of time which further complicates the nonlinearity of the problem. A binary mixture solidification in a semi-infinite medium has been studied by several investigators [1-7]. The finite medium problem was solved by Rubinsky [8] and O'Callaghan et al. [9-11]. Rubinsky used a finite element method for a given temperature function at the boundary and O'Callaghan et al. used a concentration profile obtained from the semi-infinite solution.

Analysis

Consider a finite planar layer of a liquid mixture of depth l with a uniform solute concentration C_0. The lower boundary of the layer at $z = l$ is insulated and nonpermeable to the solute. The solidification starts at time $t = 0$ by cooling the mixture from the upper boundary of the layer at $z = 0$. As the solidification continues, the solid-liquid interface at $z = s(t)$ moves toward the lower boundary.

Here we present the formulation to the problem for constant wall heat flux q_w cooling at the upper boundary. Initially, the liquid mixture is assumed to be in the state of uniform cooling with an upper boundary at the phase change temperature $T_i(C_0)$. The governing equations consist of unsteady transport equations and are given in the form

$$\frac{\partial T_s(z,t)}{\partial t} = \alpha_s \frac{\partial^2 T_s}{\partial z^2} \quad \text{for} \quad 0<z<s(t), \quad t>0 \tag{1a}$$

$$\frac{\partial T_l(z,t)}{\partial t} = \alpha_l \frac{\partial^2 T_l}{\partial z^2} \quad \text{for} \quad s(t)<z<l, \quad t>0 \tag{1b}$$

$$\frac{\partial C(z,t)}{\partial t} = D\frac{\partial^2 C}{\partial z^2} \quad \text{for} \quad s(t)<z<l, \quad t>0 \tag{1c}$$

subject to the following boundary conditions

$$-k_s \frac{\partial T_s(0,t)}{\partial z} = q_w \tag{2a}$$

$$T_s[s(t),t] = T_l[s(t),t] = T_i(t) \tag{2b}$$

$$\frac{\partial T_l(l,t)}{\partial z} = 0 \tag{2c}$$

$$k_s \frac{\partial T_s[s(t),t]}{\partial z} - k_l \frac{\partial T_l[s(t),t]}{\partial z} = \rho L \frac{ds}{dt} \tag{3}$$

$$C[s(t),t] = C_i \tag{4a}$$

$$\frac{\partial C(l,t)}{\partial z} = 0 \tag{4b}$$

$$-D\frac{\partial C[s(t),t]}{\partial z} = C_i \frac{ds}{dt} \tag{5}$$

and the initial conditions

$$T_l(0,0) = T_i(C_0) = T_0, \quad \frac{\partial T_l(z,0)}{\partial t} = \text{const} \tag{6}$$

$$C(z,0) = C_0 \tag{7}$$

The phase change interface temperature T_i and concentration C_i are coupled by the assumption of local thermodynamic equilibrium, through a linear relation based on the constitutional phase diagram relation as,

$$T_i(C_i) = a' + b' C_i \tag{8}$$

where a' and b' are constants.

The problem is governed by nonlinear equations because of the moving interface during solidification and the interface depression from the buildup solute. The heat balance integral method [12] is used to obtain an analytical solution. In the solid and liquid phases parabolic temperature profiles are assumed with the boundary conditions given by equations (2) as

$$T_s(z,t) = T_i + q_w(s-z)/k_s - a_s(s^2-z^2) \tag{9a}$$

$$T_l(z,t) = T_i + 2a_l l(s-z) - a_l(s^2-z^2) \tag{9b}$$

where a_s and a_l are time-dependent coefficients to be found. Equations (9) are substituted into the integral forms of the governing equations (1a, b) and into the boundary condition (3) and the following differential equations are obtained

$$\dot{a}_s = 3\left(\frac{q_w}{2k_s s^2} - \frac{a_s}{s}\right)\dot{s} - \frac{3a_s\alpha_s}{s^2} + \frac{3}{2s^2}\dot{T}_i \tag{10a}$$

$$\dot{a}_l = \frac{3a_l}{l-s}\dot{s} - \frac{3a_l\alpha_l}{(l-s)^2} + \frac{3}{2(l-s)^2}\dot{T}_i \tag{10b}$$

$$\dot{s} = \frac{-q_w + 2a_s k_s s + 2a_l k_l (l-s)}{\rho L} \tag{10c}$$

For the solution of the concentration profile in the liquid

[1]Graduate Student, Mechanical Engineering and Material Science Department, Rice University, Houston, TX 77251
[2]Associate Professor, Mechanical Engineering and Material Science Department, Rice University, Houston, TX 77251, Assoc. Mem. ASME
Contributed by the Heat Transfer Division for publication in the JOURNAL OF HEAT TRANSFER. Manuscript received by the Heat Transfer Division May 3, 1984.

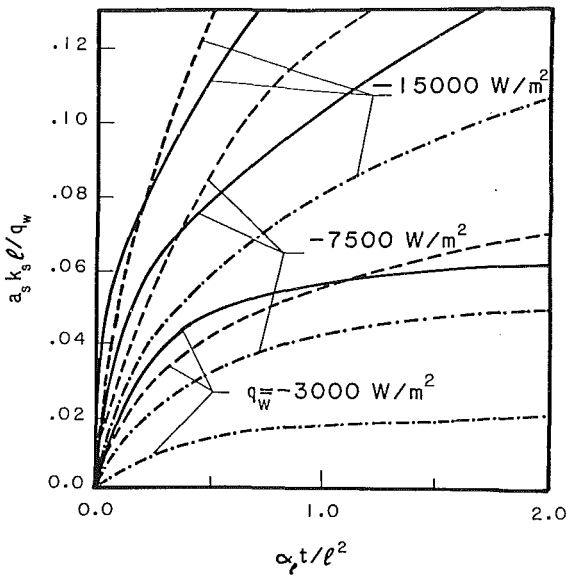

Fig. 1 Dynamic variation of the solid phase curvature parameter as a function of constant heat flux at the boundary for C_0 = 0.145 mole/L: —— present work; ---- [11]; -·-·-·- pure water

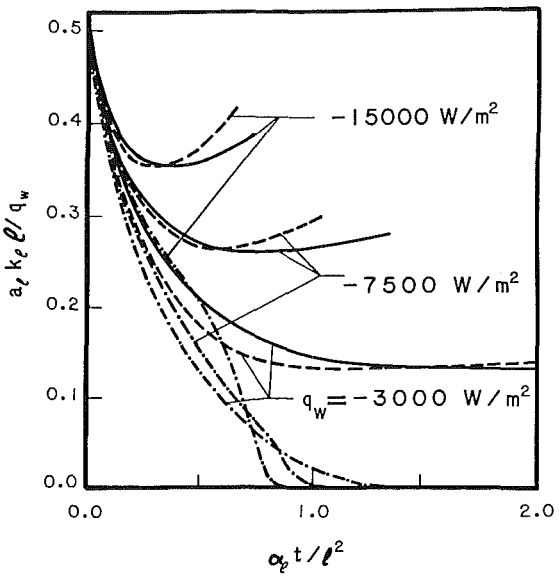

Fig. 2 Dynamic variation of the liquid phase curvature parameter as a function of constant heat flux at the boundary for C_0 = 0.145 mole/L: —— present work; ---- [11]; -·-·-·- pure water

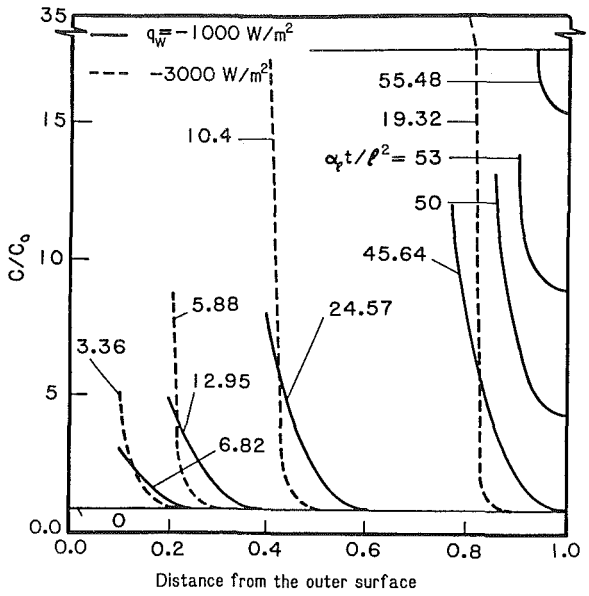

Fig. 3 Dynamic variation of the concentration profile

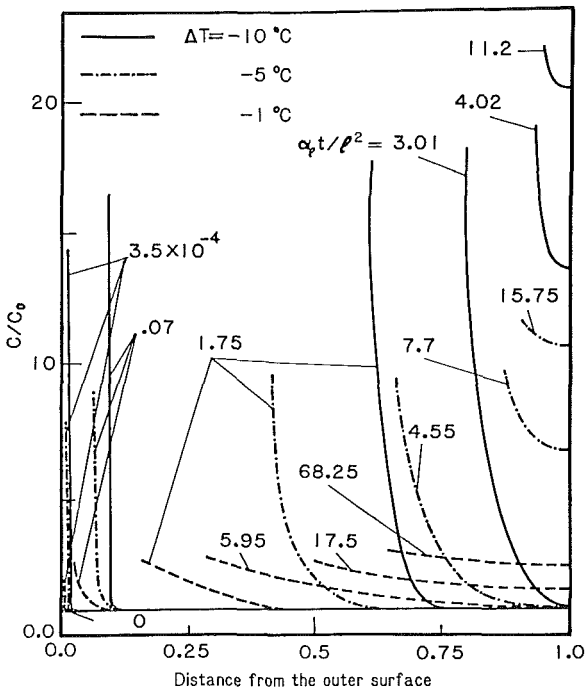

Fig. 4 Dynamic variation of concentration field in the liquid phase as a function of temperature drop at the boundary

phase a concentration boundary layer $\delta_c(t)$ is defined such that

$$C=C_0,\ \partial C/\partial z=0,\ \partial^2 C/\partial z^2=0,\quad \text{at}\quad z=s+\delta_c \tag{11}$$

where $\delta_c(t=0)=0$. Then a cubic concentration profile is assumed with the boundary conditions given by equations (4) and (11) as

$$C=C_0\left[1-\frac{\dot{s}(z-\delta_c-s)^3}{\delta_c^2(3D-\dot{s}\delta_c)}\right] \tag{12}$$

Equation (12) is substituted into the integral form of equation (1*c*) and the following differential equation is obtained

$$\dot{\delta}_c=\frac{4(3D-\dot{s}\delta_c)^2}{\delta_c(6D-\dot{s}\delta_c)}-\frac{3D\delta_c}{\dot{s}(6D-\dot{s}\delta_c)}\ddot{s} \tag{13}$$

Use of the time derivative of equation (12) at $z=s(t)$ and the application of the chain rule resulted in the necessary time derivative of the interface temperature $\dot{T}_i$ as

$$\dot{T}_i=\frac{3Db'}{(3D-\dot{s}\delta_c)}(\dot{s}\dot{\delta}_c+\delta_c\ddot{s}) \tag{14}$$

where

$$\ddot{s}=(1/\rho L)[2\dot{s}(a_s k_s-a_l k_l)+2k_s s\dot{a}_s+2k_l(l-s)\dot{a}_l] \tag{15}$$

When the concentration boundary layer δ_c reaches the lower boundary at $z=l$, the solutions given by equations (12-15) are not valid and second domain solutions are necessary for the concentration. The second domain concentration profile is obtained by setting $\delta_c=l-s$ and by changing C_0 to $p(t)$ in equation (12), and it is to be noted that

$p(t)$ is the nonpermeable surface concentration at $z = l$ and initially equal to C_0.

Results and Discussion

The quantities a_s and a_l are the quadratic coefficients in the temperature profiles, representing the spatial curvature of those profiles. These coefficients reflect the importance of the thermal mass. The variation of a_s is shown in Fig. 1 for $C_0 = 0.145$, and for saline water with $l = 5$ mm. The finite medium solution of this work approaches the semi-infinite medium solution of [11] with decreasing heat flux at the boundary. The liquid phase curvature parameter a_l is also presented in Fig. 2. The initial decrease of a_l is due to the "flattening" of the temperature profile in the liquid, because initially the insulated wall temperature is higher than the interface temperature. As the interface temperature decreases, a_l increases slightly to maintain a zero temperature gradient at $z = l$.

The concentration profile is a function of the interface velocity and consequently a function of the interface velocity gradient. If the interface velocity is larger than the mass diffusion velocity, the concentration boundary layer decreases in length although the plane at $z = s + \delta_c$ is moving downward. This causes an accumulation of solute at the interface. Therefore, the semi-infinite medium assumption for the concentration profile [11] will not be proper. The semi-infinite concentration profile assumption will be made in studying morphological instability of the freezing front with large initial solute concentrations. In Figs. 1 and 2, the solidification problem for pure water is also presented.

The concentration profiles for two different values of heat fluxes at the boundary are shown in Fig. 3. For $q_w = -3000$ W/m^2 the concentration layer becomes so thin that the interface concentration becomes too large to be physically meaningful for saline water; therefore the second domain solution is presented only for $q_w = -1000$ W/m^2.

To study solidification with a constant wall temperature boundary condition T_w, the temperature drops $\Delta T = T_w - T_i$ at the boundary ranging from -1°C to -10°C are considered. The concentration field is presented in Fig. 4. The interface concentration remained almost constant during the early times of solidification.

References

1 Weber, J. E., "Heat and Salt Transfer Associated With Formation of Sea-Ice," *Tellus*, Vol. 29, 1977, pp. 151–160.

2 Smith, V. G., Tiller, W. A., and Rutter, J. W., "A Mathematical Analysis of Solute Redistribution During Solidification," *Canadian J. of Physics*, Vol. 33, 1958, p. 723.

3 Rutter, J. W., and Chalmers, B., "Solute Redistribution During Planar Solidification," *Canadian J. of Physics*, Vol. 31, 1953, p. 15.

4 Mullins, W. W., and Sekerka, R. F., "Morphological Stability of a Particle Growing by Diffusion or Heat Flow," *J. of Applied Physics*, Vol. 34, No. 2, Feb. 1963, pp. 323–329.

5 Mullins, W. W., and Sekerka, R. F., "Stability of a Planar Interface During Solidification of a Dilute Binary Alloy," *J. of Applied Physics*, Vol. 35, No. 2, Feb. 1984, pp. 444–451.

6 Sekerka, R. F., "A Stability Function for Explicit Evaluation of the Mullins-Sekerka Interface Stability Criterion," *J. of Applied Physics*, Vol. 36, No. 1, Jan. 1965, pp. 264–268.

7 Chen, J. H., and Rubinsky, B., "Morphological Stability Analysis on a Solid-Liquid Interface During Solidification of Binary Alloys," ASME Paper No. 83-HT-24.

8 Rubinsky, B., "Solidification Processes in Saline Solutions," ASME Paper No. 82-WA/HT-1.

9 O'Callaghan, M. G., "An Analysis of the Heat and Mass Transport During the Freezing of Biomaterials," Ph.D. Thesis, Department of Mechanical Engineering, MIT, Cambridge, MA, Oct. 1978.

10 O'Callaghan, M. G., Cravalho, E. G., and Huggins, C. E., "Instability of the Planar Interface During the Freezing of Biomaterials," *Cryobiology*, Vol. 15, 1978, p. 704.

11 O'Callaghan, M. G., Cravalho, E. G., and Huggins, C. E., "Instability of the Planar Freeze Front During Solidification of an Aqueous Binary Solution," ASME JOURNAL OF HEAT TRANSFER, Vol. 102, Nov. 1980, pp. 673–677.

12 Ozisik, M. N., *Heat Conduction*, Wiley, New York, 1980.

Optimization of Annular Fins With Variable Thermal Parameters by Invariant Imbedding

M. N. Netrakanti[1] and C. L. D. Huang[2]

Recently, Razelos and Imre [2] have obtained optimum dimensions of a circular fin of trapezoidal profile, with variable thermal conductivity and heat transfer coefficient. They used a quasi-Newtonian algorithm to solve the nonlinear differential equation. It is well known that the set of nonlinear differential equations of this type of problem is not very stable. The numerical integration scheme must be executed cautiously. In this study, the same problem is reconsidered. The thermal conductivity is assumed to vary linearly with temperature, and the variation of the heat transfer coefficient to be a form of power law. The mathematical formulation of the problem and the nomenclature in [1] are used in this note. Heat dissipation in the fin of a given volume is maximized by the invariant imbedding technique by which the inherent instability in a numerical integration technique can be avoided. The effects of the thermal parameters α and m, and of the geometric parameter λ, on the heat dissipation of the optimal fin are discussed.

Now, the problem is stated in terms of the nondimensional quantities. For a given dimensionless volume U, we determine the thickness parameter v and the length parameter b which maximize the heat dissipation Q_h, subjected to the constraint condition

$$N_r = q/q_{nf} = q/4\pi r_i w h_{nf}(t_{nf} - t_\infty) > 1 \tag{1}$$

The dimensionless parameters are defined as

$$U = g(b)/v^2, \quad v^2 = h_a r_b^2/k_a w, \quad b = r_0/r_b$$

and

$$Q_h = (1+\alpha)\theta'(1)/v^2 \tag{2}$$

where $\theta'(1)$ satisfies the following boundary-value problem in the domain $1 \le \xi \le b$.

$$\frac{dX_1}{d\xi} = \frac{X_2}{\beta\xi(1+\alpha X_1)} = f(X_1, X_2, \xi) \tag{3}$$

$$\frac{dX_2}{d\xi} = v^2 H \xi X_1 = g(X_1, X_2, \xi) \tag{4}$$

where X_1 and X_2 are defined as $X_1 = \theta$ and $X_2 = (1+\alpha\theta)\beta\xi\theta'(\xi)$. The boundary conditions are

$$X_1(\xi = 1) = 1 \text{ and } X_2(\xi = b) = 0. \tag{5}$$

The shape of a trapezoidal annular fin can be characterized by nondimensional parameters as follows

$$\beta = \frac{y(r)}{w} = \lambda + (1-\lambda)\left(\frac{b-\xi}{b-1}\right) \tag{6}$$

where λ is the shape parameter defined by $\lambda = w_0/w$. Thus $g(b)$ can be expressed as

$$g(b) = \frac{(b-1)}{6U}[(1-\lambda)(b+2) + 3\lambda(b+1)] \tag{7}$$

The invariant imbedding technique is used to solve the problem equations (3), (4), and (5). In this problem, the missing initial condition $X_2(1)$ is of interest. The boundary conditions (5) are converted to a recursive form as

[1]Department of Mechanical Engineering, Kansas State University, Manhattan, KS 66506, Assoc. Mem. ASME

[2]Department of Mechanical Engineering, Kansas State University, Manhattan, KS 66506, Mem. ASME

Contributed by the Heat Transfer Division and presented at the 1983 ASME-JSME Thermal Engineering Conference, Honolulu, Hawaii, March 20–24, 1983. Manuscript received by the Heat Transfer Division February 18, 1983.

$p(t)$ is the nonpermeable surface concentration at $z = l$ and initially equal to C_0.

Results and Discussion

The quantities a_s and a_l are the quadratic coefficients in the temperature profiles, representing the spatial curvature of those profiles. These coefficients reflect the importance of the thermal mass. The variation of a_s is shown in Fig. 1 for $C_0 = 0.145$, and for saline water with $l = 5$ mm. The finite medium solution of this work approaches the semi-infinite medium solution of [11] with decreasing heat flux at the boundary. The liquid phase curvature parameter a_l is also presented in Fig. 2. The initial decrease of a_l is due to the "flattening" of the temperature profile in the liquid, because initially the insulated wall temperature is higher than the interface temperature. As the interface temperature decreases, a_l increases slightly to maintain a zero temperature gradient at $z = l$.

The concentration profile is a function of the interface velocity and consequently a function of the interface velocity gradient. If the interface velocity is larger than the mass diffusion velocity, the concentration boundary layer decreases in length although the plane at $z = s + \delta_c$ is moving downward. This causes an accumulation of solute at the interface. Therefore, the semi-infinite medium assumption for the concentration profile [11] will not be proper. The semi-infinite concentration profile assumption will be made in studying morphological instability of the freezing front with large initial solute concentrations. In Figs. 1 and 2, the solidification problem for pure water is also presented.

The concentration profiles for two different values of heat fluxes at the boundary are shown in Fig. 3. For $q_w = -3000$ W/m^2 the concentration layer becomes so thin that the interface concentration becomes too large to be physically meaningful for saline water; therefore the second domain solution is presented only for $q_w = -1000$ W/m^2.

To study solidification with a constant wall temperature boundary condition T_w, the temperature drops $\Delta T = T_w - T_i$ at the boundary ranging from -1°C to -10°C are considered. The concentration field is presented in Fig. 4. The interface concentration remained almost constant during the early times of solidification.

References

1 Weber, J. E., "Heat and Salt Transfer Associated With Formation of Sea-Ice," *Tellus*, Vol. 29, 1977, pp. 151–160.

2 Smith, V. G., Tiller, W. A., and Rutter, J. W., "A Mathematical Analysis of Solute Redistribution During Solidification," *Canadian J. of Physics*, Vol. 33, 1958, p. 723.

3 Rutter, J. W., and Chalmers, B., "Solute Redistribution During Planar Solidification," *Canadian J. of Physics*, Vol. 31, 1953, p. 15.

4 Mullins, W. W., and Sekerka, R. F., "Morphological Stability of a Particle Growing by Diffusion or Heat Flow," *J. of Applied Physics*, Vol. 34, No. 2, Feb. 1963, pp. 323–329.

5 Mullins, W. W., and Sekerka, R. F., "Stability of a Planar Interface During Solidification of a Dilute Binary Alloy," *J. of Applied Physics*, Vol. 35, No. 2, Feb. 1984, pp. 444–451.

6 Sekerka, R. F., "A Stability Function for Explicit Evaluation of the Mullins-Sekerka Interface Stability Criterion," *J. of Applied Physics*, Vol. 36, No. 1, Jan. 1965, pp. 264–268.

7 Chen, J. H., and Rubinsky, B., "Morphological Stability Analysis on a Solid-Liquid Interface During Solidification of Binary Alloys," ASME Paper No. 83-HT-24.

8 Rubinsky, B., "Solidification Processes in Saline Solutions," ASME Paper No. 82-WA/HT-1.

9 O'Callaghan, M. G., "An Analysis of the Heat and Mass Transport During the Freezing of Biomaterials," Ph.D. Thesis, Department of Mechanical Engineering, MIT, Cambridge, MA, Oct. 1978.

10 O'Callaghan, M. G., Cravalho, E. G., and Huggins, C. E., "Instability of the Planar Interface During the Freezing of Biomaterials," *Cryobiology*, Vol. 15, 1978, p. 704.

11 O'Callaghan, M. G., Cravalho, E. G., and Huggins, C. E., "Instability of the Planar Freeze Front During Solidification of an Aqueous Binary Solution," ASME JOURNAL OF HEAT TRANSFER, Vol. 102, Nov. 1980, pp. 673–677.

12 Ozisik, M. N., *Heat Conduction*, Wiley, New York, 1980.

Optimization of Annular Fins With Variable Thermal Parameters by Invariant Imbedding

M. N. Netrakanti[1] and C. L. D. Huang[2]

Recently, Razelos and Imre [2] have obtained optimum dimensions of a circular fin of trapezoidal profile, with variable thermal conductivity and heat transfer coefficient. They used a quasi-Newtonian algorithm to solve the nonlinear differential equation. It is well known that the set of nonlinear differential equations of this type of problem is not very stable. The numerical integration scheme must be executed cautiously. In this study, the same problem is reconsidered. The thermal conductivity is assumed to vary linearly with temperature, and the variation of the heat transfer coefficient to be a form of power law. The mathematical formulation of the problem and the nomenclature in [1] are used in this note. Heat dissipation in the fin of a given volume is maximized by the invariant imbedding technique by which the inherent instability in a numerical integration technique can be avoided. The effects of the thermal parameters α and m, and of the geometric parameter λ, on the heat dissipation of the optimal fin are discussed.

Now, the problem is stated in terms of the nondimensional quantities. For a given dimensionless volume U, we determine the thickness parameter v and the length parameter b which maximize the heat dissipation Q_h, subjected to the constraint condition

$$N_r = q/q_{nf} = q/4\pi r_i w h_{nf}(t_{nf} - t_\infty) > 1 \tag{1}$$

The dimensionless parameters are defined as

$$U = g(b)/v^2, \quad v^2 = h_a r_b^2/k_a w, \quad b = r_0/r_b$$

and

$$Q_h = (1+\alpha)\theta'(1)/v^2 \tag{2}$$

where $\theta'(1)$ satisfies the following boundary-value problem in the domain $1 \le \xi \le b$.

$$\frac{dX_1}{d\xi} = \frac{X_2}{\beta\xi(1+\alpha X_1)} = f(X_1, X_2, \xi) \tag{3}$$

$$\frac{dX_2}{d\xi} = v^2 H \xi X_1 = g(X_1, X_2, \xi) \tag{4}$$

where X_1 and X_2 are defined as $X_1 = \theta$ and $X_2 = (1+\alpha\theta)\beta\xi\theta'(\xi)$. The boundary conditions are

$$X_1(\xi = 1) = 1 \text{ and } X_2(\xi = b) = 0. \tag{5}$$

The shape of a trapezoidal annular fin can be characterized by nondimensional parameters as follows

$$\beta = \frac{y(r)}{w} = \lambda + (1-\lambda)\left(\frac{b-\xi}{b-1}\right) \tag{6}$$

where λ is the shape parameter defined by $\lambda = w_0/w$. Thus $g(b)$ can be expressed as

$$g(b) = \frac{(b-1)}{6U}[(1-\lambda)(b+2) + 3\lambda(b+1)] \tag{7}$$

The invariant imbedding technique is used to solve the problem equations (3), (4), and (5). In this problem, the missing initial condition $X_2(1)$ is of interest. The boundary conditions (5) are converted to a recursive form as

[1]Department of Mechanical Engineering, Kansas State University, Manhattan, KS 66506, Assoc. Mem. ASME

[2]Department of Mechanical Engineering, Kansas State University, Manhattan, KS 66506, Mem. ASME

Contributed by the Heat Transfer Division and presented at the 1983 ASME-JSME Thermal Engineering Conference, Honolulu, Hawaii, March 20–24, 1983. Manuscript received by the Heat Transfer Division February 18, 1983.

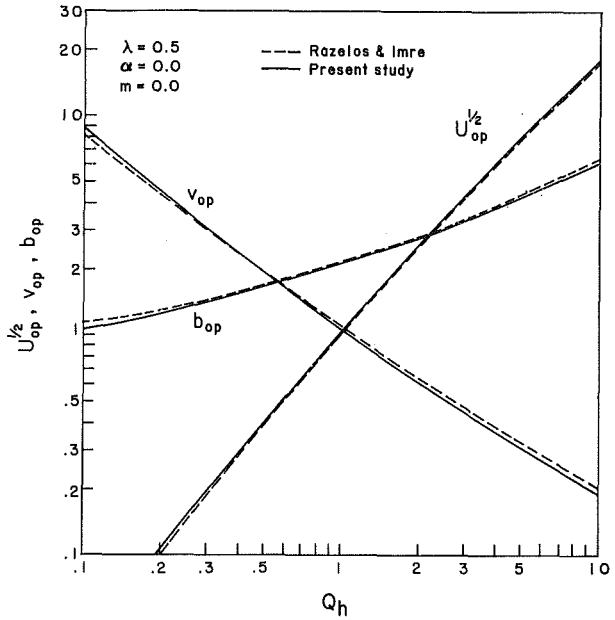

Fig. 1 Optimum volume, length, and base width versus the heat dissipation

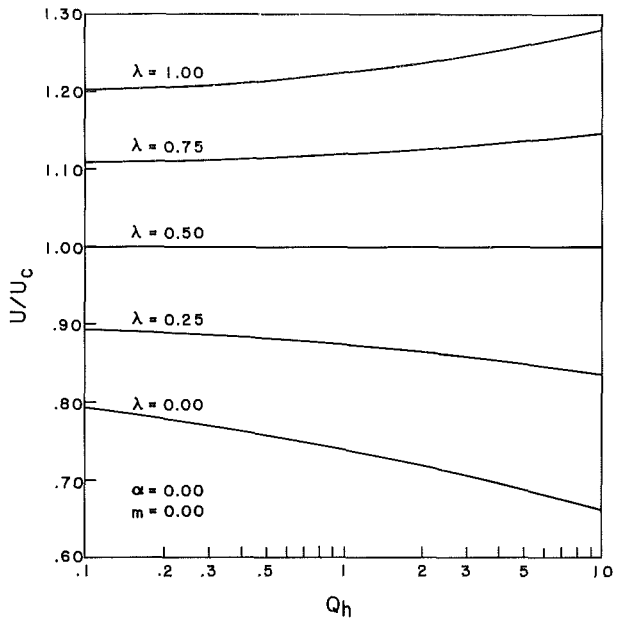

Fig. 2 Effect of slope parameter λ on the optimum volume

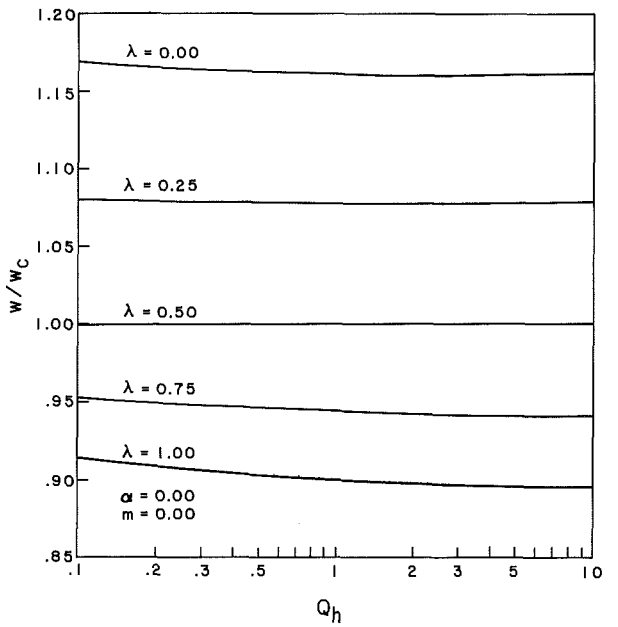

Fig. 3 Effect of the slope parameter λ on the optimum base thickness

$$X_1(a)=c,\ X_2(b)=0. \tag{8}$$

a denotes the recursive duration, and c is the initial state of the process. The missing initial state of the process $X_2(a)$ is not only a function of the starting duration a, but also a function of the starting state c. Thus the function $R=X_2(a)$ can be expressed as

$$X_2(a)=R(c,a) \tag{9}$$

By changing successively the value of duration a, a family of problems that have the same physical processes can be generated. Clearly, we cannot evaluate the values of R at all possible real values of c and a. Hence, some discrete values of c and a must be chosen. The equation governing the whole imbedding process for the missing initial condition R(i.e., $X_2(a)$) can be shown [2] as

$$R(c,a)=R(c+f(c,R(c,a),a)\Delta,a+\Delta) - g(c,R(c,a),a)\Delta \tag{10}$$

where the functions f and g are given in equations (3) and (4). Equation (10) can be solved in a backward recursive fashion, by implementing the condition

$$R(c,b)=0 \tag{11}$$

which follows readily from the boundary condition (8b). In this study $\Delta=0.01$, $\delta=0.1$. Since the function R is represented by a set of values at grid points or in a tabular form, a scheme of interpolation has been used to create the R value at a point of interest, which is different from the grid points.

Adopting a backward recursive approach, we first obtain $R(c,b-\Delta)$, that is when the duration $a=b-\Delta$. For this duration, R is calculated for all the values of c at the grid points. All these R values are stored in the computer memory to be used in the next step of the recursive process, when we try to obtain $R(c,b-2\Delta)$. This backward recursive process is continued by reducing the value of a at each step until $a=1$, because the value $R(1,1)$ is of interest. In summary of the optimization process, a value of U is selected first. With a value of b assumed, the corresponding value of v^2 is calculated directly from (2). By the invariant imbedding method, $X_2(1)$ is obtained. The objective function Q_h is then evaluated by equation (2). Next, the value of b is incremented by Δ, and Q_h calculated again. The value of b is incremented, until the maximum value of Q_h is reached. The corresponding optimized values of b and v are denoted as b_{op} and V_{op}. With some experience, the initial assumed value of b can be selected close to its optimum value.

Figure 1 shows the optimum values of U, v, and b versus Q_h for the case with $\lambda=0.5$, $m=0.0$, and $\alpha=0.0$. For the purpose of comparison, the case is called the base case. The dotted line shows the results obtained by Razelos and Imre [2]. It can be seen that the variation in the base thickness of the fin (the nondimensional parameter v) plays an important role in the heat transfer process. A change in Q_h from 0.2 to 5 increases b_{op} by a factor of 4, whereas v_{op} decreases by a factor of 14. Figures 2 and 3 show the effects of the geometric parameter λ on the optimum cases. We note that as λ decreases, the ratio U/U_c decreases; that is, as we change the shape of a fin from a constant thickness to a triangular fin, less volume is needed for a fin which has the same capacity for heat dissipation. Also, as λ decreases, the base thickness increases. Hence, for

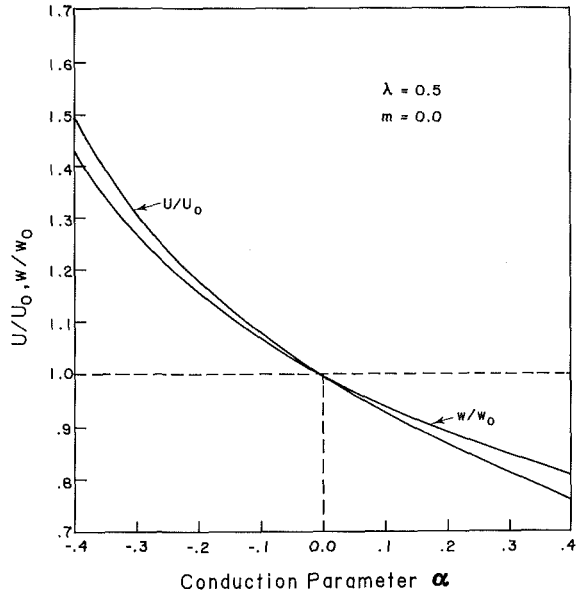

Fig. 4 Effect of the conductivity parameter α on the optimum volume and optimum base thickness

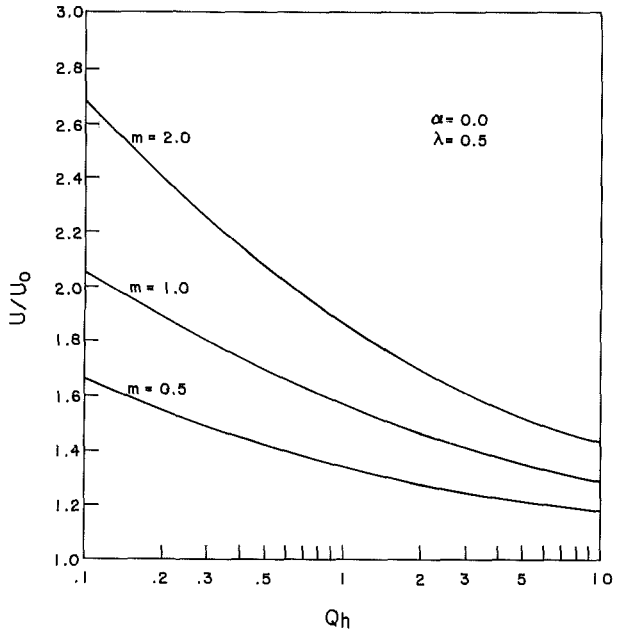

Fig. 5 Effect of the index m on the optimum volume

a fin with a constant slope the triangular fin has the smallest volume and the largest base thickness. Also, we note that the effects of λ variation on the optimum cases are more significant in the case of higher values of Q_h. Figure 4 illustrates the effects of α on the optimum cases. Both curves pass through the (0, 1) point. For a given value of heat dissipation, we require larger volumes than required for the base case when $\alpha<0.0$, and smaller volumes where $\alpha>0.0$. Figures 5 and 6 show the effects of the index m on the optimum cases. For the same value of heat dissipation, as m increases, the volume and the base thickness increases. This is because the heat transfer coefficient has decreased.

In conclusion, the invariant imbedding approach has been effectively applied to the problem of the fin optimization, with variable thermal parameters. For this optimization problem, the invariant imbedding approach requires much less computation time than the time required by the quasi-Newtonian approach, because the quasi-Newtonian algorithm

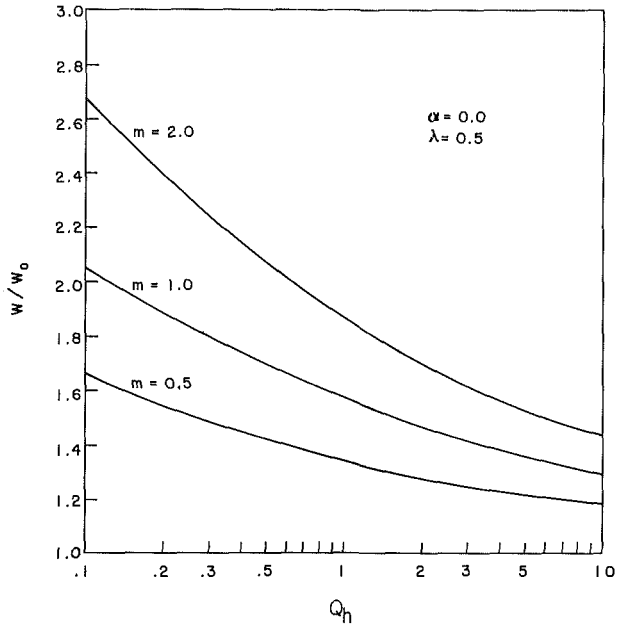

Fig. 6 Effect of the index m on the optimum base thickness

involves integration processes and iterations until convergence of the sequence of the computed values is reached. Besides, the invariant imbedded approach is much more stable than the quasi-Newtonian approach, because the invariant imbedding approach automatically takes care of any possible mathematical singularities.

References

1 Razelos, P., and Imre, K., "The Optimum Dimensions of Circular Fins With Variable Thermal Parameters," ASME JOURNAL OF HEAT TRANSFER, Vol. 102, No. 3, Aug. 1980, pp. 420-425.

2 Lee, E. S., *Quasilinearization and Invariant Imbedding, Mathematics in Science and Engineering*, Vol. 41, Academic Press, New York, 1968.

Optimum Use of Longitudinal Fins of Rectangular Profiles in Boiling Liquids

S. Biyikli[1]

Nomenclature

A = conduction area of fin
A_c = convection area of fin
A_p = profile area of fin
H = height of fin
$h(x)$ = local heat transfer coefficient
h_m = mean heat transfer coefficient
q = heat transfer rate
$(q/A)_0$ = base heat flux of fin
$(q/A)^*$ = surface heat flux without fin
r = aspect ratio
T_0 = base temperature of fin
T_s = saturation temperature of liquid
$\Delta T(x)$ = local temperature difference
$(\Delta T)_m$ = mean temperature difference
ΔT_0 = base temperature difference $= T_0 - T_s$
ΔT_{0p} = optimum base temperature difference
W = width of fin

[1]Research Associate, Department of Mechanical Engineering, University of Southern California, Los Angeles, CA 90089-1453; Assoc. Mem. ASME.

Contributed by the Heat Transfer Division for publication in the JOURNAL OF HEAT TRANSFER. Manuscript received by the Heat Transfer Division April 14, 1984.

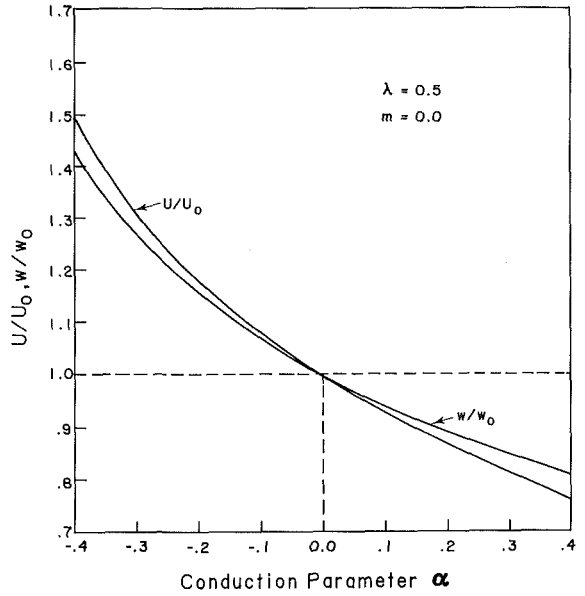

Fig. 4 Effect of the conductivity parameter α on the optimum volume and optimum base thickness

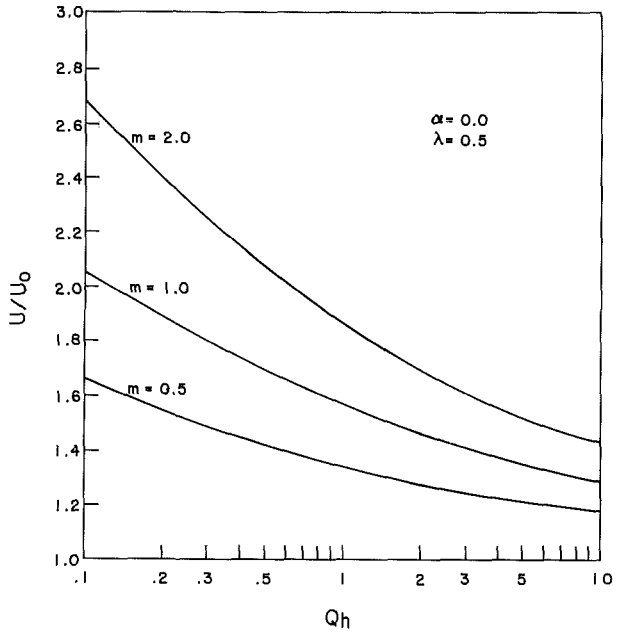

Fig. 5 Effect of the index m on the optimum volume

a fin with a constant slope the triangular fin has the smallest volume and the largest base thickness. Also, we note that the effects of λ variation on the optimum cases are more significant in the case of higher values of Q_h. Figure 4 illustrates the effects of α on the optimum cases. Both curves pass through the (0, 1) point. For a given value of heat dissipation, we require larger volumes than required for the base case when $\alpha<0.0$, and smaller volumes where $\alpha>0.0$. Figures 5 and 6 show the effects of the index m on the optimum cases. For the same value of heat dissipation, as m increases, the volume and the base thickness increases. This is because the heat transfer coefficient has decreased.

In conclusion, the invariant imbedding approach has been effectively applied to the problem of the fin optimization, with variable thermal parameters. For this optimization problem, the invariant imbedding approach requires much less computation time than the time required by the quasi-Newtonian approach, because the quasi-Newtonian algorithm

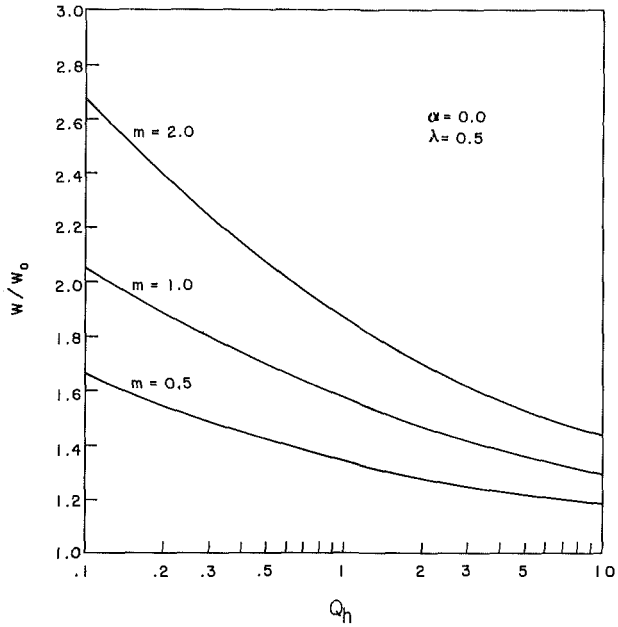

Fig. 6 Effect of the index m on the optimum base thickness

involves integration processes and iterations until convergence of the sequence of the computed values is reached. Besides, the invariant imbedded approach is much more stable than the quasi-Newtonian approach, because the invariant imbedding approach automatically takes care of any possible mathematical singularities.

References

1 Razelos, P., and Imre, K., "The Optimum Dimensions of Circular Fins With Variable Thermal Parameters," ASME JOURNAL OF HEAT TRANSFER, Vol. 102, No. 3, Aug. 1980, pp. 420-425.

2 Lee, E. S., *Quasilinearization and Invariant Imbedding, Mathematics in Science and Engineering*, Vol. 41, Academic Press, New York, 1968.

Optimum Use of Longitudinal Fins of Rectangular Profiles in Boiling Liquids

S. Biyikli[1]

Nomenclature

A = conduction area of fin
A_c = convection area of fin
A_p = profile area of fin
H = height of fin
$h(x)$ = local heat transfer coefficient
h_m = mean heat transfer coefficient
q = heat transfer rate
$(q/A)_0$ = base heat flux of fin
$(q/A)^*$ = surface heat flux without fin
r = aspect ratio
T_0 = base temperature of fin
T_s = saturation temperature of liquid
$\Delta T(x)$ = local temperature difference
$(\Delta T)_m$ = mean temperature difference
ΔT_0 = base temperature difference $= T_0 - T_s$
ΔT_{0p} = optimum base temperature difference
W = width of fin

[1]Research Associate, Department of Mechanical Engineering, University of Southern California, Los Angeles, CA 90089-1453; Assoc. Mem. ASME.

Contributed by the Heat Transfer Division for publication in the JOURNAL OF HEAT TRANSFER. Manuscript received by the Heat Transfer Division April 14, 1984.

Introduction

For many years fins have been used primarily in contact with fluids having poor heat transfer characteristics, and with the heat transfer coefficient between the fin and the fluid fairly constant along the length of the fin. In recent years, however, the use of fins in boiling liquids has been increasing. When heat is transferred from a fin to a boiling liquid, an interesting situation occurs in which the heat transfer coefficient is not constant along the length of a fin. The use of fins with boiling liquids in reboilers, and refrigeration equipment is common and they are attractive for cooling of nuclear reactors. Although the phenomenon of boiling along the length of longitudinal fins has been studied by previous investigators [1–9], there is a need for further information regarding optimum use of longitudinal fins of rectangular profiles in boiling liquids for engineering applications.

The objective of the present study is to develop design charts for longitudinal fins of rectangular profiles in boiling water, isopropyl alcohol and Freon-113.

Analysis of Fin Performance

The steady-state one-dimensional heat conduction equation is solved numerically for longitudinal fins of rectangular profile (fin material is copper) in boiling water, isopropyl alcohol, and Freon-113, employing the assumptions of Hsu [8]. It was shown by Shih and Westwater [6] that one-dimensional conduction calculations are identical to two-dimensional calculations for copper fins. The heat transfer coefficient, $h(x)$, is assumed to be proportional to the temperature difference, as reported by Haley and Westwater [4]. The solution is obtained by finite differencing with successive overrelaxation. The results are used to explain the effect of aspect ratio, r, profile area, A_p, and base temperature difference, ΔT_0, on heat transfer from fins. The description of heat transfer leads to design curves for rectangular fins.

The heat transfer rate from a fin can be expressed using Newton's law of cooling

$$q = \frac{A_c}{H}\int_0^H h(x)\,\Delta T(x)\,dx \qquad (1a)$$

or

$$q = A_c h_m (\Delta T)_m \qquad (1b)$$

where h_m and $(\Delta T)_m$ are the mean values of the heat transfer coefficient and temperature difference along the fin, and A_c is the convection area of the fin. For a given fin material and boiling liquid, from the physics of the problem it can be shown that $h_m(\Delta T)_m$ is only a function of r, A_p, and ΔT_0, i.e.,

$$h_m(\Delta T)_m = f(r, A_p, \Delta T_0) \qquad (2)$$

The base heat flux $(q/A)_0$ is also a function of r, A_p, and ΔT_0.

Effects of r, A_p, *and* ΔT_0. The variation of the local heat transfer coefficient over the fin as a function of r depends on what value the base temperature difference is kept. When the base temperature difference corresponds to nucleate boiling, increasing r decreases the tip heat transfer coefficient. Hence, the mean heat transfer coefficient (h_m) decreases with increasing r. When the base temperature difference is at transition or film boiling, the local heat transfer coefficient at first increases, then decreases with increasing r. Thus, h_m passes through a maximum with increasing r when ΔT_0 is at transition or film boiling.

The variation of the heat transfer coefficient over the fin as a function of A_p depends also on what value the base temperature difference is kept. h_m decreases with increasing A_p for the case where the fin base is in transition boiling and the fin tip is in nucleate boiling. h_m increases with increasing A_p for the case where the tip of the fin is also in transition boiling. Very low values of the heat transfer coefficient are observed compared to the cases where the tip of the fin is in nucleate boiling. It is seen here that when nucleate boiling disappears from the fin, h_m becomes very low.

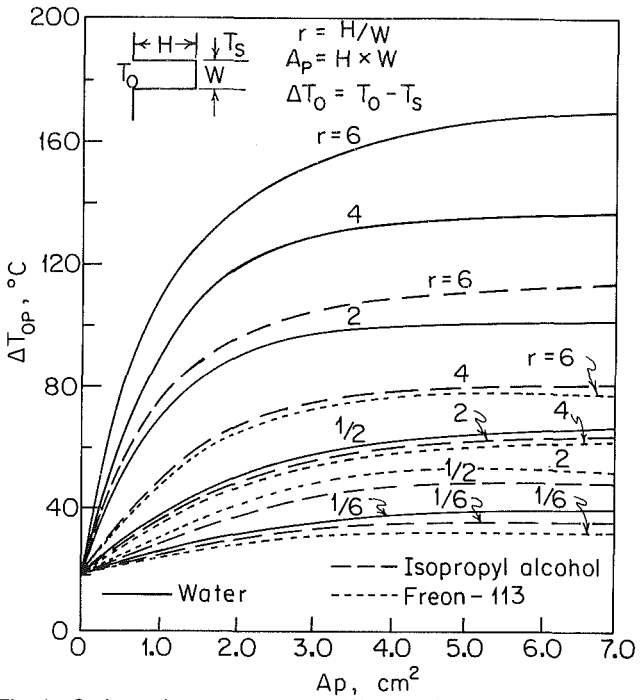

Fig. 1 Optimum base temperature difference for rectangular fins in boiling water, isopropyl alcohol, and Freon-113

Base heat flux from a fin in a boiling liquid increases with increasing base temperature difference and, after reaching a maximum point, it starts to decrease. When r is small, the base heat flux reaches a maximum soon after the burnout point is exceeded. With larger values of r, the maximum base heat flux occurs at higher values of ΔT_0.

Design Curves for Rectangular Fins

The base heat flux as a function of base temperature difference at constant A_p and r passes through a maximum. The base temperature difference corresponding to this maximum base heat flux may be called the optimum base temperature difference, (ΔT_{0p}), of the fin at that A_p and r. For a given A_p and r, when the base temperature difference is at the optimum value, the maximum base heat flux will be obtained from the fin.

The optimum base temperature difference, ΔT_{0p}, as a function of profile area for different aspect ratios is given in Fig. 1 for water, isopropyl alcohol, and Freon-113. When A_p is zero, i.e., when there is no fin on the surface, the optimum base temperature difference is 19°C. This corresponds to the burnout point in the boiling heat transfer curves of water, isopropyl alcohol, and Freon-113 in [4]. When a fin is attached to the surface, the optimum base temperature difference is greater than the burnout point temperature difference regardless of the dimensions of the fin. The optimum base temperature difference increases with increasing profile area at constant r as seen in Fig. 1.

The maximum base heat fluxes for longitudinal fins of rectangular profiles as a function of profile area for different aspect ratios in boiling water, isopropyl alcohol, and Freon-113 are given in Fig. 2. When A_p is zero, i.e., when there is no fin on the surface, the maximum base heat flux is the burnout heat flux of the surface at $\Delta T_{0p} = 19$°C. When A_p is very small, the maximum base heat flux is quite high. Increasing

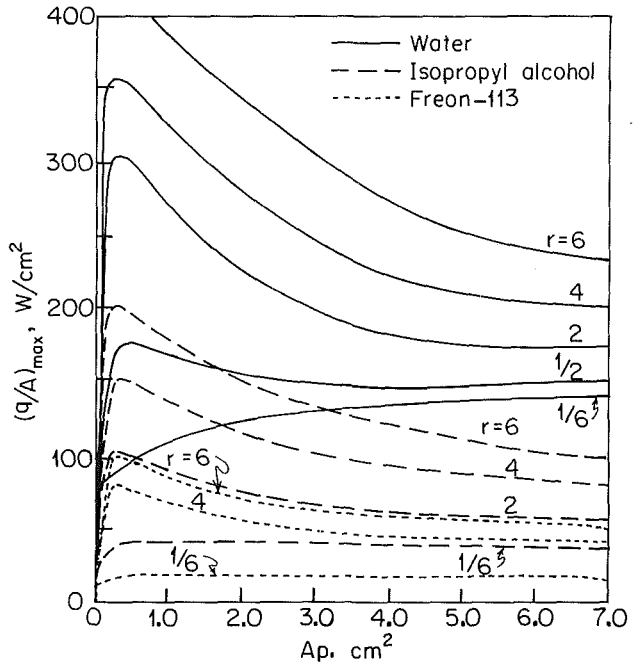

Fig. 2 Maximum base heat flux for rectangular fins in boiling water, isopropyl alcohol, and Freon-113

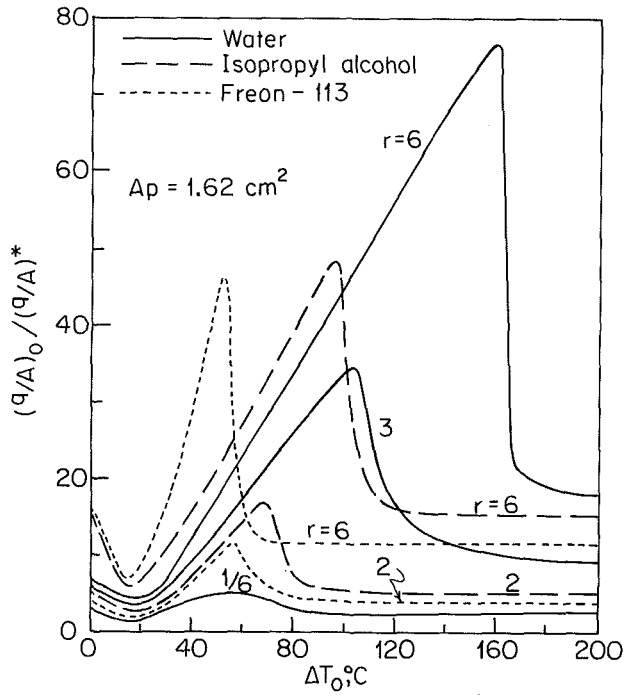

Fig. 3 Fin effectiveness for rectangular fins in boiling water, isopropyl alcohol, and Freon-113

A_p at constant r increases the base area of the fin, and the maximum base heat flux decreases. When r is increased at a given A_p, the base area decreases so that the maximum base heat flux increases with increasing r.

Fin effectiveness is defined as the ratio of the base heat flux of a fin to the surface heat flux without a fin at the same base temperature difference. Figure 3 shows the fin effectiveness as a function of base temperature difference, for different aspect ratios for a given profile area. For other fin profile areas the variations of the curves are similar except the point corresponding to the maximum fin effectiveness increases and occurs at increasing base temperature differences with increasing profile area. Increasing the base temperature difference in nucleate boiling decreases the fin effectiveness. A minimum is observed at the burnout point. For ΔT_0 close to burnout, the fin effectiveness may be less than 1, i.e., the heat flux from the fin base is less than the surface heat flux at the same base temperature difference. For these cases a fin acts as an insulator on the surface. With further increase in ΔT_0, fin effectiveness increases, reaches a maximum, and then decreases. The base temperature difference corresponding to maximum fin effectiveness may not coincide with the optimum base temperature difference for maximum base heat flux for the same fin. The former may be higher than the latter. Fin effectiveness is seen to improve with increasing aspect ratio.

Summary and Conclusions

In this work, the boiling heat transfer phenomenon is explained for longitudinal fins of rectangular profiles in boiling water, isopropyl alcohol, and Freon-113. Preliminary design curves are developed for longitudinal fins of rectangular profiles in the boiling liquids. It may be concluded that:

1 Performance of a fin changes depending on the base temperature and size of the fin in a boiling liquid. Performances of fins improve with increasing aspect ratio.

2 Use of fins when the base of the fin is in transition or film boiling is more effective than when it is in nucleate boiling. When the base temperature difference is at burnout point a fin may act as an insulator on the surface.

Acknowledgments

The author wishes to thank Dr. A. Umur and Dr. M. F. Modest for their helpful suggestions.

References

1 Haley, K. W., and Westwater, J. W., "Heat Transfer From a Fin to a Boiling Liquid," *Chemical Engineering Science*, Vol. 20, 1965, p. 711.

2 Cash, D. R., Klein, G. J., and Westwater, J. W., "Approximate Optimum Fin Design for Boiling Heat Transfer," ASME JOURNAL OF HEAT TRANSFER, Vol. 93, 1971, pp. 19–24.

3 Lai, F. S., and Hsu, Y. Y., "Temperature Distribution in a Fin Partially Cooled by Nucleate Boiling," *AIChE Journal*, Vol. 13, 1967, pp. 817–821.

4 Haley, D. W., and Westwater, J. W., "Boiling Heat Transfer From Single Fins," *Proc. Int. Heat Transfer Conf. (3rd)*, Vol. 13, Paris, 1966, pp. 245–253.

5 Klein, G. J., and Westwater, J. W., "Heat Transfer From Multiple Spines to Boiling Liquids," *AIChE Journal*, Vol. 17, 1971, pp. 1050–1056.

6 Shih, C. C., and Westwater, J. W., "Effect of Geometry and Wall Thickness on Heat Transfer From Longitudinal Fins to Boiling Liquids," *Proc. Int. Heat Transfer Conf. (5th)*, Vol. 4, Tokyo, 1974, pp. 15–19.

7 Ouchi, M., and Takeyama, T., "Experimental and Analytical Study of a Fin in Boiling Water," *Trans. JSME*, Vol. 44, 1978, pp. 154–161.

8 Hsu, Y. Y., "Analysis of Boiling on a Fin," NASA Technical Note, NASA-TNO-4797, 1968.

9 Siman-Tov, M., "Analysis and Design of Extended Surfaces in Boiling Liquids," *Chem. Eng. Prog. Symp. Series*, Vol. 66, No. 102, pp. 174–184.

Surface Tension Effects on Convective Boiling Heat Transfer in Compact Heat Exchangers With Offset Strip Fins

V. P. Carey[1]

Nomenclature

Bo = Bond number = $(\rho_f - \rho_g) g\, d_{hs}^2 \sin\theta/\sigma$
d_h = hydraulic diameter of passage between fin

[1]Department of Mechanical Engineering, University of California, Berkeley, CA 94720, Assoc. Mem. ASME

Contributed by the Heat Transfer Division for publication in the JOURNAL OF HEAT TRANSFER. Manuscript received by the Heat Transfer Division July 12, 1984.

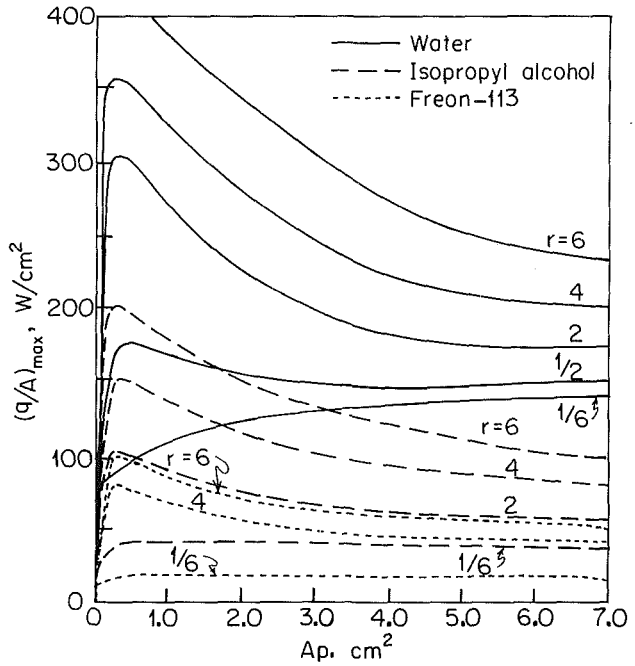

Fig. 2 Maximum base heat flux for rectangular fins in boiling water, isopropyl alcohol, and Freon-113

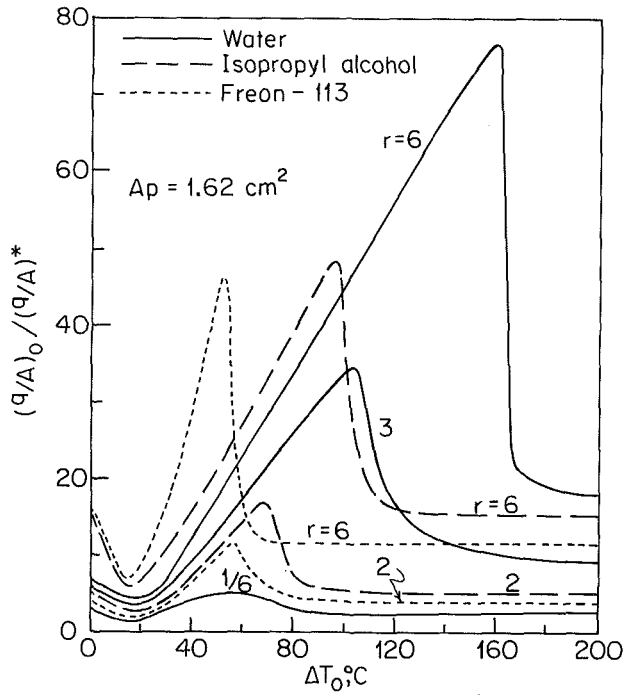

Fig. 3 Fin effectiveness for rectangular fins in boiling water, isopropyl alcohol, and Freon-113

A_p at constant r increases the base area of the fin, and the maximum base heat flux decreases. When r is increased at a given A_p, the base area decreases so that the maximum base heat flux increases with increasing r.

Fin effectiveness is defined as the ratio of the base heat flux of a fin to the surface heat flux without a fin at the same base temperature difference. Figure 3 shows the fin effectiveness as a function of base temperature difference, for different aspect ratios for a given profile area. For other fin profile areas the variations of the curves are similar except the point corresponding to the maximum fin effectiveness increases and occurs at increasing base temperature differences with increasing profile area. Increasing the base temperature difference in nucleate boiling decreases the fin effectiveness. A minimum is observed at the burnout point. For ΔT_0 close to burnout, the fin effectiveness may be less than 1, i.e., the heat flux from the fin base is less than the surface heat flux at the same base temperature difference. For these cases a fin acts as an insulator on the surface. With further increase in ΔT_0, fin effectiveness increases, reaches a maximum, and then decreases. The base temperature difference corresponding to maximum fin effectiveness may not coincide with the optimum base temperature difference for maximum base heat flux for the same fin. The former may be higher than the latter. Fin effectiveness is seen to improve with increasing aspect ratio.

Summary and Conclusions

In this work, the boiling heat transfer phenomenon is explained for longitudinal fins of rectangular profiles in boiling water, isopropyl alcohol, and Freon-113. Preliminary design curves are developed for longitudinal fins of rectangular profiles in the boiling liquids. It may be concluded that:

1 Performance of a fin changes depending on the base temperature and size of the fin in a boiling liquid. Performances of fins improve with increasing aspect ratio.

2 Use of fins when the base of the fin is in transition or film boiling is more effective than when it is in nucleate boiling. When the base temperature difference is at burnout point a fin may act as an insulator on the surface.

Acknowledgments

The author wishes to thank Dr. A. Umur and Dr. M. F. Modest for their helpful suggestions.

References

1 Haley, K. W., and Westwater, J. W., "Heat Transfer From a Fin to a Boiling Liquid," *Chemical Engineering Science*, Vol. 20, 1965, p. 711.

2 Cash, D. R., Klein, G. J., and Westwater, J. W., "Approximate Optimum Fin Design for Boiling Heat Transfer," ASME JOURNAL OF HEAT TRANSFER, Vol. 93, 1971, pp. 19–24.

3 Lai, F. S., and Hsu, Y. Y., "Temperature Distribution in a Fin Partially Cooled by Nucleate Boiling," *AIChE Journal*, Vol. 13, 1967, pp. 817–821.

4 Haley, D. W., and Westwater, J. W., "Boiling Heat Transfer From Single Fins," *Proc. Int. Heat Transfer Conf. (3rd)*, Vol. 13, Paris, 1966, pp. 245–253.

5 Klein, G. J., and Westwater, J. W., "Heat Transfer From Multiple Spines to Boiling Liquids," *AIChE Journal*, Vol. 17, 1971, pp. 1050–1056.

6 Shih, C. C., and Westwater, J. W., "Effect of Geometry and Wall Thickness on Heat Transfer From Longitudinal Fins to Boiling Liquids," *Proc. Int. Heat Transfer Conf. (5th)*, Vol. 4, Tokyo, 1974, pp. 15–19.

7 Ouchi, M., and Takeyama, T., "Experimental and Analytical Study of a Fin in Boiling Water," *Trans. JSME*, Vol. 44, 1978, pp. 154–161.

8 Hsu, Y. Y., "Analysis of Boiling on a Fin," NASA Technical Note, NASA-TNO-4797, 1968.

9 Siman-Tov, M., "Analysis and Design of Extended Surfaces in Boiling Liquids," *Chem. Eng. Prog. Symp. Series*, Vol. 66, No. 102, pp. 174–184.

Surface Tension Effects on Convective Boiling Heat Transfer in Compact Heat Exchangers With Offset Strip Fins

V. P. Carey[1]

Nomenclature

Bo = Bond number = $(\rho_f - \rho_g) g\, d_{hs}^2 \sin\theta/\sigma$
d_h = hydraulic diameter of passage between fin

[1]Department of Mechanical Engineering, University of California, Berkeley, CA 94720, Assoc. Mem. ASME

Contributed by the Heat Transfer Division for publication in the JOURNAL OF HEAT TRANSFER. Manuscript received by the Heat Transfer Division July 12, 1984.

d_{hs} = hydraulic diameter of small passage at end of fin
f = friction factor
F = multiplier in Chen correlation $= h_c/(h_f \, \mathrm{Pr}_f^{0.296})$
G = mass flux
h = heat transfer coefficient
h_c = convective boiling heat transfer coefficient
h_{cmin} = minimum convective boiling heat transfer coefficient
k_f = thermal conductivity of liquid
L = strip length of offset fin
p = pressure
Pr_f = liquid Prandtl number
Re = Reynolds number $= Gd_h/\mu_f$
Re_f = liquid Reynolds number $= G(1-x)d_h/\mu_f$
We = Weber number $= G^2 d_{hs}/\sigma\rho_f$
x = mass quality
X_{tt} = Martinelli parameter $= [(dp/dz)_{Ff}/(dp/dz)_{Fg}]_{tt}^{1/2}$
z = axial distance along flow direction
α = void fraction
δ = fin thickness
θ = angle between channel axis and horizontal
μ = absolute viscosity
ν = kinematic viscosity
ρ = density
σ = surface tension
ϕ_f = two-phase multiplier
Ω = parameter defined in equation (5)

Subscripts

f = liquid properties, or corresponding to liquid portion flowing alone in the channel
$f0$ = corresponding to entire flow as liquid
F = friction component
g = vapor properties
tt = corresponding to turbulent liquid and vapor flow

Introduction

The space and weight savings and high efficiency associated with offset strip fin compact heat exchanger geometries has led to their increased use as evaporators in refrigeration, air-conditioning, and cryogenic applications. The need to understand and predict heat transfer in applications of this type has prompted several recent studies of boiling in plate-fin heat exchanger geometries. The boiling heat transfer performance of offset strip fin geometries in thermosyphon boiler configurations has been investigated by Westwater and coworkers [1–3], and Galezha, Usyukin, and Kan [4]. These studies all consider moderate to high wall superheat levels where nucleate boiling effects are important.

In a series of recent papers, Robertson [5, 6] and Robertson and Lovegrove [7] have examined forced convective boiling heat transfer in offset strip fin geometries at very low wall superheat levels, where nucleate boiling effects are negligible. Film flow models for predicting convective boiling heat transfer in offset strip fins at high quality have also been proposed by Robertson [6] and Yung, Lorentz, and Panchal [8].

At high qualities and moderate to high flow rates, the convective boiling heat transfer coefficients measured by Robertson and Lovegrove [5, 7] are consistent with the trends predicted by the film-flow models mentioned above. At low qualities and low flow rates, however, the trend in the data is quite unusual. At the low temperature differences in these experiments, nucleate boiling effects are negligible. Hence, as the quality approaches zero, one might expect the heat transfer coefficient to decrease to the value for single-phase liquid flow. Instead, the measured coefficients level off at a value about a factor of two higher than the single phase coefficient. In the studies mentioned above, no satisfactory explanation of this trend has been offered.

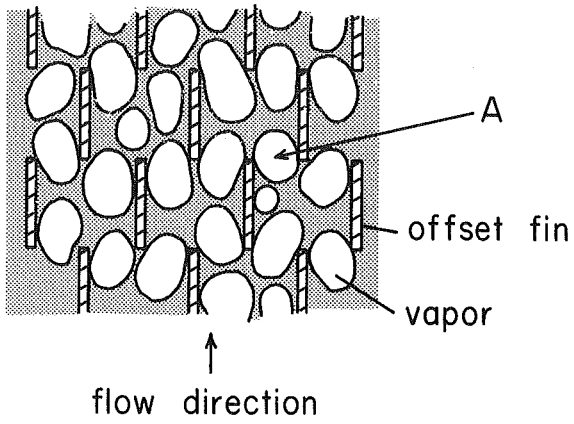

Fig. 1 Schematic plan cross section of two-phase flow through an offset strip fin array at low quality

The present note examines the effects of surface tension on convective boiling heat transfer in compact offset fin geometries at low wall superheat levels. Theoretical arguments and experimental evidence are presented which suggest that the high heat transfer coefficients obtained by Robertson et al. [5, 7] at low flow and quality may be due to the effects of surface tension on vapor motion through the fin matrix. It is also shown that the arguments advanced here may be used to develop a modified form of the Chen [9] correlation that predicts convective boiling heat transfer coefficients which agree closely with available data.

Analysis and Discussion

As pointed out by Robertson et al. [7], at low mass flux and quality the vapor flux is low and a form of slug flow is likely to occur in small offset fin geometries. A plan cross section of such a flow in an offset fin matrix is shown schematically in Fig. 1. It can be seen that vapor bubbles must squeeze through the narrow passage where one fin ends and another begins. When the liquid–vapor interface contacts the fin, surface tension forces will affect the bubble motion.

To determine the effect of surface tension on vapor motion through the matrix, the following model is considered. A bubble at the narrow passage at location A in Fig. 1 can only pass through if there is a net downstream force on the bubble. This condition is stated quantitatively as

$$\left(-\frac{dp}{dz}\right)_F A_{os} d_{hs} > \sigma P_s - (\rho_f - \rho_g) g \, V_b \sin\theta \qquad (1)$$

Here A_{os} is the open area of the small channel at location A, P_s is its perimeter, and V_b is the volume of the bubble. The left side of relation (1) represents the downstream force due to the friction pressure gradient acting across the bubble. The pressure drop due to acceleration is assumed small compared with the friction component. The right side of relation (1) contains terms representing the surface tension and buoyancy forces acting on the bubble. The friction pressure gradient is evaluated using the two-phase multiplier ϕ_f as

$$\left(\frac{dp}{dz}\right)_F = \left(\frac{dp}{dz}\right)_f \phi_f^2 = \left[\frac{2f_f G^2}{d_h \rho_f}(1-x)^2\right]\phi_f^2 \qquad (2)$$

To evaluate the friction factor f_f in equation (2), the correlation of Wieting [10] for single phase turbulent flow in offset fin geometries is used

$$f_f = \gamma_1 \mathrm{Re}_f^{-0.198}, \qquad \gamma_1 = 1.136(L/d_h)^{-0.781}(\delta/d_h)^{0.534} \qquad (3)$$

Using the fact that $P_s/A_{os} = 4/d_{hs}$ and assuming that $V_b/A_{os} \cong d_{hs}$, (1)–(3) may be combined to yield

$$\phi_f > \Omega/(1-x)^{0.9} \qquad (4)$$

where

$$\Omega = \left[\frac{2\ \mathrm{Re}^{0.198}}{\gamma_1 \mathrm{We}} \left(\frac{d_h}{d_{hs}} \right) (1 - 0.25\ \mathrm{Bo}) \right]^{1/2} \tag{5}$$

Equation (4) implies that a minimum value of ϕ_f equal to $\Omega/(1-x)$ is required before the drag due to the frictional pressure drop can overcome the combined effects of surface tension and buoyancy. Collier [11] points out that for pipe flows, ϕ_f, given approximately by $\phi_f = (1-\alpha)^{-1}$, is a monotonically increasing function of α. If this is also true for the two-phase flow through offset fin surfaces, equation (4) also implies that a minimum value of α must be attained before pressure forces on the bubble will overcome the retarding effects of surface tension and push the bubbles through the matrix. If α is below this minimum value in a boiling system, bubbles will be held back until vapor generation raises α to the required minimum value. Only then will some of the vapor start to move through the matrix.

The fact that surface tension can hold back vapor in compact heat exchanger geometries has been demonstrated in experiments at the University of California at Berkeley. An offset fin surface 6.4 cm wide with $L = 0.159$ cm, $H = 0.386$ cm, 2.76 fins per cm, and $\delta = 0.020$ cm was installed in a clear plexiglass channel. For this configuration, d_h was 0.359 cm and d_{hs} was 0.226 cm. A steady flow of water at room temperature was pumped through the channel. Once a steady liquid flow was established, a small quantity of air was introduced into the flow upstream of the surface.

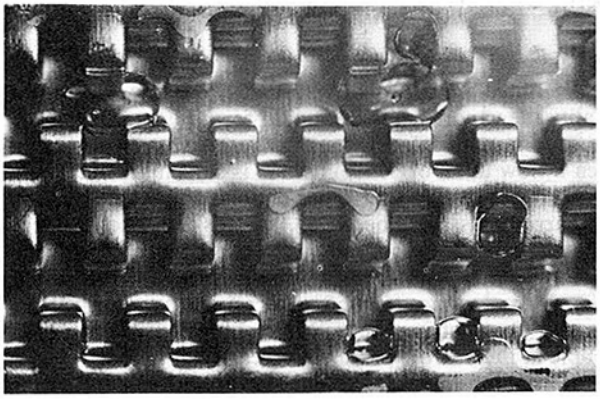

Fig. 2 Photograph of air bubbles held in place by surface tension in an offset strip fin matrix; the channel is horizontal with pure water flowing from right to left at a mass flux of 60 kg/m^{2}s; both the water and air are at 20°C

At low flow, the bubbles were observed to be held back at the narrowest passages in the matrix. When the flow was increased, however, the increased drag released the bubbles and pushed them downstream through the matrix. A photograph taken of bubbles held in place at low flow is shown in Fig. 2. The surface is horizontal and the mass flux G is 60 kg/m^{2}s. The value of Ω for the conditions in the photograph is 10.5. As will later be seen, values of Ω for the experimental conditions investigated by Robertson and Lovegrove [5, 7] range between 3 and 25. This suggests that the same retarding effect on vapor motion may have been present at low quality in the boiling experiments of Robertson and Lovegrove [5, 7] for low flow rates.

For convective boiling in vertical round tubes, Bennett and Chen [12] used a modified Chilton-Colburn analogy to show that

$$\frac{h_c}{h_f} \mathrm{Pr}_f^{-0.296} = \phi_f^{0.89} \tag{6}$$

It is not clear, *a priori*, whether equation (6) is also valid for the offset fin geometry considered here. However, it does strongly suggest that $(h_c/h_f)\ \mathrm{Pr}_f^{-0.296}$ is likely to be some monotonically increasing function R of ϕ_f

$$\frac{h_c}{h_f} \mathrm{Pr}_f^{-0.296} = R(\phi_f) \tag{7}$$

Since equation (4) implies that a minimum value of ϕ_f is required for vapor motion to occur, equation (7) implies that there is a minimum value of the heat transfer coefficient associated with this condition. Combining (4) with (7) and assuming x is small compared to 1, this minimum h_c value is given by

$$h_{c\min} = h_{f0} \mathrm{Pr}_f^{0.296} R(\Omega) \tag{8}$$

For each of their test runs, the measured values of h_c obtained by Robertson and Lovegrove [5, 7] appear to level off at a minimum value as $x \to 0$. To evaluate the validity of equation (8), all the lowest h_c values obtained by Robertson and Lovegrove [5, 7] were normalized with $h_{f0}\ \mathrm{Pr}^{0.296}$ and plotted versus Ω. Here h_{f0} was determined using the single-phase heat transfer correlation of Wieting [10] for turbulent flow in offset fin geometries

$$h_{f0} = 0.242 (L/d_h)^{-0.322} (\delta/d_h)^{0.089} (k_f/d_h) \mathrm{Pr}_f^{1/3} \mathrm{Re}^{0.632} \tag{9}$$

As seen in Fig. 3, equation (8) with

$$R(\Omega) = 1.0 + 0.34\ \Omega^{0.68} \tag{10}$$

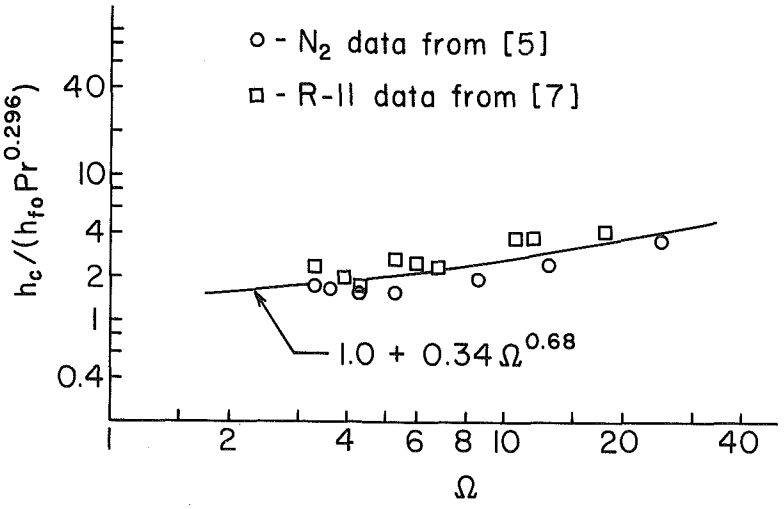

Fig. 3 Correlation of the minimum h_c values for each run measured by Robertson and Lovegrove [5, 7] with Ω

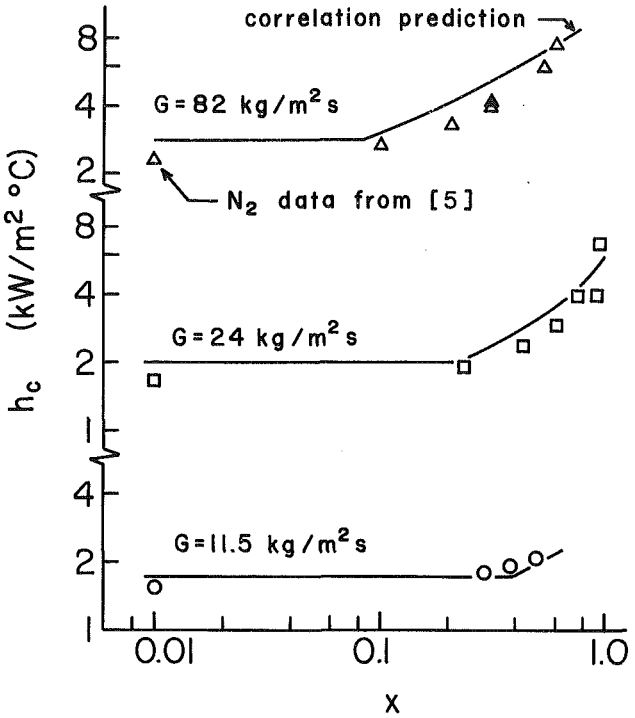

Fig. 4 Comparison of the predicted variation of h_c with values measured by Robertson [5] for N_2 at 3 bar

fits all the minimum h_c values very well. Since these data for N_2 and R-11 cover a wide range of pressure (3 to 7 bar) and mass flux conditions (11.5 to 157 kg/m^{2}s), the good agreement with this correlation appears to support the theoretical model of surface tension effects postulated above.

At moderate and high qualities, h_c will, in general, be above its minimum value. For these circumstances, a modified version of Chen's [9] method is proposed for predicting h_c. Following the same reasoning as Bennett and Chen [12], the convective boiling heat transfer coefficient is postulated as

$$h_c = h_f \mathrm{Pr}_f^{0.296} F(1/X_{tt}) \tag{11}$$

where, from Wieting's [10] correlations for turbulent flow, h_f and $1/X_{tt}$ are given by

$$h_f = 0.242(L/d_h)^{-0.322}(\delta/d_h)^{0.089}(k_f/d_h)\mathrm{Pr}_f^{1/3}\mathrm{Re}_f^{0.632} \tag{12}$$

$$\frac{1}{X_{tt}} = \left[\frac{\nu_g}{\nu_f}\right]^{0.099}\left(\frac{\rho_f}{\rho_g}\right)^{0.401}\left(\frac{x}{1-x}\right)^{0.901} \tag{13}$$

When converted to values of $F = h_c/h_f\,\mathrm{Pr}_f^{0.296}$ and $1/X_{tt}$, the data of Robertson et al. [5, 7] for $h_c > h_{cmin}$ were found to agree closely with the curve given by

$$F = 1.65\left(\frac{1}{X_{tt}} + 0.60\right)^{0.78} \quad \text{for} \quad \frac{1}{X_{tt}} > 0.1 \tag{14}$$

which is only slightly different from Chen's [9] empirical correlation for convective boiling in circular pipes.

To predict the value of h_c for any set of conditions, h_c is first calculated by the modified Chen correlation using equations (11)–(14) and then h_{cmin} is calculated using

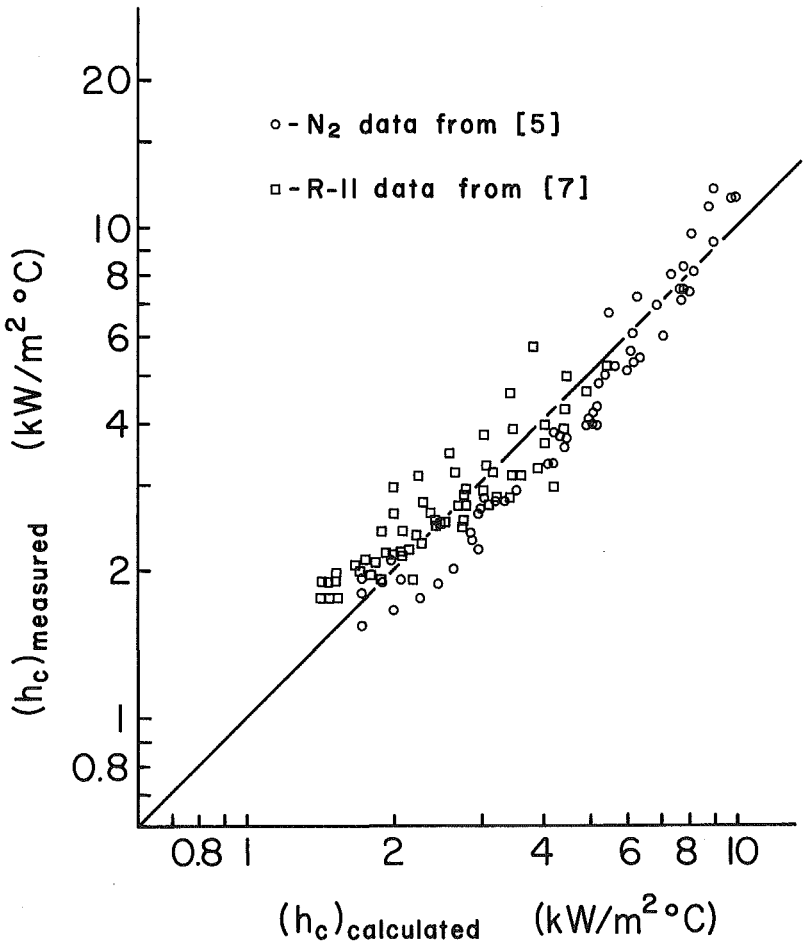

Fig. 5 Comparison of all the measured h_c values obtained by Robertson and Lovegrove [5, 7] with the corresponding values predicted by the h_{cmin}-Chen correlation method

equations (8)–(10). If h_c calculated by the modified Chen technique is less than h_{cmin}, h_c is taken to be h_{cmin}. Otherwise, the value from the Chen correlation is used. The variation of h_c with x predicted in this way is compared with the corresponding N_2 data of Robertson [5] at various flow rates in Fig. 4. It can be seen that the predicted value of h_c decreases as $x \rightarrow 0$ until it reaches a minimum value and then levels off. The data in each case behave in the same manner and agree well with the predicted values.

The procedure described above was used to predict h_c values corresponding to all the R-11 and N_2 data of Robertson et al. [5, 7]. Figure 5 shows a plot of the measured versus the predicted values of h_c. It can be seen there that the agreement is quite good. The mean absolute deviation between the measured and predicted values is only 13.8 percent, which is about the level of accuracy usually obtained with Chen's correlation for convective boiling in round tubes.

Conclusions

An analytical model of surface tension effects during convective boiling in offset fin heat exchanger geometries has been presented. This model indicates that to maintain vapor flow through the matrix, the void fraction must be above a certain minimum value. It further predicts that there is a minimum heat transfer coefficient associated with this minimum void fraction condition which depends primarily on the dimensionless parameter Ω. The measurements of forced convective boiling heat transfer coefficients obtained by Robertson et al. [5, 7] exhibit trends which are completely consistent with the predictions of this model. This suggests that the leveling-off of the measured heat transfer coefficients obtained in these studies, as $x \rightarrow 0$, may be due to the effects of surface tension on vapor motion.

A method of predicting forced convective heat transfer coefficients in offset strip fin geometries was also presented that accounts for surface tension effects. This method was found to predict values of h_c which agreed well with the data of Robertson et al. [5, 7]. More data are needed to fully assess the accuracy of the model of surface tension effects proposed here. However, the good agreement of its predictions with the limited existing data suggests that it may have value as a means of predicting the effects of surface tension on forced convective boiling in offset strip fin geometries.

References

1 Pantisidis, H., Gresham, R. D., and Westwater, J. W., "Boiling of Liquids in a Compact Plate-Fin Heat Exchanger," *Int. J. Heat and Mass Transfer*, Vol. 18, 1975, pp. 37–42.

2 Chen, C. C., Loh, J. V., and Westwater, J. W., "Prediction of Boiling Heat Transfer Duty in a Compact Plate-Fin Heat Exchanger Using the Improved Local Assumption," *Int. J. Heat and Mass Transfer*, Vol. 24, 1981, pp. 1907–1912.

3 Chen, C. C., and Westwater, J. W., "Application of the Local Assumption for the Design of Compact Heat Exchangers for Boiling Heat Transfer," ASME JOURNAL OF HEAT TRANSFER, Vol. 106, 1984, pp. 204–209.

4 Galezha, V. B., Usyukin, I. P., and Kan, K. D., "Boiling Heat Transfer With Freons in Finned-Plate Heat Exchangers," *Heat Transfer—Soviet Research*, Vol. 8, 1976, pp. 103–110.

5 Robertson, J. M., "Boiling Heat Transfer With Liquid Nitrogen in Brazed-Aluminum Plate-Fin Heat Exchangers," *AIChE Symposium Series*, Vol. 75, 1979, pp. 151–164.

6 Robertson, J. M., "The Correlation of Boiling Coefficients in Plate-Fin Heat Exchanger Passages With a Film-Flow Model," *Proceedings, 7th International Heat Transfer Conference*, Vol. 6, Munich, 1982.

7 Robertson, J. M., and Lovegrove, P. C., "Boiling Heat Transfer With Freon 11 (R11) in Brazed Aluminum Plate-Fin Heat Exchangers," ASME JOURNAL OF HEAT TRANSFER, Vol. 105, 1983, pp 605–610.

8 Yung, D., Lorenz, J. J., and Panchal, C., "Convective Vaporization and Condensation in Serrated-Fin Channels," ASME HTD, Vol. 23, 1980, pp. 29–37.

9 Chen, J. C., "Correlation for Boiling Heat Transfer to Saturated Fluids in Convective Flow," *Industrial and Engineering Chemistry Process Design and Development*, Vol. 5, 1966, pp. 322–329.

10 Wieting, A. R., "Empirical Correlations for Heat Transfer and Flow Friction Characteristics of Rectangular Offset-Fin Plate-Fin Heat Exchangers," ASME JOURNAL OF HEAT TRANSFER, Vol. 97, 1975, pp. 488–490.

11 Collier, J. G., *Convective Boiling and Condensation*, 2nd edn., McGraw-Hill, New York, 1981.

12 Bennett, D. L., and Chen, J. C., "Forced Convective Boiling in Vertical Tubes for Saturated Pure Components and Binary Mixtures," *AIChE Journal*, Vol. 26, 1980, pp. 454–461.

On the Steady-State Velocity of the Inclined Toroidal Thermosyphon

M. Sen,[1,2,3] E. Ramos,[2,4] and C. Treviño[1]

Introduction

The toroidal thermosyphon consists of a closed loop of tubing in the form of a torus, filled with a fluid and heated over part of its length and cooled over another part. In the presence of gravity, buoyancy forces due to temperature differences set the fluid in motion. Thus a circulation is created which transfers energy by convection from the heated section of the loop to the cooled one. A recent review of natural circulation loops has been carried out by Mertol and Greif [1].

Creveling et al. [2] made theoretical and experimental investigations of the dynamics of a toroidal thermosyphon where the heated and cooled regions were the lower and upper halves, respectively. They observed that, depending on the heat input, the flow velocity could be steady, oscillatory in one direction, or oscillatory in both directions.

The steady-state velocity in a toroidal thermosyphon with displacement of the heated and cooled sections with respect to gravity was analyzed by Damerell and Schoenhals [3]. Using the results of a one-dimensional model, they affirm that the maximum flow rate is attained for zero inclination when heating occurs from directly below and cooling directly above. For this inclination, three steady-state velocities are also predicted, one of them being the zero velocity solution. Finally, their analysis also predicted that at least one steady-state velocity can be obtained for all angles of inclination. These results are all based on a small-parameter approximation.

In the present note a similar theoretical analysis on the inclined toroidal loop is made in order to obtain an exact expression for the steady-state velocity. Some important qualitative differences with the approximate calculations of Damerell and Schoenhals [3] are found.

Analysis and Results

We consider the thermosyphon shown in Fig. 1 of [3]. This is a toroidal geometry which is heated with constant heat input of over half its length and cooled by means of a heat exchanger with constant heat transfer coefficient h and wall temperature T_0 on the other half.

The heated and cooled sections are inclined an angle θ_0 with respect to the horizontal plane. We make the usual Boussinesq approximation with the assumption of linear variation of fluid density with temperature. In the steady state, the buoyancy force on the fluid is exactly balanced by the viscous

[1]Departamento de Fluidos y Termica, Facultad de Ingenieria, UNAM, 04510 Mexico, D.F., Mexico

[2]Departamento de Energía Solar, Instituto de Investigaciones en Materials, UNAM, 04510 México, D.F., Mexico

[3]Mem. ASME

[4]Present address: Laboratorio de Energía Solar, IIM-UNAM, 62580 Temixco, Mor. Mexico

Contributed by the Heat Transfer Division for publication in the JOURNAL OF HEAT TRANSFER. Manuscript received by the Heat Transfer Division June 13, 1984.

equations (8)-(10). If h_c calculated by the modified Chen technique is less than h_{cmin}, h_c is taken to be h_{cmin}. Otherwise, the value from the Chen correlation is used. The variation of h_c with x predicted in this way is compared with the corresponding N_2 data of Robertson [5] at various flow rates in Fig. 4. It can be seen that the predicted value of h_c decreases as $x \rightarrow 0$ until it reaches a minimum value and then levels off. The data in each case behave in the same manner and agree well with the predicted values.

The procedure described above was used to predict h_c values corresponding to all the R-11 and N_2 data of Robertson et al. [5, 7]. Figure 5 shows a plot of the measured versus the predicted values of h_c. It can be seen there that the agreement is quite good. The mean absolute deviation between the measured and predicted values is only 13.8 percent, which is about the level of accuracy usually obtained with Chen's correlation for convective boiling in round tubes.

Conclusions

An analytical model of surface tension effects during convective boiling in offset fin heat exchanger geometries has been presented. This model indicates that to maintain vapor flow through the matrix, the void fraction must be above a certain minimum value. It further predicts that there is a minimum heat transfer coefficient associated with this minimum void fraction condition which depends primarily on the dimensionless parameter Ω. The measurements of forced convective boiling heat transfer coefficients obtained by Robertson et al. [5, 7] exhibit trends which are completely consistent with the predictions of this model. This suggests that the leveling-off of the measured heat transfer coefficients obtained in these studies, as $x \rightarrow 0$, may be due to the effects of surface tension on vapor motion.

A method of predicting forced convective heat transfer coefficients in offset strip fin geometries was also presented that accounts for surface tension effects. This method was found to predict values of h_c which agreed well with the data of Robertson et al. [5, 7]. More data are needed to fully assess the accuracy of the model of surface tension effects proposed here. However, the good agreement of its predictions with the limited existing data suggests that it may have value as a means of predicting the effects of surface tension on forced convective boiling in offset strip fin geometries.

References

1 Pantisidis, H., Gresham, R. D., and Westwater, J. W., "Boiling of Liquids in a Compact Plate-Fin Heat Exchanger," *Int. J. Heat and Mass Transfer*, Vol. 18, 1975, pp. 37-42.

2 Chen, C. C., Loh, J. V., and Westwater, J. W., "Prediction of Boiling Heat Transfer Duty in a Compact Plate-Fin Heat Exchanger Using the Improved Local Assumption," *Int. J. Heat and Mass Transfer*, Vol. 24, 1981, pp. 1907-1912.

3 Chen, C. C., and Westwater, J. W., "Application of the Local Assumption for the Design of Compact Heat Exchangers for Boiling Heat Transfer," ASME JOURNAL OF HEAT TRANSFER, Vol. 106, 1984, pp. 204-209.

4 Galezha, V. B., Usyukin, I. P., and Kan, K. D., "Boiling Heat Transfer With Freons in Finned-Plate Heat Exchangers," *Heat Transfer—Soviet Research*, Vol. 8, 1976, pp. 103-110.

5 Robertson, J. M., "Boiling Heat Transfer With Liquid Nitrogen in Brazed-Aluminum Plate-Fin Heat Exchangers," *AIChE Symposium Series*, Vol. 75, 1979, pp. 151-164.

6 Robertson, J. M., "The Correlation of Boiling Coefficients in Plate-Fin Heat Exchanger Passages With a Film-Flow Model," *Proceedings, 7th International Heat Transfer Conference*, Vol. 6, Munich, 1982.

7 Robertson, J. M., and Lovegrove, P. C., "Boiling Heat Transfer With Freon 11 (R11) in Brazed Aluminum Plate-Fin Heat Exchangers," ASME JOURNAL OF HEAT TRANSFER, Vol. 105, 1983, pp 605-610.

8 Yung, D., Lorenz, J. J., and Panchal, C., "Convective Vaporization and Condensation in Serrated-Fin Channels," ASME HTD, Vol. 23, 1980, pp. 29-37.

9 Chen, J. C., "Correlation for Boiling Heat Transfer to Saturated Fluids in Convective Flow," *Industrial and Engineering Chemistry Process Design and Development*, Vol. 5, 1966, pp. 322-329.

10 Wieting, A. R., "Empirical Correlations for Heat Transfer and Flow Friction Characteristics of Rectangular Offset-Fin Plate-Fin Heat Exchangers," ASME JOURNAL OF HEAT TRANSFER, Vol. 97, 1975, pp. 488-490.

11 Collier, J. G., *Convective Boiling and Condensation*, 2nd edn., McGraw-Hill, New York, 1981.

12 Bennett, D. L., and Chen, J. C., "Forced Convective Boiling in Vertical Tubes for Saturated Pure Components and Binary Mixtures," *AIChE Journal*, Vol. 26, 1980, pp. 454-461.

On the Steady-State Velocity of the Inclined Toroidal Thermosyphon

M. Sen,[1,2,3] E. Ramos,[2,4] and C. Treviño[1]

Introduction

The toroidal thermosyphon consists of a closed loop of tubing in the form of a torus, filled with a fluid and heated over part of its length and cooled over another part. In the presence of gravity, buoyancy forces due to temperature differences set the fluid in motion. Thus a circulation is created which transfers energy by convection from the heated section of the loop to the cooled one. A recent review of natural circulation loops has been carried out by Mertol and Greif [1].

Creveling et al. [2] made theoretical and experimental investigations of the dynamics of a toroidal thermosyphon where the heated and cooled regions were the lower and upper halves, respectively. They observed that, depending on the heat input, the flow velocity could be steady, oscillatory in one direction, or oscillatory in both directions.

The steady-state velocity in a toroidal thermosyphon with displacement of the heated and cooled sections with respect to gravity was analyzed by Damerell and Schoenhals [3]. Using the results of a one-dimensional model, they affirm that the maximum flow rate is attained for zero inclination when heating occurs from directly below and cooling directly above. For this inclination, three steady-state velocities are also predicted, one of them being the zero velocity solution. Finally, their analysis also predicted that at least one steady-state velocity can be obtained for all angles of inclination. These results are all based on a small-parameter approximation.

In the present note a similar theoretical analysis on the inclined toroidal loop is made in order to obtain an exact expression for the steady-state velocity. Some important qualitative differences with the approximate calculations of Damerell and Schoenhals [3] are found.

Analysis and Results

We consider the thermosyphon shown in Fig. 1 of [3]. This is a toroidal geometry which is heated with constant heat input of over half its length and cooled by means of a heat exchanger with constant heat transfer coefficient h and wall temperature T_0 on the other half.

The heated and cooled sections are inclined an angle θ_0 with respect to the horizontal plane. We make the usual Boussinesq approximation with the assumption of linear variation of fluid density with temperature. In the steady state, the buoyancy force on the fluid is exactly balanced by the viscous

[1]Departamento de Fluidos y Termica, Facultad de Ingenieria, UNAM, 04510 Mexico, D.F., Mexico

[2]Departamento de Energía Solar, Instituto de Investigaciones en Materials, UNAM, 04510 México, D.F., Mexico

[3]Mem. ASME

[4]Present address: Laboratorio de Energía Solar, IIM-UNAM, 62580 Temixco, Mor. Mexico

Contributed by the Heat Transfer Division for publication in the JOURNAL OF HEAT TRANSFER. Manuscript received by the Heat Transfer Division June 13, 1984.

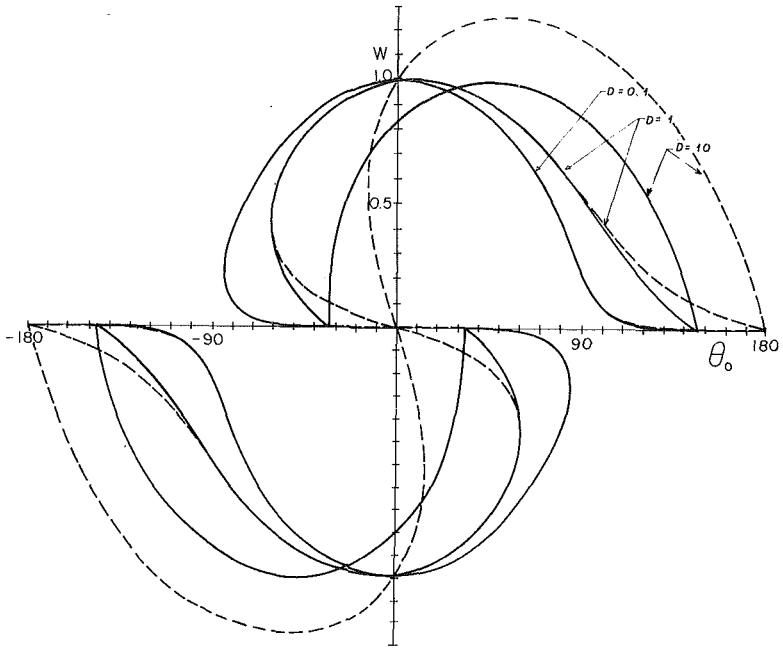

Fig. 1 Fluid velocity w as a function of thermosyphon inclination θ_0 for different values of D: continuous lines represent exact solution and broken lines approximate solution given in [3]

force which is approximated by that corresponding to Poiseuille flow in a straight circular pipe. This balance can be expressed as [4]

$$\frac{8\mu v}{\rho r^2} = \frac{\beta g}{2\pi}\int_{-\pi}^{\pi}(T-T_0)\cos\theta\, d\theta, \tag{1}$$

where v, T, μ, ρ, and β are the fluid velocity, temperature, dynamic viscosity, density and coefficient of volumetric expansion, respectively; r is the tube sectional radius, θ is an angular coordinate along the torus, and g is the acceleration due to gravity. The density ρ is taken at the reference temperature T_0.

Neglecting axial heat conduction, the temperature of the fluid satisfies the following energy balance equation

$$\frac{\rho C v}{R}\frac{dT}{d\theta} = \begin{cases} \dfrac{-2h}{r}(T-T_0) & \theta_0 \le \theta < \theta_0 + \pi \\ \dfrac{2q}{r} & \theta_0 - \pi \le \theta < \theta_0 \end{cases} \tag{2}$$

where C is the fluid specific heat, R is the radius of the torus, and q is the heat input per unit area.

Following the notation used by Greif et al. [4], the nondimensional velocity and temperature are defined as

$$w = v/V, \qquad \phi = (T-T_0)h/q$$

respectively, where

$$V = \left(\frac{g\beta Rrq}{2\pi C\mu}\right)^{1/2}. \tag{3}$$

Accordingly, equations (1) and (2) become

$$w = \frac{\pi}{4D}\int_{-\pi}^{\pi}\phi\cos\theta\, d\theta \tag{4}$$

and

$$\pi w\frac{d\phi}{d\theta} = \begin{cases} -D\phi \text{ for } \theta_0 \le \theta \le \theta_0 + \pi \\ D \text{ for } \theta_0 - \pi \le \theta < \theta_0 \end{cases} \tag{5}$$

where $D = 2\pi Rh/\rho CrV$.

Upon integrating equation (5) and substituting in equation (4), the following relation between w and θ_0 is found:

$$G(w,\theta_0,D) = w^2 - \frac{\cos\theta_0}{2} - \frac{[(D/w)\cos\theta_0 + (D/\pi w)^2\pi\sin\theta_0]}{4[1+(D/\pi w)^2]}\coth(D/2w) = 0. \tag{6}$$

If there is a velocity w^* such that $G(w^*, \theta_0, D) = 0$, then $G(-w^*, -\theta_0, D) = 0$. This property of the velocity was deduced by Damerell and Schoenhals [3] on physical grounds. For $\theta_0 = 0$, $G(w, 0, D)$ is an even function of w and therefore symmetric steady-state solutions for the fluid velocity are possible. In this special case, equation (6) reduces to a version of the expression given by Greif et al. [4].

An approximation can be obtained on expanding the expressions in equation (6) for $D/w << 1$ and retaining terms only up to order D/w. Multiplying then by w we get

$$w^3 - w\cos\theta_0 - \left(\frac{D}{2\pi}\right)\sin\theta_0 = 0 \tag{7}$$

which is the form reported by Damerell and Schoenhals[5] [3]. The approximate solution obtained from equation (7) is shown by broken lines in Fig. 1, indicating either one possible solution or three for different ranges of θ_0. Obviously, this approximation is not valid near $w=0$. For example, for $\theta_0 = 0$, equation (7) has three roots $w = -1$, 0, and 1. The zero root is spurious and does not satisfy the exact equation (6) in addition to being physically inexplicable here since axial heat conduction has been neglected. Only when this effect is taken into account is the zero-velocity purely conductive solution possible.

A convenient form of equation (6) is obtained by solving for the angle of inclination θ_0 in terms of the nondimensional velocity w

$$\theta_0 = \arccos\left\{\frac{c}{(a^2+b^2)^{1/2}}\right\} + \arctan\left\{\frac{b}{a}\right\} \tag{8}$$

where

$$a = \frac{1}{2} + \frac{(D/w)\coth(D/2w)}{4[1+(D/\pi w)^2]}$$

$$b = (D/\pi w)(a-1/2)$$

and

$$c = w^2.$$

[5] The parameter B used by them is $D/2\pi$ here.

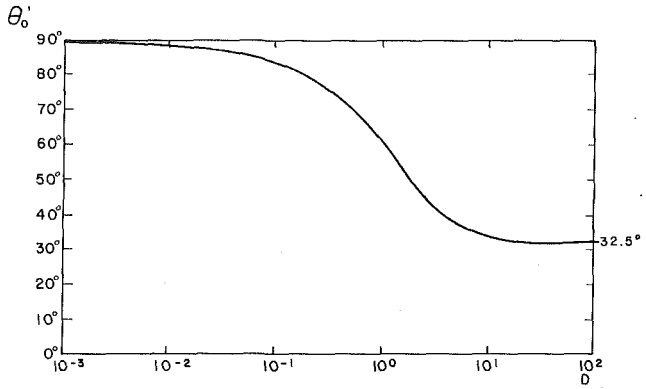

Fig. 2 Variation of maximum thermosyphon inclination for three possible solutions θ_0' as a function of D

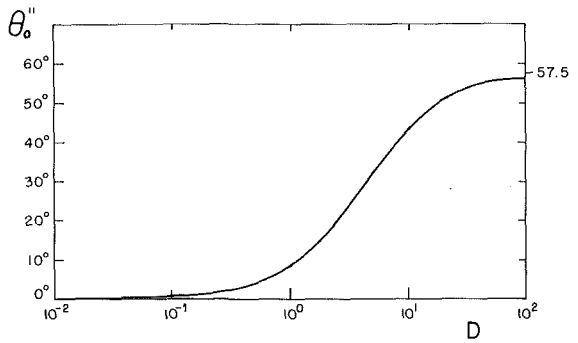

Fig 3 Variation of thermosyphon inclination θ_0'' at which maximum velocity occurs as a function of D

It is readily seen then that there are two values of θ_0 for each value of w. Furthermore, as $w \to 0$, $\theta_0 \to \arctan(\pm 2/\pi)$, the negative sign being applicable as w vanishes from above and the positive sign as w vanishes from below. We have then

(*a*) $\lim_{w \to 0^+} \theta_0 = -32.5$ deg and 147.5 deg

(*b*) $\lim_{w \to 0^-} \theta_0 = -147.5$ deg and 32.5 deg.

These details are indicated in Fig, 1 which shows the steady-state velocity as a function of θ_0 obtained from equation (6), for different values of the parameter D. Regions of zero, one, two, and three steady-state solutions can be identified. For -180 deg $< \theta_0 < -147.5$ deg and 147.5 deg $< \theta_0 <$ 180 deg no steady-state solution is possible. In the range -147.5 deg $< \theta_0 < -\theta_0'$ and $\theta_0' < \theta_0 <$ 147. 5 deg, where θ_0' is shown in Fig 2, there is only one velocity. Three velocities are obtained for $-\theta_0' < \theta_0 < -32.5$ deg and 32.5 deg $< \theta_0 < \theta_0'$. Two velocities are possible for -32.5 deg $< \theta_0 <$ 32.5 deg, straddling the zero inclination case.

In the $D \to 0$ and $D \to \infty$ limits, equation (6) becomes

$$w^2 - \cos\theta_0 = 0 \tag{9}$$

and

$$w^2 - \frac{\cos\theta_0}{2} - \frac{\pi}{4}\sin\theta_0 = 0 \tag{10}$$

respectively. From these expressions, limiting values of θ_0' are easily obtained. At $\theta_0 = \theta_0'$, $d\theta_0/dw = 0$ which gives $\theta_0' \to 90$ deg as $D \to 0$ and $\theta_0' \to 32.5$ deg as $D \to \infty$, as shown in Fig. 2.

It is also noticed from Fig. 1 that the maximum velocity for a given value of the parameter D is attained near $\theta_0 = 0$ for small D, being different for larger D. Figure 3 shows the angle θ_0'' at which the maximum velocity is attained as a function of the parameter D. Again from equations (9) and (10) we find that as $D \to 0$, $\theta_0'' \to 0$ and as $D \to \infty$, $\theta_0'' \to 57.5$ deg.

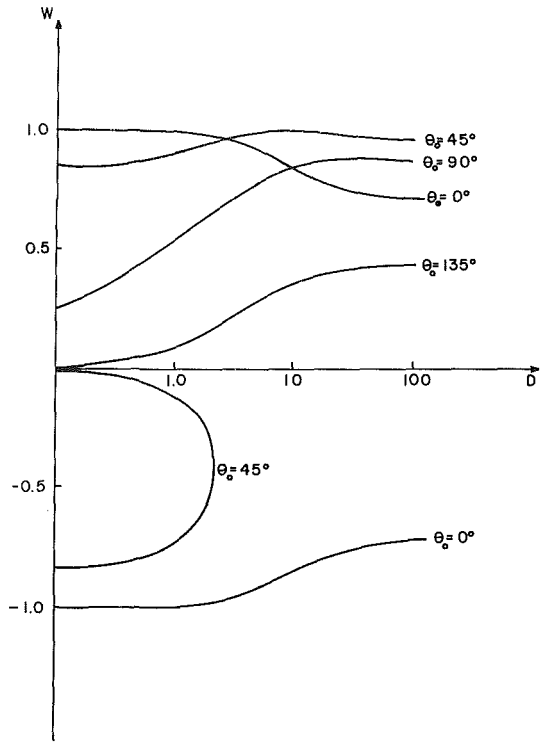

Fig. 4 Velocity w as a function of D for different thermosyphon inclinations θ_0

Figure 4 shows the steady-state velocity as a function of D for different angles of inclination θ_0. For $\theta_0 = 0$, the values of w correspond to those given in tabular form in [4]. Moreover only at this inclination, the positive and negative velocities are equal in magnitude for any D, such that the two branches of the curve are symmetric. For $\theta_0 = 45$ deg, the two branches are not symmetric while for $\theta_0 = 90$ and 135 deg, only the positive branch exists.

Conclusions and Discussion

Several properties of the steady-state velocity of the inclined toroidal thermosyphon have been discussed. In particular it has been demonstrated that the flow can have zero, one, two, or three steady-state velocities. Also it was found that the maximum velocity is not always attained for zero angle of inclination. The approximate solution is practically indistinguishable from the exact for small D/w, but substantially different for larger values of this parameter. More significant, however, are the qualitative differences between the two solutions. The approximate solution does not indicate that two steady-state velocities or none are possible over some ranges of the angle of inclination. Steady-state velocities, which can sometimes be experimentally observed in the inclination range for which the present analysis indicates no possible solution, must be dominated by axial heat conduction.

Although for particular angles of inclination there is more than one steady-state velocity, the stability of the solutions has not been discussed. We may expect, for example, that when three steady-state velocities are possible, the middle one would be unstable as discussed by Benjamin [5].

The study presented here has been performed for a toroidal loop; however, other geometries can be similarly analyzed since the only major modification required would be in the expression for the buoyancy term in equation (1). In fact, a thermosyphon of arbitrary geometry can be expected to exhibit similar qualitative properties as the one described above. Indeed, for a square geometry in special, a diagram

similar to Fig. 1 is obtained but limiting angles of ∓ 63.4 deg and $\pm$ 116.6 deg as $w \to 0^{\pm}$ are found. Actually, experiments performed with this geometry confirm the salient features of the one-dimensional analysis, especially with respect to the velocity-inclination diagram. In particular, stable steady-state velocities have been observed in all four quadrants of the diagram. Detailed results are available in [6].

References

1 Metrol, A., and Greif, R., "A Review of Natural Circulation Loops," in: *Natural Convection: Fundamentals and Applications*, W. Aung, S. Kakac, and R. Viskanta, eds., Hemisphere, 1985 (to be published).

2 Creveling, H. F., de Paz, J. F., Baladi, J. Y., and Schoenhals, R. J., "Stability Characteristics of a Single-Phase Free Convection Loop," *J. Fluid Mech.*, Vol. 67, 1975, pp. 65-84.

3 Damerell, P. S., and Schoenhals, R. J., "Flow in a Toroidal Thermosyphon With Angular Displacement of Heated and Cooled Sections," ASME JOURNAL OF HEAT TRANSFER, Vol. 101, 1979, pp. 672-676.

4 Greif, R., Zvirin, Y., and Mertol, A., "The Transient and Stability Behavior of a Natural Convection Loop," ASME JOURNAL OF HEAT TRANSFER, Vol. 101, 1979, pp. 684-688.

5 Benjamin, T. B., "Applications of Leray-Schauder Degree Theory to Problems of Hydrodynamic Stability," *Math. Proc. Camb. Phil. Soc.*, Vol. 79, 1976, pp. 373-392.

6 Acosta, R., and Manero, E., "Theoretical and Experimental Study of Thermosyphons in One- and Two-Phases" (in Spanish), Bachelor's Thesis, Faculty of Engineering, UNAM, Mexico City, 1984.

Lateral-Edge Effects on Natural Convection Heat Transfer From an Isothermal Vertical Plate

E. M. Sparrow[1,2] and L. F. A. Azevedo[1]

Nomenclature

- A = surface area = HW
- F = frame width, Fig. 2
- g = acceleration of gravity
- H = plate height, Fig. 1
- h = average heat transfer coefficient = $Q/A(T_w - T_\infty)$
- k = thermal conductivity
- L = length of shroud, Figs. 2 and 3
- Nu = Nusselt number = hH/k
- Pr = Prandtl number
- Q = rate of heat transfer
- Ra = Rayleigh number = $[g\beta(T_w - T_\infty)H^3/\nu^2]$Pr
- T_w = plate surface temperature
- T_∞ = temperature of fluid environment
- t = thickness of shroud, Figs. 2 and 3
- W = plate width, Fig. 1
- β = thermal expansion coefficient
- ν = kinematic viscosity

Introduction

Although natural convection from an isothermal vertical plate has been extensively investigated [1, 2], certain key issues remain unresolved. One of these is the response of the plate heat transfer to the boundary conditions at the lateral edges of the plate. The basic issue is whether the heat transfer would be different if the edges were unshrouded (permitting possible lateral inflow of fluid toward the plate) or if they were shrouded (thereby blocking the possible inflow). Also of relevance is the nature of the shrouds, e.g., their thickness and the distance that they project forward of the surface of the plate.

It appears that there is no quantitative information available on the lateral-edge effect, and the present Note provides initial results relevant to this effect. These results, while not complete, yield definitive conclusions for a certain range of plate height-width ratios and Rayleigh numbers. The experiments were performed in water using a plate assembly with a demonstrated capability [3] for providing data of very high accuracy. The availability of this highly precise plate assembly and the total absence of quantitative information on the lateral-edge effect prompted the undertaking of these experiments.

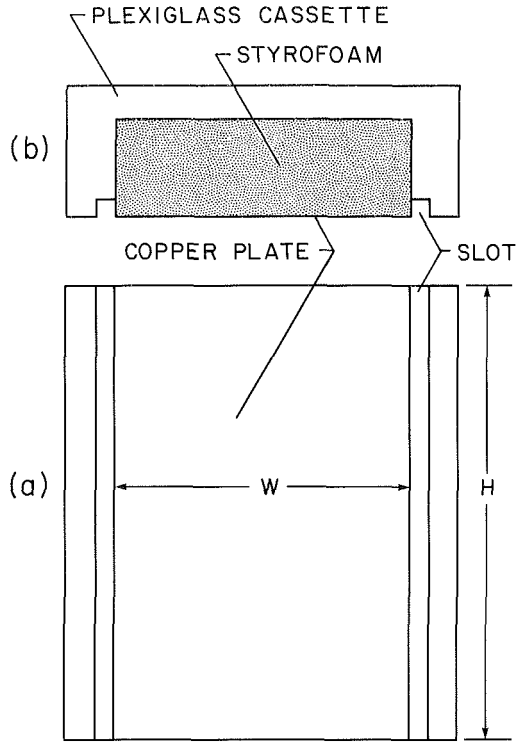

Fig. 1 Vertical plate assembly

Experiments

The vertical plate assembly used in the experiments is pictured schematically in Figs. 1(*a*) and 1(*b*) which are, respectively, elevation and plan views. The assembly consists of a heated copper plate backed by a 3.2-cm-thick block of water-tolerant, closed-pore styrofoam insulation which is housed in a C-shaped plexiglass holder (termed a cassette). As seen in the figure, only the front face of the copper plate was exposed to the fluid environment. The face dimensions of the plate, denoted by H and W in the figure, were 14.52 and 9.67 cm, respectively, and the thickness was 0.635 cm.

The plate was grooved on its rear face to accommodate electrical resistance wire. Three separately controlled heater circuits were employed to facilitate the attainment of temperature uniformity, which was achieved to within one percent of the surface-to-ambient temperature difference. The plate temperature was measured by eight embedded thermocouples.

As indicated in the figure, slots were cut in the cassette adjacent to the lateral edges of the plate. These slots served to

[1]Department of Mechanical Engineering, University of Minnesota, Minneapolis, MN 55455

[2]Fellow ASME

Contributed by the Heat Transfer Division for publication in the JOURNAL OF HEAT TRANSFER. Manuscript received by the Heat Transfer Division November 2, 1984.

similar to Fig. 1 is obtained but limiting angles of ∓ 63.4 deg and $\pm$ 116.6 deg as $w \to 0^{\pm}$ are found. Actually, experiments performed with this geometry confirm the salient features of the one-dimensional analysis, especially with respect to the velocity-inclination diagram. In particular, stable steady-state velocities have been observed in all four quadrants of the diagram. Detailed results are available in [6].

References

1 Metrol, A., and Greif, R., "A Review of Natural Circulation Loops," in: *Natural Convection: Fundamentals and Applications*, W. Aung, S. Kakac, and R. Viskanta, eds., Hemisphere, 1985 (to be published).

2 Creveling, H. F., de Paz, J. F., Baladi, J. Y., and Schoenhals, R. J., "Stability Characteristics of a Single-Phase Free Convection Loop," *J. Fluid Mech.*, Vol. 67, 1975, pp. 65-84.

3 Damerell, P. S., and Schoenhals, R. J., "Flow in a Toroidal Thermosyphon With Angular Displacement of Heated and Cooled Sections," ASME JOURNAL OF HEAT TRANSFER, Vol. 101, 1979, pp. 672-676.

4 Greif, R., Zvirin, Y., and Mertol, A., "The Transient and Stability Behavior of a Natural Convection Loop," ASME JOURNAL OF HEAT TRANSFER, Vol. 101, 1979, pp. 684-688.

5 Benjamin, T. B., "Applications of Leray-Schauder Degree Theory to Problems of Hydrodynamic Stability," *Math. Proc. Camb. Phil. Soc.*, Vol. 79, 1976, pp. 373-392.

6 Acosta, R., and Manero, E., "Theoretical and Experimental Study of Thermosyphons in One- and Two-Phases" (in Spanish), Bachelor's Thesis, Faculty of Engineering, UNAM, Mexico City, 1984.

Lateral-Edge Effects on Natural Convection Heat Transfer From an Isothermal Vertical Plate

E. M. Sparrow[1,2] and L. F. A. Azevedo[1]

Nomenclature

- A = surface area = HW
- F = frame width, Fig. 2
- g = acceleration of gravity
- H = plate height, Fig. 1
- h = average heat transfer coefficient = $Q/A(T_w - T_\infty)$
- k = thermal conductivity
- L = length of shroud, Figs. 2 and 3
- Nu = Nusselt number = hH/k
- Pr = Prandtl number
- Q = rate of heat transfer
- Ra = Rayleigh number = $[g\beta(T_w - T_\infty)H^3/\nu^2]$Pr
- T_w = plate surface temperature
- T_∞ = temperature of fluid environment
- t = thickness of shroud, Figs. 2 and 3
- W = plate width, Fig. 1
- β = thermal expansion coefficient
- ν = kinematic viscosity

Introduction

Although natural convection from an isothermal vertical plate has been extensively investigated [1, 2], certain key issues remain unresolved. One of these is the response of the plate heat transfer to the boundary conditions at the lateral edges of the plate. The basic issue is whether the heat transfer would be different if the edges were unshrouded (permitting possible lateral inflow of fluid toward the plate) or if they were shrouded (thereby blocking the possible inflow). Also of relevance is the nature of the shrouds, e.g., their thickness and the distance that they project forward of the surface of the plate.

It appears that there is no quantitative information available on the lateral-edge effect, and the present Note provides initial results relevant to this effect. These results, while not complete, yield definitive conclusions for a certain range of plate height-width ratios and Rayleigh numbers. The experiments were performed in water using a plate assembly with a demonstrated capability [3] for providing data of very high accuracy. The availability of this highly precise plate assembly and the total absence of quantitative information on the lateral-edge effect prompted the undertaking of these experiments.

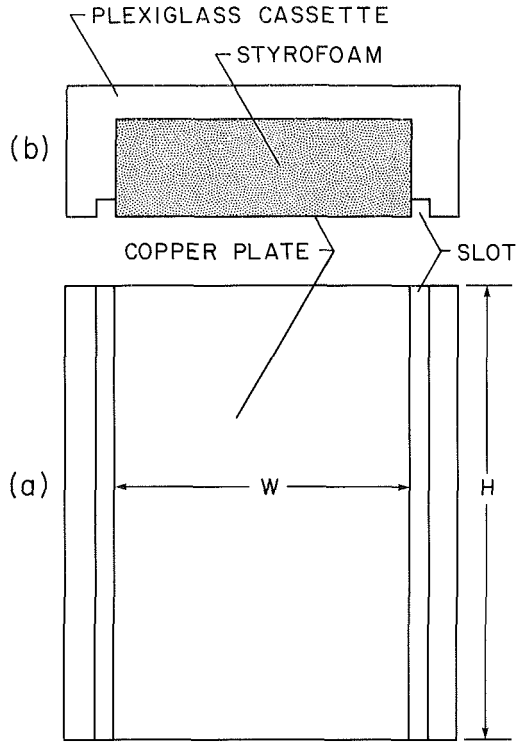

Fig. 1 Vertical plate assembly

Experiments

The vertical plate assembly used in the experiments is pictured schematically in Figs. 1(*a*) and 1(*b*) which are, respectively, elevation and plan views. The assembly consists of a heated copper plate backed by a 3.2-cm-thick block of water-tolerant, closed-pore styrofoam insulation which is housed in a C-shaped plexiglass holder (termed a cassette). As seen in the figure, only the front face of the copper plate was exposed to the fluid environment. The face dimensions of the plate, denoted by H and W in the figure, were 14.52 and 9.67 cm, respectively, and the thickness was 0.635 cm.

The plate was grooved on its rear face to accommodate electrical resistance wire. Three separately controlled heater circuits were employed to facilitate the attainment of temperature uniformity, which was achieved to within one percent of the surface-to-ambient temperature difference. The plate temperature was measured by eight embedded thermocouples.

As indicated in the figure, slots were cut in the cassette adjacent to the lateral edges of the plate. These slots served to

[1]Department of Mechanical Engineering, University of Minnesota, Minneapolis, MN 55455

[2]Fellow ASME

Contributed by the Heat Transfer Division for publication in the JOURNAL OF HEAT TRANSFER. Manuscript received by the Heat Transfer Division November 2, 1984.

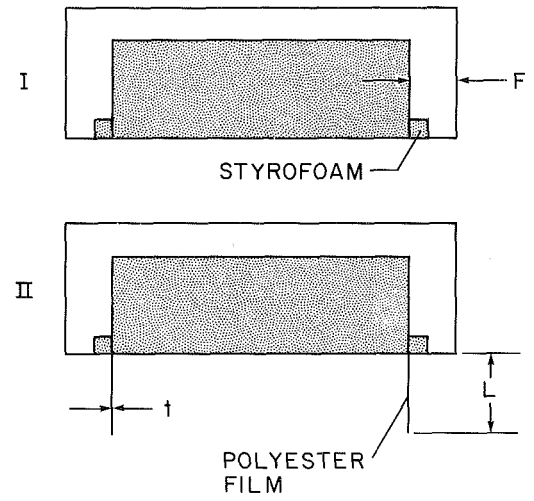

Fig. 2 Lateral-edge configurations I and II

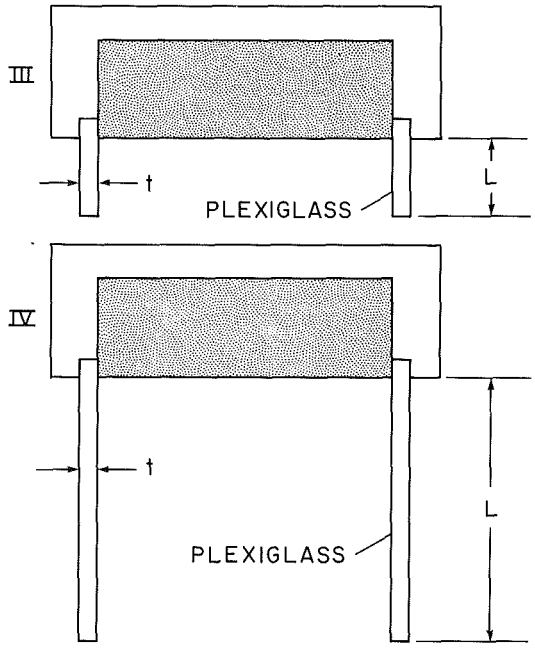

Fig. 3 Lateral-edge configurations III and IV

house various inserts which yielded the desired range of lateral-edge boundary conditions. The inserts and the resulting lateral-edge configurations are pictured in Figs. 2 and 3. In configuration I, strips of styrofoam were inserted into the slots, and the exposed faces of the strips were covered by polyester tape to achieve hydrodynamic smoothness. Therefore, configuration I corresponds to the case of unshrouded and insulated lateral edges. The dimension F of the frame which extends beyond the respective edges is given in Table 1.

For configuration II, a thin polyester film, 0.011 cm thick, was used as the shroud. The film was secured to the side of the copper plate and stiffened along its outboard edges by thin strips of wood. Styrofoam was used to fill the slots. Configuration II corresponds to a hydrodynamic blockage which is totally devoid of heat loss capability. Both the t and L dimensions are listed in Table 1.

The shroud in configuration III is of identical length to that of configuration II, but it is made of plexiglass and, as a consequence, it is substantially thicker (0.635 cm versus 0.011 cm). This configuration was employed to investigate the possibility that the shroud might function not only as a hydrodynamic blockage but also as a heat conducting fin. The shroud in configuration IV is a longer version of that in configuration III, providing more decisive hydrodynamic blockage.

Table 1 Dimensions defining the lateral-edge configurations (all dimensions in cm)

Case	L	t	F
I			1.4
II	2.54	0.011	
III	2.54	0.635	
IV	8.50	0.635	

The experiments were performed utilizing a tank-in-tank arrangement. The water in the inner tank served as the fluid environment for the vertical plate, while the water in the intertank space functioned as a buffer which thermally decoupled the fluid environment from the laboratory. A temperature controller/circulator was situated in the intertank space to provide a uniform, preset temperature at the boundaries of the inner tank. A sheet of insulation lined with impermeable plastic served to cover the top of both tanks.

Both tanks were of plexiglass, with respective dimensions of 73.7 × 43.2 × 45.7 cm and 101.6 × 66 × 48.3 cm (length × width × depth). Distilled water was supplied to both the inner tank and the intertank space. A vertical array of three thermocouples, respectively situated at distances of 7.6, 17, and 24 cm above the floor of the inner tank, measured the temperature of the water ambient of the vertical plate. The thermocouples were displaced horizontally from the plate by about 30 cm.

The plate was supported by a pair of struts, each attached to a side of the cassette and anchored to the floor of the tank, and positioned so as not to have any influence on the fluid flow. The leading edge of the plate was situated 12.7 cm above the floor, while the water level was maintained 12.7 cm above the trailing edge of the plate.

A data run was initiated only when the inner tank was free of stratification and when the temperatures in the inner tank and the intertank space were identical (as measured by ASTM-certified thermometers). The fulfillment of the latter condition ensured the absence of extraneous buoyancy-induced motions in the inner tank. Steady state was attained within fifteen minutes following the application of power to the plate heating circuits.

Results and Discussion

The average heat transfer coefficients and the corresponding Nusselt numbers for the vertical plate were evaluated from their standard definitions

$$h = Q/A(T_w - T_\infty), \qquad \mathrm{Nu} = hH/k \tag{1}$$

where Q was obtained from the electric power input, and the surface area A is equal to HW. The Nusselt number results will be parameterized by the Rayleigh number Ra

$$\mathrm{Ra} = [g\beta(T_w - T_\infty)H^3/\nu^2]\mathrm{Pr} \tag{2}$$

In both Nu and Ra, the thermophysical properties were evaluated at the mean of T_w and T_∞.

For the operating conditions of the experiments, Ra ranged from about 8.5×10^7 to 10^9, while the Prandtl number varied from about 4.75 to 5.25. Over this small Prandtl number range, the Nusselt number is essentially a unique function of the Rayleigh number (i.e., negligible separate effect of the Prandtl number).

The experimentally determined Nusselt numbers are plotted as a function of the Rayleigh number in Fig. 4, where the data corresponding to the various lateral-edge configurations are identified in the legend. Also appearing in the figure is a solid line representing the well-established Churchill–Chu

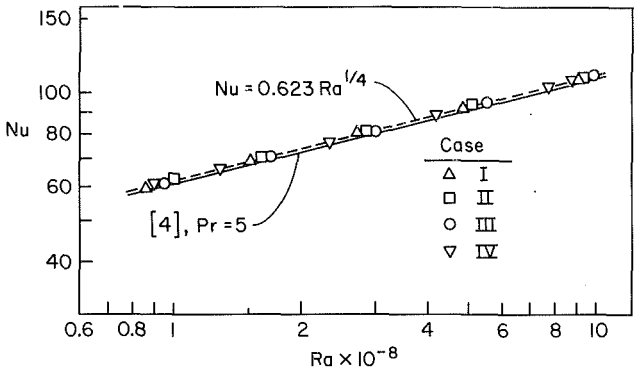

Fig. 4 Nusselt number results for the various lateral-edge configurations

correlation, equation (5) of [4], which was evaluated for Pr = 5.

Inspection of the figure indicates that the data for the four investigated lateral-edge configurations are in remarkable mutual agreement. Indeed, it is compellingly clear that all the data belong to a single set, independent of the lateral-edge configuration. A further affirmation of the inherent unity of the data is that the extreme deviation of any point from the least-squares fit represented by the dashed line in Fig. 4 is only 1.1 percent. The equation of the fitted line is

$$\mathrm{Nu} = 0.623\mathrm{Ra}^{1/4} \tag{3}$$

Also of interest is the excellent agreement (deviation ~ 2½ percent) between the present data and the Churchill-Chu correlation – an agreement made noteworthy by the scatter exhibited by other data presented by Churchill and Chu in Fig. 1 of [4].

The results obtained here indicate an indifference of the plate heat transfer to the boundary conditions at the lateral edges of the plate. In reflecting on this finding, it is relevant to take note of the H/W (height/width) ratio of the plate. In this regard, it is reasonable to expect that the lateral-edge conditions will play a greater role when H/W is large, i.e., when the plate is relatively narrow. In the present experiments, where $H/W = 1.5$, the plate is more narrow than wide, but not very narrow.

Since the lateral-edge effects were found to be negligible for $H/W = 1.5$, it can be expected that this finding will continue to be valid for all $H/W < 1.5$ (i.e., for wider plates). Furthermore, considering the totality of the indifference to lateral-edge effects encountered here, it does not appear unreasonable to extrapolate this indifference to $H/W > 1.5$, certainly to 2, and perhaps to 3 or 4.

Another factor which might influence the importance of the lateral-edge effects is the magnitude of the Rayleigh number. With water as the fluid environment, high Rayleigh numbers are naturally encountered. Intermediate and low Rayleigh numbers can be obtained when air is used as the fluid environment. Such experiments were outside the scope of the present investigation and remain to be carried out.

References

1 Ede, A. J., "Advances in Natural Convection," *Advances in Heat Transfer*, Vol. 4, 1967, pp. 1–64.

2 Jaluria, Y., *Natural Convection Heat and Mass Transfer*, Pergamon Press, Oxford, 1980.

3 Sparrow, E. M., and Azevedo, L. F. A., "Vertical-Channel Natural Convection Spanning Between the Fully Developed Limit and the Single-Plate Boundary Layer Limit," *International Journal of Heat and Mass Transfer*, in press.

4 Churchill, S. W., and Chu, H. H. S., "Correlating Equations for Laminar and Turbulent Free Convection From a Vertical Plate," *International Journal of Heat and Mass Transfer*, Vol. 18, 1975, pp. 1323–1329.

Mass Transfer to Natural Convection Boundary Layer Flow Driven by Heat Transfer

K. R. Khair[1] and A. Bejan[1,2]

The phenomenon of combined mass and heat transfer effected by natural convection has received considerable attention due to its many applications in diverse fields such as chemical engineering, environmental dynamics, and architectural design. The present study is concerned with a limiting facet of the combined mass and heat transfer natural convection phenomenon, namely, the mass transfer rate associated with a vertical natural convection boundary layer flow driven solely by the buoyancy effect due to temperature variations within the fluid (the flow in this limit may be referred to as "heat-transfer-driven" [1,2]). Given the possible interplay between temperature and concentration variations in providing the buoyancy effect for driving the flow, the limit addressed by this study is conceptually analogous to determining the heat transfer rate associated with flows driven solely by buoyancy due to concentration variations.

Part of the motivation for developing the similarity solutions reported below was provided by the apparent mismatch between the lack of generality of existing integral and similarity solutions [3–7] and the generality of the scale analysis results [1] reproduced here in Table 1. The mismatch stems from the fact that with the exception of [7], the previous studies focused on relatively narrow ranges of Prandtl and Schmidt numbers, whereas the scaling results summarized in Table 1 cover the entire Pr–Sc domain. For example, the first integral analysis of the phenomenon [3] is valid only for Pr and Sc values of order unity; one of its results is that the ratio between mass transfer and heat transfer in heat-transfer-driven flows must scale as $\mathrm{Le}^{1/2}$. The same scaling is supported by subsequent studies (e.g., [4–6]), and it is clearly in agreement with the scales of Table 1 at the multiple intersection represented by Pr ~ 1 and Sc ~ 1 (or Le ~ 1).

However, the scale analysis [1, 2] produced six different scales for the mass transfer rate, scales labeled (*a*)–(*f*) in Table 1, one different scale for each of the six subdomains delineated by Pr ~ 1, Sc ~ 1, and Le ~ 1 in the Pr-Sc plane. Partial support for the transition from the $\mathrm{Le}^{1/3}$ scaling of case (*a*) to the $\mathrm{Le}^{1/2}$ scaling of case (*b*) was provided in [8] by using the Gebhart and Pera similarity results for Pr = 0.7 and Pr = 7 flows driven by a combination of temperature and concentration buoyancy effects, and by approximating via graphic interpolation the results that would correspond to heat-transfer-driven flows. To provide a rigorous test of all the scales of Table 1, and to develop more accurate Sherwood number predictions for both large and small values of Pr, Sc, and Le, is the main purpose of the present study.

Consider the two-dimensional boundary layer flow driven along a vertical impermeable wall by the combined buoyancy effect due to the wall reservoir temperature difference $T_0 - T_\infty$ and the wall-reservoir constituent concentration difference $C_0 - C_\infty$. In the Cartesian system of coordinates (x, y) where y is measured vertically from the bottom edge of the wall and x is measured horizontally away from the wall into the fluid reservoir (T_∞, C_∞), the boundary layer approximated equations that govern the conservation of mass, momentum, energy, and constituent are

[1]Department of Mechanical Engineering and Materials Science, Duke University, Durham, NC 27706.

[2]Assoc. Mem. ASME

Contributed by the Heat Transfer Division for publication in the JOURNAL OF HEAT TRANSFER. Manuscript received by the Heat Transfer Division October 31, 1984.

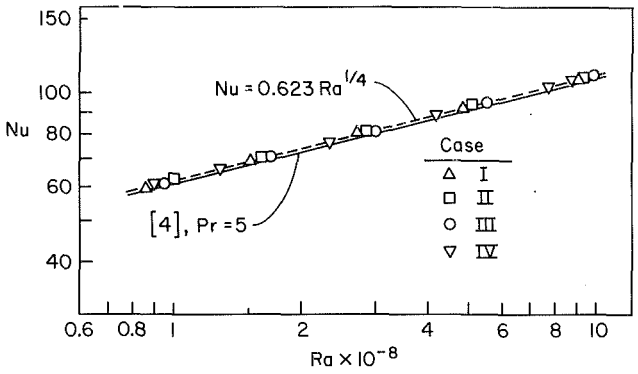

Fig. 4 Nusselt number results for the various lateral-edge configurations

correlation, equation (5) of [4], which was evaluated for Pr = 5.

Inspection of the figure indicates that the data for the four investigated lateral-edge configurations are in remarkable mutual agreement. Indeed, it is compellingly clear that all the data belong to a single set, independent of the lateral-edge configuration. A further affirmation of the inherent unity of the data is that the extreme deviation of any point from the least-squares fit represented by the dashed line in Fig. 4 is only 1.1 percent. The equation of the fitted line is

$$\mathrm{Nu} = 0.623\mathrm{Ra}^{1/4} \tag{3}$$

Also of interest is the excellent agreement (deviation ~ 2½ percent) between the present data and the Churchill–Chu correlation – an agreement made noteworthy by the scatter exhibited by other data presented by Churchill and Chu in Fig. 1 of [4].

The results obtained here indicate an indifference of the plate heat transfer to the boundary conditions at the lateral edges of the plate. In reflecting on this finding, it is relevant to take note of the H/W (height/width) ratio of the plate. In this regard, it is reasonable to expect that the lateral-edge conditions will play a greater role when H/W is large, i.e., when the plate is relatively narrow. In the present experiments, where $H/W = 1.5$, the plate is more narrow than wide, but not very narrow.

Since the lateral-edge effects were found to be negligible for $H/W = 1.5$, it can be expected that this finding will continue to be valid for all $H/W < 1.5$ (i.e., for wider plates). Furthermore, considering the totality of the indifference to lateral-edge effects encountered here, it does not appear unreasonable to extrapolate this indifference to $H/W > 1.5$, certainly to 2, and perhaps to 3 or 4.

Another factor which might influence the importance of the lateral-edge effects is the magnitude of the Rayleigh number. With water as the fluid environment, high Rayleigh numbers are naturally encountered. Intermediate and low Rayleigh numbers can be obtained when air is used as the fluid environment. Such experiments were outside the scope of the present investigation and remain to be carried out.

References

1 Ede, A. J., "Advances in Natural Convection," *Advances in Heat Transfer*, Vol. 4, 1967, pp. 1–64.

2 Jaluria, Y., *Natural Convection Heat and Mass Transfer*, Pergamon Press, Oxford, 1980.

3 Sparrow, E. M., and Azevedo, L. F. A., "Vertical-Channel Natural Convection Spanning Between the Fully Developed Limit and the Single-Plate Boundary Layer Limit," *International Journal of Heat and Mass Transfer*, in press.

4 Churchill, S. W., and Chu, H. H. S., "Correlating Equations for Laminar and Turbulent Free Convection From a Vertical Plate," *International Journal of Heat and Mass Transfer*, Vol. 18, 1975, pp. 1323–1329.

Mass Transfer to Natural Convection Boundary Layer Flow Driven by Heat Transfer

K. R. Khair[1] and A. Bejan[1,2]

The phenomenon of combined mass and heat transfer effected by natural convection has received considerable attention due to its many applications in diverse fields such as chemical engineering, environmental dynamics, and architectural design. The present study is concerned with a limiting facet of the combined mass and heat transfer natural convection phenomenon, namely, the mass transfer rate associated with a vertical natural convection boundary layer flow driven solely by the buoyancy effect due to temperature variations within the fluid (the flow in this limit may be referred to as "heat-transfer-driven" [1,2]). Given the possible interplay between temperature and concentration variations in providing the buoyancy effect for driving the flow, the limit addressed by this study is conceptually analogous to determining the heat transfer rate associated with flows driven solely by buoyancy due to concentration variations.

Part of the motivation for developing the similarity solutions reported below was provided by the apparent mismatch between the lack of generality of existing integral and similarity solutions [3–7] and the generality of the scale analysis results [1] reproduced here in Table 1. The mismatch stems from the fact that with the exception of [7], the previous studies focused on relatively narrow ranges of Prandtl and Schmidt numbers, whereas the scaling results summarized in Table 1 cover the entire Pr–Sc domain. For example, the first integral analysis of the phenomenon [3] is valid only for Pr and Sc values of order unity; one of its results is that the ratio between mass transfer and heat transfer in heat-transfer-driven flows must scale as $\mathrm{Le}^{1/2}$. The same scaling is supported by subsequent studies (e.g., [4–6]), and it is clearly in agreement with the scales of Table 1 at the multiple intersection represented by Pr ~ 1 and Sc ~ 1 (or Le ~ 1).

However, the scale analysis [1, 2] produced six different scales for the mass transfer rate, scales labeled (*a*)–(*f*) in Table 1, one different scale for each of the six subdomains delineated by Pr ~ 1, Sc ~ 1, and Le ~ 1 in the Pr-Sc plane. Partial support for the transition from the $\mathrm{Le}^{1/3}$ scaling of case (*a*) to the $\mathrm{Le}^{1/2}$ scaling of case (*b*) was provided in [8] by using the Gebhart and Pera similarity results for Pr = 0.7 and Pr = 7 flows driven by a combination of temperature and concentration buoyancy effects, and by approximating via graphic interpolation the results that would correspond to heat-transfer-driven flows. To provide a rigorous test of all the scales of Table 1, and to develop more accurate Sherwood number predictions for both large and small values of Pr, Sc, and Le, is the main purpose of the present study.

Consider the two-dimensional boundary layer flow driven along a vertical impermeable wall by the combined buoyancy effect due to the wall reservoir temperature difference $T_0 - T_\infty$ and the wall-reservoir constituent concentration difference $C_0 - C_\infty$. In the Cartesian system of coordinates (x, y) where y is measured vertically from the bottom edge of the wall and x is measured horizontally away from the wall into the fluid reservoir (T_∞, C_∞), the boundary layer approximated equations that govern the conservation of mass, momentum, energy, and constituent are

[1]Department of Mechanical Engineering and Materials Science, Duke University, Durham, NC 27706.

[2]Assoc. Mem. ASME

Contributed by the Heat Transfer Division for publication in the JOURNAL OF HEAT TRANSFER. Manuscript received by the Heat Transfer Division October 31, 1984.

$$\frac{1}{\mathrm{Pr}}\left(\frac{1}{2}f'^2-\frac{3}{4}ff''\right)=f'''+\theta+Nc \tag{1}$$

$$-\frac{3}{4}f\theta'=\theta'' \tag{2}$$

$$-\frac{3}{4}\mathrm{Le}fc'=c'' \tag{3}$$

The similarity formulation of the above equations is the same as on pp. 125–130 of [1]; hence

$$\eta=\frac{x}{y\mathrm{Ra}^{-1/4}},\quad \psi=\alpha\mathrm{Ra}^{1/4}f(\eta)$$

$$\theta=\frac{T-T_\infty}{T_0-T_\infty},\quad c=\frac{C-C_\infty}{C_0-C_\infty} \tag{4}$$

where ψ is the streamfunction ($u=\partial\psi/\partial y$, $v=-\partial\psi/\partial x$), u and v are the horizontal and vertical velocity components, and Ra is the local Rayleigh number $\mathrm{Ra}=g\beta(T_0-T_\infty)y^3/(\alpha\nu)$. As in the usual notation, g, β, α, and ν are the gravitational acceleration, coefficient of thermal expansion, thermal diffusivity and kinematic viscosity, respectively. The boundary conditions for solving equations (1)–(3) are

$$f=0,\ f'=0,\ \theta=1,\ c=1,\ \text{at}\ \eta=0$$
$$f'=0,\ \theta=0,\ c=0,\ \text{as}\ \eta\to\infty \tag{5}$$

Table 1 Mass transfer rate scales in heat-transfer-driven vertical boundary layer flow [1, 2]

	Fluid Properties	Sherwood Number Scales
a)	Pr > 1, Le > 1	$\mathrm{Sh}\sim \mathrm{Le}^{1/3}\,\mathrm{Ra}^{1/4}$
b)	Pr > 1, Le < 1 (Sc > 1)	$\mathrm{Sh}\sim \mathrm{Le}^{1/2}\,\mathrm{Ra}^{1/4}$
c)	Pr > 1, Le < 1 (Sc < 1)	$\mathrm{Sh}\sim \mathrm{Le}\,\mathrm{Pr}^{1/2}\,\mathrm{Ra}^{1/4}$
d)	Pr < 1, Sc > 1	$\mathrm{Sh}\sim \mathrm{Le}^{1/3}\,\mathrm{Pr}^{1/12}\,\mathrm{Ra}^{1/4}$
e)	Pr < 1, Sc < 1 (Le > 1)	$\mathrm{Sh}\sim \mathrm{Le}^{1/2}\,\mathrm{Pr}^{1/4}\,\mathrm{Ra}^{1/4}$
f)	Pr < 1, Sc < 1 (Le < 1)	$\mathrm{Sh}\sim \mathrm{Le}\,\mathrm{Pr}^{1/4}\,\mathrm{Ra}^{1/4}$

In general, the solution depends on the Prandtl number $\mathrm{Pr}=\nu/\alpha$, the Lewis number $\mathrm{Le}=\alpha/D$ (where D is the mass diffusivity of the constituent whose concentration is C), and the buoyancy ratio $N=\beta_C(C_0-C_\infty)/[\beta(T_0-T_\infty)]$, where β_C is the concentration expansion coefficient, $\beta_C=-\rho^{-1}\cdot\{\partial\rho/\partial C)_P$. In the present study N is set equal to zero, as the main objective of the study is to provide a rigorous test for the mass transfer scaling laws of *heat-transfer-driven flows* advanced in [1].

The problem formulated as equations (1)–(5) was solved numerically based on the standard shooting method, for a total of 48 cases covering evenly the Prandtl number range 0.01–1000 and the Lewis number range 0.01–100 (see Table 2). Since the Schmidt number is the same as the product Pr•Le, the data collected in Table 2 cover the Schmidt number range 10^{-3}–10^5. The equations were integrated using the fourth-order Runge–Kutta method. With only one exception, the results compiled in Table 2 were obtained using the shooting success criterion

$$\max(f',\theta,c)\le 10^{-5} \tag{6}$$

The exception was the case of f' at $\mathrm{Pr}=10^3$, where the best we could achieve was $f'\cong 2\times10^{-4}$ at $\eta=150$ (for the same case, θ and c become less than 10^{-5} at $\eta\cong 6$). Since relative to the thermal and velocity boundary layers the concentration boundary layer can become considerably thicker as the Lewis number becomes smaller than unity (Fig. 1) we used a variable step size $\Delta\eta$ in order to control the time required by one integration. Thus, for Pr = 10, 100, 1000 and Le = 0.01, 0.03, 0.1, 0.3 we used $\Delta\eta=0.01$ for $0<\eta<10$, $\Delta\eta=0.05$ for $10<\eta<100$ and $\Delta\eta=0.1$ for $\eta>100$. For the remaining cases (all Pr values and $\mathrm{Le}\ge 1$; and Pr = 0.72, 0.01 and Le < 1) we used the uniform step $\Delta\eta=0.003$.

Listed in Table 2 are the final numerical results for the dimensionless concentration gradient evaluated at the wall, $-c'(0)$. These numerical values are proportional to the local mass flux $j''=-D(\partial C/\partial x)_{x=0}$ or to its dimensionless counterpart, the Sherwood number

$$\mathrm{Sh}=\frac{j''y}{D(C_0-C_\infty)}=-c'(0)\mathrm{Ra}^{1/4} \tag{7}$$

The Rayleigh number dependence of Sh, predicted by the scale analysis results listed in Table 1, is confirmed by equation (7) and the fact that the $c'(0)$ values of Table 2 depend only on Le and Pr. It remains to show that $c'(0)$ depends on Le and Pr in the manner of cases $(a)-(f)$ of Table 1.

Figure 2 tests the validity of scaling results (a), (b), and (c)

Table 2 Summary of similarity results for mass transfer in heat-transfer-driven natural convection boundary layer flow (the numbers in the array represent the value of $-c'(0)$)

Prandtl number	Lewis Number									
	0.01	0.03	0.1	0.3	1	3	10	30	50	100
Pr = 0.01 f''(0) = 0.44104 θ'(0) = -0.1803			0.02986	0.0758	0.1803	0.3461	0.6391	1.0497	1.3009	1.7178
Pr = 0.72 f''(0) = 0.8806 θ'(0) = -0.3871	0.0105	0.0279	0.08273	0.1914	0.3871	0.6390	1.0326	1.334	1.855	2.3668
Pr = 10 f''(0) = 1.0542 θ'(0) = -0.465	0.02672	0.06631	0.1501	0.2707	0.465	0.7217	1.1312	1.6765	2.006	2.5524
Pr = 100 f''(0) = 1.1428 θ'(0) = -0.4898	0.04915	0.09627	0.17906	0.29635	0.4898	0.74927	1.1661	1.7223	2.0537	2.6167
Pr = 1000 f''(0) = 1.15205 θ'(0) = -0.4985	0.06144	0.10692	0.18837	0.30492	0.4985	0.7592	1.1788	1.7392	2.0781	2.6408

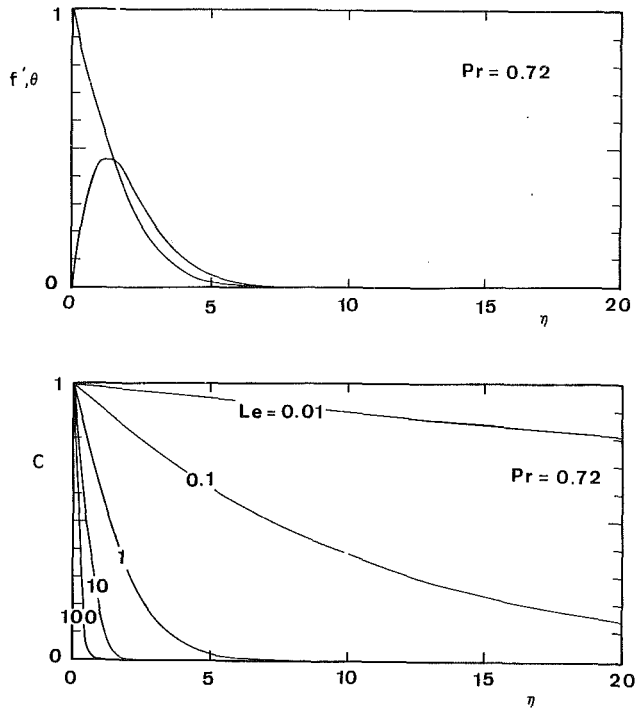

Fig. 1 Sample of similarity profiles for velocity, temperature and concentration (Pr = 0.72, 0.01 ≤ Le ≤ 100)

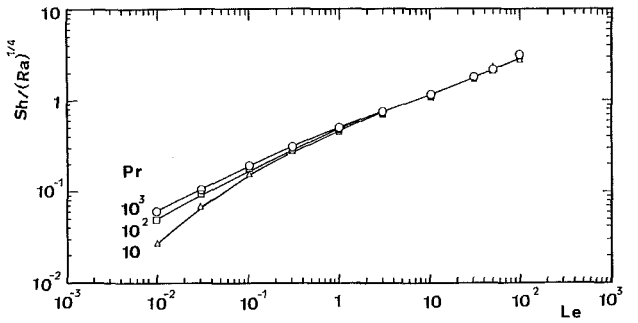

Fig. 2 The dependence of the Sherwood number scaling law on Lewis number (Pr = 10, 100, 1000)

of Table 1 against the numerical similarity results reported for $Pr > 1$ fluids in Table 2. The ratio $Sh/Ra^{1/4}$ increases monotonically with Le; however, the rate of the increase depends on both Le and Pr. Looking first at the high Prandtl number data ($Pr = 100$ and 1000), we see that they are effectively correlated by one curve on the $Sh/Ra^{1/4}$–Le plane. Furthermore, the slope of this curve on the log-log plane changes visibly from 1/2 in the $Le < 1$ range to 1/3 when $Le > 1$. Noting that these data correspond to fluids with Schmidt numbers greater than unity, we conclude that they validate scaling laws (*a*) and (*b*) of Table 1.

Figure 2 shows also that the behavior of $Sh/Ra^{1/4}$ versus Le changes as the Prandtl number drops to the point that the Schmidt number becomes smaller than unity (see the $Pr = 10$ data below $Le = 0.1$). Under these circumstances, the $Sh/Ra^{1/4}$–Le curve shows a slope of 1 on the log-log plane. In addition, the ratio $Sh/Ra^{1/4}$ evaluated at constant Lewis number varies as $Pr^{1/2}$ (this trend could be illustrated further by plotting the $Le = 0.01$, $Pr = 0.72$ and 10 data of Table 2 on a log-log graph of $Sh/Ra^{1/4}$ versus Pr). Put together, the behavior exhibited by the similarity results of Fig. 2 in the limit of small Schmidt numbers confirms the validity of scaling result (*c*) of Table 1.

Figure 3 shows the alignment of the $Pr = 0.01$ data on the $Sh/(Ra\ Pr)^{1/4}$–Le plane. The data correspond to moderate

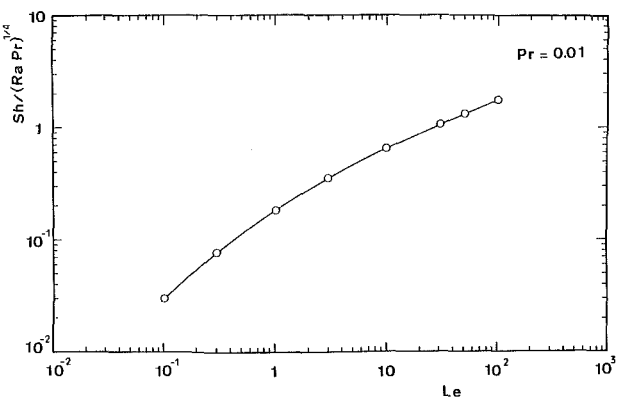

Fig. 3 The dependence of the Sherwood number scaling law on Lewis number (Pr = 0.01)

and low Lewis numbers so that the Schmidt numbers are consistently smaller than unity. Thus, Fig. 3 constitutes a test of the validity of mass transfer scales (*e*) and (*f*): As predicted by scale analysis, the Lewis number influence on $Sh/(Ra \cdot Pr)^{1/4}$ changes from being proportional to Le when $Le < 1$ to being proportional to $Le^{1/2}$ when $Le > 1$.

Regarding the mass transfer scale (*d*) (which varies as $Le^{1/3}$, Table 1), the fact that the analysis that yields scale (*d*) is analogous to the analysis that leads to scale (*a*) (see Fig. 9.5 of [1]), and the success registered in validating (*a*) based on similarity results (Fig. 2 in this paper), are signs that scaling law (*d*) is correct.

The conclusion of the present study is that similarity solutions obtained for a wide spectrum of fluid properties ($0.01 \le Pr \le 1000$, $0.01 \le Le \le 100$, $10^{-3} \le Sc \le 10^5$) validate the mass transfer scales anticipated based on pure scaling arguments in [1]. From an engineering standpoint, the similarity results compiled in Table 2 provide a more accurate alternative to evaluating the mass transfer rate to natural convection vertical boundary layer flows driven by heat transfer.

Acknowledgments

This study was supported in part by the National Science Foundation through Grant No. MEA-82-07779. The present report was prepared during A. Bejan's sabbatical leave from Duke University and his term as F. Mosey Visiting Scholar to the Faculty of Engineering of the University of Western Australia. The support received from Duke University and the University of Western Australia is gratefully acknowledged.

References

1 Bejan, A., *Convection Heat Transfer*, Wiley, New York, 1984, pp. 318–324.

2 Bejan, A., *Solutions Manual for Convection Heat Transfer*, Wiley, New York, 1984, pp. 172–177.

3 Somers, E. V., "Theoretical Considerations of Combined Thermal and Mass Transfer From a Vertical Flat Plate," *ASME Journal of Applied Mechanics*, Vol. 23, 1956, pp. 295–301.

4 Mathers, W. G., Madden, A. J., and Piet, E. L., "Simultaneous Heat and Mass Transfer in Free Convection," *Ind. Engng. Chem.*, Vol. 49, 1957, pp. 961–968.

5 Wilcox, W. R., "Simultaneous Heat and Mass Transfers in Free Convection," *Chem. Engng. Sci.*, Vol. 13, 1961, pp. 113–119.

6 deLeeuw Den Bouter, J. A., DeMunnik, B., and Heertijes, P. M., "Simultaneous Heat and Mass Transfer in Laminar Free Convection From a Vertical Plate," *Chem. Engng. Sci.*, Vol. 23, 1968, pp. 1185–1190.

7 Gebhart, B., and Pera, L., "The Nature of Vertical Natural Convection Flows Resulting From the Combined Buoyancy Effects of Thermal and Mass Diffusion," *Int. J. Heat Mass Transfer*, Vol. 14, 1971, pp. 2025–2050.

8 Bejan, A., "The Method of Scale Analysis: Natural Convection in Fluids," *Natural Convection: Fundamentals of Applications*, S. Kakac, W. Aung, and R. Viskanta, eds., Hemisphere, Washington, D.C., 1985.

Effect of the Prandtl Number on Heatup of a Stratified Fluid in an Enclosure

Jae Min Hyun[1]

1 Introduction

Heatup refers to the transient adjustment process of a contained fluid in response to changes in thermal forcing at the boundaries [1]. As a classical model in simple geometry, [2] considered the linearized heatup process of a thermally stratified Boussinesq fluid in a cylinder of radius a and height h, the axis of which is parallel to gravity g. At the initial state, the fluid is at rest and the temperature distribution is linear in the vertical coordinate z, i.e., $T_i(z) = T_b + \Delta T_i z/h$, where T_b is the temperature at the bottom endwall at $z=0$. The initial stratification of the fluid system is characterized by the Brunt-Väisälä frequency $N_i = [\alpha g \Delta T_i/h]^{1/2}$, where α is the coefficient of volumetric expansion. At $t=0$, the temperature of the container wall is impulsively altered to a new vertically linear temperature profile, $T_f(z) = T_i(z) + 2\epsilon\Delta T_i(z/h - 0.5)$, corresponding to the new Brunt-Väisälä frequency $N_f[=N_i + \Delta N]$ and is maintained so thereafter.

Here, attention is restricted to the situations in which the overall Rayleigh number $\mathrm{Ra}[=\alpha g \Delta T_i h^3/\nu\kappa]$ is sufficiently large that the boundary layers exist on the walls. References [2] and [3] analyzed the cases when the temperature changes are small, i.e., $\epsilon \ll 1$, and thus $\Delta N/N_f \ll 1$; this permits linearization of the equations. Under the assumption that the Prandtl number Pr is of order unity, analytical solutions were derived for the transient temperature and velocities in the core [2, 3]. It was clearly demonstrated that a meridional circulation, which is driven by a buoyant sidewall boundary layer pumping mechanism, redistributes the fluid, thereby bringing about the new equilibrium state of stratification N_f. The time scale for the overall adjustment in the core was found to be the buoyant convective time scale $t_h \sim \mathrm{Pr}^{1/2}\mathrm{Ra}^{1/4}N_f^{-1}$, rather than the diffusive time scale $t_d \sim \mathrm{Pr}^{1/2}\mathrm{Ra}^{1/2}N_f^{-1}$. The subsequent numerical study [4] supported the qualitative correctness of the analyses of [2, 3] in representing the overall flow trend over the time span $0(t_h)$.

All the previous investigations cited above were undertaken for the Prandtl number of order unity, and the cases for extreme values of Pr have not been analyzed. However, flows with extreme values of Pr are of interest in certain technological applications. The heatup process of a fluid of very large Pr finds applications in the heating of containers of a highly viscous fluid such as fuel oil. Knowledge of the heatup process of a fluid of very small Pr is relevant to the motion of liquid metals. The objective of this study is to examine the details of the flow with extreme values of Pr. It is of particular interest to inquire as to whether the analytical solutions of [2, 3] can still provide useful descriptions of the flow in these cases.

Another important motivation for this study is to demonstrate the existence of an oscillatory behavior in the transient flow field, a topic of considerable current interest [4-9]. Recently [5, 6], relying on elaborate scaling schemes, argued that the general character of unsteady natural convection in an enclosure depends crucially on the relative values of Ra and $\mathrm{Pr}^4 A^{-4}$, A being the aspect ratio, height/width. In particular, [5, 6] predicted that for the regime $\mathrm{Ra} > \mathrm{Pr}^4 A^{-4}$, the flow approaches steady state in a decaying oscillatory manner due to the presence of internal waves. The specific flows that were exemplified in [5] were started by instantaneously raising and lowering the opposite end temperatures in the enclosure. There have been laboratory experimental efforts [7] to verify the predictions of [5] by using two different aspect ratios for a fixed value of Pr = 6 for water. In this note, by varying Pr for fixed aspect ratio $A=1$, we shall demonstrate that the present heatup flow is indeed characterized by an oscillatory approach to steady state in the regime $\mathrm{Ra} > \mathrm{Pr}^4 A^{-4}$.

In line with the method of [4], we acquired numerical solutions to the unsteady Navier-Stokes equations for the model problem of [2]. Since $A=1$, this note considers the effect of Pr, not of A. We note that the thermal boundary conditions for [5] are not exactly the same as those in the present problem. However, the vital mechanism to drive buoyant convective motion is essentially the same for the two cases. For flows $\mathrm{Ra} \gg 1$ so that distinct vertical boundary layers are formed, the pumping by the boundary layer is the principal mechanism [2, 3, 5].

2 Formulation

The governing time-dependent Navier-Stokes equations for an incompressible, Boussinesq fluid written for cylindrical coordinates (r, ϕ, z) are standard and will not be repeated here (see, e.g., equations (1)-(5) of [4]). The velocity components in the r, z direction are u, w, respectively. The finite-difference numerical model of [10] was modified to apply to the present problem. The numerical techniques and the details on the implementation of the methods were given in [4, 10].

3 Results and Discussion

Computations were performed for several sets of experimental parameters. For all cases, $\mathrm{Ra} = 2.89\times10^7$, $A(\equiv h/a) = 1.0$, $\epsilon = 0.0005$ were used to simulate the linearized heatup process considered in [2, 3]. Three different values for the Prandtl number, $\mathrm{Pr}=100.0$, $\mathrm{Pr}=5.7$, $\mathrm{Pr}=0.1$, were chosen to represent respectively the flow regimes of $\mathrm{Pr} \gg 1$, $\mathrm{Pr} \sim 0(1)$, $\mathrm{Pr} \ll 1$.

Since the present model configuration is antisymmetric about the cylinder middepth plane $z=h/2$, the ensuing discussion will be concerned with the flow in the bottom half of the cylinder.

Guided by the analyses of [2, 3], the results will be presented using the following nondimensional quantities:

$$\begin{aligned} &R = r/a,\ Z = z/h,\ \tau = t/(\mathrm{Pr}^{1/2}\mathrm{Ra}^{1/4}N_f^{-1}),\\ &\theta = (T-T_i)/[2\epsilon\Delta T_i(Z-0.5)],\\ &U = u/(2^{1/2}\epsilon\mathrm{Pr}^{-1/2}\mathrm{Ra}^{-1/4}hN_fR),\\ &W = w/[2^{3/2}\epsilon\mathrm{Pr}^{-1/2}\mathrm{Ra}^{-1/4}(h^2/a)N_f(Z-0.5)] \end{aligned} \tag{1}$$

Therefore, the lowest-order analytical solutions for the core region are [2, 3]

$$U, W = \exp(-\tau) \tag{2a}$$

$$\theta = 1 - \exp[-2^{1/2}(h/a)\tau] \tag{2b}$$

We observe that (2a) does not meet the motionless initial conditions. The theory scales the equations by using the time scale t_h. Therefore, the boundary layers are considered to be formed instantaneously, and to remain quasi-steady throughout the heatup process. These arguments were clearly explained in [3].

Figure 1 illustrates the results for Pr = 100.0. Note that this case belongs to the regime $\mathrm{Ra} < \mathrm{Pr}^4 A^{-4}$, as was classified by [5].

Figure 1(A) depicts the temperature evolution in the core. The theoretical prediction (2b) almost overlaps the curve for $Z=0.42$ in Fig. 1(A). It is evident that the overall temperature adjustment is accomplished over the convective time scale $0(t_h)$. The numerical results for the positions away from the endwall boundary, as seen by the curves for $Z=0.25$ and

[1]Department of Mechanical Engineering, Clarkson University, Potsdam, NY 13676, Mem. ASME.

Contributed by the Heat Transfer Division for publication in the JOURNAL OF HEAT TRANSFER. Manuscript received by the Heat Transfer Division November 27, 1984.

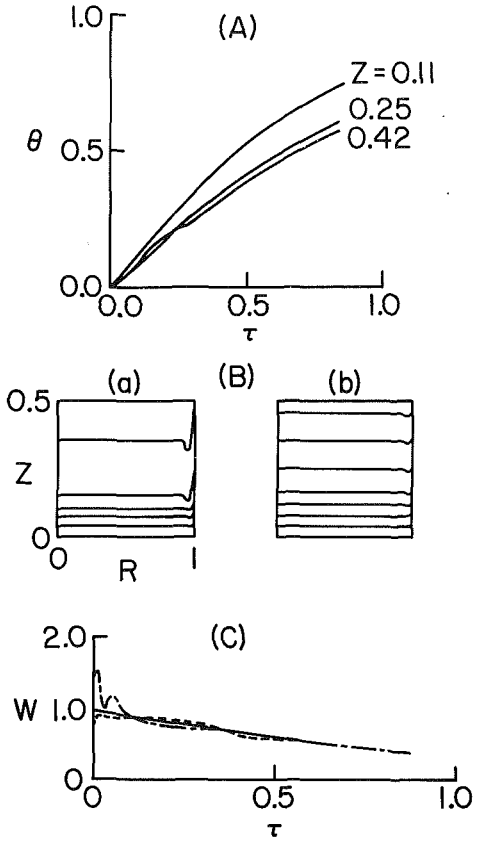

Fig. 1 Results for Pr = 100.0, Ra = 2.89×10^7, $A = 1.0$: (*A*) scaled temperature θ versus time τ at R = 0.5; the theoretical prediction equation (2*b*) overlaps the curve for $Z = 0.42$ within graphic resolution; (*B*) plots of isotherms, $\Theta = (T - T_i)/\epsilon\Delta T_i$; the contour value increases from -1.0 at $Z = 0$ to 0.0 at $Z = 0.5$ with equal increment; times are (*a*) $\tau = 0.184$, (*b*) $\tau = 0.490$; (*C*) scaled vertical velocity *W* versus τ at $Z = 0.24$; —·— $R = 0.29$; — — — — $R = 0.63$; —— equation (2*a*)

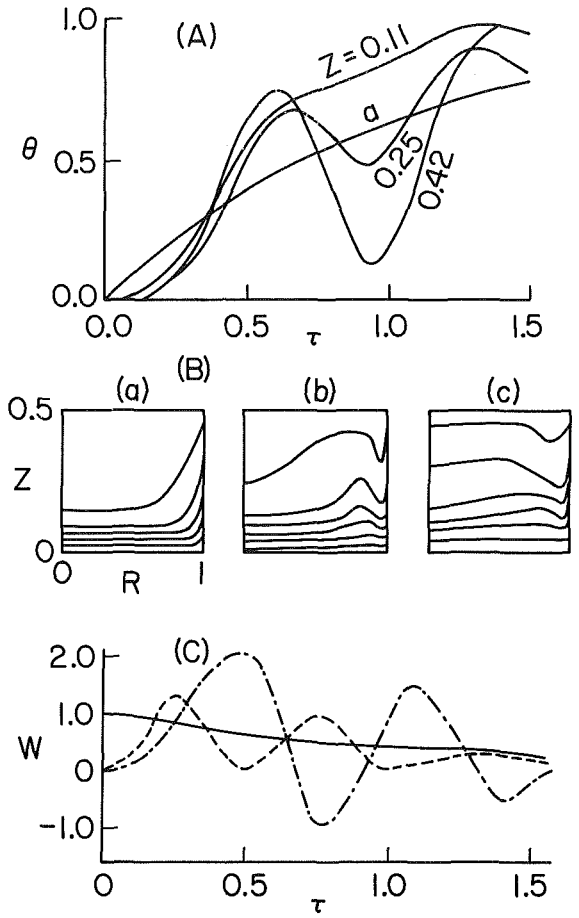

Fig. 2 Same as Fig. 1, except Pr = 0.1: (*A*) equation (2*b*) is denoted by *a*; (*B*) times are (*a*) $\tau = 0.151$, (*b*) $\tau = 0.293$, (*c*) $\tau = 0.435$; (*C*) —·— $R = 0.20$; — — — — $R = 0.65$; —— equation (2*a*)

$Z = 0.42$, are in satisfactory agreement with the theoretical prediction (2*b*). In a region close to the endwall (see curve for $Z = 0.11$), the numerical results indicate that the adjustment process proceeds faster. This is attributable to the increased diffusive effects in the regions near the boundary walls.

Figure 1(*B*) displays the contour plots of the temperature deviation $\Theta \equiv (T - T_i)/\epsilon\Delta T_i$. The temperature field in the core is substantially uniform in the horizontal direction, which is a well-known property in stratified fluids.

Figures 1(*A*) and 1(*B*) suggest that the temperature adjustment process is monotonic. It is also important to recognize that the analytical solution (2*b*) provides a correct description of the temperature evolution in the core.

Figure 1(*C*) exemplifies the velocity evolution. Internal-gravity oscillations are evident at early times. However, because of high viscous effects, these oscillations are damped after one or two cycles. The subsequent evolution of velocities is quite monotonic, and this behavior is depicted well by the theoretical prediction (2*a*).

It is seen in Fig. 1 that, even after $0(t_h)$, flows are still changing slowly. These remaining small changes toward the complete steady state are achieved over the diffusive time scale $0(t_d)$. In this note, we are not interested in these small changes. It is unnecessary and impractical to integrate the equations to $0(t_d)$, which is an order of magnitude larger than $0(t_h)$, to depict the essential features of the transient flows [11].

In summary, the principal phase of the heatup process for large Pr is monotonically varying; the impact of the internal-gravity oscillations on the overall adjustment process is minimal. The analytical solutions give an adequate approximation to this case. These flow characteristics are consistent with the general flow properties in the transient convective flow regime $\mathrm{Ra} < \mathrm{Pr}^4 A^{-4}$, as stated in [5] (note $A = 1$ in the present study).

Figure 2 presents the results for Pr = 0.1. This case belongs to the regime $\mathrm{Ra} > \mathrm{Pr}^4 A^{-4}$.

The temperature evolution in the core, as illustrated in Fig. 2(*A*), is highly oscillatory in time and in space. To ascertain that these oscillations are indeed the internal-gravity oscillations, we calculate the frequencies β of the internal-gravity oscillations [4, 12, 13]

$$\beta = N_i \left[\frac{(\alpha_n A/m\pi)^2}{1 + (\alpha_n A/m\pi)^2} \right]^{\frac{1}{2}} \tag{3}$$

where α_n are zeros of the first-order Bessel function, m is any integer. The calculated value for the nondimensionalized period of the most dominant mode ($m = 2$, $n = 1$) is 0.734. This is in fair agreement with the period of oscillations detectable in Fig. 2(*A*), establishing that the oscillatory nature is due to the presence of the internal-gravity oscillations. (Similar checks on the internal-gravity oscillations were conducted in the studies of spin-up phenomena of stratified rotating fluids; see, e.g., [12, 13].) In a region close to the endwall (see curve for $Z = 0.11$), the temperature evolution is less oscillatory. This is attributable to the enhanced influence of the diffusive effects near the endwall, which damps the internal-gravity oscillations.

Figure 2(*b*) shows the contour plots of the temperature deviation. The transient temperature field is not uniform in the horizontal direction, owing to the presence of the internal-gravity oscillations.

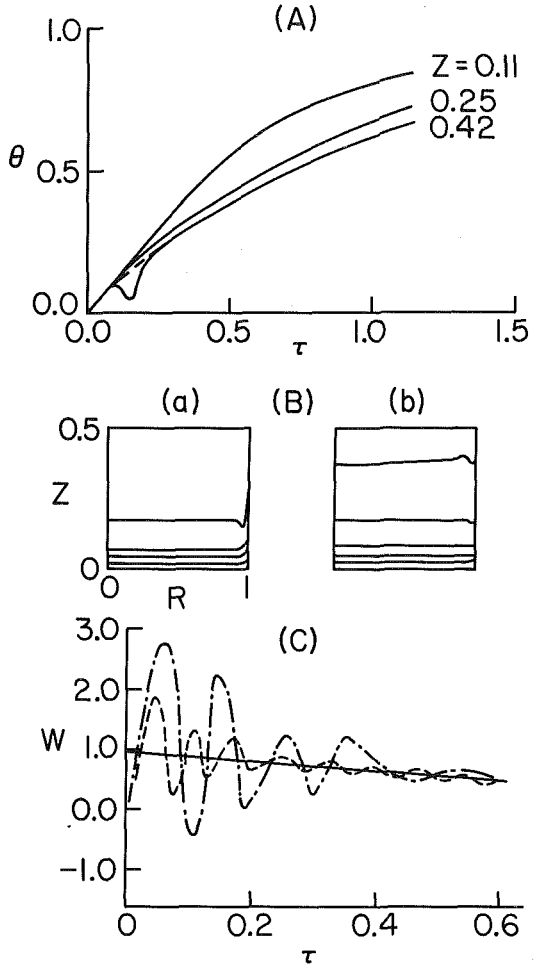

Fig. 3 Same as Fig. 1, except Pr = 5.7: (*A*) equation (2*b*) is shown in dotted line; (*B*) times are (*a*) $\tau = 0.144$, (*b*) $\tau = 0.502$; (*C*) —·— $R = 0.24$; — — — — $R = 0.63$; —— equation (2*a*)

The velocities, as illustrated in Fig. 2(*C*), rise sharply to peak values at early times; subsequently, the velocities behave in a decaying oscillatory manner.

Figure 2 points to the inadequacy of the analytical solutions (2) to represent the significant aspects of the true heatup process for small values of Pr. The internal-gravity oscillations have a pronounced influence on the flows with small values of Pr. It is also apparent in Fig. 2 that the length of time required for a substantial accomplishment of adjustment process far exceeds the usual convective time scale $0(t_h)$. The decay of internal-gravity oscillations persists to a larger time on the diffusive time scale $0(t_d)$. Since the diffusive time scale is an order larger than the convective time scale, it was not possible to continue the computations to $0(t_d)$ for the present case. These distinct features of the flow are consistent with the general flow characteristics expounded in [5] for the regime $\mathrm{Ra} > \mathrm{Pr}^4 A^{-4}$.

Figure 3 shows the results for $\mathrm{Pr} = 5.7$, representing the cases for $\mathrm{Pr} \sim 0(1)$. Note that $\mathrm{Ra} > \mathrm{Pr}^4 A^{-4}$. The qualitative flow patterns are intermediate between the two flows with extreme values of Pr discussed above. The superposition of the internal waves for early times in the temperature plot is apparent in Fig. 3(*A*). However, the impact of the internal waves on the overall temperature field is quite minor. This is consistent with the fact that the temperature field reacts weakly to high-frequency changes in the flow field [14]. On the other hand, the velocities, as displayed in Fig. 3(*C*), are highly oscillatory during the principal phase of the transient process. We also note that the internal waves damp out within the convective time scale $0(t_h)$. Further details on the flow pertaining to $\mathrm{Pr} \sim 0(1)$ have been given in [4].

4 Conclusion

The heatup process of a stratified fluid with large Rayleigh number is considered. When Pr is very large, the adjustment process is substantially monotonic, and the analytical solutions of [2] and [3] provide a qualitatively accurate description of the overall transient process. The internal-gravity oscillations are damped. When Pr is very small, the evolutions of the flow and temperature fields are highly oscillatory due to the dominant presence of the internal-gravity oscillations. The analytical solutions do not represent the transient flow details in this case. The results for extreme values of Pr are consistent with the flow characteristics described in [5] for the regimes $\mathrm{RA} < \mathrm{Pr}^4 A^{-4}$ and $\mathrm{Ra} > \mathrm{Pr}^4 A^{-4}$, respectively.

References

1 Veronis, G., "The Analogy Between Rotating and Stratified Fluids," *Annual Review of Fluid Mechanics*, Vol. 2, 1970, pp. 37–66.

2 Sakurai, T., and Matsuda, T., "A Temperature Adjustment Process in a Boussinesq Fluid via a Buoyancy-Induced Meridional Circulation," *Journal of Fluid Mechanics*, Vol. 54, 1972, pp. 417–421.

3 Jischke, M. C., and Doty, R. T., "Linearized Buoyant Motion in a Closed Container," *Journal of Fluid Mechanics*, Vol. 71, 1975, pp. 729–754.

4 Hyun, J. M., "Transient Buoyant Convection of a Contained Fluid Driven by the Changes in the Boundary Temperatures," ASME *Journal of Applied Mechanics*, Vol. 52, 1985, pp. 193–198.

5 Patterson, J., and Imberger, J., "Unsteady Natural Convection in a Rectangular Cavity," *Journal of Fluid Mechanics*, Vol. 100, 1980, pp. 65–86.

6 Patterson, J. C., "On the Existence of an Oscillatory Approach to Steady Natural Convection in Cavities," ASME JOURNAL OF HEAT TRANSFER, Vol. 106, 1984, pp. 104–108.

7 Yewell, R., Poulikakos, D., and Bejan, A., "Transient Natural Convection Experiments in Shallow Cavities," ASME JOURNAL OF HEAT TRANSFER, Vol. 104, 1982, pp. 533–538.

8 Ivey, G. N., "Experiments on Transient Natural Convection in a Cavity," *Journal of Fluid Mechanics*, Vol. 144, 1984, pp. 389–401.

9 Staehle, B., and Hahne, E., "Overshooting and Damped Oscillations of Transient Natural Convection Flows in Cavities," *Proceedings, The Seventh International Heat Transfer Conference*, Munich, Vol. 2, 1982, pp. 287–292.

10 Warn-Varnas, A., Fowlis, W. W., Piacsek, S., and Lee, S. M., "Numerical Solutions and Laser-Doppler Measurements of Spin-up," *Journal of Fluid Mechanics*, Vol. 85, 1978, pp. 609–639.

11 Allen, J. S., "Upwelling of a Stratified Fluid in a Rotating Annulus. Steady State. Part 2. Numerical Solutions," *Journal of Fluid Mechanics*, Vol. 59, 1973, pp. 337–368.

12 Lee, S. M., "An Investigation of Stratified Spin-up Using a Rotating Laser-Doppler Velocimeter," M.S. Thesis, Florida State University, 1975.

13 Hyun, J. M., Fowlis, W. W., and Warn-Varnas, A., "Numerical Solutions for the Spin-up of Stratified Fluid," *Journal of Fluid Mechanics*, Vol. 117, 1982, pp. 71–90.

14 Kublbeck, K., Merker, G. P., and Straub, J., "Advanced Numerical Computation of Two-Dimensional Time-Dependent Free Convection in Cavities," *International Journal of Heat and Mass Transfer*, Vol. 23, 1980, pp. 203–217.

Effect of Frictional Heating and Compressive Work in Rotating Axisymmetric Flow

J. W. Chew[1]

1 Introduction

Owing to the high rotational speeds that occur in gas turbine engines, frictional heating and compressive work can have an important effect on the heat transfer at the surface of an engine component. To gauge this effect it is useful to

[1]Theoretical Science Group, Rolls-Royce Limited, Derby, England.

Contributed by the Heat Transfer Division for publication in the JOURNAL OF HEAT TRANSFER. Manuscript received by the Heat Transfer Division April 24, 1984.

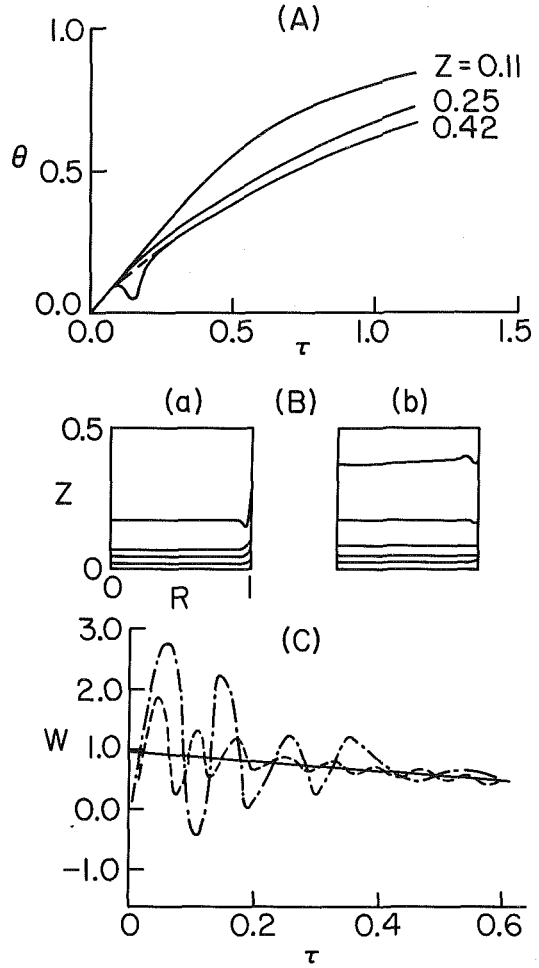

Fig. 3 Same as Fig. 1, except Pr = 5.7: (*A*) equation (2*b*) is shown in dotted line; (*B*) times are (*a*) $\tau = 0.144$, (*b*) $\tau = 0.502$; (*C*) —·— $R = 0.24$; — — — — $R = 0.63$; —— equation (2*a*)

The velocities, as illustrated in Fig. 2(*C*), rise sharply to peak values at early times; subsequently, the velocities behave in a decaying oscillatory manner.

Figure 2 points to the inadequacy of the analytical solutions (2) to represent the significant aspects of the true heatup process for small values of Pr. The internal-gravity oscillations have a pronounced influence on the flows with small values of Pr. It is also apparent in Fig. 2 that the length of time required for a substantial accomplishment of adjustment process far exceeds the usual convective time scale $0(t_h)$. The decay of internal-gravity oscillations persists to a larger time on the diffusive time scale $0(t_d)$. Since the diffusive time scale is an order larger than the convective time scale, it was not possible to continue the computations to $0(t_d)$ for the present case. These distinct features of the flow are consistent with the general flow characteristics expounded in [5] for the regime $\mathrm{Ra} > \mathrm{Pr}^4 A^{-4}$.

Figure 3 shows the results for $\mathrm{Pr} = 5.7$, representing the cases for $\mathrm{Pr} \sim 0(1)$. Note that $\mathrm{Ra} > \mathrm{Pr}^4 A^{-4}$. The qualitative flow patterns are intermediate between the two flows with extreme values of Pr discussed above. The superposition of the internal waves for early times in the temperature plot is apparent in Fig. 3(*A*). However, the impact of the internal waves on the overall temperature field is quite minor. This is consistent with the fact that the temperature field reacts weakly to high-frequency changes in the flow field [14]. On the other hand, the velocities, as displayed in Fig. 3(*C*), are highly oscillatory during the principal phase of the transient process. We also note that the internal waves damp out within the convective time scale $0(t_h)$. Further details on the flow pertaining to $\mathrm{Pr} \sim 0(1)$ have been given in [4].

4 Conclusion

The heatup process of a stratified fluid with large Rayleigh number is considered. When Pr is very large, the adjustment process is substantially monotonic, and the analytical solutions of [2] and [3] provide a qualitatively accurate description of the overall transient process. The internal-gravity oscillations are damped. When Pr is very small, the evolutions of the flow and temperature fields are highly oscillatory due to the dominant presence of the internal-gravity oscillations. The analytical solutions do not represent the transient flow details in this case. The results for extreme values of Pr are consistent with the flow characteristics described in [5] for the regimes $\mathrm{RA} < \mathrm{Pr}^4 A^{-4}$ and $\mathrm{Ra} > \mathrm{Pr}^4 A^{-4}$, respectively.

References

1 Veronis, G., "The Analogy Between Rotating and Stratified Fluids," *Annual Review of Fluid Mechanics*, Vol. 2, 1970, pp. 37–66.

2 Sakurai, T., and Matsuda, T., "A Temperature Adjustment Process in a Boussinesq Fluid via a Buoyancy-Induced Meridional Circulation," *Journal of Fluid Mechanics*, Vol. 54, 1972, pp. 417–421.

3 Jischke, M. C., and Doty, R. T., "Linearized Buoyant Motion in a Closed Container," *Journal of Fluid Mechanics*, Vol. 71, 1975, pp. 729–754.

4 Hyun, J. M., "Transient Buoyant Convection of a Contained Fluid Driven by the Changes in the Boundary Temperatures," ASME *Journal of Applied Mechanics*, Vol. 52, 1985, pp. 193–198.

5 Patterson, J., and Imberger, J., "Unsteady Natural Convection in a Rectangular Cavity," *Journal of Fluid Mechanics*, Vol. 100, 1980, pp. 65–86.

6 Patterson, J. C., "On the Existence of an Oscillatory Approach to Steady Natural Convection in Cavities," ASME JOURNAL OF HEAT TRANSFER, Vol. 106, 1984, pp. 104–108.

7 Yewell, R., Poulikakos, D., and Bejan, A., "Transient Natural Convection Experiments in Shallow Cavities," ASME JOURNAL OF HEAT TRANSFER, Vol. 104, 1982, pp. 533–538.

8 Ivey, G. N., "Experiments on Transient Natural Convection in a Cavity," *Journal of Fluid Mechanics*, Vol. 144, 1984, pp. 389–401.

9 Staehle, B., and Hahne, E., "Overshooting and Damped Oscillations of Transient Natural Convection Flows in Cavities," *Proceedings, The Seventh International Heat Transfer Conference*, Munich, Vol. 2, 1982, pp. 287–292.

10 Warn-Varnas, A., Fowlis, W. W., Piacsek, S., and Lee, S. M., "Numerical Solutions and Laser-Doppler Measurements of Spin-up," *Journal of Fluid Mechanics*, Vol. 85, 1978, pp. 609–639.

11 Allen, J. S., "Upwelling of a Stratified Fluid in a Rotating Annulus. Steady State. Part 2. Numerical Solutions," *Journal of Fluid Mechanics*, Vol. 59, 1973, pp. 337–368.

12 Lee, S. M., "An Investigation of Stratified Spin-up Using a Rotating Laser-Doppler Velocimeter," M.S. Thesis, Florida State University, 1975.

13 Hyun, J. M., Fowlis, W. W., and Warn-Varnas, A., "Numerical Solutions for the Spin-up of Stratified Fluid," *Journal of Fluid Mechanics*, Vol. 117, 1982, pp. 71–90.

14 Kublbeck, K., Merker, G. P., and Straub, J., "Advanced Numerical Computation of Two-Dimensional Time-Dependent Free Convection in Cavities," *International Journal of Heat and Mass Transfer*, Vol. 23, 1980, pp. 203–217.

Effect of Frictional Heating and Compressive Work in Rotating Axisymmetric Flow

J. W. Chew[1]

1 Introduction

Owing to the high rotational speeds that occur in gas turbine engines, frictional heating and compressive work can have an important effect on the heat transfer at the surface of an engine component. To gauge this effect it is useful to

[1]Theoretical Science Group, Rolls-Royce Limited, Derby, England.

Contributed by the Heat Transfer Division for publication in the JOURNAL OF HEAT TRANSFER. Manuscript received by the Heat Transfer Division April 24, 1984.

consider a simple example. Owen [1] has shown that for a "free disk" (i.e., a disk rotating in an infinite quiescent environment) the temperature rise of an adiabatic disk due to frictional heating is $\Omega^2 r^2/2C_p$, where Ω, r, and C_p denote angular velocity, radius, and specific heat at constant pressure, respectively. For a typical H. P. compressor disk of radius 300 mm rotating at 10,000 rpm this expression gives a temperature rise of about 50 K.

The main aims of this note are to clarify the effects of compressive work and frictional heating in axisymmetric swirling flow and to give formulae for use in engineering calculations. The results may be applied in calculating heat transfer in rotating disk systems using integral methods and may be helpful in interpretation of experimental rig or engine measurements at high rotational speed. As most of the available Nusselt number correlations for calculating heat transfer from rotating bodies are based on experimental work at somewhat lower rotational speeds than are encountered in the engine, this work may also be useful in extrapolating such correlations to engine conditions.

2 The Reynolds Analogy

The analogy between the equations for tangential momentum and energy conservation for the boundary layer flow of a fluid near a plane disk has been shown by Dorfman [2] for incompressible flow neglecting frictional effects, and by Owen [1] for compressible flow including frictional effects. This analogy can be extended to boundary layer flow on a more general body of rotation provided the radius of curvature of the body in the plane of symmetry is much greater than the boundary layer thickness and the variation of radius r across the boundary layer is small compared to r.

A surface coordinate system in the plane of symmetry is employed. The distance along the surface in this plane is s and the distance along the normal to the surface is n. Velocity components for the s, n, and tangential directions are denoted u_s, u_n, and v, respectively, and the body radius is r. Under the foregoing assumptions, and also assuming that the effective Prandtl number is unity the tangential momentum and energy conservation equations may be written in the form

$$\rho\left[\frac{u_s}{r^2}\frac{\partial(r^2\Phi)}{\partial s}+\frac{u_n}{r^3}\frac{\partial(r^2\Phi)}{\partial n}\right]=\frac{1}{r^3}\frac{\partial}{\partial n}\left(r^3\mu_e\frac{\partial\Phi}{\partial n}\right) \tag{1}$$

Here ρ denotes density, μ_e is the effective viscosity, and Φ denotes either the nondimensional tangential velocity G or stagnation enthalpy θ defined by

$$G=\frac{v}{\Omega r},\quad \theta=\frac{h-h_{\text{ref}}}{cr^2} \tag{2}$$

where Ω is the rotational speed of the body, $h = C_pT + 0.5[u_s^2 + u_n^2 + v^2]$ is the stagnation enthalpy, and c is an as yet unspecified dimensional constant. It will be shown later that the analogy between G and θ will hold for certain boundary conditions on h in which c appears as a constant of proportionality. The subscript ref indicates a reference value. Note that, in addition to the assumptions mentioned above, the effects of density variations in the viscous terms of equation (1) have been neglected.

Since the equations for G and θ are identical it follows that if the boundary conditions on G and θ are the same, then the solutions for G and θ will be identical. Without making any new assumptions it may then be shown that

$$\frac{\partial T}{\partial n}=\frac{1}{C_p}\frac{\partial}{\partial n}[cr^2G-0.5(u_s^2+u_n^2+v^2)] \tag{3}$$

and hence, for an effective Prandtl number of unity, the heat flux to the surface is given by

$$q_0=\left[\mu_e\left(v\frac{\partial v}{\partial n}-\frac{c}{\Omega}\frac{\partial(rv)}{\partial n}\right]_{n=0}\right. \tag{4}$$

It is consistent with the earlier assumptions to assume $v\partial r/\partial n$ is small compared to $r\partial v/\partial n$. For a body rotating with angular velocity Ω equation (4) then gives

$$q_0=\tau_{\phi,0}r\Omega\left(\frac{c}{\Omega^2}-1\right) \tag{5}$$

where $\tau_{\phi,0}$ is the tangential shear stress at the surface.

For the boundary conditions on θ and G to be the same we require

$$h_0=h_{\text{ref}}+cr^2 \tag{6}$$

$$\bar{h}=h_{\text{ref}}+\frac{cr\bar{v}}{\Omega} \tag{7}$$

where the overline denotes a value at the boundary layer edge. If the equations for G and θ are similar outside the boundary layer, which is the case if viscosity and heat conduction are negligible, equation (7) may be replaced by conditions at the other boundaries.

If follows from equations (5) and (6) that q_0 is zero when $c=\Omega^2$, and the adiabatic surface temperature is given by

$$T_{0,\text{ad}}=T_{\text{ref}}+\frac{\Omega^2r^2}{2C_p} \tag{8}$$

where $T_{\text{ref}}=h_{\text{ref}}/C_p$. This agrees with Owen's [1] result for a plane disk and gives the surface temperature rise due to the combined effect of friction and compressive work. The temperature distribution in adiabatic conditions may be written

$$T_{\text{ad}}=T_{\text{ref}}+\frac{(\Omega^2r^2-U^2)}{2C_p} \tag{9}$$

where $U=(u_s^2 + u_n^2 + [v - \Omega r]^2)^{1/2}$ is the magnitude of the velocity relative to the surface. Alternatively we may write

$$T_{\text{ad}}=\bar{T}_{\text{ad}}+\frac{(\bar{U}^2-U^2)}{2C_p} \tag{10}$$

where $\bar{T}_{\text{ad}}$ and $\bar{U}$ satisfy equation (9). Equation (10) is identical to the expression for the temperature rise due to friction in flow over a flat plate, with $\bar{T}_{\text{ad}}$ corresponding to the free-stream temperature (see Schlichting [3]).

Consider now a surface with the quadratic temperature distribution

$$T_0=T_{\text{ref}}+\left(\frac{c}{\Omega^2}-\frac{1}{2}\right)\frac{\Omega^2r^2}{C_p} \tag{11}$$

which satisfies equation (6). Introducing a Nusselt number $\text{Nu} = rq_0/k(T_0-\bar{T}-T_{0,\text{ad}}+\bar{T}_{\text{ad}})$, and a rotational Reynolds number $\text{Re}_\phi = \rho\Omega b^2/\nu$, equation (5) gives

$$\text{Nu}=\text{Re}_\phi\frac{\tau_{\phi,0}}{\rho\Omega^2b^2(1-\bar{v}/\Omega r)} \tag{12}$$

For the free disk $\bar{v} = 0$, $\bar{T} = \bar{T}_{\text{ad}}$ and equation (12) reduces to the result derived by Owen [1] and shows that in this case frictional effects can be taken into account by use of the adiabatic disk temperature in defining the Nusselt number.

The above analysis can be applied to the case of swirling flow near a stationary surface by simply taking the limit $\Omega\to 0$. For these conditions the adiabatic surface temperature is a constant, although as shown by equation (9) the temperature of the fluid will be nonuniform.

3 The Influence of Prandtl Number and Arbitrary Temperature Distribution

The analysis in the previous section is only valid for a Prandtl number of unity and with a surface temperature varying quadratically with radius. The effect of relaxing these conditions is now discussed.

In the limit $r\to\infty$, $\Omega\to 0$ such that Ωr is fixed curvature effects will be negligible and, if the dissipation is dominated by either the tangential or radial velocity component, the flat

plate formula for $T_{0,ad}$ should apply to the present problem. Thus, to reproduce results for the flat plate in these conditions a recovery factor R is introduced to account for the effect of Prandtl number (Pr) on frictional heating. The adiabatic disk temperature is then given by

$$T_{0,ad} - \bar{T}_{ad} = \frac{R\bar{U}^2}{2C_p} \tag{13}$$

where R is usually taken as $Pr^{1/2}$ for laminar flow and $Pr^{1/3}$ for turbulent flow. For lack of further information it is reasonable to use the flat plate values for R throughout. Assuming that the effect of Prandtl number on Nusselt number can be carried by a factor ϕ (Pr), equation (12) can then be generalized to include the effect of Prandtl number as follows

$$Nu = \phi Re_\phi \frac{\tau_{\phi,0}}{\rho\Omega^2 b^2(1 - \bar{v}/\Omega r)} \tag{14}$$

with $\bar{T}_{0,ad} - \bar{T}_{ad}$ used in the definition of Nu, being calculated from equation (13).

It is beyond the scope of the present work to give a full treatment of the effect of surface temperature distribution; only the influences of friction and compressive work on the heat transfer are considered. From the fact that the energy equation is linear in temperature it follows that, for forced convection, allowance for frictional and compressive effects may be made simply by subtracting the adiabatic temperature difference $T_{0,ad} - \bar{T}_{ad}$ from the true value of $T_0 - \bar{T}$ before applying a Nusselt number correlation which neglects these effects. This result applies for any surface temperature distribution, although it does assume that the effect of temperature distribution on the effective thermal conductivity is negligible. In free convection the velocities depend on the temperature field and the situation is more complex. However, if a Nusselt number relationship similar to equation (14) is used, in which the effect of temperature on velocity does not appear explicitly, it is again valid to carry the dependence on frictional and compressive effects in the manner described above.

4 A Numerical Example

The above results are now illustrated by the example of laminar radial outflow through a rotating cavity as shown in Fig. 1. As indicated in the figure the flow for this case can be divided into a source region, Ekman layers on the two disks, a central core, and a sink layer. Elliptic flow calculation methods have been applied to this case [4] and numerical results for the adiabatic disk temperature distribution are available. Figure 2 shows these results for flow rates given by $C_w = 79$ and 605 where $C_w = m/\mu b$; m is the mass flow rate and b the cavity radius, with a rotational speed corresponding to $Re_\phi = 2.5 \times 10^4$. The reference temperature in this case, T_{ref}, is equal to the fluid inlet temperature.

At the higher flow rate ($C_w = 605$), for which the source region of flow extends to $r/b \simeq 0.8$ the numerical results for Pr = 1 are very close to equation (8). Reducing the Prandtl number to 0.718 induces a general reduction in disk temperature. The maximum effect occurs close to the edge of the source region. Here the difference is about 15 percent of the disk temperature at this point. This is consistent with assuming $\bar{T}_{ad}$ is equal to the inlet air temperature and $\bar{u} \simeq \Omega r$ in equation (13), as would be expected in the source region of flow. At higher radii, in the Ekman layer region, the swirl of the central core becomes significant giving $\bar{U} < \Omega r$. This leads to increased significance of the compressive work terms in the energy equation and a corresponding reduction in the importance of the frictional terms. As only the frictional terms are influenced by Prandtl number the reduction in disk temperature is less in the Ekman layer region.

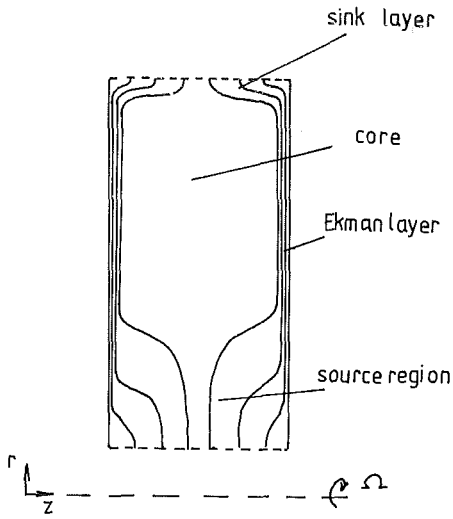

Fig. 1 Radial outflow through a rotating cavity

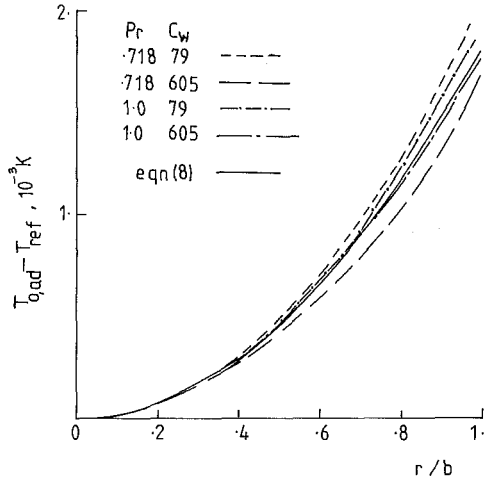

Fig. 2 Radial variation of adiabatic disk temperature: radial inlet, $Re_\phi = 2.5 \times 10^4$

At the lower flow rate ($C_w = 79$) the source region of flow extends only to $r/b \simeq 0.3$ and the flow on the disks is dominated by the Ekman layers. Consequently the temperature difference across the disk boundary layer due to friction and the influence of Prandtl number will be small. However, the temperature will still increase according to equation (8) due to the radial pressure gradient. In fact the numerical results fall slightly above the theoretical result. This is attributed to radial heat conduction in the central core and is consistent with an approximate analytic solution, given in [4], which includes this effect and predicts increases in adiabatic disk temperature of 4.4 percent and 6.3 percent for Pr = 1 and 0.718, respectively.

Acknowledgments

This paper is published with the permission of Rolls-Royce Limited.

References

1 Owen, J. M., "The Reynolds Analogy Applied to the Flow Between a Rotating and a Stationary Disc," *Int. J. Heat Mass Transfer*, Vol. 14, 1971, pp. 451-460.

2 Dorfman, L. A., *Hydrodynamic Resistance and Heat Loss of Rotating Solids*, Oliver and Boyd Limited, Edinburgh, 1963, Chap. 5, pp. 77-98.

3 Schlichting, H., *Boundary-Layer Theory*, 6th ed., McGraw-Hill, New York, 1968, Chap. 13, pp. 656-676.

4 Chew, J. W., "Computation of Flow and Heat Transfer in Rotating Cavities," D. Phil. thesis, University of Sussex, U.K., 1982.

Journal of Heat Transfer

Discussion

Forced Convection Heat Transfer From Nonisothermal Thin Needles[1]

M. M. Hasan.[2] The authors analyzed the laminar forced convection heat transfer problem from nonisothermal thin needles and obtained similarity solutions for certain types of the power law variations of the free-stream velocity, the surface temperature, or the surface heat flux. However, this reader finds some inconsistencies in the analysis because of the following reason.

One of the main assumptions of the forced or mixed convection problem along a thin needle is that the pressure gradient along the needle is neglected but the effect of the transverse curvature is retained (e.g., see references cited in original paper). The authors retained the axial pressure gradient term in the axisymmetric boundary layer momentum equation

$$u\frac{\partial u}{\partial x}+v\frac{\partial u}{\partial r}=U\frac{dU}{dx}+\frac{\nu}{r}\frac{\partial}{\partial r}\left(r\frac{\partial u}{\partial r}\right)$$

where x and r are the axial and radial coordinates, respectively. But in doing so the authors have erroneously suggested that if the body shape of the needle is represented by

$$R(x)=\left(\frac{\nu}{u_1}a\right)^{1/2}x^{(1-m)/2} \tag{5}$$

the free-stream velocity can be represented by the expression of the form $U=u_1x^m$. Consider the three cases the authors tried to address in their paper.

1 $m=0$, giving $R(x)\propto x^{1/2}$. This represents a paraboloid. For this case the free-stream velocity becomes $U=u_1x^0=$ const!

2 $m=1$, giving $R(x)=$ const, a vertical cylinder, and $U=u_1x$!

3 $m=-1$, $R(x)\propto x$. This represents a cone. In this case, the free-stream velocity becomes $U=u_1x^{-1}$, retarding flow.

Therefore, this reader is of the opinion that the solution provided by the authors does not represent a physically correct situation. The point is, given a body shape, the expression for the free-stream velocity in general cannot be represented by $U=u_1x^m$; rather, it should be obtained from the potential flow solution.

References

19 Sparrow, E. M., Eichhorn, R., and Gregg, J. L., "Combined Forced and Free Convection in a Boundary Layer Flow," *Physics of Fluids*, Vol. 2, 1959, pp. 319–328.

Authors' Closure

We thank Professor Hasan for his interest in our paper. Unfortunately, it appears that he overlooked the fact that the axial pressure gradient may be *externally* imposed in many applications. For a thin needle, the pressure gradient along it due to the presence of the needle may be neglected as discussed in the paper. The axial pressure gradient term retained in the momentum equation takes account of the externally imposed free-stream velocity which may result from the contouring of a channel wall far from the needle. Thus, the solutions presented in the paper do represent physically correct and realistic situations.

In the study of the general problem of boundary layer flow and heat transfer, it is common to impose certain variations for both free-stream velocity (or pressure gradient) and wall temperature (or heat flux). In their similarity analysis of the combined forced and free convection in a two-dimensional boundary layer flow, Sparrow et al. [19] considered a physical model relating to the simultaneously imposed power function variations in both free-stream velocity and surface temperature.

[1] By J. L. S. Chen and T. N. Smith, published in the May 1978 issue of the JOURNAL OF HEAT TRANSFER, Vol. 100, No. 2, pp. 358–362.

[2] Assistant Professor, Department of Mechanical and Aerospace Engineering, University of Missouri—Rolla, Rolla, MO 65401; Assoc. Mem. ASME